Effect of carbonate platform controls on large scale platform heterogeneity and seismically imaged geometries.

A thesis submitted for the degree of
Doctor of Philosophy
at the University of London

Georgios Antonatos

Department of Earth Sciences
Royal Holloway
University of London

January 16, 2019

Declaration

I, Georgios Antonatos, hereby declare that the thesis and work presented in it is entirely my own. Where I have consulted the work of others, this is clearly stated. No part of this work has previously been submitted for a degree at the University of London or any other university. The copyright of this thesis rests with the author and no quatation from it or information derived from it may be published without the author's prior consent.

Signed

Date

Abstract

Hydrocarbon exploration is based on identification of reservoir location, geometry and size from the interpretation of seismic images. The inherited uncertainty of the estimations about reservoir volume and properties is improved by accurate prediction of facies distribution imaged on seismic sections.

Carbonate platform's heterogeneity at all scales, large scale, whole platform geometry and sub-seismic facies distribution is achieved with a modified version of the CarboCAT. The modifications developed for this project include wave energy calculation, cross-platform sediment transportation and deposition of siliciclastic sediments.

The seismic behaviour of the produced stratigraphic models is studied with generation of synthetic seismic images using a new model. The new model uses grain texture and porosity to calculate the pseudo-acoustic impedance of Carbo-CAT generated carbonate strata. The new model is validated using sensitivity analysis based on a real seismic image of a carbonate platform.

The modified version of CarboCAT is used to reproduce the platform geometry of Upper Cretaceous (Santonian) outcrops in South-Central Pyrenees, Spain and the Cenomanian-Turonian Mishrif formation, South Iraq. Modelling of the Santonian outcrops reveals the controls on platform development and the non-uniqueness of the platform strata. Modelling of the Cenomanian-Turonian Mishrif formation shows the platform's internal structure and calculates the connectivity and volume of specific strata of interest.

Sensitivity analysis demonstrates the effect of cross-platform sediment transportation and grain size on large scale platform geometry. Furthermore, the interaction of sediment transportation and production on the formation of autocycles, compartmentalisation of platform interior and specific facies distribution is studied.

Acknowledgements

Contents

List of Figures

List of Tables

Symbols

C	siliciclastic concentration
D	diffusion coefficient for siliciclastics
d	wave break depth (m)
E	wave energy
F	wave fetch area (m)
Fo	external forces (N)
f	frequency (Hz)
g	gravitational constant (m/s^2)
H	wave height (m)
K	Elastic tensor
k	kinetic energy
L	wave length (m)
l	turbulent length scale
p	carbonate production (m/My)
R	reflectivity
r	surface or bottom roughness
Re	reflection coefficient
s	grain size (m)
T	wave period(s)
t	time
Tr	transmission coefficient
u	wind speed (m/s^2)
V	velocity of seismic waves
W	work (J)
Z	(pseuso) acoustic impedance
z	water depth (m)
ϵ	energy dissipation rate (W)
ρ	density (kg/m^3)
σ	strain
APD	aggradation to progradation to degradation
A/S	accommodation supply ratio
CA	cellular automata
CCD	carbonate compensation depth
EMT	elapsed model time

ESL	eustatic sea level
$FRWST$	forced regressive system tract
$FSST$	falling stage system tract
FTP	flat-topped platform
HST	highstand system tract
LST	lowstand system tract
PA	progradation to agradation
PAR	photosynthetically active radiation
R	retrogradation
RSL	relative sea level
SFM	stratigraphic forward model
SMB	Bretschneider-Svedrup-Munk model
TST	transgressive system tract

1 Introduction

1.1 Problem statement

Hydrocarbon exploration is based on identification of reservoir location and properties from seismic images. Interpretation of seismic images aims to provide estimations about the location, volume, and geometry of the reservoirs present. However, even high quality seismic images have limitations. Different platform geometries have different lithofacies distributions and thus the location and properties of carbonate reservoirs vary from one platform to the next. Even platforms with similar geometries can have very different facies distributions. Facies with seismically indistinguishable physical properties but which affect reservoir properties are particularly problematic. Furthermore, strata heterogeneity present in every carbonate formation cannot be resolved at sub-seismic scales.

Estimation of reservoir parameters from interpretation of seismic images always includes some uncertainty. Efficient hydrocarbon exploration requires accurate prediction of the reservoir location and parameters. The inherited uncertainty can be decreased with the prediction of reservoir location, size, geometry and lithofacies distributions for each platform.

Lithofacies can recognised on seismic images using specific seismic phases and frequencies. Furthermore, lithofacies distributions can be estimated from analysis of seismic images. Even though the achieved results improve the seismic interpretation, the distributions still contain a high degree of uncertainty for efficient exploration. More details and reduced uncertainty of the estimations of facies distributions are required.

Stratigraphic forward modelling predicts facies distribution in three dimensions, maps heterogeneity at multiple scales and calculates platform evolution through time. Several models have been developed in order to predict lithofacies distribution. The models calculate numerical facies distribution using advanced algorithms to compute carbonate production, transportation and deposition. To date, no one model incorporates both heterogeneity at all scales and accurate descriptions of physical processes that control platform evolution.

1.2 Aims and Objectives

The aims of this thesis are:

- to predict facies distributions and rock properties of carbonate strata at sub-seismic scales;

- to study heterogeneity of carbonate platforms at wide range of scales (from large scale, whole platform to sub-seismic scale);

- enhance prediction of facies distribution and reservoir properties from seismic images of carbonate platforms.

The objectives for achieving these aims are:

- improve the existing stratigraphic forward model (CarboCAT);

- study the effect of allogenic and autogenic processes on carbonate platform heterogeneity;

- identify the controls on large scale platform geometry;

- study the formation and distribution of specific carbonate lithofacies;

- identify the controls on the elastic properties of carbonate strata;

- generate synthetic seismic images;

- identify the signature of heterogeneity on seismic images.

2 Stratigraphic theory

This chapter is divided in two sections. The first section is a review of the processes controlling deposition of carbonate strata that are relevant to the numerical modelling used for the goals of this project. Numerical modelling was performed with CarboCAT **Burgess2013**. The second section discusses the main principles of sequence stratigraphic and provides a description of the geometry of carbonate accumulations.

2.1 General principles

2.1.1 Geochemistry of carbonates

The carbonate strata are mainly composed of calcium carbonate $CaCO_3$. Calcium carbonate, an ionic complex of carbonic acid,$(CO_3)^{2-}$ and Ca^{2+} metallic cation (eq.2.1). $CaCO_3$ forms when the calcium ions concentration reaches a supersaturated stage and calcium bond with carbonate ions. The supersaturation stage for the calcium ions depends on the amount of carbonate ions present and thus the pH of the water (**Gebauer2008**).

$$Ca^{+2} + 2HCO_3^{-1} = CO_2 + H_2O + CaCO_3 \qquad (2.1)$$
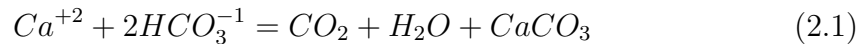
The above process is called abiotic precipitation because formation of calcium carbonate occurs naturally depending on the concentrations of the elements in the water. Precipitation of calcium carbonate can be also be biotically controlled, when living biota in the water use the process to build skeletal structures. Furthermore, biotically induced formation of $CaCO_3$ is possible when the biota simply initiate the formation of calcium carbonate without any further control on the process (**Schlager2005**).

Formation of $CaCO_3$ is not explicitly modelled as described in eq.(2.1) for this project. Biotically controlled carbonate production is modelled here as the volume of in-situ produced carbonate material (see section 3.2).

Calcium carbonate in carbonate sediments appear in three poly-morphs, calcite, aragonite and vaterite. The rhombohedral mineral calcite is the most abundant and thermodynamically stable. Aragonite is the orthorhombic form of $CaCO_3$, is also common and about 1.5 times more soluble than calcite. Solubility is the maximum amount of solute (in this case carbonate mineral) that can be dissolved in 1 litre of water (**Morse1990**).

Because aragonite molecule structure is denser compared to calcite (density 2940 kg/m^3 of aragonite compared to 2720 kg/m^3 of calcite) under high pressure $CaCO_3$ is crystallised as aragonite. Vaterite is the hexagonal form of $CaCO_3$. Vaterite is only observed in natural systems as metastable form relative to calcite. Vaterite is 3.7 times more soluble than calcite.

Even though Ca^{2+} is by far the most common element that forms ionic complexes with the carbonic acid, several other minor elements do it as well. The most common metallic anions observed in carbonate sediments are Mg^{2+}, Fe^{2+}, Mn^{2+}, Sr^{2+}, Co^{2+} and Zn^{2+}. Substitution of the Ca^{2+} from magnesium or manganese and iron (the most common cases) produce a range of carbonate structures with crystals in various crystal systems and various degrees of stability (**Morse1990**).

From all the metallic anions that substitute Ca^{2+} in the ionic complexes, the most important one is magnesium. Magnesian calcites $Ca(Mg)CO_3$ are an important subgroup of $CaCO_3$ minerals. The substitution of Ca^{2+} with Mg^{2+} affects the solubility of the calcites. A magnesian calcite with approximately 11% mole $MgCO_3$ can be as stable as a pure aragonite. The most important product of magnesium substitution is the formation of dolomite, $CaMg(CO_3)_2$.

Dolomite is one of the most abundant sedimentary carbonate minerals. For a wide range of temperatures (from 500^oC to 1100^oC) and up to 50 mole % Mg^{2+} instead of Ca^{2+}, a two phase product of calcilte/dolomite is stable. The stable calcite becomes progressively enriched in magnesium (dolomite) with increasing temperature. For lower temperatures, equivalent to the surface temperature, a calcite containing no magnesium would be stable and would coexist with a 50-50 mole % dolomite. For mineral compositions with more than 50% mole Mg^{2+}, dolomite is the more stable mineral phase and shallow waters are supersaturated with respect to this carbonate mineral (**Morse1990**).

Modern shallow-marine sea waters are super-saturated with respect to most carbonate minerals. The saturation level of sea water changes mainly with depth, with deep waters being under-saturated with respect to most carbonate minerals. The water depth at which sea water becomes under-saturated with respect to calcite and thus the rate of dissolution of calcite increases is called lysocline. Modern shallow marine carbonate sediments consist primary of aragonite and magnesian calcites. Palaeozoic carbonate sediments tended to be more calcitic. Mesozoic and Tertiary carbonates become progressively more aragonitic (**Moore2001**).

2.1.2 Carbonate accumulations

Carbonate sediments are the result of mainly biotic actions. Though abiotic precipitation of carbonate sediment is an important producing factor, the great majority of carbonate sediments are in-situ produced in shallow, warm waters by carbonate secreting organisms (**Emery1996**).

Inorganically dominated carbonate production is mainly comprised of coated grains, ooids, peloids and clasts. In contrast, organically produced carbonate sediments are in the form of highly structured $CaCO_3$ skeletal material of organisms such as corals, foraminifera, bivalves and algae (**Emery1996**).

The necessary materials for the carbonate producing biota derive from dissolved minerals of the sea and photosynthesis. Photosynthesis can be very simply described as:

$$CO_2 + H_2O + \text{solar energy} = O_2 + CH_2O \qquad (2.2)$$
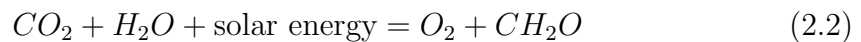
where CH_2O is called formaldehyde and is a very simple organic compound.

The survival and growth of the carbonate producing biota is directly related to photosynthesis. Photosynthesis produces the necessary organic matter and oxygen for the organisms and also removes CO_2 from the water. Reduced amounts of dissolved CO_2 in the sea water changes the pH of the water and favours the formation of $CaCO_3$ as described in eq.(2.1).

Carbonate accumulations show similarities that are directly related to environmental conditions controlling production, transportation and accumulation of sediment. The general characteristics of carbonate accumulations are (**Schlager2005**):

- carbonate biota tend to build elevated localised accumulations. Optimal conditions in an area allow carbonate bodies to rise above sea floor, forming a carbonate build-up;

- carbonate production is highest at the light saturated zone due to photosynthesis and thus carbonates build up to or close to the sea surface;

- the spatial distribution of environmental factors that control production and transportation creates differential production rates at different areas. Areas with higher production rates build higher than adjacent areas;

- carbonate accumulations tend to steepen with height of production and are generally steeper than the siliciclastic accumulations (**Schlager1986**). Binding of slope sediment and early cementation are the main reasons of steeper carbonate slopes. Low gradient carbonate slopes are also common.

The sediment fabric and grain size are related to slope height and angle. The composition of slope sediment is controlled by sediment reaction to gravity field, shear stress and transportation type. Grain supported fabrics build slopes with angles varying from 12° to 40°, whereas mud supported fabrics show slope angles up to 15° (**Kenter1990**).

Modelling of organically produced sediments in CarboCAT is linked to photosynthesis and more specifically light. Calculation of in-situ carbonate production for this project, is directly related to the amount of light available in the water column. Calculation of in-situ carbonate production is a measure of the final outcome of the photosynthetic process only, but photosynthesis itself is not modelled. Furthermore, simulated carbonate accumulations display all four of the characteristics mentioned by **Schlager2005** (see section 3.2).

2.1.3   Controls on carbonate production

Production of carbonate material is a property of the carbonate secreting organisms and is controlled by a number of factors. Additionally to light, necessary for photosynthesis, and water temperature, necessary for the carbonate biota to survive, a number of controls have been identified (**Pomar2004**):

- nutrients;

- water energy conditions;

- water chemistry;

- depth of the sea floor;

- competitive displacement;

- substrate requirements;

- biological and evolutionary trends.

Unlike siliciclastic systems where strata geometry is controlled by hydrodynamic conditions only, in carbonate systems strata geometry and facies distribution is an interplay between physical controls and biological production. The biological production has three broad environmental controls. First, ecological requirements, that change as the biota evolve, second, atmospheric and oceanic chemistry and third, regional hydrodynamic settings (**Pomar2008a**).
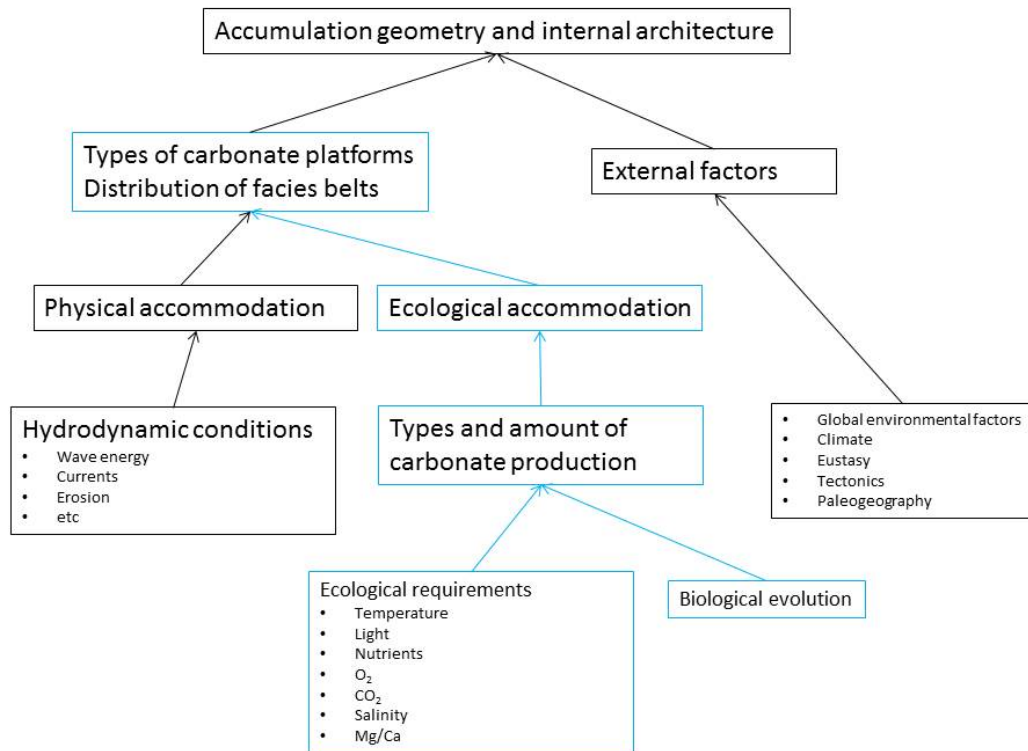
Figure 2.1: Diagram of the relationship of physical and biological controls on carbonate accumulations. Black squares mark external (to the producing biota) factors equivalent to siliciclastic strata. Blue squares are biologically controled factors. Redrawn from **Pomar2008a**

Ecological requirements are the optimal conditions in terms of water temperature, concentrations of O_2 and CO_2, Ca^{2+} in the water, nutrients supply, light and water salinity that are necessary for the living biota to grow. Different species have different optimal ecological conditions while the species evolve as the conditions change. The regional hydrodynamic conditions control nutrient availability and water energy conditions in the direct environment of the producing biota. (Fig.2.1).

A number of additional factors can affect carbonate production in each area as well. These factors range from over-fishing which causes increased fleshy macro-algal abundance on reefs (**Zaneveld2016**), to dredging for coastal construction (**Erftemeijer2012**), to sewage pollution (**Wear2015**), to tourism that might disturb or completely alter the local conditions, among others. Even though these factors can have a significant effect on carbonate producing communities, it is only the factors that affect carbonate production globally that are discussed here.

Most studies on the controls on carbonate production focus on coral production since corals are the most common reef builders in modern carbonate settings.

Corals (and all the other carbonate producing organisms that produced highly structure skeletal material) have adapted to live and thrive within specific environmental and ecological conditions. Environmental conditions that show values outside the optimal range for corals, are defined as stressors.

The effect of stress on coral communities depends on the ability of the corals to counter-balance the stress (resilience) and the magnitude of the stress. If the stress effects overcome the resilience of the corals, a disease is formed. A disease is any disorder of vital body functions or organs of the coral and their symbiotic zooxanthellae (**Sutherland2004**).

Zooxanthellae is a photosynthetic algae that lives in a mutualistic symbiosis on the coral tissue. The coral provides a protected environment and compounds for photosynthesis and the zooxanthellae provide oxygen and other products of photosynthesis necessary for the coral survival (**noaa**).

The disease induction mechanisms are associated with pathogens such as bacteria, cyanobacteria and fungi. Corals and zooxanthellae are resilient to almost all diseases but environmental or anthropogenic stress factors enhance the action of the pathogens (**Sutherland2004**).

The same factors that cause stress to corals, generate favourable conditions for other benthic communities that compete with corals and cause further reef degradation. Macro-algae and cyanobactieria are the most hurtful of these competitors which are both greatly benefited from increased nutrients influx (eutrophication) and raised water temperatures. **Bakker2017** reported that the benthic communities of the Caribbean reefs of Curacao and Bonnaire are dominated by cyanobacterial and algal mats. Similar trends of coral shift have been reported all over the world (**Bakker2017**).

2.1.4 Ecological conditions

2.1.4.1 Temperature

The global spatial distribution of modern coral reefs (Fig.2.2) reveals that the great majority of reefs is located in waters with surface temperature in the range of $20 - 30^{o}C$. Water temperatures higher that the optimal temperature window for corals cause stress which can lead to disease and in extreme cases even death.

The most common temperature related disease in modern corals is bleaching. Bleaching occurs when corals expel their symbiotic zooxanthellae and lose their colour. Bleaching is not always terminal for the corals. It directly leads to lower reproductive outcome, skeletal growth and calcification rates (**Sutherland2004**). When temperature conditions return to normal it is possible for corals to regain their symbiont and recover from bleaching but repeated events or the stress from other factors can cause coral mortality.
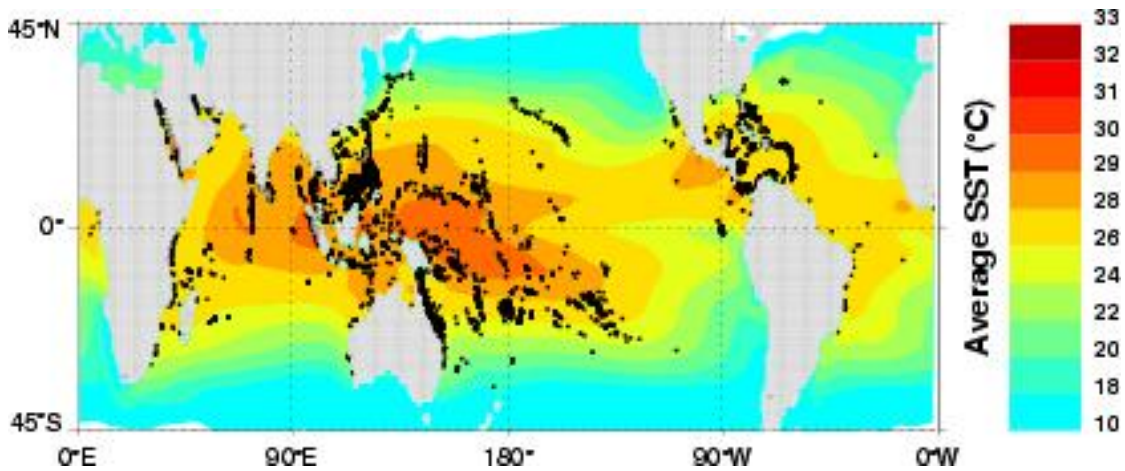
Figure 2.2: Global distribution of modern coral reefs with average sea surface temperature (SST). Most coral communities thrive in waters where temperature rarely falls below 22^oC. The 20^oC isotherm (green colour region) loosely follows the 30° latitude indicating the significance of temperature over light (solar radiation). After https://biomessixth10.wikispaces.com/Coral+Reef+Home.

Bleaching is caused by microbial communities on the mucus layer of the corals. The mucus environment of corals is rich in nutrients and thus is a host of wide variety of microbial communities. Most of the microbial communities are beneficial to the corals with some pathogens in low numbers through the effect of coral induced antibiotics. Thermal stress causes loss of antibiotic activity or pathogens became immune to them. Both cases result to a shift from mucus dominated by beneficial microbes to pathogen domination (**Mao-Jones2010**).

Once the shift has occurred, corals expel their zooxanthellae and all the symbions and bleaching takes place. Normal temperature conditions after bleaching are not enough for coral recovery. Full recovery of corals occurs when pathogen population decreases which requires water temperature to drop to unfavourable levels for the pathogen (**Mao-Jones2010**).

2.1.4.2   Nutrients

Despite their high production rates, corals thrive in low nutrient environment (**Hallock2005**). The ability of corals to survive in nutrient poor environments is attributed to symbiotic zooxanthellae. The symbiosis is mutually beneficial only in environments with low nutrient supply. High nutrient supply tends to destabilise the system and negatively effect the corals in a predictable manner. The response of corals to increased nutrification is (**Hallock2005**):

- decline in the coral population;

- increase in benthic macroalgae population;

10

- increase in cyanobacterial densities;

- increased rates of bio-erosion;

- loss of reef structure.

While low or medium flows of organic matter can have positive effects on both corals and zooxanthellae since they gain some of the required energy from the available organic matter, it is the flows of high amount of organic mater that causes problems. Higher concentrations of organic matter disproportionally benefit organisms that compete with corals (**Fabricius2005**).

Moreover, dissolved inorganic matter and specifically nitrates and phosphates directly harms corals as inorganic matter is used preferentially by zooxanthellae. As the zooxanthellae populations grow they deplete the available CO_2 for photosynthesis and the depleted CO_2 becomes a limiting factor for calcification. (**Fabricius2005**).

2.1.4.3 Water chemistry

Photosynthesis alters the chemistry of sea water (eq.2.2) by reducing the water's acidity and promoting calcification. The form of the produced $CaCO_3$ (calcite or aragonite) depends on the concentration of Ca^{2+} and more specifically the Mg/Ca ratio. Mg/Ca ratio higher than 4 favours formation of aragonitic shells which are more stable and stronger than the calcitic shells (**Hallock2005**).

In Cretaceous and Paleogene shallow, tropical seas the Mg/Ca ratio were around 3 and thus the most abundant form of $CaCO_3$ was calcite. In the Neogene the Mg/Ca ratio of the tropical, shallow seas typically exceeded 3 and thus aragonite became the most efficient $CaCO_3$ form.

As atmospheric concentration of CO_2 increases, more $(CO_2)_{aq}$ enters the sea water and reacts with the available carbonic acid CO_3^{2-} (eq.2.3). Decreased concentrations of carbonic acid reduce the calcium carbonate or aragonite saturation state. Aragonite saturation Ω is defined as the ratio of the product of the ions concentration of calcium carbonate to its solubility (**Hoegh-Guldberg2007**) (eq.2.4)

$$H_2O + (CO_2)_{aq} + CO_3^{2-} \Rightarrow 2HCO_3^- \tag{2.3}$$
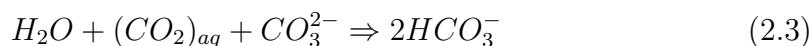
$$\Omega = \frac{[Ca^{2+}][CO_3^{2-}]}{K} \tag{2.4}$$

Carbonate accretion becomes zero (and as a result reef accretion becomes negative under the effect of erosion) when aragonitic saturation drops to values of 3.3 or lower which corresponds to CO_2 atmospheric concentration of 380ppm. Modern days CO_2 concentrations of 400ppm and increasing means the optimal conditions
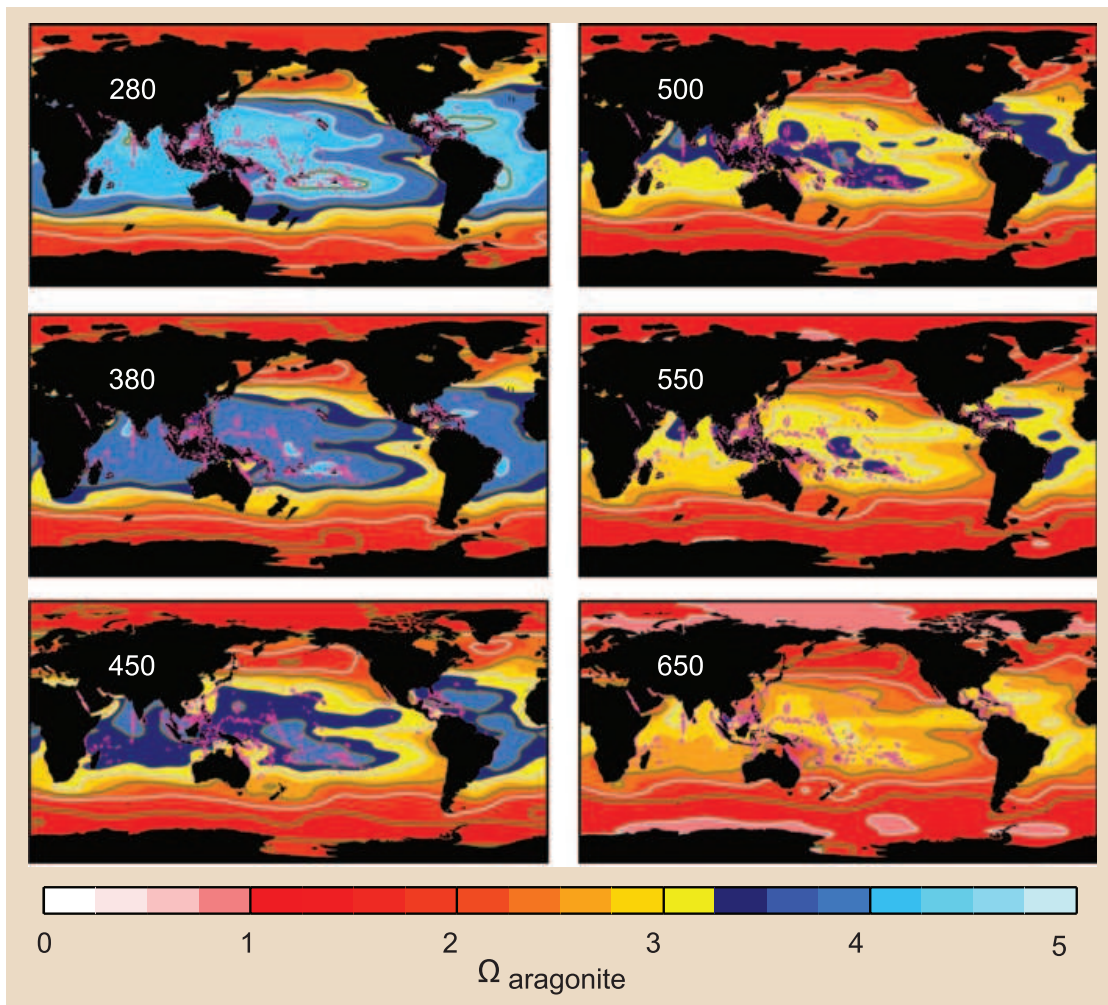
Figure 2.3: Global distribution of aragonite saturation Ω predicted to occur at different atmospheric CO_2 concentrations (number on the top left in ppm). Pink dots indicate locations of modern shallow reefs. Today's atmospheric CO_2 concentration of 400ppm corresponds somewhere between the middle and the bottom panel of the left side. The 3.3 threshold for reef conservation corresponds to dark blue indicating that favourable water conditions are shrinking. Modified from **Hoegh-Guldberg2007**.

for new reefs are very restricted and existing reefs are in danger of loosing mass (Fig.2.3) (**Hoegh-Guldberg2007**).

2.1.4.4 Siliciclastic sediment supply

Additionally to carbonate sediment produced in-situ, siliciclastic sediment may be supplied to a carbonate system from external sources. The majority of sediment supplied to carbonate systems is via rivers which carry the products of land or coastal erosion. The erosional material delivered to a carbonate platform will be

here collectively referred to as siliciclastics in order to differentiate it from organic clasts or dissolved organic matter.

Depending on the hydrodynamic conditions around the source, larger grain size siliciclastics are deposited within a few kilometres from the river mouth, while fine grains may stay in suspension and transported longer distances. Both deposited and suspended siliciclastics are stressors for carbonate producing organisms. The effect of siliciclastics on carbonate production is directly related to concentration of siliciclastics. In coral colonies, siliciclastic stress increases linearly with the duration of particle suspension and the amount of sediment supply (**Fabricius2005**).

High supply rates that completely cover the corals can kill exposed coral tissue within a period of few days. Lower supply rates that do not completely cover corals reduce photosynthesis by increasing light attenuation in the case of suspended sediment. Deposited sediment increases the energy requirements of the corals since the settled particles need to be removed (**Fabricius2005**).

Suspended particles scatter the available light in the water column. Light scattering is related to the mean size of the particles and apparent density (dry weight / wet volume). More importantly maybe, light scattering depends on the particles "wet" size. As suspended particles bound together, they trap some water in the spaces between the solid matter. This process results to formation of bigger but less dense particles with smaller specific scattering coefficient compared to equal size "dry" particles (**Bowers2009**).

Photosynthetically active radiation (PAR) attenuation coefficient is mainly related to changes in suspended particulate matter during both the wet and dry conditions. Attenuation of PAR from dissolved organic matter and water is less significant (**Lund-Hansen2010**).

Storlazzi2015 studied light attenuation in the laboratory and confirmed that higher suspended sediment concentrations, finer grain size and longer suspension times have higher PAR attenuation coefficients. The authors identified that sediment grain colours also affect light attenuation with darker or red grain colours attenuating PAR more efficiently.

Photosynthetically active radiation is a spectral integral of solar radiation in the visible light spectrum from 400 to 700nm. The 400-700nm wavelengths are utilised by photosynthetic organisms. Because PAR covers a range of wavelengths, the attenuation coefficient K(PAR) varies at different water depths. The upper-most portion of the water column shows very high K(PAR) because longer wavelengths ($\approx 700nm$) are absorbed faster than shorter wavelengths ($\approx 400nm$) (**Storlazzi2015**).

The removal of settled siliciclastic particles increases the energy requirements of the carbonate producers. The same time, reduced PAR from light scattering and absorption due to suspended particles restricts photosynthesis and thus energy

production. The limited available energy results to reduced rates of calcification and reduced tissue thickness of each animal which combined affect colony survival (**Fabricius2005**). Table 2.1 illustrates a summary of the effect of each main parameter of the terrestrial run off on coral communities.

Table 2.1: Summary of direct effects of terrestrial sedimentation on the growth and survival of adult coral colonies. The arrows indicate the relative strength and effect of each parameter. Arrows pointing up or down: positive or negative effect. Half arrows: weak effect, single arrows: moderate effect, double arrows: Strong effect. Dash indicates no effect. N:Nitrates, P:Phosphates, POM:Particulate organic matter. Modified from **Fabricius2005**

	Disolved N	Disolved P	POM	Light reduction	Siliciclastics
Calcification	↓	↓	↿	⇓	⇓
Tissue thickness	–	–	↑	↓	⇓
Zooxanthellae density	⇑	–	↿	↿	↓
Photosynthesis	↑	↑	↑	⇓	⇓
Adult colony survival	–	–	↑	↓	⇓

A new algorithm has been developed in CarboCAT to simulate the introduction and deposition of siliciclastic material on a carbonate platform. The algorithm also calculates the effect of siliciclastics on carbonate production based on the concentration of siliciclastics and the size of the clasts (see section 5.5)

2.1.5 Physical energy

2.1.5.1 Wave energy

The lateral distribution of facies reflects energy levels, topography and organic activity. Topography is directly related to the geometry of the platform while organic activity is controlled by the physical properties of the platform (**Lucia1999**). Key controls of the energy distribution over the platform are the platform topography and wind waves.

Wind or wind-generated waves are water particle oscillations in the water free surface. The factors that influence the formation, size and shape of actual wind waves are (**SPM1984**):

- wind speed. The strength of the wind defines the amount of energy that is transferred to the water molecules;

- wind duration. The time for which the wind has blown over a given area;

- fetch area. The uninterrupted distance of open water over which the wind blows;

- water depth.

A set of wind and fetch conditions can generate a specific wind wave in deep water or fully developed sea. Not fully developed or limited sea conditions imply that the water depth limits the size of the generated wind wave. Wind waves are also called gravity waves because the returning force necessary for bringing equilibrium is gravity.

Wind waves are usually defined by their height, length and period (Fig.2.4). Wave height is the vertical distance from the top of the crest to the bottom of the trough. Wave length is the horizontal distance between two successive crests and wave period is the time in seconds between successive crests passing a given point.
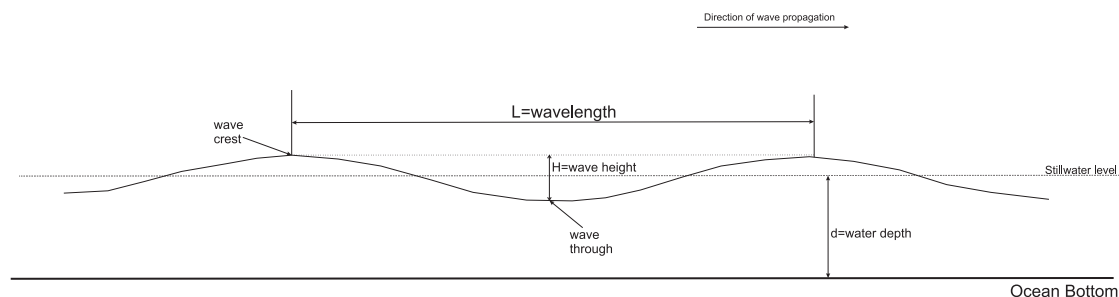
Figure 2.4: Wave characteristics (**SPM1984**)

15
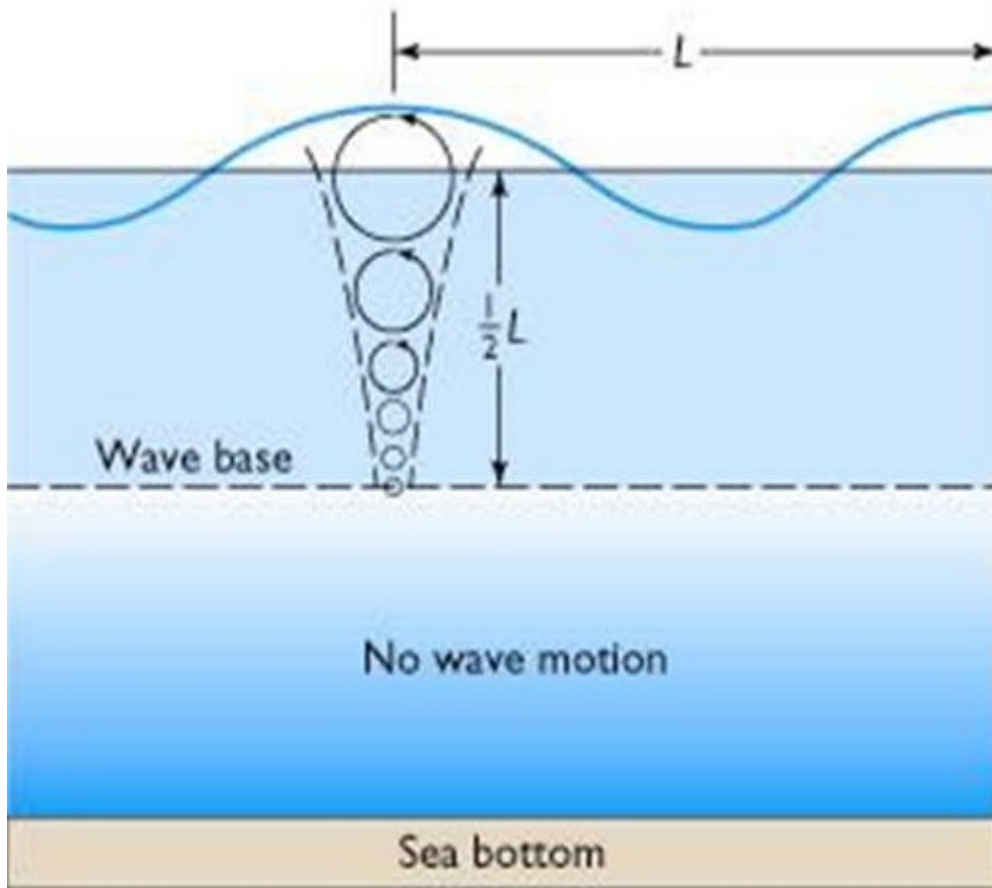
Figure 2.5: Sketch showing the wave base and particle movement of a wave. The size of the oscillation decreases with depth and becomes zero at the wave base. Below wave base there is no water movement from the wave. In deep water waves do not affect the sea bottom.

Wind conditions over the fetch area generate waves that move in the wind direction. Wave propagation in deep water carries forward only the waveform and energy, but not mass. Water particles oscillate in nearly circular paths and return to their initial positions when the waveform has passed them. The size of these orbits is defined by the wave height and length, is greatest at the surface and decreases fast with depth. Below a certain depth which is equal to half the wave length, water particles stay still. The maximum depth that a wind wave can move water is called wave base (see Fig.2.5). If the water depth is less than the wave base, the wave is in touch with the sea floor, water action does not decease with depth and orbits are more elliptical.

The maximum depth that wave motion reaches is controlled by its length while the wave height contains the wave energy. The wave's energy is proportional to the square of its height (**SPM1984**).

$$E = \frac{\rho g H^2}{8} \tag{2.5}$$

where E is the wave energy in J/m^2, ρ is the water density in kg/m^3, g is the acceleration of gravity in m/s^2 and H is the wave height in m.

16

The maximum height of a propagating wave in deep water depends on the amount of energy that has passed to the water column from the wind. The wave height is limited by the maximum wave steepness which is defined as the ratio of the wave height to wave length. Waves with steepness values less than 0.14 are stable whereas steepness values greater than 0.14 cause instability.

Waves that move from deep water to more shallow water change their shape as a function of depth. For water depths less than the wave base, waves are in contact with the sea floor, grow taller and their steepness changes. When the steepness reaches the instability threshold, the wave breaks and its energy is dissipated very fast. The depth at which the wave breaks depends on the wave height and it is called break depth (**SPM1984**).

Bretschneider1958 revised a prediction system developed earlier by Sverdrup and Munk in what is often called the SMB method from the initials of the researchers that developed it. The SMB method predicts wave height, length and period for both deep and shallow water from the wind speed and fetch length.

The wave height H for deep water for any fetch length and wind conditions is calculated from the SMB method using eq.(2.6). The wave period T is given from eq.(2.7) and the wave length L from eq.(2.8). The Sverdrup-Munk-Bretschneider Nomogram (Fig.2.6) allows visual estimation of the maximum wave height for different fetch sizes and wind speed conditions.

$$\frac{gH}{u^2} = 0.283 \tanh\left(0.0125\left(\frac{gF}{u^2}\right)^{0.42}\right) \tag{2.6}$$

$$\frac{gT}{u} = 2.4\pi \tanh\left(0.077\left(\frac{gF}{u^2}\right)^{0.25}\right) \tag{2.7}$$

$$L = \frac{gT^2}{2\pi} \tag{2.8}$$

where g is the acceleration of gravity in m/s^2, u is the wind speed in m/s and F is the fetch length in m

Eq.(2.6) and eq.(2.8) calculate the maximum wave height and the maximum wavelength that can be generated for any given wind conditions and fetch dimensions. Waves with smaller heights and wavelengths than the maximum predicted are also generated under the same conditions.

Furthermore, eq.(2.6) and eq.(2.8) do not include the effect of wind duration on wave generation. For both equations it is assumed that wind blows enough time over the fetch area to generate the calculated waves. In reality, wind conditions and thus wave energy are highly variable with time ranging from wind gusts, in a time scale of minutes, to seasonal wind patterns in a time scale of months.
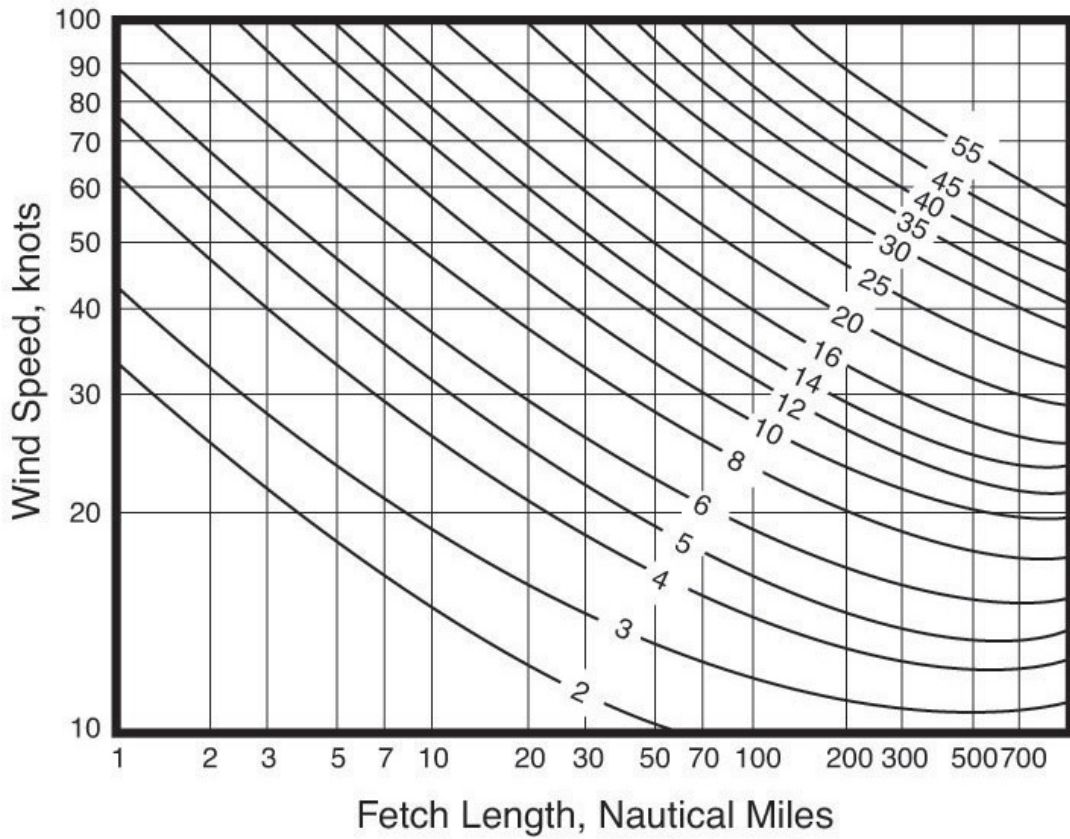
Figure 2.6: Simplified Sverdrup-Munk-Bretschneider Nomogram. The diagram displays the maximum wave height in feet generated from different fetch areas and wind conditions. From **noaa**
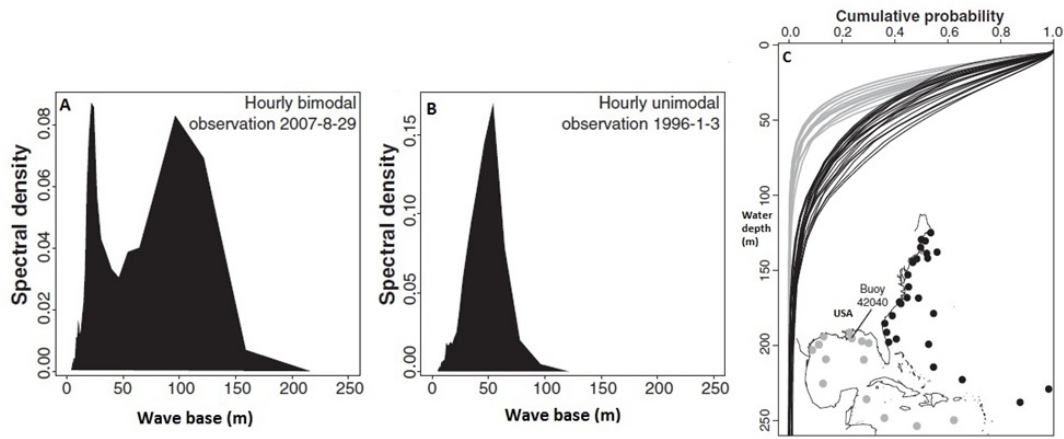
Figure 2.7: Examples of wave size as spectral density from the buoy 42040 (map inset in C) at two different days. A-Hourly observations that show bimodal wave energy distribution. Two different water depths (20m-fair weather wave base and 105m-storm weather wave base) can be identified. B-Hourly observations that show unimodal energy distribution and one wave base for all waves. C-Cumulative probability of a wave encountering the sediment-water interface. Data from two groups of buoys were used. One group (grey dots and lines) in the gulf of Mexico and a different group (black dots and lines) in the west Atlantic. Modified from **Peters2012**.

All these imply that both break depth and wave base are actually not well defined water depth surfaces but zones of water depths. **Peters2012** using data from buoys in the Gulf of Mexico and west Atlantic identified both bimodal and unimodal wave energy distributions with wave base. The authors also identified that despite the time variability of the wave size, the cumulative probability of a wave to affect the sediment-water interface decreases smoothly with water depth (Fig.2.7).

A new algorithm has been developed in CarboCAT to simulate the effect of wind generated waves on carbonate production. The algorithm takes as input wind conditions and fetch area length and calculates wave energy distribution, wave base and break depth. Furthermore, model runs have been used to study the effect of wave energy on small and large scale facies distribution (see section 5.4)

2.1.5.2 Erosion and transportation

Erosion is defined as the removal of weathered sediment or rocks by the forces of water, wind or ice. Physical, chemical and biological processes are responsible for the breakdown and removal of carbonate rocks. Physical or mechanical erosion breaks the rocks into small clasts through mechanical stress. Chemical erosion dissolves the rocks into solution, while bio-erosion is referred to the disintegration of rocks caused by an organism (**Pidwirny2006**).

Mechanical erosion is unevenly distributed over carbonate depositional environments. It is more intense at platform margins where wave energy is higher and less intense in restricted environments and deep waters. Various sources supply the necessary energy for physical erosion. Mechanical erosion is fuelled mainly by the wave energy and gravity.

Gravity moves a body of sediment vertically and horizontally from unstable slopes towards an equilibrium point, usually to the basin of the system (**Peel2014**). Slope stability characterises conditions in which geologic materials move spontaneously on surface slope. A measure of the stability of single grain on a horizontal surface is called angle of repose. The angle of repose is the steepest angle relative to the horizontal plane to which motion does not occur. The angle or repose depends on the shape of the grain (**Julien2010**).

Slope stability is modelled in CarboCAT but the angle of repose is not explicitly defined. Slope stability is quantified as the maximum bathymetric difference threshold above which sediment is mobilised and the threshold is defined for each numerical facies (see section 3.2). The effect of slope stability in whole scale platform geometry is studied with a series of model runs (see section 7).

Dissolution of carbonates due to chemical erosion is very limited at the surface waters and small water depths but much more intensive in the deep ocean. Shoal waters are practically saturated with respect to calcite and only the high magnesium contents dissolve. Deep oceans are unsaturated with respect to $CaCO_3$ and higher dissolution occurs. Moreover, carbonates dissolve above sea level in the presence of fresh water.

Bio-erosion of carbonates is particularly intensive because they consist of relatively soft minerals. The organic matter in the carbonate minerals is an incentive for organisms to attack the grains. Bio-erosion increases with nutrient supply and is responsible for limited growth and accumulation rates of carbonates.

Depending on the grain size of the eroded material and the forces exerted on each grain, material can be picked up, a process known as entrainment and moved smaller or larger distances, a process known as transportation (Fig.2.8).

Sediments in transportation are distinguished in two groups:

- bedload. The portion of the sediment that is moving along the bed and most of the time maintains contact with the bed;

- suspended load. The portion of the sediment that is carried in suspension and almost never touches the bed.

Generally, silt and clay size particles enter suspension while sand and coarser material roll and slide in contact with the bed.

When the energy exerted on the sediment particles drops below a specific value for each grain size and type of transportation, erosion stops and the sediment is
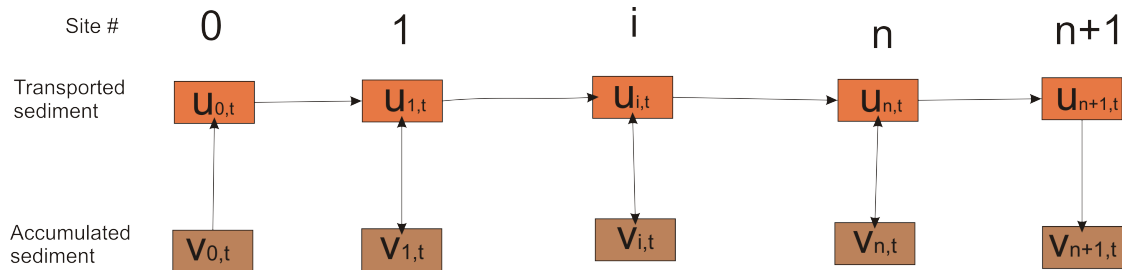
Figure 2.8: For each site within a carbonate system, sediment accumulation (with volume v) is the sum of in-situ produced sediment and deposition of transported sediment. At any site, not all in-situ produced material accumulates. Depending on the hydrodynamic conditions at each site, a portion of the in-situ produced material is available for transportation (with volume u) or a portion of the transported material gets deposited. For perfect sources (site 0) all the accumulated sediment comes from in-situ production. For perfect sinks (site n+1) all the accumulated sediment is deposited transported material. Arrows pointing upwards indicate removal of sediment from a site. Downward arrows indicate sediment deposition. Modified from **Tipper2016**.

deposited. The amount of deposited sediment depends mainly on the energy level at the position of deposition.

A new sediment transportation algorithm has been developed in CarboCAT. The new transportation algorithm simulates bedload transportation of sediment clasts from water currents. The algorithm calculates the total shear stress exerted on carbonate clasts from water currents and the gravitational forces. Transportation is performed when the total shear stress exceeds an energy grater than the threshold for entrainment while deposition occurs when the energy drops below the threshold. Furthermore, transportation is also initiated when the bathymetry exceeds the slope stability threshold for each facies (see section 5.6).

2.1.5.3 Water Depth

Almost all controls on facies distribution (wave energy, light penetration, water temperature and nutrient supply) are water depth-dependent and scale-dependent processes. For large scales (whole platform scale) there is a deterministic relationship between facies distribution and water depth.

This deterministic relationship allows for interpretation of water depth and sedimentological environments from strata geometries and their lateral and vertical distribution. Deep basin depositional environments accumulate sediments that have different lithological properties and texture from sediments deposited on the

slope and both differ from sediments deposited in shallow tidal flats.

For smaller scales (outcrop or smaller) or shallow water depths the interplay between all the physical processes that control facies distribution poses a question to what extent water depth uniquely controls facies.

Rankey2004 performed statistical analysis of the biological habitats and sedimentological facies from a shallow (water depths less than 9m), carbonate platform at Key Largo, Florida and concluded that water depth does not uniquely control water facies distribution. The author also identified that for water depths greater than 10m there is 0 % uncertainty in the prediction of facies distribution compared to 83% uncertainty for water depths less than 8m

Purkis2005 studied a shallow sub-tidal Holocene carbonate ramp between Abu Dhabi and Dubai with maximum water depth 6m below the lowest tide and found that fractal output patterns for all lithofacies are present in the ramp for a wide range of observational scales (from 10^3 to 10^6 m^2). Fractal properties indicate scale invariance and thus a fractal carbonate depositional system will look the same in all scales. Fractal properties imply that the controlling factors create a scale invariant facies distribution and thus there is no deterministic relationship between water depth and facies distribution.

Bosence2008 studied the peritidal facies transitions in the depositional margin of a carbonate mount in Florida Keys and concluded, contrary to the previous studies, that facies transitions followed water depth very closely. **Maloof2012** studied peritidal carbonate accumulations as well at Triple Goose Creek, northwest Andros island, Bahamas and also concluded that the distribution of facies is a function of water depth and not random.

Purkis2012a studied the lateral anisotropy of facies on the Saipan island, a modern rimmed lagoon north of Guam in the Marianne Archipelago. They measured the anisotropy along all directions for multiple scales (from 100m to 1km with lateral resolution of 4m) on the platform. Statistical analysis using Markov chains of the measured anisotropy revealed that assessment of anisotropy varies little when measured on scales of hundreds of meters to a few km and as result the use of water depth dependent depositional environments is justified. Even though some areas follow a water depth dependent relation, some others could not be constrained to water depth only. An almost equal prevalence of strongly isotropic and strongly anisotropic areas exists (**Purkis2012a**).

Purkis2015 used remote sensing imagery, field observations and hydrodynamic models for two reef-rimmed shore-attached carbonate platforms in the Red Sea to show that the combination of water depth and hydrodynamic conditions explained facies distribution very well. Furthermore, the authors concluded that facies distributions though are not related either to water depth or energy levels when the parameters are considered isolated from each other.

The results of **Purkis2015** that facies distribution is controlled by water depth and energy conditions agree with the conclusions of all the previously mentioned studies and define the limits of the deterministic water depth-facies relationship.

Hydrodynamic conditions are variable only above the wave base and below the break depth and thus this is the scale where the deterministic relationship is not valid. The failure of the deterministic relationship generates exchangeable facies across some water depth ranges.

For large scale (whole platform) facies distribution is only controlled by water depth because energy levels are high only on the top few tens of meters water depth. For smaller scales and water depths above the wave base, facies distribution is better predicted by the combination of water depth and energy conditions. For even smaller scales (10-100s of meters or above the break depth or peritidal environments) the deterministic water depth relationship appears valid again due to very low energy conditions.

Modelling of carbonate strata with CarboCAT involves a wide range of scales from big scale-whole platform geometries to small scale-facies transitions relationships. Implementation of facies competition rules, wave energy conditions and sediment transportation allows simulation of all physical controls on facies distribution.

2.1.6   Carbonate factories

The carbonate factory is an open dynamic system as the environmental conditions affect the ability of the living biota to grow which in turn modify the environmental conditions around them. The carbonate factory is a spatially and temporally dynamic system, capable of occurring at a range of depths depending on the environmental factors and the available biota (**Wright2005**).

Based on the character of biogenic carbonate production of Mesozoic and Cenozoic, three carbonate factories have been identified, the benthic automicrite factory, neritic lime-mud factory and the skeletal factory (**Pomar2008**).

The benthic automicrite factory represents a type of carbonate facies precipitated by the interplay of inorganic and organic chemical reactions. The factory is light independent and represents biotically induced carbonate production. Precipitation of $CaCO_3$ occurs from microbes and bacteria associated with degradation of organic matter. The main source of the necessary organic matter was mainly photosynthetic metazoan communities (sponges) and cyanobacteria.

Precipitation of $CaCO_3$ in the neritic lime-mud factory is the result of microbial calcification. Micritic carbonate precipitates occur when photosynthesis from cyanobacteria, algae and phytoplagton is de-coupled from cell growth in well lit and nutrients rich environments. The abundance of nutrients provide the necessary energy for photo-autotrophic cells which use photosynthesis to fix carbon excess.
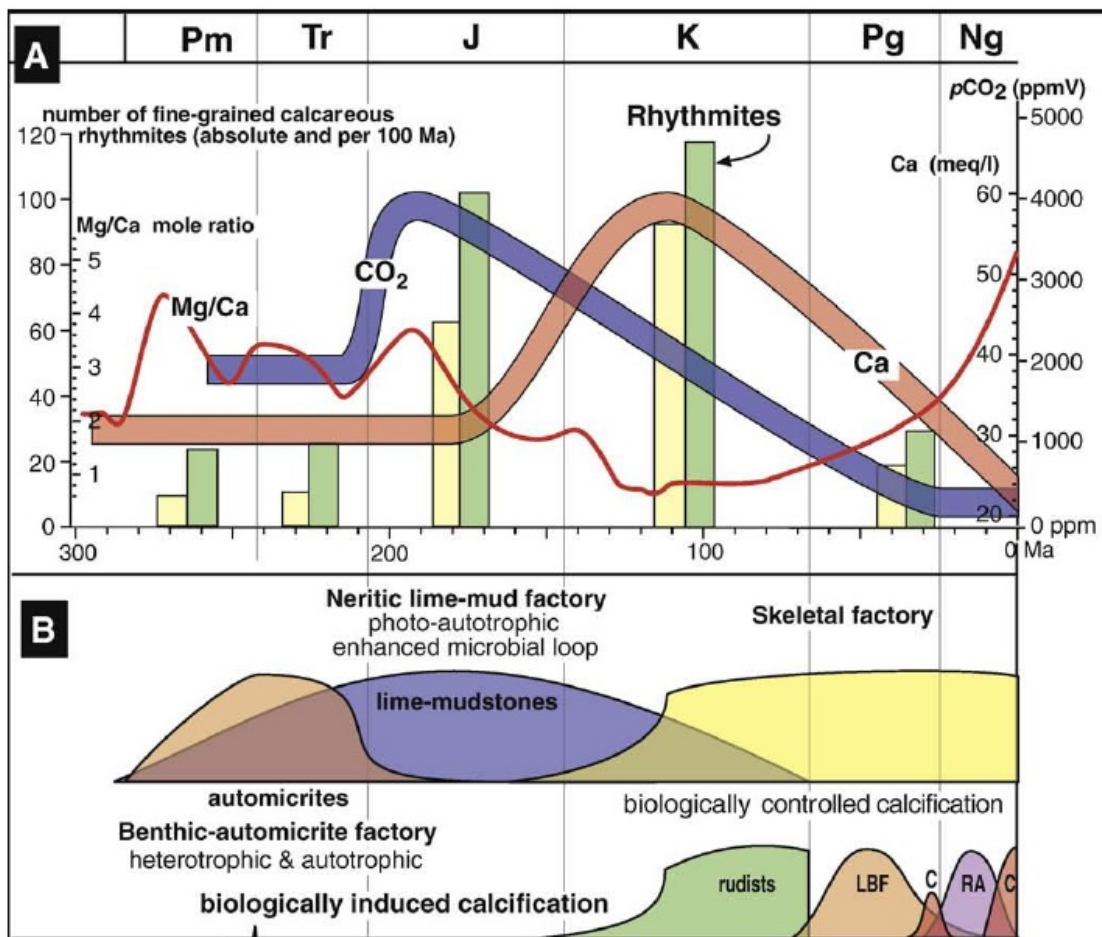
Figure 2.9: A. Time variations in the Mg/Ca ratio in the seawater, atmospheric CO_2, occurance of fine-grained calcareous limestones-marl alterations and smoothed average calcium concentration. B. Resulting predominant type of carbonate factory over the Mesozoic and Cenozoic. Pm:Permian, Tr: Triassic, J: Jurassic, K: Cretaceous, Pg:Palaiogene, Ng:Neogene; LBF: Large benthic foraminifera, C: Corals, RA: Crystalline red algal. Modified from **Pomar2008**

The skeletal factory is the main biotically controlled carbonate precipitation process. $CaCO_3$ is formed as highly structure crystals either for building of hard shells (skeleton) or regulation of pH and concentration of Ca^{2+} in the environment of the living biota. The skeletal factory operates in rather narrow range of environmental conditions.

Pomar2008 identified the environmental conditions in terms of concentrations of CO_2, O and Ca and the Mg/Ca ratio for the Mesozoic and Cenozoic and estimated the importance of each factory through time (Fig.2.9).

Based on the mean temperature of the sea water, carbonate factories are distinguished in tropical, cool water and mud-mound factories (**Schlager2003**) (Fig.2.10-A). The tropical shallow-water factory is dominated by biotically controlled (mainly photo-autotrophic) and abiotic precipitates; cool-water factory, dominated by biotically controlled (mainly heterotrophic) precipitates and the mud-mound factory, dominated by biotically induced (mainly microbial) and abi-
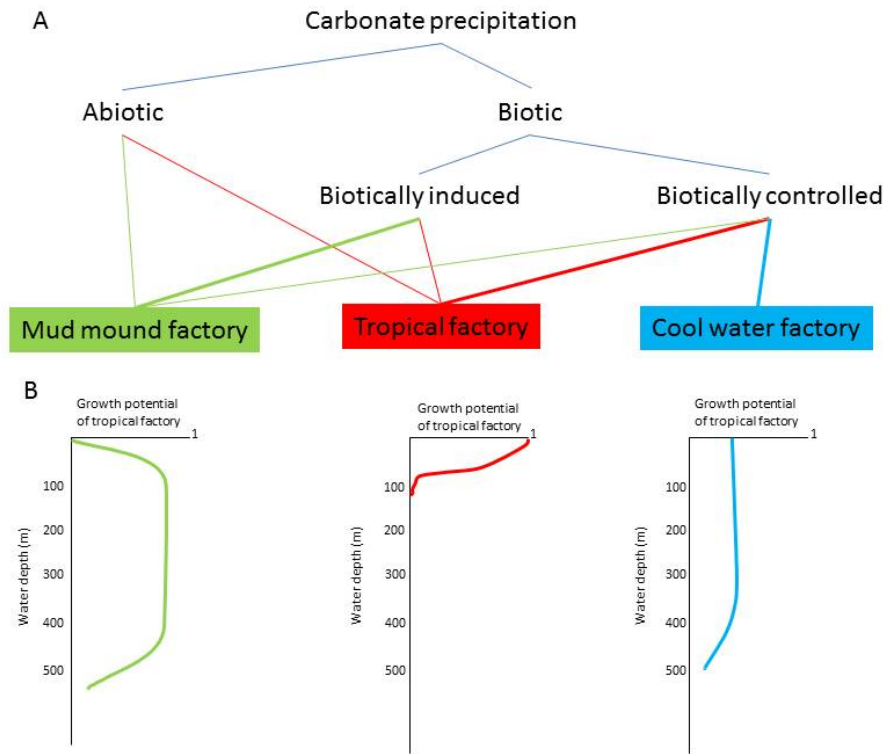
Figure 2.10: Carbonate factories and their growth potential. A-The three temperature based carbonate factories and their main precipitation modes (thicker lines). The tropical and the cool water factories are mainly comprised of biotically controlled preciitation. Biotically induced precipitatin dominates the mud mound factory. B-Production potential with depth of the three factories. The tropical factory shows the highest rates concentrated in the euphotic zone. The other two factories are light independent with unknown lower limits of production. Both factories have lower production rates than the the tropical one. Modified from **Schlager2003**.

otic precipitates.

The mud-mound factory corresponds to the benthic automicrite factory of **Pomar2008** while the tropical factory corresponds to both niritic-lime and skeletal factories of **Pomar2008**.

The ability of carbonate factories to grow and thus produce sediment is called growth potential. The growth potential is a property of the dynamic system and varies with factories (Fig.2.10-B) and with time (**Schlager2005**). The growth potential is a measurement of the maximum amount of sediment that can be produced from each factory. The amount of sediment that is actually produced depends on the ecological and physical conditions in each area and the available accommodation.

Growth rates of carbonate factories are related but are not the same as deposition and accumulation rates. Growth rates and local hydrodynamics conditions

| IP: | 11.4 g x cm^{-2} x year^{-1} | | IP: | 4.7 g x cm^{-2} x year^{-1} | IP: | 3.9 - 4.4 g x cm^{-2} x year^{-1} |
| PCP: | 28.5 kg x m^{-2} x year^{-1} | | PCP: | 11.7 kg x m^{-2} x year^{-1} | PCP: | 8.0 - 9.8 kg x m^{-2} x year^{-1} |
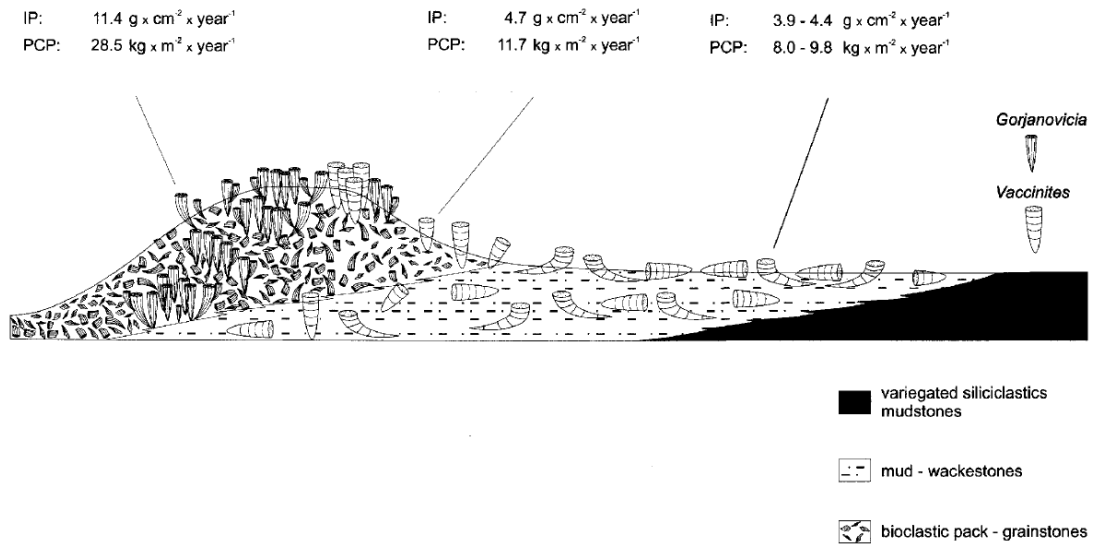
Figure 2.11: Distribution of morphotypes and growth potential of Vaccinites and Gorjanovicia rudists species in differetn depositional environments. IP: individual production, PCP: potential community production. Horizontal distance is several kilometres and exaggerated vertical scale. Modified from **Steuber2000**.

control the amount of deposited material and thus the depositional rates. High depositional rates imply high growth rates but the reverse relationship is not always valid. Highly energetic environments could show low depositional rates even for high growth rates factories.

Hydrodynamic conditions, erosion, transportation and growth rates also control the accumulation of sediment. High accumulation rates imply high depositional rates and thus growth. Low accumulation rates or even depositional hiatuses do not uniquely indicate low (or lack of) growth rates.

Growth potential shows a specific spatial distribution over a carbonate platform with growth potential on platform margins significantly higher than the inner shelf lagoonal settings (Fig.2.11). Low turbulence on the interior prevents the transportation of bioclastic material which restricts the number of individuals that could establish. Moreover, bio-deposits and inorganic sediment stays longer in suspension on the interior affecting the water chemistry and physical conditions (**Steuber2000**).

Mallela2007 studied coral reef encrusted communities along a gradient of riverine influence (decreased turbidity, light attenuation, sedimentation and nutrient supply with increasing distance away from the river mouth) in Jamaica and concluded that elevated riverine input and reduced wave energy were associated with lower carbonate production. Clear waters due to high wave action show higher density of encrusted coral communities and thus higher $CaCO_3$ productivity.

Modelling of carbonate production in CarboCAT simulates all three carbonates factories of **Schlager2003**. The tropical shallow-water factory with highest

production rates concentrated in the euphotic zone is simulated using an euphotic factory in CarboCAT. The two light-independent, cool water and mud mound factory, are simulated using an oligophotic/aphotic factory in CarboCAT (see section 5.1).

Growth rates of carbonate factories are simulated in CarboCAT as production rates of numerical facies. Each numerical facies has a fully defined production rate that represents the maximum amount of sediment that can be produced from that facies under optimal conditions (see section 3.2). The amount of sediment that actually accumulates in each position, which represent the accumulation rate at this position, is calculated based on sediment transportation and deposition based on hydrodynamic conditions.

2.1.7   Population dynamics

Carbonate producing organisms that comprise the carbonate factories do not live isolated from each other but are part of bigger populations. A population is a group of individuals of the same species who live together in the same habitat. Furthermore, populations of other animals might be present in the same area. The interactions and the relations between members of the same population and between members of different populations control the size of the populations and their lateral expansion(**Turchin2003**).

In areas with more than one populations, all populations have to co-exist in a finite space and share some finite resources. Relationships develop between different populations and members of the same population in order to survive. The most important relationship models are predator-prey relationship, competition and cooperation (**Turchin2003**).

The predatory prey model consists of a population of predators that foray on a population of preys. Members of these populations cannot co-exist next to each other since the predator consumes the prey. The survival of both population depends on the survival of the other (**Turchin2003**).

A competitive situation occurs when several species compete for the same resources. In this case the populations can exist next to each other and the size of each population affects the size of the other. If one population goes extinct, the size of the other population increases to a number controlled by the available resources (**Turchin2003**).

The opposite situation is cooperation or symbiosis. There are three possible types of symbiosis commensalism, mutualism and parasitism Commensalism describes the relationship between two living organisms where one benefits while the other is neither harmed nor benefited. Mutualism is a relationship between species when both species benefit from each other. An example of mutualistic relationship is the corals-zooxanthellae symbiosis. Parasitism describes the relationship that

one of the symbiotic species benefits in the expense of the other (**Paracer2000**).

Modelling of carbonate strata includes modelling of the lateral distribution of carbonate factories or living biota. A number of modelling approaches have been adopted to simulate the dynamics between carbonate populations (see section SFM). Population dynamics in CarboCAT is replicated using cellular automata that describe competition of factories for space (see section 3.2).

2.2 Sequence stratigraphy

2.2.1 Definitions

Sequence stratigraphy originated in the early 20th century using the concepts of seismic stratigraphy. Seismic stratigraphic is a method to interpret and describe strata geometries of siliciclastic strata on passive margins imaged on seismic sections (**Payton1977**). As soon as the method was applied to different environments, for different purposes and by different workers a process of adjustments, re-defining and improvements has started.

The term sequence describes a stratigraphic unit bounded by sub-aerial uncomformities and emphasises the importance of such sequence define uncomformities. A depositional sequence is defined as a relatively conformable succession of genetically related strata bounded by sub-aerial unconformities or their correlative conformities (**Mitchum1977a**). The **Mitchum1977a** definition of sequence follows a seismic stratigraphic context while several other types of sequences (genetic, depositional among others) have been defined. All the types of sequences refer to strata that were deposited during a full stratigraphic cycle of change in accommodation or sediment supply (**Catuneanu2009**).

A parasequence is defined as relatively conformable succession of genetically related beds or bedsets bounded by flooding surfaces (**Catuneanu2009**). By definition, parasequences can only be mapped within shallow-water systems, where flooding surfaces have meaning. Parasequences thus are geographically restricted to shallow-water portions of a platform while sequences are scale independent (spatially and temporally) since they represent full sedimentary cycles (**Catuneanu2009**).

The analysis of the relationships between genetically related strata in a chronological framework is the goal of sequence stratigraphy. All the definitions that have been published over the years for sequence stratigraphy stress (**Catuneanu2009**):

1. the cyclicity of the strata. A sequence represents the product of the rock record of a stratigraphic cycle;

2. the temporal framework of facies or depositional systems;

3. genetically related strata;

4. the interplay of accommodation and sedimentation.

Sequence stratigraphy was developed based on and refers to mainly siliciclastic strata. The sequence stratigraphy concepts though apply the same way to carbonate systems as apply to siliciclastic systems. Both carbonate and siliciclastic strata are subdivided by similar surfaces that are responses to changes in base level. The main differences in the case of carbonate systems are related to the nature of the carbonate strata and the fact they are produced in-situ by biological factors instead of supplied from external sources (**Catuneanu2009**).

The same principles used by sequence stratigraphy as a method to describe strata geometries to predict strata geometries, positions and properties in areas where no available information exists. The predictive and descriptive powers of sequence stratigraphy makes it both a model and a method. **Burgess2016b** suggests that sequence stratigraphy is a paradigm, both a method and a model, stressing the danger of the paradigm dominating the way of thinking. Such scenario would actually prevent questioning and testing of sequence stratigraphic theory and ideas.

This project uses numerical modelling to simulate observed and interpreted strata geometries. Having this in mind, this project works as a method to describe strata geometries and analyse their controls. In a wider perspective though, the numerical models generated here provide information about large scale features (whole platform geometry) and smaller scale features (position and geometry of geobodies) that either have not or could not be observed. In this sense, predictions can be made based on the numerical models.

2.2.2 Accommodation

A rather straightforward and simple definition of accommodation is the available space for sediments to accumulate. The above definition is provided by **Jervey1988** who also noted that accommodation for marine sedimentation is roughly equivalent to water depth.

Muto2000 indicated that according to this definition accommodation is a potential space that might be filled or not, without specified boundaries. This creates two significant problems. First accommodation cannot be explicitly defined and thus measured, and second it has dimensions of length which is not directly comparable to carbonate production which is defined a rate.

The lack of boundaries in the definition of accommodation leaves the lateral extent of the space undefined. Without definition of the lateral boundaries, accommodation for a carbonate platform could be anything from the water depth at the position of the deposited sediments to the whole space covered by all the oceans

on the Earth. This two extreme cases would have provided completely different values for the accommodation of the carbonate platform.

Muto2000 also proposed a definition of accommodation as "the thickness measured at a specified site and time, of a space which becomes filled with sediments during a specified time interval". This definition makes accommodation a precise and measurable quantity with magnitude which is related to sedimentation. Maybe more importantly, accommodation over some time period in a specific area allows for direct comparison with sedimentation rates for the same time and place.

Accommodation according to **Muto2000** differs from the water depth in any location. Even though it is commonly assumed that "the space that becomes filled with sediment" represents the space between sea floor and sea surface, there are a number of factors that prevent sediments to accumulate up to the sea surface. The maximum thickness of sediments that can accumulate in any area is defined by the stratigraphic base level in this area.

Stratigraphic base level is an equilibrium surface above which sediment bypasses the area or erosion re-mobilises the deposited material (**Muto2000**, **Shanley1994**). Base level depends on the hydrodynamic conditions in each area but it is not directly related to wave base (**Peters2012**). Furthermore, for any given energy conditions, base level also depends on sediment grain size.

Deposition of sediments is controlled by the wave base at specific time and place but the type of strata formed at each location are not indicative of the wave base position. **Peters2012** showed that formation and preservation of sedimentary structures indicate the position of specific hydrodynamic conditions relative to the wave base and not the absolute position of the wave base.

The above discussion about accommodation refers mainly to siliciclastic strata, where sediment supply and accommodation are independent from each other. For carbonate strata though, the situation is different as accommodation and sediment production are interdependent. Hydrodynamic conditions and relative sea level movements define the accommodation for carbonates to accumulate and carbonate production actively modifies the available accommodation. Furthermore, carbonates have the ability to build wave resistant structures above the base level and thus change the energy conditions in their environment (**Schlager2005**).

The accommodation concept for carbonates has been extended to include physical accommodation controlled by hydrodynamic conditions (similar to siliciclastics) and ecological accommodation which is controlled by the factors that affect the capacity of carbonate producing organisms to build above the hydrodynamic thresholds (**Pomar2008a**).

Pomar2001a defined the ecological accommodation studying a rimmed platform directly overlain a distally steepened ramp in Upper Miocene platforms of the Balearic islands. The base level for the two platforms was different (Fig.2.12)

even though the mean relative sea level remained approximately static and the hydrodynamic conditions did not change. The necessary accommodation for the rimmed platform to develop was created by the ability of carbonate biota to build above the base level of the distally steepened ramp.

(a)

(b)
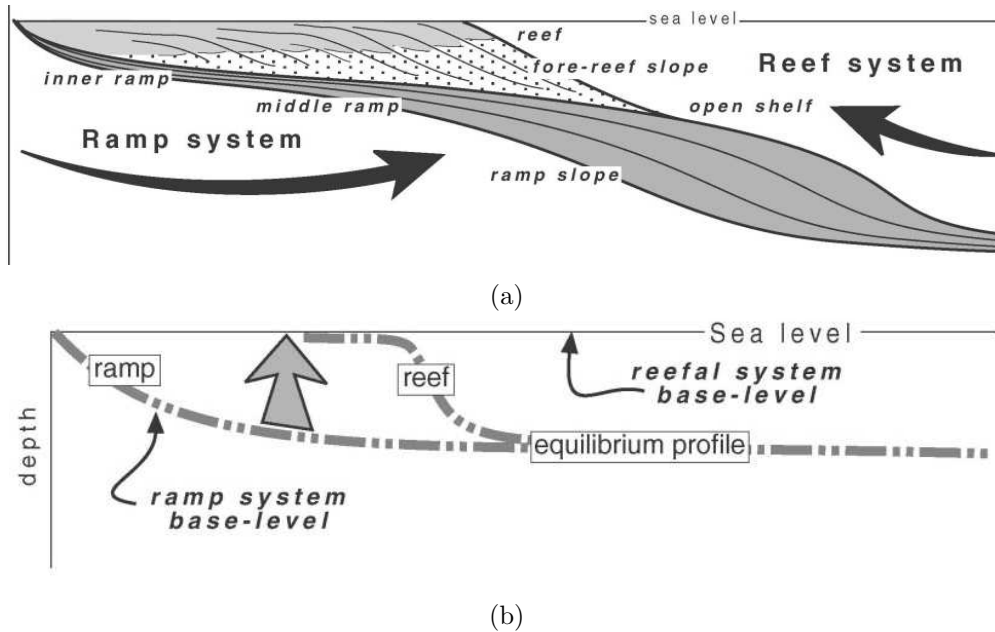
Figure 2.12: (a)-Diagram showing the stratigraphic relationship of the two Late Miocene sequences. A rimmed platform overlain a distally steepend ramp. Sea level oscillations and hydrodynamic condtions (not shown in the diagram) were the same during the deposition of both sequences. (b)-Ramp and reef base level and the biotically generated ecological accommodation. A decrease in the nutrient supply from the land to the platform allowed frame-building, euphotic producing organisms to modify the hydrodynamic conditions and create the necessary ecological accommodation. Modified from **Pomar2001a**.

While accommodation according to **Muto2000** has physical meaning of the observed thickness of deposited sediments at specific time and place, the distinction between ecological and physical accommodation cannot be physically identified on carbonate strata.

Accommodation refers to a specific thickness of strata deposited at a specific area over a specific time interval. Recognition of physical and ecological accommodation would imply that it is possible to identify which part and how much strata have been deposited under the control of physical processes and which part under ecological control.

Physical and ecological accommodation are interpretations of the changes of

base level based on the assumption that physical processes (deposition of sediment decreases the water depth and thus changes the hydrodynamic conditions) and ecological processes (carbonate factories build wave resistant structures) act independently.

2.2.3   A/S ratio

In the early stages of the development of sequence stratigraphy (and in some cases even today, **Burgess2016b**) eustatic changes of the sea level in the studied area were assigned more significance than sediment supply in the interpretation of stratal geometries and stacking patterns. **Galloway1987** studied the depositional and structural architecture of Cenozoic siliciclastic sediments on the continental margin of the Gulf of Mexico and identified that beyond eustatic movements, subsidence and sediment supply also affect the architecture of the strata.

Burgess2001 used numerical forward modelling of a carbonate system and concluded that in the absence of unambiguous sub-aerial exposure, which directly indicates control by relative sea level, changing productivity and variable supply rates is a plausible alternative.

The interplay between multiple controlling factors that collectively can be group as sediment supply and relative sea level movement (**Burgess2006a**) as the main control of depositional systems is a powerful tool to both describing strata geometries and predicting strata positions and relationships. The interplay has been quantified by the use of the accommodation-supply ratio (A/S).

In its most general form, the A/S ratio concept is used to describe shoreline trajectories of siliciclastic systems based on measurable quantities. A/S ratio higher than one means that accommodation is created faster than sediment is supplied and implies backstepping of the shoreline. A/S ratio lower than one means that sediment supply is greater than accommodation creation and implies basinward movement of the shoreline and progradation, while A/S ratio equal to one implies equal rates of accommodation creation and sediment supply and thus aggradation.

Because the A/S ratio's was originally developed for siliciclastic systems, there are two important points that need to be addressed when the A/S ratio concept is used in carbonates. Firstly, in carbonate depositional systems, sediment is not supplied into the system but is produced in situ. Secondly, both quantities must be uniquely defined and refer to the same area or point of a sedimentation system that will allow to measure them and more importantly compare them with each other in a meaningful way.

A more general definition of the A/S ratio for carbonate systems, which has been adopted for this project, is the accommodation-sedimentation ratio (A/S).

Sedimentation rate in this sense takes into account in-situ carbonate production (or growth) rates, possible sediment supply into the carbonate system and the effect of sediment re-distribution due to erosion and transportation.

2.2.4   Temporal evolution of carbonate accumulation

The A/S ratio theory predicts that changes in the bathymetric profile and strata geometry of a platform occur only when the A/S ratio is changing, ignoring the temporal evolution of the platforms. Considering all controls on platform evolution constant (A/S ratio constant), the bathymetric profile and strata geometry of a platform are not static through time.

A static system is a system which lacks any movement or change. Carbonate platforms are dynamic systems characterised by constant change and activity. Sediment is produced in-situ, it gets eroded, transported shorter or longer distances and it is deposited and accumulated constantly.

Some of the processes active on dynamic platform are complementary (in-situ accumulation and deposition of transported sediment build topography) while others are opposing (sediment entrainment and transportation remove sediment from a site). If the opposing forces acting on dynamic system are balanced then the system is in equilibrium. Carbonate platforms in dynamic equilibrium constantly change but their large scale geometry and profile are balanced and appear stable through time. Stable systems are firmly fixed systems that are not likely to change.

Dynamic external forcing produces dynamic platforms. The magnitude and frequency of the changes on the platform can be related to magnitude and frequency of the change of the external forcing. Changes on the bathymetric profile and strata geometry on a platform that are related to changes of the external forcing are called allogenic changes. External forcing is defined as any process acting from outside a system with specified spatial extent and limiting boundaries.

Stable external forcing also generates dynamic platforms (Fig.2.13). Depending on the magnitude of the complementary and opposing forces on a carbonate platform, a dynamic platform generated by steady external forcing might be in or out of equilibrium. Dynamic platforms out of equilibrium show changes with magnitude and frequency not related to the magnitude and frequency of the external forcing. The changes on the platform are characterised as autogenic processes (**Muto2014**).

Muto2016 suggested that if the change of a depositional system is greater than the magnitude of the external forcing, autogenetic processes are active. Thus the stratigraphic configuration of a depositional system does not always directly relate to the state of the external forcing.

This project uses numerical modelling to examine the effect of stable external forcing, more specifically cross-platform sediment transportation, to large scale
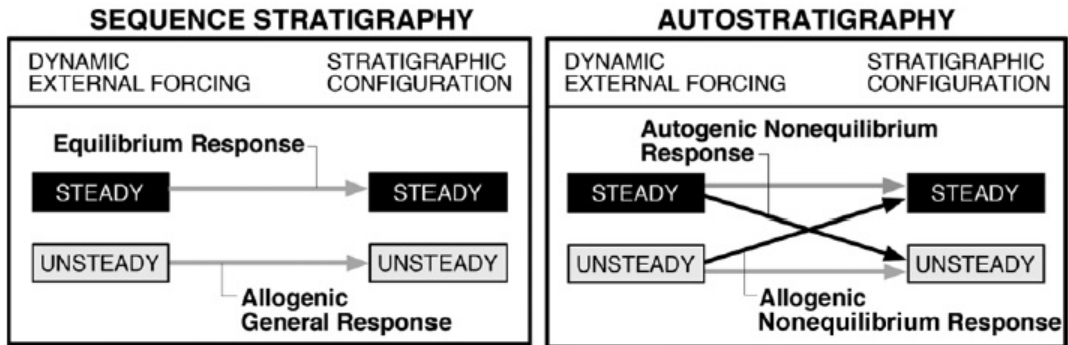
Figure 2.13: Sequence stratigraphy assumes that external forcing and strata geometry are in equilibrium (left). Autogenetic effects generate additional responces to external forcing (right). From **Muto2016**.

platform geometry of platforms and if platforms can reach dynamic equilibrium for all cases of external forcing (see section).

2.2.5 Geometry of carbonate accumulations

The dictionary definition of the platform is a flat surface that is raised higher than the sea-floor around it. Carbonate platforms are classified based on their large scale geometry which varies between to end members of carbonate ramps and flat-topped platforms (FTP) (**Williams2011**).

Carbonate ramps are bodies built away from positive areas with gentle regional paleo-slopes and without an apparent break in slope (**Wilson1975**). A more complete definition distinguishes ramps from FTPs based on their slopes. Ramps as gently slopping platforms with slopes less than 1° that lack a marked break in slope. FTPs are defined as platforms marked by a pronounced increase in slope from few degrees to over 45° into deep water (**READ1982**).

A few slope values have been suggested as the threshold between ramps and FTPs. **Lucia1999** uses the angle of 2°, while **Schlager2005** suggests 1.5^o as the threshold. Accurate platform classification requires identification of geomorphic features in combination with the slope angle but the 1° value is generally accepted. The ramp-FTP platform geometry represents only the two end members of the whole seaward dipping profile of a carbonate platform.

Williams2011 studied through numerical modelling a wide range of platform geometries and their facies distribution and concluded that a continuum of forms exists between the end members and that classification of any platform as either ramp or FTP is based on rather arbitrary criteria. The continuum is formed as

multiple parameters such as sediment production, transportation, hydrodynamic conditions, relative sea level movements and subsidence among others control the formation and evolution of platform geometry.

The continuum of platform geometries due to sediment transportation is examined in this project. Numerical models are used to study the evolution of a homoclinal ramp with various transported fractions and two different slope stability values. Continuum of geometries allows the formation of all platform types between ramps and FTPs (see section 7).

Based also on their large scale geometries, carbonate ramps are further distinguished in homoclinal and distally steepened ramps. Homoclinal ramps are typically low gradient systems with slopes of one to few meters per km of horizontal distance (**READ1982**). They typically show facies distribution that is mainly controlled by wave energy with high energy near-shore facies passing down to slope, deep water, low energy deposits (Fig.2.14).

Distally steepened ramps share the same facies distribution with homoclinal ramps but have a major break in slope. The slope break is usually offshore compared with the position of the wave agitated facies. The distal steeper portion shows gradients considerably less than the gradients in FTPs beyond the slope break (**Burchette1992**)

The transition from relatively flat or very low angle platform top to the usually steeper platform slope defines a geomorphic feature on FTPs that is called platform margin. Platform margin is typically located at the outer edge of the FTPs and signifies the position where low wave energy environments pass to higher energy environments. The part of the carbonate platform that is located landwards from the margin is called platform interior or inner shelf (Fig.2.14).

The platform margin in FTPs is the preferred location for frame-builders that form organic reefs. Reefs raise above the internal area and a platform rim is formed (**Schlager2005**).

Rims are wave resistant structures that form semi-continuous to continuous barriers along the platform margin which restrict circulation and wave action (**READ1982**). Rims typically are located at the platform margin but not all platform margins are rimmed. Rims may originally form between the shore and the geomorphic platform margin and rapidly prograde to the the platform edge. The area landwards from the rim is called lagoon and it is a low energy area usually not very deep, separated (or partly separated) from the sea by the reefs (Fig.2.14a).

Wave energy conditions and facies grain size have been used to distinguish platform segments on carbonate ramps that lack platform margins and platforms without pronounced slope break. Grain size is medium to fine in low energy, platform interior environments but coarse to fine near high energy environments

Non-rimmed carbonate shelf

inner shelf
grainstone/packstone

outer shelf
packstone/wackestone

slope
redeposited limestone

deep water carbonate
mudstone

(a) FTP geometry and facies distribution

Sabkha

Tidal Flats

Lagoon

Shoal

Shallow Open
Marine

Inner Ramp

Outer Ramp

Fairweather
wave base

Storm wave
base
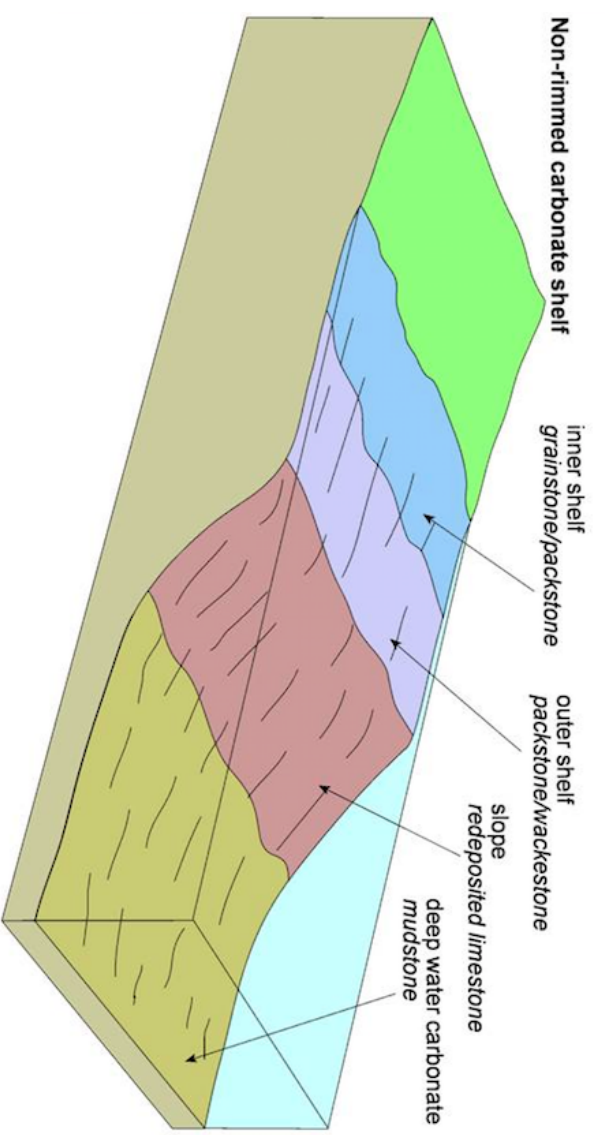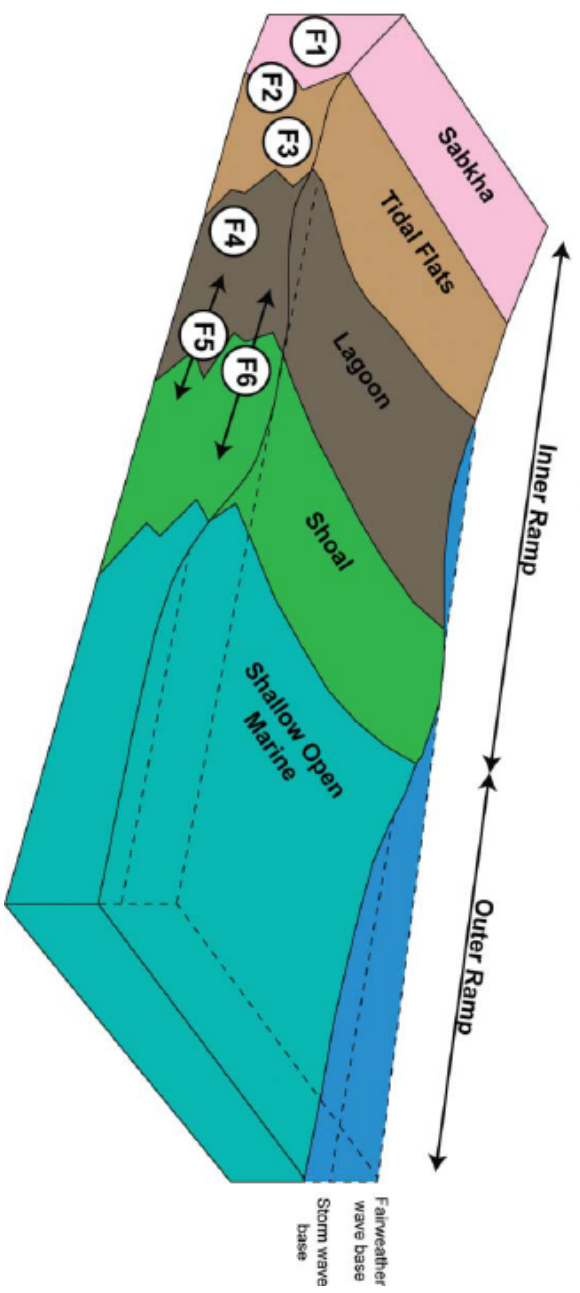
(b) Ramp geometry and facies distribution

Figure 2.14: Schematic of an FTP platform (a) and a ramp platform (b) geometry. The platform margin (geomorphic transition from outer shelf to slope in FTP) can be rimmed. Due to lack of geomorphic features in ramp geometries facies distribution follows hydrodynamic conditions. Modified from **Baniak2014**

36

(**Simo1993**) (Fig.2.14b).

2.2.6   System tracts

Carbonate facies models of ramps and FTPs and facies belts represent a static description of facies distribution over a carbonate platform. Relative sea level through geologic time rarely (if ever) stays constant. The changes in relative sea level affect the carbonate producing organisms and control the geometry of the platform.

Genetically associated stratigraphic units that were deposited during specific phases of relative sea level movements form subdivisions of a sequence and are called system tracts. System tracts are defined based on stacking patterns of the consisting strata, the position of the strata within the sequence and types of bounding surfaces. Even though the system tracts were initially defined based on the geometry of siliciclastic units, the concept has been expanded to include carbonates as well (**Hanford1993**). The system tracts reflect the interplay of relative sea level changes and carbonate production. Four system tracts are currently in use: (**Catuneanu2002**) (Fig.2.15)

- falling stage system tract (FSST). Strata that are deposited during falling sea level form the falling stage systems tract on the marine part of the platform. Depending on the magnitude of the relative sea level fall, the platform margin and the interior might get exposed. Shallow deposits prograde on slope or basinal age equivalent sediments. The FSST is called forced regressive system tract (FRST or FRWST);

- lowstand system tract (LST). It forms during the very early stage of sea level rise. The rate of carbonate production is higher than the rate of accommodation creation. Typical stacking patterns for LST consist of aggradation or progradation. A new margin with lagoon can form, lower and more distal than the HST margin. The LST is bounded by the sub-aerial unconformity and its marine correlative conformity;

- transgressive system tract (TST). As the rate of sea level rise increases, the accommodation creation rate becomes bigger than the production rate. Typical stacking patterns for TST consist of mainly retrogradation with some aggradation may be possible. TST is bounded by the maximum regressive surface at the base and the maximum flooding surface at the top;

- highstand system tract (HST). The highstand system tract occurs during the late phase of relative sea level rise when the rate of production exceeds the accommodation creation. Aggradation and progradation with normal

37
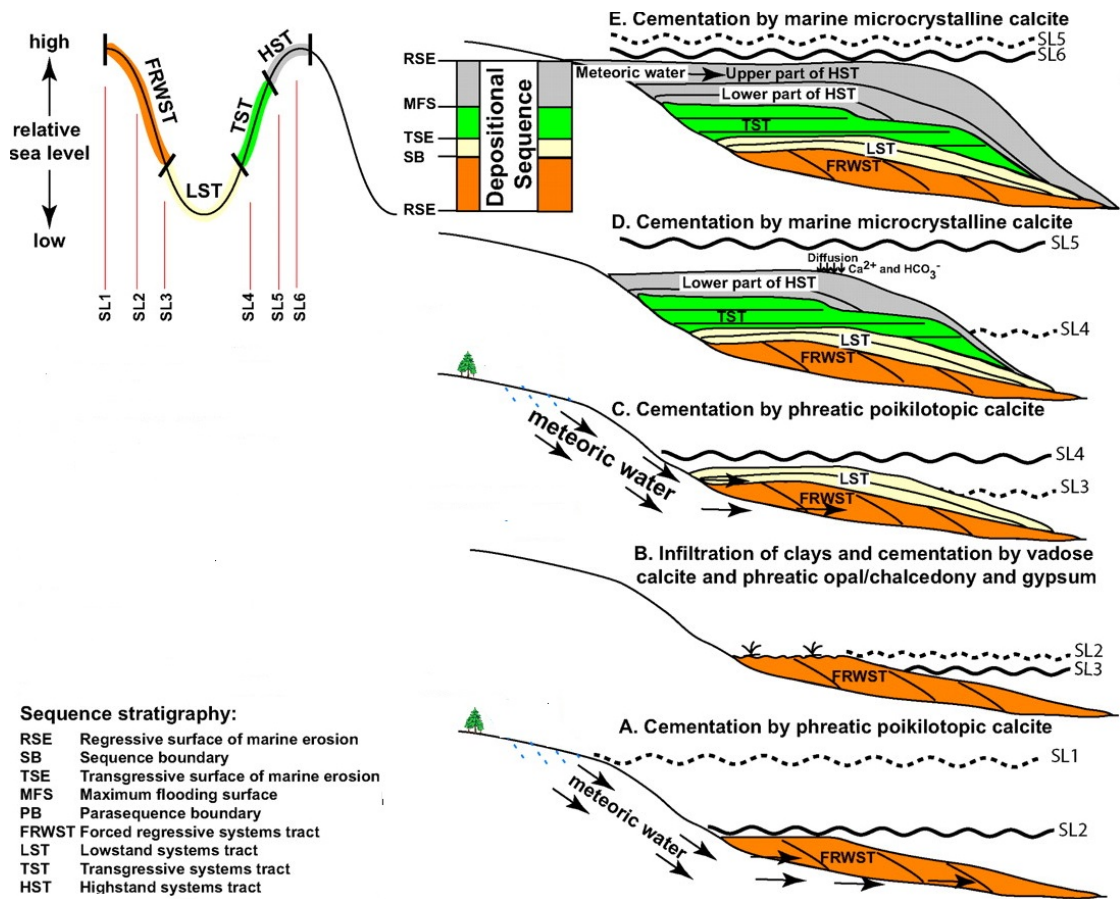
Figure 2.15: Cartoon depicting an ideal sequence with four system tracts on a FTP. During HST reefs form at the margin. Sea level drops below the margin and the margin and the interior get exposed during the FSST. Modified from geologyin.com

regression occurs. Reefs can form on the margin with lagoons on the interior. The HST is bounded by the maximum flooding surface at the base and by a composite surface at the top.

The FSST was described by **Hunt1992**. Older classifications of the system tracts also known and as the Exxon sequence stratigraphic model, include only the first three tracts. The results of natural process that are acting over shorter time scales are not preserved in geologic record. The effect of minor cycles in relative sea level, climate and wave action on carbonate production that can be studied only in modern systems, mainly create erosional and non-depositional discontinuities (**Hampson2003**).
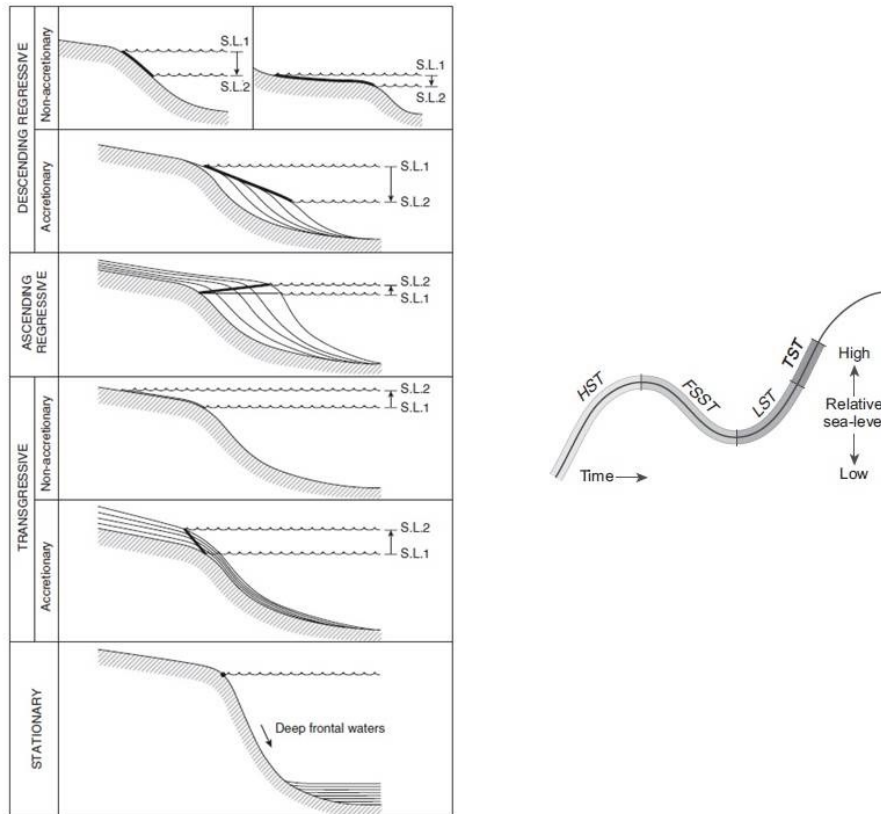
Figure 2.16: Shoreline trajectories (left) in relation to relative sea level movements and system tracts (right). Descending regressive shoreline trajectories correspond to FSST, while ascending regressive trajectories to either HST or LST. Transgressive shoreline trajectories correspond to TST. Stationary trajectories indicate stabilazation of shoreline position for some time and do not correspond to any system tract. Modified from **Helland-Hansen2009**.

2.2.7 Shoreline and shelf-edge trajectory

Relative sea level movements in combination with sediment supply define the system tracts and the position of the shoreline. Shorelines move laterally and vertically as a function of relative sea level change, sediment supply and and basin physiography. The cross-sectional shoreline migration path along the depositional dip is the shoreline trajectory (**Helland-Hansen1994**).

Based on the lateral and vertical movement of the shoreline trajectory **Helland-Hansen2009** identified six shoreline trajectory classes and linked them to system tracts (Fig.2.16). Lack of movement of the shoreline does not generate a trajectory but it is assigned a stationary trajectory. Stationary trajectories indicate that the shoreline has been fixed in front of steep slopes with sediment bypass to the basin. Stationary shoreline trajectories are indicative of FTPs.

The long term and large-scale effect of the interplay between sediment supply and accommodation is mapped by shelf-edge trajectory (**Helland-Hansen2009**). Even though self-edge trajectories can be seen as the long term result of stacked shoreline trajectories, shelf-edge (or margin) and shoreline are not the same.

Shoreline is the position where the bathymetry meets the sea level. Shelf-edge is a geomorhic feature of a platform, independent of the sea level position. Shelf-edge trajectories tend to be fixed or migrate basinward. Shelf-edge trajectories are subdivided into ascending, descending or flat.

A new algorithm has been developed in CarboCAT that identifies the platform margin position for every cross-section along the depositional dip. Cross-sectional plots of the margin position are analogous to shelf-edge trajectories because the new algorithm uses geomorphic features of the platform to identify the margin (see section 5).

2.2.8 Issues

2.2.8.1 Method, model, paradigm

One of the most fundamental issues with the duality of method and model is the need of clear distinction between observations and interpretations. Attention must be paid that all terms and definitions used by sequence stratigraphy to describe strata geometries are objective and do not confuse observations and interpretations.

Unfortunately, the most commonly used terminology contains several examples of observation-interpretation mixing. For example, the LST and the HST terms used to describe observable strata geometries while the same time assume that the strata formed during a specific point on the relative sea level curve. All cases of relative sea level curve are an interpretation based on some geometry (even sub-aerial exposure signifies relative sea level fall but not its magnitude) thus should not be used in the description of strata geometries.

The above definitions and terminology of sequence stratigraphy implicitly include another problematic issue. All terms describe variability of facies and strata along the depositional dip, ignoring variability along the depositional strike. **Madof2016** showed that along strike variability cannot be predicted by studying strata geometries along the dip (as it is usually the case from 2D along the dip seismic sections) and thus the results obtained from along the dip sections cannot always be generalised to 3D models.

In order to avoid the problem with the along the strike variability, all model runs generated in this project are three dimensional and were evaluated based on at least two along the dip cross sections at different positions on the platform.

Neal2009 identified the confusion between model and method in the definition
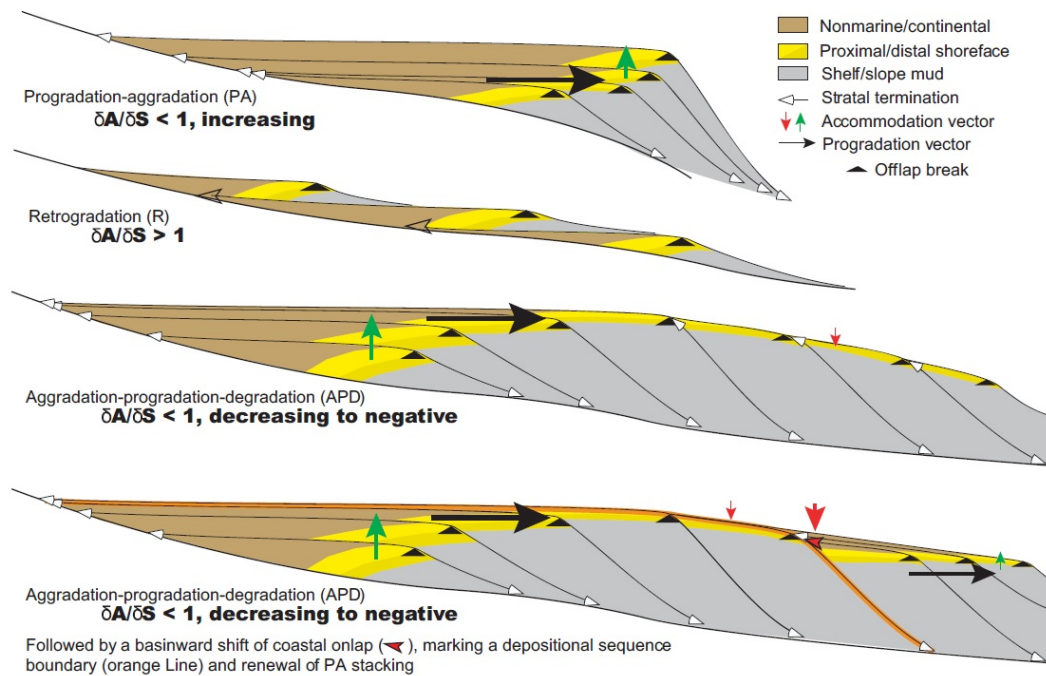
Figure 2.17: Stratal stacking patterns associated with changing rates of coastal accommodation creation rate δA and sedimentation rate δS. Following a sequence boundary (transition from APD to PA) the motif observed in the geologic record is progradation to aggradation (PA), retrogradation (R) and aggradation to progradation to degradation (APD). Negative accomodation rates indicates a decrease in accommodation through time (**Neal2009**).

of system tracts and proposed a physical stratigraphic, observation based strata recognition method. The authors defined an accommodation succession as the repeated pattern of progradation to aggradation (PA) followed by retrogradation (R) followed by aggradation to progradation, degradation (APD) and possible basinward shift.

The stacking patterns that comprise the accommodation succession (Fig.2.17) are defined based on the accommodation rate (δA) relative to sedimentation rate (δS):

1. $\frac{\delta A}{\delta S} < 1$ and increasing: Sedimentation rate is higher than the accommodation creation rate but the accommodation rate increases faster than the sedimentation rate. The progradation to aggradation (PA) stacking is defined;

2. $\frac{\delta A}{\delta S} < 1$ and decreasing: Sedimentation rate is higher than the accommodation creation rate and the sedimentation rate increases faster than the accommodation rate. The aggradation to progradation to degradation (APD) stacking is defined;

3. $\frac{\delta A}{\delta S} \geq 1$: Accommodation rate is higher than the sedimentation rate. The retrogradation (R) stacking is defined;

Based on the observational approach a sequence is defined at the beginning of increasing accommodation rate. The higher sedimentation rate generates strata
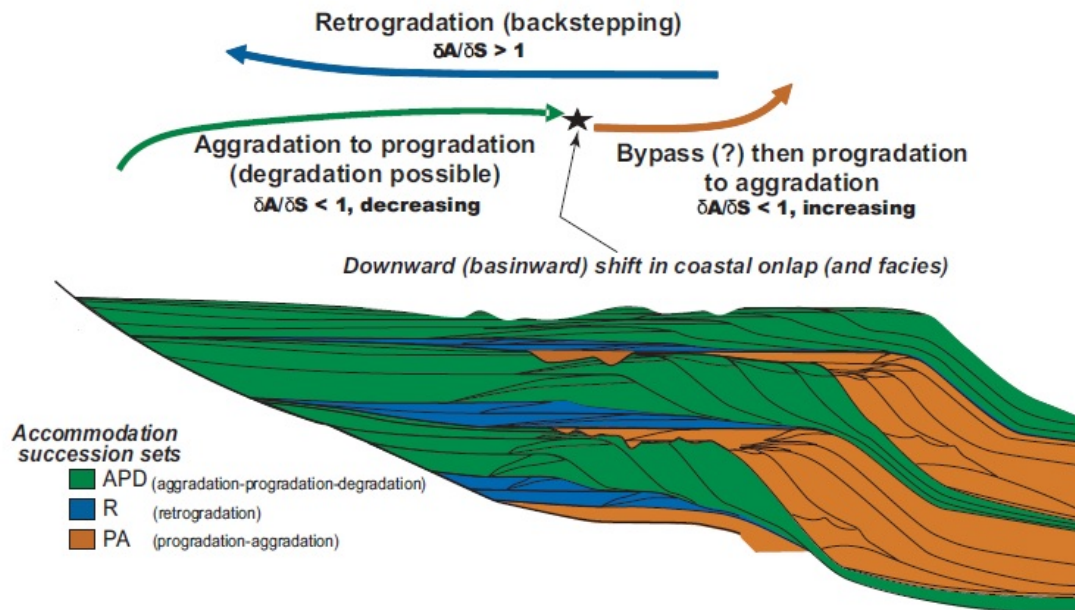
Figure 2.18: Accommodation succession and depostional sequences. The repeated stacking motif from PA to R to APD defines the depositional sequences. Modified from **Neal2009**.

progradation which turns to aggradation as soon as the accommodation creation rate is comparable to sedimentation rate ($\frac{\delta A}{\delta S} < 1$ and increasing, PA).

As the accommodation creation rate becomes greater than the sedimentation rate ($\frac{\delta A}{\delta S} \geq 1$), strata retrograde and the R stacking is formed. When accommodation creation rate slows down or sedimentation catches up with accommodation creation ($\frac{\delta A}{\delta S} < 1$ and decreasing) strata initially aggrade and then prograde. For cases with decreased accommodation a down-ward shift of proximal facies on top of distal ones is observed. A sequence boundary is readily identified at the end of this stage (Fig.2.18)

The use of objective criteria for the definition of sequences make stratigraphic interpretations more reliable, repeatable and independent of sea level terminology. System tracts are characterised by their key bounding surfaces and stacking patterns only, regardless of their position on a platform. Sequences are identified as the succession of strata starting with PA stacking and finishing at the end of the APD stacking. Furthermore, sequence boundaries are uniquely identified as surfaces that separate degradational (APD) below from progradation-agradation (PA) stacking patterns above. (**Neal2016**).

The observational approach **Neal2009** manages to separate observations from

interpretation in strata description but implicitly assumes that accommodation is the dominant control in strata formation. **Burgess2006a** showed that considering accommodation as the dominant control on sedimentary systems, underestimates the complexity of the systems. **Catuneanu2009** also pointed the role of additional controls on strata formation.

2.2.8.2 Uniquness of strata geometry

The large number of factors that control production of carbonate material, accumulation of carbonate sediment and the ultimately the formation of carbonate strata contribute to the complexity of carbonate accumulations and the uniqueness of strata geometries. Unique strata geometries are formed from a specific combination of parameter values. As a result, any other parameters values combination generates strata geometries that differ from each other.

Burgess2015 showed that the non-uniqueness of strata geometries is a serious issue for both obtaining a single explanation of the processes that formed some strata and for the ability to correlate strata. Non uniqueness occurs when the similar strata geometries are generated by different parameter values of controlling processes or from entirely different processes.

Even though it is logical to assume that the interplay of multiple controls can generate similar strata geometries, the non-uniqueness of strata is part of an active scientific debate. The value of non-unique strata geometries and numerical forward modelling results for sequence stratigraphy has been questioned (**Catuneanu2016**). **Burgess2017** disproved the arguments of **Catuneanu2016** and stressed that the best way to study the topic is by combining outcrop, seismic and numerical forward analysis.

Catuneanu2016 did not directly addressed the issue of non-uniqueness but provided some terminology. The authors identified 'unique' and 'non-unique' controls on the strata architecture and 'diagnostic' and 'non-diagnostic' criteria for identification of bounding surfaces.

This work tries to contribute to the ongoing debate about non-uniqueness by using numerical model to study Upper Cretaceous (Santonian) outcrops in South-Central Pyrenees, Spain (see chapter 8).

2.2.8.3 Cyclicity and strata order

Carbonate strata are typically interpreted to be part of repeated cycles with a specific hierarchy of high and low frequency sequences. The criteria for identifying this high and low frequency sequences are arbitrary but the cycles are commonly assumed to be the result of external forcing (**Muto2016**). Another assumption regarding carbonate strata is that external forcing (allogenesis) generates ordered strata while autocyclicity produces disordered strata geometries.

Carbonate strata cyclicity has been interpreted to include up to fifth order cycles with temporal duration of tens of thousands of years and strata forming metre thick parasequences with ordered vertical thickness patterns and vertical facies succession. The high frequency sequences and ordered strata have been assigned to high frequency external forcing and more specific eustatic sea level oscillations. Any observed discrepancies from the ordered strata thickness and facies transition have been attributed to the effect of autocyclicity (**Lehrmann1999**).

Numerical forward modelling examples show that for a wide range of allocyclic forcing parameters the resulting strata do not show the required evidence of hierarchy. High amplitude of relative sea level oscillations and introduction of stochastic elements in spatial distribution of sediment production and transportation tens to decrease the order of the generated strata (**Burgess2006**). Furthermore, sensitive dependence of strata geometries to initial conditions (**Burgess2005**), carbonate facies distribution based on facies mosaics (**Wright2005**) and carbonate facies distribution with water depth (see section 2.1.5.3) are processes that generate disordered allogenic strata.

Moreover, autocyclic strata are not necessarily any less ordered than fully allocyclic strata (**Burgess2006**). Numerical forward modelling showed that for a wide range of allocyclic forcing parameters the resulting strata geometries do not show the relevant stacking patterns. Furthermore, two forcing parameters with different frequencies must have significant difference in their amplitudes in order to generate distinctive strata cyclicity (**Pollitt2015**).

This project tries to contribute to the effect of autogenetic processes on strata geometry by studying the effect of allogenic and autogenic processes in carbonate platforms and more specifically on platform interior facies distribution. The newly developed sediment transportation algorithm is used to examine the formation and development of platform interior shoal bodies as the result of autogenetic processes with cross-platform sediment transportation conditions (see section 7).

3 Stratigraphic forward models

Stratigraphic forward modelling in this project was performed with CarboCAT. This chapter is a short review on other available stratigraphic forward models and a presentation of the original CarboCAT model. The chapter is divided in two sections. The first section presents some stratigraphic forward models and the second section is an in depth presentation of CarboCAT.

3.1 Review of SFM

Stratigraphic forward modelling is the quantification and simulation of the physical and biological processes acting over geological times to reproduce the morphology and internal structure of strata (**Watney1999**).

Stratigraphic forward models (SFM) are widely used to predict the behaviour of strata under known conditions. Realistic representation of natural processes involved in strata formation and behaviour by sophisticated SFM improves the degree of confidence of the predictions. The non-linearity of some process related to development and evolution of sediments and the sensitive dependence on initial conditions though, may limit the predictive power to general statistical properties (**Burgess2004**).

A number of stratigraphic forward models have been developed over the years for predicting both siliciclastic and carbonate strata architectures. Numerous models have been created to perform simple tasks (**Kaufman1991**), simulate specific features of siliciclastic platforms (**Pirmez1998**) or specific stratigraphies of carbonate platforms (**Bosence1994**, **Burgess2003**) to mention few among many.

More advanced models describe carbonate production, transportation and deposition and have been used to predict platform geometries and facies distributions for the whole platform. The research in the field is still active and improvements are still being developed.

All models simulate time iteratively. Each iteration is a time step that represents a finite amount of elapsed model time. The duration of each time step varies with model and modelling requirements.

A review of all the stratigraphic forward models that have been produced is difficult and starts with the first modern stratigraphic model by **Sloss1962**. **Paola2000** offers a review of quantitative stratigraphic models. SFM use a variety of mathematical approaches to model physical processes. The mathematical approaches include geometric models, diffusion models, fuzzy logic models and hydraulic models, all with strong and weak points (**Huang2015**).

The following short list consists of all purpose numerical SFM that simulate whole platform geometry. The purpose of the list is not to present and evaluate all SFM but rather to introduce models that simulate large scale (whole platform) and small scale (platform segment) facies heterogeneity and to examine their relation to CarboCAT.

A summary of input data for accumulation rates, lag time (start up phase) and accommodation is given in **Enos1991** where data are grouped in by depositional setting.

3.1.1   Synthetic stratigraphy of carbonate platform and basin system

A simple forward stratigraphic model was described by **Bice1988**. This model simulates a FTP with fixed segment lengths and a constant time step of 10ky. The model includes water depth-dependent carbonate production and subsidence as the sum of a constant function applied to the whole platform and sea level oscillations with a cosine function with variable period and amplitude.

The model constitutes one of the first attempts to model the whole platform geometry. Even though the model lacks transportation of sediments and does not describe carbonate heterogeneity, it contains the basic concepts that are used by most stratigraphic models that deal with carbonate strata. The basic concepts consist of initial bathymetry, eustatic sea level, subsidence rate and water depth-dependent production.

3.1.2   SEDPACK

SEDPAK is a 2D SFM developed **Strobel1989** that simulates evolution of mixed siliciclastic, carbonate platforms. Input parameters include initial bathymetry of the model, sea level fluctuations, subsidence rates, location and slip rates of possible faults and deposition and transportation of two siliciclastic facies (sandstone and shale) and one carbonate facies.

The initial bathymetry of the model is defined as the elevation points of 300 evenly spaced vertical columns (the vertical columns represent and will be referred here to as grid cells) along the transverse axis of the modelled platform. Accommodation is calculated based on sea level fluctuations and structural movements. The sea level curve for all time steps is calculated based on a second order sinusoidal curve. Structural movements can be subsidence and faulting with all faults assumed to extend to the bottom of the platform.

Carbonate production is calculated based on a water depth-dependent production rate and some limiting factors. The limiting factors include wave energy, the presence of reefs at the margin and the amount of siliciclastic material. The volume of siliciclastic material is user defined input.
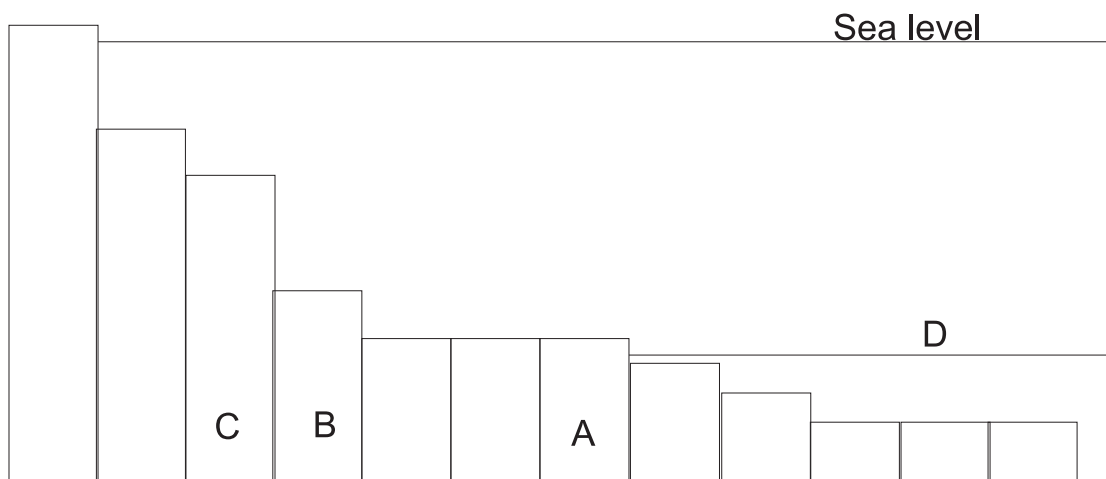
Figure 3.1: Effect of wave energy on carbonate production in SEDPAK. The effect of wave energy is restricted to grid cells above the user defined break depth (line D) and horizontal distance up to 3 cells away from the break point. The first grid cell seawards above the break depth threshold is A and thus waves affect cells A to B. Grid cell C is farther from the horizontal distance for wave action and thus waves do not affect carbonate production on cell C. From **Strobel1989**.

Carbonate production occurs only on grid cells that are below sea level with each factor limiting the amount of carbonate accumulation calculated from the water depth-dependent production rate. The effect of wave energy is quantified based on a user defined break depth and a user defined distance from the break depth (Fig.3.1).

Carbonate production also differs between lagoons and open sea conditions with different maximum production rates for each segment and is limited by the presence of siliciclastic material.

Sediment transportation and deposition (for both siliciclastics and carbonates) is performed based on the angle of stability between adjacent grid cells and a pre-defined distance for transportation for each facies and preserves mass. The angle of stability is defined as the maximum height difference between two adjacent grid cells above which no sediment deposition is allowed.

Depositional triangles (Fig.3.2) are used to define the amount of the deposited material on each position based on the distance from the source. The area of the triangle represents the available amount for deposition whereas the base length corresponds to maximum transportation distance for each facies.

Transportation of sediment in pre-defined distances is probably a good approximation for siliciclastic sediments even though it does not take into account the dynamic nature of the processes involved. Contrarily, the use of depositional triangles for carbonate strata generates linear belts with artificial boundaries on facies distribution.

47
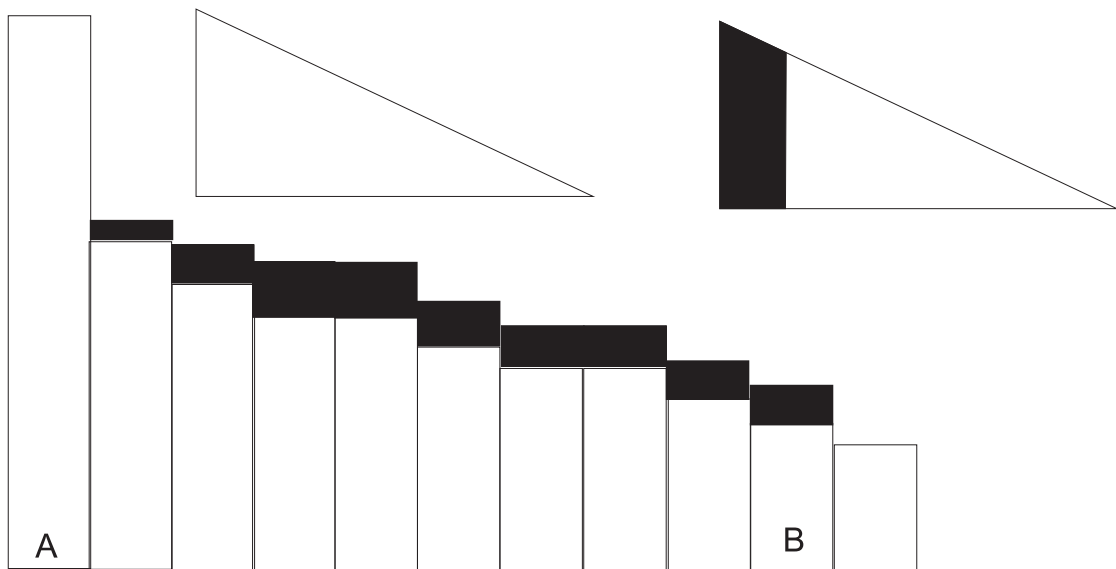
Figure 3.2: Sediment deposition based on angle of stability (bottom) and depositional triangles (top). (BOTTOM)-The height difference between grid cell A and the adjacent grid cell is higher than the stability angle and thus no sediment is deposited on A. The height difference between all other grid cells from there to B allows sediment deposition (black areas). (TOP) -A depositional triangle represents the total volume of material for deposition. The base represents the distance from the source and the height the thickness of the material that can be deposited at each distance (left triangle). Every time deposition occurs (black area on the right triangle) the relevant distance is removed from the base and the new height is defined. From **Strobel1989**

3.1.3   CYCOPATH

A two dimensional modelling of cyclostratigraphic pathways within carbonate platform, CYCOPATH 2D, was introduced by **Demicco1998**. CYCOPATH 2D incorporates sediment production, subsidence, sea level fluctuations and sediment transportation to calculate cyclic carbonate platform sedimentation.

Input parameters for CYCOPATH 2D consist of the width of the platform, initial bathymetry as the elevation of four points of the platform, subsidence rate and sea level fluctuations. Carbonate production is calculated based on depth-dependent rates. Sediment transportation and deposition is calculated from user defined percentages of carbonate material, horizontal distance for transportation, thickness of deposited sediment and preserves the geometry of the bathymetry.

CYCOPATH 2D was designed to generate large scale, whole platform cyclostratigraphic packages from relative sea level movements and various sediment transportation and deposition conditions. For this purpose CYCOPATH 2D distinguishes facies based on their depth of deposition and the model is able to reproduce the cyclic stratigraphy of sub-facies in shallowing upwards sequences.

The most important characteristic of CYCOPATH 2D is that it can generate both autocycles and allocycles in carbonates by changing the sediment transportation and deposition conditions. Sediment transportation in CYCOPATH 2D is performed based on a pre-described geometry.

Starting from the first grid cell below the sea level, a pre-defined proportion of the in-situ produced sediment is moved seawards, a pre-defined horizontal distance, where the material is deposited. Deposited material can vertically build-up to a pre-defined height above sea level (that represents the supratidal height) and form a tidal flat wedge. As the volume of the remaining material decreases, the thickness of the deposited material also decreases.

When the maximum elevation of the deposited material drops below a user defined water depth threshold the tidal flat is terminated and a new transportation/tidal flat cycle is initiated. Tidal flat drowning is generated by limited sediment deposition or by rising relative sea level. Cycles are formed when a tidal flat is flooded and carbonate production occurs above it.

Allocycles form under external forcing of eustatic sea level fluctuations. Autocycles are generated by transportation of sub-tidal sediments and deposition of supratidal flats (Fig.3.3).

Since the target of CYCOPATH 2D is to reproduce cyclostratigraphic packages, the model does not include dynamic conditions that control lateral sediment distribution and transportation and does not contain facies heterogeneity observed on carbonate platforms.

3.1.4 SEDTEC2000

A forward stratigraphic model (SEDTEC 2000) that predicts rock textures within simulated stratigraphies was presented by **Boylan2002**. The model simulates seven different types of sedimentary processes and their simulated lithofacies on a cross section. It incorporates carbonate production, fluctuating sea level, siliciclastic sediment supply, subsidence and differential compaction.

Carbonate productivity in SEDTEC 2000 is water depth-dependent and it is differentiated in three types based on the position on the platform, as interior, margin and pelagic. Each type has a different maximum production rate and all types are also restricted by distance from open water and siliciclastic sediment supply.

Entrainment and sedimentation in SEDTEC 2000 is performed based on sediment flux, a depth dependent erosion rate and a depth dependent sedimentation rate. The sediment flux at each point of the model is calculated based on a finite difference approach and the sediment supply.
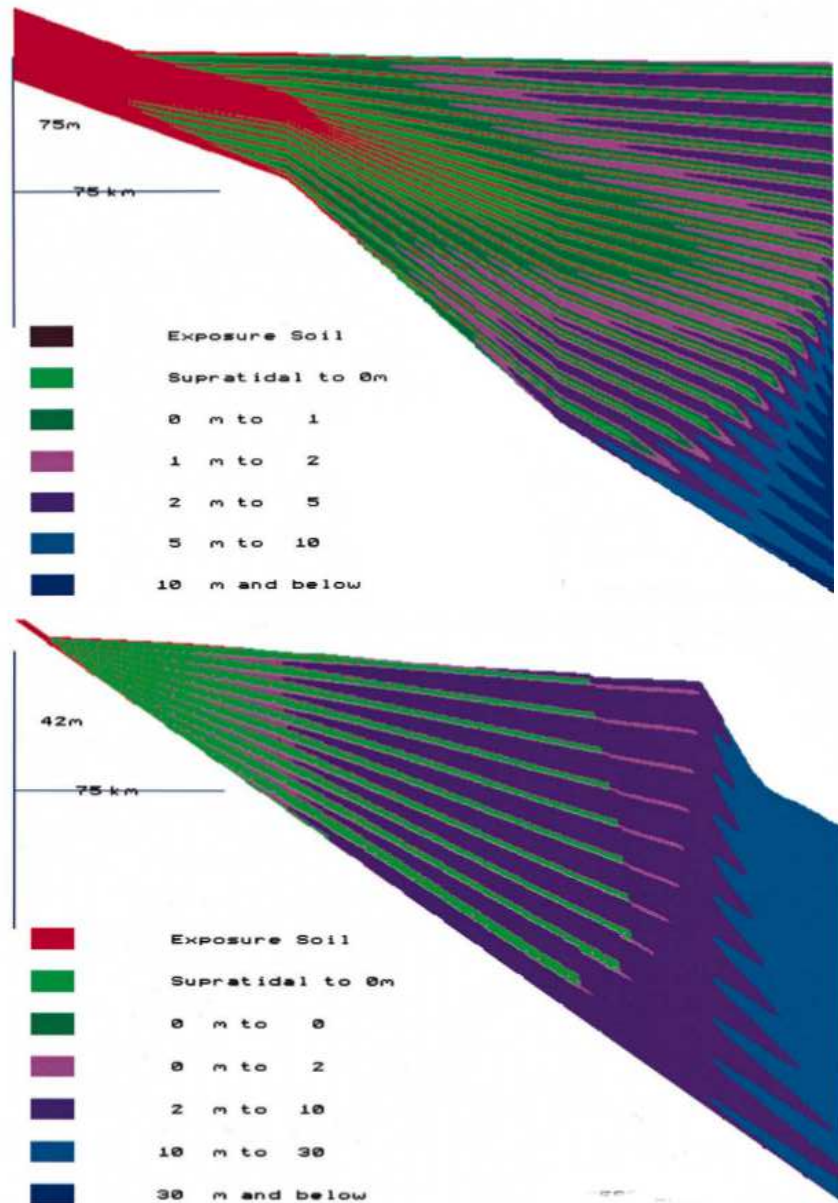
Figure 3.3: Examples of allocycles (TOP) and autocycles (BOTTOM) generated with CYCOPATH 2D. Allocycles are drowing of tidal flats under the influence of eustatic sea level oscillations. Autocycles are formed from transportation and deposition of sub-tideal sediments. From **Demicco1998**.

SEDTEC 2000 distinguishes seven sedimentary types based on the depositional environment and their products. The sedimentary types include restricted, shallow water environments that generate fine grain sediments, unrestricted, shallow water environments with in-situ produced coarse grain sediments and coarse or fine reworked material, unrestricted, deep water environments with pelagic sediments, and siliciclastic material with fine or coarse grain texture.

The sediments from each of the above types are characterised accordingly and keep the same character for the whole model even if the sediments have been transported, in a later time, to different depositional environments on the simulated platform.

Restricted and unrestricted waters are defined based on a water depth threshold that distinguishes shallow from deep water and a distance threshold away from the first deep water point. SEDTEC 2000 records the deposition depth and position of each point on the platform and the proportions for each process in that position. Combining these proportions, the material can be labelled as fine or coarse grained, as platform interior, margin or pelagic and as mud or grain dominated. This allows to characterise simulated facies based on the **Dunham1962** classification

SEDTEC2000 simulates large scale, whole platform heterogeneity and smaller scale, platform segments heterogeneity as well. The model provides a direct link between simulated sediment types and lithology and realistic description of natural processes for carbonate production and transportation. Facies can be plotted based on water depth at the point of deposition, depositional environment or facies texture (Fig.3.4).

Facies characterisation in SEDTEC2000 is performed based on user defined thresholds for water depth of deposition and dominant sedimentary processes. Even though the thresholds can be selected to representative values for each modelled area, the use of thresholds introduces artificial boundaries to the modelled facies and includes an element of interpretation in the model.

3.1.5 SIMSAFADIM

Simulation of Stratigraphic Architecture and Facies Distribution Model (SIMSAFADIM) is a three dimensional stratigraphic forward model for production, transportation and deposition of carbonates introduced by **Bitzer2002**. SIMSAFADIM is the three dimensional extension of a carbonate ecology model presented by the same authors (**Bitzer2001**) which includes simulation of flow, transportation and depositional process. An extended model that includes the effect of siliciclastic material on carbonate production was presented by **Gratacos2009**.
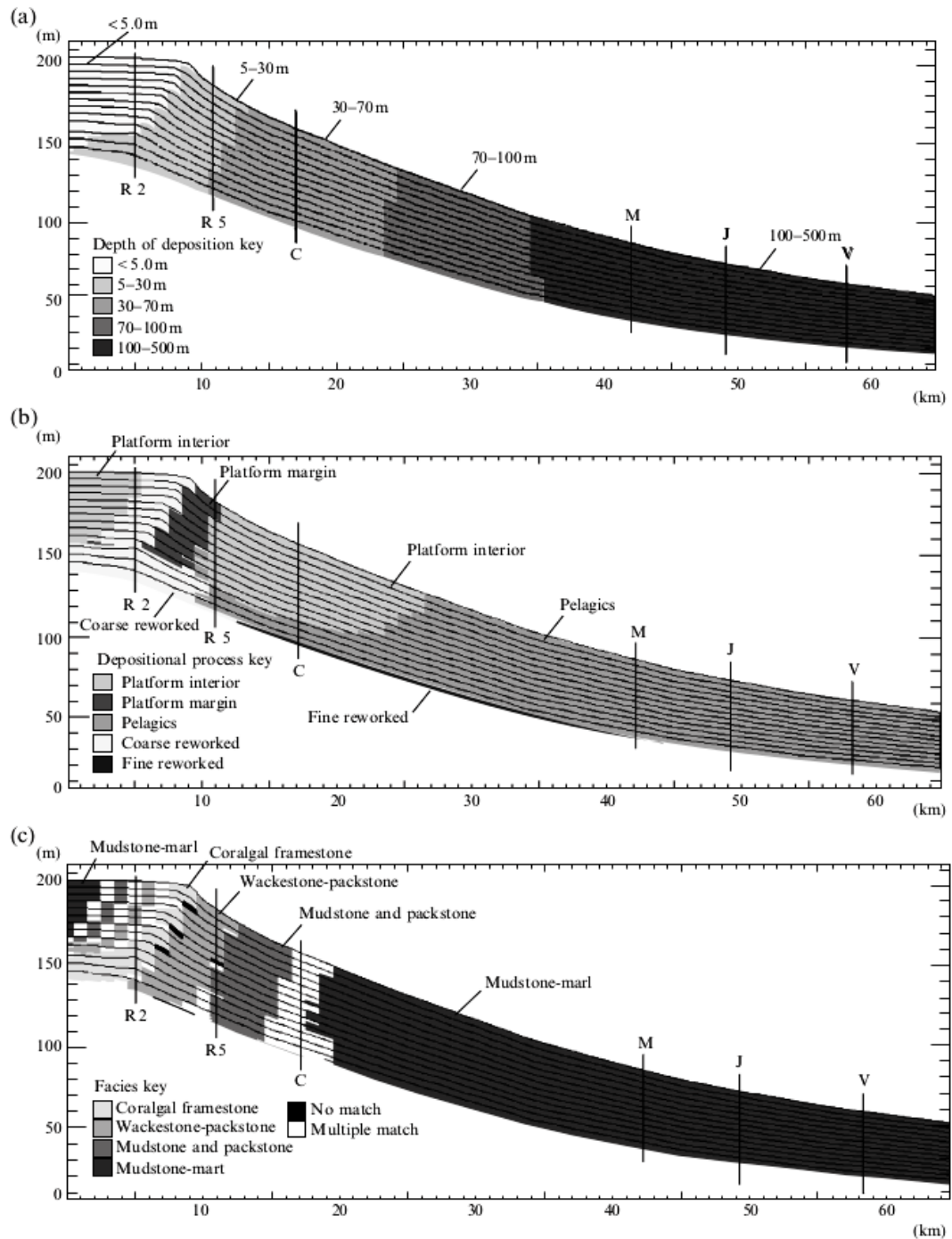
Figure 3.4: Possible outputs of SEDTEC2000 simulated stratigraphies. (a) Water depth of deposition display. Depending on the used thresholds, sub-tidal, peri-tidal and supra-tidal facies can be recognised. (b) Dominant processes of deposition display. Platform segments can be distinguished. (c) Textural distribution of simulated facies display. Modified after **Boylan2002**.

Carbonate production is modelled based on a predator-prey model while sediment transportation and deposition are based on advective, dispersive and diffusive terms. The model incorporates siliciclastic input that effects carbonate production.

The population of each species for each iteration is calculated based on a equation that includes internal competition of the population, effect from each of the other populations, the effect of siliciclastic mud and the effect of the carbonate material from the other populations. A simplified version of the population equation is shown in eq.(3.1).

$$\frac{dx_1}{dt} = \alpha * x_1 - f_{12} - f_{13} - f_{14} - f_{15} - g_1 - h_1 \tag{3.1}$$

where x_1 is the population of species 1, α is a coefficient that controls how quickly the population is growing and describes internal competition, f_{12} to f_{15} are the effect of the other carbonate species in the model on species 1 (the model considers five different carbonate species),the effect of each population is proportional to the populations size, g_1 describes the effect of siliciclastics on the species and h_1 the effect of the carbonate mud material produced from the other species. Positive values of $f_{12}, ..., f_{15}$, g_1 and h_1 reduce the growth of species and negative values increase it.

Once the number of each species has been calculated the produced carbonate material is computed. Carbonate production in SIMSAFADIM is water depth dependent. Each species has a different optimal water depth where it produces its maximum amount and a maximum depth below which no production occurs. All populations die above sea level. Carbonate production is calculated as the sum of all the material produced from all species. The spatial distribution of carbonate sediment is calculated as the percentage of the total carbonate material from each species for each model location.

Transportation and deposition in SIMSAFADIM are performed based on fluid flows and simulate suspended float transportation of carbonates. The material available for transportation from each species is released to the water column and is transported or deposited by water currents. Current velocities for each point on the platform are calculated based on water depth and taking into account diffusion, dispersion and advection terms.

3.1.6 CARBONATE3D

A three dimensional, numerical stratigraphic forward model, CARBONATE3D, that simulates stratigraphic and sedimentological development of mixed carbonate siliciclastic platforms was developed by **Warrlich2002**.

Carbonate production in CARBONATE3D is divided in three carbonate factories: benthic, shallow, open marine production; benthic, shallow, restricted production; and pelagic, open marine production. Each factory has its own maximum production rate. A stress function that limits carbonate production is defined for each factory.

The stress function eq.(3.2) includes terms that describe restrictions due to water depth, distance from open water and transported sediment. The restriction from the transported sediment is a measurement of the effect of sediment influx and turbidity in the water column.

$$
\begin{aligned}
P(x,y) &= SM \\
S &= D(z)U(x,y)L
\end{aligned}
\tag{3.2}
$$

where P is the carbonate production rate, S is the stress function, M the maximum production rate for each factory, D is the water depth effect, U is the effect due to distance from open water and L is the effect of transported sediment. Open water is defined as the first point seawards below a pre-defined water depth.

The stress function S is defined for each of the three factories according to the relevant conditions. The effect of water depth D is assumed to be the same for all factories. A number of depth dependent production rates can be adopted to describe different production profiles and can simulate marine or pelagic sedimentation.

Entrainment and deposition in CARBONATE3D is performed based on the shear stress over the platform, a deposition rate and the sediment type. The sediment type is defined by two parameters, the nature of the sediment and the grain size. Each parameter has two possible values. Sediments can be carbonates or siliciclastics and have coarse grained, or fine grained texture.

The volume of the available material for transportation and deposition is defined from a disintegration rate which depends on water depth and distance from the open water. Sediments disintegrate also from areas with slopes higher than the critical angle. The critical angle of failure is independent of water depth and depends only on the grain size.

Entrainment is calculated based on a critical shear stress. The critical shear stress for entrainment is calculated based on eq.(3.3)

$$
\tau_e = \theta \Delta \rho D
\tag{3.3}
$$

where θ is related to the angle of repose (in degrees) for each sediment type, $\Delta \rho$ (kg/m^3) is the excess density from the submerged sediment and D the grain size (mm).

The shear stress field is calculated as the sum of of the shear stress from currents, waves and slopes. The slope shear stress depends on the topography of the platform while the current and wave shear stresses depend only on water depth. Entrainment occurs when the local shear stress value is greater than the critical shear stress threshold for each sediment type.

Deposition occurs when the shear stress is below the critical shear stress threshold calculated in eq.(3.3). The transportation direction for each sediment type is controlled by its grain size. Coarse grained sediment follows the slope shear stress gradient while fine grained the wave/current shear.

The deposition rate is proportional to the sediment load in the water column and a characteristic transport distance. A short transport distance leads to deposition of most sediment close to the area where the shear stress becomes low enough for deposition. The characteristic transport distance is unique for each sediment type.

CARBONATE3D achieves simulation of facies heterogeneity at large, whole platform scale and smaller, platform interior and slope scale. Smaller scale, interior, margin, slope level heterogeneity is possible by distinguishing open water from lagoon environments, adjusting carbonate production accordingly and including the effect of wave energy and shear stress for sediment transportation.

A new algorithm developed for cross-platform sediment transportation in CarboCAT (see section 5.6) calculates shear stress the same way, eq.(3.3), as the CARBONATE3D. Cross-platform sediment transportation in CarboCAT represents entrainment, transportation and deposition of carbonate clasts from locally induced water currents and thus is related to shear stress levels on the platform. The development of new wave algorithm in CarboCAT (see section 5.4) also allows for distinguishing open water from lagoon environments and alter carbonate production accordingly.

3.2 CarboCAT

CarboCAT stands for Carbonate Cellular Automata and it is a deterministic, numerical model that calculates carbonate strata distribution in three dimensions. CarboCAT was originally developed by **Burgess2013** and several tools have been developed which can be found in relevant publications.

CarboCAT was selected based on numerous advantages over the other stratigraphic forward models. Firstly, CarboCAT is a deterministic numerical model that simulates the 3D distribution of carbonate facies. Secondly, it simulates whole platform scale and platform interior, margin and slope scale heterogeneity. CarboCAT also includes calculation of spatial competition of facies and thus attains simulation of smaller scale heterogeneity as well.

Thirdly, CarboCAT includes sediment transportation based on the bathymetric gradient and local hydrodynamic conditions. Furthermore, the effect of wave action on carbonate production is simulated based on waves generated from wind conditions over the modelled platform. Also, four in-situ producing factories and their equivalent transported factories allow for modelling facies heterogeneity with CarboCAT.

CarboCAT also accounts for formation of autocycles. Autocycles in CarboCAT are based on the interaction of sediment transportation with bathymetry and the effect of tidal movements on the modelled carbonate platform. Additionally, CarboCAT uses the concept of factories to represent the modelled lithology. Numerical factories can represent lithologies or single producing organisms based on the model cell size. Because numerical factories are directly represented in CarboCAT, no arbitrary thresholds are required. CarboCAT outcome is purely model results, completely separated by interpretation.

Furthermore, ecological simulation of carbonates in CarboCAT is performed with a competition for space approach. For this reason, in CarboCAT, each model cell can be occupied by one producing factory at each time.

3.2.1 CarboCAT formulation

CarboCAT is written in Matlab as a series of Matlab files (.m files) which contain different functions. The input parameters for CarboCAT consist of:

- the model dimensions y and x are the platform's map view dimensions;

- the total elapsed model time t and the duration of each time step;

- the subsidence rate;

- the initial bathymetry of the model;
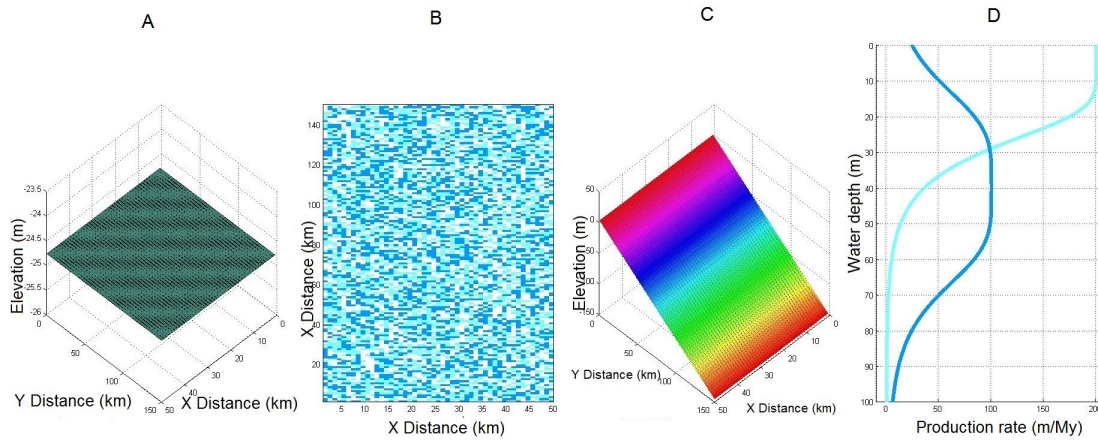
Figure 3.5: The graphical user interface in CarboCAT. The user can select the appropriate input parameters files and display them. Two in-situ producing factories (light blue and blue) are shown in this example. (A)-Total applied subsidence. (B)-Initial factory distribution. (C)-Final model bathymetry and (D)-Water depth-dependent carbonate production rates for each factory. All values shown here are for demonstrative purposes.

- the number of in-situ producing numerical factories, their spatial distribution and their production profiles;

- the eustatic sea level movements.

A Graphic User Interface (GUI) front end (Fig.3.5) allows the user to select the input parameters, visualise them and run the model. A number of Matlab graphics windows are generated to plot the model output.

CarboCAT divides the whole platform in a user defined number of model cells. Any number of model cells can be used and thus model cells in CarboCAT are scale independent. Their dimensions depend on the number of cells that are used and can range from a few meters to several kilometres based on the platform dimensions, the required model resolution and the PC characteristics.

This scale independence of CarboCAT is a powerful tool that allows studying heterogeneities at any scale and performing dynamic analysis of the modelled processes. Dynamic analysis requires more detailed description of the processes involved and more accurate definition of the problem in hand compared with a kinematic analysis.

Since no particular scale is required for the models cells in CarboCAT, the size of the model cell is defined based the modelling requirements. Model cells dimensions of a few hundred metres or even a km would suffice for large scale modelling of whole carbonate platforms with tens or hundreds of km horizontal dimensions. Modelling of smaller scale structures or specific areas of a carbonate platform, like platform interiors or slopes, with features tens or hundreds of metres in size, would require CarboCAT model cell dimensions of a few metres.

57

Based on the scale of the grid cell, each factory in CarboCAT can represent either a whole carbonate factory (see section 2.1.6) or different producing organisms. In case the grid cell size is selected to be several hundred metres or even kilometres, a CarboCAT factory is more likely to simulate a whole carbonate factory. Grid cells with size in the order of a few meters can represent single producing organisms.

Sediment transportation in CarboCAT can also represent different processes, based on the size of the grid cell. Modelling of large scale, whole platform geometries with model cell size of a kilometre could represent sediment transportation due to oceanic currents from salinity or temperature differences over a carbonate platform. Model cell of a few meters for modelling local features on the interior could represent sediment transportation due to local sources or tidal currents.

The calculated data from each function are stored in 3x3 arrays with dimensions as y, x and t, the user defined constant parameters. Each array is characterised as either *glob* or *stats*. *glob* and *stats* are two groups of functions and variables. Functions declared as *glob* or *stats* share the same copy of the *glob* or *stats* variables respectively. Any change or assignment to any of the variables in the group is immediately available to all other functions in the same group.

Usually the *glob* group contains arrays that are related to factories status or distribution and the *stats* group contains arrays that store some calculated property or statistics of the factories. The model preserves mass in the sense that the total mass in the model is deposited somewhere without any mass loss.

3.2.1.1 Model parameters

The majority of the necessary model parameters are defined in one file (Fig.3.6) that is input into CarboCAT. The model parameters can be organised in three groups that describe the geometry of the carbonate model, define carbonate production and control sediment transportation.

The first group includes parameters that define the geometry of the platform and are used to calculate the time duration of the platform, the subsidence rate, the eustatic sea level movements (ESL) and the initial distribution of factories.

The total duration of the platform, or the elapsed model time (EMT) is calculated based on the total duration of the modelled platform and the user defined time-step. Subsidence calculation is performed before the execution of the main code and produces a total subsidence rate map per time-step. Periodic eustatic sea level movement are described as the sum of two sinusoids. The initial topography and initial facies distribution are user defined as matrices with the bathymetry of each model cell and the factory in each model cell (see section 3.2.4.1, Fig.3.5), at the beginning of the model.

```
1   LongRamp              Model Name
2   100                      total Iterations
3   0.05                      timestep( My)
4
5   1                       Eustasy period 1 (My)
6   0                         Eustasy amplitude 1 (m)
7   1                       Eustasy period 2 (My)
8   0                         Eustasy amplitude 2 (m)
9
10  1                        Timesteps per CA iteration at max prod rate
11  1                        Timesteps per CA iteration at min prod rate
12
13  500                       Bathimetry difference between cells that get disconected in CA
14
15  2                        Number of producing factories
16
17  200                     Lithology 1 carb Production Rate (mMy-1)
18  3000                      Lithology 1 Surface light intensity
19  0.1                       Lithology 1 extinction coefficient
20  300                       Lithology 1 saturating light
21  4                         Lithology 1 transport product facies
22  0.5                     Lithology 1 max transported fraction of total production
23  1.5                     Lithology 1 minimum gradient for transport, m per km
24
25
26  100                     Lithology 2 carb Production Rate (mMy-1)
27  3000                     Lithology 2 Surface light intensity
28  0.1                      Lithology 2 extinction coefficient
29  50                       Lithology 2 saturating light
30  5                        Lithology 2 transport product facies
31  0.5                     Lithology 2 max transported fraction of total production
32  1.5                     Lithology 2 minimum gradient for transport, m per km
33
34
35  params/CARules2_4_10_6_10.txt                    CA rules input file
36  params/initialFaciesMapRandom_2facies_50_150.txt      initial condition facies map
37  params/initialTopographyLongRamp.txt            initial water depth map
38  params/subsidenceConst20m_50_150.txt                subsidence rate map
```

Figure 3.6: Initial model parameters file for two producing factories. All values shown here are for demonstrative purposes. Each line in the file is related to the specific parameter described on the right and thus all values in the file have to be in the same order.

59

The second parameter group includes parameters that define the production profiles of each factory and the cellular automata rules (see section 3.2.4.1). The volume of the produced material is calculated based on a water depth-dependent production profile for each facies and is calculated based on eq.(3.4) (**Bosscher1992**).

$$p_z = p_m \tanh\left(\frac{I_0 \exp(-kz)}{I(c)}\right) \qquad (3.4)$$

where z is the water depth in meters. The user defined parameters are p_m the maximum production rate in m /My , I_0 the surface light intensity in $\mu E m^{-2} s^{-1}$, I the saturation light intensity in $\mu E m^{-2} s^{-1}$, c the extinction coefficient. k is a constant.

Production of material from each factory corresponds to the growth rate of the relevant carbonate factory. The maximum carbonate production rates are usually obtained from production rates of modern carbonate systems. Alternatively, production rates can be inferred from accumulation rates of ancient carbonate systems.

The third group includes parameters that control sediment transportation. Sediment transportation in CarboCAT is performed as a single flow from each model cell (the source cell) that moves material to one or more model cells (destination cells). The path of each sediment flow and the amount of transported material are controlled by the local bathymetry and the user defined parameters for transportation.

The user defined parameters are:

- transported fraction of total production - The portion of the in-situ produced material that becomes available for transportation at each time step for each facies. Practically speaking, this parameter defines the volume of the material that is available for transportation;

- minimum gradient for transportation - The bathymetric threshold between two adjacent model cells for the transportation routines to initiate;

- the transported factory for each in-situ producing factory.

Transported material in CarboCAT is identified as factories and each transported factory represents a different model cell state. Definition of transported factories is user defined. Each transported factory can be uniquely assigned to one in-situ producing factory or more than one in-situ producing factories may generate the same transported factory or transported factories can be linked to transportation distance, with the user having the freedom to define the preferred definition
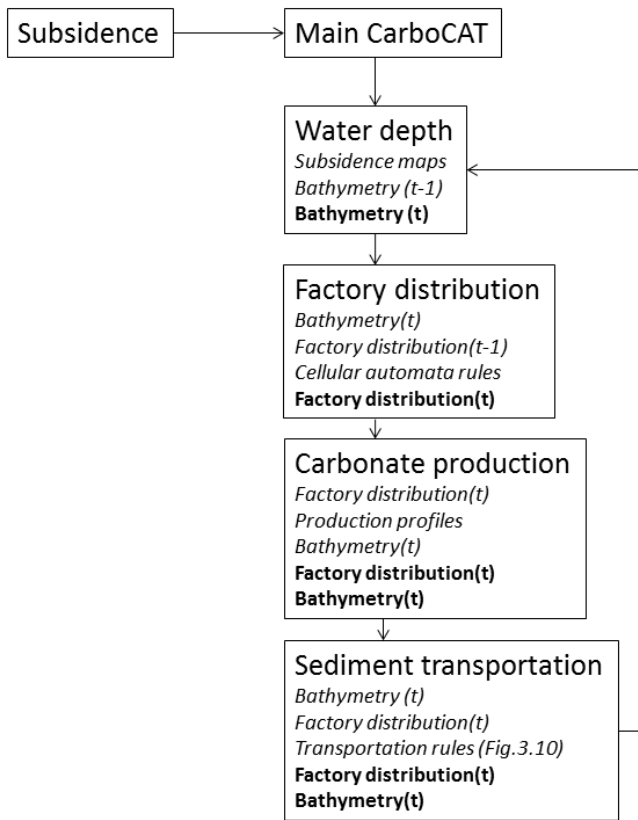
Figure 3.7: Chart showing the successive steps of CarboCAT. Rectangulars represent a set of Matlab functions. Each function takes as input one or more user defined parameters (see section 3.2.1.1) and the relevant arrays from either *glob* or *stats* groups and updates them. *t* is the current iteration. In italics: function input parameters and variables. In bold: output variables. Variables as both input and output imply that they are updated.

3.2.2 Main algorithm

Once the model parameters have been defined, CarboCAT is ready to run. Before the execution of the main CarboCAT code, tectonic subsidence is calculated based on the characteristics of possible faults in the platform. Tectonic subsidence is calculated by a standalone code developed to model carbonate systems in extensional environment (**Kozlowski2017**). The outcome from the tectonic subsidence code, one subsidence rate map per iteration, is used as input in the main CarboCAT code.

The main CarboCAT code, for each iteration and for each model cell, calculates the water depth based on the subsidence rate maps and the eustatic sea level movements. The water depth is used for the calculation of the new in-situ producing factories distribution based on the factories distribution from the previous time-step and the new bathymetry. Once the new factories distribution has been calculated, carbonate production is computed. After carbonate production has been computed, sediment transportation is performed. The processes of the main CarboCAT code are repeated until the total number of iterations has been reached (Fig.3.7).

3.2.3 Subsidence calculation

The subsidence calculated in the model generates the necessary accommodation for sediments to deposit. Since only subsidence is calculated in the model, accommodation in CarboCAT can be calculated only after the model has finished and sediment has been deposited. Accommodation can be measured as the thickness of the deposited material at each model cell for a specific time and varies with position on the platform (**Muto2000**).

3.2.4 Main CarboCAT code

3.2.4.1 Factories distribution

Factories distribution in CarboCAT is computed based on competition of producing factories for space and is described by the cellular automata. Cellular Automata (CA) are mathematical models that consist of a number of discrete sites (cells) with a finite set of possible values. The value of each particular cell is determined by the previous values of a neighbourhood of cells and a set of simple rules. At each discrete time step the rules are applied simultaneously to all cells and the new state of each cell is calculated. (**Wolfram1984**).

CA allows modelling of apparent randomness produced by a deterministic and thus better constrained method (**Burgess2013**). The complex behaviour generated by CA can be classified in four basic classes based on the patterns generated by the CA. Recognition of classes was based on one-dimension, two states CA. Recognition of classes in a two dimensional CA may not be as straight forward. The four classes are (Fig.3.8) (**Wolfram2002**, Chapter 6):

- class 1 is characterised by uniformity. Almost all initial conditions lead to exactly the same uniform final state;

- class 2 is characterised by repetition. There are many different final states consisting of set of simple structures that either remain the same or repeat every few steps;

- class 3 is characterised by complicated behaviour. Small scale structures occur in a otherwise random pattern;

- class 4 is a mixture of order and randomness. Localised structures are produced on their own, move around and interact with each other in complicated ways.
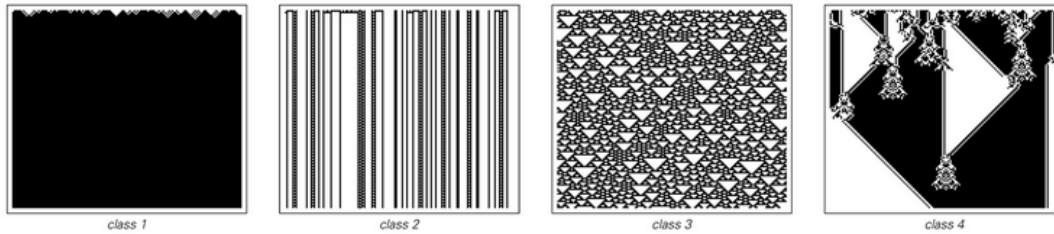
Figure 3.8: Examples of the four basic classes of behaviour in the evolution of CA with random initial conditions. From **Wolfram2002**.
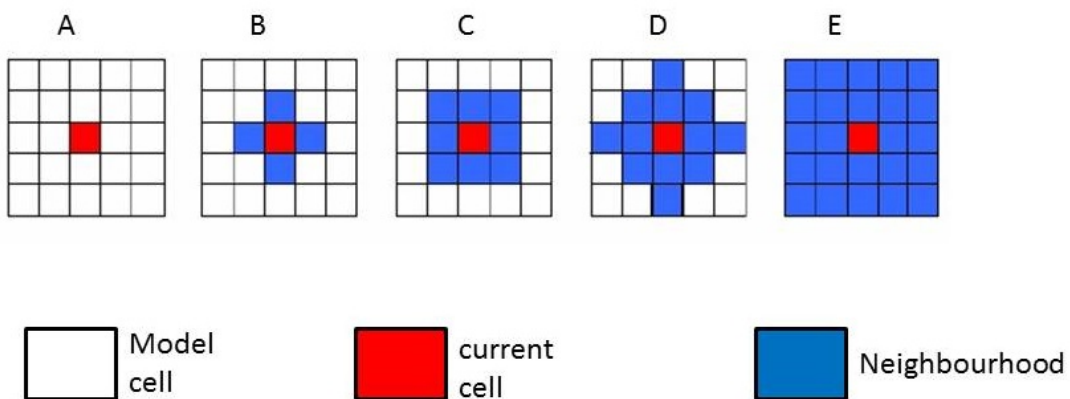
Figure 3.9: The cellular automata neighbourhood for a current cell (red) and different neighbourhood definitions. The current cell itself belongs to the neighbourhood as well. (A). Neighbourhood consisting of only the current cell. (B). Von Neumann neighbourhood consisting of five cells. (C) Moore neighbourhood of nine (current and eight adjacent) cells. (D) Neighbourhood consisting of 13 cells. (E) Neighbourhood consisting of 25 cells. This is the neighbourhood used for all the model runs in this project.

The neighbourhood of any cell in CA defines the number and distribution of surrounding cells, which combined with the CA rules control the state of each cell (Fig.3.9). CA rules define the minimum and maximum neighbours for the survival (cell remains in the same state) or triggering of new state (empty cells change their state). The size of the neighbourhood and the CA rules are user define parameters in CarboCAT.

In CarboCAT, a model cell occupied by one factory remains in its current state and thus the factory survives, only if the number of cells N with the same state in the neighbourhood is (**Burgess2013**).

$$s_{min} \leq N \leq s_{max}$$

for this factory, otherwise becomes empty.

Empty model cells can be colonised by producing factories only if the number of model cells N with one state in the neighbourhood is

$$c_{min} \leq N \leq c_{max}$$

for this factory, otherwise the model cell remains empty. A model cell might remain empty if none of the producing factories match the criteria for colonisation.

If more than one producing factories are present, CarboCAT provides two options for defining the order with which factories are checked for colonisation of empty model cells. The first option shifts the order in which producing factories are checked after each colonisation event. In a model run with two producing factories, factory 1 is checked first for colonising the first empty model cell. Factory 2 is checked only if factory 1 can not colonise the cell. For the second empty model cell on the platform and in the same iteration, the order has shifted and factory 2 is checked first for colonising the cell.

The second option, the order with which factories are checked is linked to their production rates at the water depth at which the cell is located. For the example with two producing factories, the factory with the highest production rate at the location of an empty model cell is checked first and the factory with lowest production rate, second.

3.2.4.2 Carbonate production rate calculation

Carbonate production in CarboCAT is calculated based on the production profiles for each producing factory and the factories distribution (Fig.3.7). Production occurs only on model cells that are under water and occupied by a producing factory. The amount of the in-situ produced material is calculated based on eq.(3.4).

The material that is actually produced is controlled by the competition for resources factor, with maximum production occurring only under optimal conditions. The optimal conditions are defined as the number of model cells with the

same state in the neighbourhood of each cell. If N is the number of model cells with the same state as the producing cell then (**Burgess2013**):

- if $N \leq s_{min}$ then no production occurs;

- if $s_{min} \leq N \leq n_{opt}$ then $P = P(z)\frac{N-(s_{min}-1)}{n_{opt}-(s_{min}-1)}$;

- if $N = n_{opt}$ then $P = P_z$;

- if $n_{opt} \leq N \leq s_{max}$ then $P = P(z)\frac{(s_{max}+1)-N}{(s_{max}+1)-n_{opt}}$;

- if $N \leq s_{max}$ then no production occurs.

where n_{opt} is the number of neighbours required for maximum production for each facies.

Model cells with more or fewer neighbours than the optimal range represent over-populated or under-populated areas respectively which limit the production rate compared to the production calculated with the depth production rate only.

Model cells above sea level, do not produce any material and there is the option to keep their previous state or become empty. As soon as the cells return below sea level, CA checks their state according to the new conditions in respect to the number of cells with the same state and adjusts their state as necessary. Empty model cells represent a depositional hiatus.

3.2.4.3 Carbonate transportation calculation

Sediment transportation is performed after in-situ production has been calculated (Fig.3.7). Sediment transportation is performed only from cells that meet all of the following four conditions (Fig.3.10):

1. are below sea level;

2. are occupied by a producing factory;

3. the available thickness for transportation exceeds the minimum threshold for transportation;

4. the bathymetric gradient with the adjacent model cells is greater than the minimum gradient for transportation threshold.

Because several flow paths can terminate in the same grid cell (destination cell), every time deposition of transported material occurs at a cell, the factory and the thickness of the deposited material is noted. A model cell may contain only one (or none) in-situ factory but several transported factories for each iteration.
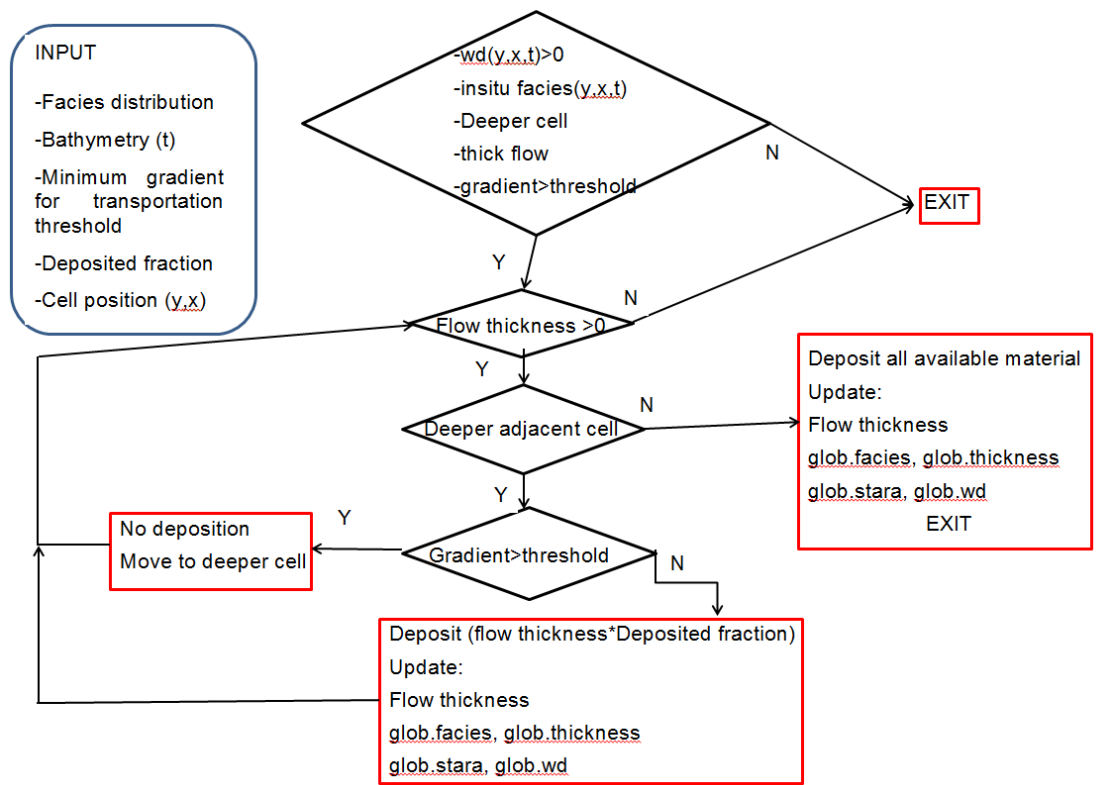
Figure 3.10: Flow chart showing the CarboCAT transportation routine. Diamonds represent conditionals and rectangulars Matlab functions. The algorithm is executed until there is no deeper cell or no more material to be deposited.

Deposition of transported material increases the bathymetric gradient at the destination cell. If the local gradient exceeds the minimum threshold for deposition, sediment deposition at the destination cell stops and sediment flows bypass the cell. Material is thus spread farther into the platform.

The minimum gradient for transportation which defines if sediment transportation or deposition will occur can have different values for each factory. Factories that represent carbonate strata with fine grain size can be assigned relatively low minimum gradients for transportation. Factories that represent strata with coarser grains are assigned higher minimum gradients.

A new algorithm has been specifically developed for sediment transportation from areas with low slope gradients and thus simulate cross platform sediment transportation (see section 5.6).

4 Seismic theory

Seismology is the study of the structure of the Earth using the propagation of seismic waves through the Earth. Seismic waves are elastic waves generated by natural and artificial sources. Earthquake seismology is the section of seismology that studies the generation and propagation of seismic waves from natural sources like earthquakes. Exploration seismology (or seismic exploration) studies the propagation of artificially generated seismic waves.

This chapter is a discussion about the basic principles of seismology in general and their application to carbonate rocks and the study of their structure and properties in particular. The chapter is divided in 3 sections. The first section presents the general principles of elasticity and wave propagation through the Earth and shortly discusses implications of wave propagation through the heterogeneous Earth. The next section presents the applications of seismology specifically to carbonates rocks. The last section discusses the concept of synthetic seismic imaging.

4.1 Elasticity and seismic wave propagation

Propagation of seismic waves through the earth materials is described by the generalised wave equation (**Cheng2014**)

$$Fo_i + (\nabla K_{ijkl} \nabla) v_{i,j} = \rho \frac{\partial^2 v_{i,j}}{\partial t^2} \tag{4.1}$$

where Fo are the body forces related to gravitational effects and the source terms, K is the elastic tensor that relates stresses applied to materials to the generated strain and v is the particle displacement.

External forces acting upon an infinitesimal cube in static equilibrium create some stress (τ) on the cube which in turn causes internal deformation of the cube and generates strain (σ). In general, the stress-strain relationship is complex and depends on a number of parameters such as pressure, temperature, stress rate, strain history of the material involved and stress magnitude among others.

The elastic behaviour of most Earth materials for the stresses involved in exploration seismology allows for defining a relatively simple stress-strain relationship. The most general form of the stress-strain relationship is a constitutive law for linear elasticity and is called the generalised Hook's law.

$$\tau_{ij} = K_{ijkl} \sigma_{kl} \tag{4.2}$$

where the indexes follow the summation convention. Indexes range from 1 to 3 (the Cartesian coordinates) while repeated indexes in a product indicate summation. W_{ijkl} is the elastic tensor which is also called stiffness matrix.

The generalised Hook's law assumes there is no energy loss as the material deforms under the effect of the applied stress (perfect elasticity). Materials obeying eq.(4.2) are called perfectly elastic. The generalised Hook's law as the stress-strain relationship is valid only for small magnitude stresses which are not common within the Earth's interior. Eq.(4.2) is assumed to be valid for small perturbations in stress with respect to the initial state of stress at which the strain is assumed to be zero.

The elastic tensor W_{ijkl} is a fourth order tensor with 81 components. Due to the symmetry of stress and strain tensors and thermodynamic considerations, the number of independent parameters reduce to 21 which is the minimum number of parameters necessary to define the stress-strain relationship for general elastic solids. Assuming isotropic materials and thus the same properties in all directions, the number of independent parameters reduces to 2 and the elastic tensor becomes

$$K_{ijkl} = \lambda \delta_{ij} + \mu(\delta_{il}\delta_{jk} + \delta_{ik}\delta_{jl}) \quad (4.3)$$

where λ and μ are called the Lamé parameters and δ_{ij} is the Kronecker delta function.

Using eq.(4.3), the generalised Hook's law for isotropic, perfectly elastic materials in static equilibrium takes the form of (eq.4.4)

$$\tau_{ij} = \lambda \delta_{ij} \epsilon_{ii} + 2\mu \epsilon_{ij} \quad (4.4)$$

The two Lamé parameters λ, μ in eq.(4.4) are also called elastic parameters or elastic moduli. The shear modulus μ is a measure of the resistance of the material to shearing. Fluids have zero shear modulus.

Practically, it is very difficult to explicitly solve eq.(4.1). High computational cost and the difficulties in separating all the wavefields involved, have led to a number of models that approximate solutions of the generalised wave equation (**Cheng2014**).

The body forces in eq.(4.1) are related to gravitational effects and the source terms. Gravitational effects are equal to elastic effects for signal frequencies in the range $10^{-3} - 10^{-4} Hz$ (**Scales1997**). Exploration seismics are generally interested in signal frequencies of a few tens of Hz and thus gravity effects can be neglected without significant loss. Further assuming that we are located on the far field of the source, the source effect on the particle motion is negligible.

Further simplification of the generalised wave equation is to assume that the media through which the waves propagate are homogeneous layers with velocity changes only at the boundaries between the layers. In this case the gradients of the Lamé parameters become zero within each medium.

By ignoring body forces and assuming homogeneous media eq.(4.1) simplifies to:

$$\rho\frac{\partial^2 v}{\partial t^2} = (\lambda + 2\mu)\nabla(\nabla v) - \mu\nabla \times (\nabla \times v) \qquad (4.5)$$

Eq.(4.5) will be referred here to as the homogeneous media wave equation. The homogeneous media wave equation is a much simpler equation than eq.(4.1) and several methods to solve it exist. Despite its practicality and extensive use, eq.(4.5) is valid only for layered, homogeneous, isotropic media with velocity changes only at boundary surfaces.

4.2 Implications of wave propagation

Seismic waves are the propagation of energy outwards from a source. The energy propagates through materials by setting the particles of the material in motion and thus the wave-front contains the wave energy as the potential energy of the oscillating particles. The potential energy of propagating waves is also called strain energy and is generated from the resistance of the material to the deformation (strain) caused by the applied stress.

Assuming that the material particles were initially static, the average stored work (strain energy) during a complete wavelength (λ) of a propagating wave for an infinitesimal volume is

$$W = \frac{1}{\lambda}\int_0^\lambda \frac{1}{2}k^2 A^2 G dx = 2\pi^2 \rho A^2 \omega^2 \qquad (4.6)$$

where $k = 2\pi/\lambda$, A is the amplitude of the propagating wave and μ is the shear modulus of the material through which the wave propagates.

The energy of a propagating plane wave is proportional to the square of the pulse amplitude and proportional to the square of its frequency.

The energy density in the propagation direction per unit time per unit area perpendicular to the wave-front is given by:

$$E^{flux}(t_1) = 2\pi^2 V_1 A_1^2 \rho_1 \omega^2 dS_1 \qquad (4.7)$$

where A_1 is the wave amplitude at time t_1, ω is the angular frequency and dS_1 is the surface area of the wave-front.

The energy density of the wave at a later time t_2 is:

$$E^{flux}(t_2) = 2\pi^2 V_2 A_2^2 \rho_2 \omega^2 dS_2 \qquad (4.8)$$

and because the energy flux remains the same through time

$$\frac{A_2}{A_1} = \sqrt{\frac{dS_1 \rho_1 V_1}{dS_2 \rho_2 V_2}} \qquad (4.9)$$

which means that the amplitude of a propagating wave varies inversely as the square root of the surface area of the wave front as the wave-front spreads out, and the elastic properties (velocity and density) of the medium through which the wave propagates.

4.2.1 Partioning of energy at an interface

When propagating body waves encounter areas where the elastic properties of the material change, the waves' propagation direction, velocity and amplitude change to accommodate the changes in the elastic parameters.

Assuming that the change in the elastic properties of the material occurs only at either sides of an interface between two mediums with constant properties and using ray theory, the change in direction and amplitude of the body waves can be calculated.

The direction of propagation of each wave is calculated using the Snell's law

$$\frac{V_1}{V_2} = \frac{\sin \theta_1}{\sin \theta_2} \qquad (4.10)$$

where V_1, V_2 are the wave velocities above and below the interface and θ_1, θ_2 are the incident angle and the angle of refraction.

The energy partitioning at the interface is controlled by the changes in the elastic properties across the interface. Conservation of energy at the interface requires the stress and strain on either side of the interface to be the same.

The energy partitioning is quantified with the reflection Re and transmission Tr coefficients. The reflection coefficient is defined as the ratio of the amplitude of the reflected wave to the amplitude of the incident wave of the same type. Similarly the transmission coefficient is the ratio of the amplitude of the transmitted wave to the amplitude of the incident wave of the same type.

$$
\begin{aligned}
Re &= \frac{A_2}{A_1} \\
Tr &= \frac{A_3}{A_1}
\end{aligned}
$$

where A_1, A_2, A_3 are the amplitudes of the incident, reflected and transmitted waves respectively.

Reflection and transmission coefficients and thus the partitioning of wave energy depends on the angle of incidence at the interface. Zoeppritz derived the

70

reflection and transmission coefficients of a plane wave at a plane interface between two material with different elastic properties for any angle of incidence.

A special case of Re and Tr is the normal to the interface incident angle. In this case the angle effect on energy partitioning disappears and the reflection and transmission coefficients are calculated from:

$$
\begin{aligned}
Re_0 &= \frac{\rho_2 V_{P2} - \rho_1 V_{P1}}{\rho_1 V_{P1} + \rho_2 V_{P2}} \\
Tr_0 &= \frac{2\rho_2 V_{P2}}{\rho_1 V_{P1} + \rho_2 V_{P2}}
\end{aligned}
\tag{4.11}
$$

where ρ is the density (kg/m^3) of the medium through which the seismic wave propagates and V is the seismic wave velocity through the medium.

The Earth, through which seismic waves propagate, is a laterally and vertically heterogeneous medium. The scale length of heterogeneities in the Earth ranges over 8 orders of magnitude from global heterogeneities with scale length tens od thousands of kilometres to well log heterogeneities with scale a few millimetres (**Wu1988**).

The effect of heterogeneities to the propagating seismic waves depends on the scale length of heterogeneities compared to the wavelength of the wave. **Wu1988** defined several different propagations regimes based on the relation between the wavelength of the propagating wave and the size of the heterogeneity.

Depending on the propagation regime various analytical methods have been used to describe the scattering of the propagating waves.The analytical methods vary from Rayleigh scattering for very small heterogeneities to ray theory, to Born and Rytov approximations to finite difference methods to parabolic approximations for very large (global scale) heterogeneities (**Wu1988**).

4.3   Controls on acoustic impedance of carbonate rocks

Most of the work regarding velocities, densities and acoustic impedance calculations has focused primarily on siliciclastic strata. Reflectivity in siliciclastic strata, in most cases, is generated by lithological differences of the strata. Carbonate depositional environments and carbonate strata differ from siliciclastics in ways that directly effect reflectivity.

The main factors controlling the elastic properties of carbonates in decreasing order are (**Eberli2003**):

1. diagenetic process that directly affect the amount and type of porosity. Cementation, that can take place even in very shallow depths and early ages fills the primary porosity and lithifies the sediments, is the most important control on elastic properties. Compaction becomes more important at greater burial depths;

2. porosity and pore type. There is a general trend of decreasing V_P with increasing porosity but with large scatter. Velocity changes follow much more closely the type of porosity. Inter-particle porosity has less effect in velocity compared to micro-porosity, moldic and intra-particle porosity;

3. grain size and shape. The grain shape and the grain-to-matrix diameter control the size and types of grain contact and the elastic properties;

4. mineralogy. Mineralogy in carbonates is less important than in siliciclastics. There are some velocity differences between dolomites and calcites as dolomites are denser but there is no clear separation.

Reflection coefficients higher than ±0.02 generate reflections that can be imaged with modern seismic techniques (**Palaz1997**). Reflection coefficient of ±0.02 corresponds to 5% difference in acoustic impedance between two facies. Low impedance contrasts between similar mineralogicaly carbonate facies generate reflected waves with low amplitude irrespective of the layers thickness involved.

Because of early cementation and diagenesis, the velocities of carbonates are generally higher than the velocities of siliciclastics at comparable depths. Higher velocities imply that for a given frequency the wavelengths of propagating waves are longer in carbonates than in siliciclastics which directly affects the resolution of the seismic images.

The depositional environment affects carbonate strata geometry and their reflectivity. The typical carbonate platform geometry (see section 2.1.2) shows significant changes in reflectivity. Carbonate platform interiors with restricted water circulation may contain tens or hundreds of meters thick sediments but display very low reflectivity. The combination of similar deposited facies with lower resolution in carbonates, generally generates low reflectivity on carbonate platform interiors (**Palaz1997**).

Contrary to platform interiors, slopes usually show better reflectivity. Even though sediment thickness is less on the slopes, greater facies heterogeneity (in the form of deposited transported facies and breccias among others) on the slope and possible presence of siliciclastics generate brighter reflections (**Palaz1997**).

4.3.1 Porosity and fluids substitution

Porosity affects the wave propagation through carbonate strata. Porosity as empty spaces in the crystals of the medium, controls the elastic properties of the medium, with higher porosity indicating more empty spaces and thus less dense crystal structures. Additionally to the effect of porosity on the density of the crystal, the type and shape of porosity also affects the elastic properties of carbonates.

Elongated, interconnected pores result to lower velocities compared to poorly connected, spherical pores for the same porosity. Flat elongated pores are more compressible than spherical ones and thus elongated pores have greater effect on the bulk modulus of the surrounding crystal frame (**Wang2001**).

The type of fluid present in the pores and the degree of fluid saturation also affects the elastic properties of carbonates. Porous rocks saturated with less compressible fluids have high velocities and thus higher impedances compared to unsaturated or completely dry pores. Dry pores contain air in their pore space which air is more compressible compared to water or other fluids.

Hydrocarbon gases are highly compressible under reservoir conditions with bulk moduli values of $0.01 - 0.2 GPa$. Other fluids present in many reservoirs is carbon dioxide and hydrocarbon oils. The elastic properties of these fluids are pressure and temperature dependent and formulas have been developed to estimate them (**Wang2001**).

Water shows abnormal properties relative to other fluids since under atmospheric pressure water shows maximum density at 4^oC and has high boiling points. Unlike other hydrocarbon fluids in which acoustic velocities decrease monotonically with increasing temperature, acoustic velocity in water increases with increasing temperature.

Acoustic velocity of water reaches a maximum value at around 73^oC, and then decreases as temperature further increases at atmospheric pressure. Special formulas that take into account the amount of dissolved material in the water have been developed for calculating the elastic properties of water (**Wang2001**).

The effect of fluids on the elastic properties of strata is quantified with Gassmann equation. Gassman equation calculates the bulk modulus of saturated rocks based on the porosity of the strata, the bulk moduli of the rock frame and the mineral matrix and the pore filling fluids (**Smith2003**).

$$K_{sat} = K^* + \frac{(1 - \frac{K^*}{K_o})^2}{\frac{\phi}{K_{fl}} + \frac{(1-\phi)}{K_o} - \frac{K^*}{K_o^2}} \qquad (4.12)$$

where K_{sat} is the bulk modulus of the saturated rock, K^* the bulk modulus of the rock frame, K_o the bulk modulus of the mineral matrix, K_{fl} the bulk modulus of the pore fluid and ϕ the porosity.

Eq.(4.12) is based on some assumptions. First, assumption is that the rock matrix and the pore frame are homogeneous and isotropic. Most rocks can be considered isotropic over one wavelength in typical exploration cases. Problems arise for cases where several minerals with large contracts in elastic properties are present.

Second, assumption is that the pores are interconnected and fluid can flow freely. Carbonates that might have multiple types of porosity and low porosity
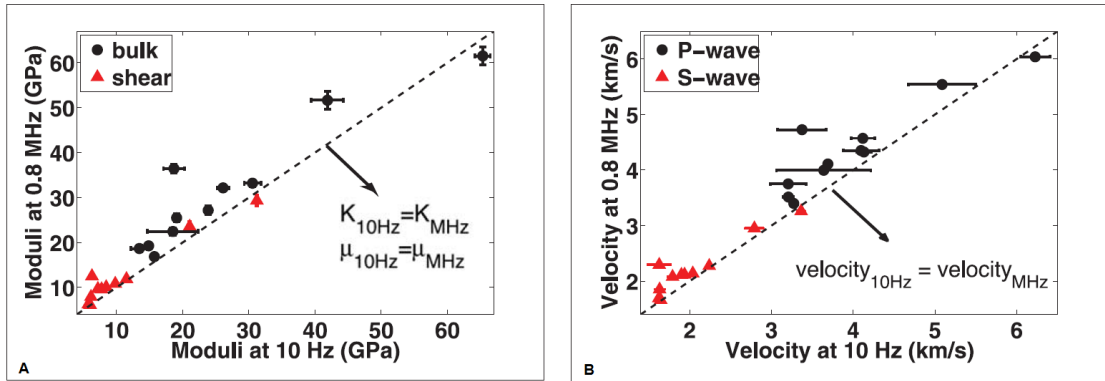
Figure 4.1: (A) Bulk and shear moduli of carbonate samples at 31 MPa differential pressure and fully brine saturated conditions at seismic frequency (10 Hz) and ultrasonic frequency (0.8MHz). The dashed line represents where the moduli at both frequencies are equal. On average, there is a 23% increase for the bulk modulus and 12% for the shear modulus from 10Hz to 0.8 MHz. (B) P-waves and S-waves velocities of carbonate samples at the same conditions as (A) at 10Hz and 0.8MHz frequencies. The dashed line represents where the velocities at both frequencies are equal. On average, there is 9.5% increase in the P-wave velocity and 5.8% increase in the S-wave velocity from low to high frequencies. Modified after **Adam2008**.

rocks violate this assumption. Third, the pore fluids do not interact with the pore matrix, which is not valid for many carbonate rocks.

Furthermore, Gassmann equation is derived for zero frequency and is valid for low frequencies and long wavelengths. For higher frequencies other formulations have been derived (**Smith2003**) but the Gassmann equation is still used.

Seismic velocities, bulk and shear moduli of carbonate strata are dispersive, their values increase with increasing frequency (Fig.4.1). The dispersivity of the elastic moduli is attributed to changes on pore fluid behaviour with frequency (**Adam2008**).

The pore fluids have more time (at low, seismic frequencies) or less time (at high, ultrasonic frequencies) to relax after the wave has passed. Additionally, preferential propagation of the waves through faster paths at high frequencies effect the elastic moduli as well (**Adam2008**).

Presence of fluids in the pores (fluid saturation) affect the shear modulus, contrary to the Gassmann assumption, with both strengthening and weakening effects (Fig.4.2). The change in the shear modulus is a result of interactions between the pore fluid and the rock, which interactions alter the rock frame properties (**Baechle2005**).

Shear weakening and strengthening by fluid substitution is controlled by pore
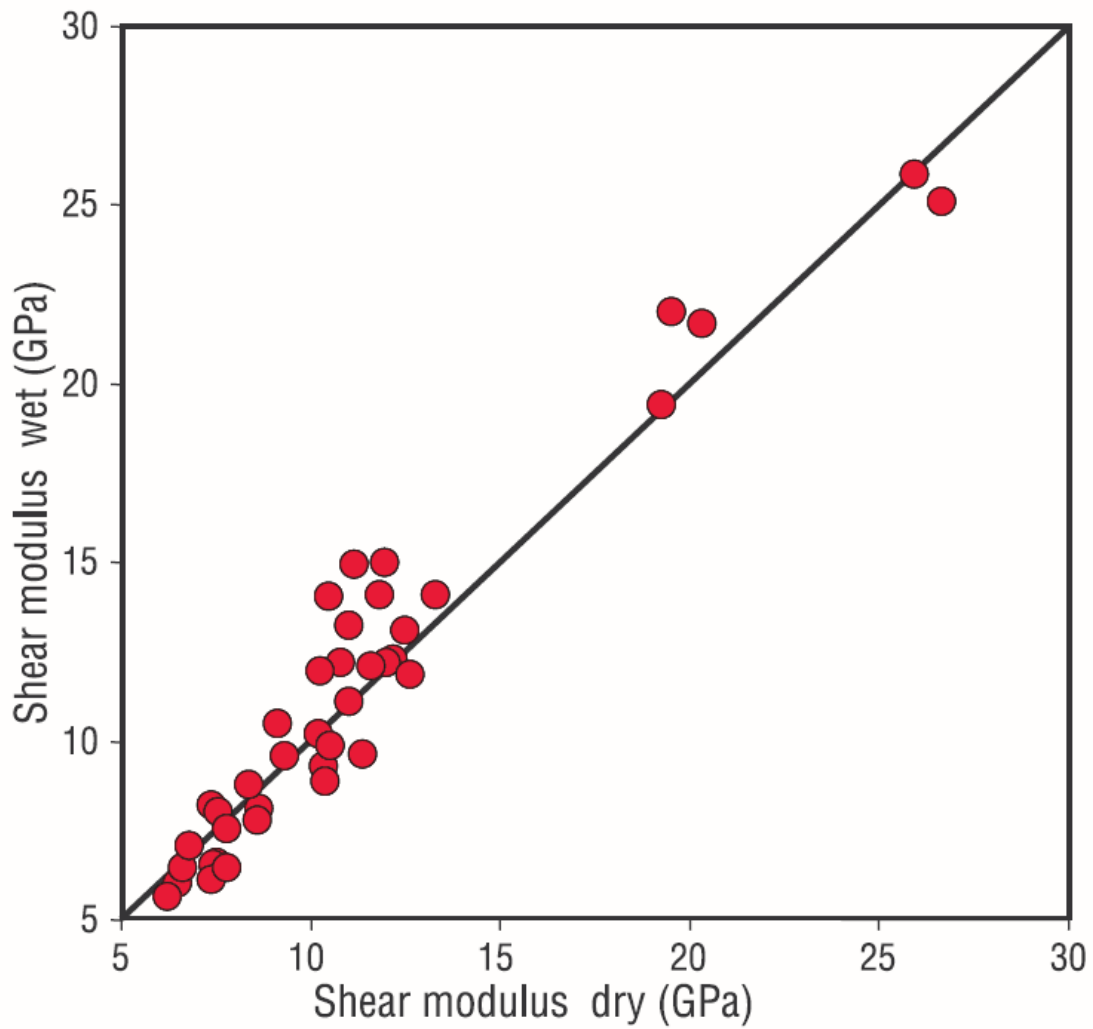
Figure 4.2: Changes in shear modulus of carbonates with saturation. Both shear strengthening and weaking occur. The line indicates where dry and saturated shear moduli are equal. From **Baechle2005**.
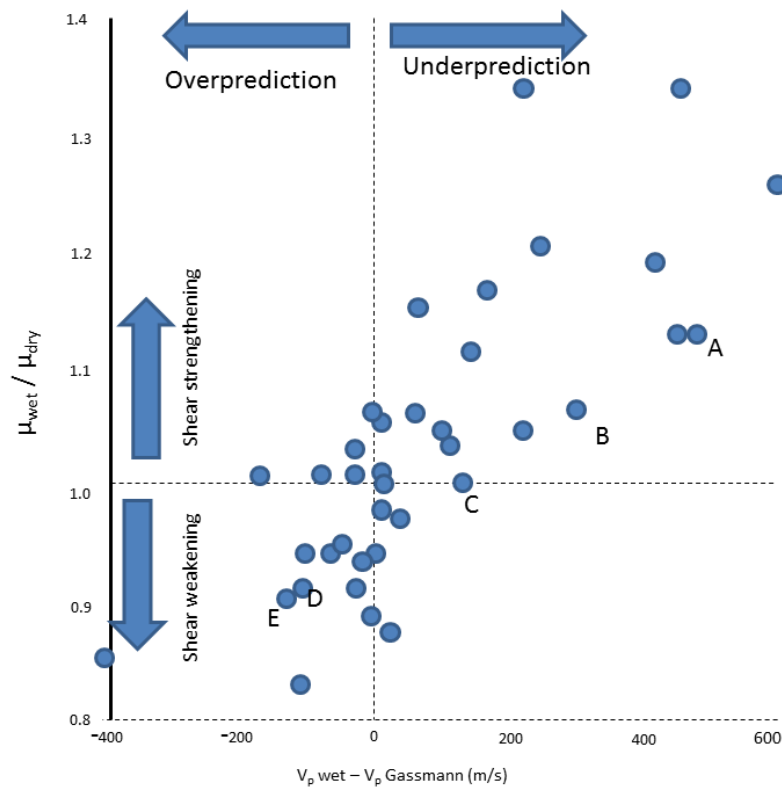
Figure 4.3: Plot of μ_{wet}/μ_{dry} versus $V_{Pwet} - V_{PGass}$ at 40 MPa effective pressure, displaying the changing shear-moduli effect on velocity prediction. Points A and B represent re-crystallised limestones with intercrystalline porosity. Point C represents a framestone with intraparticle porosity. Points D and E represent grain-stones samples with high amount of micro-porosity. Modified after **Baechle2009**.

types and grain-to-grain contact for any reservoir effective pressure. The differential or effective pressure of a reservoir is the difference between the overburden and the fluid pressure of the reservoir. The overburden pressure is the confined pressure exerted to the reservoir rocks by the overburden strata. The fluid pressure is the pressure from the fluid mass in the reservoir.

High amount of micro-porosity is related to shear weakening with fluid saturation. High amount of inter-crystalline or inter-granular porosity tend to show shear strengthening with saturation (Fig.4.3) (**Baechle2009**).

The general porosity in carbonates should be distinguished to two types. Macroporosity, usually inter-grain similar to siliciclastic strata and micro-porosity characteristic of carbonates (**Baechle2008**). Micro-porosity has more significant effects on elastic properties of carbonates than macro-porosity (Fig.4.4-A and B). Micro-porosity produces low seismic velocities independent of the stiffness of the mineral grain.

Micro-porosity could be in the form of intra-grain, vuggy or moldic porosity. Micro-porosity changes the elastic properties of the rock matrix which is considered soft material. The effect of micro-porosity on the elastic properties is best described by assigning a softer matrix stiffness (K_o') due to micro-porosity compared to the stiffness of the matrix related to macro-porosity (K_o in eq.(4.12)) (Fig.4.4-C)
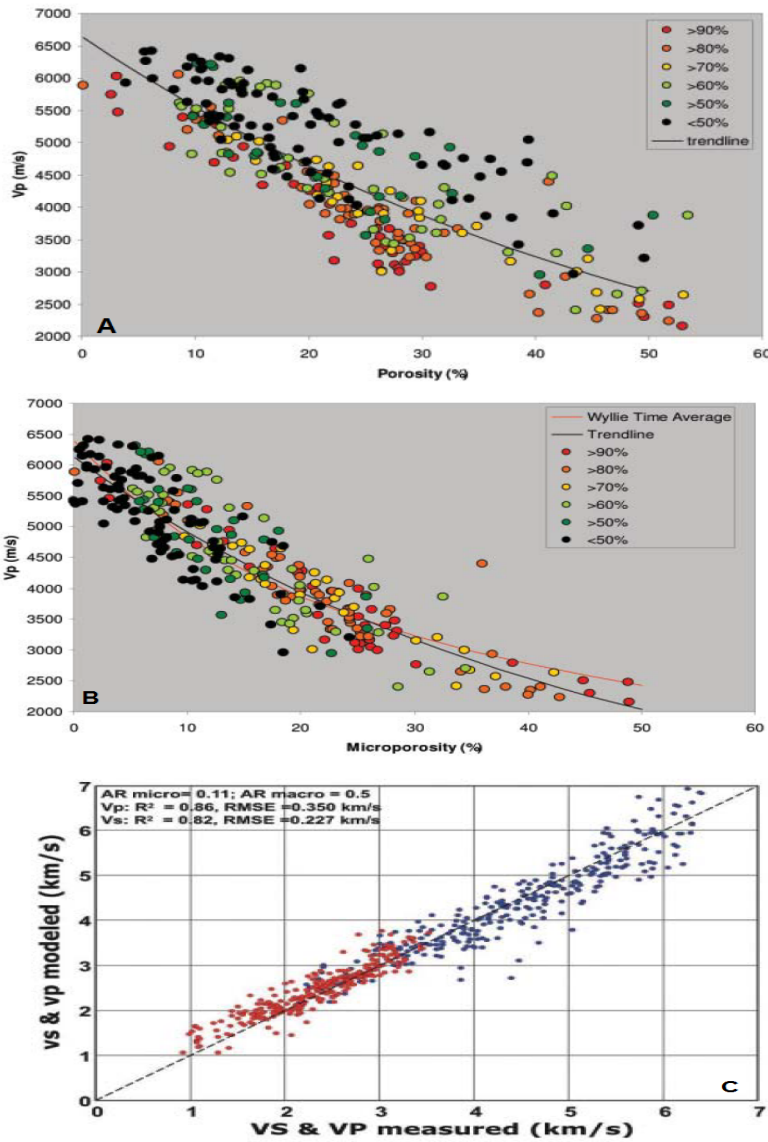
Figure 4.4: (A) Plot of porosity versus P-wave velocity with color indicating the percentage of total porosity due to microporosity. (B) P-wave velocity versus microporosity only excluding the macro-pores. There is less scattering in the effect of microporosity to V_p. (C) Measured V_P (blue dots) and V_S (red dots) versus calculated velocities using the two stiffness method. The dashed line indicates where the measured and calculated velocities are equal. Modified after **Baechle2008**

(**Baechle2008**).

Shear weakening is attributed to large surface area of matrix-fluid interaction for micro-porous rocks. Inter-crystalline or inter-granular porosity are usually re-

lated to higher permeability which allows out of phase movements of the fluid and the solids and generation of shear strengthening (**Verwer2010**).

Besides pore type, pore shape also controls the elastic properties of carbonates. Ellipsoidal pores with various aspect ratio exert a major control on the variation of elastic velocities with porosity. The effect of pore shape is more apparent for fluid saturated rocks (**Sayers2008**).

The pore aspect ratio is a measurement of the shape of the pores. It is defined as the ratio between the longest and the shortest axis of the average pores. Elongated pores have high aspect ratios, while symmetrical pores have lower aspect ratios. Spherical pores have aspect ratio one. Even though pores in carbonates are unlikely to be exactly ellipsoidal, the various aspect ratio values accounts for several possible pore shapes from spherical pores to crack-line shapes.

Low aspect pores have the greatest effect in decreasing the elastic moduli of carbonates. Because acoustic impedance of carbonates is sensitive to the presence of low aspect ratio pores and fractures, vertical pores and fractures have a significant effect on the normal incidence acoustic impedance (**Sayers2008**).

The equivalent elastic medium method has been suggested for modelling microporous cemented grainstones. The equivalent elastic medium is composed by two end members, a pure calcite host without pores and a porous medium with micritic grains. All the pore space of the modelled strata is located within the micritic porous medium. The porous medium is composed of spherical inclusions which contain pores with the same aspect ratio (equivalent pore aspect ratio, EPAR) as the modelled strata (**Fournier2011**).

Fournier2014 showed that the EPAR of the elastic medium is a useful parameter for identifying pore types from velocity-porosity measurements and quantifying the effect of cementation on the elastic properties of limestones. The effect of aspect ratio in the prediction of elastic properties of microporous limestones with a wide range of textures (grainstones, packstones, wackestones, mudstones and several in between classes) at several effective pressure regimes, low (5-7.5 MPa), moderate (20MPa) and high (40-50 MPa) was shown by **LimaNeto2015**.

Pore shape parameters that refer and describe individual pores and pore shape parameters that refer to the entire pore system of the rocks were evaluated based on their effectiveness to predict velocities of carbonate rocks. The geometric pore-shape parameters that are more closely related to the effect of porosity on the elastic properties of carbonate rocks are (**Weger2009**):

- perimeter over Area (PoA). PoA is defined as the ratio of the total perimeter that encloses the pore space to the total pore space area. Small values indicate a simple pore geometry;

- dominant Pore Size (DomSize). DomSize is defined as the upper boundary of pore sizes that compose 50% of the porosity. DomSize is an indication of the dominant pore size range;

- gamma (γ). γ is defined as the perimeter over an area of an individual pore normalised to a circle. Perfect round pores have γ values 1;

- aspect Ratio (AR);

- amount of micro-porosity.

Each geometric pore-shape parameter when used in addition to porosity improves the correlation between measured and estimated velocities (Table 4.1). Combinations of several pore-shape parameters in addition to porosity also improve the prediction of velocities but not more than single parameters (**Weger2009**).

Table 4.1: Corellation between measured and estimated velocities based on the coefficients of regression. Each pore-shape parameter improves the correlation (R^2) between measured and estimated velocities. PoA and DomSize show the most significant correlation. Combinations of parameters do not offer better estimations compared to single parameters. See text for parameter explanation. From **Weger2009**

Estimators used for velocity prediction	R^2
Porosity	0.542
Porosity and AR	0.549
Porosity and γ	0.639
Porosity and DomSize	0.768
Porosity and % microposity	0.769
Porosity and PoA	0.786
Porosity and PoA and AR	0.788
Porosity and PoA and DomSize	0.800
Porosity and PoA and γ	0.810
Porosity and PoA and % microporosity	0.820
Porosity and PoA and % microporosity and AR	0.822
Porosity and PoA and % microporosity and γ	0.832
Porosity and PoA and % microporosity and DomSize	0.840
Porosity and PoA and % microporosity and AR and DomSize	0.841
Porosity and PoA and % microporosity and DomSize and γ	0.844
Porosity and PoA and % microporosity and DomSize and AR and γ	0.845

4.3.2 Grain texture and fabric

The effect of rock fabric on the elastic properties of carbonates has been demonstrated with the use of the Poisson's ratio. Granular fabric rocks typically demonstrate high Poisson's ratio values and relatively low P-wave velocities, while recrystallised rocks show low Poisson's ratio and relatively high P-wave velocities (Fig.4.5). Siliciclastic and mixed siliciclastic-carbonate sedimentary rocks also display the same behaviour and thus the Poisson's ratio is a good indicator of the rock texture irrespective of the strata type. (**Kenter2007**).

Rock texture (granular or crystalline) is a major control on the elastic properties of carbonates. Dry, granular textures demonstrate lower P-wave velocities and wider range of Poisson's ratio values than dry, crystalline textures. Dry, granular textures show V_P values from $2000 - 4500m/s$ while crystalline textures have V_P higher than $4500m/s$ (**Verwer2008**).

Granular texture refers to depositional textures where grain-to-grain contacts support the frame with various amounts of cement and little matrix. Granular textures usually contain inter-granular porosity and relatively high permeabilities. The initial rock texture of carbonates is preserved with very low influence of diagenetic processes. Acoustically, granular textures are not very efficient in wave propagation due to energy scattering at the grain boundaries (**Verwer2008**).

Crystalline textures refers to rock frame consisting of interlocking crystals. Crystalline textures are dominated by re-crystallised or cemented fabric without any initial granular texture. Porosity is usually low as the result of cementation and compaction. Crystal compaction and cementation of pore spaces generates an efficient, acoustically, connected framework (**Verwer2008**).

Several diagenetic paths based on the V_P-Poisson's ratio crossplots can be identified (Fig.4.6). Compaction of grains rapidly decreases the Poisson's ratio and increase their P-wave velocity but preserves the granular texture. Cementation of the rock changes the texture from granular to crystalline with significant increase in V_P but relatively constant Poisson's ratio. If dissolution occurs before cementation then a V_P and Poisson's ratio decrease is observed before the effects of cementation (**Verwer2008**).

Coarse grain samples (0% micrites) generally show elastic moduli strengthening trend with fluid substitution with a negative correlation with confining pressure. The negative correlation with pressure remains but trend reverses to elastic moduli weakening for fine grain and mud supported samples (Fig.4.7) (**Husseiny2015**).

The fraction of micro-crystalline matrix (rock texture) and its distribution are related to porosity and they are characteristic of the effect of diagenetic processes on porosity and thus the elastic properties of carbonates. For coarse grain supported matrix ($0 - 10\%$ micrite) with inter-granular porosity, the micritic content fills the porous between the grains. Dissolution of the grains generates more mi-
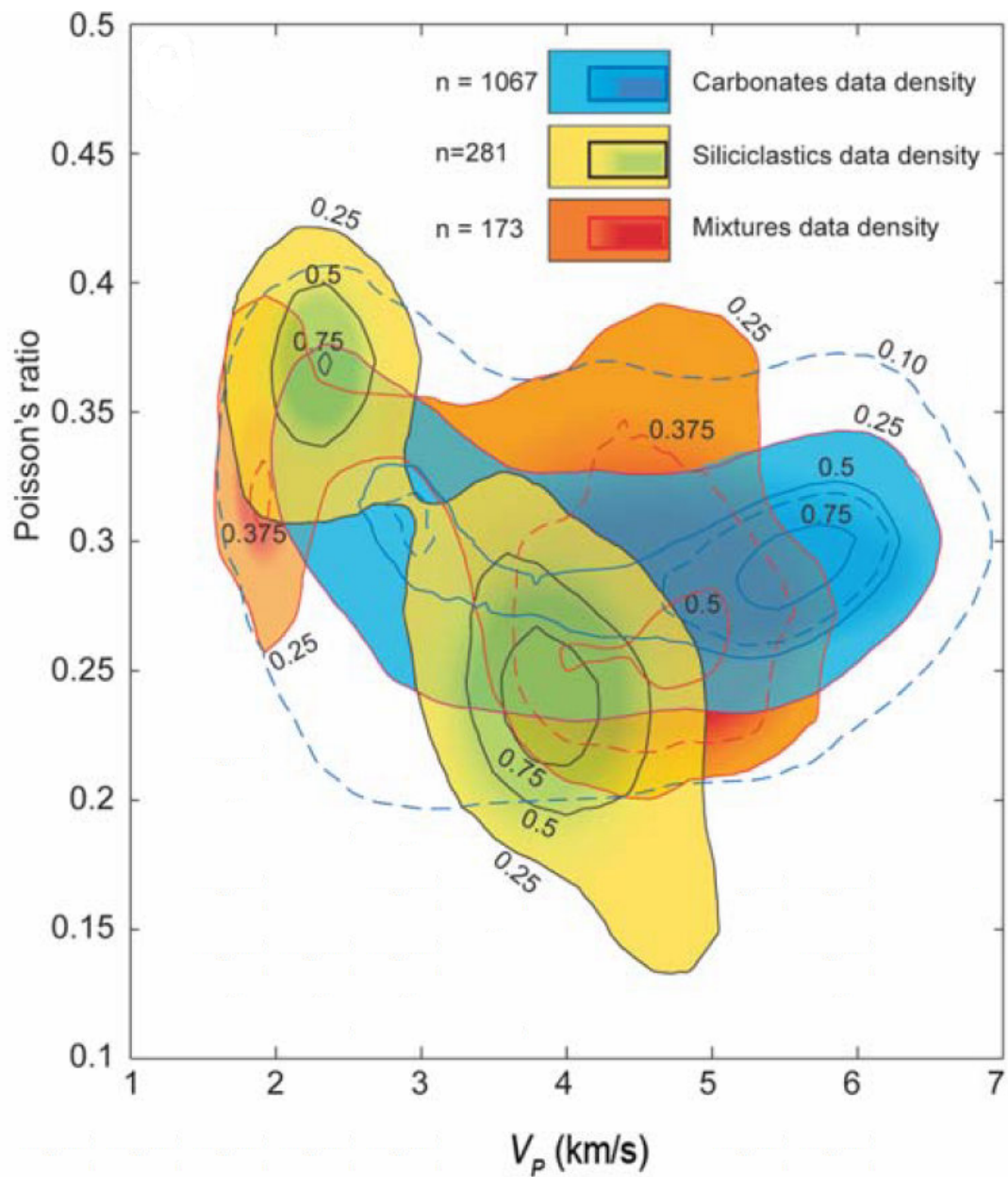
Figure 4.5: Carbonate fabric rock identification based on Poisson's ratio versus V_P. Carbonates (blue area) show a clear V-shape distribution with granular strata on the left side and crystalline strata on the right separated by a relatively low Poisson's ratio (≈ 0.3) area at $4km/s$. Modified after **Kenter2007**.
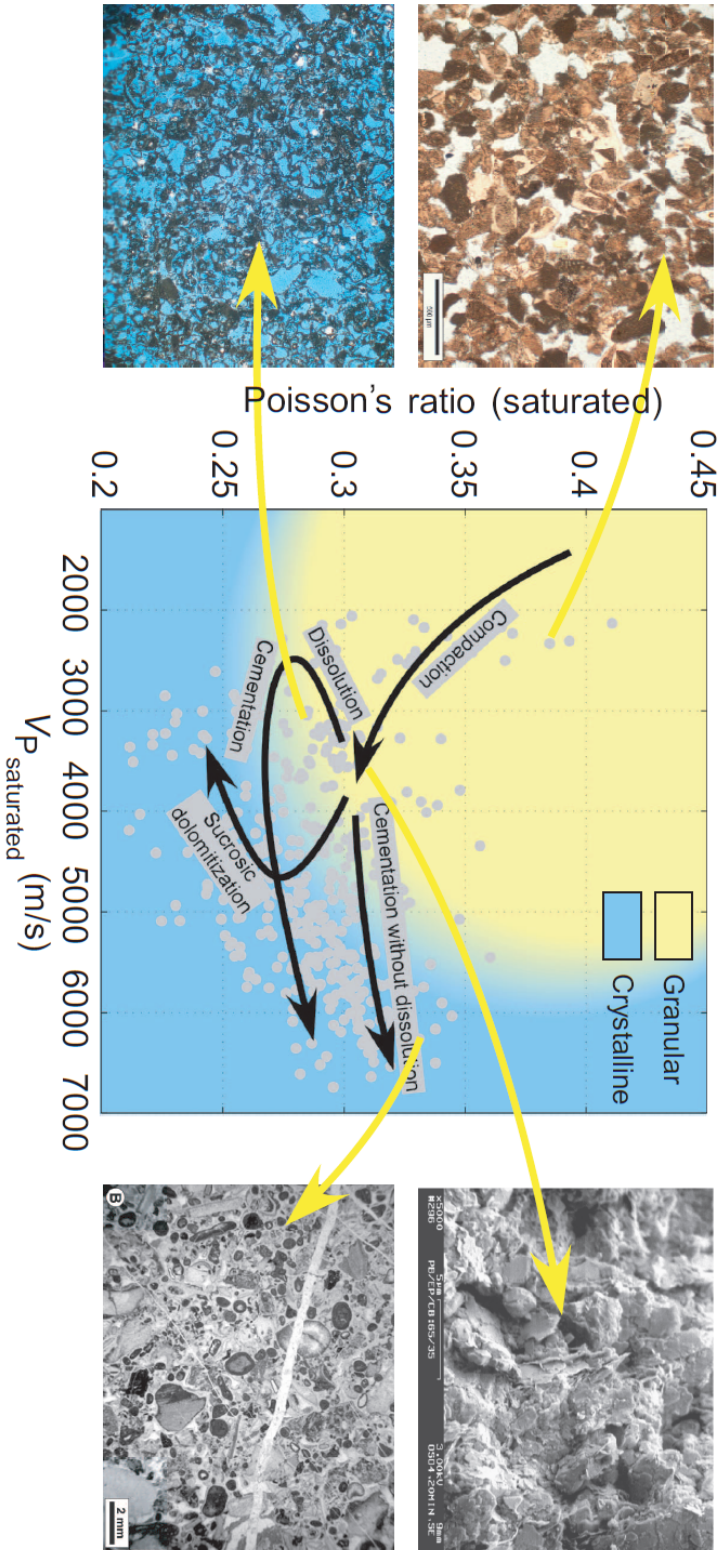
Figure 4.6: Saturated V_P versus Poisson's ratio crossplot with diagenetic paths superimposed and photomicrographs with particular rock textures: A poorly cemented grainstone (upper left), a re-crystallised grainstone (lower left), chalk (upper right) and densely cemented grainstone (lower right). Yellow colour signifies granular textures and blue crystalline texture. The transition from granular to crystalline is not a sharp boundary and occurs at $\approx 4500m/s$ at 0.28 Poisson's ratio but at $\approx 5500m/s$ at 0.4 Poisson's ratio. From **Verwer2008**.
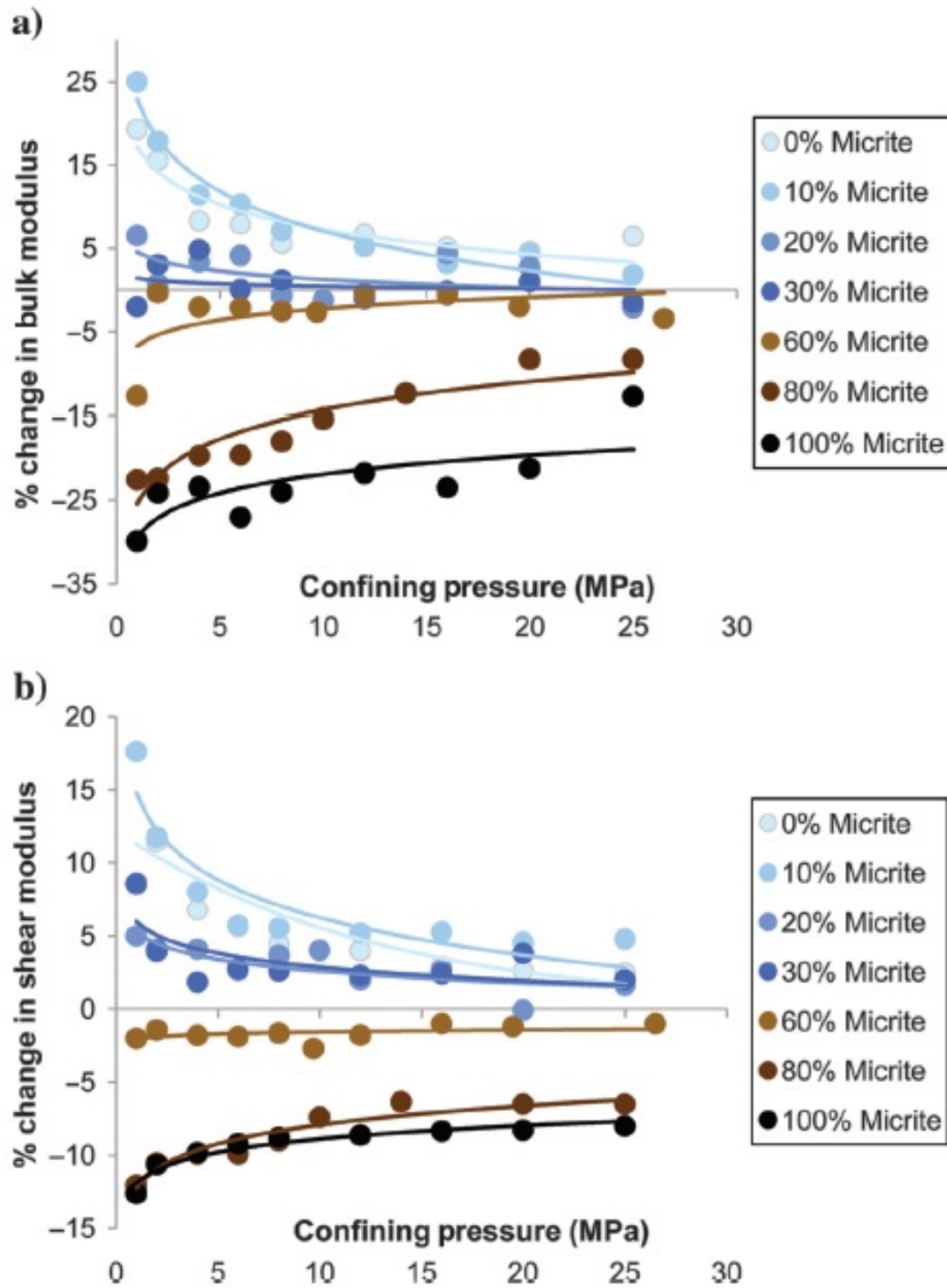
Figure 4.7: Percentage change in bulk modulus (a) and shear modulus (b) for samples fully saturated with CO_2-rich water. The change is calculated as $\frac{modulus_{sat} - modulus_{dry}}{modulus_{dry}}$. From **Husseiny2015**.
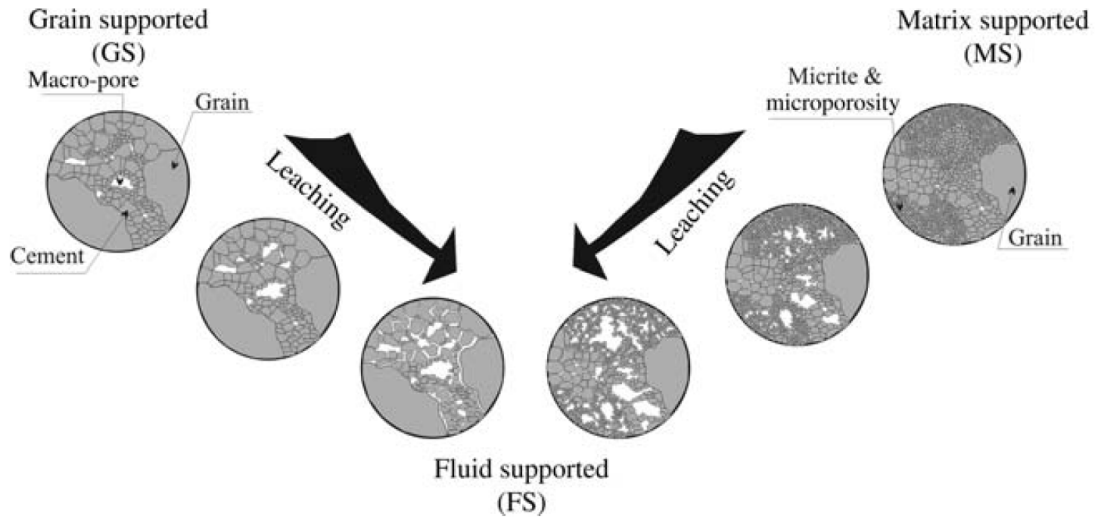
Figure 4.8: Conceptual model of the evolution of the calcite grain, micrite mixture based on grain-micrite-pore fraction. From **Vanorio2011**.

critic material and increases the porosity of the formation. Dissolution of mud-supported matrix ($> 50\%$ micrite) removes micritic crystalls increasing the porosity leading to a fluid-supported matrix (Fig.4.8). The above processes assumes no cementation is talking place and dissolution is caused by chemical reactivity of the carbonate matrix (**Vanorio2011**).

The micro-structure of carbonates can be described by the grain-micrite matrix ratio (GMR). GMR expresses the relative amount of coarse and fine texture carbonate material and has been shown to correlate with current action, the energy levels of the depositional setting and the elastic properties of the strata. Strata with high GMR typically demonstrate lower P-wave velocities compared with lower GMR strata (Fig.4.9) (**Vanorio2011**).

Grainstones and packstones usually show inter-grain porosity and high permeability. Constant stress and the presence of diagenetic fluids favour dissolution of the grains and the high permeability allows mechanical removal of the micritic products. Dissolution of the matrix reduces the stiffness of the grain contacts and causes reduction in the elastic moduli of the rocks. For high confining pressures, grain compaction reduces the rock-fluid surface and limited interactions occur which ultimately leads to constant elastic moduli (Fig.4.10) (**Vanorio2013**).

Chemical dissolution of the rock frame was quantified measuring the concentration of the dissolved Ca^{2+} in the saturating solution. Higher Ca^{2+} concentration means higher chemical dissolution of the frame. Mechanical dissolution and compaction were measured with changes in the length of the samples as an indication
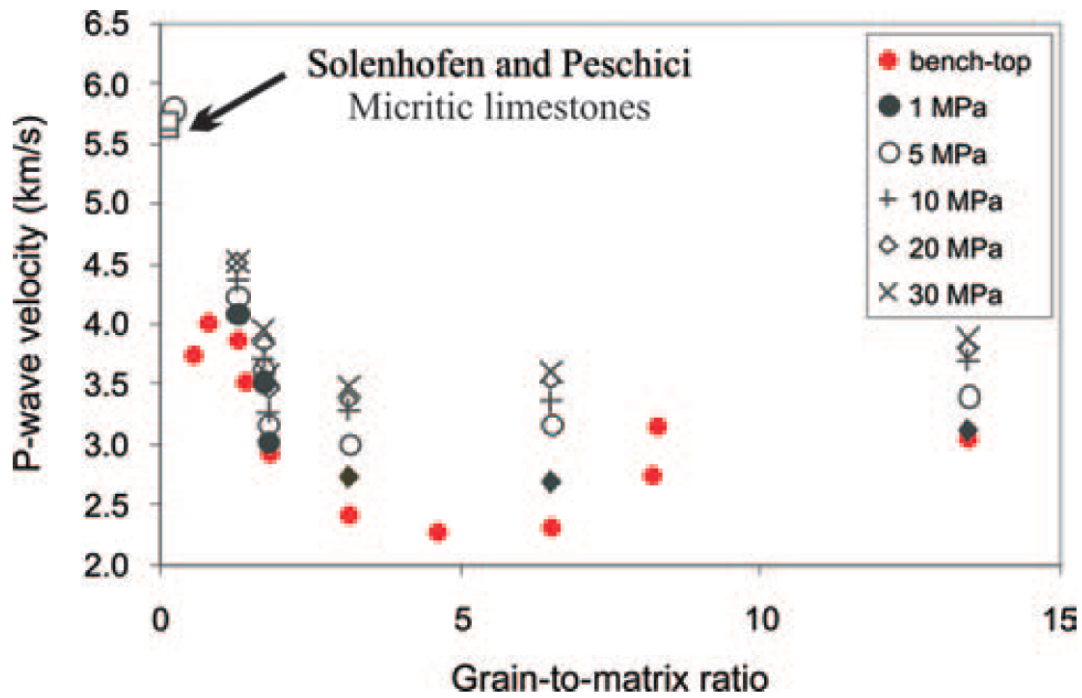
Figure 4.9: Variation of P-wave velocity as a function of grain to matrix ratio (GMR). From **Vanorio2011**.

of the generated strains from the confining pressure. Elastic properties were measured for various degrees of confining pressure and saturation levels. CO_2-rich water fluid was used for saturation (**Vanorio2013**).

In tight mudstones the initially interlocked micritic crystals show only micro-porosity and low permeability values. Stress has little effect on the micro-structure and low permeability does not allow removal of the chemical dissolution products. If cementation occurs under high stress, the micro-porosity remains low but the tighter structure generates higher permeability which results to high flow rates and un-balanced rock-fluid interactions (Fig.4.11) (**Vanorio2013**).

4.3.3 Summary

The factors which control the elastic properties of carbonate strata are diagenetic processes, porosity and pore type, grain size and texture and mineralogy. Each of these factors affect the elastic properties of the medium through which the seismic waves are propagate (Table 4.2). Mineralogy mainly defines the elastic properties and density of the matrix or crystals that propagate the wave energy.

Diagenesis can positively (elastic parameter values increase) or negatively (elastic parameter values decrease) influence the elastic parameters of carbonate strata. Compaction and cementation decrease the porosity of the strata and produce denser strata with generally high velocities. Dissolution and leaching generate

85
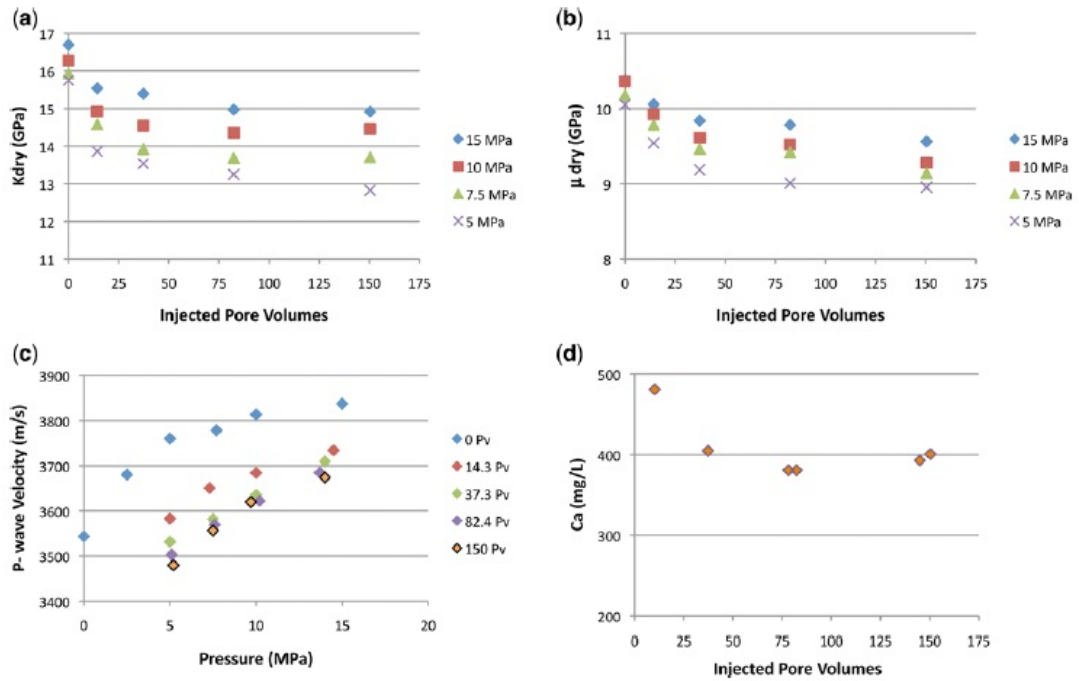
Figure 4.10: Variation of bulk modulus (a), shear modulus (b), V_P (c) and dissolution (d) of micritic-rich grainstone at several saturation level and confining pressure. Bulk, shear moduli and dissolution levels initailly decrease with increasing saturation and quickly obtain a constant value for all pressures. From **Vanorio2013**.
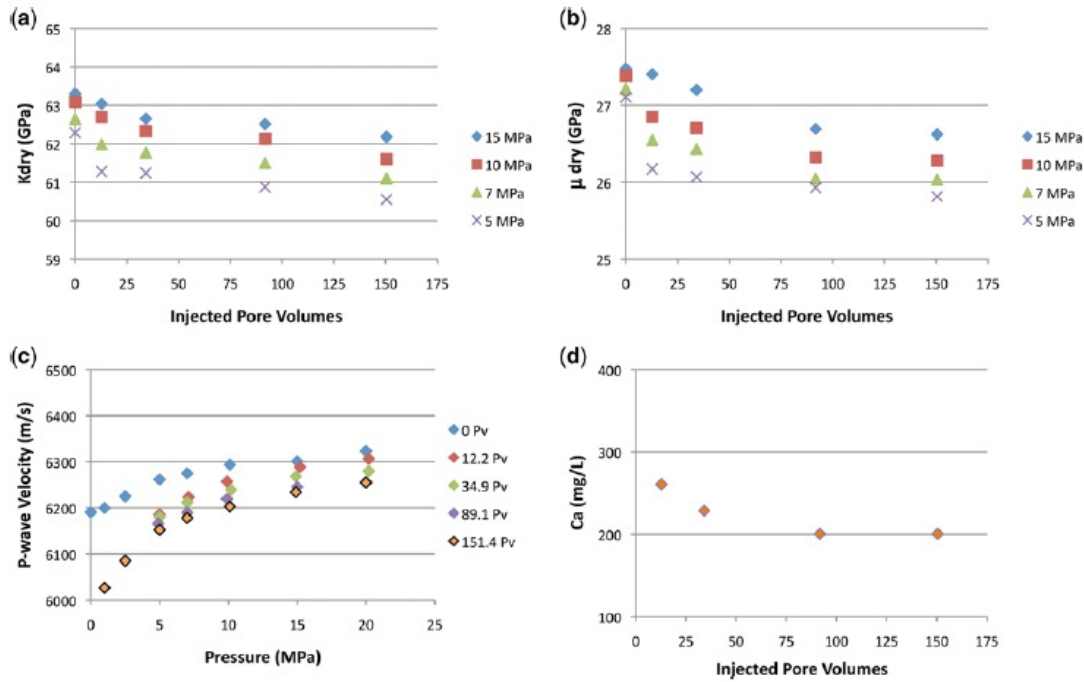
Figure 4.11: Variation of bulk modulus (a), shear modulus (b), V_P (c) and dissolution (d) of mudstone at several saturation level and confining pressure. Bulk and shear moduli decrease with increasing saturation. Dissolution levels initially decrease with increasing saturation and quickly obtain a constant value. From **Vanorio2013**.

higher porosity and are related to lower velocities.

Macro-porosity, the measure of empty spaces in the crystal, generally decreases the strata velocity but there is considerable scatter between porosity and velocity values. Microporosity has more significant effect on the elastic properties of carbonates. Inter-crystalline or inter-granular microporosity is usually related to high permeabilities which allow out of phase movements of pore fluids and generate shear strengthening of the strata.

Rock texture affects the elastic properties by controlling the medium through which the wave propagate. Granular fabrics with the initial rock textures preserved, show relatively low P-velocities. Seismic energy is scattered at the grain boundaries. Crystalline textures consist mainly of interlocking crystals with low porosity (due to cementation) and provide an efficient, acoustically connected network for seismic energy.

Table 4.2: Parameters controlling the velocity and density of carbonate strata. The direction of the arrow indicates increasing (upwards) or decreasing (downwards) parameter values. Simple arrows show weak effect and double arrows significant effect on the parameter values

Control	V_P	Density
Mineralogy	Defines the elastic properties of the medium	Defines the medium
Macro-porosity	↓	⇓
Micro-porosity		
Inter-granular	⇑ shear strengthening	↓
Intra-granular	⇓ shear weakening	↓
Grain texture		
Granular	⇓ scattering at grains	-
Crystalline	⇑ connected network	-
Diagenesis		
Cementation, compaction	⇑	⇑
Dissolution, leaching	⇓	⇓

4.4 Synthetic seismic images

If seismic interpretation is the prediction of geologic strata from seismic images, generation of synthetic seismic images or simply synthetics can be seen as the reverse process. Generation of synthetics is the process of predicting the seismic recordings from a known stratigraphic model. The seismic response of any model can be predicted by solving the generalised wave equation, eq.(4.1).

The solutions of the equation would, theoretically, fully describe the wave propagation through the assumed structure and allow detailed prediction of seismic recordings at any position of the model. Synthetic seismograms as the results of seismic forward modelling have been used to relate the elastic properties of strata to their seismic response.

Practically, it is very difficult to solve the wave equation in order to calculate the response of the strata. Synthetics are calculated from measured variations in the physical properties of the strata in boreholes during exploration surveys. So any attempt to generate synthetic seismic images involves calculation of the acoustic impedance of the strata.

Rock physics models are formulas that relate elastic properties, usually acoustic impedance, to physical properties, usually mineralogy, porosity and fluid saturation of the rocks. Depending on generated outcome rock physics models can be distinguished in 3 groups:

1. Theoretical models. A general, theoretical relationship is used to describe the elastic properties-porosity relationship.

2. Empirical models. The elastic properties are obtained from the best fit model for the available data. The use and accuracy of empirical models have increased with increasing computational power and inversion techniques (**Aleardi2017**).

3. Analogue models. An area with known, well defined mineralogy and elastic properties can be used as an analogue for the studied area.

The most common physical properties of strata measured in boreholes or well-logs are mineralogy, density, fluid saturation, elastic wave velocities and porosity. Elastic properties of carbonate rocks are measured from samples on laboratory experiments and include the elastic moduli (usually shear and bulk moduli) and porosity. Thus rock physics models link the elastic properties-porosity of the constitute parts of strata to the impedance-porosity relation of the strata.

4.4.1 Upscaling of elastic properties

Calculating the effectively equivalent elastic properties of a homogeneous volume from the elastic properties of its constitute volumes is called upscaling and it is the scope of the elastic effective medium theory. The effective medium and constitute volumes are defined based on the wavelength of elastic waves. Strata that are several times thicker than the wavelength can be considered as a mixture of volume fractions which properties and spatial arrangement control the elastic properties of the effective medium.

For wavelength to layer thickness ratio λ/d between 0.1 and 10, strata velocities are better predicted using ray theory whereas for λ/d ratios greater than 15 wave velocities are better predicted using effective theory. The λ/d ratio value of 10 is used as threshold, a value which is consistent with the predictions of scatter theory for wave propagation (**Marion1994**).

The difference between the effective elastic properties of strata and the elastic properties of the layers are attributed to three reasons (**Tiwary2009**). The first is the scale effect. The physical and elastic properties of material depend on the scale of investigation and frequency. The fine-scale distribution of the elastic properties and the heterogeneity of the constitute volumes have significant effects on the coarse-scale, effective properties of the volume (**Moulton1998**).

The second reason is elastic scattering. Heterogeneities that are comparable in size to the wavelength, scatter the elastic energy and thus less energy reaches the measuring instruments. The third reason is attenuation due to pores. Partially or fully saturated pores in the material generate pressure disequilibrium with the rest surrounding material and thus effect the wave propagation (**Tiwary2009**).

Several methods applicable to specific strata types and environments have been suggested for calculating effective properties of strata. **Chapman2003** showed

that scale-dependent anisotropy occurs in fractured strata, with the size of the fractures playing a controlling role. **Gold2000** suggested an upscaling method for isotropic heterogeneous strata based on smoothing with frequency dependent radius. **Torquato2000** presented a method for random heterogeneous material based on the micro-structure of the strata. **Lopez2017** established a rock-physics model for an offshore oil reservoir and the surrounding shale.

The simplest upscaling method is calculating the effective properties of strata as simple averaging of the elastic properties of their layers. Each constitute layer is assumed to be homogeneous with thickness significantly less than the dominant wavelength and the thickness of the strata. The effective elastic moduli and density are calculated from eq(4.13)

$$
\begin{aligned}
K* &= \tfrac{1}{L} \sum_1^N d_i K_i \\
\mu* &= \tfrac{1}{L} \sum_1^N d_i \mu_i \\
\rho* &= \tfrac{1}{L} \sum_1^N d_i \rho_i
\end{aligned}
$$

$$(4.13)$$

where $K*, \mu*, \rho*$ are the effective bulk modulus, shear modulus and density respectively, L is the averaging window length, d is the thickness and K, μ, ρ the bulk modulus, shear modulus and density of the each layer respectively.

Instead of calculating an exact value for each elastic property, the bound method predicts the upper and lower bounds of the effective elastic properties of strata based on volume fractions and the elastic moduli of the constituent material. The Hashin-Shtrikman-Wapole bounds can be written as (**Mavko2009**):

$$
\begin{aligned}
K^{HSW\pm} &= K_1 + \frac{f_2}{(K_2-K_1)^{-1}+f_1(K_1+4/3\mu_m)} \\
\mu^{HSW\pm} &= \mu_1 + \frac{f_2}{(\mu_2-\mu_1)^{-1}+f_1[\mu_1+\mu m/6(\frac{9K_m+8\mu_m}{K_m+2\mu_m})]^{-1}}
\end{aligned}
$$

where subscripts 1,2 refer to the properties of the two components, f_1, f_2 are the volume fractions of each component. The maximum or the minimum bounds are calculated when K_m and μ_m are the maximum or minimum elastic moduli respectively.

The effective elastic parameters and effective stiffness matrix of a layered package consisting of fine layers with known elastic parameters is transversely anisotropic even if the layers are isotropic. Conversely, any homogeneous transversely isotropic medium can be considered the long wave equivalent of at least four homogeneous isotropic layers (**Backus1962**).

The effective properties of a stratified package composed of isostropic, porous layers depend on the degree of hydraulic communication between the layers. For

hydraulically communicating layers the effective properties of the package can be estimated using the simple averaging equations (eq.4.13). Hydraulically isolated layers generate effective properties of the package better described by the bounds theory (**Wollner2016**).

Tiwary2009 compared the most commonly used upscaling techniques and concluded that the upscaling results depend on the applied method and they vary considerably. Upscaling methods that have more physical background and integrate frequency and heterogeneity effects, perform better.

4.4.2 Thin beds and tuning

The reflectivity of strata for any angle of incidence is calculated using the Zoeppritz reflection and transmission coefficients. Zoeppritz reflection and transmission coefficients were calculated assuming a plane horizontal boundary between two half-spaces that show only small differences ($\frac{\Delta c}{c} << 1$ and $\Delta i \approx \tan i$) in their elastic properties (**Aki1980**). As a result of the above, the majority of the incident energy will be transmitted.

The semi-infinite thickness of the layers on either side of a boundary means that only one reflection event will occur and thus there is no interference with the amplitude of the reflected wave. Geological strata though have a finite thickness and two boundaries. An upper boundary with the formation above the strata and a lower boundary with the formation below them. The two boundaries generate two reflections, one at each boundary and the two reflected waves interfere with each other. The interference of the reflected waves with each other is called tuning.

The thickness d of a layer embedded in a homogeneous medium, compared to the wavelength λ of the wave inside the layer controls the interference of the reflected waves from the top and bottom boundaries of the layer. The time delay between the top and bottom reflections for layers thicker than $\lambda/2$ is enough for the two reflections not to interfere. Reflections from layers with thickness less than $\lambda/2$ show some interference. The interference between top and bottom reflections can be observed for layers as thin as $\lambda/8$, which is defined as the thin layer threshold (**Widess1973**).

The $\lambda/8$ limit is the minimum layer thickness (or distance between top and bottom boundaries) identified by **Widess1973** to generate a composite reflection with waveform as the derivative of the single reflection waveform. In practise, the resolution limit for thin beds in seismic signals is considered as $\lambda/4$ below which thin beds can be detected but not resolved (**Kallweit1982**).

The $\lambda/4$ resolution threshold defines the spatial resolution limit for strata. Resolution is defined as the minimum distance (horizontally or vertically) between two points that can be identified as separate events in a seismic image. Seismic resolution is a measure of how large an object needs to be in order to be seen in a

seismic image. Based on the strata vertical and horizontal dimensions 4 cases can be identified (**Zeng2015**).

1. spatially resolved. Both vertical and horizontal dimensions are greater than $\lambda/4$. Top, bottom and lateral boundaries of beds can be determined;

2. vertically resolved. Strata thickness is greater than $\lambda/4$ but lateral dimensions are less than $\lambda/4$. The top and bottom boundaries only can be determined;

3. horizontally resolved. Strata lateral dimensions are greater than $\lambda/4$ but thickness is not. The lateral boundaries only can be detected;

4. spatially unresolved. Both vertical and lateral dimensions are less than $\lambda/4$. Neither the vertical nor the lateral boundaries can be detected.

Because interference from top and bottom reflections occurs, the amplitude of the reflected wave from a thin layer differs from the amplitude estimated with the Zoeppritz reflection coefficient. The reflected amplitude A_d of a layer with thickness d embedded in a homogeneous isotropic medium based on the amplitude A_m of a normal incident monochromatic sine wave with period equal to the wavelet period is given by (**Widess1973**) :

$$A_d = \frac{4\pi A_m k d}{\lambda_d} \tag{4.14}$$

where λ_d is the wavelength inside the layer and k is the ratio of the acoustic impedances $k = \frac{V_2 \rho_2}{V_1 \rho_1}$.

The linear relation between reflected amplitude and layer thickness, eq(4.14) is a special case of equal magnitude and opposite polarity reflections of the top and bottom boundaries. The reflected amplitude response A_R of thin beds with different polarities and magnitudes between the top and bottom boundaries is calculated from (**Chung1995**):

$$A_R = A \left[(r_1 + r_2)^2 \left[1 - 2 \left(\frac{\pi d}{\lambda_d} \right)^2 \right]^2 + M^2 (r_2 - r_1)^2 \left(\frac{2\pi d}{\lambda_d} \right)^2 \right]^{1/2} \tag{4.15}$$

where A is the amplitude of the incident wave, r_1 the reflection coefficient of the upper boundary, r_2 the reflection coefficient of the bottom boundary, d the thickness of the layer, λ_d the wavelength inside the layer and M is a source related parameter with value 1 for the a sine monochromatic wave and 0.75 for a Ricker zero phase wavelet.
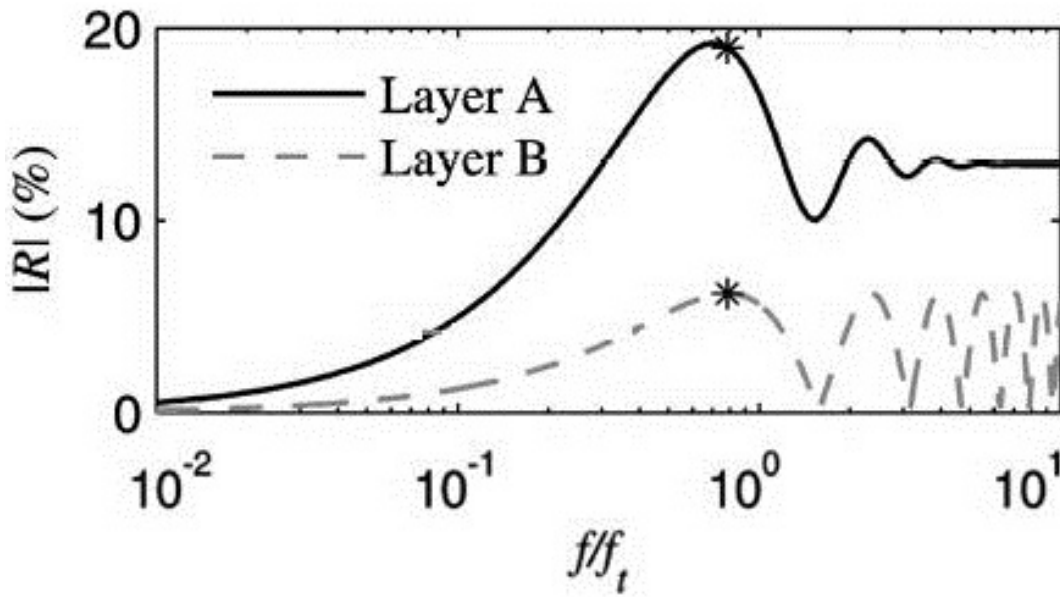
Figure 4.12: Absolute values of the reflection coefficient of an attenuating layer (Layer A) and an elastic layer (Layer B) for different frequencies. Small values of the f/f_t ratio indicate thin layers compared to the wavelength while big values inidcate thick layers compared to the wavelength. For higher values of the f/f_t ratio (thick layers, not shown here) the reflection coefficient is constant and calculated by the Zoeppritz equations. Modidfied after **Quintal2011**.

Thin layers are defined relative to the wavelength inside the layer. Because wavelengths are frequency dependent, tuning generates frequency dependent signals. The normal incidence reflection coefficient R of layer embedded in an elastic background medium is also frequency dependent for both elastic and attenuating layers (Fig.4.12) (**Quintal2011**):

$$R = \frac{1-k}{1+k}\left(1 - \frac{4ku}{(1+k)^2 - u(1-k)^2}\right) \tag{4.16}$$

where k is the acoustic impedance ratio, and u is frequency dependent parameter defined as:

$$u = \exp\left(-\frac{i4f}{f_t}\right)$$

where f is the frequency and f_t is the tuning frequency defined as

$$f_t = \frac{V}{\pi d}$$

where V is the velocity of the layer and d its thickness.

Small values of f/f_t ratio correspond to thin layers compared to the wavelength whereas big values of f/f_t ratio indicate thick layers compared to the wavelength.

Assuming a V_P of $4000m/s$ for a pure calcite with 10% porosity (**Assefa2003**) and a high frequency (100 Hz) zero-phase Ricker wavelet source, the $\lambda/4$ resolution limit for spatially resolved beds is 10m, the **Widess1973** thin bed $\lambda/8$ limit is 5m

93

and the detectable $\lambda/25$ limit is 1.6m. Strata thickness from SFM performed for this project (see section 8 and section 9) show that numerical facies thickness ranges from several metres to less than a metre while their lateral dimensions are in the range of a few hundred metres.

The above mentioned numerical facies dimensions indicate that the simulated facies are horizontally resolved only. The facies thicknesses are comparable with a high frequency wavelength in carbonates, indicating the influence of tuning on the calculated reflection coefficients. Furthermore, the numerical facies thickness are not one order of magnitude greater than a typical wavelength (**Marion1994**) and thus the acoustic impedance of the numerical facies must be calculated using effective theory.

4.4.3   Pseudo acoustic impedance

The above limitations, effective acoustic impedance and thin layer tuning, make clear that the actual reflectivity of strata can only be estimated. The effective impedance of strata is an estimation of their actual acoustic impedance. Furthermore, calculation of strata reflectivity using Zoeppritz equations is a rather bad estimation of the actual reflectivity of the strata when thin layers are involved.

Additionally, smoothed transitions between layers with more or less similar elastic properties, which are very common in carbonate depositional settings and the SFM results for this project, that cannot be approximated as boundaries further complicate the calculation of strata reflectivity.

Because the actual acoustic impedance and reflectivity can only be estimated, any method used to calculate acoustic impedance and reflectivity of strata is an approximate or pseudo-impedance method that calculates an approximate or pseudo-reflectivity of the strata. If calculated pseudo-impedance is well correlated to the actual impedance, then changes in the pseudo-impedance will correspond to changes in the actual impedance.

The most commonly used and simple pseudo-acoustic impedance method is to assume that the effective acoustic impedance of the heterogeneous strata is the simple averaging of the acoustic impedance of the constitute homogeneous layers. The acoustic impedance of each of these homogeneous layers is calculated as the product of the seismic velocity and density irrespective of layer thickness and material distribution.

The above method, which here will be referred to as the average impedance method, has been applied by many authors and researchers in almost all rock types. The average impedance method is a theoretical rock physics model that reliably calculates acoustic impedance of homogeneous siliciclastic strata with thickness one order of magnitude greater than the dominant wavelength.

The average impedance reflectivity method is based primarily on mineralog-

94

ical differences obtained from velocity differences of the modelled strata. The most popular velocity transformations fail to extract adequate mineralogical information from seismic data without prior knowledge of the sedimentary system (**Kenter2007**).

The most popular velocity transforms, namely the Wyllie time-average equation and the modified time-average equation are based on siliciclastic data sets with one or two mineral systems. Both transformations show high relative errors in modelled seismic velocities (Fig.4.13).
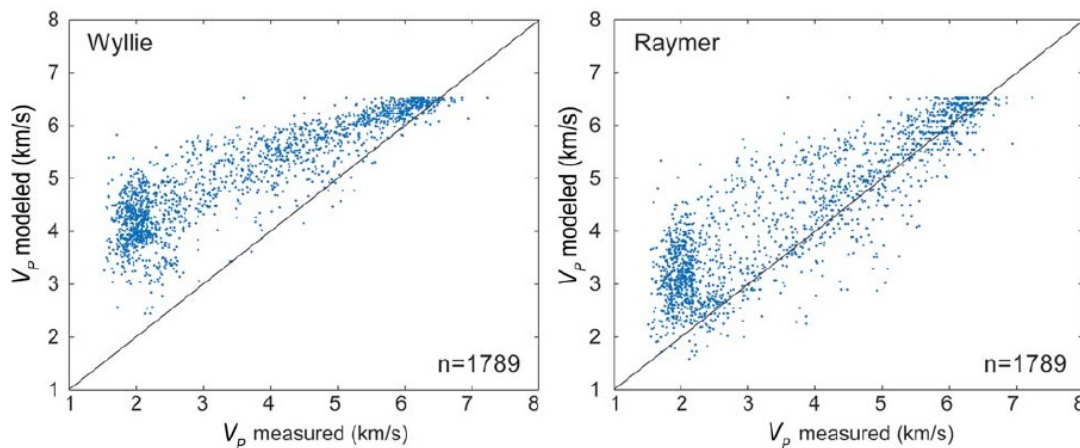

Figure 4.13: Evaluation of the time-average equation (Wyllie) and the modified time-average equation (Raymer). Crossplots of modelled against measured V_P. The black lines show where the modelled and measured velocities are equal. Modified after **Kenter2007**.

It can be proven mathematically that any parameter can be used to calculate pseudo-impedance and pseudo-reflectivity, provided that the used parameter is well correlated with the real impedance. Table 4.2 shows that for carbonate strata, the parameters that, potentially, can be used to calculate pseudo-reflectivity include porosity (and more specifically microporosity), grain texture and diagenetic processes.

The new method developed for calculating synthetic seismic images for this project, estimates a pseudo-acoustic impedance based on the texture and the porosity of numerical facies (see section 6). Using the concept of grain-to-matrix ratio (GMR) numerical facies are characterised as having granular or crystalline texture based on the energy levels of their depositional environments and different elastic properties are assigned to each texture type. Further differentiation between numerical facies with the same texture is achieved with the assumption of different porosity type based on the differential effective models.

The quality of any pseudo-acoustic impedance method depends on how well the method is correlated to the real acoustic impedance and not how the pseudo-reflectivity is calculated. A pseudo-acoustic impedance method that can be considered a good candidate for calculating reflectivity must be proven to be well correlated to real reflectivity and must use reasonable parameters to calculate pseudo-reflectivity.

5 New developments in CarboCAT

Stratigraphic forward modelling for this project is performed with a modified version of CarboCAT. The original version of CarboCAT **Burgess2013** is presented in section 3.2. The modified version of CarboCAT which will be here referred to as the new CarboCAT, includes a number of functions that simulate physical processes not previously included in CarboCAT.

New CarboCAT provides the option to select the functions that will be used in each model run. The selection is done in a new parameters file with all the available functions in a pre-defined order. All functions are independent of each other and new CarboCAT can run with any combination of functions. The selection file is an input parameters file for the new CarboCAT.

The list of functions that the user can choose from includes:

- the order of factories which will be used from cellular automata to check the model cell status. The available options are the order based on the factory production rate at each model cell or a pre-defined order (paragraph 3.2.4.1). The function was developed by **Kozlowski2017**;

- the transportation algorithm. The options are the steepest descent (section 3.2.4.3) or the new cross-platform algorithm (section 5.6);

- the wave energy routine (section 5.4). The function can be activated or de-activated;

- the siliciclastic routine (section 5.5). Siliciclastic strata are deposited on the platform if the function is activated;

- carbonate concentration can be active or not. Developed by **Kozlowski2017**;

- soil formation can be active or not. Developed by **Kozlowski2017**;

- the option to select the state of re-flooded model cells. The state of a cell that has been sub-aerially exposed and later re-submerged by a rising relative sea level can be either the last cell state prior to exposure or it can be empty.The selection file allows the user to pick which one will be active;

- eustatic sea level input method (section 5.2). The new option allows for any sea level to be given as an input from an external file;

- boundary conditions for the edge of the platform. The function provides the options of wrapping around the edge of the grid or mirroring for model cells at the edges of the grid where the neighbour area used in cellular automata is beyond the grid limits. The function was developed by **Kozlowski2017**.

97

This chapter presents the modifications that were developed for this project, based on the requirements of the modelled areas. More specifically, a method to input non-periodic eustatic sea level movements, an algorithm that simulates the dispersion, deposition and interaction of siliciclastics with carbonates and a routine that incorporates wave energy and its effect on facies distribution were developed for modelling the Upper Cretaceous (Santonian) outcrops in South-Central Pyrenees, Spain (see chapter 8).

Furthermore, a new sediment transportation algorithm that allows shoal formation was written for the Cenomanian-Turonian Mishrif formation (see chapter 9) which contains platform interior shoals.

5.1 Carbonate production profiles

New CarboCAT incorporates three different profiles for water depth-dependent carbonate production (Fig.5.1). The first production profile simulates euphotic carbonate production according to **Bosscher1992**. Production is directly related to the amount of light in the water column. Production rates are maximum at the top few meters of water depth and then decrease with water depth. A water depth cut-off defines the depth below which no carbonate production exists (curve A, Fig.5.1). This production profile is equivalent to the tropical factory of **Schlager2003**.

The second production profile can simulate either oligophotic or aphotic production profiles. The profile provides the option of highest production rates to occur at some water depth range and decrease exponentially above and below these depths (curve B, Fig.5.1 for an oligophotic example). Production profiles with maximum production below the euphotic zone are similar to the mud mound factory production profile of **Schlager2003**.

The third production profile can be assumed to simulate inorganic or biotically-induced pelagic production. As discussed in section 2.1.4.3, dissolved carbonic acid triggers inorganic precipitation of carbonate minerals (section 2.1.1). Production rates are zero at the sea surface (or above some specific water depth e.g break depth) and increase linearly with water depth reaching their maximum value at the base of the euphotic zone. For water depths greater than the euphotic zone, production rates remain constant and equal to the their value at the base of the euphotic zone (curve C, Fig.5.1). If necessary, a carbonate compensation depth (CCD) can be defined and thus carbonate production would seize for water depths greater than the CCD.

Practically, the three production curves represent three equations with different parameters. The three water depth-dependent production profiles are available for all factories but only one can be used for each factory in each model run.
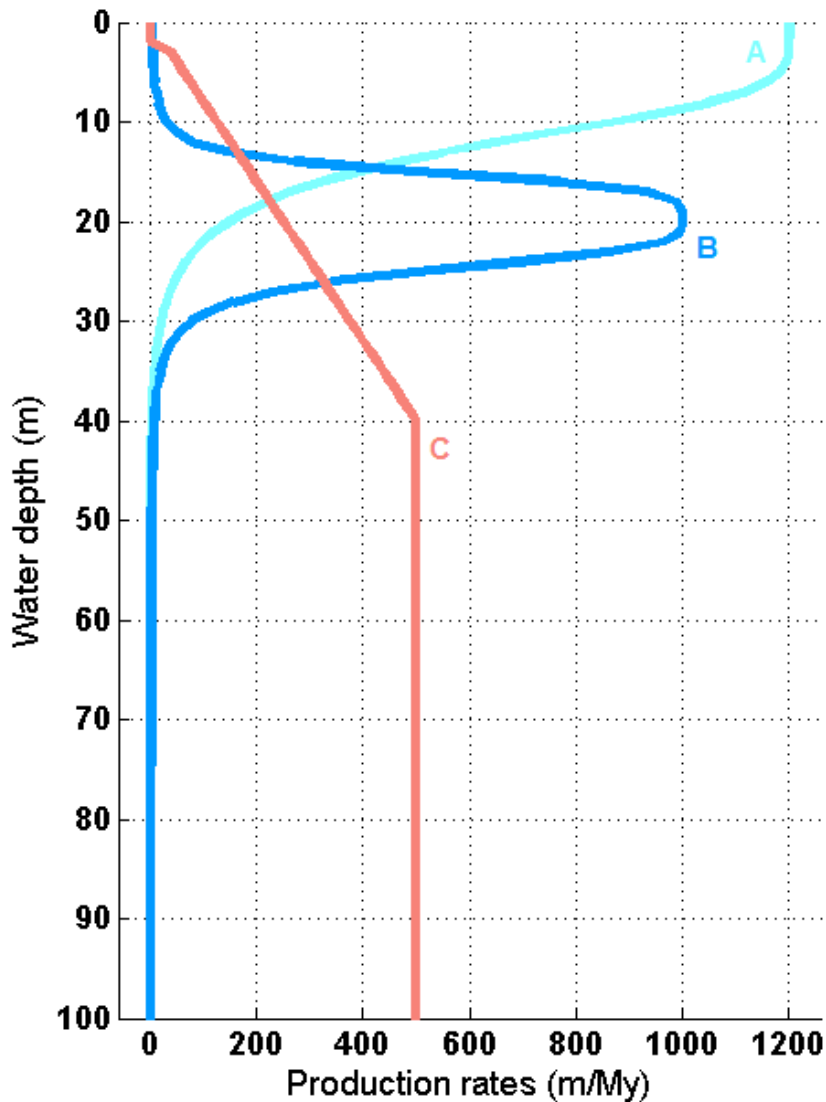
Figure 5.1: Depth dependent production profiles with euphotic zone at 40m and break depth at 3m water depth. A. Euphotic, (**Bosscher1992**) production profile. Production rate is maximum at the top 4m water depth and decreases with water depth. B. Oligophotic production profile. C. Pelagic production profile. Production is zero above the break depth, increases linearly with water depth and reaches its maximum value at the bottom of the euphotic zone.
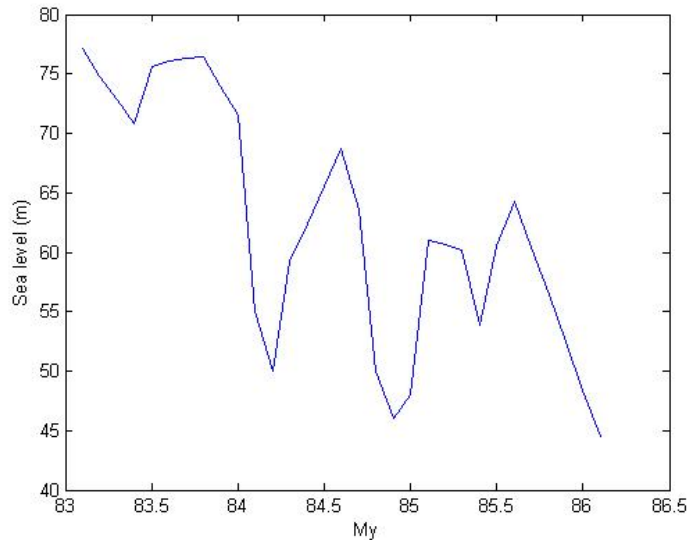
Figure 5.2: Example of a known eustatic sea level movement generated with the new routine and can be imported to new CarboCAT. Sea level movement for the Santonian with resolution 100ky from **Kominz2008**.

5.2 Sea level oscillations routine

Eustatic sea level movements that cannot be defined as a periodic signal could not previously be described in CarboCAT. Models of global sea level fluctuations are available for the Phanerozoic (**Kominz2008**, **Miller2005**). Also local sea level curves can be reconstructed by various methods. In order to address the non periodic sea level movements and being able to use known sea level curves a new algorithm was developed.

The new routine provides the option using any known sea level curve as input in new CarboCAT instead of calculating a eustatic sea level curve. The selection for the sea level curve is done in the functions parameters file. Known sea level movements are input in new CarboCAT in chronological order from the oldest value to the newest, as vectors with size equal to the number of time-steps in the model run.

Depending on the model requirements and the available data, any sea level curve can be used. As an example, a Santonian sea level curve with 100ky resolution as estimated by **Kominz2008** is generated with the new function and can be imported in new CarboCAT (Fig.5.2).

The known sea level curve is digitised (if not already in a digital form) and if necessary, interpolation can be performed so the time-step of the sea level curve is the same as the time-step of the CarboCAT model run.
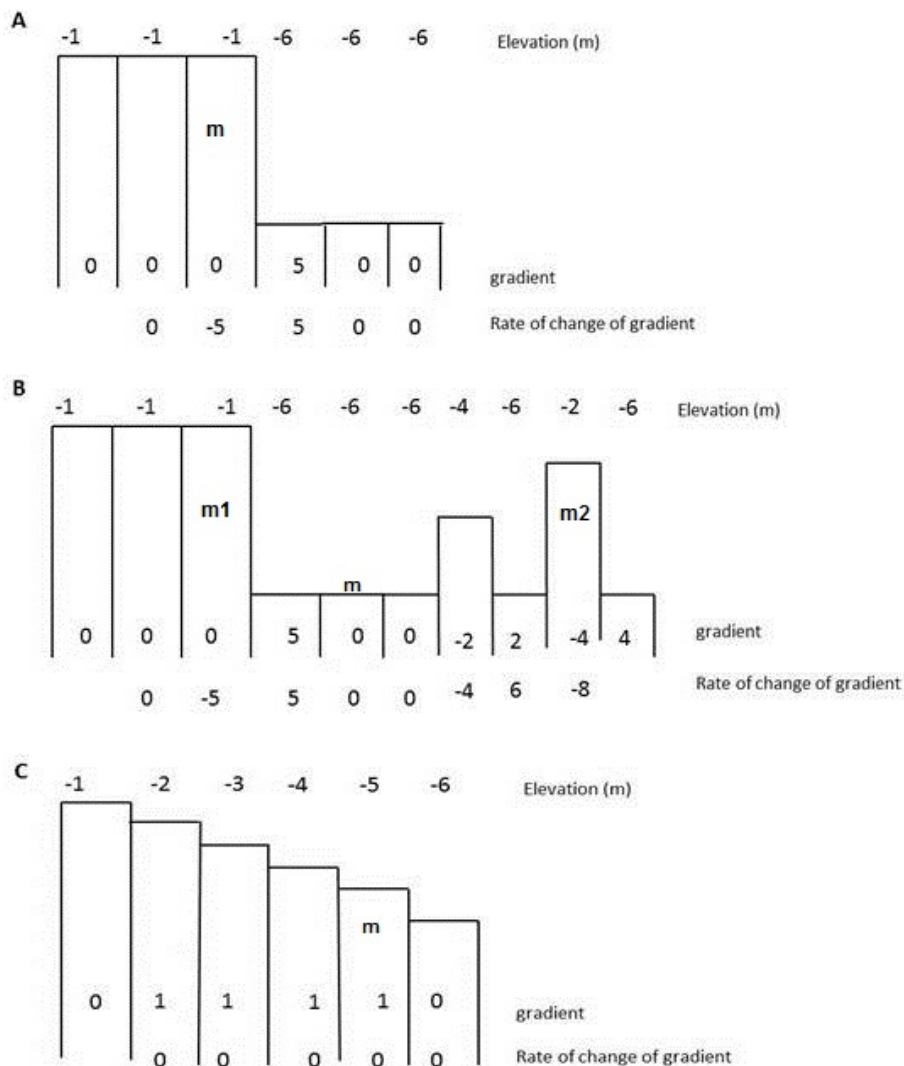
Figure 5.3: Hypothetical, cell based bathymetries, with the elevation (top row of numbers), gradient (middle row of numbers) and rate of change of gradient (bottom row of numbers) for each cell. (A)-Ideal FTP with a steep platform margin. Both the maximum gradient and the maximum rate of change of gradient identify the same cell (m) as the platform margin. (B)-In-situ carbonate production creates local build-ups. Based on the maximum gradient value, the margin is placed on m1, while based on the maximum rate of change of gradient value, m2 is the margin. In this case the algorithm picks cell m, as the platform margin. (C)-Bathymetry without pronounced geomorhic features. The algorithm picks cell m as the margin, based on the larger scale platform geometry (not shown in the figure).

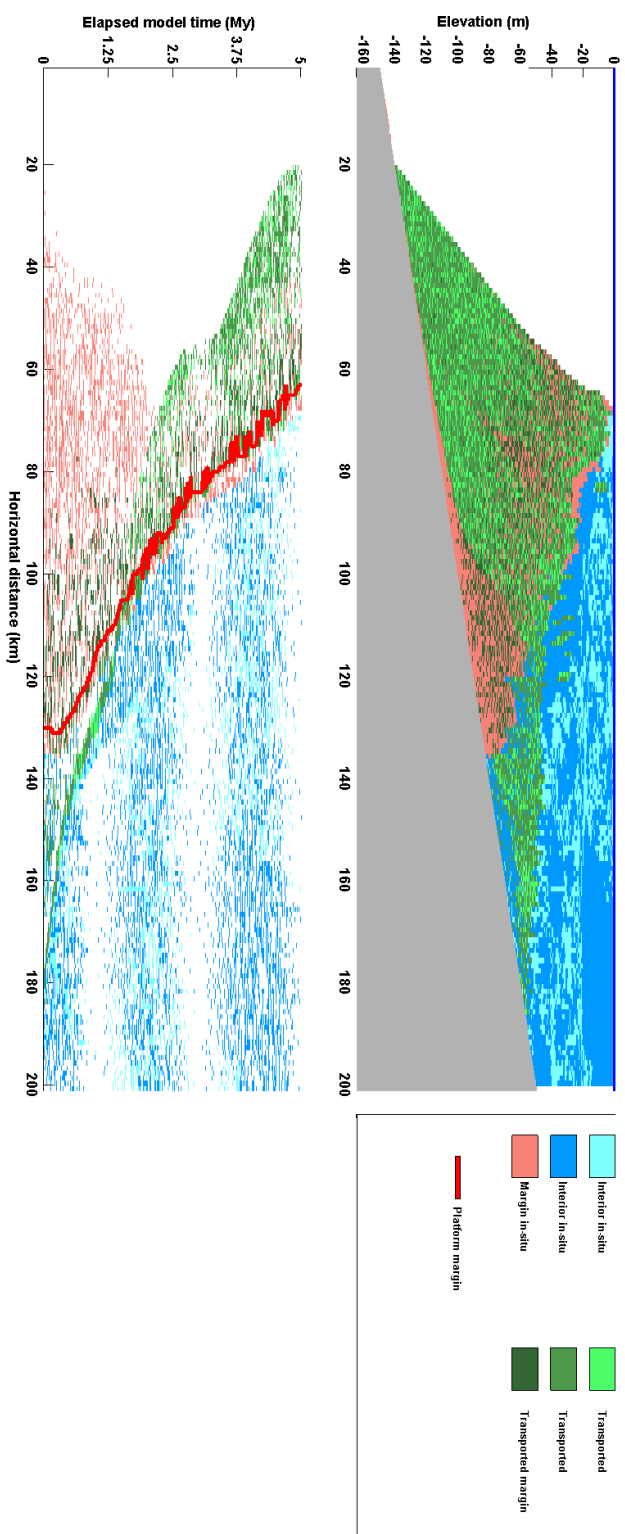Figure 5.4: TOP-Cross section along the depositional dip at x=15 of a 200x20 carbonate platform with 3 in-situ produced facies. BOTTOM -Chrono-strat section along the same position as A with the platform margin position (red line) superimposed.

5.3 Platform margin routine

A new algorithm was developed to calculate the position of the platform margin for each time step. The platform margin position is calculated as the average position of the highest bathymetric gradient and the highest rate of change of the bathymetric gradient (Fig.5.3). The bathymetric gradient is calculated as the elevation difference between two adjacent model cells. The rate of change of gradient is calculated using the central difference method eq.(**??**)

The calculation of the platform margin position (Fig.5.4) is performed independently and is not required by the transportation routines. The calculation of the platform margin position allows, among other possibilities, for calculating the amount of sediment deposited at each platform segment (interior, slope) and the dimensions of each segment.

The platform margin routine is based on geomoprhic features of the platform to locate the margin. This implies that the margin routine performs best on FTPs with well developed margins and steep slopes. For ramp style geometries that lack platform margins or for the early stages of platform development when carbonate production occurs over much of the platform (0-0.2 My elapsed model time in Fig.5.4), there are no pronounced geomorphic features. The algorithm in such cases may generate results that look erroneous, but actually indicate the weakness of the specific method to identify platform margins.

In order to deal with cases where carbonate production generates locally irregular bathymetry a platform margin position is calculated for each transect along the depositional dip for each time step. If the platform margin position is used in any other function, the position of the margin is calculated as the average position of all the transects for this time step.

The platform margin routine does not require any input from the user. The algorithm is executed and the platform margin position is calculated for each iteration for all models runs. The user can choose whether to plot or not the position of the platform margin on the final cross sections plots. The movement of the platform margin position generates a platfrom margin trajectory.

The platform margin trajectory in new CarboCAT is equivalent to the shelf-edge trajectory of **Helland-Hansen2009**. The platform margin position is calculated for each time-step in CarboCAT but refers to the geomorphic feature of the platform and is not directly related to the sea level position.

5.4 Wave energy distribution routine

The wave energy algorithm calculates water energy conditions over the platform due to wind-generated propagating waves. The calculated wave energy is used to distinguish depositional environments and factories based on energy conditions.
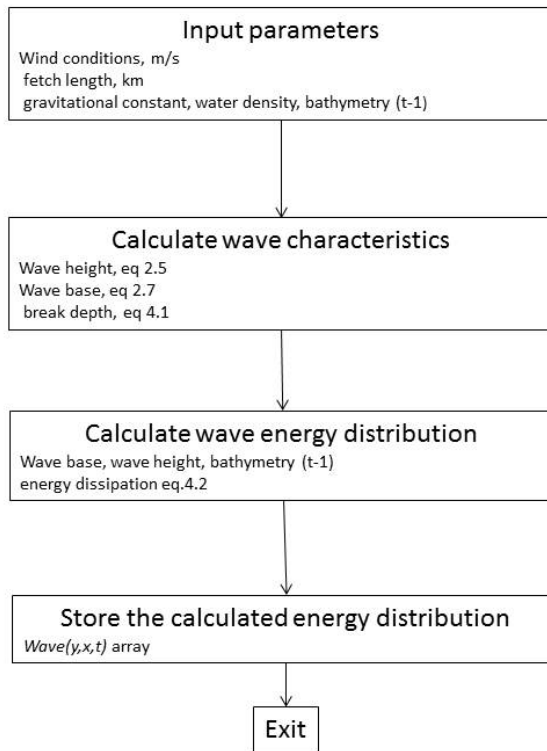
Figure 5.5: Wave fuction flow. The function, if activated from the functions parameter file, is executed for each time step for all model cells. The input parameters are show for each step.

Each depositional environment can have any number of factories assigned to it and each factory can be assigned to one or more depositional environments. Furthermore, a combination of wave energy dependent and energy independent factories can be used in the algorithm. Wave energy-independent factories are assigned to all depositional environments.

5.4.1 Description of the algorithm

The algorithm takes as input the fetch area size, wind conditions, water density, gravitational constant and the bathymetry of the model and calculates wave height, break depth, wave base (section 2.1.5.1) and the energy distribution over the whole platform for each time step and for each model cell (Fig.5.5). Initial fetch area, wind conditions and water density have to be defined at the beginning of the model runs and remain constant for the whole model time.

The function is executed after the calculation of the water depth and before the computation of new factories distribution (Fig.3.7). The function stores the calculated wave energy in an new array which is called *wave* accessible to all other CarboCAT functions. The *wave* array is a three dimensional array with y and x dimensions corresponding to the platform dimensions and t is the temporal

dimension.

For any given fetch length and wind conditions the wave height of the biggest generated wave is calculated using eq.(5.1)

$$\frac{gH}{u^2} = 0.283 \tanh \left(0.0125 \left(\frac{gF}{u^2} \right)^{0.42} \right) \qquad (5.1)$$

where H is the wave height in m, g the gravitational constant in m/s^2, u the wind velocity in m/s and F the fetch length in m,

and the wave length from eq.(5.2).

$$L = \frac{gT^2}{2\pi} \qquad (5.2)$$

where L is the wave wavelength (m), g the gravitational constant in m/s^2, T the wave period (s).

The break depth is calculated from the wave height using eq.(5.3) and the wave base depth as half the wavelength (**SPM1984**).

$$H = 0.78d \qquad (5.3)$$

where H is the wave height (m) and d is the break depth (m).

Fair weather conditions and light winds ($\leq 10m/s$) generate waves with wave height that does not dependent on the fetch length. Alternatively, wave height from stronger winds ($> 15m/s$) is highly dependent on the fetch length (Fig.5.6).

The algorithm provides two options for the calculation of wave height based on wind conditions. If wind conditions are known or can be assumed as fair weather, the algorithm provides the option to define a constant wave height irrespective of fetch length. If there is data support for stronger wind conditions, the algorithm allows for calculating an active fetch area for each iteration.

The active fetch area (Fig.5.7) is defined by subtracting the length of the platform interior from the predefined initial fetch area. The length of the platform interior is calculated in new CarboCAT from the platform margin location routine, independently from the wave algorithm. The active fetch area may change for each iteration and is used for calculating the wave height for eq.(5.1).

Waves that propagate in areas with water depths less than the wave base are in touch with the sea floor and thus lose some energy as they propagate. In order to take into account the effect of energy loss, wave energy distribution over the whole platform is calculated using the kinetic energy dissipation rate due to water depth (**Terray1995**).

$$\frac{\varepsilon H}{u^2} = 0.3 \left(\frac{z}{H} \right)^{-2} \qquad (5.4)$$
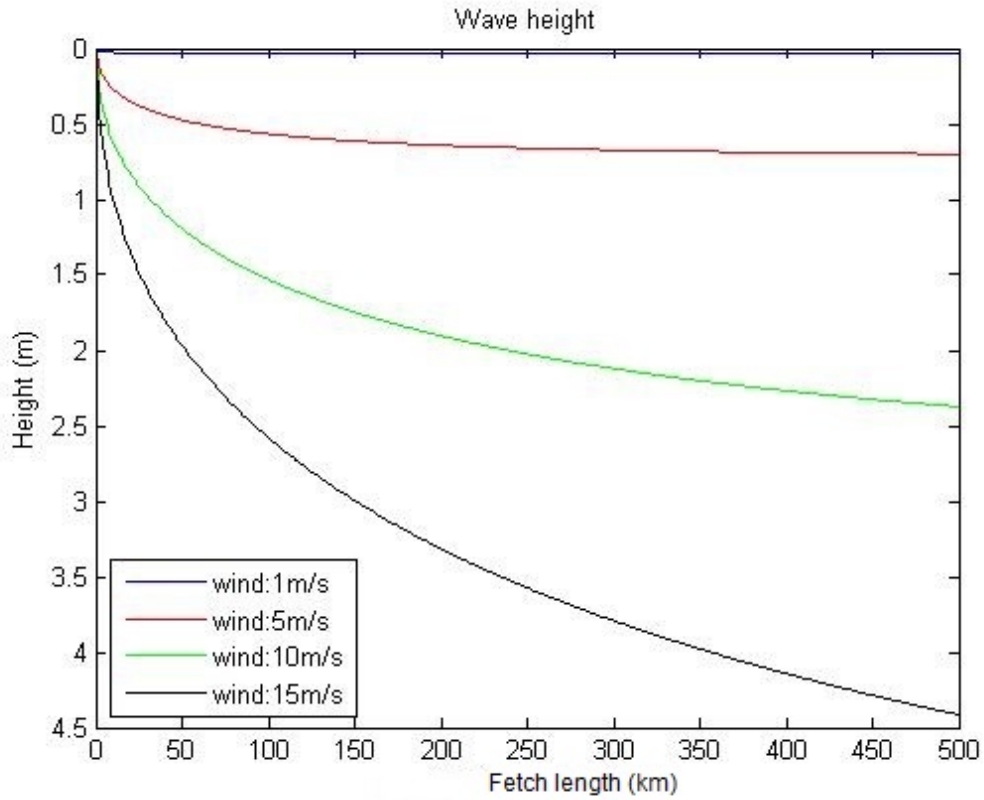
Figure 5.6: Wave height of the biggest wave generated from different fetch lengths and wind conditions. Light winds ($< 5m/s$) generate waves with height less than 2m irrespective of the fetch length. Wave height from stronger winds ($> 10m/s$) strongly depends on the fetch length. Small fetch lengths (less than 100km) generate waves with up to 2m heights while waves with height more than 4m can be generated by large (more than 300km) fetch.
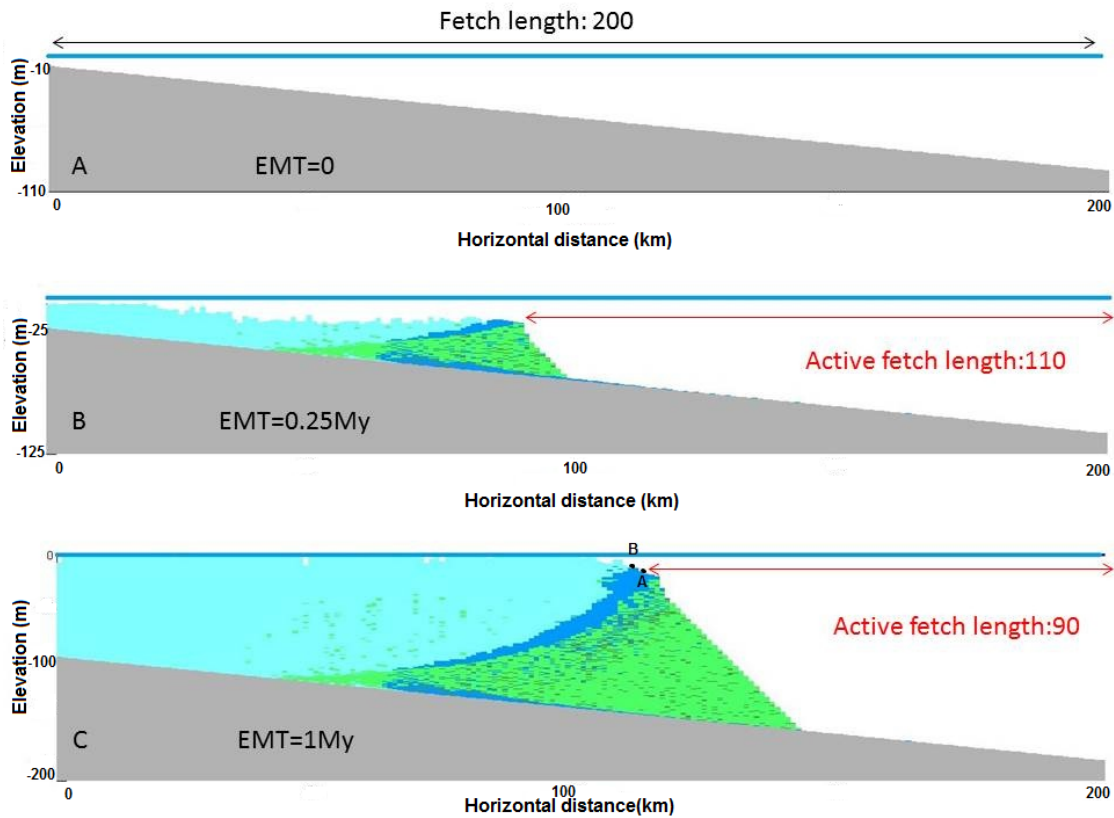
Figure 5.7: (A): Cross section of a homoclinal ramp with length 200 km, subsidence rate 100m/My and minimum water depth 10m. The fetch area has been defined as the whole ramp. (B):At 0.25My EMT carbonate production (light blue, low energy factory, blue, high energy factory and green colours) has built close to the sea level and has decreased the water depth at horizontal distances 0-90 km. The active fetch area at this point is restricted by the position of the margin. (C): At 1My EMT carbonate production has prograded farther, restricting the active fetch length to only 90 km. Water depth at point A is 10m and at point B 5m.

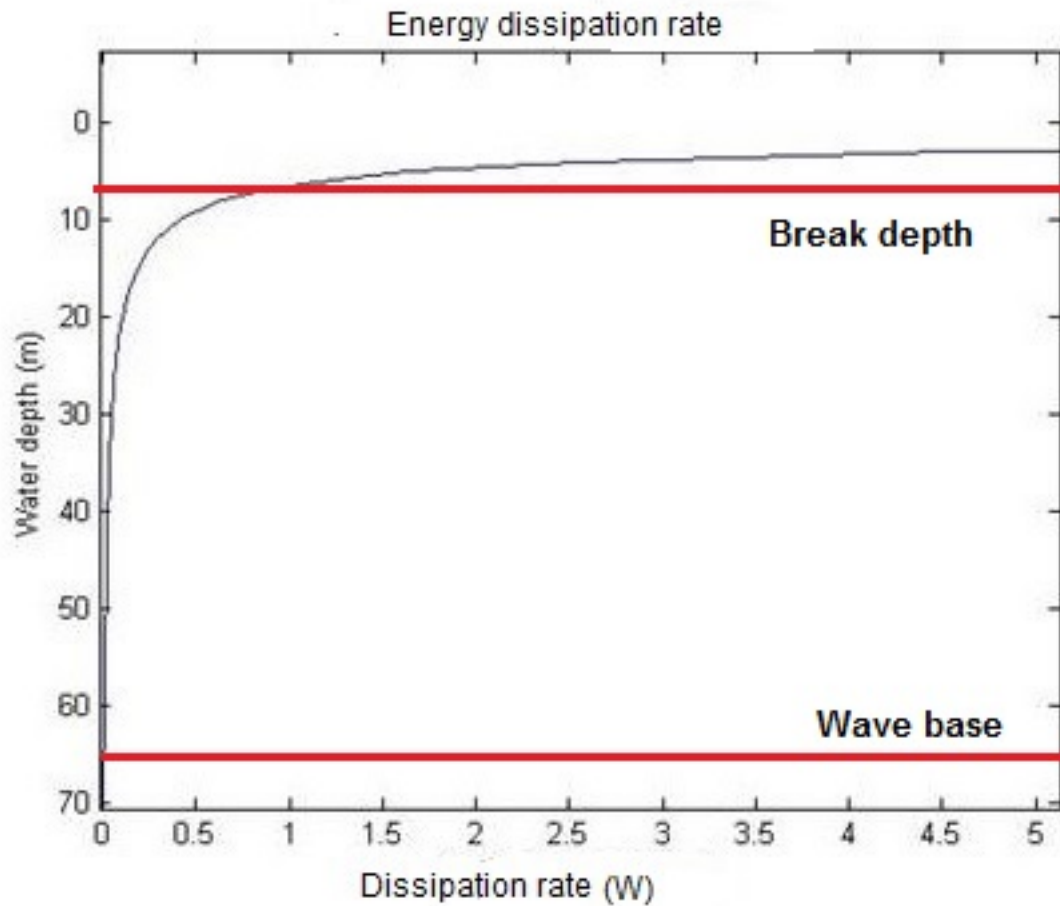Figure 5.8: Energy dissipation rate with water depth calculated from eq.(5.4) for a wave with height 5m. Energy dissipation rate becomes greater than 1W at 6.41m water depth which corresponds to the break depth and zero at 64m which is the wave base of the wave. The dissiaption rate is less than 0.1W below 20m and becomes greater than 0.5W only above 9m water depth indicating that most of the wave energy is lost at or above the break depth.

where ε is rate of energy dissipation in W, H is the wave height in m, u is the wave velocity in m/s and z is water depth in m.

The energy dissipation rate with water depth (Fig.5.8) calculated from eq.(5.4) reveals that energy loss occurs only above wave base and energy loss is minimal below break depth. Almost all of the energy dissipation occurs at or very close to break depth. The wave energy is dissipated very fast above the break depth.

For water depths less than the wave break, waves still contain some energy. The oscillation paths of the water molecules of waves that have broken become more elliptical and wave energy is transformed into turbulent kinetic energy.

Turbulent kinetic energy dissipation rate ε_t of a wave that has broken depends on the the kinetic energy of the wave, k, and the turbulent length scale, l. l depends on the surface roughness of the sea as the wave propagates and the bottom

roughness and is defined as eq.(5.5) (**Craig1994**):

$$l = \alpha(r_o - z) \qquad\qquad -(z_{max} - r_o + r_z)/2 \le z \le 0$$
$$l = \alpha(z_{max} + r_z + z) \qquad -z_{max} \le z \le -(z_{max} - r_o + r_z)/2 \qquad (5.5)$$

where z is the water depth, r_o is the surface roughness, r_z is the bottom roughness, z_{max} is the maximum water depth and α is a constant.

The turbulent kinetic energy dissipation rate is related to l based on eq.(5.6) (**Craig1994**)

$$\epsilon_t = \frac{\nu^3}{\beta l} \qquad (5.6)$$

where β is a constant of proportionality and ν is friction velocity.

ε_t is calculated by eq.(5.7) (**Jones2008**)

$$\frac{\partial k_t}{\partial t} - \frac{\partial \nu}{\partial z}\frac{\partial k_t}{\partial z} = \nu\left((\frac{\partial u}{\partial z})^2 + (\frac{\partial \nu}{\partial z})^2\right) - \varepsilon_t \qquad (5.7)$$

where k_t is the turbulent kinetic energy, ν is kinematic viscosity and z the height from the sea-bed.

Calculation of k_t and ϵ_t with linear models is not appropriate (eq.5.7) and includes parameters that are not calculated in CarboCAT.

The wave height calculated with eq.(5.1) is the maximum generated height for the given wind and fetch conditions and thus the wave break from eq.(5.3) is the deepest possible. A wave with height 5m and break depth 6.41m would pass point A(water depth 10m) in Fig.5.7-C but would break before point B (water depth 5m). Point B is still a high energy area, because waves with height less than 3.5m move farther into the platform.

Calculating the energy distribution of only the biggest generated waves and assuming a single water depth for break depth and a single water depth for wave base is consistent with the results of **Peters2012** regarding wave penetration.

In order to take into account the effect of smaller waves that penetrate some distance farther from the break depth of the biggest wave, to include the effect of turbulent kinetic energy and the variability of wave energy with time (see section 2.2.2) the algorithm allows for some small but non zero wave energy on a number of model cells more proximal than the break depth along the wave propagation direction. The exact number of model cells with lower wave energy is calculated based on the bathymetry of the model and the break depths of waves smaller than the eq.(5.1) calculated.

The algorithm calculates the wave energy over the whole platform assuming that waves generated at the most distal part (or outside) the modelled platform and propagate in a straight line towards the more proximal part of the platform.

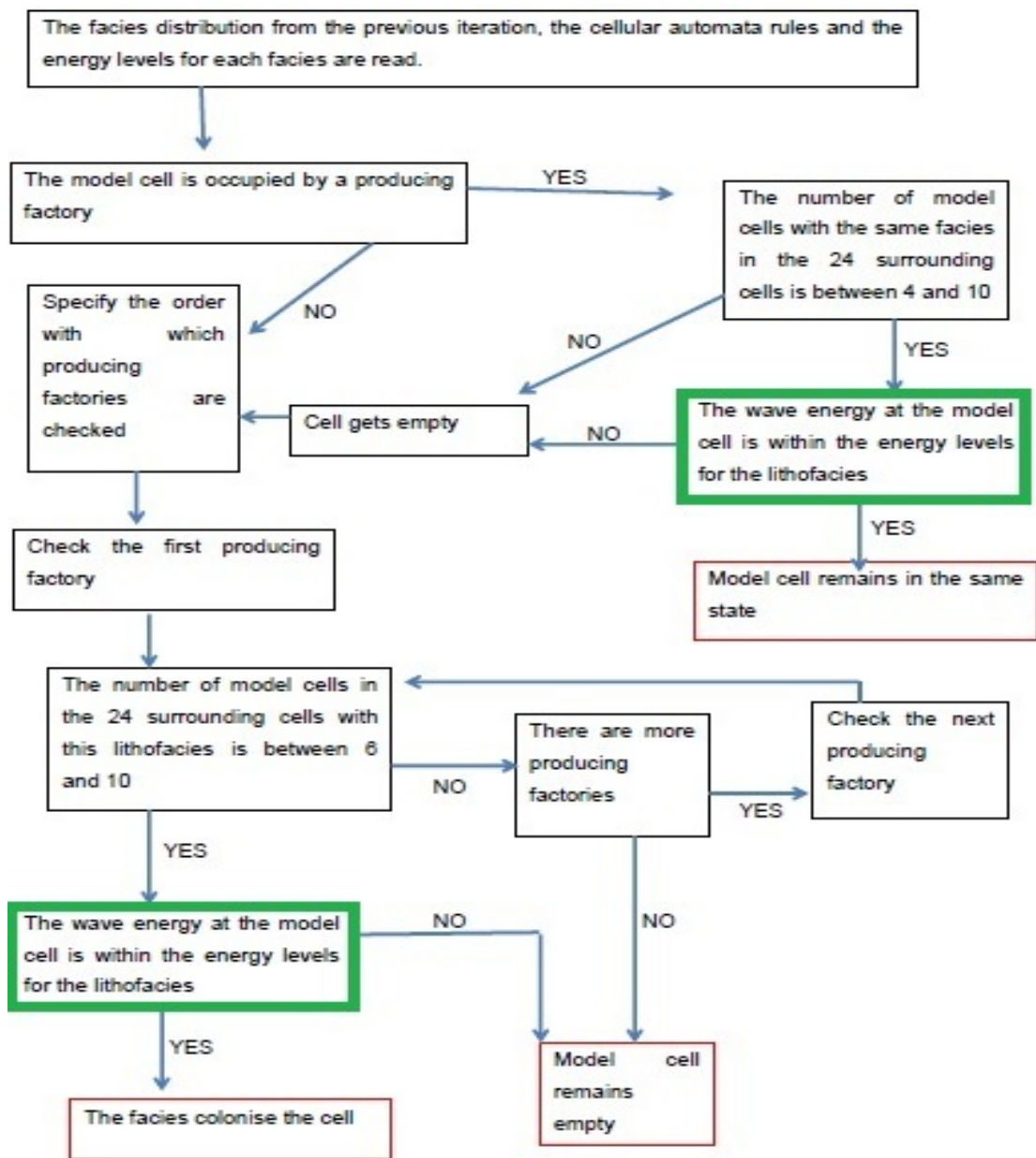Figure 5.9: Diagram showing calculation of factories distribution from cellular automata and the additional control from wave energy (green rectangulars). Black rectangulars indicate functions and red rectangulars termination of the code. Cellular automata rules for this example include 24 cells neighbourhood size, minimum four and maximum ten cells for factory survival and minimum six and maximum ten cells for factory colonisation.

Wave energy distribution is calculated for each transect along the depositional dip and it is not affect by wave energy or bathymetry outside the transect.

The wave energy routine is executed before the factories distribution for each time step and thus factories distribution can be affected from the wave energy. The wave algorithm implements an additional condition to the cellular automata rules that define the occupation and colonisation of a model cell from each factory.

Factories occupy or colonise a model cell if the relevant spatial conditions specified by the cellular automata rules are met and the wave energy at that model cell has the proper value for their type. If the wave energy value at a model cell is not the within the thresholds for the relevant type, factories are not allowed to occupy or colonise a model cell even if the other conditions have been met (Fig.5.9).

5.4.2 Algorithm examples

.

Fig. 5.10 shows the wave energy distribution over a platform as a function of the bathymetry over time. Early in the model, waves travel uninterrupted across the whole ramp. Deposition on the platform decreases the water depth at the most proximal part of the platform and waves break farther from the shore. The formation of a wave resistant platform margin causes the wave to break directly on the margin and a low energy interior is formed. Waves have no effect below the wave base.

Wave energy controls the factory distribution and thus the lithology and facies distribution over the platform. Factories can be low, high wave-energy or wave energy-independent. Factory distribution without wave energy (Fig.5.11-A) is controlled only by the water depth dependent-production profiles (right part of Fig.5.11).

Wave energy control affects the facies distribution with the high energy facies preferentially concentrating in front (relative to the wave propagation direction) of the low energy facies.

The size and distribution of the high energy area are controlled by the height of the biggest wave used in the calculation of the wave energy. Small waves with shallow break depth initially penetrate farther in the platform and generate a wide, prograding high energy environment (Fig.5.11-B). Bigger waves with deeper break depths generate a high energy environment confined around the initial position of their break depth and a laterally extensive, low energy environment (Fig.5.11-D).

Based on the bathymetry of the model and the height of the waves, three depositional environments are defined:
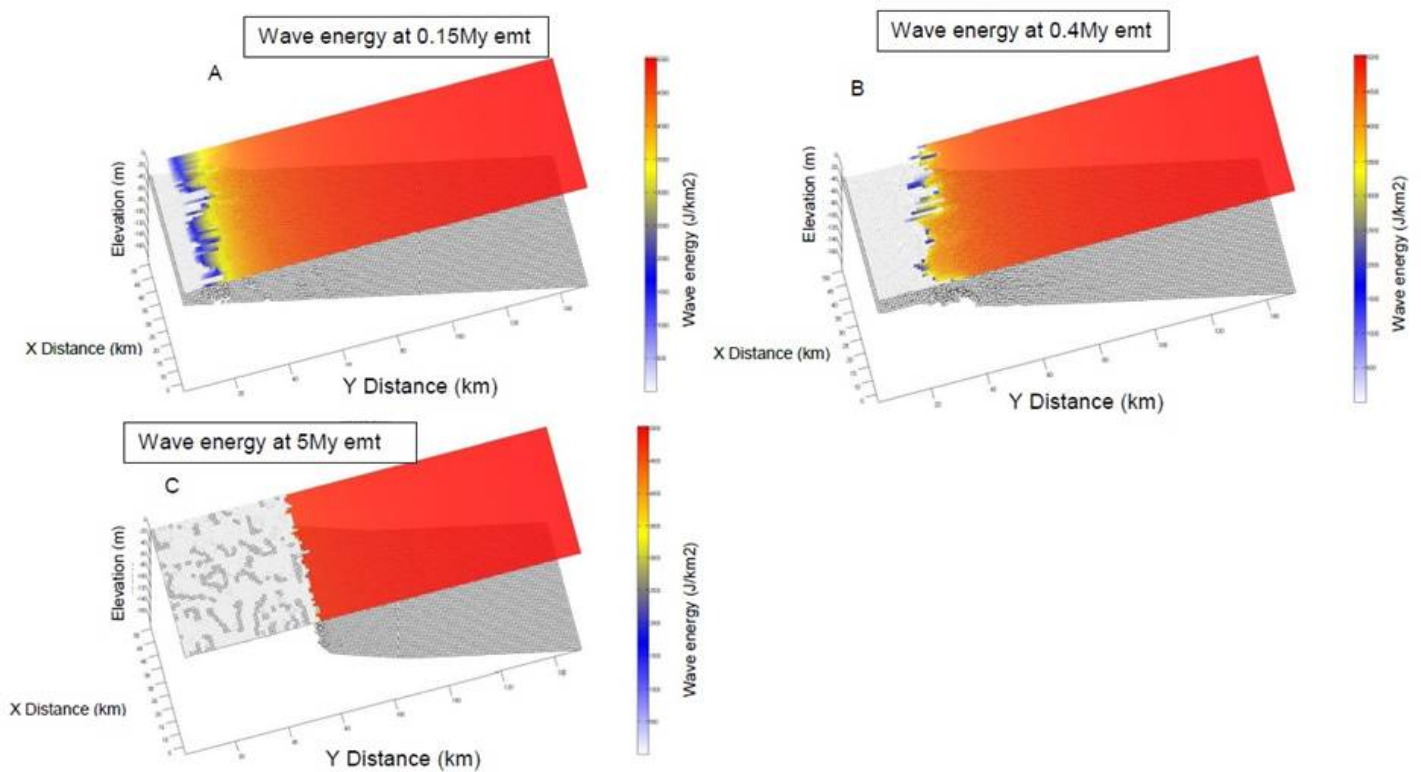
Figure 5.10: Wave energy distribution over a carbonate platform for a wave with height of 2m and wave length of 48m. The breaking depth of the modelled wave is 2.3m. and the wave base is 24m. A modelled platform of 150x50 cells with duration 5 My, initial bathymetry a homoclinal ramp, constant sea level and constant spatially and temporally subsidence was used. The bathymetry of the platform is also shown. (A) Energy distribution at 0.15 My EMT. Waves travel undisturbed from the basinal part of the ramp (y=150) and break to the more shallow part of the ramp (y=18).(B) Energy distribution at 0.4 My EMT. As the platform is formed and the platform top aggrades, platform top water depth decreases and waves break farther from the shore (y=45). (C) Energy distribution at 5 My EMT. FTP has been formed and waves break directly at the platform margin (y=58). The grey patches on the interior are bathymetric highs
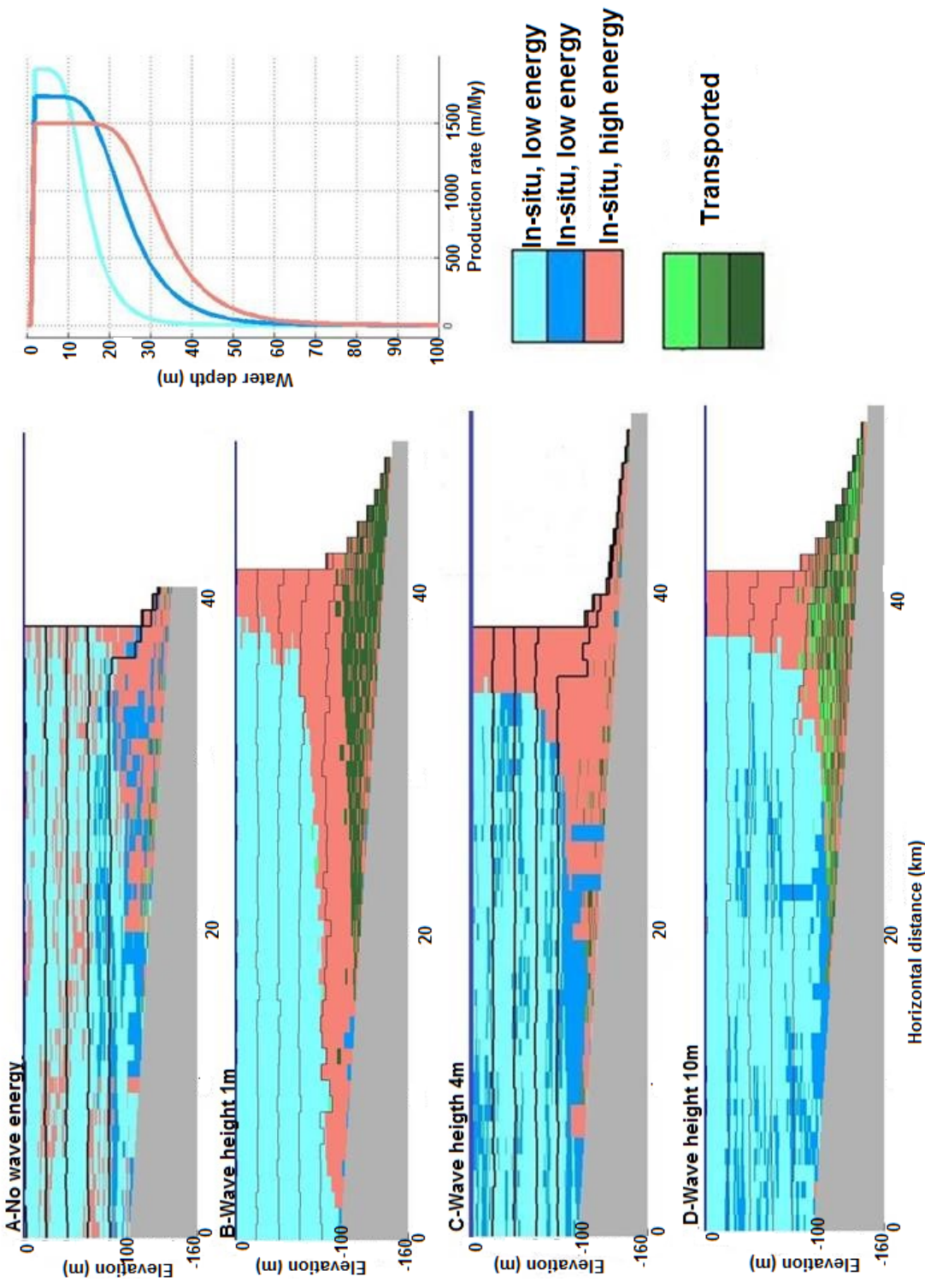
Figure 5.11: Factory distribution with different wave heights. A carbonate platform with initial bathymetry a homoclinal ramp with water depth 0m at the most proximal part (0 km horizontal distance) and three insitu producing factories has been used for all cases. Waves propagate from distal areas (> 40 km) towards 0km. All cross sections are generated at the same point. (A) No wave energy control or energy independent factories. (B) Wave height 1m and break depth 1.28m (initially located at 2km). The limited low energy environment shows very small water depths and as a result only the more shallow of the low energy facies survives.(C) Wave height 4m and break depth 5.12m (initially located at 8km). (D) Wave height 10m and break depth 12.8m (initially located at 16km). The smallest wave used for the energy calculation behind the break depth, was 1m and thus the length of the high energy part of the margin is always the same.

113

1. low energy, platform interior;

2. high energy, platform margin and upper slope;

3. below wave base, lower slope or basin.

Even though the algorithm is efficient for its purpose, further developments could be implemented. Wave propagation currently described as straight lines, can be improved to include wave refraction and diffraction. Moreover, the concept of fetch area can be expanded. Fetch area is assumed to be only the more distal platform part. Creation of local fetch areas in other parts of the platform that locally generate smaller waves can be introduced.

5.5 Siliciclastic input routine

A new algorithm has been developed that simulates the deposition of siliciclastic strata in new CarboCAT. The algorithm assumes that the source of siliciclastic material is located outside the boundaries of the modelled platform and the volume of the siliciclastic material through time is known. The algorithm models suspended load and calculates the effect of siliciclastics on carbonate production as well.

5.5.1 Description of the algorithm

Siliciclastic material is introduced from outside the platform as a separate factory without in-situ production. The siliciclastic material is diffused from a point or a line source into the platform. The algorithm uses Fick's second law to compute the concentration of siliciclastic material with time (Fig.5.12) and the results are stored in two new three dimensional arrays.

The *concentration* array stores the concentration of siliciclastic material on each model cell for each time step. The *productionBySiliciclasticMap* array stores the effect of the siliciclastics on carbonate production for each model cell for each time step.

Both the concentration and the siliciclastic effect arrays are accessible by all other functions and can be used where necessary. For consistency throughout new CarboCAT it is important to update the strata array using the siliciclastic concentration data array in the production function as well. The production function also updates the strata array and care must be taken not to overwrite the siliciclastic updates.

Suspended load and the use of diffusion for computing the concentration of siliciclastic dispersal, limits the grain size of the material that can be modelled.
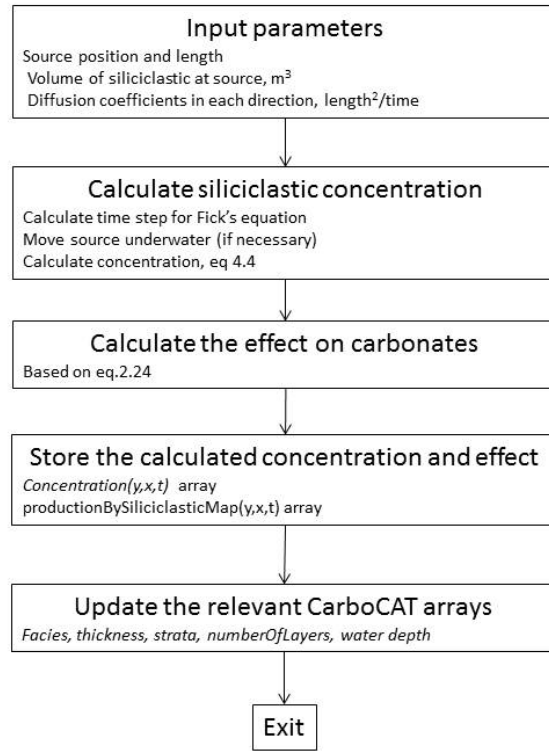
114

Figure 5.12: Siliciclastic algorithm and the relevant equations in each step. The function is executed (if activated from the functions parameter file) for each iteraton before the calculation of carbonate production.

The grain size of the simulated siliciclastic material with the diffusion algorithm is assumed to be sand or finer.

Fick's second law is a second order differential equation which predicts how diffusion causes concentration to change with time. The general 3D equation is

$$\frac{\partial C}{\partial t} = D\nabla^2 C \tag{5.8}$$

where C is the concentration and D is the diffusion coefficient with dimensions $(length^2/time)$.

The diffusion algorithm uses the 2D version of eq.(5.8)

$$\frac{\partial C}{\partial t} = D_x\frac{\partial^2 C}{\partial x^2} + D_y\frac{\partial^2 C}{\partial y^2} \tag{5.9}$$

where D_x $(length^2/time)$ and D_y $(length^2/time)$ are the diffusion coefficients along the x and y directions.

Eq.(5.9) calculates the diffusion of material in the two horizontal directions over the platform. The distance over which siliciclastic material is dispersed in each direction is only controlled by the diffusion coefficient in that direction and the volume of siliciclastics.

115

For stability of the solution and in order to avoid numerical errors, the time step t in eq.(5.9) is different from the main model time step. The time step in the diffusion equation is defined based on eq.(5.10) (**Kajishima2017**).

$$\frac{D\Delta t}{\Delta x^2} \leq \frac{1}{2} \tag{5.10}$$

where Δt is the time step for the diffusion equation and Δx is the size of the CarboCAT model cell. The time step for the diffusion equation depends on the model cell dimensions and it is not related to the main model time step. Reducing the spatial size by half, increases the time step by a factor of four. Typical values for the time step for the diffusion equation are in the order of a few hundred years.

In practise, for each time-step in CarboCAT the diffusion equation is solved with a time increment Δt, as many times as necessary depending on the size of Δt and the main model time step. For example, a main model time step of 1 ky would require the diffusion equation to be solved ten times, assuming that the Δt is hundred years.

Siliciclastic strata once deposited based on the diffusion equation remain in their position unlike the carbonate strata. Siliciclastic strata affect the bathymetry, the wave energy distribution and carbonate production but are not included in the transportation algorithms. Neither the siliciclastic nor the transportation algorithms include reworked siliciclastic strata.

The siliciclastics diffusion algorithm is executed before the calculation of carbonate production. The effect of siliciclastic material on each factory is calculated separately and two options are available. The first option limits the carbonate production in the presence of siliciclastics, simulating the effect of mud or clay on carbonates. The second option does not limit carbonate production.

The effect of the concentration of siliciclastics in the water column on carbonate production is quantified based on the production rate for each facies with water depth (**Bosscher1992**) eq.(3.4).

$$p_z = p_m \tanh\left(\frac{I_0 \exp(-kz)}{I(c)}\right)$$

where z is the water depth in meters, p_m is the maximum production rate in m /My, I_0 is the surface light intensity, I is the saturation light intensity, c is the extinction coefficient and k is a constant.

Saturation light intensity depends on water conditions while each species shows different sensitivity to I. The effect of siliciclastics on carbonate production is calculated based on the concentration of siliciclastics at each model cell and the user defined sensitivity of each factory to siliciclastic material. For each factory, a concentration of siliciclastic material that completely kills carbonate production is defined.

The algorithm reduces carbonate production (increases I because I is in the denominator in eq.(3.4)) for each factory based on eq.(5.11)

$$I_c = I/(1 - \frac{C_{(y,x)}}{C_{(factory)}}) \qquad (5.11)$$

where I_c is the saturation light intensity, $C_{(y,x)}$ is the concentration of siliciclastic material on each model cell and $C_{(factory)}$ is the concentration that completely kills carbonate production for each factory (Fig.5.13).

When the concentration of the siliciclastic material $C_{(y,x)}$ reaches the concentration that completely kills carbonate production $C_{(factory)}$, the denominator in eq.(5.11) becomes zero and the value for saturation intensity light reaches infinity. Infinite saturation light intensity in eq.(3.4) implies that carbonate production is zero.

The user defined parameters necessary for the algorithm are:

- the length of the source. A point or a line source can be used;

- the diffusion coefficients in each horizontal direction on the platform;

- the volume of the siliciclastic material that inputs the platform per time step;

- the position of the source relative to the platform;

- the sensitivity of each factory to the presence of siliciclastic material.

5.5.2 Results

Siliciclastic material is introduced and dispersed from a point source outside the carbonate platform. Introduction of siliciclastic material in a mixed carbonate, siliciclastic platform generates three distinct and uneven in size zones. The zones are controlled by the concentration of siliciclastics and the sensitivity of the carbonate factory (Fig.5.14):

- zone A is dominated by siliciclastic strata that completely fill the available accommodation. The size of zone A is directly controlled by the volume of siliciclastic material supplied at the source;

- zone B lays at the periphery of zone A and marks the area of interaction between siliciclastic and carbonate strata. The accommodation is not completely filled by siliciclastic strata but their presence decreases carbonate production. The effect of siliciclastics on carbonate production in zone B is controlled by the sensitivity of the carbonate facies to the presence of siliciclastics;
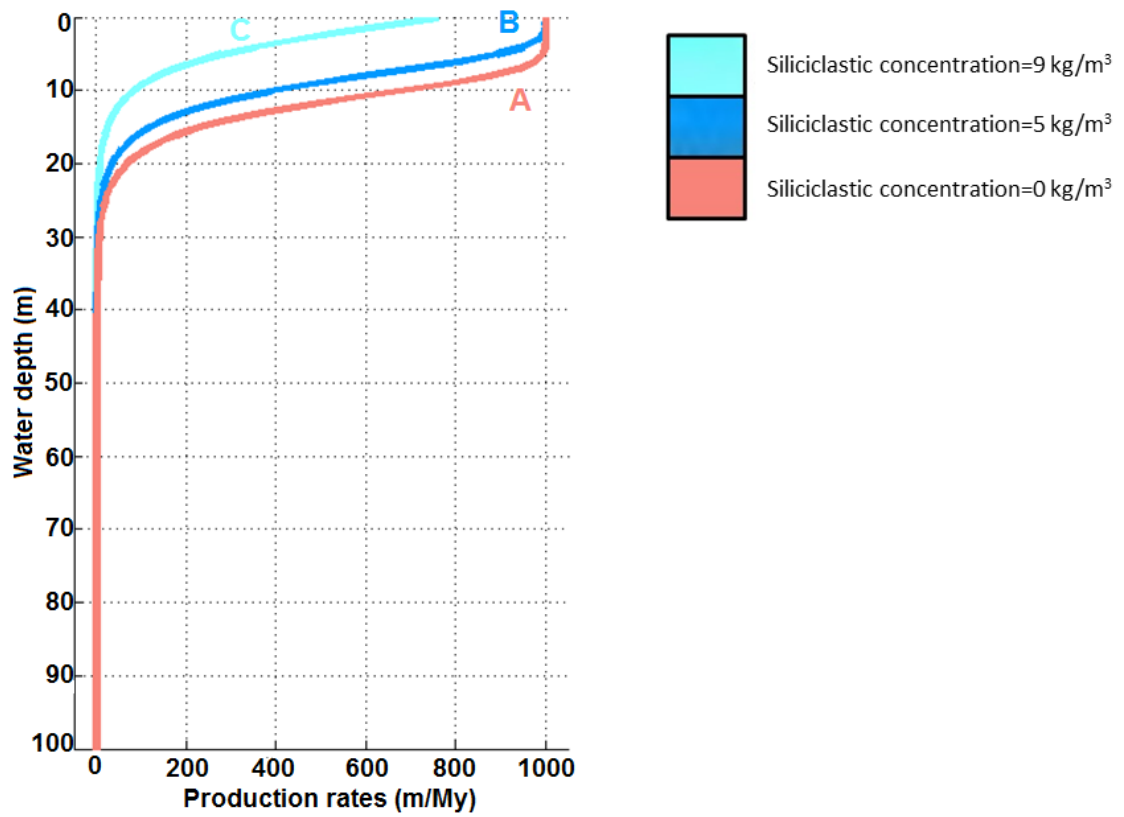
Figure 5.13: Impact of siliciclastic concentration on carbonate production. A factory with production rate 1000 m/My, surface light intensity 3000 $\mu Em^{-2}s^{-1}$, extinction coefficient 0.25, saturation light intensity 300 $\mu Em^{-2}s^{-1}$ and 10 kg/m^3 concentration of siliciclastic material for complete production shut down is shown. Line A shows the factory production profile without siliciclastics. The factory has maximum production rate at the top 5m water depth and production cut-off at 42m water depth. Siliciclastics with concentration of 5 kg/m^3 (line B) limits the maximum production zone to the top 3m and the product cut-off to 32m water depth. 9 kg/m^3 concentration of siliciclastic material (line C) decreases the maximum production rate to 760 m/My and the production cut-off water depth to 24m.
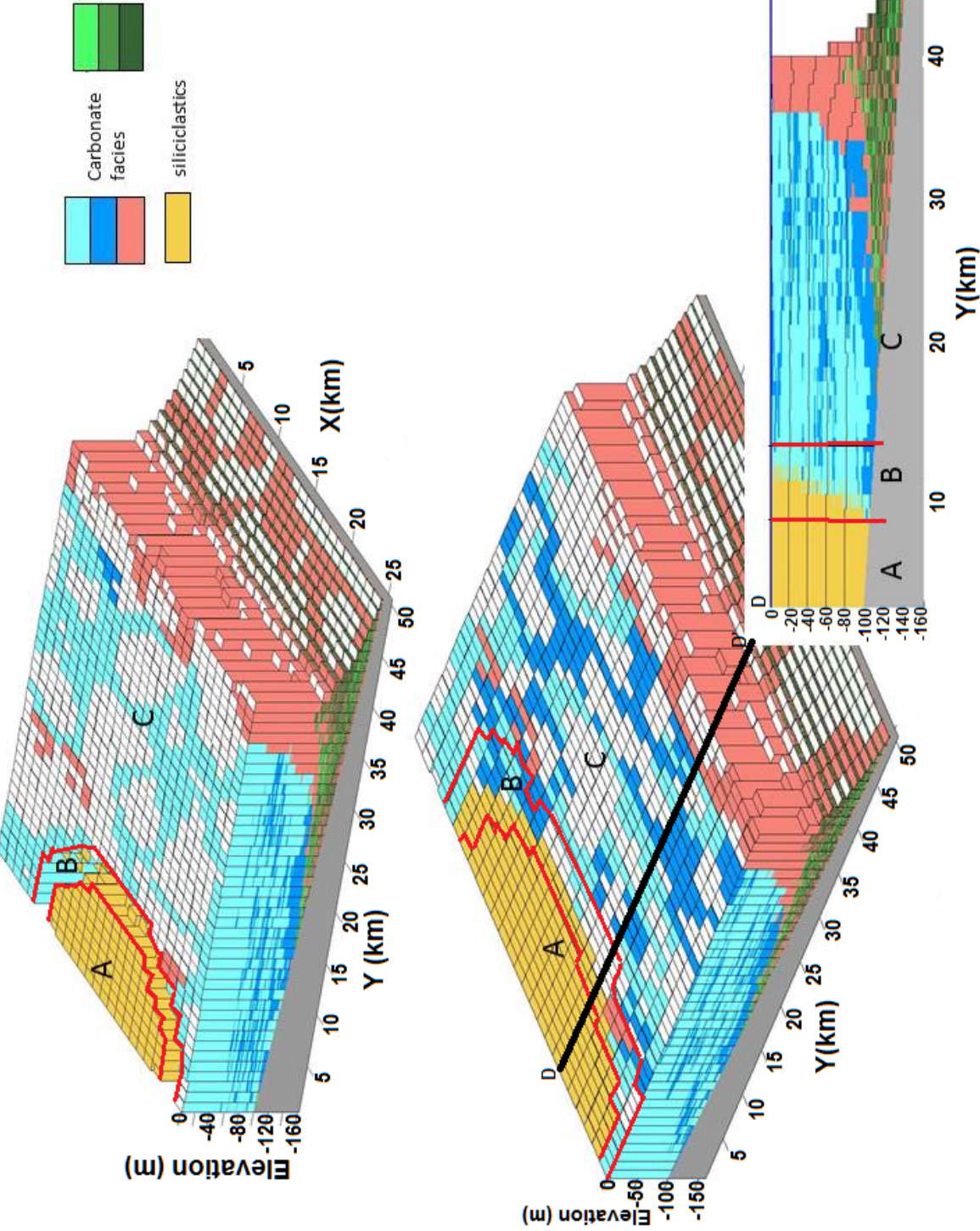
Figure 5.14: 3D models of a mixed carbonate-siliciclastic platform with 3 zones. Siliciclastic material is introduced from a point source outside the platform (y=0) at x=12. Based on the their volume, siliciclastic strata occupy the whole available accommodation in an area around the point source (zone A). The presence of siliciclastic material farther from zone A limits carbonate production in zone B. Outside zone B there is no effect on carbonate strata from siliciclastics (zone C). TOP. Any concentration of siliciclastics complete kills carbonate production (shut down siliciclastic concentration is any positive number). Zone B remains partially empty. BOTTOM. Siliciclastic strata limit but not completely kill carbonate production. The structure of zone B can be better seen on the inserted cross section. The boundaries of each zone are also shown (red lines).

119

- zone C occupies the remaining platform space and represents the area where there is no siliciclastic effect on carbonate production.

Further development of the siliciclastic algorithm could be introduced to improve the algorithm's outcome. Currently all siliciclastic material is assumed to be of the same grain size. Introduction of multiple size and coarser material could be modelled. The effect of siliciclastics based on their grain size on each numerical carbonate facies can be implemented. Moreover, siliciclastic material could be assigned to an extra numerical facies which would allow computation of secondary transportation of siliciclastic strata under the same hydrodynamic conditions as the carbonate strata.

5.6 Cross-platform transportation routine

The steepest descent algorithm describes sediment transportation in well developed platform margins and slopes. In the relatively flat platform interiors steepest descent moves material short distances or not at all. In order to take into account sediment movement due to water currents on the platform top a new algorithm was developed. Water currents over a carbonate platform can be regional oceanic currents related to thermal or density differences in the area of the platform. The cross-platform algorithm simulates movement of carbonate clasts based on platform interior energy conditions.

5.6.1 Description of the algorithm

The routine moves material across the relatively flat platform interior along a user defined transportation direction and the algorithm conserves matter. Sediment transportation is based on the local hydrodynamic conditions on the platform. The energy (τ) calculation for each model cell includes shear energy from water currents ($\tau_{current}$) and shear energy from the bathymetry of the platform (τ_{slope}), eq.(5.12).

$$\tau = \tau_{slope} + \tau_{current} \qquad (5.12)$$

The method for estimating the shear energy on the platform is the same as the sediment dispersal method in CARBONATE3D (**Warrlich2008**). CARBONATE3D (see section 3.1.6) describes sediment entrainment, transportation and deposition of carbonate clasts with different grain sizes, based on the energy conditions on a platform. The cross-platform sediment transportation algorithm also describes sediment transportation of carbonate clasts with several grain sizes and thus uses the same method and the same equations.

The shear energy due to bathymetry (τ_{slope}) is a measure of the local bathymetric gradient in each model cell and is calculated from eq.(5.13) (**Warrlich2008**).

$$\tau_{slope} = \Delta\rho g s \sin(\alpha) \qquad (5.13)$$

where $\Delta\rho$ is the excess density of the submerged sediment in relation to water density, g is the gravitational constant (m/s^2), s is the grain size (m) and α the maximum bathymetric angle (^{o})at each model cell.

Carbonate facies density is not calculated in CarboCAT, so the densities of all modelled carbonate facies are assumed to be similar. The effect of grain size on sediment transportation is studied in section 7.1.

τ_{slope} has its maximum value at and around well developed platform margins where high gradients are dominant. More proximal than the margin, the relatively flat platform interior is characterised by significantly lower bathymetric gradients.

More distal than the margin and down the geomorphic slope, the bathymetric gradients are also small but τ_{slope} is non-zero and thus can move sediment (Fig. 5.15).

A user defined energy threshold is used to distinguish the margin from the interior and the upper slope. Areas with τ_{slope} above the threshold trigger the termination of the cross-platform sediment transportation algorithm and the transition to steepest descent transportation algorithm.

The second term in eq.(5.12) describes the shear energy from water currents active in the area of the platform. The current shear energy is calculated from eq.(5.14) (Fig.5.16) (**Warrlich2008**)

$$
\begin{aligned}
\tau_{current} &= E * \frac{z}{z_b} \qquad z \leq z_b \\
&= E, \qquad z_b < z < z_D \\
&= E \exp(-\frac{z - z_D}{\sigma_D}), \qquad z > z_D
\end{aligned}
\tag{5.14}
$$

where E (J/m^2) is the maximum shear energy value, z_b is the top depth interval of maximum shear energy (m), z_D is the deposition threshold water depth (m) and σ_D is a scaling factor (m).

The currents capacity to carry sediment is a function of water depth. For shallow water depths, the currents are moving fast and have high energy levels. For water depths greater than a threshold (z_b), controlled by local conditions for each case, currents expand, slow down and lose sediment transport capacity (Fig.5.16).

Current energy very close to sea surface (z_a in Fig.5.16) is affected by bathymetric features that build above sea level. Currents are moving fast due to small water depths but sub-aerially expose features (islands) block the current path since there is no space for the water to move. The effect of islands to platform interior is studied in section 7.2.

Shear energy due to water currents has its maximum value on the platform top where water depths are regularly small. $\tau_{current}$ at platform margins is significantly higher than the interior because shear energy at the margin is controlled by the propagating waves and not the water currents. Far from the margin and down the depositional slope, water depths typically exceed several tens of meters and thus slopes have very low $\tau_{current}$ (Fig.5.17)

In terms of eq.(5.12), platform interiors are relatively low energy environments due to the shear energy from water currents. Platform margins are high energy environments due to high bathymetric gradients and wave action. Upper slopes are relatively high energy environments due to wave actions and bathymetric gradients.
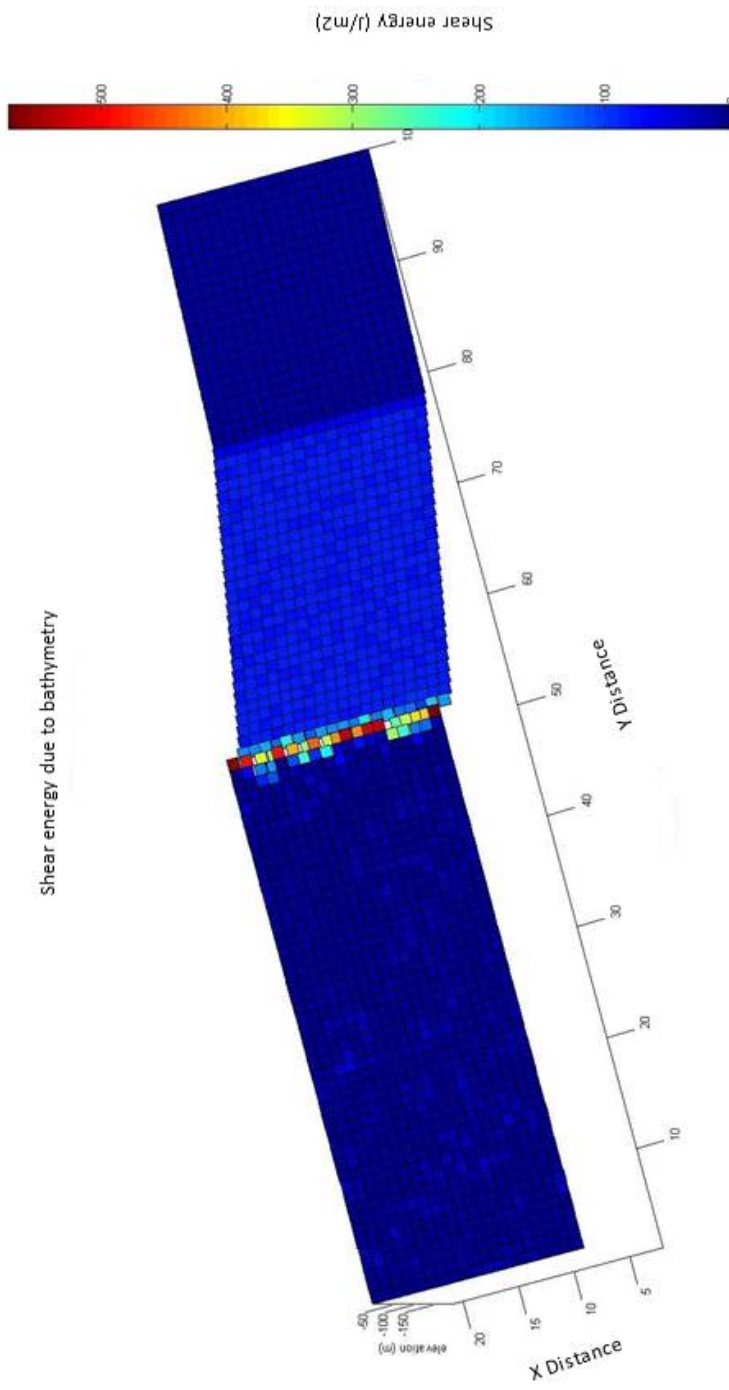
Figure 5.15: 3D plot with the shear slope energy over a 100x20 platform with homoclinal ramp initial bathymetry, constant ESL constant temporaly and spatialy subsidence rate. The high bathymetric gradients at the margin (Y=50) show the highest energy levels while the upper slope (Y=55-78) has intermediate energy values. More proximal than the margin (Y<50) and more distal than the upper slope (Y>78) the relatively flat platform interior and the lower slope respectively show significantly lower energy values. An energy threshold of 250 J/m2 can be used to distinguish the margin from the interior and the upper slope.
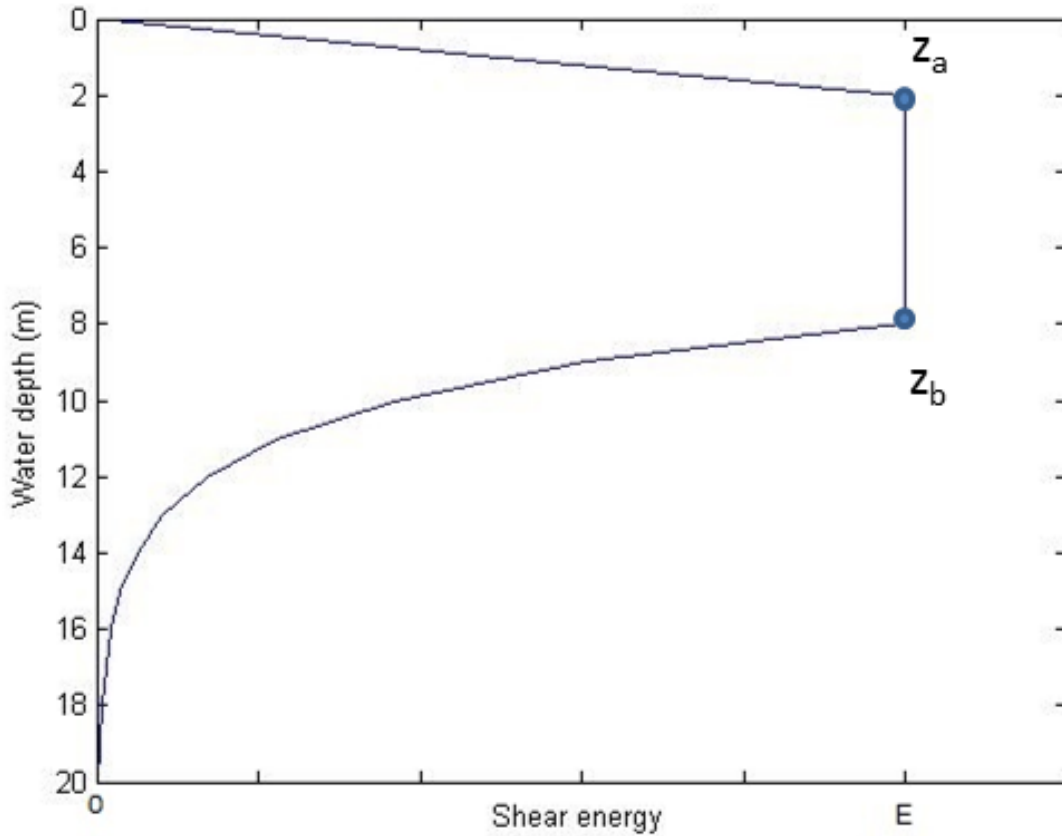
123

Figure 5.16: Shear energy from water currents with water depth. The energy of the water currents is maximum for shallow water depths and decreases with water depth below a threshold (z_b) as the currents expand and slow down. Energy levels very close to the surface (above z_a) are effected by islands that act as barriers to the current movement. The water depth of points z_a and z_b are controlled by the local conditions. Their values here have been selected for demonstrative purposes.
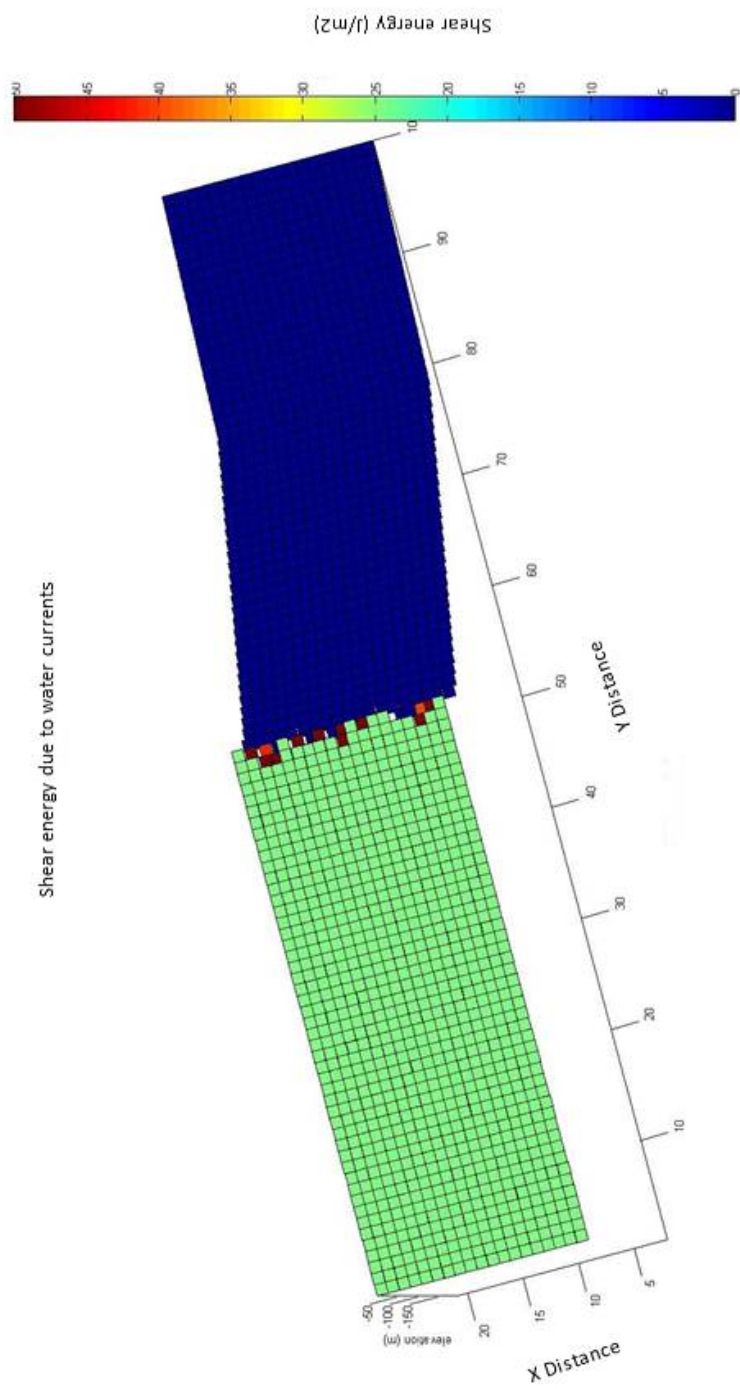
124

Figure 5.17: 3D plot with the shear current energy over a 100x20 platform with homoclinal ramp initial bathymetry, constant ESL constant temporaly and spatialy subsidence. The shallow platform interior (0-50 Y distance) shows some intermediate energy values and is followed more distally by a narrow belt of higher energy, the platform margin (Y=50). More distal, the deep slope environment shows minimum current energy. A threshold value of 10-20 J/m2 can be used to distinguish interior-margin from the slope.

The necessary user defined, input parameters for the cross platform algorithm are:

- the energy threshold for entrainment/deposition;

- the energy threshold for transition from cross platform to steepest descent;

- the transportation direction. The transportation direction defines the direction towards which the material will be moved from each model cell. The transportation direction can be chosen freely and can be even altered with time. Moreover, the transportation direction can be changed locally if necessary.

Here must be noted that the transportation parameters, namely the amount of material available for transportation, the local bathymetric gradient threshold for deposition and the deposited fraction, that were discussed in section 3.2.4.3 are still in use and must also be defined.

For each iteration the algorithm checks all model cells and it is executed (Fig.5.18) only if all of the following criteria are met:

- the cell contains in-situ produced material (source cell);

- the amount of material available for transportation is greater than the thickness threshold;

- the cell is below or at sea level;

- the total shear energy is greater than the entrainment threshold.

A special boundary condition has been created for the case the boundaries along the strike direction have been reached. The boundary condition or wrapping condition, assumes that equal amount of material that exits the platform from one side, enters the platform from the other side. Thus the algorithm moves the material from one side of the modelled platform to the other (Fig.??-B). The wrapping condition implies that the modelled area is part of a bigger platform with sediment flows controlled by large scale currents.

5.6.2 Results

Fig.5.19 shows the effect of the cross platform algorithm in the redistribution of the material and the geometry of a platform compared to the material distribution and platform geometry from the steepest descent algorithm only. The reworked
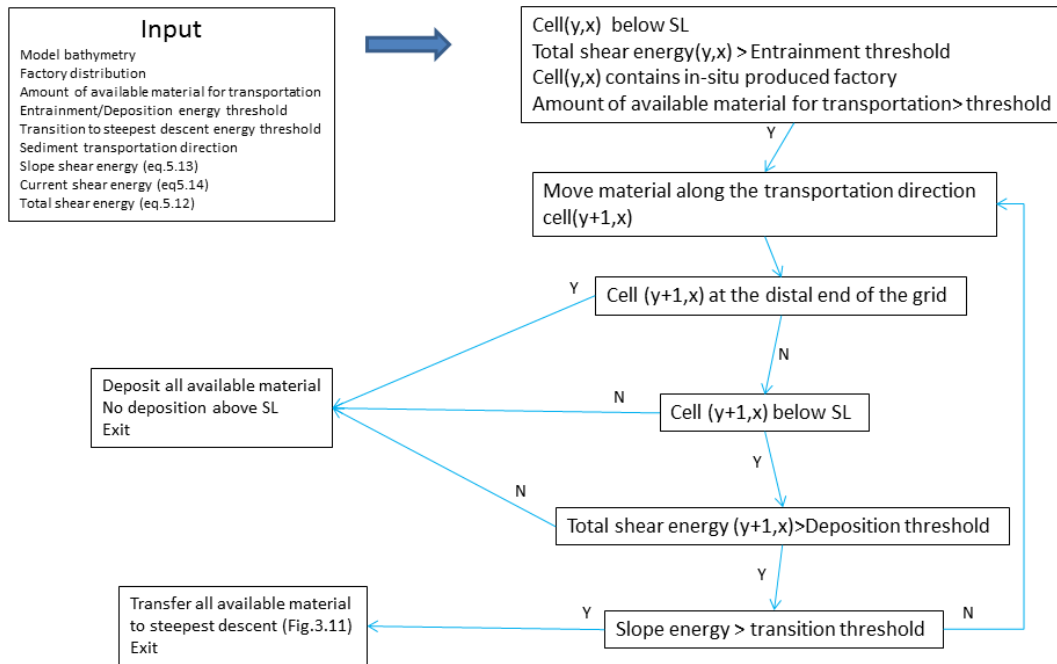
Input
Model bathymetry
Factory distribution
Amount of available material for transportation
Entrainment/Deposition energy threshold
Transition to steepest descent energy threshold
Sediment transportation direction
Slope shear energy (eq.5.13)
Current shear energy (eq5.14)
Total shear energy (eq.5.12)

Cell(y,x) below SL
Total shear energy(y,x) > Entrainment threshold
Cell(y,x) contains in-situ produced factory
Amount of available material for transportation> threshold

Move material along the transportation direction cell(y+1,x)

Cell (y+1,x) at the distal end of the grid

Deposit all available material
No deposition above SL
Exit

Cell (y+1,x) below SL

Total shear energy (y+1,x)>Deposition threshold

Transfer all available material
to steepest descent (Fig.3.11)
Exit

Slope energy > transition threshold

Figure 5.18: Flow chart describing the cross-platform sediment transportation algorithm. The algorithm terminates by passing the material to the steepest descent algorithm, or reaching a point with total shear energy is less than the deposition theshold or when it moves to the distal end of the grid. The algorithm conserves mass.

material for the model run with the steepest descent algorithm (Fig.5.19-A) consists of transported material from the margin facies only, has small thickness and gets deposited near the platform margin.

Reworked material from the interior facies is only observed in the early stages of the platform (0-0.20 My EMT Fig.5.19-B). As soon as the relatively flat platform interior is formed, only the local bathymetric gradients at the platform margin can exceed the threshold for transportation. As a result, material from the interior remains in its place or is moved very small distances.

The cross platform algorithm moves material along the relatively flat platform interior to the higher bathymetric gradient margin. The reworked material with cross-platform algorithm is comprised of rework material from the margin and the platform interior. The reworked from the margin still concentrates around the geomorphic margin but now an extensive slope (40 km) is dominated by thick transported material from the platform interior. A secondary effect of more reworked material being deposited is that the platform margin progrades more. The platform margin is located at 45km when the cross platform algorithm is used compared with the 35km with the steepest descent only (Fig.5.19-C).

The effect of the cross platform algorithm can be quantified in terms of deposited volumes on each platform area (Fig.5.20). The measured volumes represent material that got deposited either in-situ or by transportation at each specific platform segment for each factory for the model runs in Fig.5.19. The platform top environment represents the low wave energy part of the platform and the geomorphic margin. The slope environment represents the actual geomorphic slope (Fig.5.19 for reference).

Interior facies refer to low energy factories and margin facies to high energy factories. Both interior and margin facies have been mainly produced from factories on the platform top and their distinguish is based on their position on the platform top and their energy levels.

The cross platform algorithm transports 30% of the interior facies to the slope where it gets deposited (trans slope, red line Fig.5.20a). As a result the in-situ produced material in the platform top (in-situ, top, blue line, Fig.5.20a) represents only 2/3 of the total produced material (total, black line, Fig.5.20a).

Material from the platform top that gets deposited on the slope with the cross platform algorithm, reduces the water depth and allows for in-situ production of high energy, margin facies on the slope (in-situ slope, orange line, Fig.5.20c).

With the steepest descent algorithm only, because of low bathymetric gradients on the platform top, interior facies remain where have been produced and almost all of the material deposited on the platform top is in-situ produced (in-situ, top, blue line, Fig.5.20b). Sediment deposition on the platform top is due to locally produced bathymetric depressions (trans top, green line, Fig.5.20b) and represents

less than 10% of the total produced material.

Cross-platform sediment transportation across the highly productive platform top generates volumetrically significant deposits (Fig.5.20) to the slope. Lithological and compositional differences between platform top and slope material can be used to differentiate the origin of the strata on the slope (Fig.5.19).

Lack of platform top sediments on the slope could be an indication of limited cross-platform sediment transportation or an indication of restricted production area. Restricted production area can occur during lowstand conditions and thus identification of thick sediments from the platform top on the slope can be used as indication of highstand shedding for ancient carbonate platforms (**Schlager1994**).
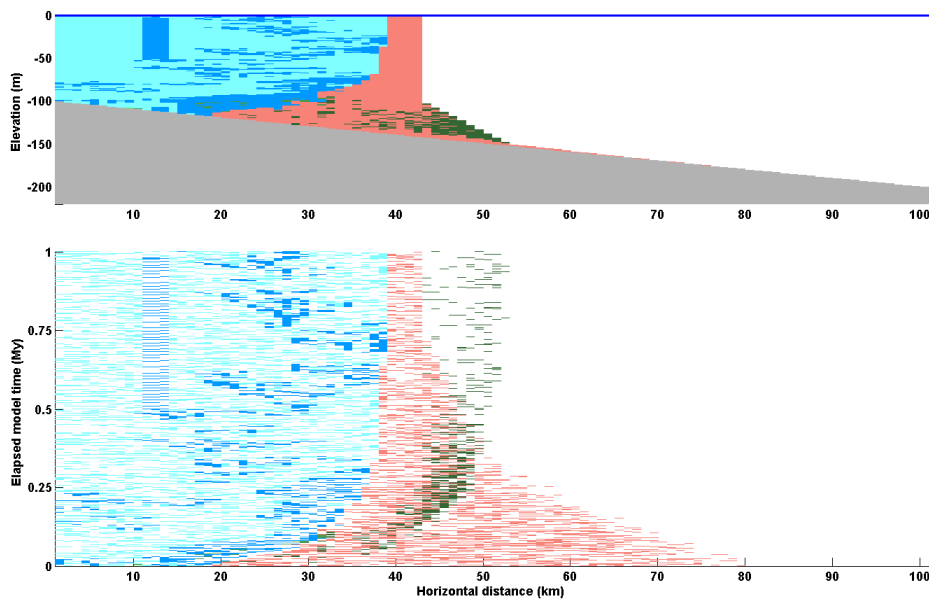
(a) Cross platfrom transportation algorithm
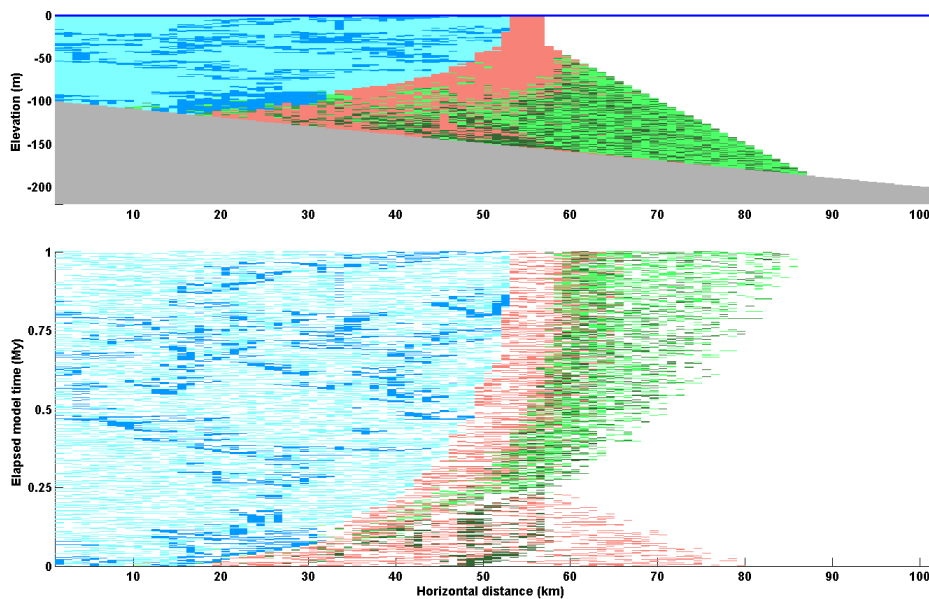
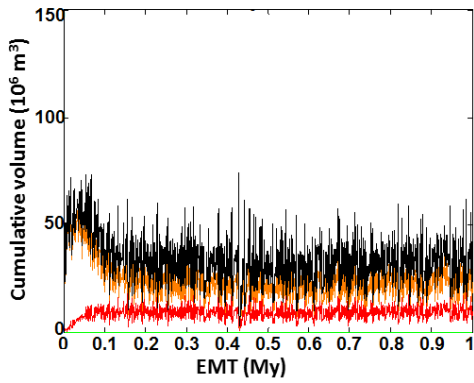(b) Steepest descent transportation algorithm only

Figure 5.19: Cross sections (TOP) and chrono stratigraphic sections (BOTTOM) along the same position of a model run with with 30% transported material (a) Steepest descent transportation algorithm only. The transported material is very thin and remains close to the margin (maximum transportation distance from the margin is 20km). The transported material consists of almost entirely of reworked margin material. (b) Cross-platform sediment transportation algorithm. The transported material is much thicker and moves farther from the margin (maximum transportation distance 40km). The margin is located 10km more distal (at 45km horizontal distance) than the margin in (a).Transported material from both the top and the margin is observed in the slope.
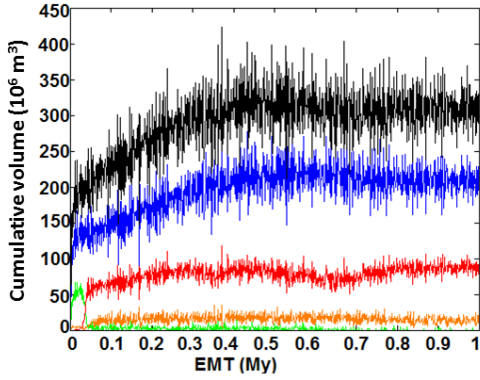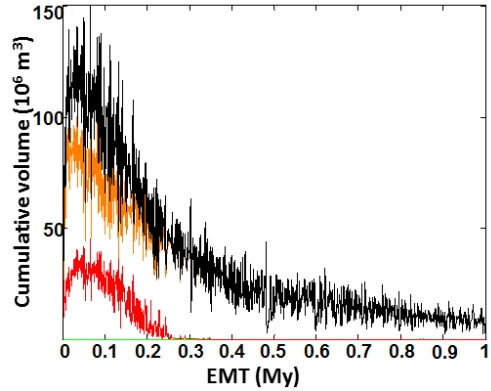
(a) Cross platform, interior facies
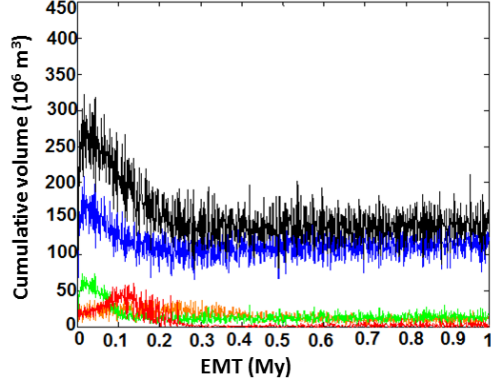
(b) Steepest descent only, interior facies

(c) Cross platform, margin facies

(d) Steepest descent only, margin facies

Figure 5.20: Deposited volumes at each area of the platform in Fig.5.19 for each numerical facies with the two transportation algorithms. The left side shows volumes with the cross-platform algorithm (which includes the steepest descent) and the right side with the steepest descent only. Top panels show platform interior facies and bottom panels margin facies. 30% of the insitu produced material is available for transportation with both algorithms. Low topographic gradients on the platform top prevents the steepest descent from moving material (top left) and only the margin facies deposits on the slope (red line, bottom, left). The cross platform algorithm moves material along the platform top. The material reaches and gets depsoited on the slope (top, right).

131

6 New developments in seismic imaging

Synthetic seismic imaging for this project was performed with a new pseudo-acoustic impedance method which will be here refer to as the textural impedance reflectivity method. The first section of this chapter describes the principles of the new method and how reflectivity is calculated. The second section presents synthetic seismic images generated with the textural impedance reflectivity method and compares them with synthetic seismic images generated with the average impedance reflectivity method. The third and final section discusses the results of the new method and evaluates the method.

6.1 Textural impedance reflectivity method

Elastic properties of carbonate strata are mainly controlled by diagenetic processes, porosity and texture with mineralogy having a less significant role (see section 4.3). Moreover, there are inherited limitations in the estimation of elastic properties from seismic data (see section 4.4.3).

Synthetic seismic images of carbonate strata for this project are generated using on a pseudo acoustic impedance. The pseudo acoustic impedance, developed for this project, is computed based on the rock texture of the modelled rocks. The method uses stratigraphic forward models and strata properties calculated in CarboCAT only.

The textural impedance reflectivity assumes that each numerical facies in CarboCAT has unique elastic properties and that facies beds are homogeneous with elastic properties characteristic for each facies. Textural impedance reflectivity method also assumes that the reflection coefficient between beds with different elastic properties is calculated from the normal incidence Zoeppritz equation, eq.(4.11) irrespective of the bed thickness.

For comparison and evaluation purposes in this chapter, synthetic seismic images are also generated using the average impedance reflectivity method . Synthetic seismic images with the average impedance reflectivity method are generated by assigning velocity and density values to each numerical facies from CarboCAT. The acoustic impedance of each numerical facies is calculated as the product of velocity and density. Reflectivity between beds is also calculated from the normal incidence Zoeppritz equation as above.

6.1.1 Definition of textural impedance reflecticity method

Textural impedance reflectivity method is based on the principles that:

- the major factors that control the elastic properties of carbonates are rock texture and porosity;

- factories in CarboCAT can represent either a single producing organism or a whole carbonate factory (see section 3.2) and not simple mineralogies.

Textural impedance reflectivity method uses the factory distribution, the relative position on the platform during deposition and water energy conditions calculated in CarboCAT and distinguishes numerical factories based on their texture. Strata are assigned a unique number similar to the grain to micirte ratio (GMR) concept.

GMR is the ratio of the percentage of grains divided by the percentage of micrite in a carbonate rock. GMR values greater than one indicate that more than 50% of the rock volume is grains and implies granular texture with inter-grain or inter-crystal porosity. GMR values lower than one indicate that more than 50% of the rock volume is micrite or mud which implies intra-granular or intra-crystalline porosity.

The GMR as a measure of the texture of the carbonate rocks has been linked to energy conditions of the depositional environment of carbonates. GMR values significantly lower than one (0-0.25) are related to stagnant or very low energy water. GMR values greater than one (> 10) are diagnostic of high energy, strongly agitated water conditions (**Bissell1967**).

Numerical facies that have been deposited on low energy, shallow depositional environments in CarboCAT are assumed to have fine texture and GMR values around zero by the textural impedance reflectivity method. Numerical facies deposited in deep, below wave base waters are also assumed to have fine grain texture and low GMR values. Numerical facies deposited at high energy depositional environments are considered coarse grain texture facies with high GMR values.

Textural impedance reflectivity calculates the volume of fine and the volume of coarse texture facies in each position over the platform. The ratio of the fine volume facies to the total volume of the facies on that position defines the pseudo-acoustic impedance value for the position.

$$Z_{y,x} = \frac{\text{volume of coarse material}}{\text{total volume of material}}$$

where Z is the ratio used as pseudo-acoustic impedance value for position y, x.

Pseudo acoustic impedance values calculated with the textural impedance reflectivity method vary from zero to one. Pseudo-acoustic impedance values of 0 mean that all deposited strata on one location have fine grain texture and thus lower acoustic impedance values, whereas values closer to 1 indicate that all deposited material is coarse grain and shows higher acoustic impedance values, consistent with with fig.4.4. Empty model cells are excluded from the calculation of the pseudo-acoustic impedance.

The two main texture groups (coarse or fine), if necessary, can be subdivided based on the assumed porosity type of the numerical facies. This secondary classification allows for further distinguishing fine or coarse facies depending for example on their position within the depositional environment or later diagenetic effects. The secondary, porosity type classification of numerical facies even though practical must be used with caution since neither porosity, nor diagnesis are calculated in CarboCAT and thus any secondary facies differentiation will be based on arbitrary criteria.

6.1.2 Pseudo impedance calculation

An algorithm was developed in CarboCAT to generate synthetic seismic images based on the textural impedance reflectivity method. The algorithm calculates pseudo-acoustic impedance values for the whole platform, computes strata reflectivity, and using a source signal generates synthetic seismic images.

The algorithm generates 2D synthetic seismic images for any cross section along the depositional dip of carbonate platforms generated with CarboCAT. The algorithm generates three NxM matrices, one pseudo-acoustic impedance matrix, one reflectivity matrix and the final synthetic seismic matrix for each cross section along the depositional dip. N depends on the total thickness of the strata on the cross section and M is calculated from the length of the platform.

The algorithm provides the option to calculate pseudo-acoustic impedance using any model cell size along the depositional dip. In case the cell size for the synthetic seismic image is the same as the cell size in CarboCAT, the M of the generated matrices is equal to the number of CarboCAT model cells along the depositional dip. If a smaller size cell is used for the synthetic seismic images, the algorithm interpolates the facies, facies thickness and water energy conditions between vertically and horizontally adjacent CarboCAT model cells and the M depends on the size of the synthetic seismic model cells and the size of the platform.

For each position along the cross section the algorithm calculates pseudo-acoustic impedance variation with depth based on the coarse to total material ratio and the bed thickness as computed in CarboCAT. Exposed model cells are considered by the algorithm as coarse texture material regardless of the facies they

contain. Once the pseudo-acoustic impedance with depth has been computed, the reflectivity with depth (R_{NM}) is estimated based on the normal incident reflection coefficient eq.(6.1).

$$R_{NM} = \frac{Z_{2_{ij}} - Z_{1_{ij}}}{Z_{2_{ij}} + Z_{1_{ij}}} \tag{6.1}$$

where z_1 is the pseudo-acoustic impedance of the bed above the facies transition and z_2 the pseudo acoustic impedances of the bed below the facies transition respectively, i varies from 1 to N and j varies from 1 to M Based on this formula, transition from low pseudo-acoustic impedance facies (fine grain) to higher pseudo-acoustic impedance facies (coarse grain) generates a positive amplitude reflection.

The algorithm generates the synthetic seismic image by performing 1D convolution of the reflectivity depth series with a zero phase Ricker wavelet w, eq.(6.2)(fig.6.1). 1D convolution of the source wavelet with the reflectivity series implies normal incident of the wave from the source at the facies transition. A 100Hz wavelet has been used for all examples.

$$w = (1 - 2\pi^2 f^2 t_s^2)e^{-\pi^2 f^2 t_s^2} \tag{6.2}$$

where f is the user defined frequency of the source and t_s is the sampling time.
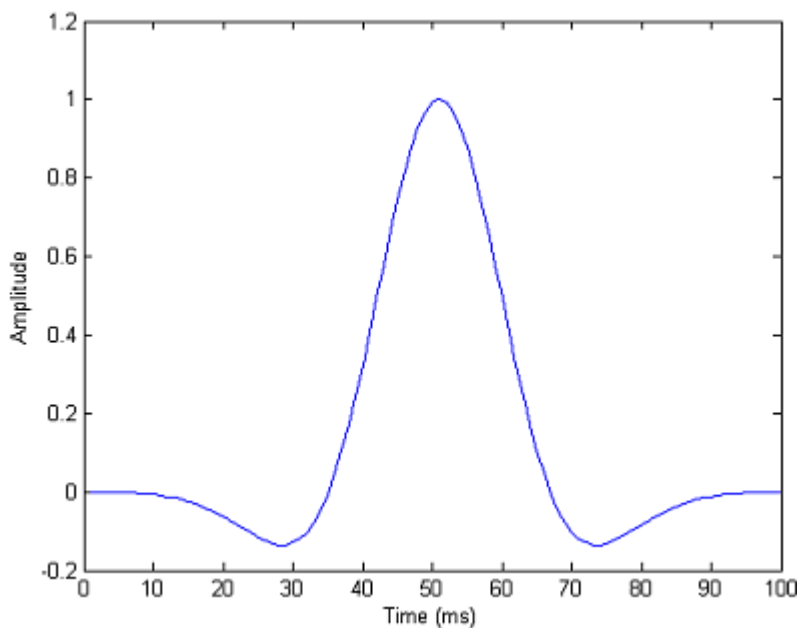

Figure 6.1: Amplitude with time of the 100Hz Ricker wavelet used for the convolution of the seismic images.

6.2 Textural impedance reflectivity examples

In order to test and evaluate the textural impedance reflectivity method, sensitivity analysis was performed as a series of models runs generated with CarboCAT. The model runs provided the opportunity to generate synthetic seismic images of carbonate platforms with known characteristics and fully controlled strata geometries.

The strata geometry and dimensions for the sensitivity analysis were obtained from an actual seismic image of a carbonate platform (Fig.6.2) from geosciences Australia web site (**ga**). The generated model runs geometrically match the carbonate platform shown on the seismic image.

Because only the geometrical characteristics of the carbonate platform in the seismic image are known, a number of assumptions were necessary for the generation of model runs. Based on assumed 2000 m/s depth conversion velocity and an assumed 5My platform duration an estimated 1600m maximum strata thickness and an 100 m/My subsidence rate was calculated. The CarboCAT model cell size was set to 500m x 500m and the time-step for the model runs was set to 2ky.

Sensitivity analysis was performed by changing the value of one model parameter at a time (Table.6.1) and running the model to obtain a numerical carbonate platform. The generated numerical model was used to calculate a synthetic seismic image with the textural impedance reflectivity method.

The goal of the analysis was to test the textural impedance reflectivity method's results based on real seismic examples and gain understanding of the features appearing in the synthetic seismic images and not to accurately model the platform shown on the seismic image.

Two groups of model runs were generated with the parameters shown on Table.6.1. The first group was generated without any heterogeneity in the models. Facies distribution was controlled only by the eustatic sea level movements. The wave energy control and the lateral heterogeneity of CarboCAT had been deactivated during the model runs.

This unrealistic selection of conditions was made for two important reasons. First the simplistic models allowed for identification of each feature on the synthetic images and its stratigraphic source under fully controlled conditions. The effect of any parameter value change was possible to be identified on the model runs and also isolated on the synthetic seismic images.

The second and most important reason was the study of the heterogeneity itself on the synthetic seismic images. The second group of model runs was generated with heterogeneity turned on (lateral facies distribution based on competition for space and wave energy). The effect of heterogeneity was possible to be identified both on the stratigraphic models and the synthetics.
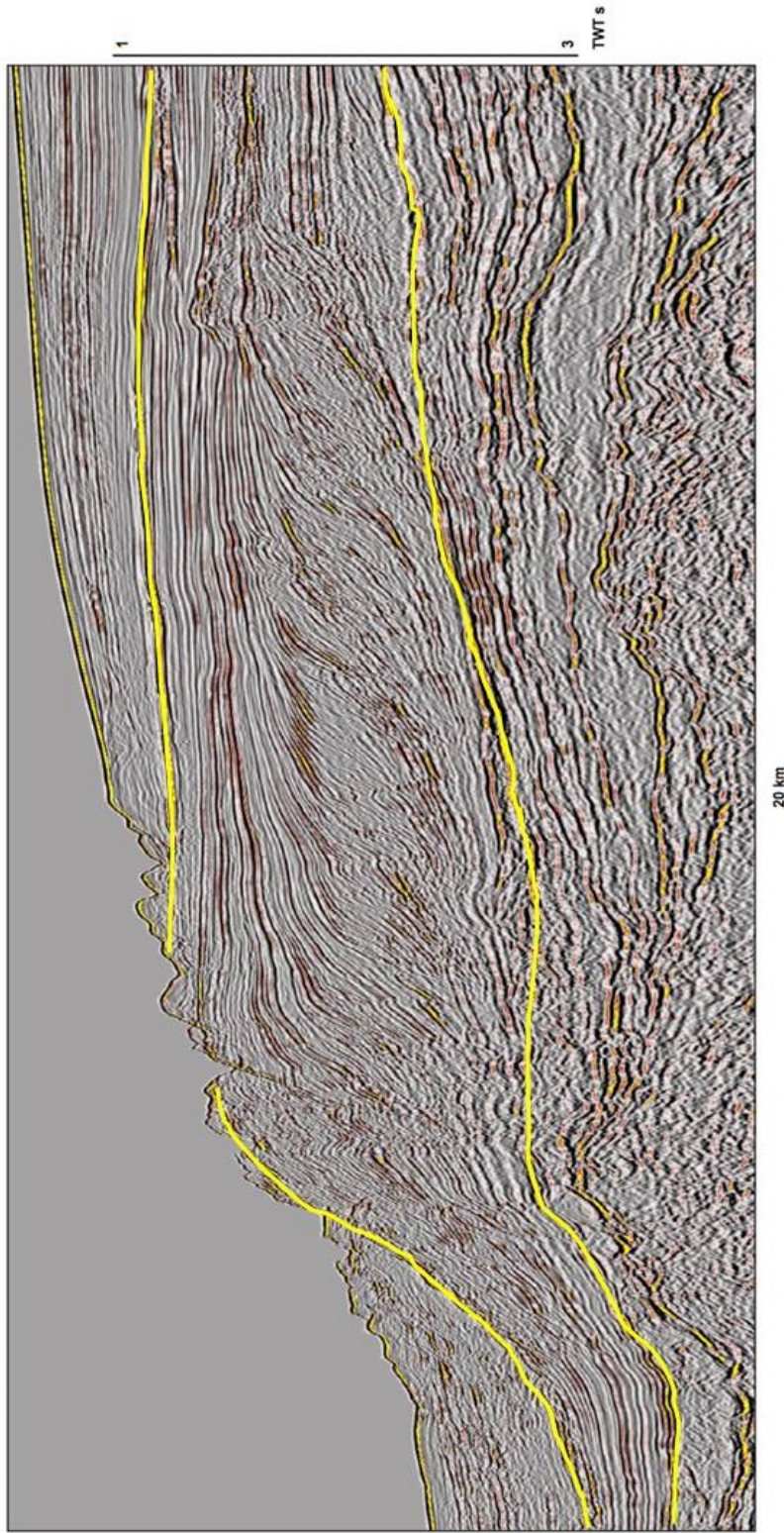
Figure 6.2: Seismic section showing a carbonate platform with clinoforms. The top and bottom boundaries of the platform have been marked (yellow line). Only geometrical characterisitics of the platform can be obtained from the image. The platform is 100 km long with 1.6s TWT maximum strata thickness. From **ga**.

137

6.2.1 Model runs without heterogeneity

Model runs without heterogeneity were generated with a modified version of CarboCAT. Lateral facies competition for space and wave energy controls were turned off. Numerical facies production profile was water depth dependent but facies distribution was linked only to eustatic sea level movements.

Two numerical facies were used the in-situ carbonate production for all model runs without heterogeneity. One numerical facies assumed to have fine texture and the other numerical facies coarse texture. The numerical facies that represent reworked material for each in-situ facies was set to have the same texture as source facies

6.2.1.1 Model run SA

Model run SA (Fig.6.3a) shows a 100km long carbonate platform with maximum strata thickness 1600m and 40km of margin progradation. Eustatic sea level movements have generated two exposure surfaces on the interior and oversimplified clinoform surfaces on the slope. Model run SA is also referred here to as the standard model without heterogeneity.

The synthetic seismic image generated with the textural impedance reflectivity (Fig.6.3b) shows two laterally extensive and bright reflections on the interior and less continuous reflections on the slope. The polarity of the interior reflections, the stratigraphic model and eq.(6.1) reveal that the positive amplitude, bright, laterally continuous reflections on the interior correspond to transitions from fine to coarse material. The positive amplitude reflections can also be traced down to the slope.

The coarse to fine material transitions that can be seen on stratigraphic section do not generate clear reflections on the synthetic image. Negative amplitude reflections that correspond to coarse to fine transition systematically appear on the most distal part of the interior and can barely be followed on the slope. Sub-aerial exposure on the interior significantly limits the thickness of the coarse material. The very thin coarse material generates weak reflections on the interior and the slope. Furthermore, positive amplitude reflections seem to originate from same position as the negative reflections.

The discontinuity of the reflection surfaces on the slope is related to spatial aliasing issues generated by the size of the CarboCAT model cell (500 x 500 m).

6.2.1.2 Model run SB

The effect of the sub-aerial exposure on the reflectivity of the models was studied with model run SB. The subsidence rate for this model run was doubled and as a result the maximum strata thickness on the platform is 1800m and the platform
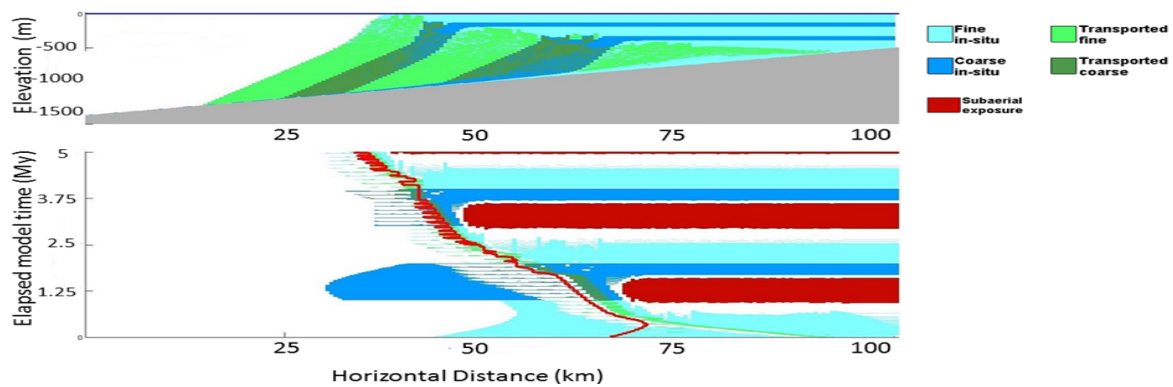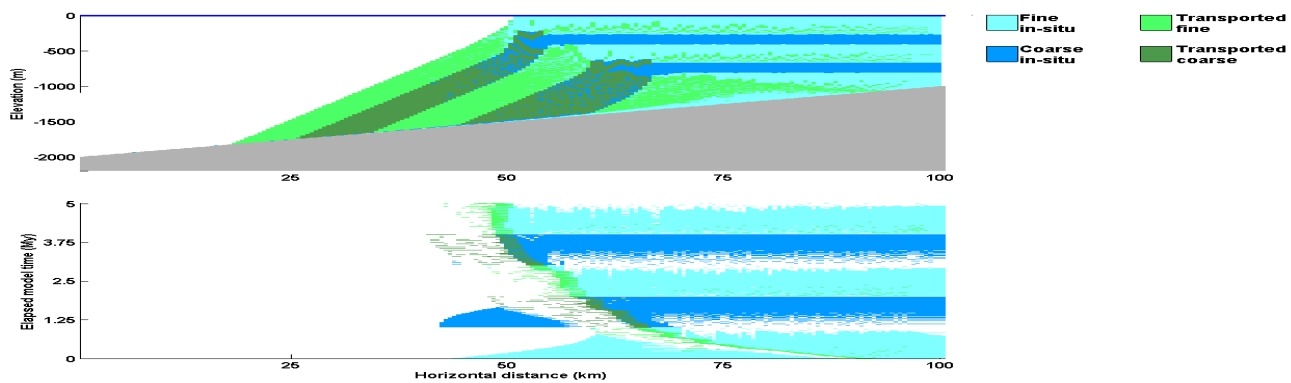
(a) Cross section and chrono-strat section
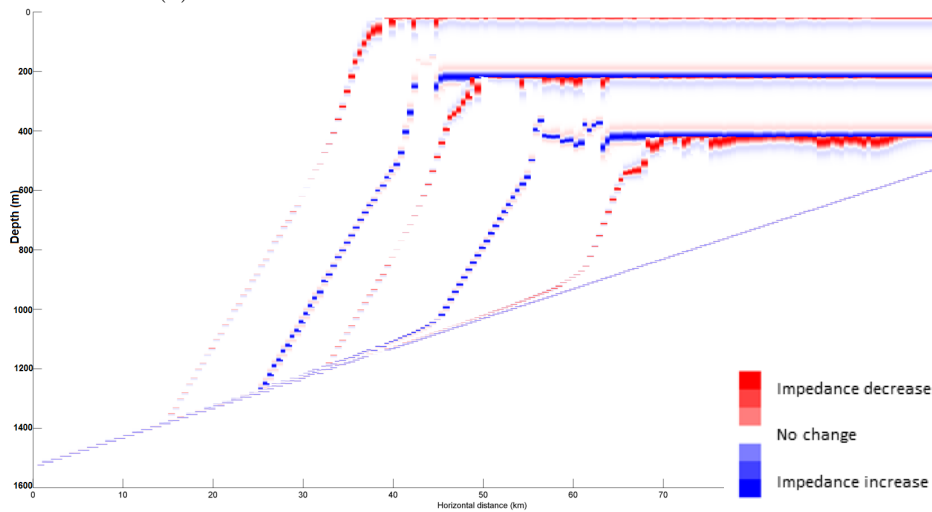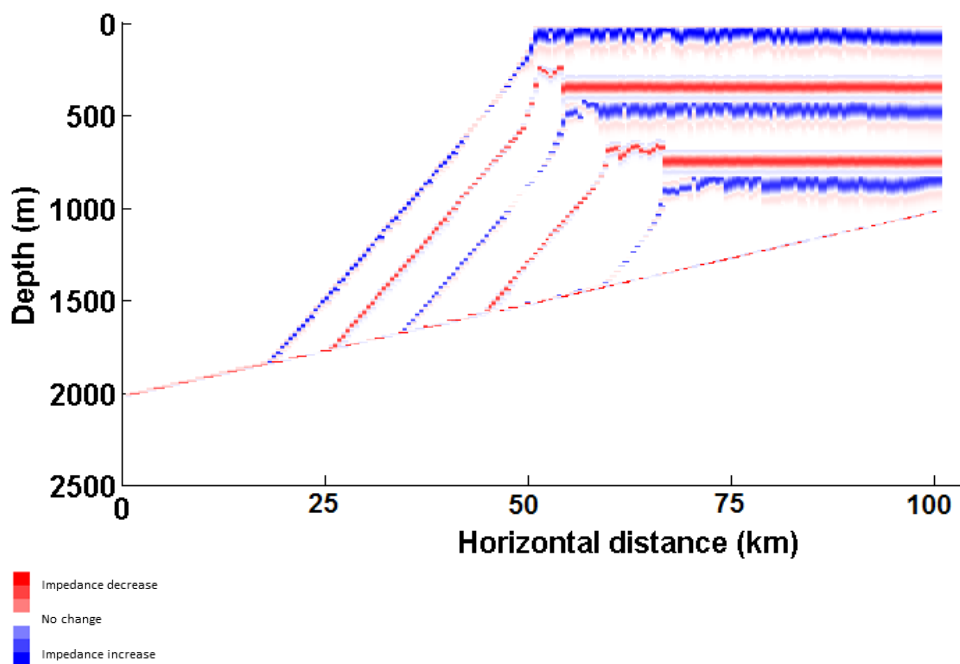

(b) Synthetic seismic image

Figure 6.3: (a) Stratigraphic model and chrono-stratigraphic model of the SA model run. Exposure surfaces on the interior and simplistic clinoforms on the slope are formed due to ESL movements. (b) Synthetic seismic image generated with the textural impedance reflectivity method. The transparency of the image is due to facile model. Bright, laterally continous reflections can be seen on the interior. The clinoform surfaces can be followed on the upper slope.

margin progrades only for 25km. The highest subsidence rate also resulted to an interior without sub-aerial exposure and thicker coarse strata (Fig.6.4a).

The synthetic seismic image generated with textural impedance reflectivity method (Fig.6.4b) shows laterally extensive reflections on the interior and simple clinoform surfaces on the slope. The polarity of the reflections on the interior and the slope follow the facies transitions from fine to coarse (positive amplitude reflections) and from coarse to fine (negative amplitude reflections).

139

(a) Cross section and chrono-strat section

(b) Synthetic seismic image

Figure 6.4: (a) Stratigraphic model and chrono-stratigraphic model of the SB model run. No exposure surfaces occur on the interior due to higher subsidence rate and simplistic clinoforms on the slope are formed due to ESL movements. (b) Synthetic seismic image generated with the textural impedance reflectivity method. The transparency of the image is due to facile model. Bright, laterally continous reflections can be seen on the interior. The clinoform surfaces can be followed on the slope.

6.2.1.3   Model runs SC,SD,SE,SF,SG

The observations made in the previous two model runs are confirmed by all the remaining models (see appendix). More specifically, sub-aerial exposure limits the thickness of the deposited coarse material and generates reflections with opposite amplitude to originate from the same point. Spatial aliasing has as a result laterally extensive surfaces to appear discontinuous on the slope.

6.2.1.4   Comments

Model runs without heterogeneity SA, SB, SC, SD, SE, SF and SG are not realistic representations of carbonate platforms. The generated synthetic seismic images are not realistic and do not resemble the real seismic image on Fig.6.2.

Despite the above limitations, model runs without heterogeneity were useful to identify some features on the images generated with the textural impedance reflectivity method:

- for constant pseudo-acoustic impedance differences reflection strength is analogous to strata thickness;

- sub-aerial exposure restricts the thickness of strata and results to weak reflections;

- laterally extensive stratigraphic features are very well mapped;

- laterally extensive reflectors are better mapped on the platform interior and upper slope compared to lower slope;

- spatial aliasing issues cause laterally extensive surfaces to appear discontinuous or to be mapped poorly.

141

Model parameter	Model SA	Model SB	Model SC	Model SD	Model SE	Model SF	Model SG
Model cell size	500m	500m	500m	500m	500m	500m	500m
Elapsed model time	5 My	5 My	5 My	5 My	5 My	5 My	5 My
Timestep	2 ky	2 ky	2 ky	2 ky	2 ky	2 ky	2 ky
Subsidence	100 m/My	200m/My	100 m/My	100m/My	100m/My	100m/My	100m/My
Initial bathymetry	Homoclinal ramp	Homoclinal ramp	Distally steepened	Homoclinal ramp	Homoclinal ramp	Homoclinal ramp	Homoclinal ramp
Production rate	250 m/My-200 m/My	250 m/My-200 m/My	250 m/My-200 m/My	500 m/My-400 m/My	250 m/My-200 m/My	250 m/My-200 m/My	250 m/My-200 m/My
Transported fraction	0.5-0.5	0.5-0.5	0.5-0.5	0.5-0.5	0.25-0.25	0.25-0.25	0.25-0.25
ESL amplitude	35m	35m	35m	35m	35m	35m	17m
ESL period	2My	2My	2My	2My	2My	1My	2My

Table 6.1: Input parameters for model runs

6.2.2 Model runs with heterogeneity

Table 6.2: Velocity, density and texture values used for each factory for generation of synthetic seismic images for each model run

Factory	Velocity-Density	Texture
insitu facies 1	$5500m/s$ - $2900kg/m^3$	fine with 15% porosity
insitu facies 2	$5000m/s$ - $3000kg/m^3$	fine with 20% porosity
insitu facies 3	$6000m/s$ - $3100kg/m^3$	coarse
reworked facies 1	$4500m/s$ - $2000kg/m^3$	fine with 25% porosity
reworked facies 2	$4000m/s$ - $2100kg/m^3$	fine with 30% porosity
reworked facies 3	$5500m/s$ - $3100kg/m^3$	coarse with 10% porosity

The effect of heterogeneity was studied with more realistic model runs that were generated without any adjustment to CarboCAT. This allowed for lateral heterogeneity to be present on the model runs and the formation of platform interior, margin, upper and lower slope with different hydrodynamic conditions and thus different facies distribution.

Using the normal CarboCAT version to study heterogeneity on seismic images caused some changes on the model parameters. In order to study the effect of heterogeneity on the interior, a third numerical facies was introduced to the model. Two low energy, fine texture numerical facies formed on the platform interior whereas a high energy, coarse texture dominates on the margin. Furthermore, production rates of the three facies show much more realistic values and were 10 times higher than the values shown on Table.6.1.

Synthetic seismic images were generated for each model run with both the textural impedance reflectivity and the average impedance reflectivity method. Table.6.2 shows the velocity and density values used for the average impedance method and the texture used for the textural impedance method for each factory. Both platform interior factories are low wave energy factories and assumed to be fine material. Secondary classification of the factories assumes a porosity for each facies. Porosity is not calculated in CarboCAT.

Furthermore, in order to address the spatial aliasing problems that appear in the synthetic seismic images without heterogeneity, the interpolation option available in the algorithm was used. The cell size for the synthetic images with heterogeneity was reduced to 50 x 50 m from the original 500 x 500 m of the CarboCAT models.

6.2.2.1 Model run SHA

Model run SHA or the standard model shows a 100km long platform and maximum strata thickness 1600m. The platform interior is 55km long with two in-situ

producing facies and the high energy margin progrades for 40km (Fig.6.5a).

The synthetic seismic image generated with the textural impedance reflectivity method (Fig.6.5b) is mainly a noisy image with some laterally extensive reflectors. Reflectivity on the interior appears noisy due to distribution of facies with similar lithological and elastic properties.

The margin and the upper slope show some more coherent reflectivity and clinoform surfaces can be traced there. As the cross platform algorithm moves material preferentially along the depositional dip on the upper slope, laterally extensive reflections are generated. Farther away from the margin and on the lower slope, the preferential deposition of facies becomes weaker and the linear reflectivity disappears.

6.2.2.2 Model run SHB

Model run SHB was generated with double the subsidence rate compared to the standard model. Because of the higher subsidence the total length of the platform is 75km, the low energy interior is 40km long, without sub-aerial exposure and the margin progrades only for 20km (Fig.6.6a).

The synthetic seismic image generated with the textural impedance reflectivity method (Fig.6.6b) shows generally low reflectivity on the interior and higher reflectivity on the slope. Reflectivity on the interior is only controlled by facies heterogeneity. Model cell based heterogeneity on the platform interior results to facies mosaic and generates noisy reflectivity. The textural similarity of the platform interior numerical facies combined with the facies mosaic prompt noisy, low reflectivity on the interior regardless of the strata thickness.

Reflectivity on the slope is also noisy but a linear trend can be recognised. The higher reflectivity is attributed to higher textural differences between the facies present on the slope. The slope is comprised of coarse, high energy in-situ produced material, its coarse reworked material and various amounts of reworked material form the interior with generally fine properties.

The faint linearity of the upper slope reflections is linked to the preferred direction of transportation along the depositional dip. The cross platform algorithm in CarboCAT (see section 5.6) moves material without deposition on the platform interior and deposits material on the slope based on the local gradient. As a result, deposition generally shows a linear trend along the depositional dip.

6.2.2.3 Model run SHE

Model run SHE was generated with half the transportation rates of the standard model. The stratigraphic model of SHE (Fig.6.7a) shows a mainly aggrading platform dominated by in-situ produced material with very little transported material

144

on the slope. Due to low transportation rates, the platform is comprised of in-situ produced vertically accumulating strata.

The synthetic seismic image generated with the textural impedance reflectivity method (Fig.6.7b) does not distinguish between interior and slope, reflectivity appears everywhere very noisy. The reflectivity on the proximal part ($> 60km$ horizontal distance) is caused by facies mosaic on the platform interior. Reflectivity on the more distal part ($< 60km$ horizontal distance) is generated by textural differences between the dominating coarse material and the very few transported deposits.

6.3 Discussion and conclusions

6.3.1 Discussion

Laterally extensive stratigraphic features generate clear, strong, reflections (Fig.6.3 and appendix A) for model runs without heterogeneity and Fig.6.5 and appendix A with heterogeneity).

Facies mosaic generated from model cell base competition for space and the use of cellular automata in CarboCAT cannot be resolved in the seismic images. Both textural impedance reflectivity method and the average impedance reflectivity show chaotic reflectivity without any linear features(Fig.6.7 and appendix A).

Reworked material probably has the most significant effect on the synthetic seismic images. Sediment transportation along preferred directions produces linear stratigraphic features. Depending on the thickness of the transported sediments, they contribute to generation of linear reflections. The transportation algorithm in CarboCAT favours deposition of transported sediment on the upper slope along the depositional dip and thus reflection surfaces (clinoforms) can be identified on the upper slope around the platform margin. Lack of preferred direction for deposition on the lower slope generates chaotic reflections that cannot be distinguished from noise. Lack of transported material generates synthetic images completely dominated by noise (Fig.6.7).

The steady dynamic state of the external forcing and the behaviour of seismic responses (reflections) reveal that autogenetic processes affect carbonate platform development and thus the generated synthetic seismic images. Synthetic seismic images for model runs without heterogeneity display reflectivity in agreement with the external forcing (Fig.6.3 and appendix A). Reflections on synthetic seismic images for model runs with heterogeneity systematically show higher magnitude of change compared to external forcing (Fig.6.5 and appendix A) implying the role of heterogeneity in autogenesis.

6.3.2   Conclusions

The textural impedance reflectivity method was evaluated based on sensitivity analysis guided by a seismic image of a carbonate platform. A series of reasonably realistic simulations were used to identify and explain the features generated with the new method. Textural impedance reflectivity results were compared and contrasted with images generated with the commonly used average impedance reflectivity method.

Both methods generated similar results regarding the position, polarity and geometry of the reflections. Minor differences between the two methods were almost exclusively related to the strength of the reflections. The similarity of the generated results between the two methods indicates the textural impedance reflectivity method is a pragmatic approach to real strata reflectivity.

Textural impedance reflectivity method is a pseudo-acoustic impedance method well correlated with the real strata reflectivity. The method is based on the main controls of the elastic properties of carbonates, namely rock texture and porosity. Textural impedance reflectivity calculates pseudo-acoustic impedance using only SFM results and measured quantities on CarboCAT without the need of arbitrary assumptions.

Heterogeneity on the platform adds noise to the generated synthetic seismic images. Heterogeneity on platform interior result to facies mosaic which cannot be resolved and appears as noise. Noise on the slope is generated by textural heterogeneity of the reworked facies combined with small thickness of the deposited strata, typically less than the vertical resolution of the wavelet.
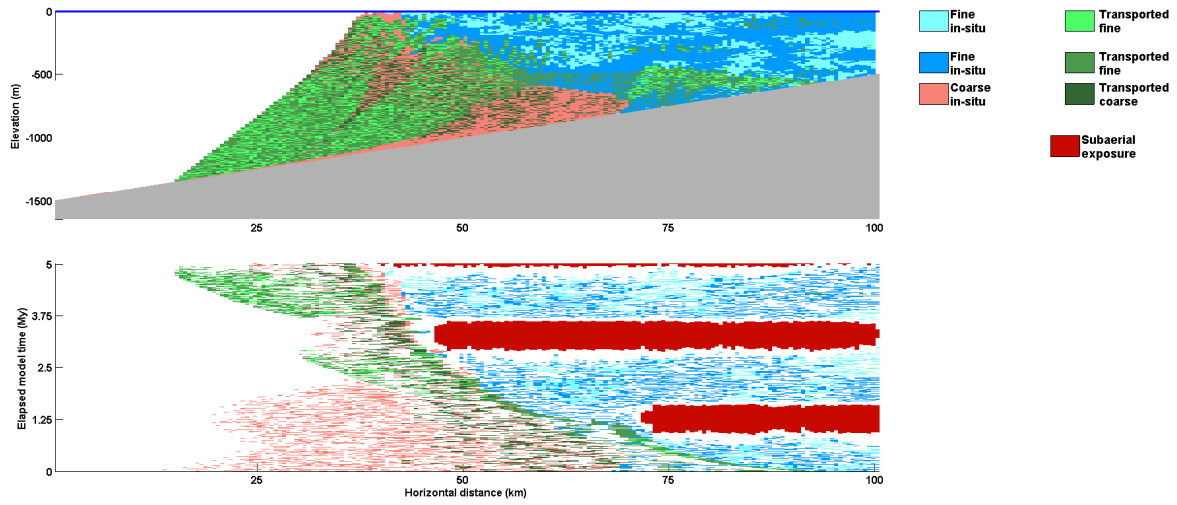
(a) Cross section and chrono-strat section
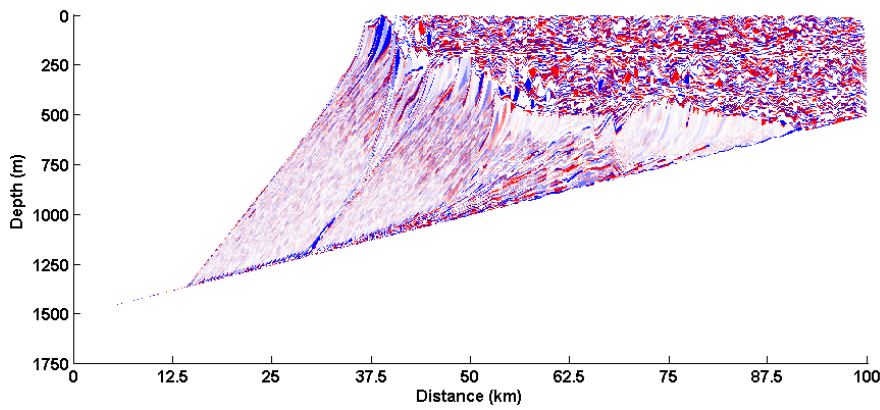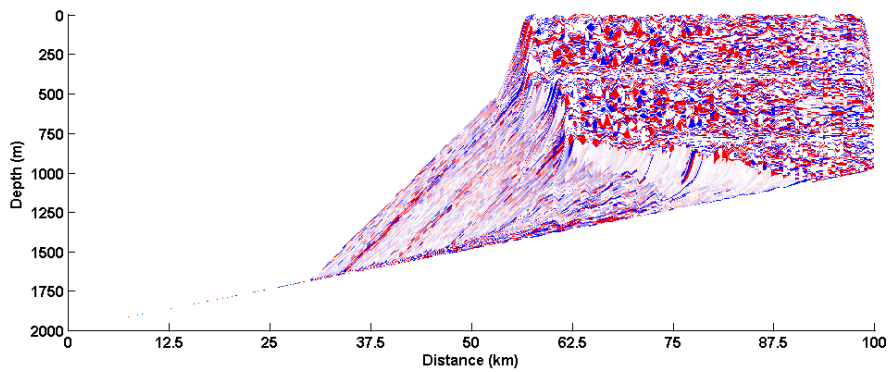

(b) Synthetic seismic image with textural impedance

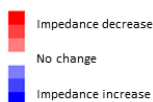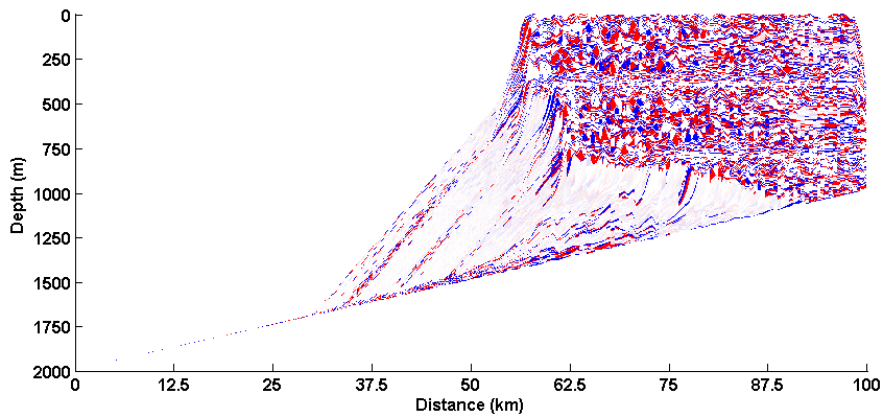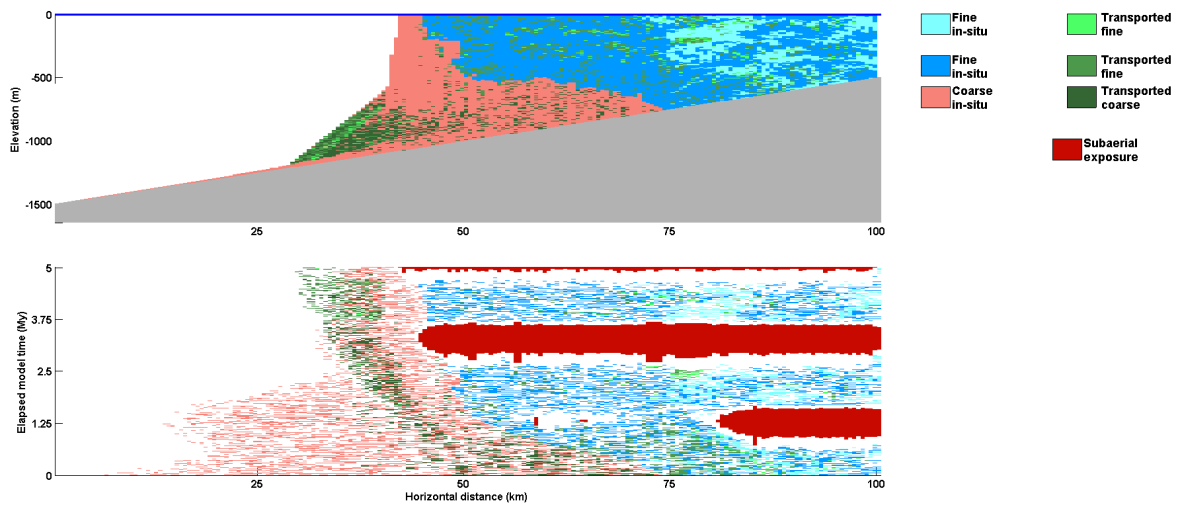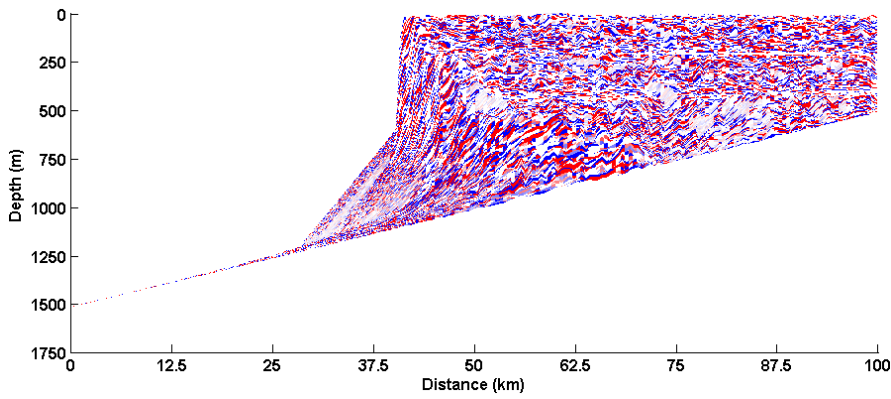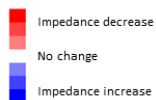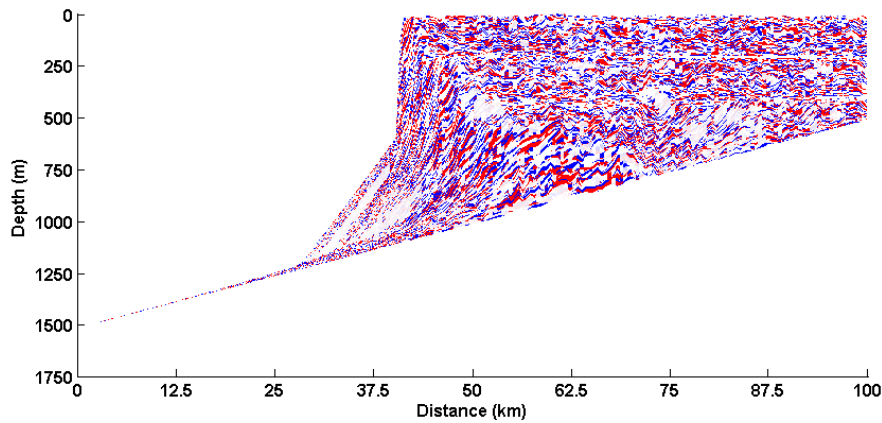(c) Synthetic seismic image with average impedance

147
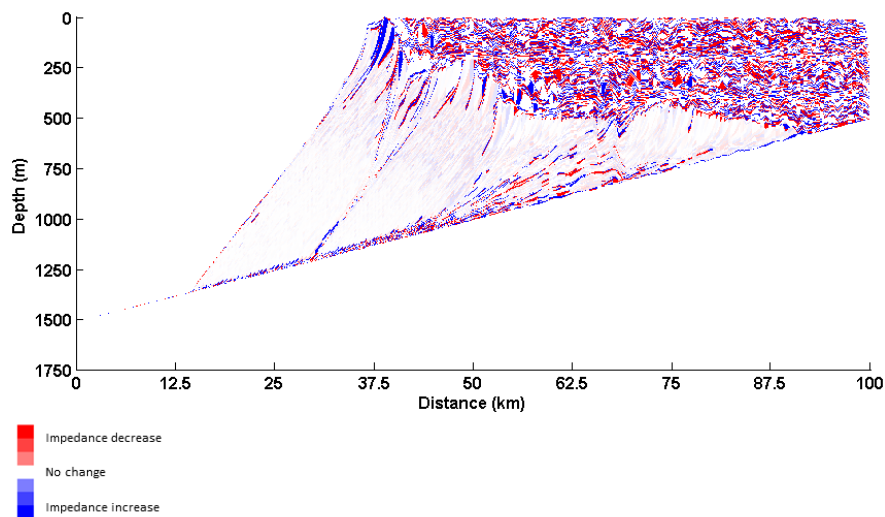
Figure 6.5: (a) Stratigraphic model and chrono-stratigraphic model of the SHA model run. The interior is dominated by low energy, fine material and the margin by high energy, in-situ produced and reworked material (b) Synthetic seismic image generated with the textural impedance reflectivity method. Only thr laterally extensive sub-aerially exposed surfaces can be identified on the interior. On the upper slope some clinoforms surfaces can be identified. (c) Synthetic seismic image generated witht the average impedance reflectivity method, for comparison.
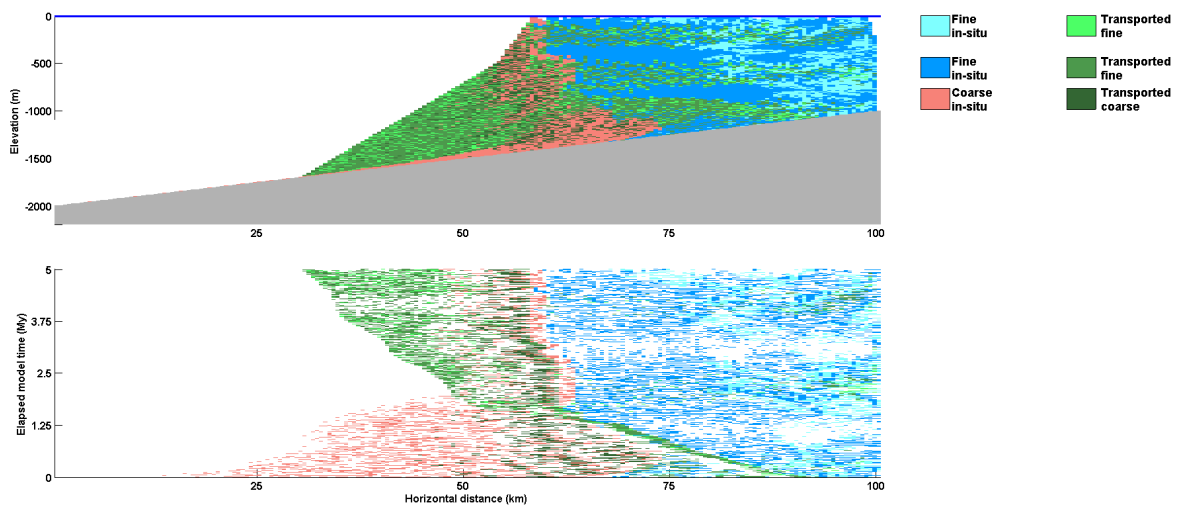
(a) Cross section and chrono-strat section

(b) Synthetic seismic image with the textural
impedance.

(c) Synthetic seismic image with average
impedance.

Figure 6.6: (a) Stratigraphic model and chrono-stratigraphic model of the SHB model run. The interior is dominated by low energy, fine material and the margin by high energy, in-situ produced and reworked material (b) Synthetic seismic image generated with the textural impedance reflectivity method. Noisy reflectivity on the interior. Linear, clinoforms surfaces can be identified on both the upper and the lower slope. (c) The sysnthetic seismic image generated with the average impedance reflectivity method.

(a) Cross section and chrono-strat section

(b) Synthetic seismic image with textural
impedance

(c) Synthetic seismic image with average
impedance

149

Figure 6.7: (a) Stratigraphic model and chrono-stratigraphic model of the SHE
model run. The interior is dominated by low energy, fine material and the margin
by high energy, in-situ produced (b) Synthetic seismic image generated with the
textural impedance reflectivity method. (c) The sysnthetic seismic image gener-
ated with the average impedance reflectivity method

7 Effects of cross platform sediment transportation on large scale platform geometry and autocyclic platform interior shoals.

This chapter studies the effect of the cross platform sediment transportation on large scale carbonate platform geometries, formation of autocycles on platform interior and platform interior facies distribution with a series of CarboCAT generated model runs. The chapter is divided in two sections. The first section presents the results of sensitivity analysis of the effect of sediment transportation rate and grain size on large scale carbonate platform geometry. The second section deals with the effect of autocycles on platform interior and facies distribution in the interior.

7.1 Cross platform sediment transportation effect on large scale platform geometry

7.1.1 Background

The large scale geometry of carbonate platforms (**Schlager2005**, **Wilson1975**) is controlled by the interaction of sediment production rate, sediment transportation rate, subsidence rate and relative sea level movements which is described by the accommodation-supply ratio (A/S, see section 2.2.3 and references therein). The interaction of the controlling factors also effects the temporal evolution of carbonate platforms. For a constant value of A/S ratio only platforms in dynamic equilibrium maintain their bathymetric profile through time (see section 2.2.4).

Based on their large scale geometries carbonate platforms are distinguished between two end members, ramps and FTP (see section 2.14). A crucial difference between the two end members is the amount of deposited material on the interior and the slope. FTPs indicate sediment deposition mainly on the interior whilst ramps show significant deposition on the slope as well as the interior.

The amount of deposited material in each carbonate platform segment is controlled by in-situ production and sediment transportation. Cross platform sediment transportation thus is a decisive factor controlling the difference between an FTP and a ramp geometry. Hydrodynamic conditions and sediment grain size are the two major controls on sediment transportation.

Hydrodynamic conditions define the amount, volumetrically, of sediment that gets entrained, transported and re-deposited. The energy required for sediment entrainment and transportation is the kinetic energy from waves (see section 2.1.5.1) or water currents (see section 2.1.5.2). Low energy environments typically include platform interior areas where the water depth is usually less than the break depth,

and deep basinal areas below the wave base or where the water currents have lost their transportation capacity.

The transportation capacity of water currents is also affected by grain size and fabric of the carbonate sediments on the platform. Muds and non-skeletal material are entrained more easily compared to skeletal grainy sediments for the same hydrodynamic conditions (**Kenter1990**). Muds and non-skeletal material tend to generate ramp style geometries whilst FTPs are favoured by coarser, skeletal material for the same hydrodynamic conditions (**Badenas2010**, **Azeredo2009**, **Pomar2001a**, **Barnaby1990**).

7.1.2 Model formulation

The effect of cross platform sediment transportation on large scale platform geometry was studied with a series of CarboCAT generated model runs. All types of carbonate platforms from in-situ dominated systems with very low transportation rates, to transport dominated systems with high transportation rates were studied. Parallel to the effect of transportation to platform geometry, the effect of sediment grain size to large scale platform geometry was also studied.

Even though CarboCAT does not model grain size directly, the effect of grain size on sediment transportation can be evaluated with the minimum gradient for transportation model parameter (see section 3.2.1.1). The minimum gradient for transportation parameter defines the bathymetric threshold between two adjacent model cells for sediment entrainment or deposition to occur. Low minimum gradient for transportation values imply that even low bathymetric differences between adjacent model cells are enough to initiate sediment entrainment or deposition. High minimum gradient for transportation values require higher bathymetric differences between adjacent model cells to initiate sediment deposition.

The minimum gradient for transportation threshold relates the shear energy of a current to the grain size of the material that can be entrained, eq.(5.13) (**Warrlich2002**).

$$\tau_{current} = \Delta \rho g s \sin(\alpha)$$

where $\Delta \rho$ is the excess density of the submerged sediment in relation to water density, g is the gravitational constant (m/s^2), s is the grain size (m) and α the maximum bathymetric angle $(^o)$ (represented in CarboCAT by the minimum gradient for transportation) for entrainment at each model cell.

All model runs in this chapter include models with both fine and coarse grain material. Low entrainment threshold in eq.(**??**) means that a current can mobilise only fine grain material, whilst high entrainment threshold means that the current mobilises fine and coarser grain material as well. For cases with only fine grain

size or only coarse grain size material, the entrainment would have no effect on the generated geometry and thus is not studied here.

Low entrainment thresholds isolate the effect of transportation on fine grain material. This allows for studying platform geometries and facies distribution of fine grain sediments only. Studying of platforms geometries and sediment distribution from high energy thresholds is possible by comparing and contrasting them with the low energy results.

Table 7.1 shows the input model parameters used for all model runs. The CarboCAT model parameter transported fraction (see section 3.2.1.1) for the platform interior factory was varied from 0.1 to 0.9 with a step of 0.1 at a time. The transported fraction for the platform margin factory was kept constant to 0.2 for all model runs because the margin factory does not contribute material to the cross platform algorithm based on the transportation direction.

Table 7.1: Transportation model runs parameter values

Model size	200 x 50 model cells
Time step	1ky
Elapsed model time	1My
Subsidence rate	100 m/My
Eustatic sea level	Constant
Initial bathymetry	Homoclinal ramp, 0.5m/cell
In-situ producing factories	Low wave energy, production rate: 1000 m/My
	High wave energy, production rate: 1100 m/My
Transportation algorithm	Cross platform + steepest descent
Transportation direction	Straight line from proximal to distal areas along the depositional dip.

The model size was selected in order to provide enough space for the platform to freely prograde for the transported dominated model runs. Subsidence and production rates where selected in order to generate FTP with steep margins for the in-situ dominated model runs.

The time-step value was obtained based on the accumulation index (AI). AI (eq.(7.1)) is defined as the ratio of the thickness of the accumulated sediments to the total accommodation (**Kozlowski2017**). Stable AI values for different time-steps indicate that the platform geometry is not affected by the length of time-step.

$$AI = \frac{\sum_{1}^{y,x,t} accumulation_{y,x,t}}{\sum_{1}^{y,x,t} accommodation_{y,x,t}} \tag{7.1}$$

where y, x are the horizontal dimensions of the platform, t is the time-step, *accumulation* is the total sediment thickness and *accommodation* is the total generated space

from subsidence and water level variations.

Eight model runs were generated with the model parameters shown on Table 7.1, transported fraction 0.5 and time steps 5ky, 4ky, 3ky, 2ky, 1ky, 0.75ky, 0.5ky and 0.25ky (Fig.7.1). The largest time step value that generates stable results was selected for the sensitivity analysis in order to minimise the required computational time.
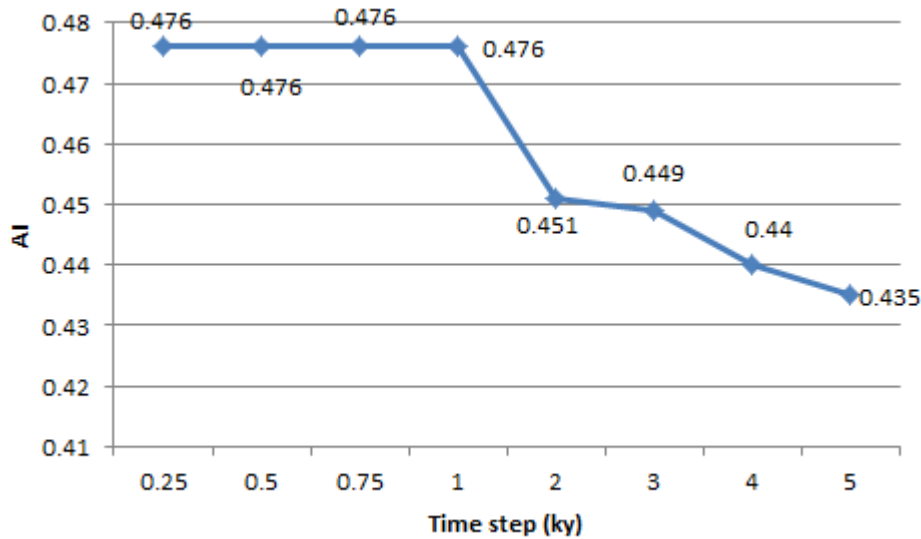

Figure 7.1: Variation of AI with different time-steps. Even though the differences between the time steps are small, stable AI values are achieved for the 250y, 500y, 750y and 1ky time-steps. The stable AI values for the 2ky and 3ky timestep indicate that for these values the platform geometry remains the same but it is ultimately values less than 1ky timestep that generate stable geometries.

The cross platform sediment transportation algorithm moves material along the preferred transportation direction without deposition, based on the total shear energy on the platform (see section 5.6). The cross platform algorithm terminates and passes all the available material to the steepest descent algorithm (see section 3.2) where the bathymetric gradient between two adjacent model cells is greater than the minimum gradient for transportation threshold. Sediment deposition with the steepest descent algorithm occurs where the local bathymetric gradient is lower than the minimum gradient for transportation threshold.

Two sets of model runs were generated (Table.7.2). The first set studied the effect of high minimum gradient for transportation threshold to the large scale platform geometry. The high minimum gradient for transportation value (5m/cell) requires bathymetric difference up of 5m between adjacent model cells in order for the transportation algorithm to change from cross platform to steepest descent.

153

This implies that, depending on the local bathymetry, the cross platform algorithm will move material longer distances without deposition before the material is passed to the steepest descent algorithm and gets deposited.

The second set studied the effect of low minimum gradient for transportation threshold to the large scale platform geometry. The low minimum gradient for transportation value (0.5m/cell) implies that in-situ production generates bathymetric differences high enough to trigger change from the cross platform algorithm and no deposition to steepest descent algorithm with deposition.

The low minimum gradient for transportation value was selected equal to the initial bathymetry of the model and the high value was selected 10 times the low value in order to favour more cross platform transportation.

Table 7.2: Transportation model runs parameter values

Model parameter	Model run 1	Model run 2
Transported fraction	0.1-0.9 step 0.1	0.1-0.9 step 0.1
Minimum gradient for transportation	0.5m/cell	5m/cell

7.1.2.1 Quantitative measurements of platform geometry

Several measurements were obtained to quantify each generated platform geometry. The volumes of the in-situ deposited and the transported and re-deposited materials were measured and presented as percentages of the total produced volume. The volumes of the material deposited on the platform interior and slope were also calculated and expressed as percentages of the total deposited volume. The generated platform geometries were classified as FTPs or ramps based on the maximum gradient of the bathymetry at the platform margin.

Additionally to FTP or ramp classification, a simple quantitative method developed for the purposes of this analysis, the clinoform characterising index (CCI) was also used. CCI (Fig.7.2) is a dimensionless number calculated for each transect along the depositional dip of the platform. CCI describes the shape of the bathymetric profile of the platform utilising three points from a cross section along the depositional dip of the platform.

The tree points necessary for the calculation of the CCI are defined as follows. The first point (A) is the position of the maximum angle of bathymetry or the platform margin position. The second point (B) is the toe of the slope, where carbonate platform sediments lay conformable to the basement. The third point (C) is the position of the maximum rate of change of the bathymetry of the segment AB (from the margin to the farthest deposition point). CCI is defined as the as the ratio of the horizontal distance (AC) to the horizontal dimension of the model cell. By definition, CCI is a positive number or zero. The CCI for the whole

154

platform is calculated as the average CCI value from all the along the depositional dip transects.
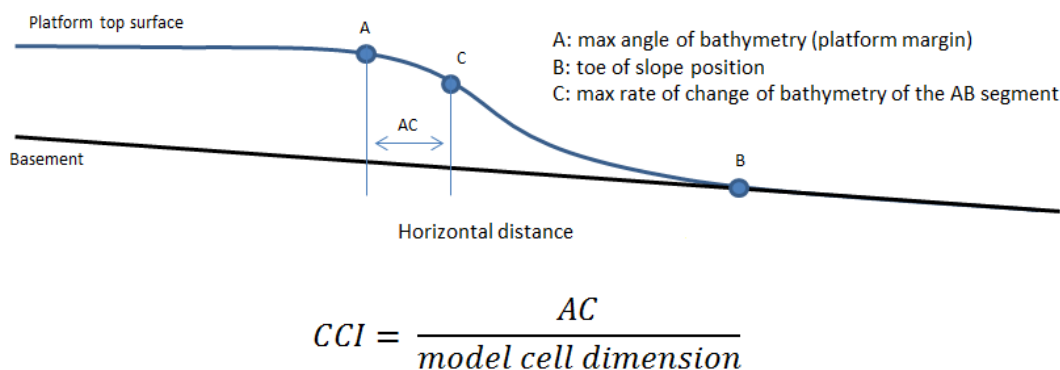

$$CCI = \frac{AC}{model\ cell\ dimension}$$

Figure 7.2: Schematic cross section of a carbonate platform for the CCI calculation. The position of the maximum angle of bathymetry (A) corresponds to the platform margin position and it is calculated in CarboCAT. The toe of the slope is (B) is the position where the slope lays conformably to the basement. The maximum rate of change of the bathymetry (C) is the position where the gradient of the bathymetry has its maximum value.

A characteristic CCI value of two was selected as a threshold between FTP and ramp style platform geometries based on sensitivity analysis (Fig.7.3):

- CCI=0. A hypothetical situation where platform margin and the maximum rate of change of the bathymetry are at the same position and implies perfectly vertical slopes;

- CCI values less than 2 indicate that the platform margin and the maximum rate of change of the bathymetry are at adjacent positions and implies FTP with steep slopes and some sediment deposition on the slope;

- CCI greater than 2 indicate that there is an offset between the platform margin and the position of maximum rate of change of the bathymetry.

The accuracy of the CCI results depends on the accuracy of the definition of the three characteristic points:

- point A, the position of the maximum angle of the bathymetry. For FTPs, point A is a well defined point and coincides with the platform margin position. For ramp style geometries where the bathymetry lacks a pronounced slope break and platform margin, point A is more difficult to identify and
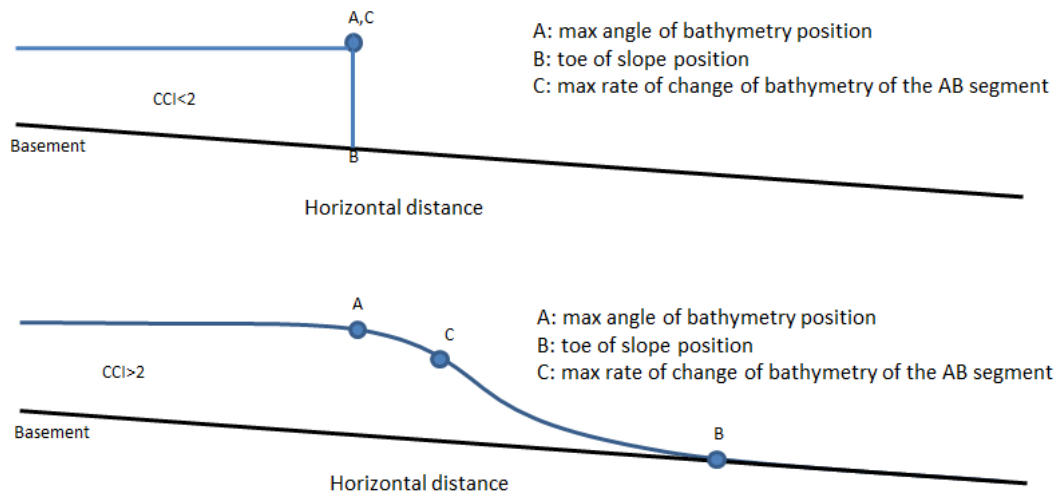
155

Figure 7.3: Schematic cross sections of carbonate platforms with different CCI values. (TOP) FTP geometry with vertical slope and no sediment depsotion beyond the platform margin. For this hypothetical platform the CCI is 0. (BOTTOM) FTP geometry with well developed slope and some offset between the margin and the maximum rate of change of bathymetry position.

could be located anywhere on the platform. Point A is calculated in Carbo-CAT with platform margin identification algorithm (see section 5);

- point B, the toe of the slope is a well defined and unique point for every along the depositional dip transect;

- point C, the position of the maximum rate of change of the bathymetry of the segment AB. Point C is also well defined.

For high gradient systems, all three points are well defined and CCI describes very well the shape of the platform profile. For low gradient systems, CCI value depends on the rather arbitrary position of the point A.

7.1.3 Model run examples

7.2 Effect of cross platform sediment transportation on autocycles and platform interior shoals

7.2.1 Background

High frequency depositional cycles like coarsening or finning upwards among others, are regularly interpreted to be the result of high frequency external forcing

(usually eustatic sea level oscillations) that indicate order in the strata. As a consequence, autocycles are assumed to be indicative of disordered strata (**Lehrmann1999**). Higher degrees of autogenesis are assumed to decrease strata order but evidence suggests that autocyclic strata are not necessary any less ordered than fully allocyclic strata (**Burgess2006** and section 2.2.8.3 for more detailed discussion).

In order to study the effect of cross platform sediment transportation on autocyclicity and the effect of autocycles on facies distribution and strata order on platform interior, a series of CarboCAT generated model runs were used. In the model runs, autocycles appear as platform interior carbonate shoals generated under constant external forcing. Shoal formation was based on the interaction of sediment transportation with the local bathymetry which generates a loop that deposits sediments on the interior and alters the bathymetry locally following the model suggested by **Ginsburg1971**.

7.2.2 Model formulation

In order to simulate the interaction between bathymetry and sediment transportation, a modified cross platform transportation algorithm was used. The cross platform algorithm moves sediment along the relatively flat platform interior without deposition, based on hydrodynamic conditions on the platform (see section 5.6).

The shear energy of locally induced currents decreases with water depth as currents expand, slow down and lose sediment transport capacity (Fig.7.4). For very shallow water depths, the velocity of the current (and thus its sediment transport capacity) increases but water currents have to stop where local bathymetric highs have reached the sea surface generating islands (zero water depth in Fig.7.4).

Islands, as structures that reach the sea surface or go above it, act as barriers to water currents since there is no available space for the current. Local bathymetric highs produced from in-situ carbonate production, can act as barriers under the effect of tidal movements (**Reeder2008**). During low tides the sea level drops and bathymetric highs that have reached or are very close to the sea level can get exposed and form temporary islands (Fig.7.5). Tidal movements are not modelled in CarboCAT but their effect can be included in the cross platform sediment transportation algorithm.

The tidal effect on cross platform sediment transportation is quantified with a water depth threshold for deposition in the cross platform transportation algorithm (Fig.7.6). The water depth threshold allowed deposition of sediment with the cross platform algorithm at bathymetric highs where the water depth on the platform is less than the threshold. The water depth threshold implies that some bathymetric areas regularly form islands that completely block the water currents and force them to deposit their sediments.

The effects of cross platform sediment transportation on autocycles and the
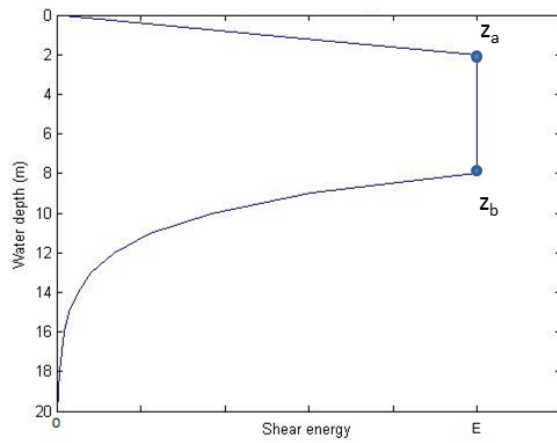
Figure 7.4: Shear energy from locally induced currents with water depth. The shear energy and thus the sediment transport capacity is maximum between water depths z_a and z_b and decreases with water depth below z_b. Above water depth threshold z_a topographic highs that reach the sea surface act as barriers to sediment transportation.
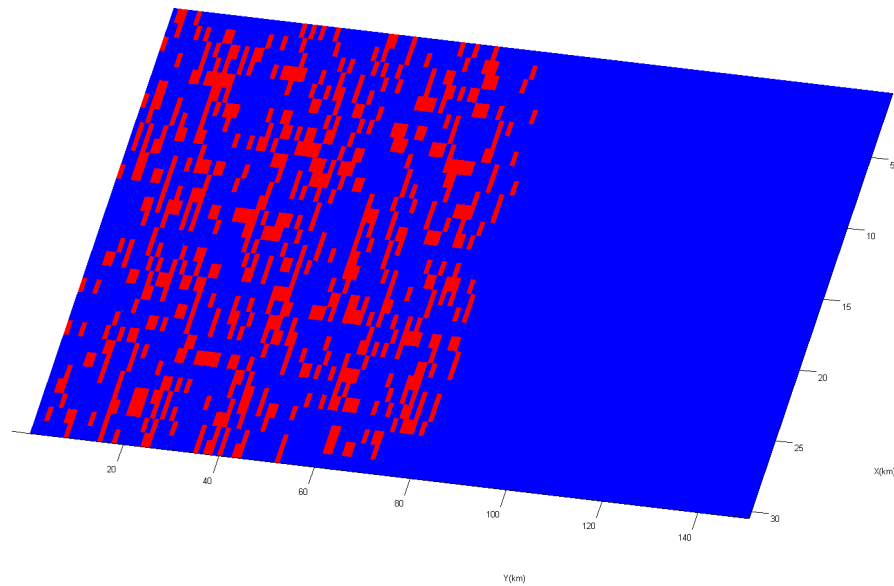

Figure 7.5: Map view of the carbonate platform used for the model runs (Table 7.3) with water current sediment transport capacity. Assuming an 1m sea level drop during low tide, a number of areas get exposed (temporaray islands, red colour) and block the current flow. Sediment transfer capacity is not affected in deeper areas (blue colour).

158
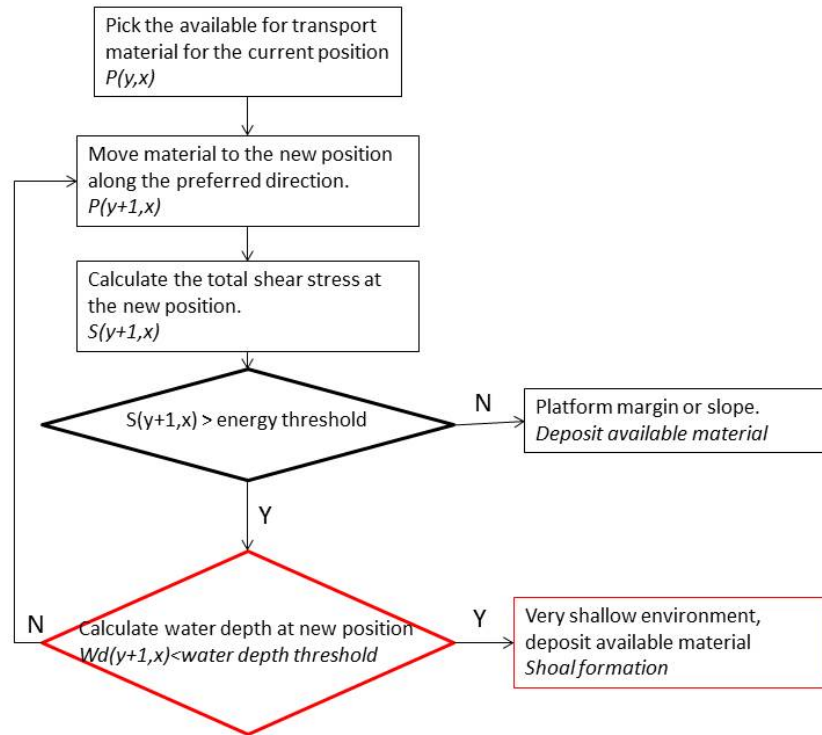
Figure 7.6: Flow chart with the cross platform transportation algorithm (black colour) and the newly developed shoal formation case with the water depth deposition threshold (red colour). All the available material is deposited (without deposition above sea level allowed) once an area shallower than the threshold has been encountered. Rectangulars represent functions in CarboCAT and diamonds conditionals.

generation and evolution of platform interior shoals were studied with a number of CarboCAT generated model runs. The input model parameters for all the model runs are listed in Table 7.3.

Table 7.3: Transportation model runs parameter values

Model size	150 x 30 model cells
Time step	1ky
Elapsed model time	1My
Subsidence rate	100 m/My
Eustatic sea level	Constant
Initial bathymetry	Homoclinal ramp, 0.5m/cell
In-situ producing factories	Low wave energy, production rate: 1000 m/My
	High wave energy, production rate: 1100 m/My
Transportation algorithm	Cross platform + steepest descent
Shoal deposition time	0.5My-1My EMT

Model size and model duration were selected in order to provide enough space and time for the shoals to form and evolve under the specific parameters used in the model runs. Production and subsidence rates were selected to generate an FTP with a wide, flat platform interior, the ideal setting for the cross platform algorithm.

Cross platform sediment transportation is active for the whole EMT but shoal formation only is prevented for the 0-0.5My EMT. This selection was done in order to make sure that only the production/transportation interaction effects shoal formation. Because of the initial bathymetry, in the early stages of the model, several areas on the platform show very shallow water depths and thus favour shoal formation without the production/transportation effect. Furthermore, preventing shoal formation for the above mentioned time, provides the option to identify the effect of shoals on the platform interior by comparing the platform situation with and without the shoals.

The effect of water depth threshold for deposition, the transportation direction and the transportation rate with the cross platform transportation algorithm on the distribution of platform interior shoals were studied with three different model runs (Table. 7.3)

Table 7.4: Model parameters for the two model runs

Model set	MS1			MS2		
Deposition threshold	0.5m			1m		
Transportation direction	Straight	Random	Bathymetry	Straight	Random	Bathymetry
Transported fraction	0.1-0.3-0.5	0.1-0.3-0.5	0.1-0.3-0.5	0.1-0.3-0.5	0.1-0.3-0.5	0.1-0.3-0.5

Three different transportation directions, all moving material towards more distal areas on the platform, were studied for each model run. The first transportation direction was a simple cross platform direction with sediment moved more distal on the platform on a straight line along the depositional dip. The second transportation direction was along the depositional dip towards more distal with a random step along the depositional strike.

The third transportation direction was bathymetry controlled with sediment moved onto local depositional highs without any preferred direction. Depositional highs are defined as areas that have built above the water depth threshold for deposition.

The straight line and random step transportation directions imply that sediment transportation is performed under the effect of strongly linear currents. The bathymetry controlled transportation direction implies that sediment is moved by the fastest moving currents at the most shallow parts of the interior which means that is more probable for the currents to meet a barrier.

The water depth depositional thresholds were selected based on the maximum water depth on the platform interior. For the model parameters used here, the maximum water depth on the interior is 5m. Since the platform interior never gets completely exposed, the deep depositional threshold was selected equal to 1m and the shallow threshold equal to 0.5m

7.2.2.1 Quantitative measurements

Several quantitative measurements were performed for each generated platform. Where appropriate, the shoal geobody dimensions and volumes, the spatial entropy, transition probability matrices and the Markov metric m from vertical succession analysis were calculated.

A new algorithm that identifies shoal geobodies for the whole 3D platform volume was developed in CarboCAT. Geobodies are defined as the extent of adjacent model cells with the a specific facies. The rest of the facies can be considered to constitute different geobodies. The boundaries of each geobody are defined as the model cells without the specific facies adjacent to geobody cells. The algorithm checks for spatially adjacent model cells in both vertical and horizontal directions while depositional hiatuses are ignored.

The algorithm also calculates the volume of each geobody as the sum of the volumes of all connected cells. Furthermore, the mean length along the depositional dip of the platform is calculated from all the lengths along all transect parallel to the depositional dip of the platform. Similarly, the mean strike length is calculated as the mean of the lengths of the geobody along all the transects parallel to the depositional strike.

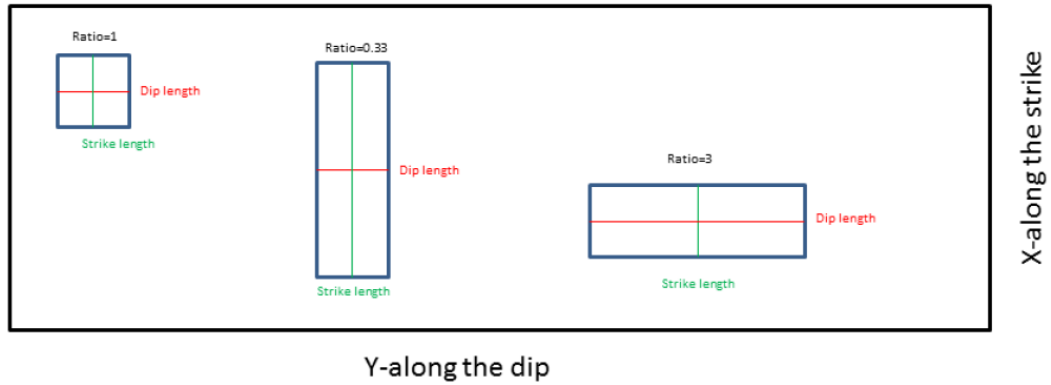The volume and dimensional calculations for all geobodies in the model runs,

161

Figure 7.7: Schematic map view of a carbonate platform with geobodies with specific dimenion ratios. Deposional dip for the platform is along the Y direction and strike along the X direction. The dip length (red) and strike length(green) of each geobody are marked.

were performed without any facies thickness threshold for cell connectivity. This means that two horizontally and vertically adjacent model cells that contained any amount of the geobody facies, were considered connected. Application of a facies thickness threshold for connectivity, based for example on fluid flow properties of the strata, will change the calculated volumes and dimensions of the geobodies.

The dimensional ratio of each geobody is defined as the ratio of the dip length to the strike length of the geobody. Ratio 1 means that the dip and strike lengths of the geobody are equal. On a map view a geobody with dimensional ratio 1 shows a square shape. Ratio greater than 1 means that the dip length of the geobody is longer than its strike length. Map view of the geobody is an elongated rectangular with the big axis parallel to the deposition dip. Ratio less than 1 means that the strike length of the geobody is longer than its dip length. Map view of the geobody is an elongated rectangular with the big axis parallel to the deposition strike (Fig.7.7).

Geobodies for all model runs are defined as the transported material that has been deposited above the depositional threshold regardless of the factory that produced the material. This simple definition of shoal geobodies allows for defining geobodies irrespective of the number of producing factories on the interior. The shoal geobody definition implies that the grain texture and properties of the reworked material differ from the texture and properties of the in-situ producing surrounding material.

Model run results were also quantified using spatial entropy calculations. Spatial entropy for each model cell is calculated by counting the number of spatially adjacent model cells with different deposited lithology and dividing by the number

162

of the adjacent model cells (8) (**Drummond1999**). Depositional hiatuses are ignored for the calculation of the spatial entropy. Spatial entropy is a measure of the facies spatial distribution and thus the facies connectivity on the platform. Low spatial entropy values indicate facies homogeneity and highly connected facies.

Transition probability matrices were also calculated where appropriate. Transition probability matrices contain values that represent the probability of vertical transition between any two faces. Each row in a transition probability matrix represent one particular facies and its probability to pass to any other facies which are represented as columns. The main diagonal of the transition probability matrices are always zero because it represents transition of one facies to itself which is ignored (**Burgess2016a**).

If more than two facies are present in a vertical succession, transition probability value of one between facies A and facies B means that facies A preferentially passes to facies B. Low transition probability values between two facies indicate that the transitions between the two facies cannot be distinguished from random. Transition probability matrices are an indication of the degree of order in a vertical facies transition (**Burgess2016a**).

Strata order is calculated based on the Markov Order Metric, m. The Markov metric m, is calculated from the off-diagonal values of transition probability matrices (TP) from eq.(7.4). Markov metric m identifies facies transition trends that could signify a relationship between facies. The metric counts the number of facies transitions between two facies and compares them to the facies transition of randomly created layers generated from 5000 iterations using a Monte Carlo approach.

Markov metric m, with a value of one indicates perfectly ordered asymmetric strata. Perfectly ordered strata with symmetric cycles have m value equal to 0.5 and lower m values indicate disordered strata or strata order that cannot be distinguished from random. (**Burgess2016a**)

$$max_{diag} = argmax_{j=1...F-1} \left[\frac{\sum diag(TP_j) + \sum diag(TP_{F-j})}{F} \right] \quad (7.2)$$

$$min_{diag} = argmin_{j=1...F-1} \left[\frac{\sum diag(TP_j) + \sum diag(TP_{F-j})}{F} \right] \quad (7.3)$$

$$m = max_{diag} - min_{diag} \quad (7.4)$$

where j is the offset value of the main diagonal, F is the number of facies, $argmin$ is a function that calculates the minimum value in a series, $argmax$ is a function that calculates the maximum value in a series and $diag$ is a function that finds the elements in diagonal with offset j from the main diagonal.

163

7.2.3   Model run examples

The model runs shown in Table 7.4 tested the effect of transported fraction, transportation direction and deposition threshold in the formation, volume and geometric characteristics of platform interior shoals.

7.2.3.1   Effect of transported fraction

The effect of transported fraction, which defines the amount of in-situ produced material that is available for transportation, was tested with model runs with low (0.1), medium (0.3) and high (0.5) transported fractions and all other parameters constant (Fig.7.8).

The interaction of local bathymetry with the straight line transportation direction generated platform interior shoals and autocycles. In-situ production generates local bathymetric highs that occasionally build above the water depth deposition threshold and block sediment transportation. Because sediment transportation is always towards more distal areas along straight lines, sediment deposition occurs on the proximal area of the bathymetric high. Sediment deposition kills the in-situ production at the bathymetric high and thus the bathymetry is controlled by the subsidence rate and the amount of deposited material (Fig.7.8).

If the amount of deposited material due to sediment transportation is just enough to fill the newly created accommodation, the shoal persists and aggardes. If the volume of the transported material deposited on the high is greater than the new accommodation, the extra material is deposited on the proximal side of the shoal and thus the shoal progrades in the opposite direction of the sediment transportation. When not enough material is deposited at the shoal to keep the bathymetry above the depositional threshold, a hiatus is generated and in-situ production can start again (Fig.7.8). The interaction of sediment transportation with local bathymetry generates an autocycle that starts with in-situ production on the bottom of the cycle, above a depositional hiatus. In-situ produced material vertically passes to transported material and the cycle terminates with a depositional hiatus on the top. The generated autocycles and the constitute shoals are diachronous features.

Sensitivity analysis demonstrates that the transported fraction affects shoal formation and size for the straight path transportation direction. For low transported fraction (0.1) relatively small shoals are formed that mainly aggrade and quickly disappear. The autocycles are composed mainly by in-situ material (Fig.7.8a). As the transported fraction increases to medium (0.3, Fig.7.8b) and high (0.5, Fig.7.8c) the generated shoals become bigger and prograde more, with the autocycles dominated by transported material.

The spatial entropy on the platform interior shows that for the first 0.5My EMT during which shoal formation is not allowed, the platform interior is highly

homogeneous because only one factory produces there. Shoal formation generates a second factory on the interior and spatial entropy increases. The increase in spatial entropy is related to the transported fraction, with higher fractions generate higher spatial entropy (Fig.7.9).

Shoal geobody measurements show that 58 geobodies are formed on the interior with mean volume $4.62*10^8 m^3$ (total interior volume is $80*10^9 m^3$) and dimensional ratio 1.74 (Table 7.5). The figures for the effect of transported fraction on shoals with random path and bathymetry controlled transported directions can be found in Appendix B.

7.2.3.2   Effect of transportation direction

The effect of transportation direction on shoal formation was tested with model runs which have different transportation directions, namely straight line, random path and bathymetry controlled and all other parameters constant, as shown in Table. 7.4.

Shoal geobodies generated with the random step (Fig.7.10b) and the bathymetry controlled transportation directions (Fig.7.10c) demonstrate some differences compared to geobodies generated with straight line transportation direction (Fig.7.10a). Because transportation includes a random step along the depositional strike not all sediment flow paths that initiate more proximal than a shoal deposit on the proximal part of the shoal.

Some flow paths deposit on the sides along the strike of the shoals. As a result of less sediment being deposited on the proximal part(along the dip) of the shoal and more sediment deposited on the strike part, dimensional ratios show a small decrease (Table 7.5).

The transportation direction does not seem to effect the spatial entropy on the platform interior (Fig.7.11). Shoal formation generates a second factory on the interior and spatial entropy increases. Since the amount of available material is the same for all transportation directions, the spatial entropy increases to 0.33 for all cases.

Similar to the spatial entropy on the platform interior, the number of isolated geobodies and their volume are not affected by the transportation direction. The number of geobodies and their volume is mainly controlled by the amount of material available and not by the way the material moves on the platform (Table 7.5).

7.2.3.3   Effect of depositional threshold

The effect of the depositional threshold on shoal formation was studied with model runs with water depth 1m for shoal formation and the rest of the parameters are shown in Table 7.4.

The deeper depositional threshold means that any given time more and bigger areas can act as sediment transportation barriers. Furthermore, more accommodation is available for sediment deposition and thus sediment deposits have to be thicker (up to 1m) to keep the bathymetry above the depositional threshold.

Comparison of model runs with water depth depositional threshold of 1m and straight line transportation direction to model runs with 0.5m depositional threshold (Fig.7.12 and 7.13) show that due to more available accommodation, Only the highest transported fraction (0.5, Fig.7.13) generates geobodies that prograde in the opposite direction of the transportation.

Further comparison of the number of geobodies, their volume and their dimensional ratio also reveals the effect of greater accommodation on the geobodies. Approximately 10% fewer geobodies are formed with the deeper depositional threshold and are volumetrically one order of magnitude bigger than the geobodies with the 0.5m depositional threshold (Table 7.6 and comparison with Table 7.5)

7.2.3.4 MS3-Deposition threshold 0.5m and straight line transportation direction.

In order to study the effect of autocycles from cross platform sediment transportation on strata order, MS3 model run included two producing factories on the platform interior. The second factory on the interior has an effect on the distribution of the in-situ produced facies and their distribution. Because all transported material is considered the same, the number of factories on the interior does not affect the characteristics of the shoals.

Model runs with water depth depositional threshold of 0.5m and straight line transportation direction towards more distal, show that aggrading geobodies are formed with low transported fraction (0.1, Fig.7.14a). Progradational geobodies with progradation towards more proximal are formed for medium (0.3, Fig.7.14b) and high (0.5, Fig.7.14c) transportation fractions.

The number of isolated geobodies on the interior decreases and the geobodies become volumetrically bigger as the transported fraction increases (Table 7.7). Because transportation moves material in straight line towards more distal, any shoal blocks all sediment transportation paths that initiate more proximal than the shoal. This generates sediment deposition always in the proximal part of the shoal and the shoals increase in length along the depositional dip and their dimensional ratio increases (Table 7.7). The rest of the figures for the data in Table 7.7

Spatial entropy on the interior for two in-situ producing factories only (0-0.5My EMT) is variable with time with a minimum value of 0.2 (Fig.7.15) . This higher spatial entropy value (compare to value 0.05 and decreasing for the one in-situ producing facies in MS1) indicates lower spatial connectivity of facies on the interior and the effect of the second in-situ producing factory.

Spatial entropy for the 0.5-1My EMT when shoals can form almost doubles in value. The increase in spatial entropy appears to be independent of the transported fraction (Fig.7.15).

Calculation of Markov metric, m, revealed that generally strata order is relatively low on the interior but autocycles increase the strata order. Even though the addition of an extra facies on the interior increases the spatial heterogeneity (Fig.7.15), shoals represent facies that form and evolve under specific conditions (bathymetry above the water depth threshold for deposition, sediment deposition on the proximal areas of the shoal), and thus generation and evolution of shoals on the interior increases the strata order (Fig.7.16).

For the low transported fraction (0.1, Fig.7.16a) the observed facies distribution has m value of 0.23 and is located within the range of the probability density function (PDF) of the random shuffling. The probability of finding a m value equal to or greater than the observed within the PDF of random shuffling (p value) is 0.449, indicating that the observed facies succession could very probably occur by chance. For the medium (0.3, Fig.7.16b) and high (0.5, Fig.7.16b) transported fractions, the calculated m values are 0.3 and 0.38 respectively. For both cases the p value is zero, an indication of ordered strata.

Transition probability matrices (TP matrices) calculated for the facies successions on the interior show that in-situ produced facies tend to vertically pass to the other in-situ produced facies. Transported facies (shoals) also tend to pass to transported facies and the probability of transported to transported facies increases with increasing transported fraction.

The high chance of vertical transition from in-situ produced to in-situ produced material and from transported to transported material is another indication of depositional autocycles on the interior. For any point on the platform a vertical succession of strata is comprised of sections dominated by in-situ produced material and sections dominated by transported material.

The calculation of Markov metric, m and TP matrices were performed assuming that any point on the platform interior is representative of the platform conditions everywhere. Markov metric m and TP matrices were calculated for the same point in each platform and the points were selected randomly in each case.
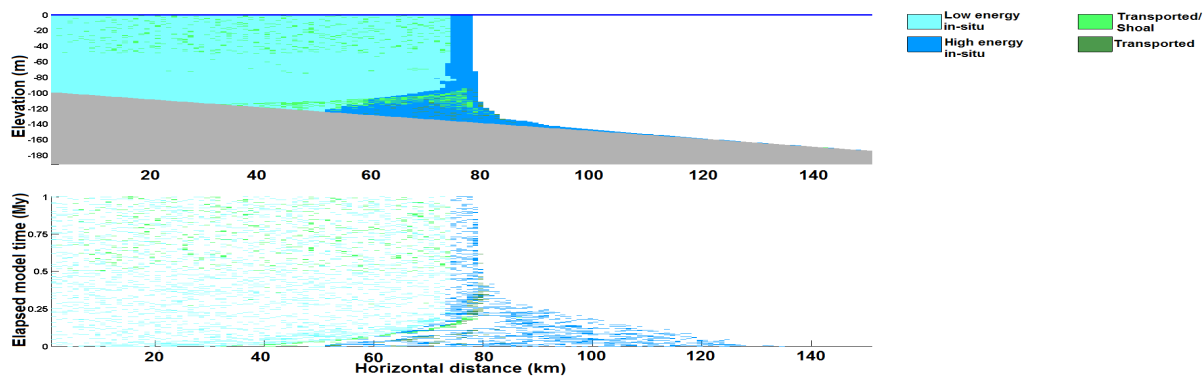
(a) Transported fraction 0.1.
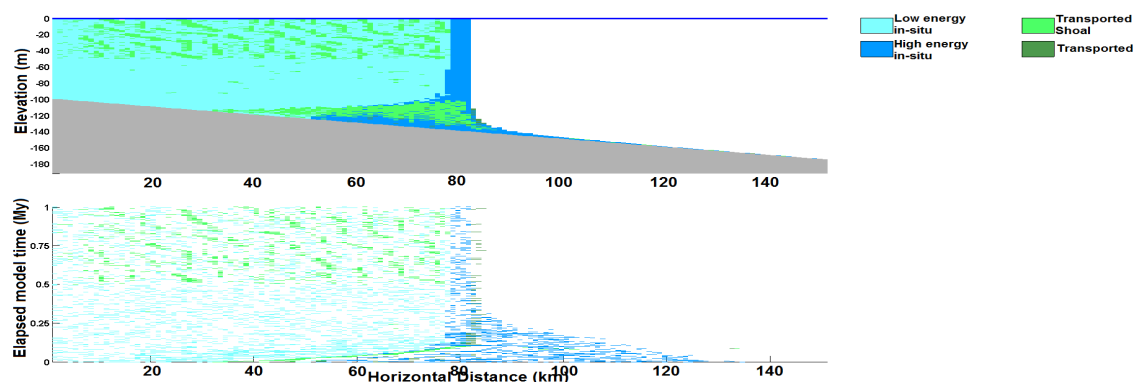
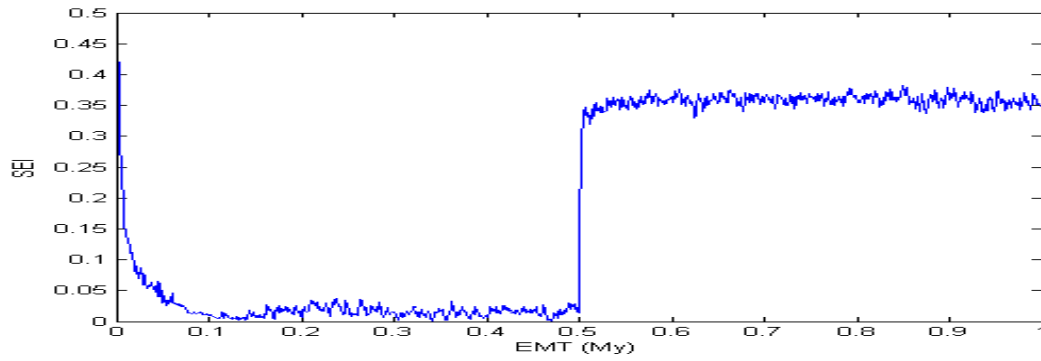(b) Transported fraction 0.3
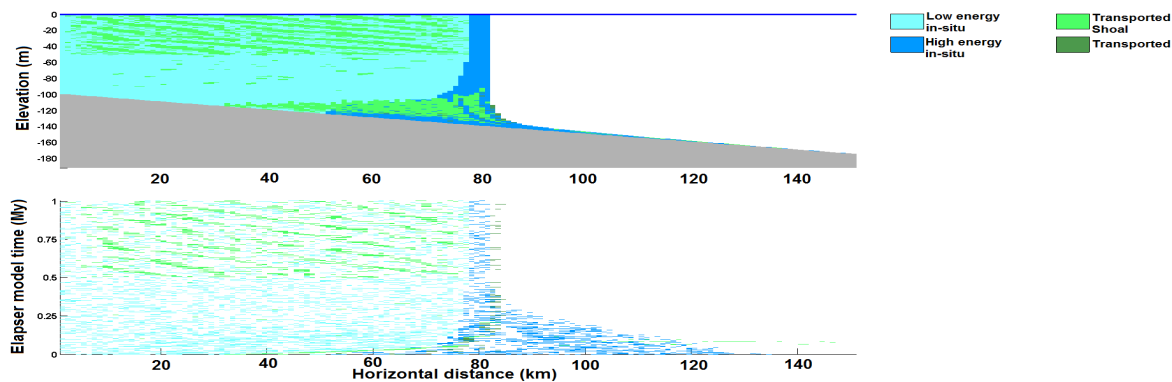
(c) Transported fraction 0.5

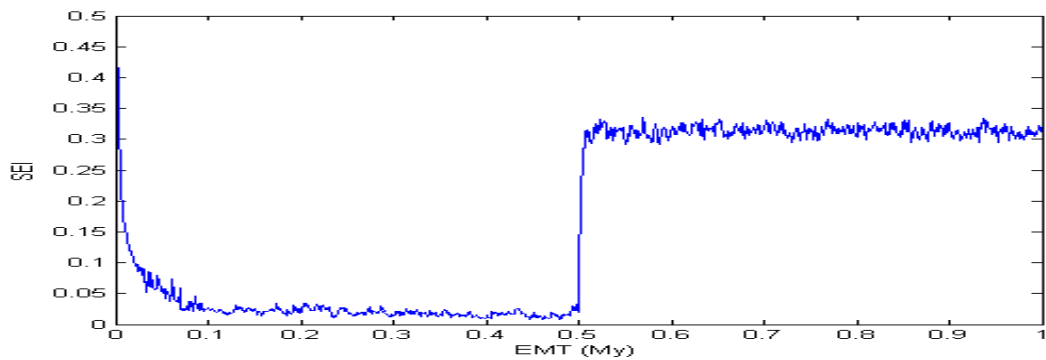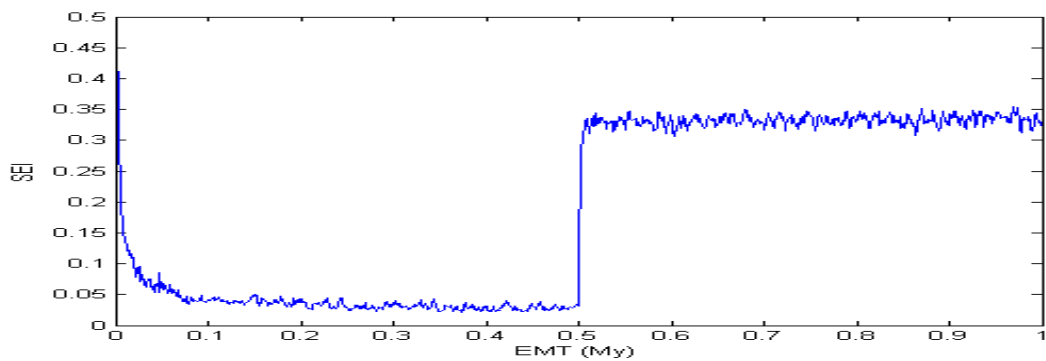Figure 7.8: Cross section (TOP) and chrono-stratigraphic section (BOTTOM) of the model runs with 0.5m water depth depositional threshold and straight line transportation direction towards higher values horizontal distance. (a) 0.1 transported fraction. Realtively small, short lived, aggrading shoals are formed. (b) 0.3 transported fraction. Most of the shoals prograde in the opposite direction of sediment transportation with a few aggrading examples. (c) 0.5 transported fraction. All geobodies highly prograde in the opposite direction of sediment transportation.
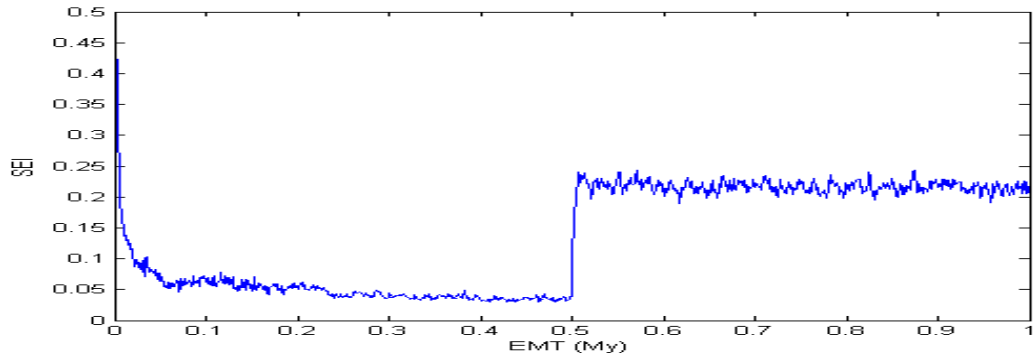
(a) Transported fraction 0.1.
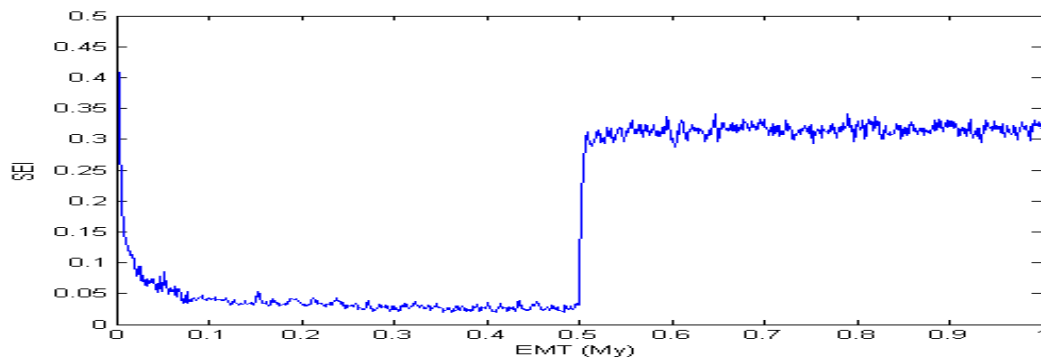
(b) Transported fraction 0.3

(c) Transported fraction 0.5

Figure 7.9: Spatial entropy with time for the model runs with 0.5m water depositional threshold and straight line transportation direction towards higher values horizontal distance. The spatial entropy increases with the addition of an extra factory and with transported fraction. (a) Transported fraction 0.1, entropy increases to 0.21. (b)Transported fraction 0.3, entropy increases to 0.32 and (c) transported fraction 0.5, entropy increases to 0.36.

169

Table 7.5: Geobody number, volume and dimensional ratio for model runs with one platform interior facies and shoal deposition threshold 1m. The volume and dimensional ratio values are mean values of all geobodies on the platform.

Transported fraction	Transportation direction								
	Straight			Path			Bathymetry		
	Number	Volume(m^3)	Ratio	Number	Volume(m^3)	Ratio	Number	Volume(m^3)	Dimension ratio
0.1	76	$8.82 * 10^8$	1.36	71	$9.18 * 10^8$	1.38	70	$9.98 * 10^8$	1.75
0.3	65	$2.43 * 10^9$	1.72	57	$2.52 * 10^9$	1.68	57	$2.32 * 10^9$	1.79
0.5	47	$4.7 * 10^9$	1.91	47	$4.4 * 10^9$	1.72	51	$3.68 * 10^9$	1.76
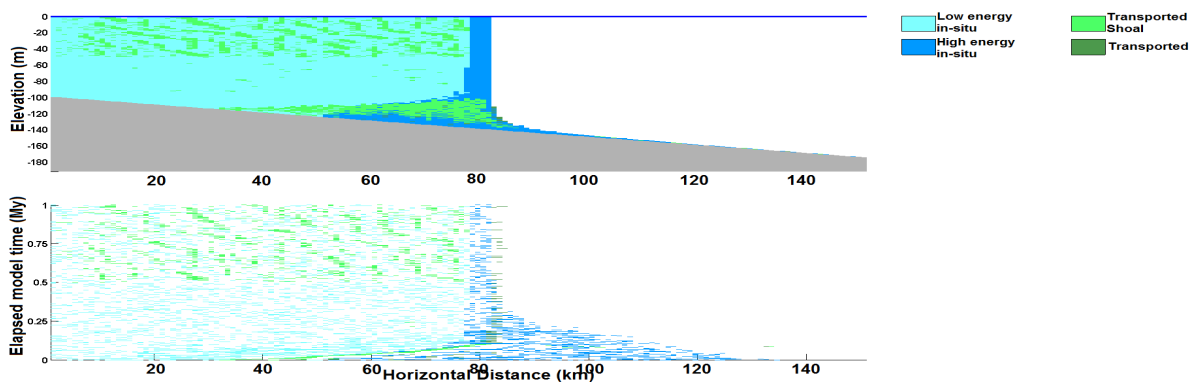
(a) Staight path transportation direction.
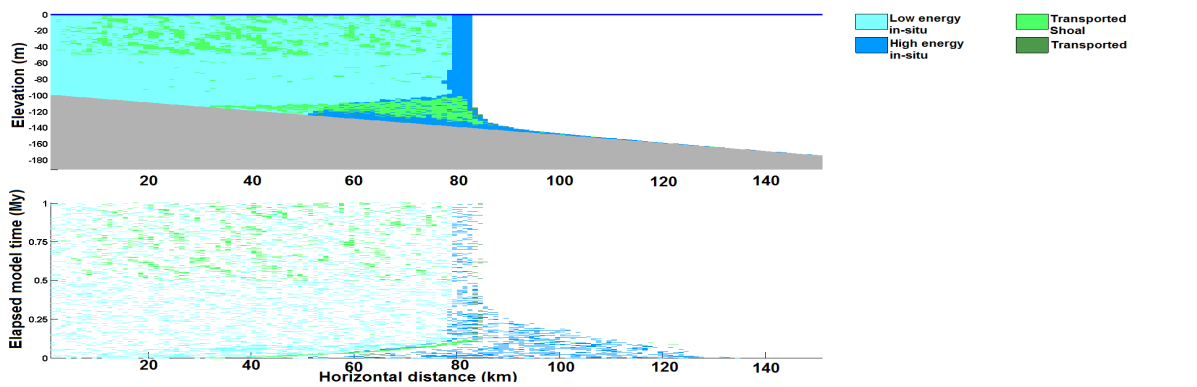
(b) Random path transportation direction
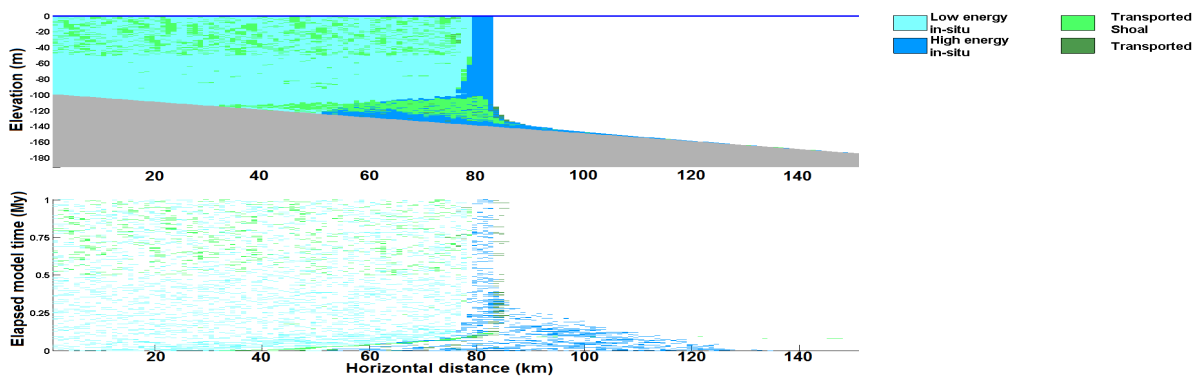
(c) Bathymetry controlled transportation direction

Figure 7.10: Cross section (TOP) and chrono-stratigraphic section (BOTTOM) of the model runs with 0.5m water depth depositional threshold and 0.3 transported fraction. (a) Straight path transportation direction Most of the shoals prograde. (b) Random path transportation direction. Most of the shoals aggrade with a few , smaller, prograding examples. (c) Bathymetry controlled transportation direction. Almost of the shoal bodies aggrade.
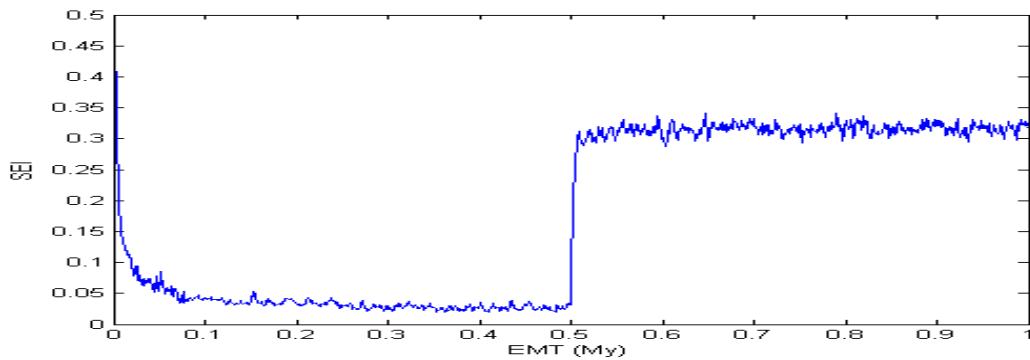
(a) Straight line transportation direction

(b) Random path transportation direction

(c) Bathymetry controlled transportation di-
rection

Figure 7.11: Spatial entropy with time for the model runs with 0.5m water depositional threshold and 0.3 transported fraction. The spatial entropy increases with the addition of an extra factory irrespective of the transportation direction.

(a) Depositional threshold 0.5m.

(b) Depositional threshold 1m
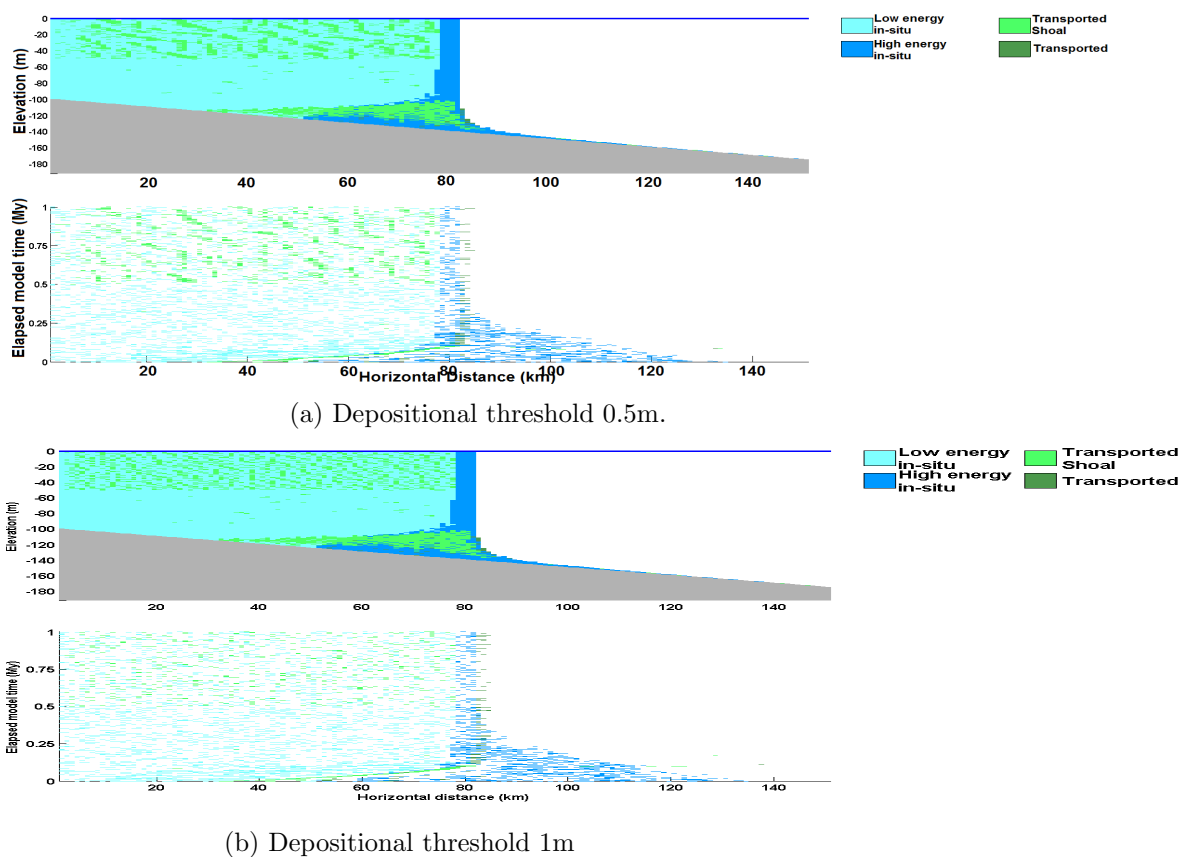
Figure 7.12: Cross section (TOP) and chrono-stratigraphic section (BOTTOM) of the model runs with 0.3 transported fraction and and straight line transportation direction towards more distal (higher values horizontal distance). (a) 0.5m depositional threshold. Most of the geobodies prograde (b) 1m depositional threshold. Only half of the geobodies aggrade.
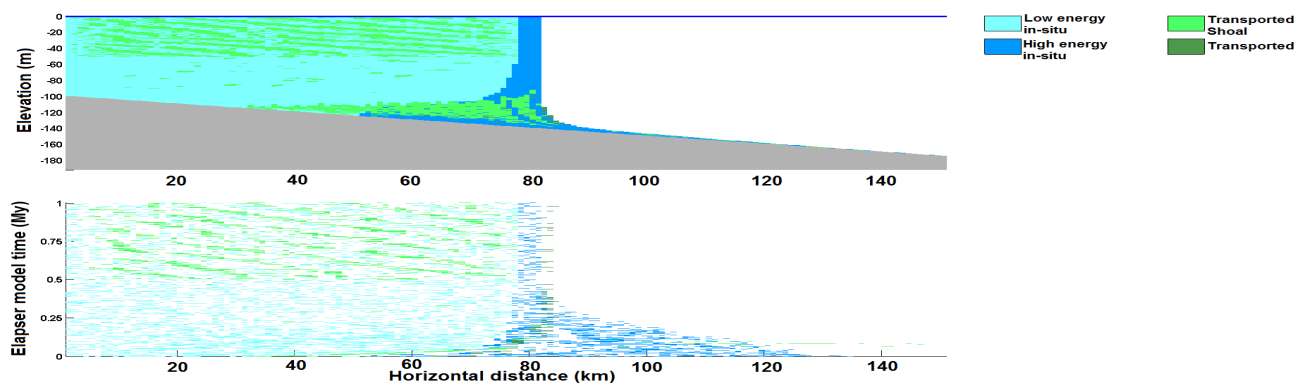
(a) Depositional threshold 0.5m.
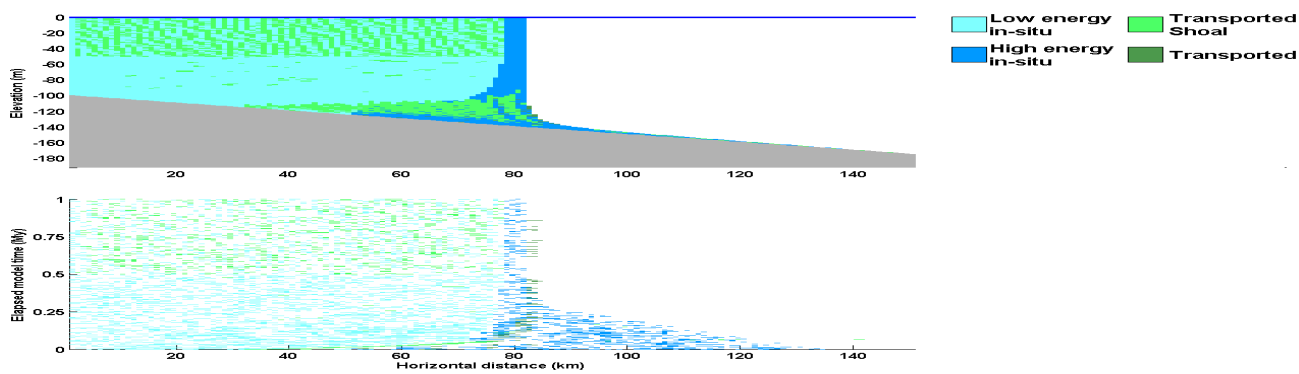
(b) Depositional threshold 1m

Figure 7.13: Cross section (TOP) and chrono-stratigraphic section (BOTTOM) of the model runs with 0.5 transported fraction and and straight line transportation direction towards more distal (higher values horizontal distance). (a) 0.5m depositional threshold. Geobodies highly prograde (b) 1m depositional threshold. Geobodies have aggradational and progradational elements.

Table 7.6: Geobody number, volume and dimensional ratio for model runs with one platform interior facies and shoal deposition threshold 1m. The volume and dimensional ratio values are mean values of all geobodies on the platform.

Transported fraction	Straight			Path			Bathymetry		
	Number	Volume(m^3)	Ratio	Number	Volume(m^3)	Ratio	Number	Volume(m^3)	Dimensional ratio
0.1	67	$1.24*10^8$	1.36	64	$1.12*10^8$	1.28	65	$1.29*10^8$	1.74
0.3	61	$1.86*10^9$	1.63	50	$2.05*10^9$	1.57	52	$3.31*10^9$	1.82
0.5	45	3.8510^9	1.87	47	$3.33*10^9$	1.66	43	$7.87*10^9$	1.75

Table 7.7: Geobody number, volume and dimensional ratio for model runs with two platform interior facies and shoal deposition threshold 0.5m. The volume and dimensional ratio values are mean values of all geobodies on the platform.

Transported fraction	Transportation direction								
	Straight			Path			Bathymetry		
	Number	Volume(m^3)	Ratio	Number	Volume(m^3)	Ratio	Number	Volume(m^3)	Dimension ratio
0.1	76	$8.82*10^8$	1.36	71	$9.18*10^8$	1.38	70	$9.98*10^8$	1.75
0.3	65	$2.43*10^9$	1.72	57	$2.52*10^9$	1.68	57	$2.32*10^9$	1.89
0.5	47	$4.7*10^9$	1.91	47	$4.4*10^9$	1.72	51	$3.68*10^9$	1.76
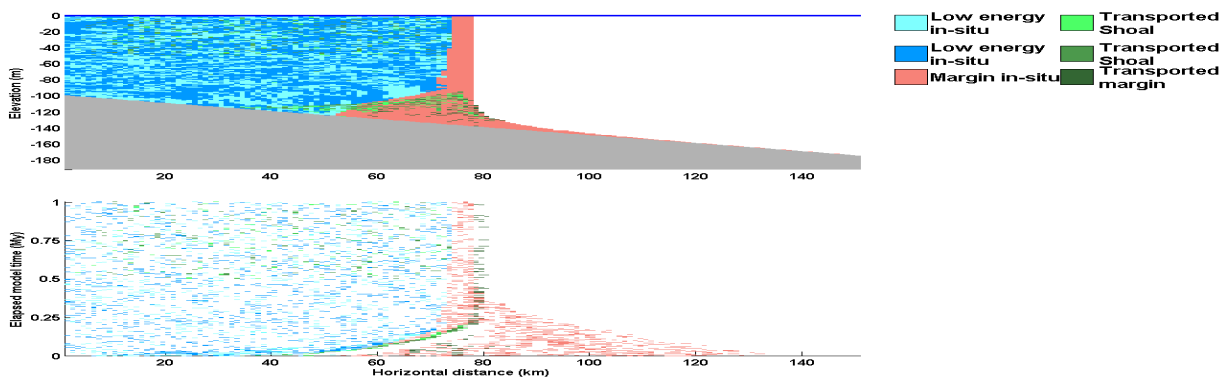
(a) Transported fraction 0.1.
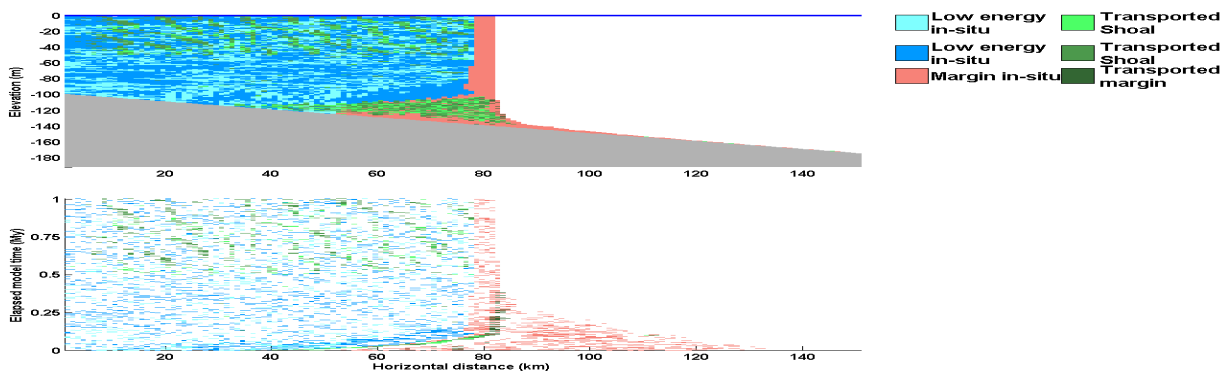
(b) Transported fraction 0.3
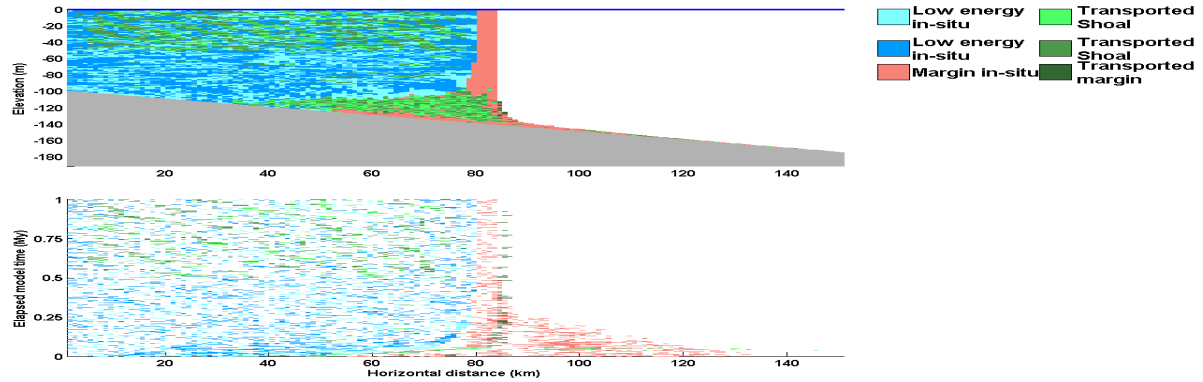
(c) Transported fraction 0.5

Figure 7.14: Cross section (TOP) and chrono-stratigraphic section (BOTTOM) of the model runs with 0.5m water depositional threshold, straight line transportation direction towards more distal (higher values horizontal distance) and two in-situ producing factories on the interior. (a) 0.1 transported fraction. Realtively small, short lived, aggrading shoals are formed. (b) 0.3 transported fraction. Prograding in the opposite direction of transportation (c) 0.5 transported fraction. Mainly geobodies prograde in the opposite direction of transportation.
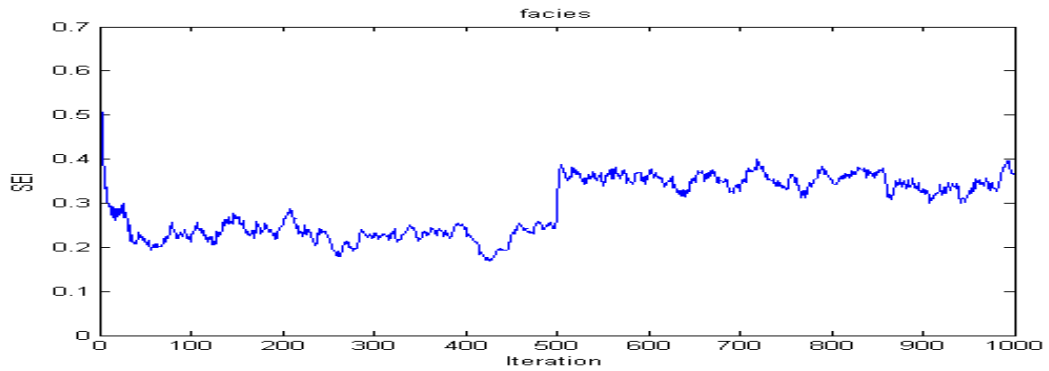
(a) Transported fraction 0.1.
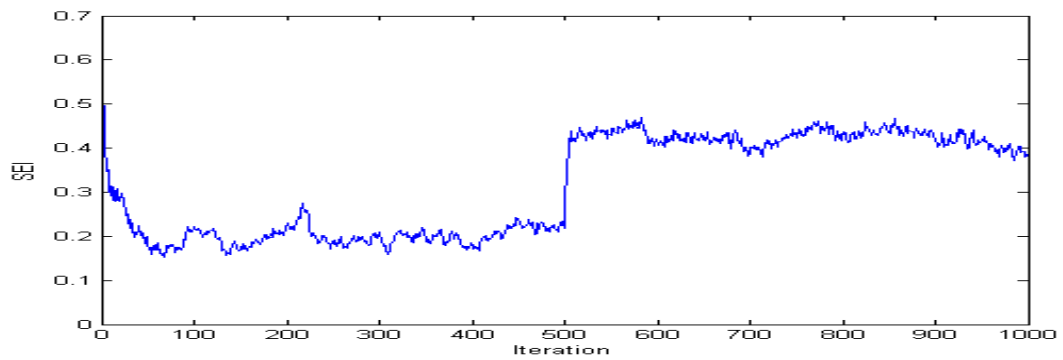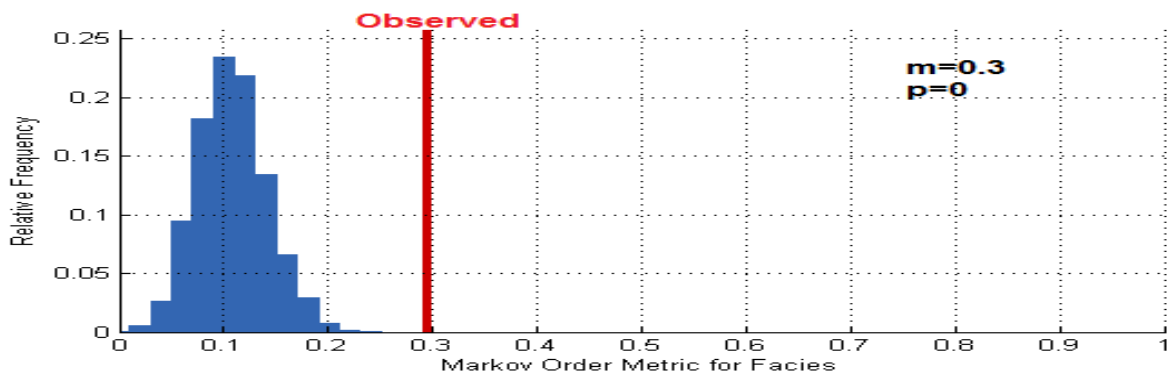

(b) Transported fraction 0.3
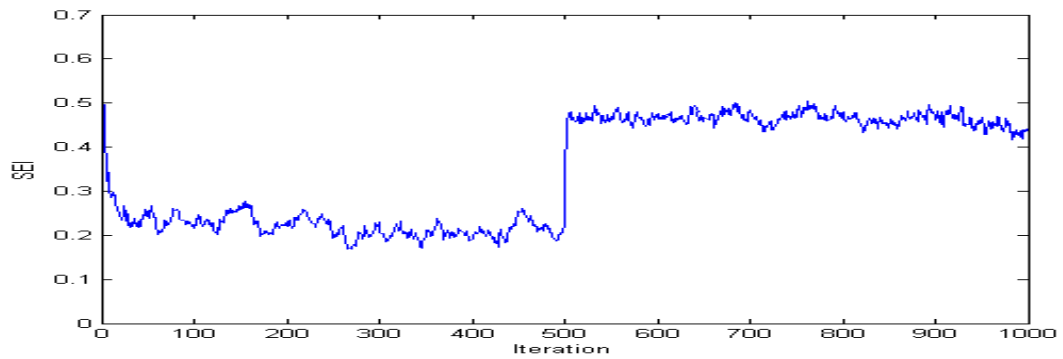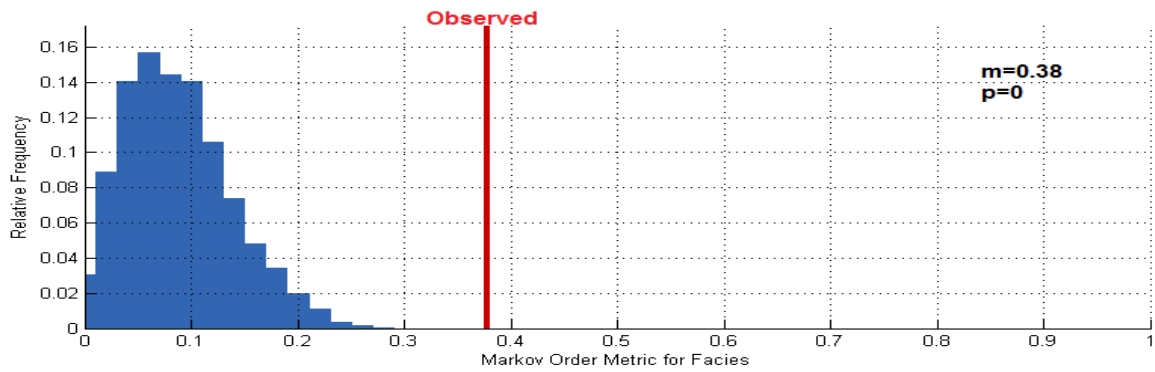

(c) Transported fraction 0.5

Figure 7.15: Spatial entropy with time for the model runs with 0.5m water depositional threshold, straight line transportation direction towards more distal (higher values horizontal distance) and two in-situ producing factories on the interior. The spatial entropy increases with the addition of an extra facies (shoals) and with transported fraction. (a) Transported fraction 0.1, entropy increases to 0.38. (b)Transported fraction 0.3, entropy increases to 0.4 and (c) transported fraction 0.5, entropy increases to 0.42.
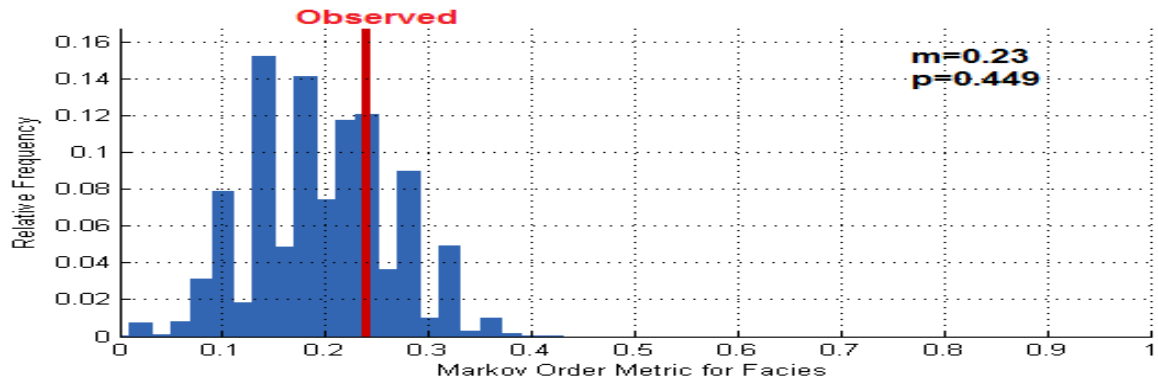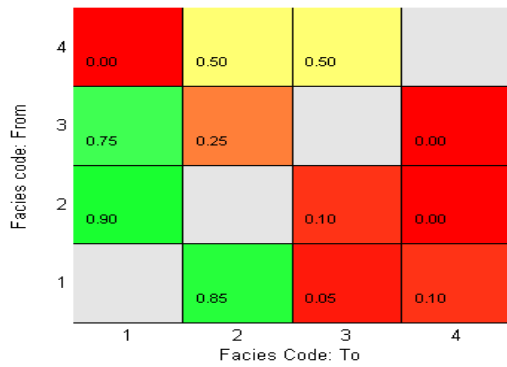
(a) Transported fraction 0.1.
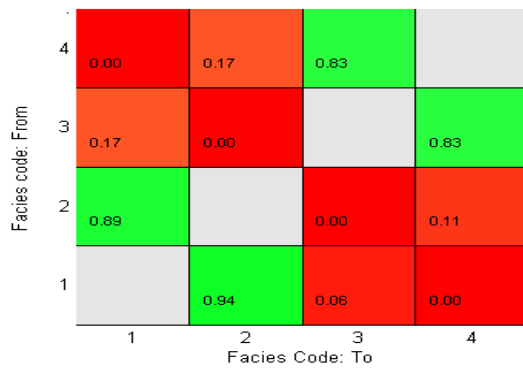

(b) Transported fraction 0.3
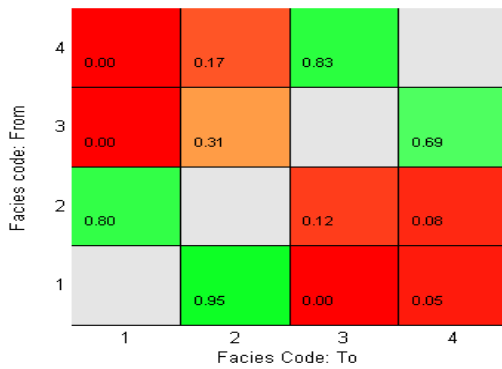

(c) Transported fraction 0.5

Figure 7.16: Calculated m values of the model run facies distribution (vertical red line) and a histogram (blue) showing the probability density function and m values from 5000 iterations of random shuffling of strata. (a) Transported fraction 0.1, the m value is 0.23 and is located within the PDF of the random shuffles. (b)Transported fraction 0.3, m is 0.3 and lies outised the range of the PDF. (c) transported fraction 0.5, with m 0.38, outside the PDF.

179

(a) Transported fraction 0.1.

(b) Transported fraction 0.3

(c) Transported fraction 0.5

Figure 7.17: Transition probability matrices of the strata successions in model runs with two in-situ producing factories in the interior, 0.5m water depth deposition threshold and straight line transportation direction towards more distal (higher values horizontal distance). Facies 1 and 2 correspond to the two in-situ producing factories on the interior. Facies 3 correspond to the transported material of factory 1 and facies 4 the transported material for factory 2. The in-situ factory on the margin and its transported material have been excluded from the calculations. (a) Transported fraction 0.1. (b)Transported fraction 0.3. (c) transported fraction 0.5.

180

8 Modelling of Upper Cretaceous (Santonian) outcrops in South-Central Pyrenees, Spain

This chapter uses CarboCAT generated stratigraphic forward models to investigate the controls on platform geometry of the Santonian outcrops in South-Central Pyrenees, Spain, evaluate different stratigraphic interpretations and study possible non-uniqueness of strata geometries. The evaluation of the model runs was performed through discussion and regular meetings with the project partner in Manchester University.

The chapter is divided into four sections. The first section presents the area of the modelled outcrops and describes their geology which is taken from **Lavi2017**. The second section presents the numerical model and the model parameters used for the model runs. The third section shows the modelling outputs as 3D plots and selected cross sections for each model run. The fourth section discusses the model runs and presents the conclusions of the work.

8.1 Location and geology

The studied area is part of the South-Central Spanish Pyrenees and is located at 42° north latitude and 1° to 2° east longitude, ca.180km NE of Barcelona, Spain. It is close to Tremp city, along the Carreu river valley.

The area is part of the Tremp Basin which is built by Upper Cretaceous strata (Fig.8.1) on the northern flank of the Sant Corneli anticline. **Skelton2003** provided a detailed description of the location of the area. The area is part of the Upper Thrust Sheet (Boixols fault) of the South Central Pyrenees zone.

The Pyrenees are a linear E-W trending mountain chain approximately 1000km long in northern Spain. They comprise of post-Hercynian rocks with a symmetrical structural axis that divides the mountain range to two zones. In the north of the axis, strata have undergone N-directed thrusting with characteristic N-verging folds. To the south of the axis post Triassic strata have undergone S-directing thrusting (**Willliams1985**).

Structurally, a Mesozoic opening between the Iberian plate to the south and the European plate to the north led to deposition of several sedimentary cycles in continental margin environment through the Mesozoic and the Cenozoic. A compressional phase during Paleogene led to the collision of the Iberian plate with the European plate, the deposition of Eocene flysch and the formation of the Pyrenees. (**Simo1986**).
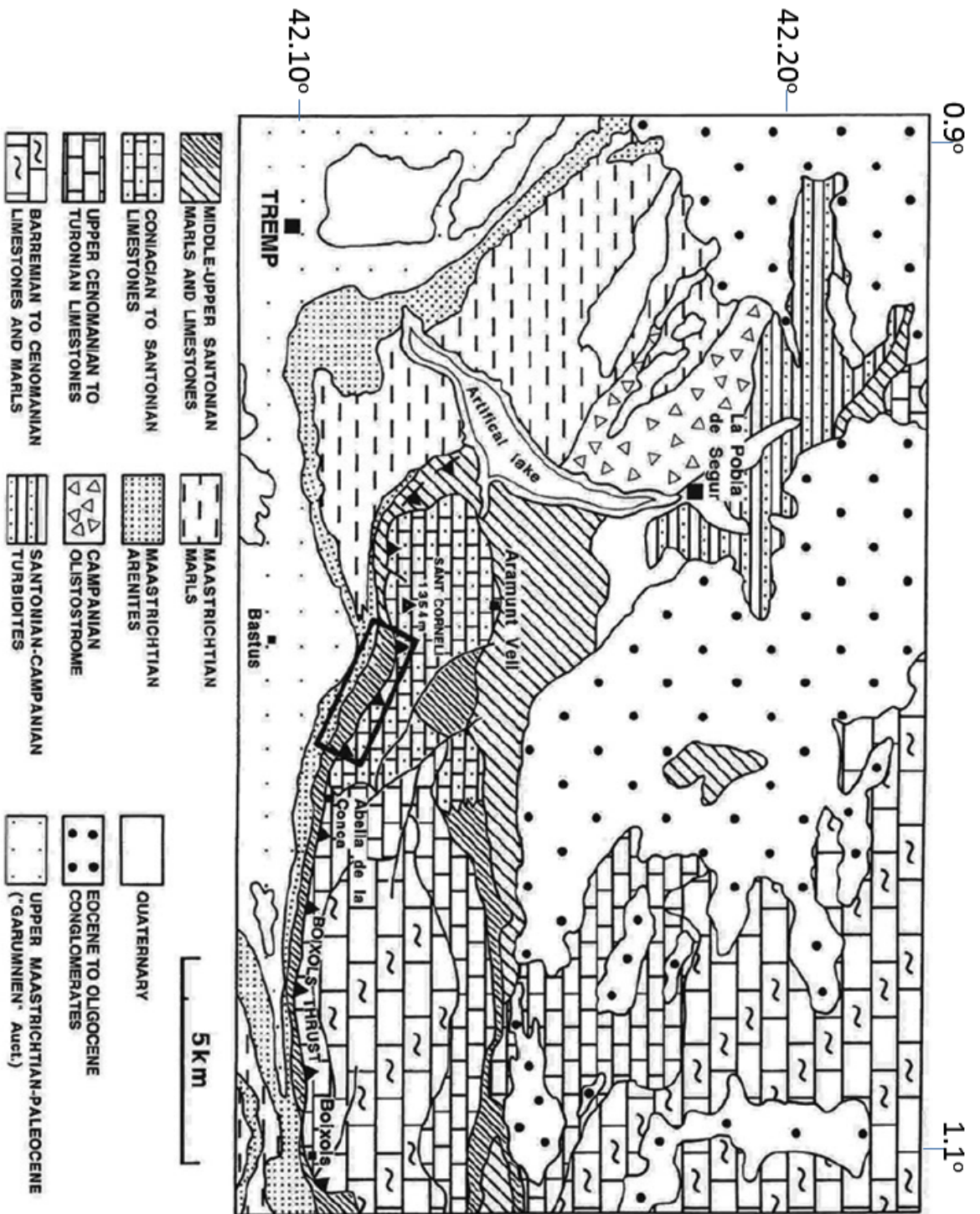
Figure 8.1: Geologic map of the studied area. The Boixols thrust is located on the south-east and the Tremp city in the south-west. The box area marks the position of the Santonian outcrops. From **Sanders2001**.

182

The main structural elements of the Pyrennes are defined as (**Puigdefabregas1986**):

- the internal metamorphic zone or North Pyrenean Fault. It corresponds to the boundary between the Iberian and European plates, and the limit of structural divergence between the North and South Pyrenean zones;

- the North Pyrenean zone. It includes basement blocks (North Pyrenean massifs) with a Mesozoic strata and a Tertiary cover;

- the South Pyrenean zone. It includes a succession of three thrust sheets. The upper thrust sheet comprised of Mesozoic-lower Tertiary strata. The Mesozoic consists of a thick, complete sequence including slope and turbidite facies in the late Cretaceous. The middle thrust sheet contains a partial Mesozoic sequence while the lower thrust sheets involve Hercynian basement rocks.

Internally the Upper Thrust Sheet of the South Pyrenean zone has been further separated to the southern Serres Marginales thrust fault, the Montsec thrust fault and the northern Boixols fault (**Villalba-Breva2013**).

In the South Pyrenean zone **Puigdefabregas1986** identified 10 depositional cycles spanning the time form Permian to Miocene. Each cycle contains several depositional sequences characterised by different tectonic events, subsidence and sediment supply patterns.

The Upper Cretaceous of the Tremp basin was mainly deposited during an extensional regime from the counter clockwise rotation of the Iberian peninsula. The tectonism due to expansion resulted to high subsidence rates and the backstepping of each sequence relative to the previous one. Sedimentation during the opening of the basin was mostly of marine-carbonate nature (**Simo1989**).

The compressional stage was marked from a 120km NW movement of the Iberian plate and the collision with the European plate. During the compressional phase, the sedimentation changed from carbonate to siliciclastic sandstones and non-marine shales (**Simo1989**).

Five carbonate platforms have been identified in the Upper Cretaceous of the Upper Thrust sheet of the South Pyrenean zone (**Simo1986**):

1. the Santa Fe sequence (upper Cenomanian); The lower boundary of Santa Fe is an angular unconformity and the upper boundary records a sea-level drop or uplift. The sequence is characterised by a thickening outwards carbonate shelf, slope breccias and basin marls;

2. the Congost sequence (Turonian to Lower Coniacian): The sequence has a NW prograding distally steepened carbonate ramp geometry, with an upper boundary produced by non- deposition and erosion;

3. the Sant Corneli sequence (Upper Coniacian to Lower Santonian): An aggradational carbonate platform with slope marls. Sant Corneli was terminated by a sea-level rise or subsidence;

4. the Vallcarga sequence (Upper Santonian-Campanian). The lower limit of the sequence represents the major marine expansion and extensive growth fault development. The beginning of the tectonic compressive stage forms the upper limit of the sequence;

5. the Aren sequence (Maastrichtian). Siliciclastic nearshore, shelf bars and slope shales developed during compressional tectonism. The upper limit is an angular unconformity in red beds;

The lower boundary of the Sant Corneli sequence is a sub-aerial exposure surface (**Simo1993**) while the upper boundary is the Upper Santonian Herba-savina clays (**Pomar2005**). The Sant Corneli sequence is comprised of three parts. A basin restricted wedge of mega-breccias, a transgressive wedge consisting of shales and a carbonate platform. The carbonate platform is built by lagoonal facies of nodular wackestones-packstones, an aggradational platform margin with coral and rudists packstones and a mud rich slope with traces of carbonate grains form the platform (**Simo1993**).

Pomar2005 identified six lithofacies based on rock textures, skeletal components and bedding, and geometric relationships in the Sant Corneli carbonate platform. Two facies assemblages were defined as rudists build ups and calcarenite wedges based on the six lithofacies. Assuming different water depths for the two assemblages and based on their stratigraphic position, a relative sea level history was estimated. Based on the estimated sea level fluctuations, sequences and para-sequences were identified.

This process-product definition of sequences was explained by changes in the dominant carbonate production as a result of changes in water depth and environmental conditions like siliciclastic influx, concentration of atmospheric CO_2 and changes in Mg/Ca ratio.

Sanders2001 also identified several sequences within the Sant Corneli platform that were attributed to a series of shallowing, aggradational and deepening, progradational successions. Sea level oscillations were assumed to be the main control of the deposition of these successions.

For the purposes of this chapter, the modelled area will be referred to as the Bastus platform. The Bastus platform is a Santonian age, 200 km long and approximately 50 km wide platform with the long axis (along the dip) oriented in N-S direction. The Bastus platform is attached to the mainland in the South with open connection to pelagic waters in the North. The initial topography of the platform is inherited by the underlain sequence and assumed to be a homoclinal

ramp. The Bastus platform represents a 3 My, low angle sequence with mixed siliciclastic and carbonate strata. The maximum thickness of the platform strata is 450 m with a well developed, low energy platform interior approximately 45 km long (**Lavi2017**). The platform strata comprised of :

- siliciclastic strata in the most proximal area (0-18km from the south) of the interior. The siliciclastic strata are well sorted, poorly consolidated sandstones with 60m maximum thickness. A carbonate-siliciclastic strata mixing zone with quartz rich bioclastic grainstones and packstones exists next and more distal from the sandstones;

- carbonate strata in the interior approximately 28km long with maximum thickness 450m. The carbonate interior is dominated by nodular wackestones / packstones with benthic foraminifera and rudists bearing wackestones/packstones as large scale patch reefs;

- wave resistant platform margin. The margin is consisting of mixed Coral-Rudists boundstones reefs and grainstones and packstones with bedded rudists debris. The maximum strata thickness is 280m;

- upper slope with nodular wackstones with foraminifera and shell fragments with maximum strata thickness ca.250m;

- extensive lower slope with pelagic calcareous muds.

8.2 Numerical forward model formulation and model parameters

The main controls on platform development and the validity of different stratigraphic interpretations of the observed geometry of the Bastus platform were studied in a series of model runs. Furthermore, a number of model runs were generated to study the uniqueness of strata geometry of the Bastus platform.

The model runs included several eustatic sea level oscillations, temporary variable production and spatially variable subsidence due to tectonic rotation. The parameter values for the model runs have been selected to represent local conditions. The main goal behind these model runs was to generate numerical forward models that depict the interpreted large scale platform geometry and stacking patterns of each platform segment. The model runs were not intended to deterministically reproduce each feature of the observed geometry.
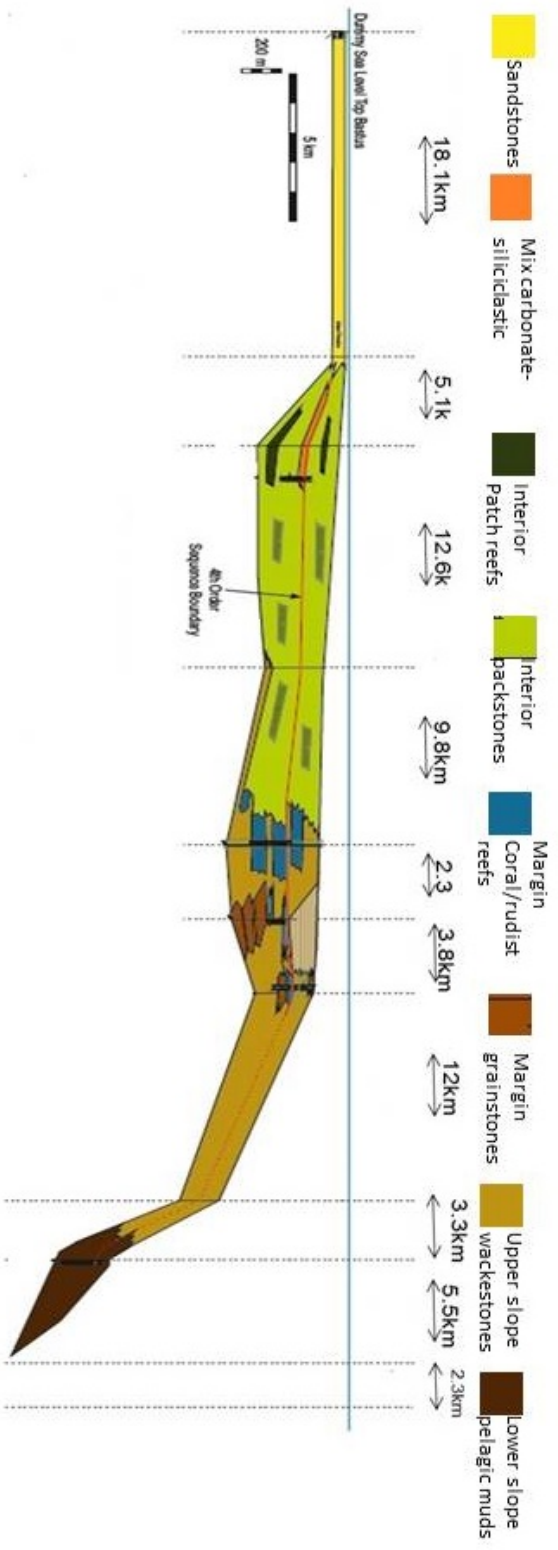
Figure 8.2: Interpreted sequence stratigraphic model with the geometry, dimensions and thickness of the Bastus platform strata. From **Lavi2017**.

186

8.2.1 Interpretation of the observed lithologies

A stratigraphic model was created based on the interpretation of the observed lithologies (Fig.8.2) (**Lavi2017**). The stratigraphic model includes:

- siliciclastic strata dominating the most proximal 18 km to the south. The volume of the siliciclastic strata increases with time and reaches its maximum value at the end of the model. The coarse sandstones with rudists were not interpreted as a different lithology but as a transition zone where siliciclastic and carbonate strata are mixed;

- a well developed, low wave energy platform interior 46 km long. The platform interior is dominated by packstones with interior patch reefs limited in areas of ca. 1km extensive representing the observed wackestones with rudists;

- wave resistant platform margin, 5 km long. The platform margin is build by coral/rudists reefs and grainstones with quartz;

- upper slope with wackestones that show mixtures of rudists and coral fragments with decreasing frequency from the margin and lower slope with pelagic muds.

Overall the Bastus platform is an aggradational platform. The platform margin aggrades with some minor progradation $< 5km$ to be possible at the bottom of platform. No significant facies change has been observed in order to define clear progradation. An observed facies transition from high energy platform margin facies to slope, below wave base pelagic facies at the geomorphic platform margin has been interpreted as a sequence boundary at 1.5 My in the platform development.

The stratigraphic interpretation that best describes the beds and surfaces correlation identified two large sequences (**Lavi2017**). A lower sequence which shows establishment, progradation and aggradation of rudist-coral build-ups and grainstone shoals along the platform margin.

The second sequence shows a distinct backstepping directly following the boundary, with a landward migration of the platform margin and absence of rudist-coral build-ups.

Two possible scenarios have been suggested for sequence boundary at the 1.5My. The first scenario includes a maximum of 5 km backstepping of the geomorphic platform margin. The second scenario assumes that there is a simple facies transition at the boundary. Neither of the two possible scenarios can be verified from field data because erosion has removed a big section of the platform margin strata (**Lavi2017**).

8.2.2 Numerical model

A series of numerical models were generated using CarboCAT in order to:

- reproduce the interpreted platform scale geometry;

- identify the controls on platform geometry;

- evaluate the possible stratigraphic interpretations and

- study the uniqueness of strata geometries on the Bastus platform.

In order to evaluate the possible stratigraphic interpretations and identify the controls on platform geometry and evolution, multiple numerical experiments were performed with different eustatic sea level oscillations and tectonic subsidence. Each numerical experiment or model run was performed by changing the value of one of the tested parameters each time. The generated platform geometry of each model run was compared with the interpreted platform geometry and the effects and importance of each model parameter were determined.

The evaluation of the model runs was done both qualitatively and quantitatively. The stacking patterns, platform margin trajectory, platform margin steepness and facies distribution of each model run was compared and contrasted against the interpreted data. Furthermore, whole platform dimensions and the platform segments dimensions and slope angles were checked against the real data as well. Models that failed any of the tests were rejected as not representative of the platform geometry and thus the effect of each control was identified.

In order to identify the controls on platform geometry it was initially assumed that the sequences were indicative of oscillating relative sea level. Periodic eustatic sea level oscillations with high and low frequency, high and low amplitudes were tested. Non-periodic eustatic sea level movements were tested as well with several amplitudes.

The lack of sub-aerial exposure anywhere on the platform that would have provided direct and clear evidence of eustatically controlled sequences, allowed for studying the non uniqueness of strata geometries. Non-uniqueness of strata geometry implies that same platform geometry can be generated by controls other than the eustatic movements (**Burgess2001**). A number of models runs examined the effect of other controls on the platform.

Model testing allows to evaluate the validity of several hypotheses in regard the controls on the platform geometry. A failure to reproduce the interpreted geometries with more than one controls would be a strong indicator of the uniqueness of strata geometry. Time variable production profiles and differential tectonic subsidence were tested with a series of model runs. Cross sections, chrono-stratigraphic sections at selected positions along each CarboCAT model run and 3D plots were generated for all model runs.

8.2.2.1 Initial conditions and input parameters

The necessary input parameters for the CarboCAT models to run (see section 3.2) can be divided into two groups. The first group contains the initial conditions which were kept constant for all model runs and the second group contains the tested parameters.

Some of the initial conditions were directly dictated by the field data while some others had to be chosen. The initial conditions directly dictated by the field data were obtained from the interpreted stratigraphic model and were:

- whole platform and platform segments dimensions. The Bastus platform is 200 km long and 50 km wide with siliciclastic strata segment 18 km long, platform interior 46 km and a platform margin 5 km long;

- strata thickness. The siliciclastic strata thickness is 60 m, platform interior strata 450 m thick, platform margin strata 280 m thick and slope strata ca.250 m thick;

- duration of platform 3 My;

- initial bathymetry as a homoclinal ramp;

- subsidence rate. The necessary subsidence rate to generate the required accommodation for sediments to be deposited was 20 m/My in the siliciclastic segment and 140 m/My in the carbonate segment;

- transported fractions. The transported fractions were calculated from sample analysis and were 30% for the interior strata and 50% for the margin strata.

The initial conditions that were not dictated by the field, were selected based on the literature or the available computational power. **Pomar2005** estimated the width of the Late Cretaceous opening between the Iberian and the European plates at about 100 km. Assuming a fetch area equal to this opening and fair weather conditions, eq.(2.7) and eq.(2.8) predict a wave base at 24 m water depth.

In order to generate models that were running in a reasonable time (ca. 2.5-3h) the CarboCAT model size selected to be 100x50 model cells and the time step of the model runs was chosen to 3 ky. The numerical model represented an area of 100 km x 50 km which implies a model cell dimension of 1 km x 1km which is the minimum estimated size of the large scale patch reefs on platform interior.

Based on the position of the platform margin at 51km from the shore and the goal of modelling platform scale geometries, the 3D CarboCAT model represents the most proximal 100km of the platform to the south. The CarboCAT model even though shorter than the total length of the Bastus platform includes platform interior, margin, upper slope and a portion of the lower slope.

8.2.2.2 Numerical factories and carbonate production

Based on the interpreted stratigraphic model, carbonate production on the Bastus platform is represented with 3 factories. Two factories represent low energy, platform interior carbonate production and one factory high energy, wave resistant platform margin production. Finally one factory simulates below wave base, slope sedimentation.

The first factory simulates the interior packstones interpreted facies. The interpreted facies represents nodular packstones with abundant benthic foraminifera (**Lavi2017**). The second factory simulates the interior patch reef interpreted facies. The patch reef interpreted facies represents wackestones with rudists which is also a benthic carbonate factory.

One factory has been selected to simulate both platform margin interpreted facies. The choice was based on the similarity of the texture and elastic properties of the two observed lithologies at the platform margin. Both lithologies can be described as a reef building carbonate factory.

The interpreted lower slope pelagic muds facies is simulated in CarboCAT with a below wave base pelagic factory. The production profile of pelagic facies is different than those of the benthic facies. The production of pelagic facies increases with water depth and reaches its maximum value at the bottom of the euphotic zone. From that water depth and deeper the pelagic facies shows constant production equal to the maximum value (see section 5.1).

The upper slope wackestones interpreted facies represents nodular wackestones with foraminifera and shell fragments strata (**Lavi2017**) and is simulated in CarboCAT by the transported factory of the interior and margin carbonate factories. The water depth-dependent production rate for each factory was defined through trial and error method with the model runs (Fig.8.3).

The production rate values for each factory were identified based on estimations from subsidence rate, strata thickness and iterative testing with the models. The production rates had to be high enough to allow the platform top to keep up with the rising relative sea level (RSL) and be within the accumulation rates of carbonate reefs and platforms for the Phanerozoic (**Enos1991**, **Steuber2000**, **McNeill2005**). The size of the euphotic zone was also selected with model run testing. Deeper euphotic zones resulted to higher platform progradation while more shallow euphotic zones showed shorter platform lengths.

Siliciclastics are included in the model. From field observations, their volume increases over time and reaches its maximum value at the end of the platform (**Lavi2017**). A time dependent volume of siliciclastics has been utilised in CarboCAT and the siliciclastic material is modelled as fine sand size clasts.
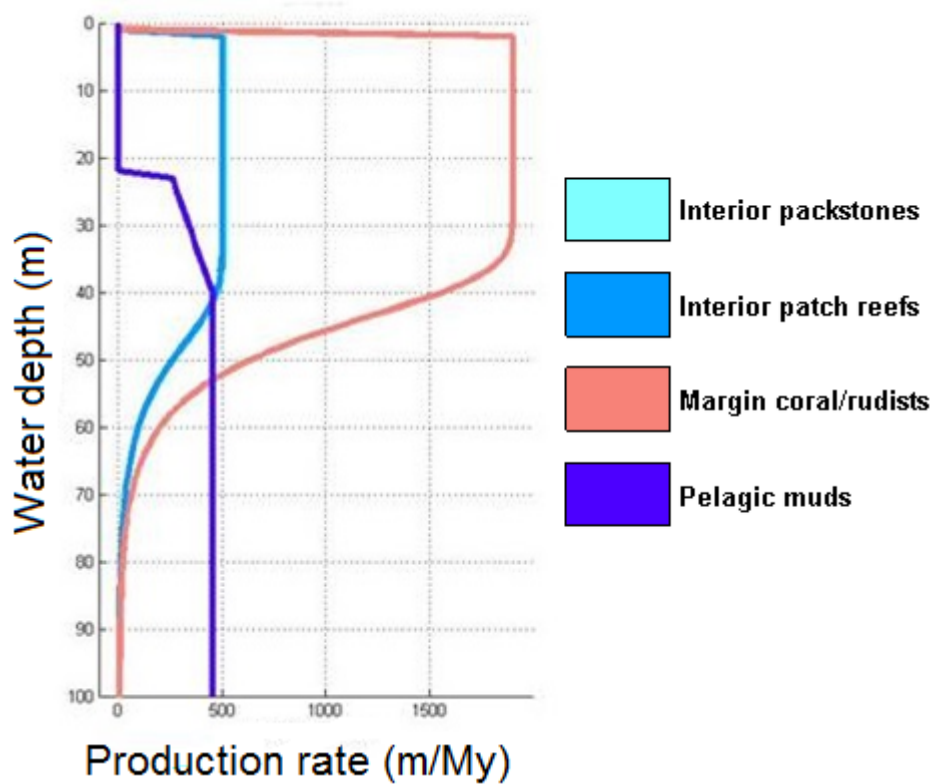
Figure 8.3: Depth dependent production profiles (colour coded) for the 3 factory and the pelagic facies in the Bastus platform. The euphotic zone extents down to 40m water depth. The three benthic factories show euphotic production profiles with no production at the top 1m and decreased production with depth below the euphotic zone. The pelagic factory shows no production above wave base (24m) and reaches its maximum value at the bottom of the euphotic zone. The two platform interior factory show the same production profile and cover each other on the plot.

Sediment transport was calculated using the cross-platform transportation algorithm in CarboCAT. When no sea level is mentioned the ESL is assumed to be constant.

The initial conditions and the input parameters for all model runs are given in Table 8.1

Table 8.1: Initial conditions and input parameters for all model runs

Model size	100km x 50 km
Number of cells	100x50
Cell size	1km x 1km
Elapsed model time	3My
Time step	3ky
Initial bathymetry	Homoclinal ramp, 0.12^o slope
Initial facies distribution	Inherited from underlain platform
Subsidence rate	0-18km:20 m/My
	19-50km: 20-140 m/My
	51-100km: 140 m/My
factory production rates	interior packstones: 500 m/My
	patch reefs: 500 m/My
	margin reefs: 1900 m/My
	pelagic muds: 450 m/My
Transported fractions	packstones 0.3
	patch reefs:0
	margin reefs: 0.5
	muds:0
Euphotic zone	40m
Wave base	24m

8.2.3 Model runs

8.2.3.1 Model runs

The effect of high frequency eustatic sea level oscillations and thus the stratigraphic interpretation that involves 5 sequences were studied with a set of model runs. A model run (EH-A1) with input parameters shown in Table 8.1 and eustatic sea level (ESL) oscillation with period 0.5My and amplitude 5m was performed. Additional a second model run (EH-A2) with the same input parameters and ESL of 0.5My oscilation period and amplitude 10m was generated. The period of the model runs was dictated by the need to generate 5 sequences within 3 My EMT.

The effect of low frequency ESL oscillations and the two sequences interpretation were also studied. A model run (EL-B1) was comprised of the input parameters shown in Table 8.1 and ESL with period of 2My and amplitude 10m. A second low frequency model (EL-B2) was generated with period 2 My and amplitude 20 m. The effect of non periodic ESL was tested with 3 model runs with constant ESL for the time period of 0-1.5 My, a "sharp" rise in sea level and then a constant ESL for the rest of the model time.

The "sharp" sea level rise was 10 m for the first model run (EN-C1), 20 m for the second (EN-C2) and 30 m for the third (EN-C3) and took place in one time step (3 ky). Since there is no direct evidence of sea level movement from the field, sea level amplitudes were selected based on reasonable values of global sea level oscillations for the Santonian (**Kominz2008**).

Tectonic subsidence as a major control in the platform geometry was examined with three model runs. Model run (R-A) used the input parameters shown in Table 8.1 and a tectonic tilting (rotation around the 0 km of the platform) of 0.05^o active for 6 ky. Model run (R-B) included tilting of 0.08^o for 6ky and model run (R-C) included tilting of 0.11^o also for 6 ky.

Finally, the role of temporary differential production rates were also examined. The production rates of all facies were significantly lowered for some period of time at the assumed sequence boundary at 1.5 My and then production was restored to its initial values. Model run (P-A) included production decreased to 10% of its input value for 150 ky. Model run (P-B1) showed complete shut of production for 300 ky, while model run (P-B2) showed production decreasing to 10% of the initial value for 300 ky. Model run (P-C1) consisted of complete production shut down for 450 ky while model run (P-C2) consisted of production decreasing to 10% of its initial value for 450 ky.

The values for tectonic subsidence, differential production rates and their duration were selected through trial and error after several model runs with two restraining conditions. First, the platform geometry of the model runs had to agree with the interpreted platform geometry. Second, the duration had to be relatively short, because longer phenomena would have generated observable traces in the field. A complete list of all the model runs is presented in Table 8.2

8.3   Stratigraphic forward modelling results

Initially, a simple numerical model was produced in order to obtain the parameter values for production rates, euphotic zone depth and initial bathymetry slope that generate a fully aggradational model which matches the dimensions of the interpreted section . This initial model was generated as a control run with temporally constant production rates, no ESL oscillations and temporally constant subsidence rate. As a result, the RSL was rising with the same rate for the whole EMT.

Table 8.2: Model runs and tested parameters

Model run	Tested parameter	Parameter value
EH-A1	High frequency eustacy	0.5My, 5m
EH-A2	High frequency eustacy	0.5My, 10m
EL-B1	Low frequency eustacy	2My, 10m
EL-B2	Low frequency eustacy	2My, 20m
EN-C1	Non periodic eustatic rise	10m
EN-C2	Non periodic eustatic rise	20m
EN-C3	Non periodic eustatic rise	30m
R-A	Tectonic rotation	0.05^o
R-B	Tectonic rotation	0.08^o
R-C	Tectonic rotation	0.11^o
P-A	Differential production	10% for 150 ky
P-B1	Differential production	0% for 300 ky
P-B2	Differential production	10% for 300 ky
P-C1	Differential production	0% for 450 ky
P-C2	Differential production	10% for 450 ky

The interpreted strata geometry of the Bastus platform was reproduced with three different model runs and more specifically:

- the non-periodic eustatic sea level rise of 30 m (EN-C3);

- tectonic rotaion of 0.05^o (R-A);

- differential production, when production drops to 10% of its initial value for 300 ky (P-B2).

8.3.1 Model run EN-C3

EN-C3 model run (Fig.8.4) was generated with input parameters as shown in Table.8.1. The sea level rose 30m at 1.5My EMT.

EN-C3 shows a mainly aggradational platform (Fig.8.5). Once the platform margin has been established (0.6 My EMT), the margin aggrades until 1.5 My EMT. At 1.5 My EMT and under the effect of ESL rise the margin retrogrades for 1 km and then aggrades for the remaining EMT. The same time (1.5 My EMT) the high energy facies retrograde for 2 km on the platform interior. The dimensions of each platform segment and the strata thickness in each segment are shown in Table.8.3.

194
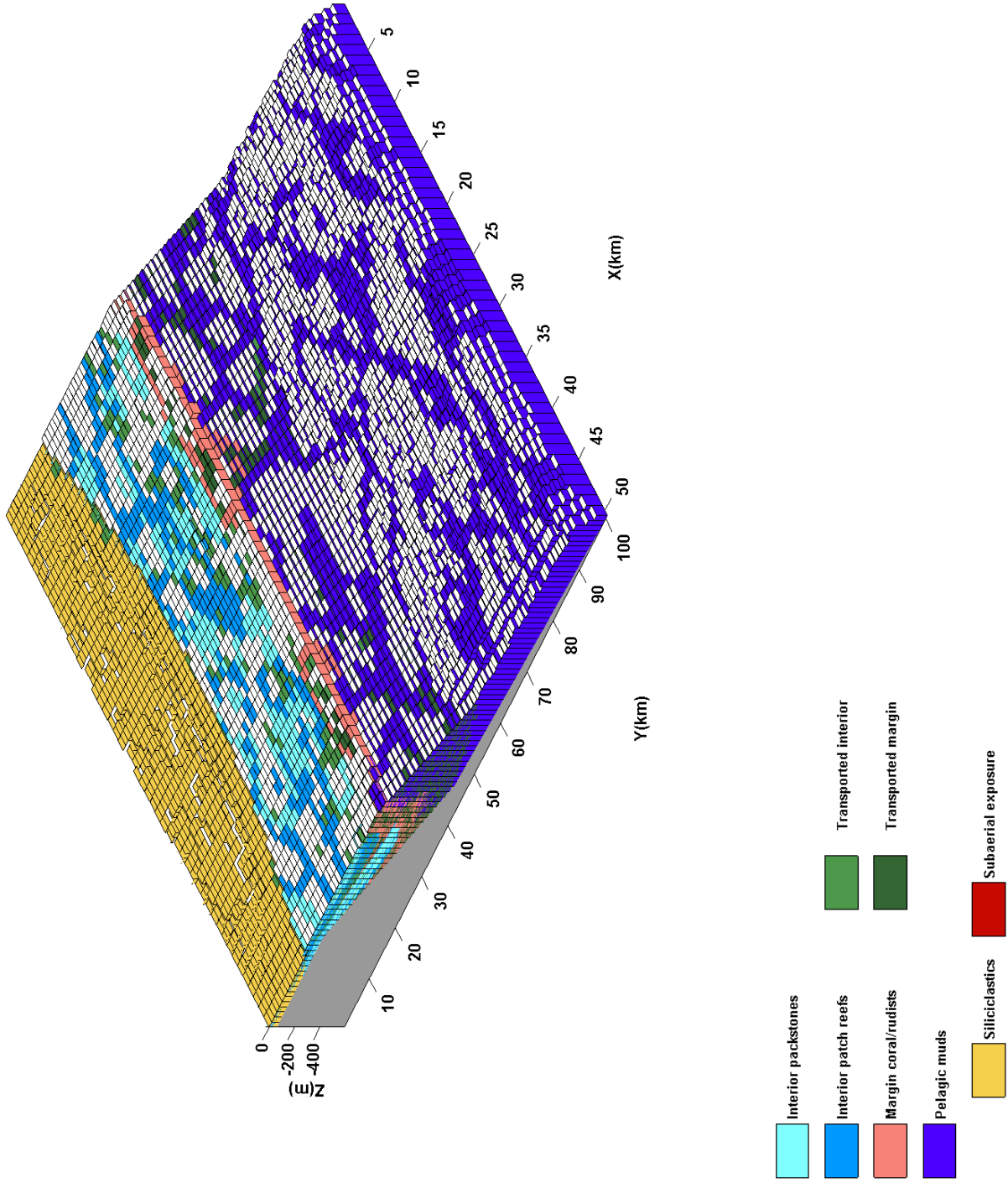
Figure 8.4: 3D plot of the EH-A1 model run.

Interior packstones

Interior patch reefs

Margin coral/rudists

Pelagic muds

Siliciclastics

Transported interior

Transported margin

Subaerial exposure

X(km)

Y(km)

Z(m)

195
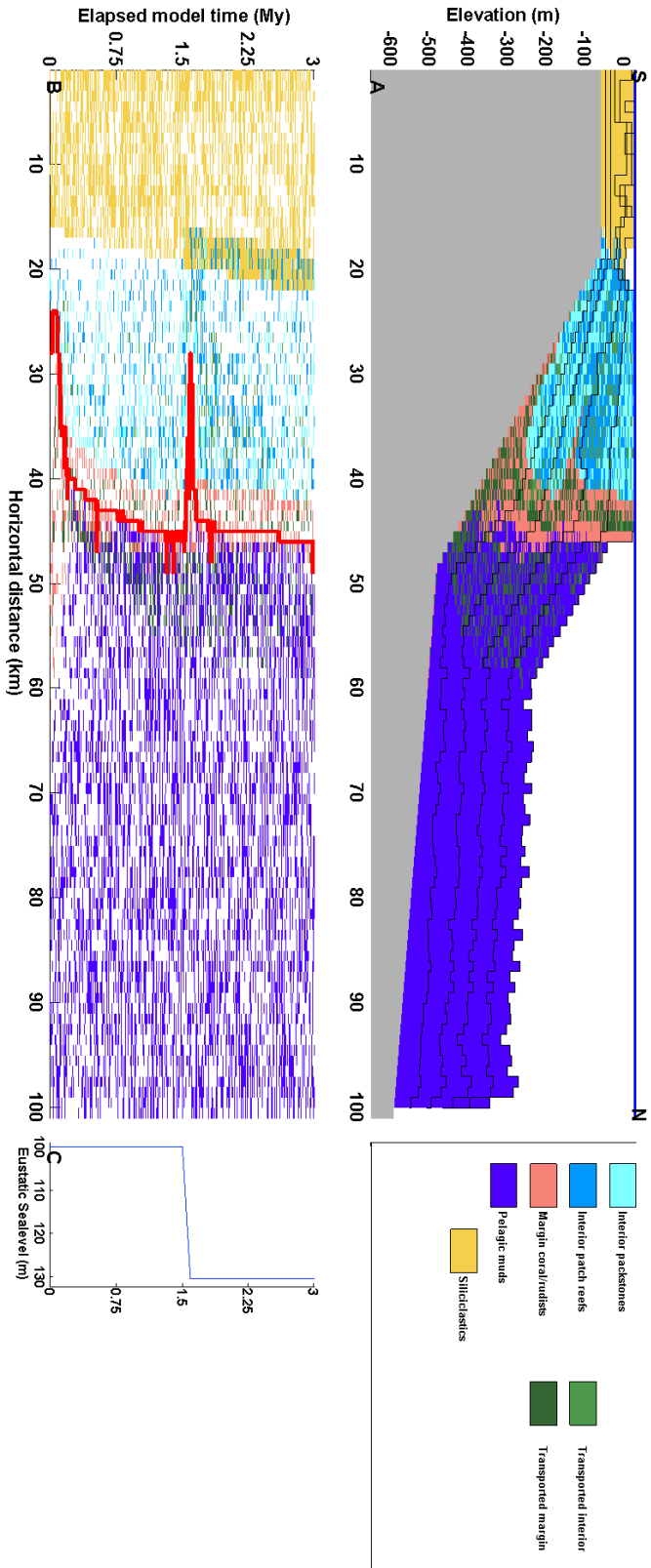
Figure 8.5: (A) Cross section along the x=25 of the 3D model. The cross section shows siliciclastic dominating the most proximal part (0-18 km), extensive platform interior (18-48 km), aggrading platform margin and upper slope extending to 65 km. (B) Chrono-strat section at the same position as (A) with the platform margin position (red line) superimposed. The platform margin progrades for 7 km once it gets established (0.6 My). (C) Eustatic sea level oscillations with period 0.5 My and amplitude 5m. Interpreted platform geometry for comparison on the top.

196

Table 8.3: Length and thickness of EN-C3 model run

Platform segment	Field values	Numerical model
Siliciclastics length	18km	18km
Siliciclastics thickness	60m	60m
Carbonate interior length	28km	25km
Carbonate interior thickness	450m	402m
Margin length	5km	5km
margin thickness	280m	327m
slope thickness	250m	274m
platform type	low angle	1.03^o

Comparison of the interpreted stratigraphic model with the EN-C3 model run shows there is a small retrogradation of the margin due to rising ESL and a transition from high energy platform margin facies to below wave base pelagic facies at the platform margin at 1.5 My EMT. The retrogradation is very small, 1 km, which is the minimum horizontal distance that can be measured and in some places on platform 2 km. The retrogradation of the high energy margin facies on the interior is much more strong (4-5 km) at the same time. The platform margin returns to the before the ESL rise position very quickly.

Overall the model run is very probable and it is a relatively good representation of the interpreted Bastus platform.

8.3.2 Model run R-A

Model run R-A (Fig.8.6) was generated with rotation of the platform of 0.05^o at 1.5My EMT. The rotation took place in 6ky. Fig.8.7 shows a mainly aggradational platform with two sequences. The platform margin mainly aggrades once the it has been established (0.6 My EMT). At 1.5 My EMT and under the effect of rotation of the platform, the margin retrogrades (5 km) generating a facies transition from high energy margin facies to pelagic facies and back-stepping of the high energy facies on the interior facies. The dimensions of each platform segment and the strata thickness in each segment are shown in Table.8.4.

The back-stepping of the platform margin at 1.5 My EMT generates two sequences and a facies transition from high energy platform margin facies to below wave base, pelagic facies at the geomorphic margin of the platform (48 km), consistent with the interpreted stratigraphic section. The stacking patterns in all platform parts remain aggradational for the entire time. Model run R-A recreates the interpreted geometry and further suggests a facies transition on the platform interior that has not been mapped.
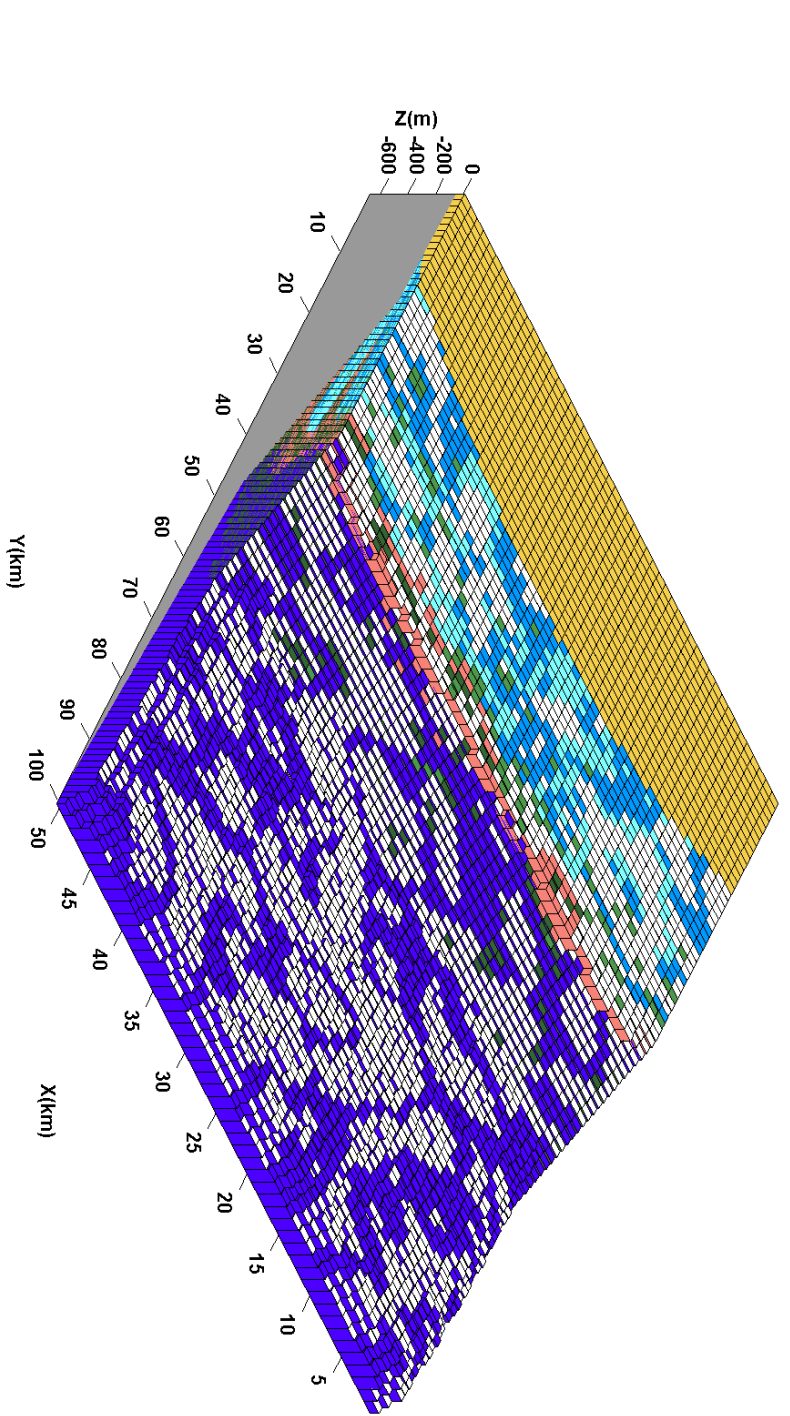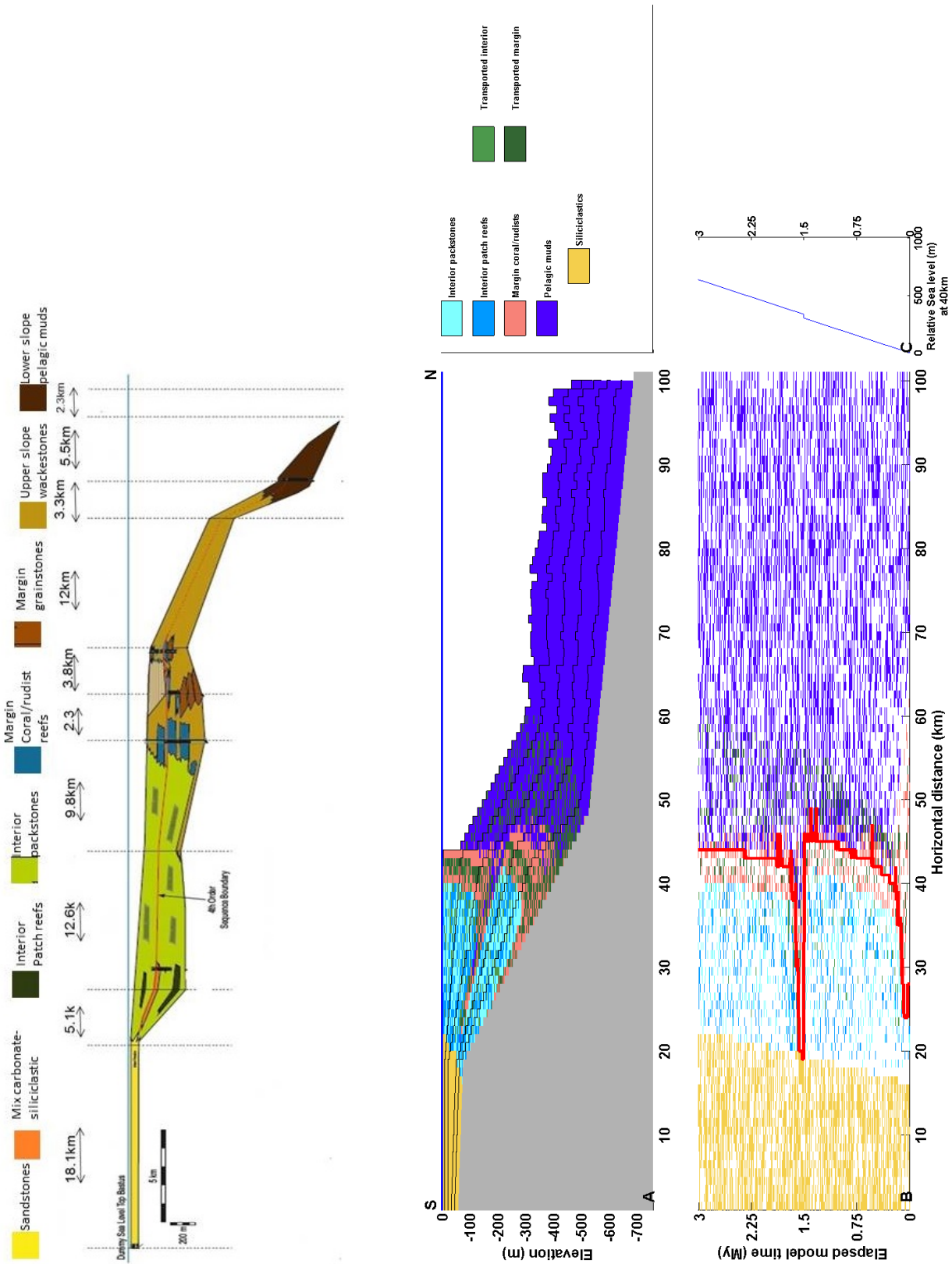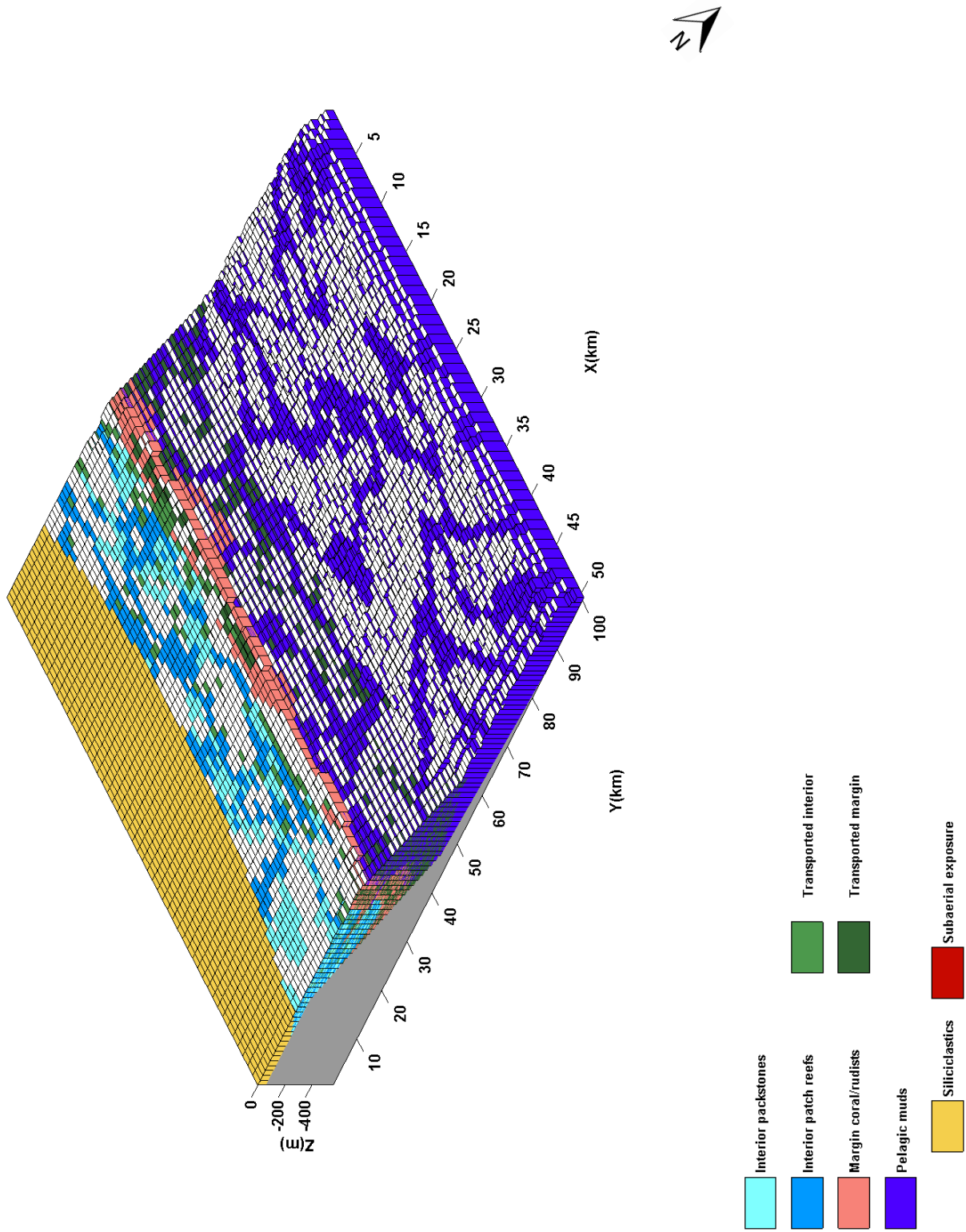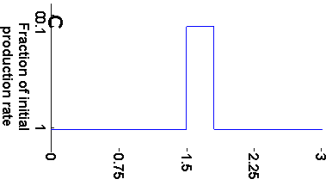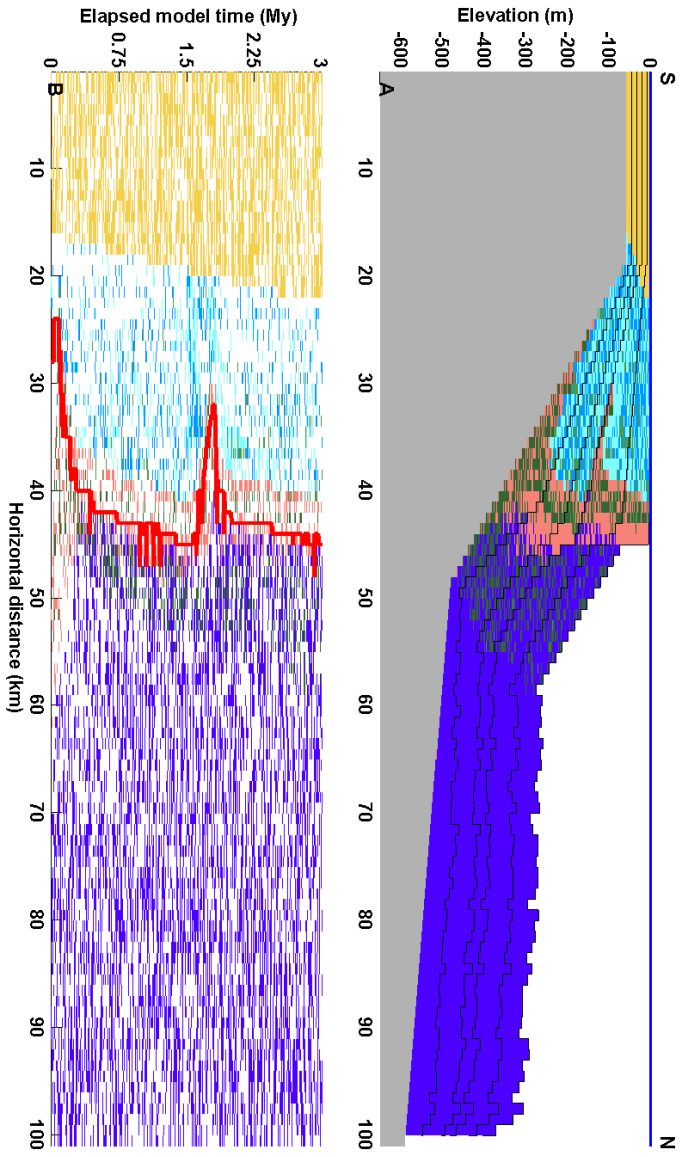
197

Figure 8.6: 3D plot of the R-A model run.

Figure 8.7: (A) Cross section along the x=23 of the 3D model. The cross section shows siliciclastic dominating the most proximal part (0-18 km), extensive platform interior (18-43 km), aggrading platform margin and upper slope extending to 61 km. (B) Chrono-strat section at the same position as (A) with the platform margin position (red line) superimposed. The platform margin progrades for 5 km once it gets established (0.6 My). (C) Relative sea level oscillations at 40 km along dip. Interpreted platform geometry for comparison on the top.

Table 8.4: Length and thickness of R-A model run

Platform segment	Field values	Numerical model
Siliciclastics length	18km	18km
Siliciclastics thickness	60m	60m
Carbonate interior length	28km	25km
Carbonate interior thickness	450m	430m
Margin length	5km	5km
margin thickness	280m	290m
slope thickness	250m	274m
platform type	low angle	1.11^o

8.3.3 Model run P-B2

Model run P-B2 (Fig.8.8 and Fig.8.9) was generated with production dropping to 10% of its initial value for 300 ky at 1.5My EMT.

Fig.8.9 shows a mainly aggradational platform with two sequences. The platform margin mainly aggrades once the platform has been established (0.6-1.5 My EMT). At 1.5 My to 1.8 My EMT and under the effect of significantly lower production, the margin retrogrades slightly (2 km). Once production returns back to initial values (1.8 My EMT) and for the remaining EMT the margin aggrades. The back-stepping generates two facies transitions from the lower to the upper sequence. One between high energy margin and below wave base, pelagic facies on the margin and one between low energy interior and high energy margin facies on the interior. The dimensions of each platform segment and the strata thickness in each segment are shown in Table.8.5.

The backstepping of the platform margin at 1.5 My EMT generates a facies consistent with the interpreted stratigraphic section. Model run P-B2 represents the interpreted geometry very well and the model dimensions and thickness agree with the observed in the field.

8.4 Discussion

The model runs presented in the previous section aimed to:

- reproduce the interpreted platform scale geometry;

- identify the controls on platform geometry;

- evaluate the possible stratigraphic interpretations;

- study non uniqueness of the strata.
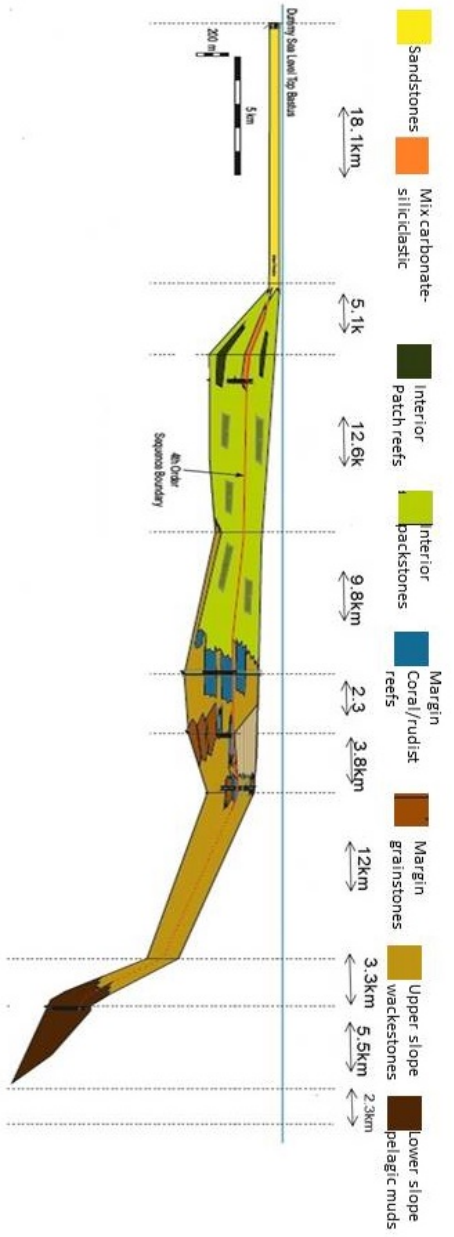
Figure 8.8: 3D plot of the R-A model run.

Figure 8.9: (A) Cross section along the x=28 of the 3D model. The cross section shows siliciclastic dominating the most proximal part (0-18 km), extensive platform interior (18-48 km), aggrading platform margin and upper slope extending to 60 km. (B) Chrono-strat section at the same position as (A) with the platform margin position (red line) superimposed. The platform margin progrades for 6 km once it gets established (0.6 My). (C) Fraction of the carbonate production with time. Interpreted platform geometry for comparison on the top.

Table 8.5: Length and thickness of P-B2 model run

Platform segment	Field values	Numerical model
Siliciclastics length	18km	18km
Siliciclastics thickness	60m	60m
Carbonate interior length	28km	25km
Carbonate interior thickness	450m	421m
Margin length	5km	5km
margin thickness	280m	302m
slope thickness	250m	270m
platform type	low angle	1.43^o

A summary of the model runs, the tested parameters and an evaluation of the models based on comparison with the interpreted geometries is given in fig.8.10

8.4.1   Eustatic sea level control

The generated model runs have examined the effect of eustatic sea level oscillations as platform control and have provided data for evaluation of 2 possible stratigraphic interpretations of the platform geometry. The first interpretation suggests a platform with 5 sequences while the second interpretation implies 2 sequences. The sequences in both interpretations are assumed to have formed under the effect of eustatic oscillations.

The high frequency model runs (EH-A1 and EH-A2 see appendix B) provide evidence that high frequency eustatic movements have no effect on the platform geometry and only affect platform interior. Both numerical models indicate that:

- for reasonable amplitude values, the margin aggrades for the whole time;

- there is sub-aerial exposure on the platform interior, contrary to the field observations;

- no sequences can be distinguished;

- no obvious system tracts exist.

Assuming that some sub-aerial exposure is present on the platform interior but was not mapped during the filed observations, a model with five sequences controlled by high frequency eustatic oscillations (**Pomar2005**) is not probable as an interpretation of the Bastus platform. For the given sedimentation and subsidence rates, the five sequences model would require eustatic sea level oscillations with amplitude higher than 30 m and periodicity of 500 ky. The amplitude and

Model run	Parameter values	Evaluation
EH-A1	ESL: 0.5My – 5m	No sequences, sub-aerial exposure, no facies
EH-A2	ESL: 0.5My – 10m	transition
EL-B1	ESL: 2My-10m	No sequences, no facies transition, sub-aerial
EL-B2	ESL: 2My-20m	exposure, wrong margin trajectory
EN-C1	Non periodic sea level rise 10m	Only EN-C3 shows two sequences with a small
EN-C2	Non periodic sea level rise 20m	facies transition at the sequence boundary.
EN-C3	Non periodic sea level rise 30m	
R-A	Platform rotation 0.05°	Two sequences, margin back-stepping and facies transition at sequence boundary, facies thickness distributions agree.
R-B	Platform rotation 0.08°	Two sequences, significant margin back-stepping and facies transition at sequence boundary. High energy facies next to siliciclastics
R-C	Platform rotation 0.11°	Shorter platform interior, 20km of back-stepping. High energy facies next to siliciclastics.
P-A	Production to 10% for 150ky	No sequences, no facies transition
P-B1	Production to 0% for 300ky	Two sequences, margin back-stepping and facies transition at sequence boundary. Depositional hiatus
P-B2	Production to 10% for 300ky	Two sequences, margin back-stepping and facies transition at sequence boundary, facies thickness distributions agree.
P-C1	Production to 0% for 450ky	Two sequences, margin back-stepping and facies transition at sequence boundary. Depositional hiatus
P-C2	Production to 10% for 450ky	Two sequences, margin back-stepping and facies transition at sequence boundary, facies thickness distributions agree. Slightly shorter platform segments

Figure 8.10: Model runs, parameter values and evaluation of each model run compared with the interpreted platform geometry

period of the required eustatic sea level oscillations imply icehouse conditions on the Upper Cretaceous but no evidence supports the icehouse hypothesis.

The low frequency models (EL-B1 and EL-B2, see appendix B) have examined the validity of the two sequences under eustatic control interpretation. The models indicate that low frequency ESL oscillations have an effect on the platform geometry and low frequency ESL is a possible control in the platform. More specifically:

- ESL amplitudes less than 10m: Have no effect on the platform geometry. Platform margin constantly aggrades. The results can not be distinguished from model runs without ESL oscillations;

- ESL amplitudes 10-30m: The platform margin progrades during ESL rise and aggrades during ESL fall;

- ESL amplitudes greater than 30m are greater than the greatest global eustatic movement suggested by the literature (**Kominz2008**).

Even though low frequency ESL oscillations are a possible control on platform evolution, the generated numerical models do not agree with interpreted geometries of the Bastus platform. Platform margin trajectories produced from the numerical models are not representative of the interpreted margin trajectory. The numerical models also failed to identify sequences and suggested some significant sub-aerial exposure in the platform interior.

It has been demonstrated that low frequency ESL oscillations, although a possible control in platform evolution are not probable to have any effect on the geometry of the Bastus platform. The two sequences model is probable but the sequences did not form under the effect of eustatic oscillations.

Model runs (EN-C1, EN-C2 and EN-C3, see appaendix A) have examined the effect of non periodic ESL movements. Two sequences were generated by non periodic ESL movements when sea level rose for 30 m which is very close to the greatest generally excepted sea level rise in the literature (**Kominz2008**).

Model runs support the interpretation with two sequences and a not extensive facies transition from non-periodic sea level movements and pose the question of how applicable are global estimations of sea level movements on the studied area. The minimum required sea level rise for generating the interpreted geometry is 30 m.

The study of eustatic sea level movements revealed that eustacy is not a control in the evolution of the Bastus platform. Relative sea level is the major control on the platform geometry but the relative sea level is affected by the high subsidence rate. The high subsidence rate (140 m/My) required for the creation of $\approx 400m$ of accommodation as indicated by the thickness of the platform strata covers any

influence from ESL. The aggrading platform margin trajectory even with the high relative sea level rise rates is consistent with the observations of **Campbell2005** about the tendancy of carbonate platforms to stack their margins and keep up with relative sea level changes.

8.4.2 Tectonic subsidence

Model runs (R-A, R-B and R-C, see appendix B) have demonstrated that spatially differential subsidence caused by tectonic tilting (rotation) of the platform is a possible control in the evolution of the Bastus platform. The model runs generate the interpreted geometry and they did so using reasonable (for the area) parameter values. The numerical models:

1. define two sequences;

2. display platform margin trajectory that matches the interpreted trajectory;

3. display facies transition from high energy, platform margin facies to below wave base, pelagic facies at the platform margin;

4. show dimensions and thickness very close to the values observed in the field;

The model runs are also predicting features of the platform that have not been observed but are very possible. Apart from the facies transition at the platform margin, the numerical models predict a transition from low energy interior strata in the lower sequence to high energy margin strata in the upper sequence at the platform interior.

Integrated evaluation via comparison of the numerical models with the interpreted geometry revealed that the most probable values of rotation for the Bastus platform are in the range of $0.05^o - 0.08^o$, with event duration of $\approx 6-10ky$. Rotation events smaller than 0.05^o would have limited effect on the platform. Rotation values greater than 0.11^o generate geometries not supported by the data, as it has been demonstrated.

The mechanisms responsible for the required tectonic tilting are very probable given the dynamic situation during the formation of the platform. The Bastus platform is part of a compressional regime caused by the convergence of the Iberian plate and the European plate during the Santonian (**Lavi2017**) and thus local tectonism that effected parts of platform is possible to have occurred.

8.4.3 Differential production

Model runs (P-A, P-B1, P-B2, P-C1 and P-C2, see appendix B) have demonstrated that temporally differential productivity over the platform was a possible control of the Bastus platform. The interpreted geometry is modelled using reasonable model parameters.

Similarly to the rotation case, the model runs also predict a transition from low energy strata to high energy platform margin strata at the boundary of the two sequences in the platform interior that has not been mapped. The similarities between the two scenarios (tectonic rotation and time variable production) extent to distances, thickness and platform interior lithofacies thickness distribution.

Integrated evaluation via comparison of the numerical models with the interpreted geometry revealed that the most probable parameter values for time variable productivity in the Bastus platform are production decrease to 10% of the initial value for 300-450 ky.

Significant reduction of the carbonate productivity could occur due to several reasons. Changes in the paleo-environment or local changes to physical or depositional conditions are possible in an tectonically active regime. Temporary barriers due to tectonic activity might had restricted the access of oceanic water to the platform or the platform interior, changing the physical and chemical conditions of the water. Suffocation of the carbonates from temporally increased siliciclastic supply is also possible.

8.4.4 Comments

The platform margin for all numerical models shows a different behaviour on the proximal part (interior to margin facies transition) and on the distal part (geomorphic margin). The numerical platform margin facies is high wave energy facies formed above the wave base and inside the euphotic zone. The numerical platform interior facies on the other hand are low (zero) wave energy facies formed in the euphotic zone. Consequently, the transition from interior to margin facies occurs where the wave energy reaches its zero value and always more proximal than the geomorphic margin.

The distal part of the margin where the geomorphic platform margin lays is controlled by different factors. The geomorphic margin is defined as the position of the maximum curvature of the topography. The topography here is built by high wave energy, above wave base margin facies next to pelagic facies below wave base and below euphotic zone. The highly productive margin facies compared with the pelagic facies tend to build steep margins and basically defines the geomorphic margin.

8.4.5 Conclusions

Numerical models of the geometry and characteristics of the Bastus platform as they were interpreted based on field observations were generated using reasonable parameter values. The importance of eustatic movements, differential tectonic subsidence and time variable production on platform evolution was examined and the controls on platform geometry and uniqueness of strata geometries were identified.

Through numerical modelling it was concluded that tectonic activity or differential productivity control the formation of the Bastus platform and its sequences and that eustatic sea level movements have limited, if any control on platform geometry. The stratigraphic interpretation of the Bastus platform with two sequences proposed here is supported by numerical modelling and agrees with stratigraphic data for the Upper Cretaceous.

The controls on the Bastus platform are:

1. subsidence is the major control on platform geometry with relative sea level movements having major effect on the platform;

2. tectonic activity that generated spatially variable subsidence. A single rotation event of the whole platform caused by the active compressional regime could have influenced the observed geometry;

3. depositional conditions that caused significant reduction in the productivity on the platform. Differences in water conditions or sediment supply affected the productivity and the evolution of the platform.

An integrated approach that included evaluation of the numerical models through comparison with interpreted data achieved further analysis of the generated results. The controls on the geometry and evolution of the Bastus platform were identified and the most reasonable values for the physical and tectonic conditions were estimated.

The integrated interpretation was not able to distinguish which of the possible mechanisms (tilting, differential production or non-periodic sea level movements) is more probable or if a combination of them controlled the platform. Such non-unique stratal geometries agree with the conclusions of **Burgess2015** that single explanation of strata history is only possible when unequivocally evidence is present (eg. sub-aerial exposure for RSL controlled strata formation).

9 Modelling of the Cenomanian-Turonian Mishrif formation, South Iraq

This work uses CarboCAT to generate stratigraphic forward models of the Cenomanian-Turonian Mishrif formation, South Iraq. The best fit models were used to generate synthetic seismic images using the two synthetic methods described in "New developments in seismic imaging" chapter.

The chapter is divided into three sections. The first section presents the area of the modelled formation and describes its geology. The second section presents the numerical model and the model parameters used for the model runs. The third section shows the generated synthetics from the stratigraphic modelling.

9.1 Geology of the modelled area

The Cretaceous of the Arabian Gulf is divided into three shallowing-upwards groups, the Thamama Group (Baressian-Aptian age), the Wasia Group (Albian-Turonian age) and the Aruma Group (Coniacian-Maastrichtian age) (Fig.9.1). All three groups show deposition of sediments with rudists at their top. The rudists build-ups mark the end of each group and constitute areas of significant hydrocarbon production (**Alsharhan1995**).

The Wasia group in the Arabian Gulf generally, is an extensive lithostratigraphic unit 600m thick with several depositional sequences. The three major sequences of the Wasia group are the Nahr Umr Formation (early Albian age), the Mauddud Formation (Late Albian) and the Mishrif Formation. Mishrif is a generic term that describes the Upper Creataceous, rudists bearing strata on top of the Wasia Group in the southern Arabian Gulf (**Burchette1993**).

The Mishrif Formation is an important reservoir formation for the whole Arabian Gulf. Only in Iraq (where this study concentrates), more than one third of the proven oil reserves are held in the Mishrif Formation of the Mesopotamian Basin. The Mishrif Formation appears throughout central and south-east Iraq, with variable thickness reaching a maximum thickness of 200m. The lower seal for the whole Mishrif hydrocarbon system in Iraq are Upper Jurassic (Kimmeridgian) Gotnia anhydrites. The upper seal is locally located in the clay layers of the Turonian Khasib Formation (**Al-Ameri2009**).

The Mishrif Formation is a 5My formation that includes strata deposited on the eastern passive margin of the Arabian craton. The Arabian craton during the Upper Cretaceous, was a shallow water, semi-arid or humid equatorial platform, more than 2000km long and 300km wide. Deformation of the Tethyan margin that created the Oman and Zagros mountains, generated a basin at the margin of the Arabian craton where deep water sediments accumulated (**Burchette1993**).

AGE IN M.A.	TIME SCALE				GROUP	FORMATION	LITHOLOGY	INTERPRETATION
65	CRETACEOUS	LATE	SENONIAN	MAASTRICHTIAN	ARUMA	SIMSIMA		Carbonate buildup.
70				CAMPANIAN		FIQA		Basinal slope and the foredeep margin
75								
80						HALUL / ILAM		Shelf limestone and platform slope
85				SANTONIAN				
				CONIACIAN		LAFFAN		Clastic influx lowstand
90				TURONIAN				Peripheral bulge erosion
		MIDDLE		CENOMANIAN	WASIA	MISHRIF		Block faulting at Fateh and Fahud. Radiolitid rudist buildup and carbonate ramp
95						SHILAIF KHATIYAH		
				ALBIAN		MAUDDUD		
100						NAHR UMR		Clastic influx lowstand
105								Sea level lowstand
110		EARLY	NEOCOMIAN	APTIAN	THAMAMA	SHUAIBA		Caprinid and caprotinid rudist buildup. Carbonate ramp shallowing-upward cycle.
115						KHARAIB		
120				BARREMIAN				
125						LEKHWAIR		
				HAUTERIVIAN				
130				VALANGINIAN		HABSHAN		
135				BERRIASIAN		SALIL RAYDA		Drowned platform / ramp
140				TITHONIAN		HITH		

LEGEND

Limestone · Anhydrite · Sandstone
Dolomitic Limestone · Marl · Rudist reefal buildup
Argillaceous Limestone · Shale · Unconformity

Figure 9.1: Lithostratigraphy of the Cretaceous of the Arabian Gulf. The major unconformities and rudists accumulations are marked. From **Alsharhan1995**.

210

Carbonate sediment deposition on the shallow-water part of the craton generated several low gradient carbonate platforms, where the Mishrif Formation accumulated. The Mishrif Formation appears in many places in the southern Arabian Gulf usually with different local names (Mishrif in South Iraq, Shilaif Formation in Abu Dhabi, Natih Formation in N.Emirates and Oman, lower Mishrif in northern Saudi Arabia and Sarvak Formation in Iran) (**Burchette1993**).

Facies distribution of the Mishrif Formation depends on the location where the Formation appears. The general model for the Mishrif Formation includes lagoon, margin, slope and basinal deposits. The lagoon was deposited in shallow, restricted to open waters. It is comprised of lime mudstones and wackestones with bioclastic packstones and grainstones locally. The margin or reef consists of coarse grain bioclastic packstones and grainstones with abundant intact rudists shells (**Alsharhan1995**).

The slope deposits are bioclastic packstones and grainstones that show a coarsening upward trend dominated by several size bioclastic fragments. Sediments were deposited at shallow to moderate water-depths and moderate to high energy conditions. Basinal, deep-water facies consist of silt to sand grade pelagic wackestones and mudstones (**Alsharhan1995**).

Specifically in South Iraq, the Wasia Group is part of the Mesopotamia Basin. The Mesopotamian Basin is bounded to the west and south-west by the Abu Jir fault zone, to the east by the Zagros mountains and the Hamrin mountains to the north-east (Fig.9.2) (**Aqrawi1998**).

The Mesopotamian Basin contains two sedimentary sequences. The lower sequence (early Aptian-early Cenomanian) includes the Nahr Umr and Mauddud Formations. The upper sequence (Cenomanian-early Turonian) includes the Ahmadi Shale Formation, the Rumaila Formation and the Mishrif Formation (Fig.9.3) (**Aqrawi1998**).

The upper boundary of the Mishrif Formation varies with location. In some locations a gradiational contact between the Mishrif Formation and the overlain Kifl Formation occurs. In other areas the Kifl Formation is absent and the Mishrif is overlain uncomfortably by the Khasib Formation (Turonian age). Both the Kifl and Khasib Formations belong to the Aruma Group (**Aqrawi1998**).

The lower boundary of the Mishrif Formation to the Rumaila Formation is gradational. In some locations the Mishrif Formation gradually passes to Rumaila Formation without any obvious boundary (Fig.9.3). The lower contact of the Rumaila/Mishrif Formation is recognised by the underlying black shales of the Ahmadi Formation (**Aqrawi1998**).
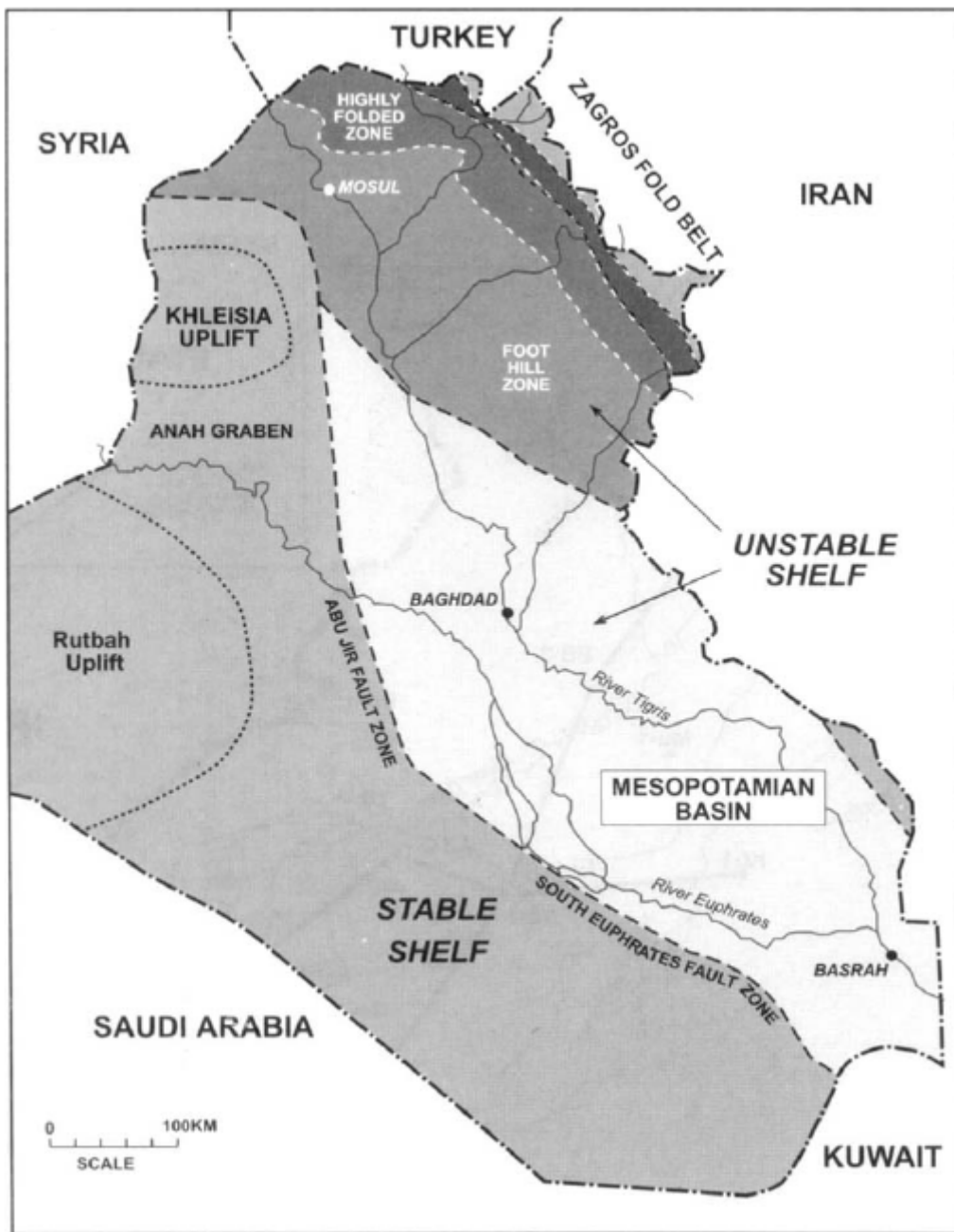
Figure 9.2: Structural map of Iraq with the location of the Mesopotamian Basin. The basin is situated on the east part of the passive margin of the Arabian craton. From **Aqrawi1998**.
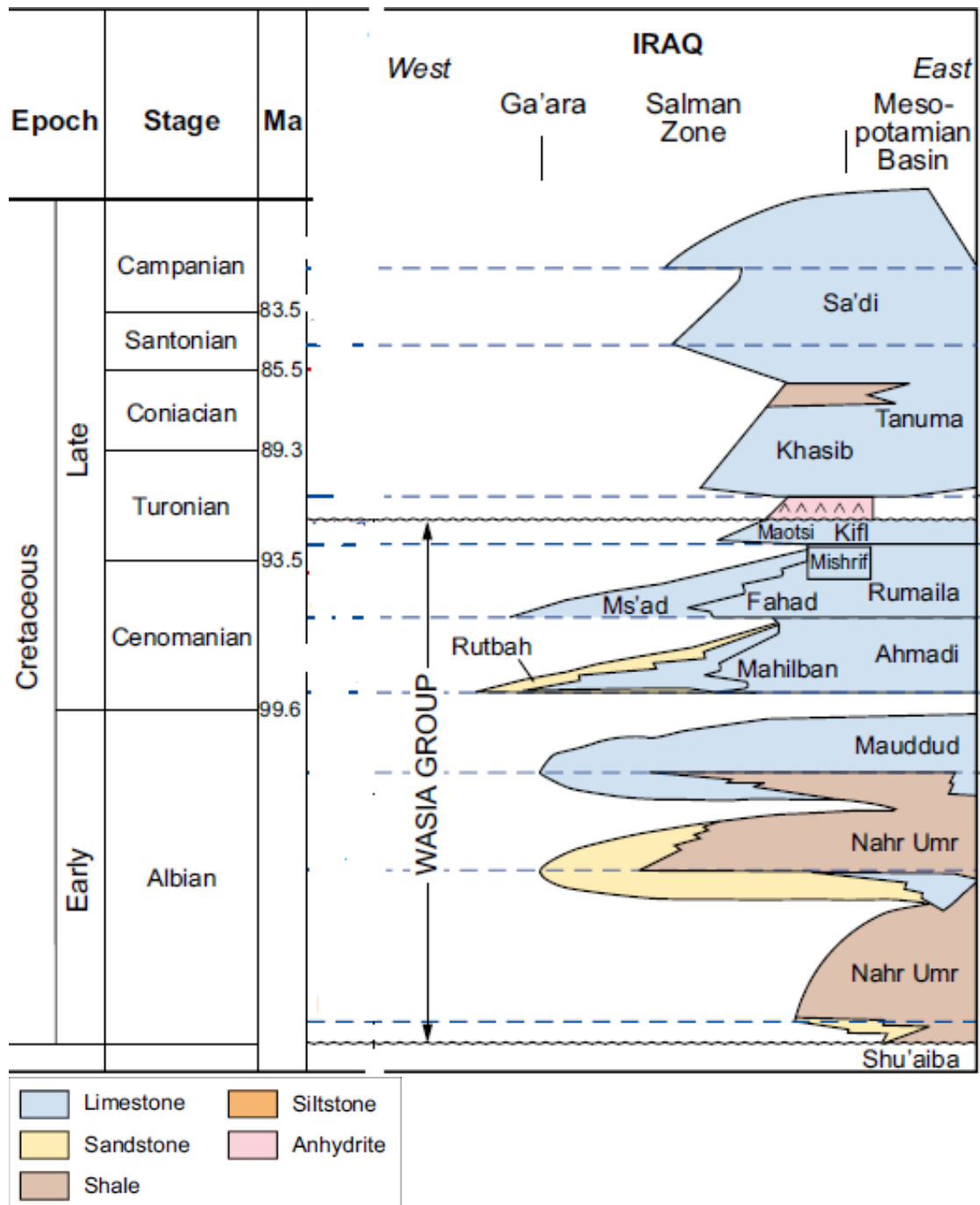
Figure 9.3: Stratigraphic section of the Cretaceous in South Iraq. The Mishrif Formation conformably overlays the Rumaila Formation and it is overlain by the Khasib and locally the Kifl Formations. Modified from **Mahdi2013**.
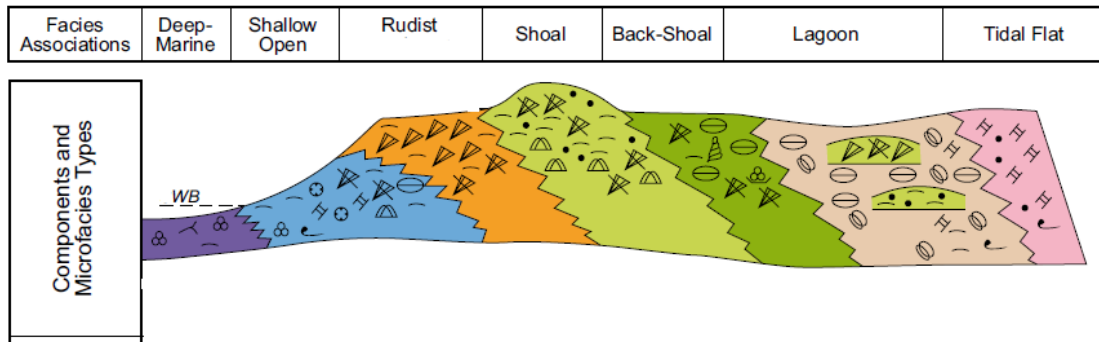
Figure 9.4: Facies associations across the Mishrif carbonate platform. WB is the wave base.

Facies distribution of Mishrif Formation in southern Mesopotamian Basin in Iraq includes 21 microfacies types which constitute seven facies associations (Fig.9.4) (**Mahdi2013**):

1. deep marine facies: Pelagic mudstones-wackestones and micro-bioclastic calcislite with lime mud and silt size skeletal grains without in-situ shallow marine macrofaunas. Some shale beds are common in several fields. These are lower slope to basin facies below the wave base;

2. shallow open-marine facies: Bioclastic wackestone-packstone and coral-algal boundstones. They consist of bioclastic microfacies with low-energy mud-supported microfacies and high-energy grain-supported microfacies. The skeletal grain show various degrees of size (silt to pebble) and sorting. Planktonic foraminifera occur but benthic foraminifera are more abundant. The facies indicate moderate to high energy environment, rework of the skeletal fragments and re-deposition on the lower slope;

3. rudist strata: Mainly rudist rudstone with radiolitid rudists as the main component with large, unbroken shells in life position. Some packstones or grainstones occur which consist of rudists fragments. Indicate high-energy platform margin environment with currents;

4. shoal: Packstones to grainstones that contain rudists bioclasts, peloids and coated grains with different sizes and sorting. Indicate very shallow, high-energy, current dominated environment. Usually overlies the rudists strata and are attributed to erosion and transportation of rudists by currents;

5. back shoal. Wackestones and packstones with bioclastic foraminifera. They are mud supported facies with bioturbated and well mixed fragments. Indicate transition between shoal and lagoon environments;

214

6. lagoon: Peloidal packstones and grainstones with abundance of benthic foraminifera and packstones-rudstones with micritised debris. Some rudist debris is present but not in significant amounts. Indicate low-energy conditions and lagoonal environment;

7. tidal flats: Mainly lime muds with cloudy texture and small shell fragments. These facies indicate tidal flats to brackish water environments. Usually observed in the upper most part of the Mishrif Formation and constitute the boundary with the overlain Kifl Formation.

The best quality reservoir parameters are located in the rudists bearing facies. The rudists reservoirs show high porosity and excellent permeability with most of the oil-fields located in the rudists bearing facies (Fig.9.5).

Rudists develop on the high energy platform margin belt or as isolated buildups on the crests of uplifted dome structures on the slope or the lagoon (shoal facies) where the environmental and hydrodynamic conditions were suitable. Erosion of the rudists buildups generated rudists fragments that were dispersed over a wide area around the buildups (back shoal or shallow-open marine facies) (**Sadooni2005**).

The rudist margin prograded towards the west-southwest into the deeper basinal limestones of the Rumaila Formation (Fig.9.6). The progradation of the rudist margin generated a facies transition from basinal, deep limestones to shallow open-marine facies and deposition of rudists strata on the west later than the east part (**Mahdi2014**).

Internally, the Mishrif Formation is divided into two depositional cycles. The lower cycle is a regressive sequence characterised by gradual facies change from basinal to shallow open-marine deposits. The cycle starts with a flooding event and the deposition of pelagic mudstones similar to the underlying Rumaila Formation (**Mahdi2014**).

Deposition of rudists grainstones occurred on the platform margin which prograded westwards generating a widespread lagoon with isolated rudist shoals. The cycle terminates with sub-aerial exposure and karstification during a relative sea level fall (**Mahdi2014**).

Diagenesis at the intra-Mishrif Formation boundary greatly enhanced the reservoir properties of the rudist bearing strata (**Aqrawi1998**). Leaching from meteoric fluids during sub-aerial exposure generated secondary porosity (**Mahdi2014**).

The upper cycle of the Mishrif Formation is thinner (compared to the lower cycle) regressive sequence. Two sedimentary sequences can be identified on the upper sequence of the Mishrif Formation. Directly above the intra-Mishrif boundary, rudists buildups with lagoon and shallow open-marine strata have retrogradated from their positions on the lower sequence (**Mahdi2014**).

Shallowing of the whole area is indicated by sub-aerial exposure on the top of the sedimentary cycle and facies transition from shallow open-marine deposits to
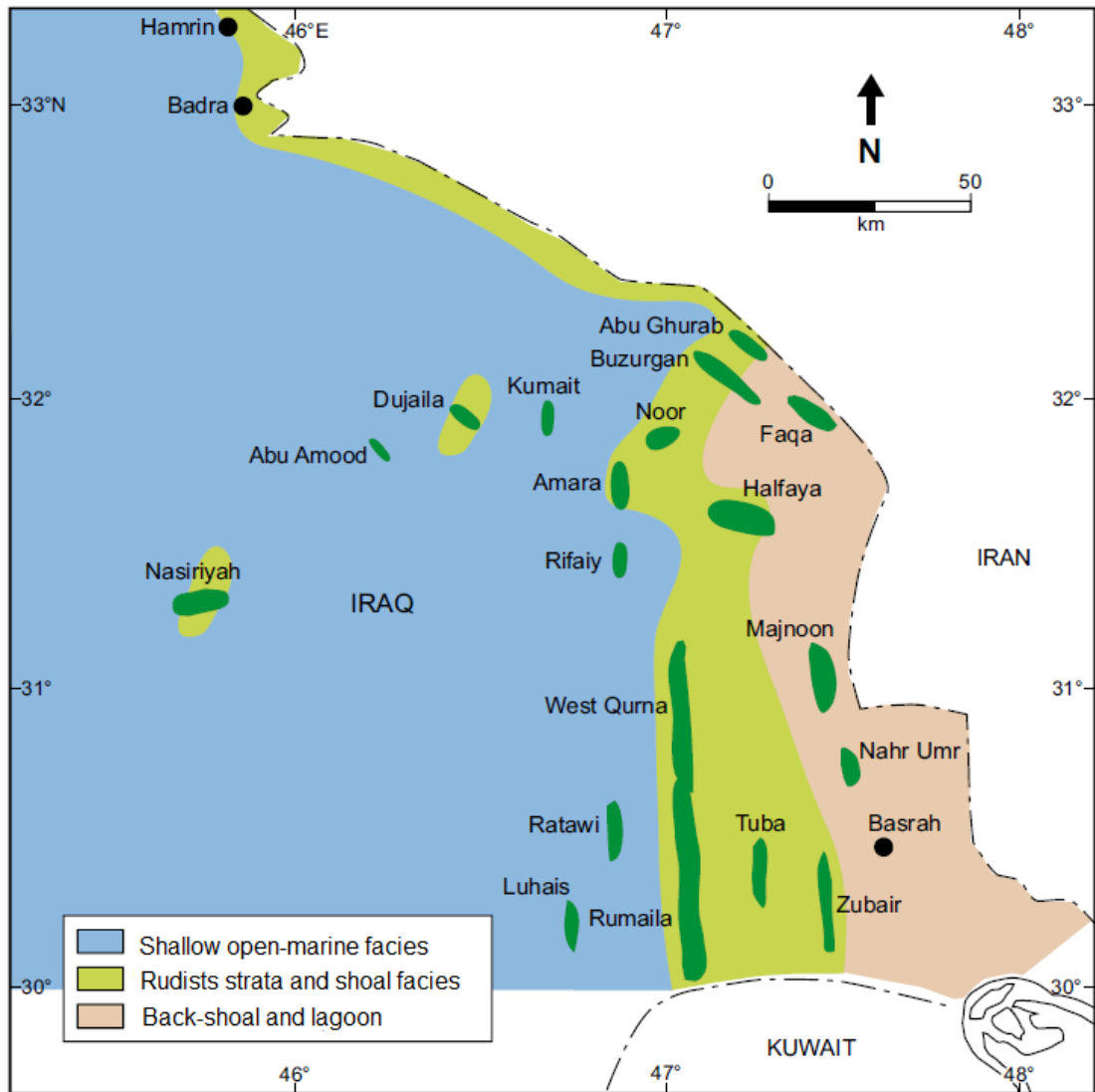
Figure 9.5: Regional paleogeographic map showing the distribution of Mishrif Formation facies in the southern Mesopotamian Basin and the position of oil fields (green colour). Modified after **Mahdi2013**.
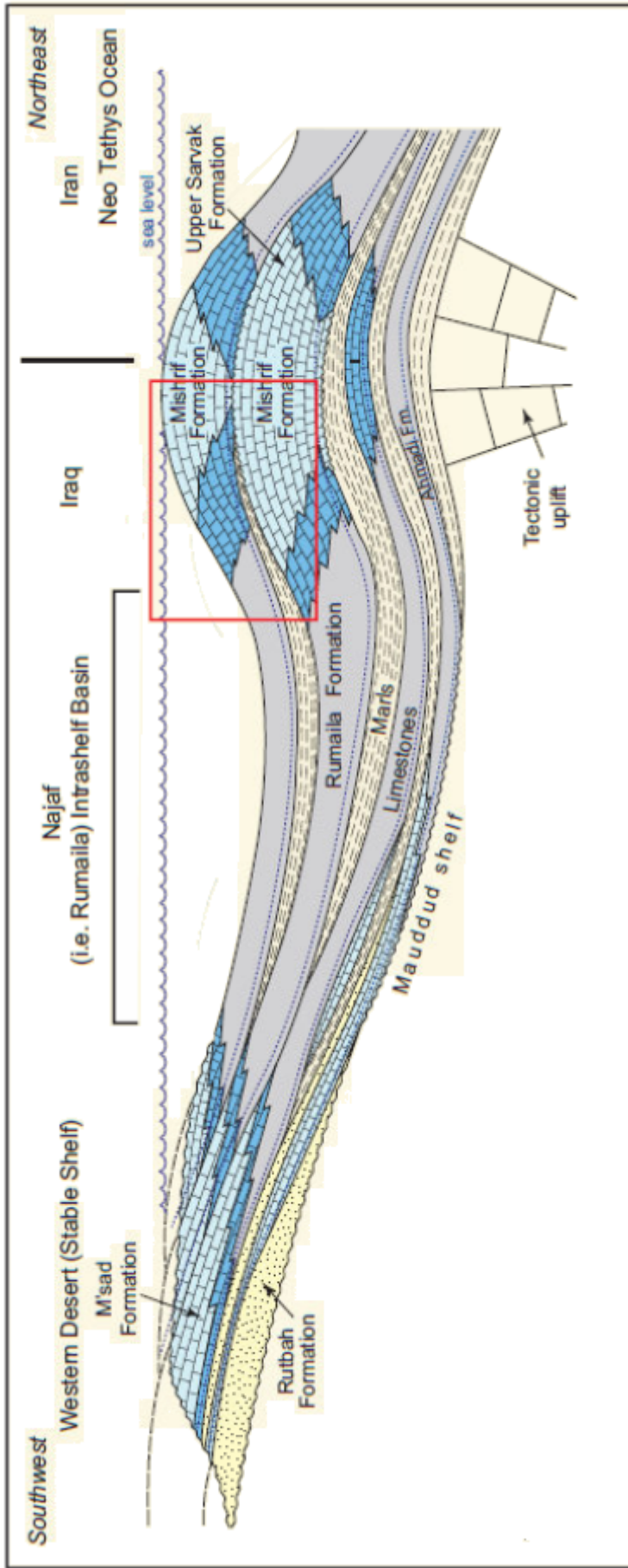
Figure 9.6: Schematic cross section showing the stratigraphic position of the Mishrif and Rumaila Formations in the Mesopotamian Basin, S Iraq (red square). The darker blue colour represents deep marine environment and the lighter blue shallow marine environment. Modified after **Mahdi2014**.

tidal flats of the second sedimentary cycle. The upper cycle terminates with the unconformable boundary with the overlain Khasib Formation (**Mahdi2014**).

9.2 Stratigraphic forward modelling of the Mishrif Formation

Stratigraphic forward modelling was performed in order to:

- generate the large scale, whole platform, geometry of the area;

- estimate the parameter values that generated the platform geometry;

- identify and measure the platform interior shoal geobodies in the platform.

The large scale, whole platform geometry was reproduced with the best-fit model run. The best-fit model is the model run that matches, within an accepted level of accuracy, all the characteristics of the modelled area at large scale and locally. The model parameter values for the best-fit model run were obtained by trial and error generating model runs and correcting the estimated model parameters. Based on discrepancies of each model run characteristics with the strata properties of the Mishrif reservoir, new model parameter values were estimated.

9.2.1 Model parameters

9.2.1.1 Strata properties

Stratigraphic forward modelling for this project was limited to the lower cycle of the Mishrif Formation. Input data were obtained from two sources. Firstly, the simplified reservoir architecture cartoon (Fig.9.7) provided by BP. Secondly, from discussions about the geometry and evolution of the entire Mishrif Formation during my visits to BP headquarters as part of the project evaluation.

The strata properties obtained from the two sources are:

- 80km x 20km platform size with the long axis (along the depositional dip) in the NE-SW direction;

- 55-60km platform top with extensive lagoon environment and high wave energy platform margin;

- platform duration of 2.5My;

- initial topography a homoclinal ramp;

- constant temporal and spatial subsidence rate;
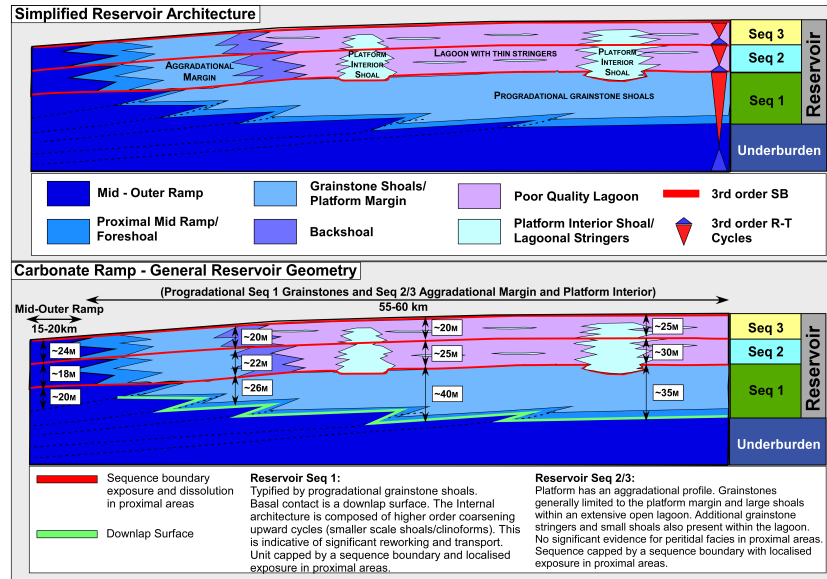
Figure 9.7: Simplified reservoir architecture of the lower cycle of the Cenomanian-Turonian Mishrif formation as provided by BP. Three sequences have been identified based on sub-aerial exposure and dissolution in proximal areas. The lower sequence (seq-1) is dominated by platform margin progradational grainstones. The upper two sequences (seq-2 and seq-3) show an extensive, mainly aggrading lagoon environment with shoal bodies.

- maximum strata thickness 90m on the platform top and dipping margin profile with decreasing strata thickness basinward;

- low gradient platform with maximum angle of bathymetry at the margin less than 1°;

- three sequences with some sub-aerial exposure and dissolution at the sequences boundaries in the proximal areas. The lower sequence (seq-1) is mainly composed of progradational grainstones, Internally, the grainstones show higher order coarsening upwards cycles with clinoforms. The upper two sequences (seq-2 and seq-3) are mainly aggradational with an extensive open lagoon. Large, mainly aggrading grainstone shoals occur within the lagoon. Some smaller grainstone shoals and stringers also occur;

- sediment transportation mainly along the platform long axis towards SW.

9.2.1.2 Model input parameters

The model input parameters were calculated based on the available strata properties and the computer characteristics used for the model runs. The calculated model parameters are:

219

- a grid with 320 x 80 model cells which correspond to a grid cell size of 250m x 250m. This is the maximum resolution that can be achieved based on the computer characteristics;

- initial bathymetry a homoclinal ramp with slope 0.05^o and minimum water depth 0m at the most shallow (proximal) part of the platform to the NE;

- subsidence rate of 20 m/My in order to generate the necessary accommodation for the deposition of 90m strata thickness;

- elapsed model time 2.5My with time step 1ky. The time step was selected as a reasonable time for modelling that is within the computational capabilities of the computer;

- eustatic sea level oscillations with period 1My and amplitude 5m. The period was calculated based on the number of sequences (3) and the total elapsed model time. The amplitude was selected as the maximum amplitude that generates limited sub-aerial exposure on the interior for the specific subsidence rate and ESL period;

- four in-situ producing factories. Two in-situ producing factories on the platform interior, one high energy factory on the margin and one below wave base, pelagic factory. Production rates for each of the lagoonal factories was 1100 m/My, for the margin factory 1500 m/My and for the pelagic factory 110 m/My;

- cross-platform sediment transportation algorithm. Sediment transportation direction was a straight line from proximal (NE) towards more distal part (SW) of the platform;

- transported fractions of 0.2 for each lagoonal factory, 0.6 for the margin factory and no transportation for the below wave base factory;

- water depth-threshold for shoal deposition 0.5m.

The number of in-situ producing factories was selected based, mainly, on the simplified reservoir architecture (Fig.9.7). The platform interior is generally characterised as poor quality lagoon which could have been modelled with one interior factory. Based on discussions during my visits to BP headquarters and examining some core samples for the modelled area, it was decided to use two platform interior producing factories.

Also from the simplified reservoir architecture, the platform margin is characterised as grainstone shoals and it is modelled with one high energy, producing

factory. The slope is divided into proximal ramp and outer ramp. The proximal ramp is dominated by grainstones/packstones with various size fragments with decreasing size away from the margin. The outer ramp is dominated by deep pelagic mudtones/wackestones (see section 9.1) and it is modelled with a pelagic, below wave base factory.

The production rates for each factory were calculated during the generation of the best-fit model. Production rates for the lagoon factories have to be high enough (compared to the accommodation creation rate) in order to build close to the sea surface and allow shoal formation. The production rate for the margin factory also has to be high enough (compared to the accommodation creation rate) to allow deposition of the two aggrading sequences (seq-2 and seq-3). The upper limit of the margin facies is defined in relation to the production rate of the pelagic factory.

The pelagic and the margin factories production rates must generate approximately 60m thick sediments on the outer ramp (Fig.9.7), a low gradient system and approximately 55-60km of margin progradation. The calculated production rates were the only combination that met all of the above criteria.

9.2.2 Results

The best-fit model run (Fig.9.8 and Fig.9.9) shows the following characteristics:

- a low gradient system with maximum bathymetric angle 0.85^o at the margin;

- extensive platform top (lagoon and margin on simplified reservoir architecture) with length 58km from the most proximal area in the NE to the platform margin;

- upper slope (proximal ramp) dominated by transported material and length 15km. Lower slope (outer ramp) comprised of pelagic, below wave base strata. Rarely some margin or transported material occurs;

- three sequences identified by limited sub-aerial exposure on the platform interior. The lower sequence (seq-1) is built mainly by high energy grainstones and progrades for 40km for 1 My EMT. The upper two sequences (seq-2 and seq-3) are dominated by slowly prograding lagoon packstones (17km progradation for 1.5 My EMT) and aggrading shoal grainstones;

- the maximum thickness on the platform top is 90m, with 60m strata thickness on the upper slope and 50m strata thickness on the lower slope.

Prograding, sigmoidal clinoforms are formed on the upper slope of the platform (Fig.9.8). The high progradation rate of seq-1 (40km over 1My EMT) generates

221
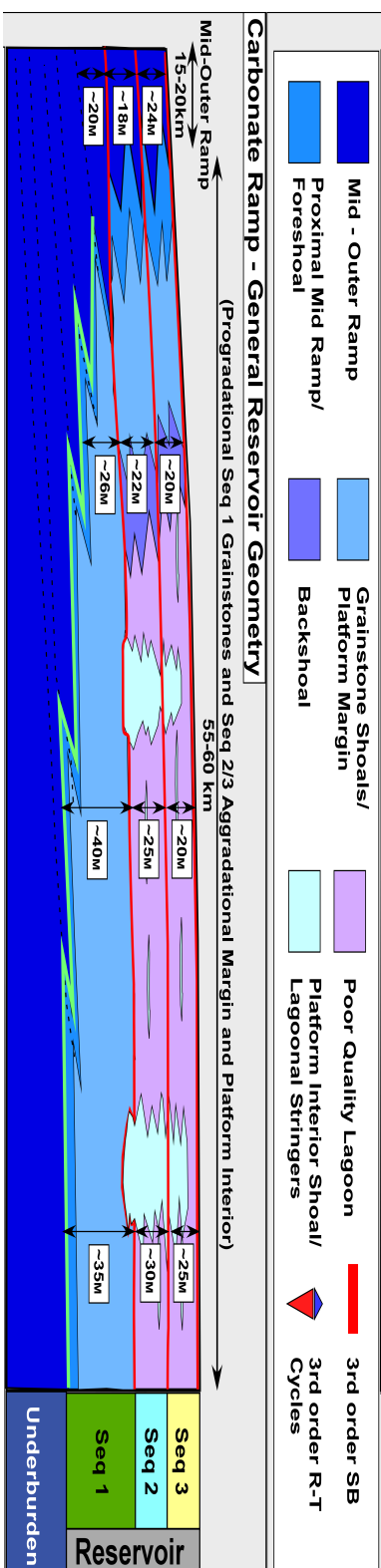
(a) Simplified reservoir architecture
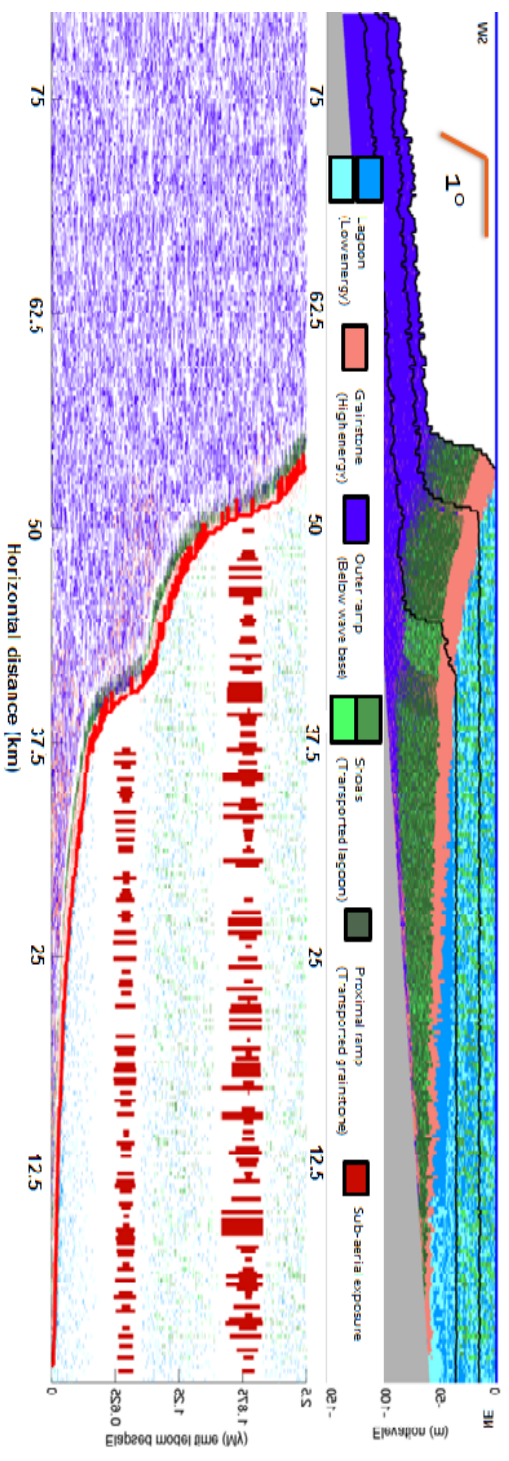
(b) Best fit model

Figure 9.8: (a) Simplified reservoir architecture of the modelled area. (b) Cross section of the best-fit model run with three sequences. The lower sequence is dominated by high-energy, platform margin, progradational strata, while the upper two sequences by low-energy platform interior strata with shoals. The proximal ramp is dominated by transported material and the outer ramp by below wave base pelagic material. The maximum slope angle at the margin is 0.85o. Three chrono-stratigraphic lines (black lines) at 1 My, 2My and 2.5My EMT respectively are shown. Chrono-stratigraphic section shows sub-aerial exposure occurs locally at the sequences boundaries. Simplified reservoir architecture sketch not to scale. Note the vertical exaggeration of the cross section.
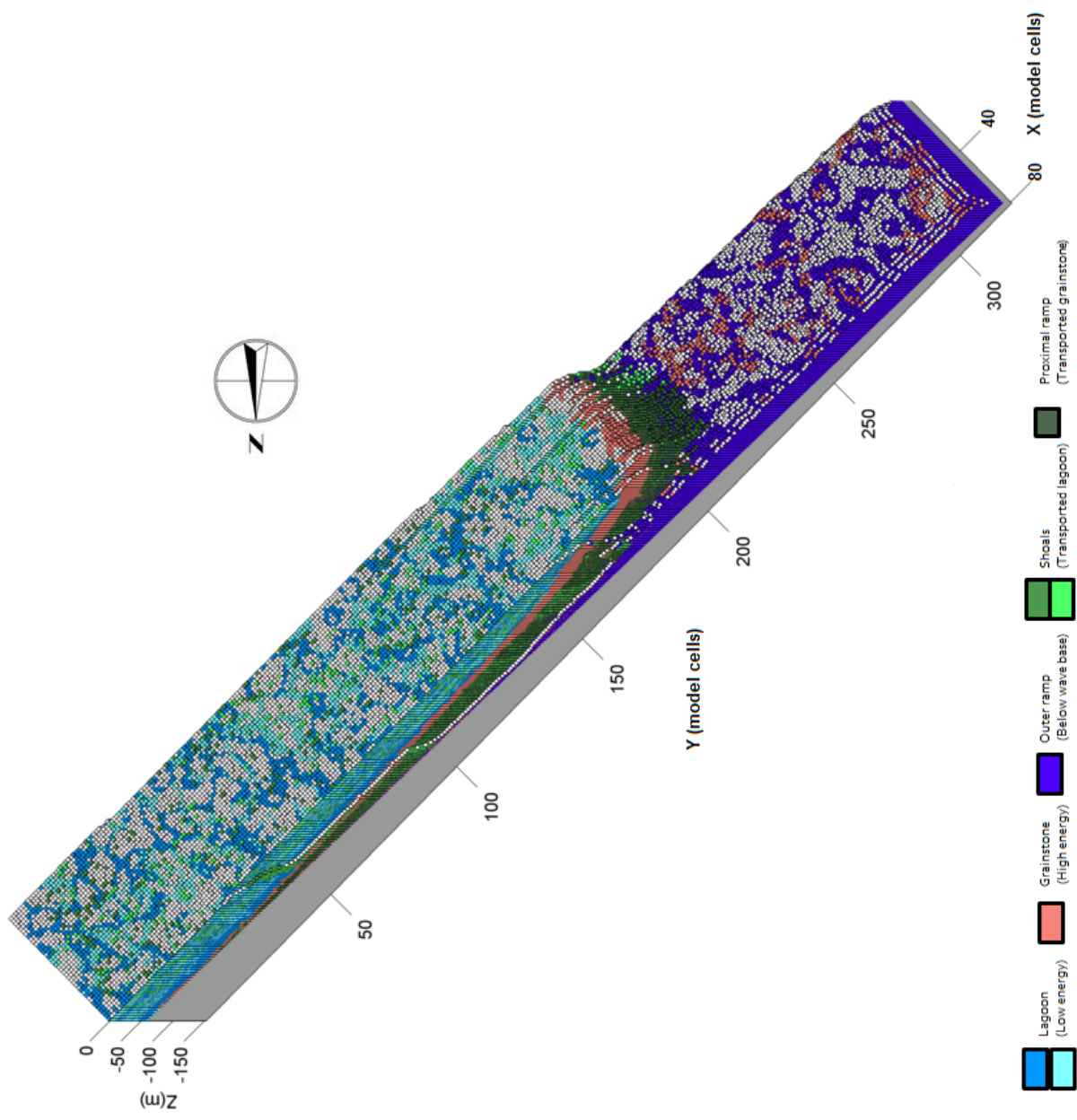
Figure 9.9: 3D plot of 80km x20km best-fit model run of simplified reservoir architecture. The long axis is in NE-SW direction with proximal on the NE and platform interior 58km long. A number of lagoonal shoals exists on the platform interior. Vertical axis not to scale.

223

prograding clinoforms with thin top. The lower progradation rate of seq-2 and seq-3 (17km over 1.5My EMT) and the formation of the aggrading interior produce prograding clinoforms with thicker tops.

A relatively small number of aggrading lagoon shoals occur on the platform interior (Fig.9.8). The number of shoal geobodies, their volume and dimensions are controlled by the interaction of sediment transportation and local bathymetry and thus are not effected by the in-situ factory that generates the shoals (Table.9.1).

Table 9.1: Volume and dimensions of shoal geobodies generated from each in-situ producing factory

Parameter	Factory 1	Factory 2
Number of geobodies	45	47
Mean volume (m^3)	$2.39 * 10^9$	$2.21 * 10^9$
Mean length (km)	2.14	2
Mean dimensional ratio	1.18	1.14

Shoal geobodies are defined as the extent of adjacent, connected, model cells throughout the platform top, that contain transported material from either lagoon factories, without any thickness threshold for the deposited, transported factories (Fig.9.10). No thickness threshold for the deposited, transported factories implies that any thickness of transported material deposited on a model cell (even 1mm) marks the cell as containing the factory and the cell can be connected to other cells with the same facies. (see section 7.2).

9.2.3 Comments

Except of transported fraction and water depth-threshold for shoal deposition, all other model parameters (subsidence rate, ESL period and amplitude, production rates and water energy levels) are defined from the input data. Transported fraction and water depth-threshold for shoal deposition values were selected in order to generate a relatively small number of aggrading shoals for the specific sediment transportation direction.

Sensitivity analysis revealed that similar shoal geometries can be achieved with different combinations of water depth-threshold and transported fractions (see section 7.2). With the available information regarding the lagoonal shoals it is not possible to distinguish which combination is more realistic and thus results from only one set are shown.

Using a thickness threshold for cell connectivity would alter the calculated volumes and dimensions of shoal geobodies. Application of a thickness threshold requires additional information regarding flow properties of the strata that is not available to me.

Geobody ID	Volume (m^3)
1	$9.74*10^8$
2	$9.61*10^8$
3	$9.58*10^8$
4	$8.23*10^8$
5	$8.2*10^8$
6	$8.1*10^8$
7	$7.91*10^8$
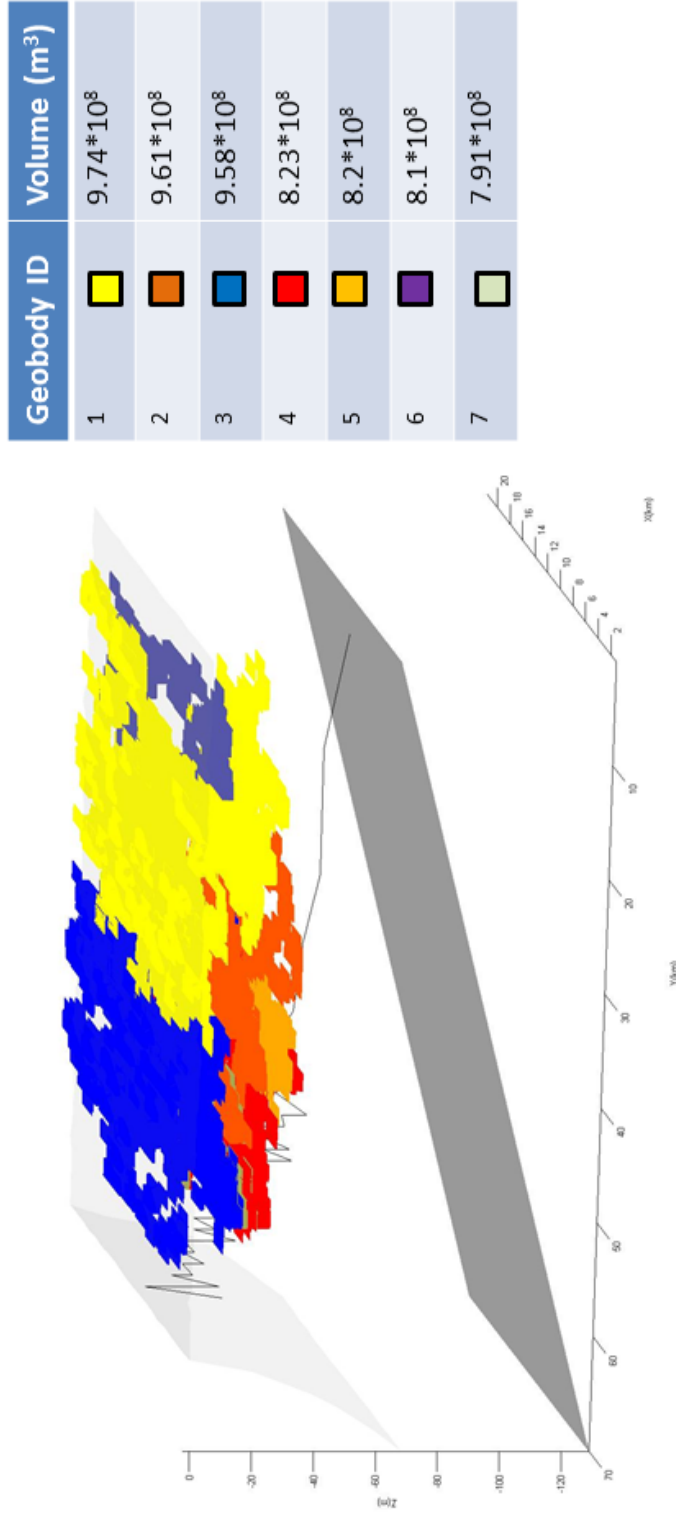
Figure 9.10: 3D distribution of platform interior shoal geobodies from either transported factories, without any thickness threshold for cell connectivity. Each geobody is the extent of vertically and horizontally adjacent model cells that contain transported material from one lagoon factory. The grey surface on the bottom of the figure is the basement while lighter, transparent grey surface on the top is the platform top surface. The black line shows the position of the platform margin.

9.3 Synthetic seismic imaging of Mishrif Formation

Synthetic seismic images were generated based on the stratigraphic forward model results using both the average impedance reflectivity method and the textural impedance reflectivity method. Data regarding the elastic properties of strata in the Mishrif Formation were obtained during my visits to BP headquarters as part of the project evaluation.

9.3.1 Elastic parameters

Elastic properties for Mishrif strata used for both methods were calculated based on:

- density for all strata was assumed to be the typical density of strata common in carbonate reservoirs. The density values used for the synthetic seismic images ranged from $2700 - 2750 kg/m^3$ for the transported factories; $2800 kg/m^3$ for the in-situ lagoon factories; and $2850 kg/m^3$ for the margin, in-situ factory;

- lagoon facies are mainly in-situ produced material with average porosity up to 15%. The high energy, in-situ, margin factory and the lagoon shoals have higher average porosity of $25 - 28\%$;

- in-situ, lagoon strata are generally mudstones with generally fine grain sizes. High energy, in-situ margin strata and lagoon shoals are mainly grainstones with coarser grain sizes.

Based on average porosity values for the Mishrif strata, P-velocities (V_P) were estimated for all strata (Fig.9.11).The estimated and calculated elastic properties are listed on Table 9.2.

A thick, homogeneous layer with velocity $4000 m/s$ and density $2600 kg/m^3$ is assumed above and below the modelled strata.

9.3.2 Results

Synthetic seismic images generated with the average impedance reflectivity method show two bright, top and bottom reflections for both low and high frequencies. Reflectivity on the platform top is noisy due to facies mosaic on the interior. Generally noisy reflectivity on the slope covers any features (Fig.9.12 and Fig.9.13).

In order to improve the produced images, the top and bottom reflections were removed from the synthetics. Furthermore, synthetics were generated using the textural impedance reflectivity method (see section 6) and textural values shown in Table 9.2.
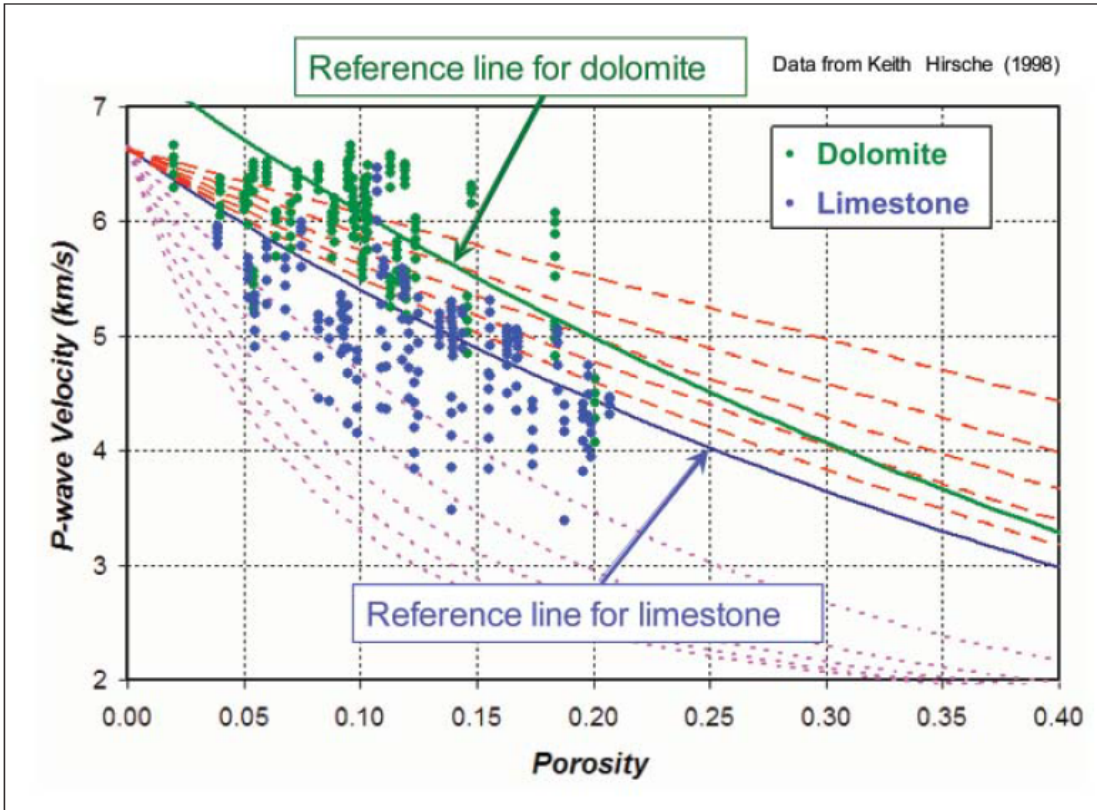
Figure 9.11: Porosity effect on P-wave velocity using laboratory data. Dashed lines above the limestone reference line indicate stiff pores and those below indicate cracks. From (**Xu2009**).

Factory	Density (kg/m^3)	Velocity (m/s)	AI ($Pa * s/m^3$)	Grain size
Lagoon1	2800	5000	14000000	75% Fine
Lagoon2	2800	4950	13860000	80% fine
Margin	2850	4000	11400000	Coarse
Below wave base	2710	5250	14227500	Fine
Transported Lagoon1	2700	3800	10260000	90% Fine
Transported Lagoon2	2700	3700	9990000	95% Fine
Transported margin	2750	3600	9900000	10% Fine

Table 9.2: Calculated elastic properties of Mishrif strata. The factories colour code refers to Fig.9.8
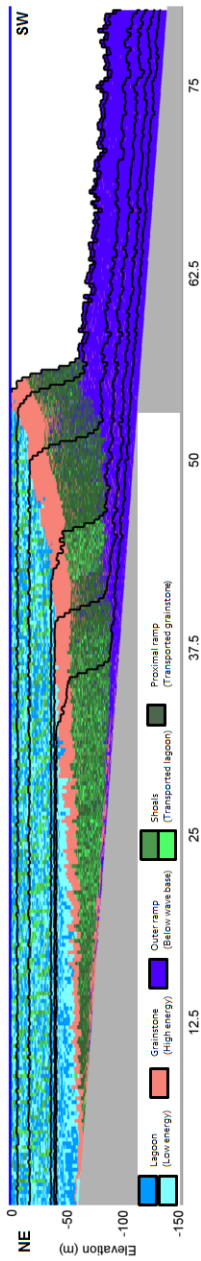
(a) Stratigraphic forward model
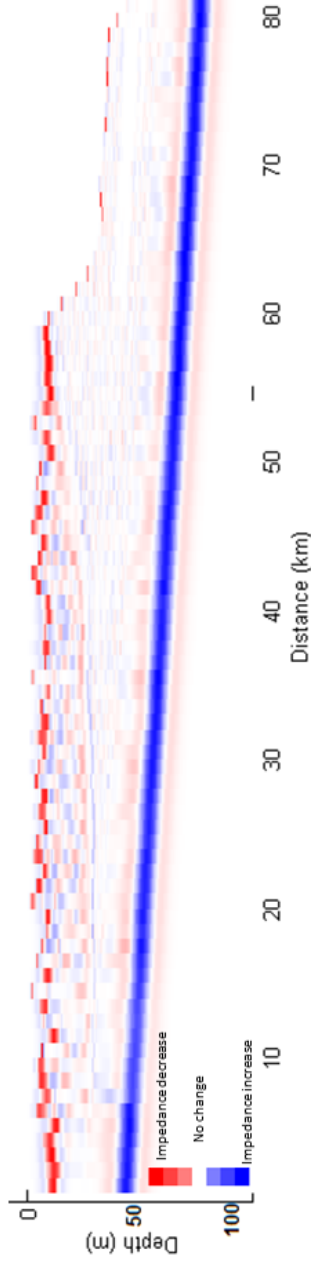
(b) Synthetic seismic image at 25Hz.

Figure 9.12: (a) Best fit model run. (b) Synthetic seismic image with the average impedance reflectivity method and 25Hz wavelet. The top and bottom reflections dominate the image. Generally noisy reflectivity on the interior and the slope.

(a) Stratigraphic forward model

(b) Synthetic seismic image at 100Hz.
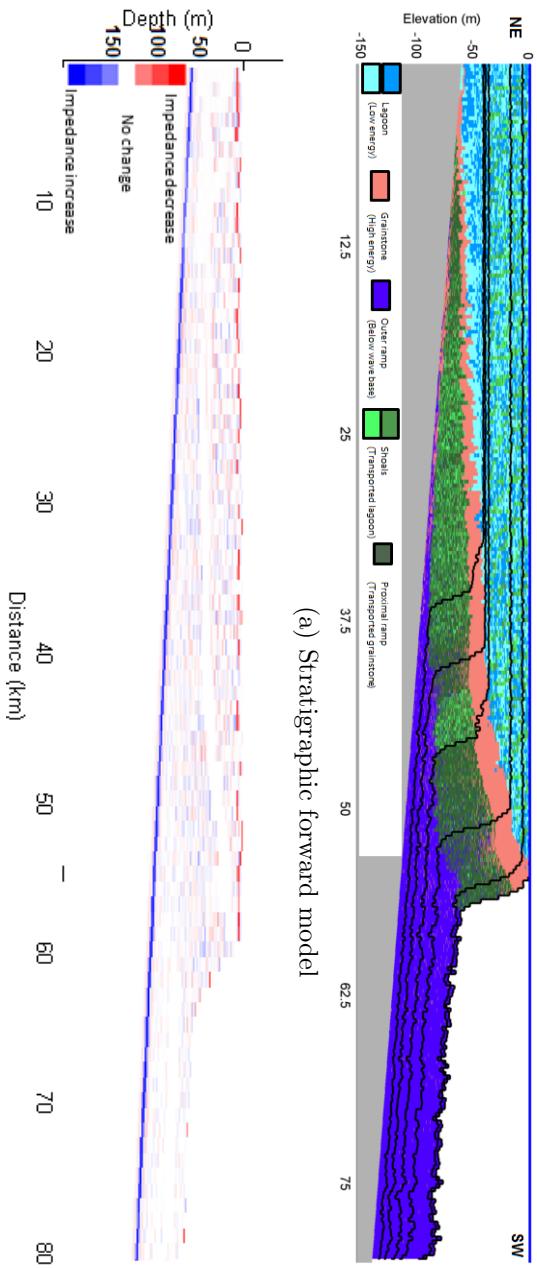
Figure 9.13: (a) Best fit model run. (b) Synthetic seismic image with the average impedance reflectivity method and 100Hz wavelet. The top and bottom reflections dominate the image. Generally noisy reflectivity on the interior and the slope.

230

The generated image (Fig.9.14) achieves excellent differentiation between the platform interior and the slope. Clinoform surfaces can be traced on the slope, while the platform top appears to be noisy. Increasing the vertical exaggeration of the synthetic image (Fig.9.15) reveals that the biggest shoal bodies can be identified in otherwise noisy interior and individual clinoforms can be identified on the slope.

(a) Stratigraphic forward model

(b) Synthetic seismic image at 25Hz.
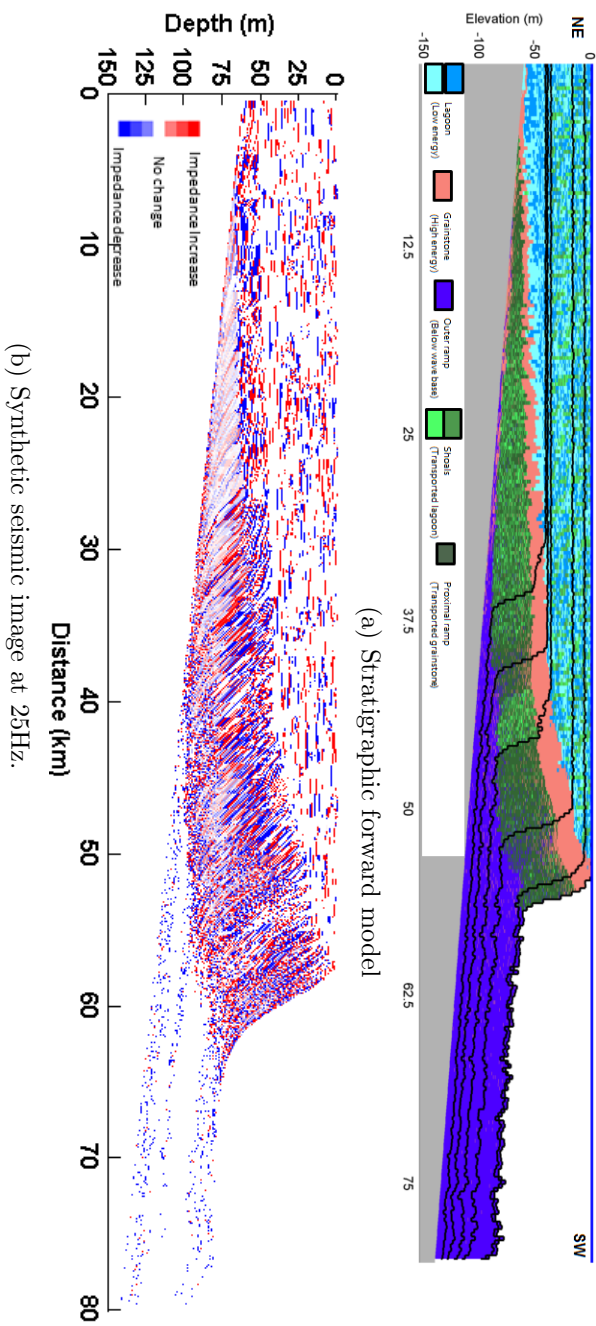
Figure 9.14: (a) Best fit model run. (b) Synthetic seismic image with the textural impedance reflectivity method and 25Hz wavelet. The platform top is generally noisy.Clinoform surfaces can be traced on the slope.

(a) Stratigraphic forward model

(b) Synthetic seismic image at 25Hz.
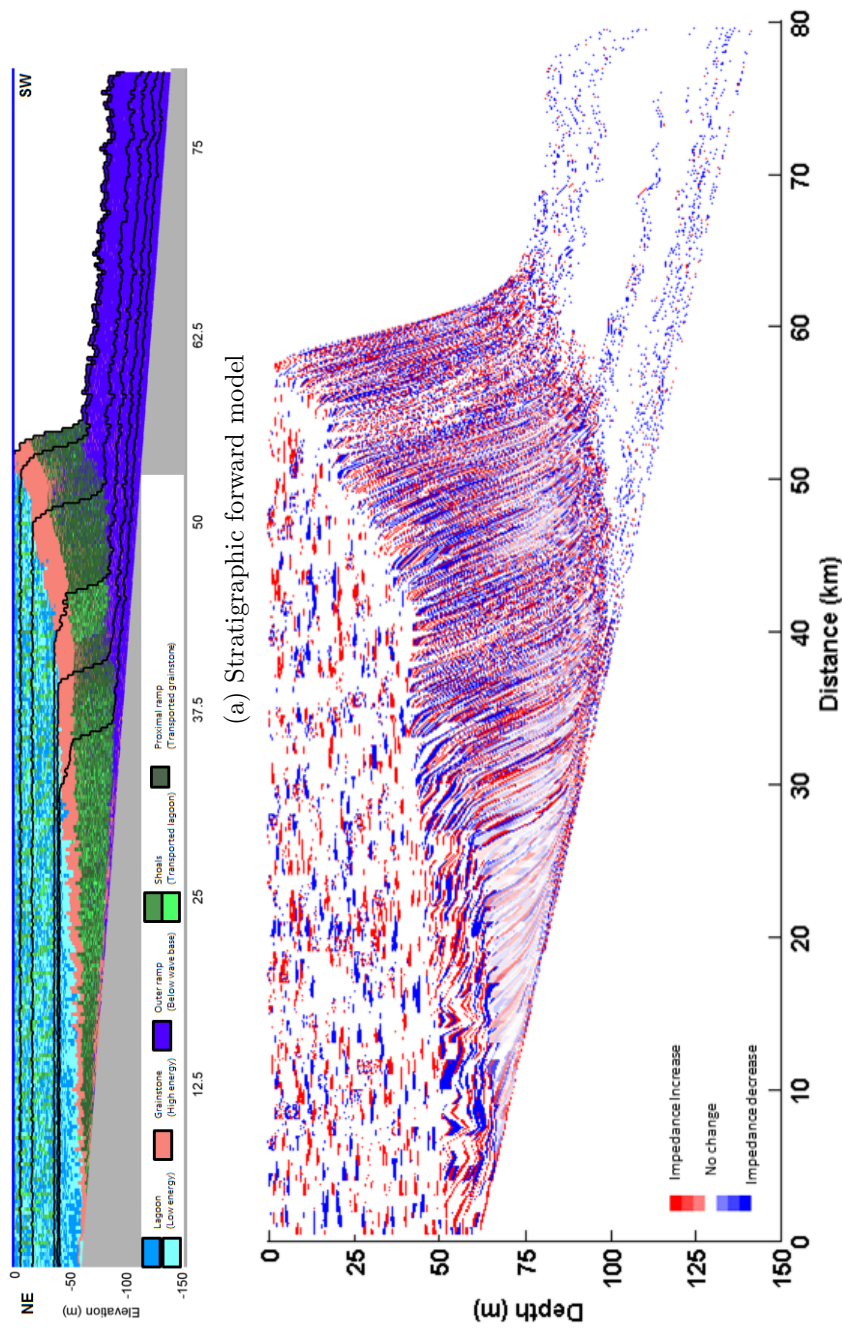
Figure 9.15: (a) Best fit model run. (b) Synthetic seismic image with the textural impedance reflectivity method and 25Hz wavelet 4x vertical exaggeration. Clinoforms dominate the slope and the seismic signal from the bigest shoals on the interior can be identified.

233

10 Discussion and conclusions

This thesis posed the questions of how to predict facies distribution and rock properties of carbonate strata at sub-seismic scales and how to study heterogeneity of carbonate platforms at all scales from seismic images.

The project developed a model that integrates stratigraphic forward modelling and synthetic seismic imaging for prediction of 3D distribution of carbonate strata and generation of synthetic seismic images. Stratigraphic forward modelling was performed with a modified version of CarboCAT. The modified version includes, among other tools, algorithms that simulate the effect of wave energy on carbonate platform geometry and on facies distribution, siliciclastic input and its effect on carbonate production, and cross-platform sediment transportation.

Accommodation in CarboCAT is in line with the **Muto2000** definition. Tectonic subsidence and eustatic sea level oscillations generate a volume available to accept sediments but the actual accommodation for a specific time at a specific location can only be measured after the model has finished and sediment has been deposited.

Ecological simulation of carbonates in CarboCAT is performed with a competition for space approach. For this reason, in CarboCAT, each model cell can be occupied by one producing factory at each time. Other approaches for calculation of the ecological effect on carbonates (predator-pray or competition for resources among others) are equally good processes involved in the ecology of carbonates.

The new cross platform sediment transportation allowed studying the effect of allogenic and autogenic processes on carbonate heterogeneity and facies distribution. Formation and distribution of specific carbonate lithofacies was allowed and examined from the dynamic interaction of depositional, entrainment and transportation processes with the local bathymetry. Enhanced prediction of lithofacies distribution and calculation of specific metrics for the position, volume and properties of specific lithofacies augmented prediction of reservoir properties and compartmentalisation.

Synthetic seismic images were generated using a new pseudo-acoustic impedance method, the textural impedance reflectivity. Textural impedance reflectivity method calculates strata reflectivity based on the texture and porosity of carbonate strata and the CarboCAT generated numerical models.

Generation of synthetic seismic images from the stratigraphic, numerical models and comparison of the synthetics with real seismic images allows for:

1. enhanced prediction of large scale platform geometry from seismic images

2. prediction of facies distribution at sub-seismic scales from seismic images

3. identification of the effect of heterogeneity on seismic images

The model also allows for testing of hypotheses regarding strata deposition and identification of the controls on large scale platform geometry. Sensitivity analysis through numerical modelling suggested that cross-platform sediment transportation of carbonates affects the large, whole platform geometry by controlling the amount of sediment deposited on the platform top and the slope producing a continuum of forms between the two end members of FTP and ramp geometries, as has been suggested by **Williams2011**.

The same model runs demonstrated that grain size of sediment is major control on the geometry of carbonate platforms. Coarse grain size sediments which require high bathymetric differences between adjacent model cells in order to be entrained, in agreement with **Kenter1990**, produce high gradient systems with relatively steep margins. Fine grain or mud sediments are more susceptible to transportation (**Beavington-Penney2005**, **Azeredo2009**) and typically produce low gradient ramps.

The effect of cross platform sediment transportation on platform geometry and facies distribution increases with increasing transportation rates. Low transportation rates generate high gradient, in-situ dominated systems with most of the material remaining on the platform interior.

High transportation rates generate low gradient systems. The platform geometry and the facies distribution of the low gradient, transport dominated systems are also a function of sediment grain size. Coarse grain sediments tend to generate low gradient systems with elongated platform interiors and slopes with clinoforms. Fine grain sediments tend to generate ramp style geometries without clear differentiation between interior, margin and slopes.

Low gradient systems have been related to several different platform geometries, from elongated, prograding platform interiors with thick deposits and clinoforms on the slope to back-stepping ramps and all cases in between based on transportation rates and grain size. Prediction of facies distribution on sub-seismic scale for low and high gradient systems shown in seismic images can be enhanced by identifying stacking patterns from the seismic data.

High gradient systems have at least one coarse grain sediment facies that usually leads to formation of steep margins and FTPs. High gradient systems may have fine grain sediments but are confined in the platform interior space. Furthermore, high gradient systems are usually in-situ dominated platforms. Identification of high gradient systems in seismic images implies that at least one coarse grain facies is present in the platform and it is located at the aggrading part of the platform or near the top of the clinoform surfaces. Clinoforms and platform interior areas may be comprised of fine grain material. Low gradient systems (ramps) are transport dominated systems and are usually built by fine grain sediment. Identification of back-stepping platforms and ramps on seismic images implies dominance

of fine grain material.

Sensitivity analysis with a modified cross-platform algorithm demonstrated that autocycles, comprised of peritidal shoals, form on the platform top from the interaction of sediment transportation and sediment production. An autocycle is comprised of in-situ produced material on the bottom that passes vertically to transported material and the cycle finishes with a depositional hiatus; after which a new cycle can form.

Autocycles were formed based on the **Ginsburg1971** method and agree with the results of **Burgess2006** and **Burgess2003**. The generated autocycles do not show pattern and spatial distribution of subtidal and supratidal areas as has been suggested by **Burgess2001a**. This indicates that the algorithm used here for the generation of autocycles does not include all the relevant processes.

The effect of transported fraction, transportation direction and bathymetric threshold for deposition on the formation of shoal geobodies was tested with the several model runs. For all transportation directions the number of isolated geobodies decreases as the transported fraction increases. Since more material is available for shoal formation, shoal geobodies overlap with each other and become volumetrically bigger.

Transportation rates control the horizontal dimensions and volume of shoals geobodies. Generally, geobody volume increases, approximately one order of magnitude, for each increase (of 0.2) in the transported fraction.

The straight line and random path transportation directions generate elongated along the dip geobodies with increasing transportation rates. Bathymetry controlled transportation generates geobodies that grow in both dip and strike directions with similar rates (Fig.10.1).

The transportation direction also controls stacking patterns of shoals. Straight line and random path transportation directions generate geobodies that prograde in the opposite direction of the transportation for medium (0.3) and high (0.5) transported fractions. Bathymetry controlled transportation generates geobodies that mainly aggrade.

The generated autocycles increased the strata order on the platform top for all transported fractions and for all transportation directions (Fig.10.2). Ordered strata from autogenic processes contradicts the suggestion from **Lehrmann1999** that ordered strata are formed from external forcing only. Models runs produced here suggest that autogenic processes generate ordered strata under spatially and temporally constant production and transportation in accordance with **Burgess2006**.

Identification of geobodies with specific lithological and elastic properties enhances prediction of facies distribution on carbonate platforms. Prediction of geobody volume, 3D distribution on the platform and connectivity of geobodies
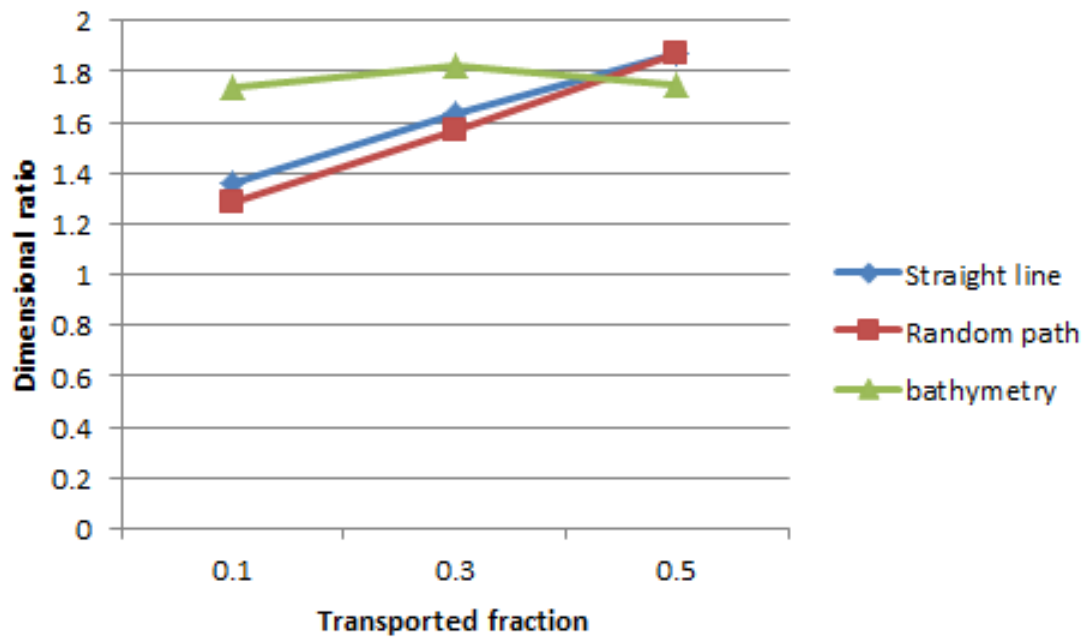
Figure 10.1: Change in dimensional ratio of shoal geobodies with transported fraction and transportation direction
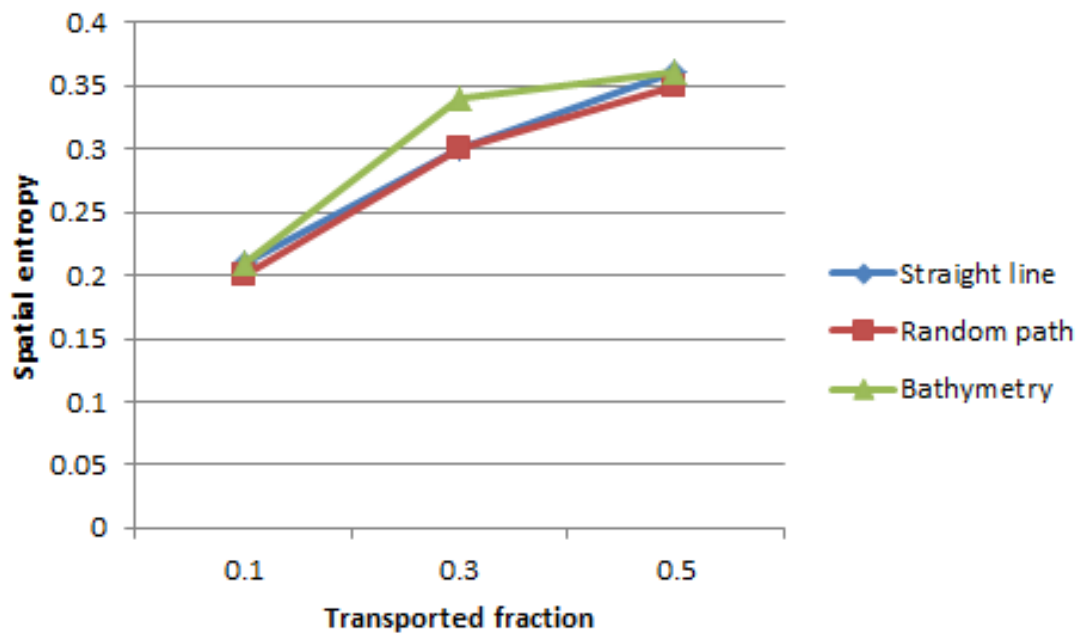
Figure 10.2: Change in spatial entropy on the platform interior with transported fraction and transportation direction

are useful tools for studying compartmentalisation of carbonate platforms or reservoirs. Exploration and production of hydrocarbons can be greatly augmented by improved interpretation of platforms imaged on seismic sections and prediction of facies distribution in sub-seismic level.

The modified version of CarboCAT was used to model Upper Cretaceous (Santonian) outcrops in South-Central Pyrenees, Spain, the Bastus platform. Several model runs identified the controls of platform geometry and enhanced the interpretation of the modelled platform by evaluating different stratigraphic interpretations. Modelling suggested that relative sea level movements are the main control on platform evolution. Variable carbonate production, differential subsidence and non-periodic eustatic sea-level movements are equally possible, secondary controls indicating the non-uniqueness of strata geometries based on outcrop data.

The extent of effect each control on the platform geometry or if interaction of the secondary controls on platform geometry cannot be distinguished based on the available field data or modelling outcomes. A more detailed field work survey that would specifically search for the effects of each secondary control in the field would be required to identify the effect of each secondary control.

Non-uniqueness of strata geometry based on outcrop data confirms and extends the observations of **Burgess2015** regarding non-uniqueness of strata based on numerical modelling only.

Evaluation of the two suggested interpretations of the Bastus platform showed that the two sequences interpretation with a back-stepping of the upper sequence at the sequence boundary, (**Lavi2017**), agrees with both field observations and numerical modelling results. The interpretation with 5 high frequency, sequences generated by eustatic sea level movements, (**Pomar2005**) can be reproduced with numerical modelling but requires unrealistic parameters and further evidence is necessary to support the hypothesis.

High resolution, synthetic seismic images of the Cenomanian-Turonian Mishrif formation, South Iraq were obtained using the model developed for this project. The CarboCAT generated best-fit model run of the interpreted geometry of the formation, identified the controls on the platform geometry and provided an alternative source of the formation of the good reservoir quality interior shoals.

Modelling suggests that the good reservoir quality interior shoals do not necessary have to be rudists formation (**Sadooni2005**) but the shoals can be formed as autogenic structures from the interaction of sediment transportation and local bathymetry.

The best-fit model run was also used to quantify the size and volume of the lagoonal shoals on the formation and thus provide information regarding the compartmentalisation of the reservoir. Based on the best-fit model run, synthetic seismic images were produced and the all formation features were linked to their

seismic signatures.

The wave energy algorithm in CarboCAT can be further developed to better simulate the interaction of waves with the bathymetry including wave reflection and diffraction. Additionally, formation of secondary fetch areas that produce smaller waves, if the conditions are appropriate, can be included in the algorithm.

The siliciclastic sediment input algorithm can be benefited by secondary transportation of the deposited siliciclastic sediment. Furthermore, the effect of grain size in both sediment transportation and siliciclastics can be quantified with an additional parameter for the in-situ produced facies.

The textural impedance reflectivity algorithm can be improved to dynamically recognise facies based on hydrodynamic and depositional conditions on the platform and to include the effect of different types of porosity and porosity shape on the elastic properties of strata.

The workflow developed integrates computational stratigraphic forward models and seismic data to enhance interpretation of seismic images for subsurface characterization. Rock properties are derived from high resolution numerical models and synthetic seismic images are generated with the new textural impedance reflectivity method. Well data, core data and field observations can be combined with the numerical models to generate a more robust estimation of the heterogeneity of the subsurface. The workflow also allows for testing several stratigraphic scenarios and validating them with observed seismic data.

A Appendix A - New developments in seismic imaging model runs

A.1 Model run SC

Model run SC was created with the initial bathymetry a distally steepened ramp (fig.A.1) while the rest of the parameters were the same as the standard model without heterogeneity. The model confirms all the observation made in the standard model without heterogeneity.

A.2 Model run SD

Model run SD (fig.A.2) was created with double the production rates of the standard model without heterogeneity. Higher production rates generate thicker sequences. The model confirms all the observation made in the standard model without heterogeneity.

A.3 Model run SE

Model run SE (fig.A.3) was created with half the transportation rates of the standard model without heterogeneity. The model confirms all the observation made in the standard model without heterogeneity. Lower volume of transported material generates weaker reflections on the slope.

A.4 Model run SF

Model run SF (fig.A.4) was created with lower eustatic sea level period compared to the standard model without heterogeneity. Only 3, thick sequences are generated, without sub-aerial exposure.

A.5 Model run SG

Model run SG (fig.A.5) was created with lower eustatic sea level amplitude compared to the standard model without heterogeneity. No sub-aerial exposure on the interior generates several proper defined reflections on the interior and the slope as well.

A.6 Model run SHC

Model run SHC (fig.A.6) shows initial bathymetry a distally steepened ramp compared to the standard model. The model confirms all the observations made in
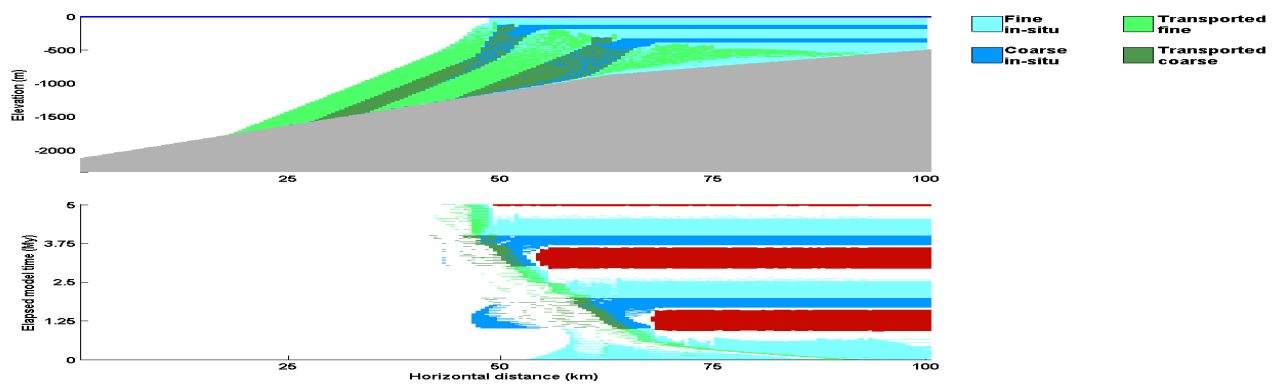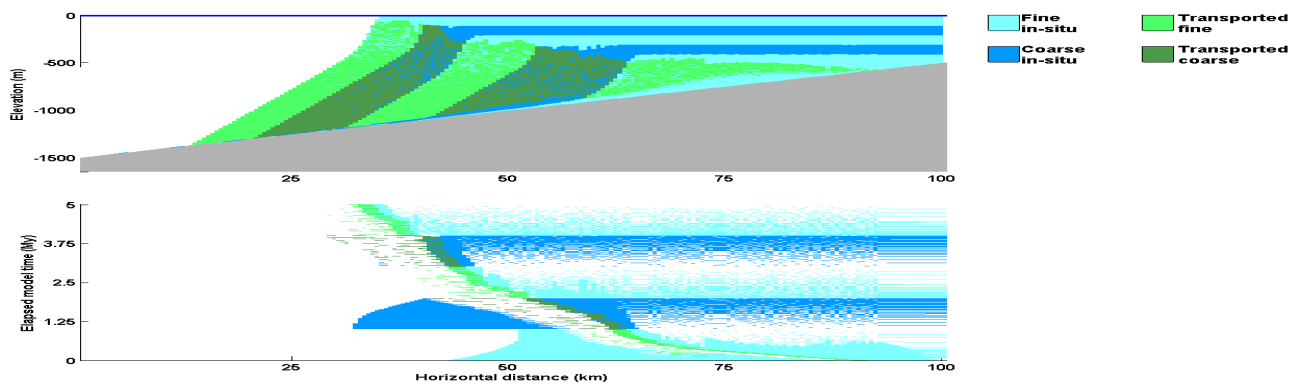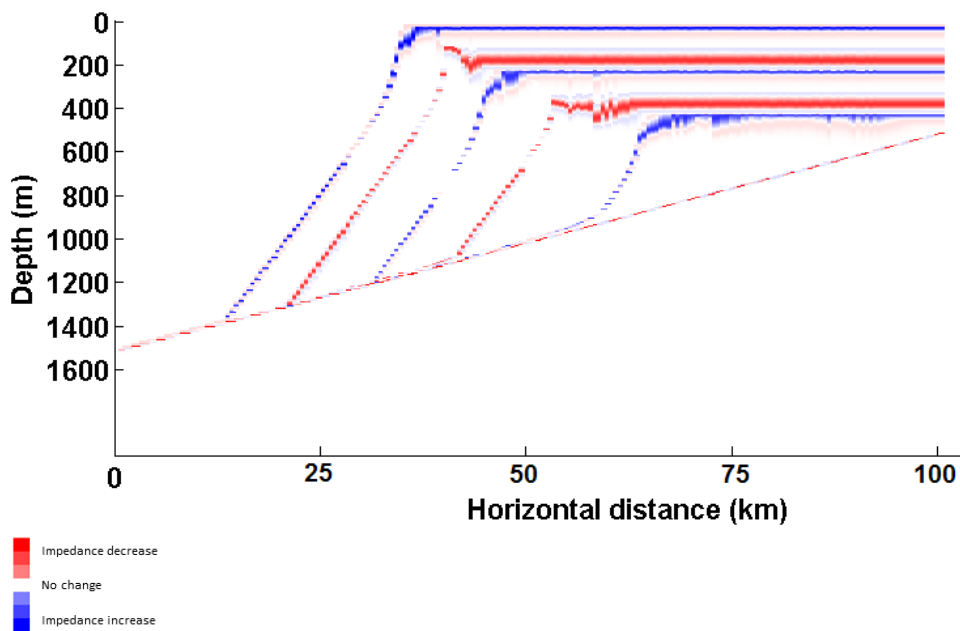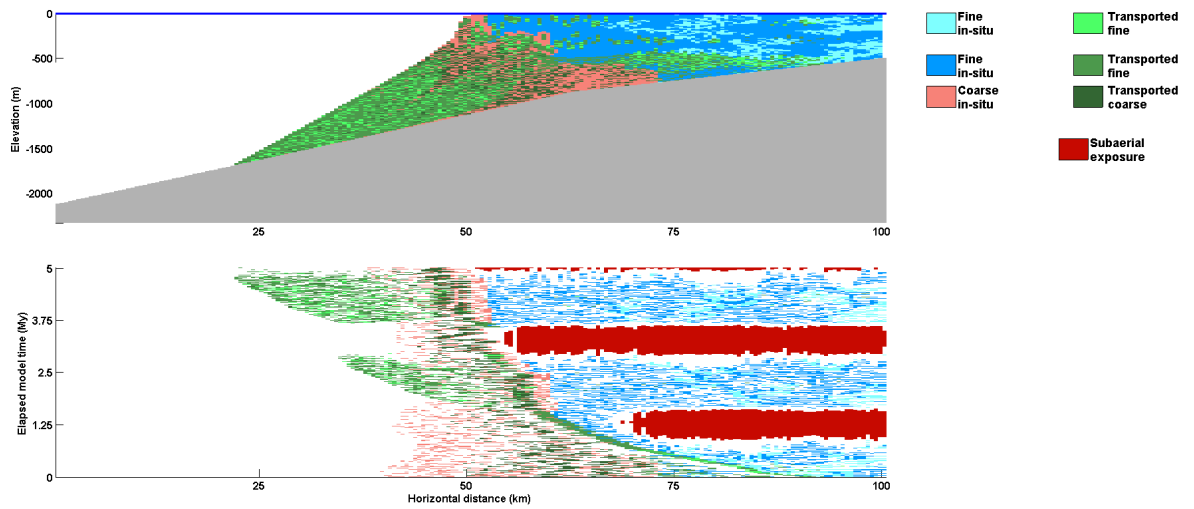
(a) Cross section and chrono-strat section
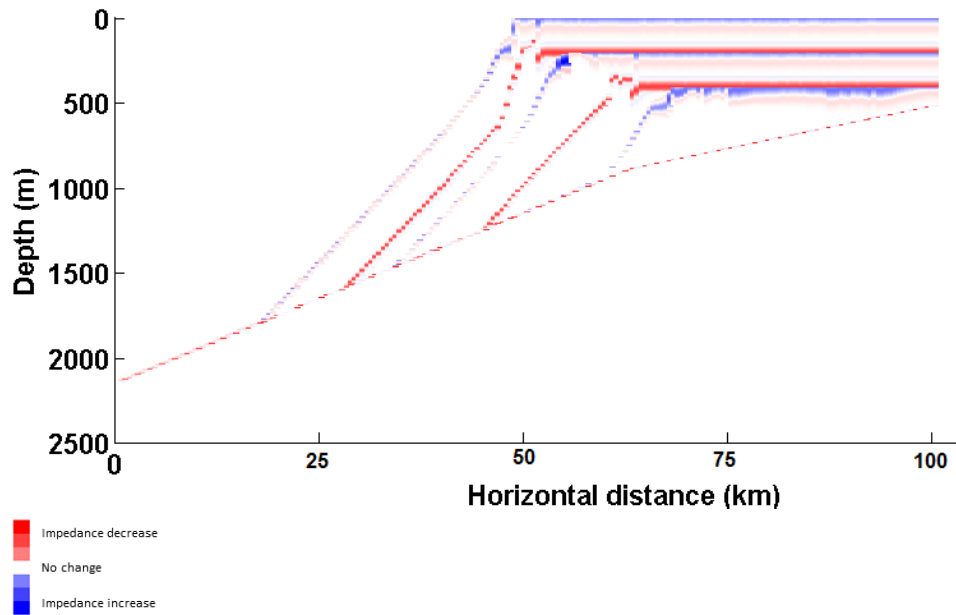
(b) Synthetic seismic image

Figure A.1: (a) Stratigraphic model and chrono-stratigraphic model of the SC model run with distally steepened initial bathymetry. Exposure surfaces occur on the interior and simplistic clinoforms on the slope are formed due to ESL movements. (b) Synthetic seismic image generated with the textural impedance reflectivity method. The transparency of the image is due to facile model. Bright, laterally continous reflections can be seen on the interior. The clinoform surfaces can be followed on the slope.

241
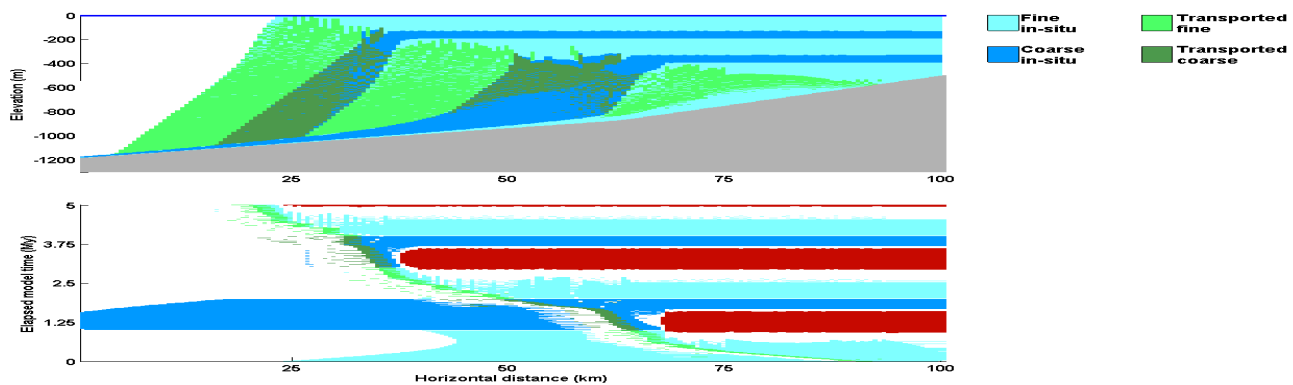
(a) Cross section and chrono-strat section
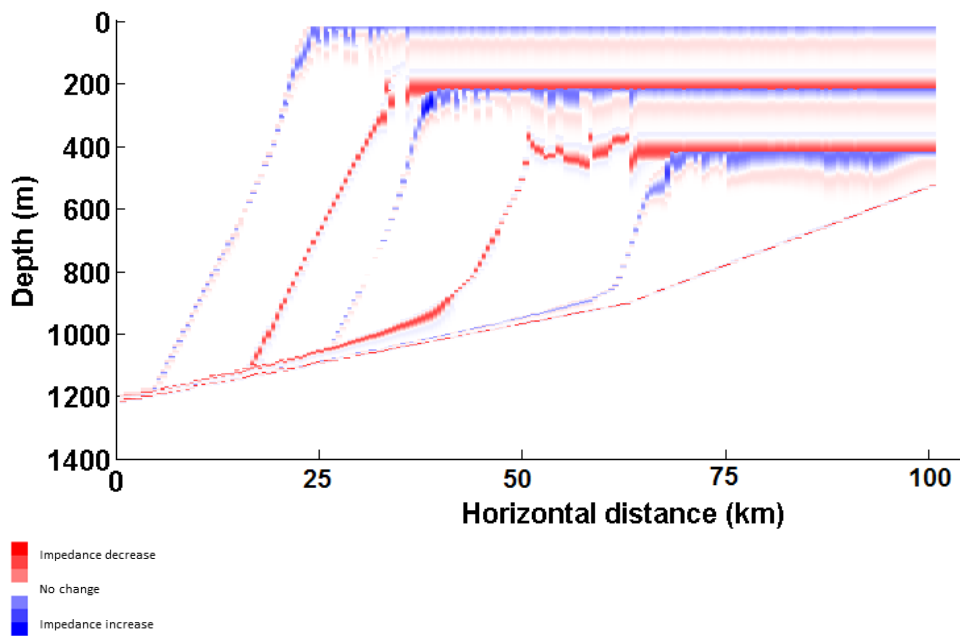
(b) Synthetic seismic image

Figure A.2: (a) Stratigraphic model and chrono-stratigraphic model of the SD model run with higher productions rates. The higher production rates fill almost all of the accommodation and generate thicj sequences. (b) Synthetic seismic image generated with the textural impedance reflectivity method. The transparency of the image is due to facile model. Bright, laterally continous reflections can be seen on the interior. The clinoform surfaces can be followed on the slope.
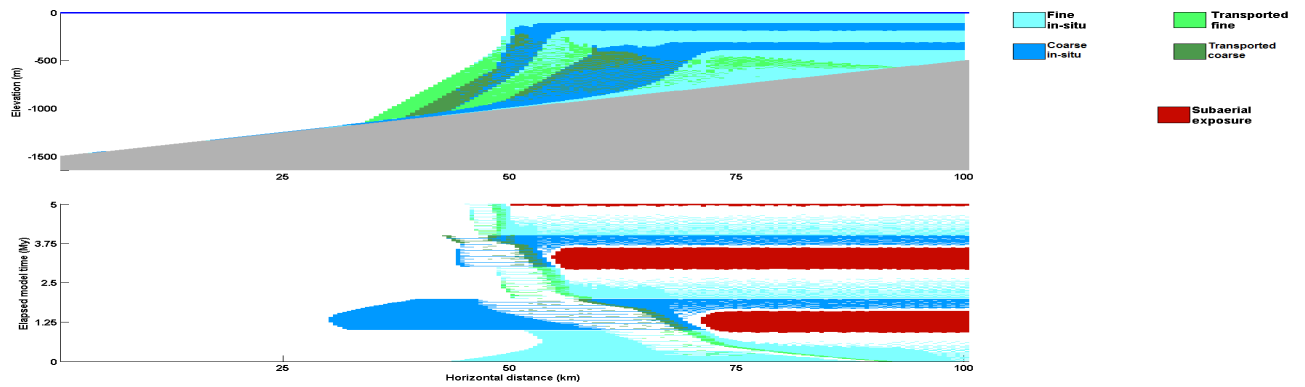
(a) Cross section and chrono-strat section
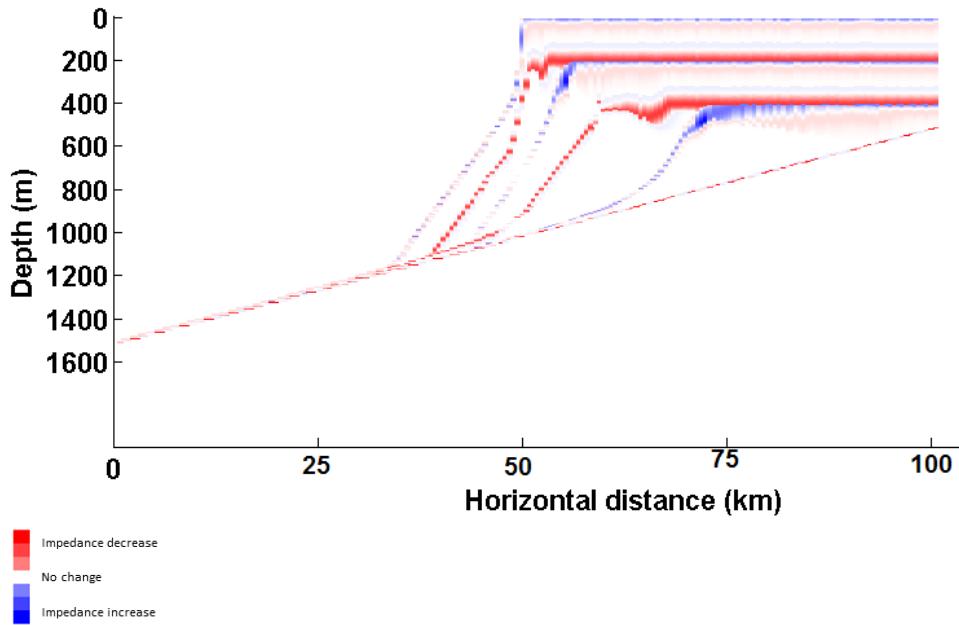
(b) Synthetic seismic image

Figure A.3: (a) Stratigraphic model and chrono-stratigraphic model of the SE model run with lower transportation rates. Exposure surfaces occur on the interior and simplistic clinoforms on the slope are formed due to ESL movements. (b) Synthetic seismic image generated with the textural impedance reflectivity method. The transparency of the image is due to facile model. Bright, laterally continous reflections can be seen on the interior. The clinoform surfaces can be followed on the slope.
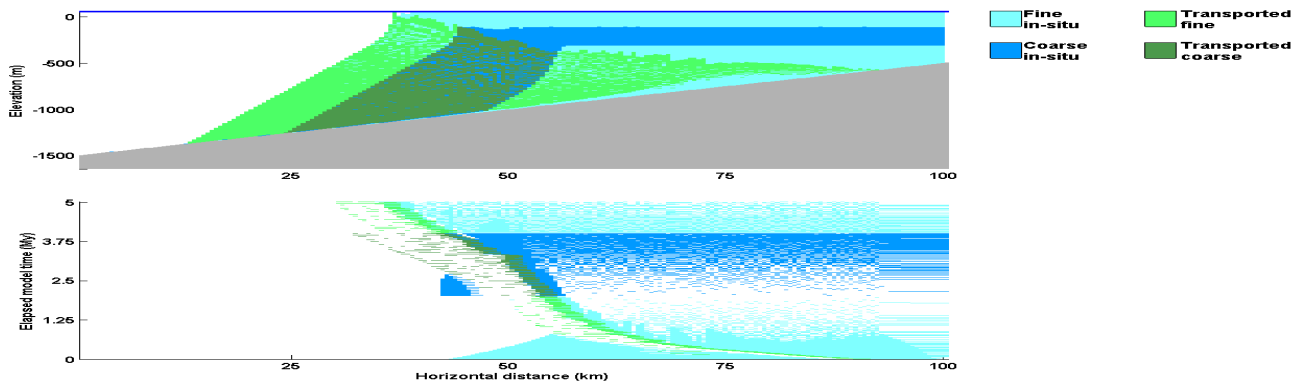
(a) Cross section and chrono-strat section
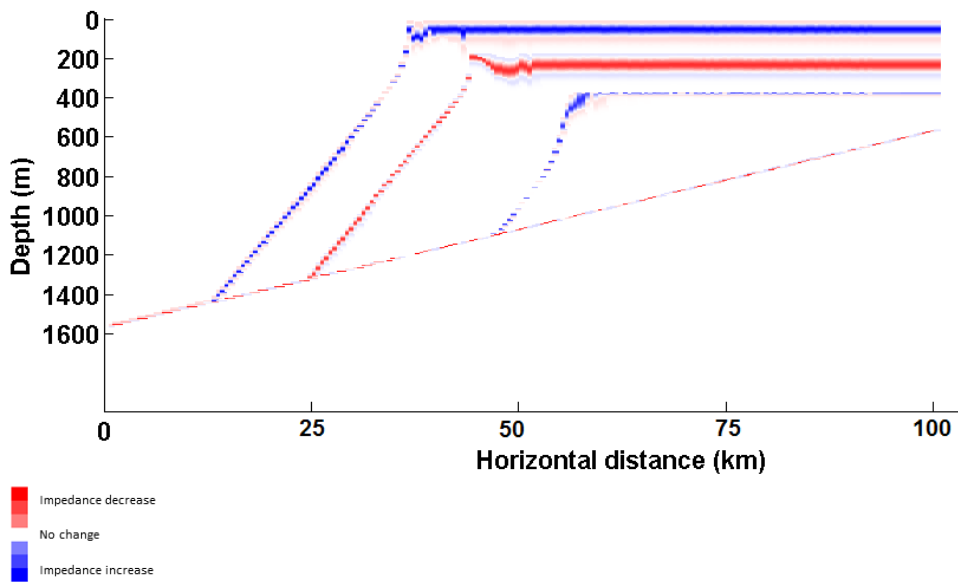
(b) Synthetic seismic image

Figure A.4: (a) Stratigraphic model and chrono-stratigraphic model of the SF model run with lower eustatic sea level period. No exposure surfaces occur on the interior. (b) Synthetic seismic image generated with the textural impedance reflectivity method. The transparency of the image is due to facile model. Bright, laterally continous reflections can be seen on the interior. The clinoform surfaces can be followed on the slope.
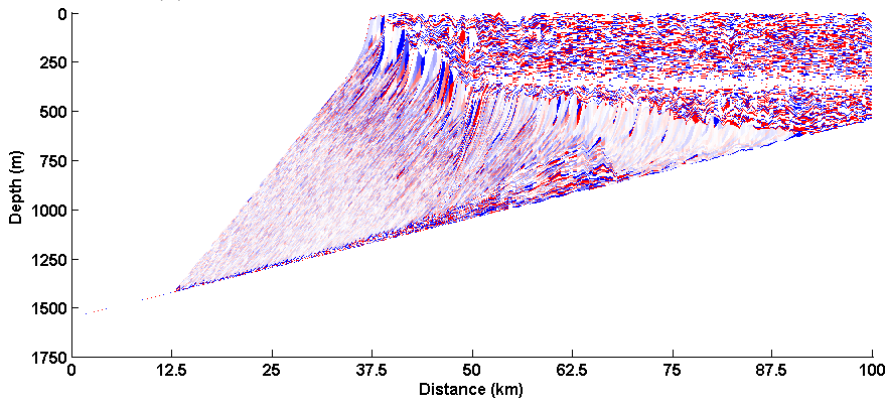
(a) Cross section and chrono-strat section

(b) Synthetic seismic image

Figure A.5: (a) Stratigraphic model and chrono-stratigraphic model of the SF model run with lower eustatic sea level amplitude. No exposure surfaces occur on the interior. (b) Synthetic seismic image generated with the textural impedance reflectivity method. The transparency of the image is due to facile model. Bright, laterally continous reflections can be seen on the interior. The clinoform surfaces can be followed on the slope.

(a) Cross section and chrono-strat section
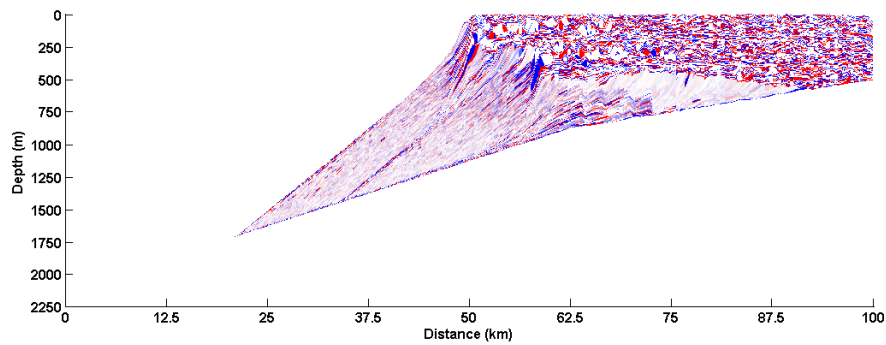
(b) Synthetic seismic image with textural impedance
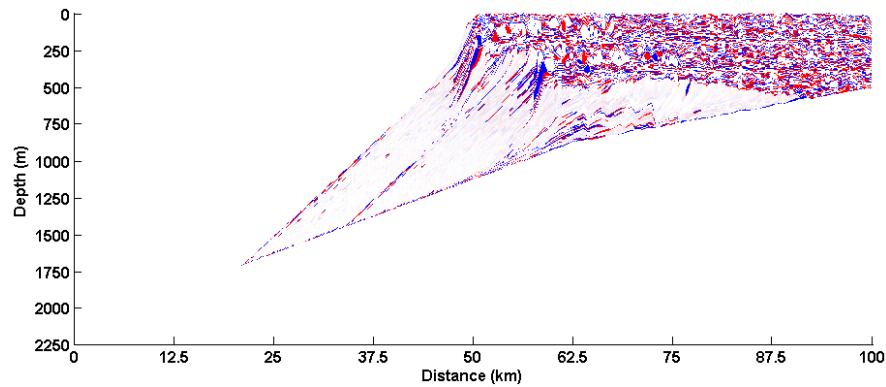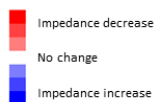

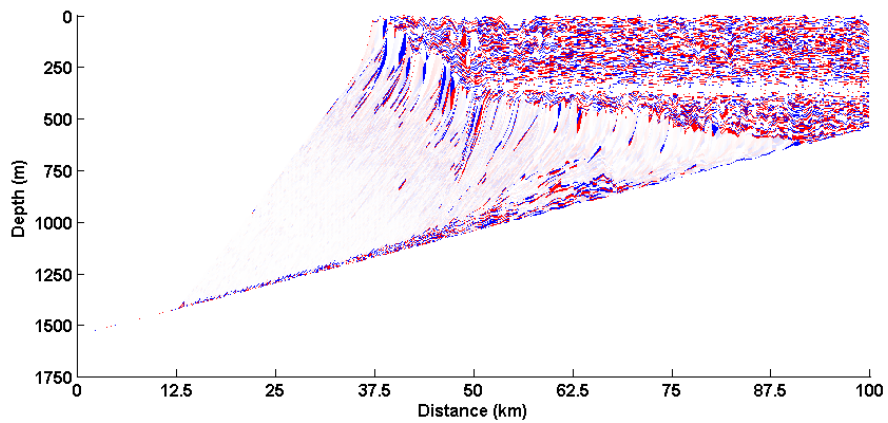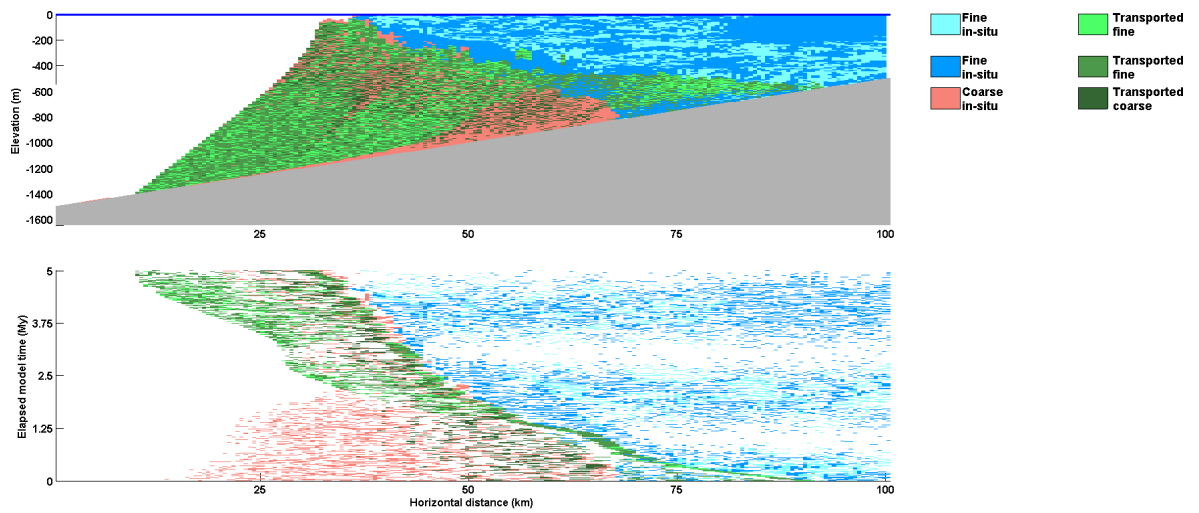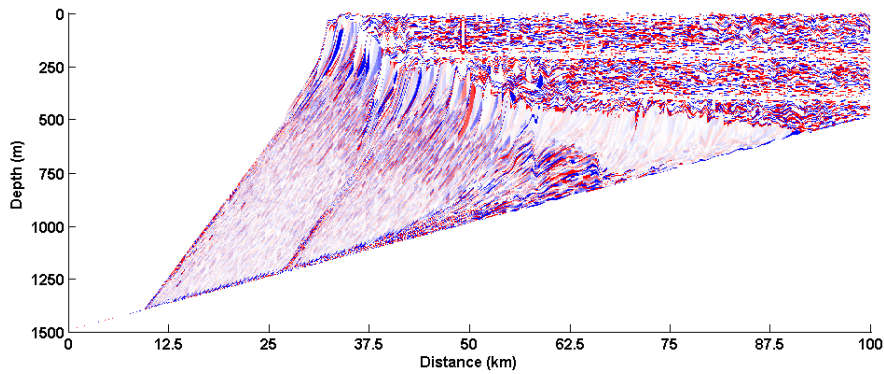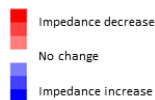(c) Synthetic seismic image with average impedance

Figure A.6: (a) Stratigraphic model and chrono-stratigraphic model of the SHC model run. The interior is dominated by low energy, fine material and the margin by high energy, in-situ produced (b) Synthetic seismic image generated with the textural impedance reflectivity method. (c) The sysnthetic seismic image generated with the average impedance reflectivity method

the standard model.

A.7   Model run SHD

Model run SHD (fig.A.7) was created with double the production rates of the standard model. Higher production rates generate thicker sequences. The model confirms all the observation made in the standard model.

A.8   Model run SHF

Model run SHF (fig.A.8) was created with lower eustatic sea level period compared to the standard model. The model confirms all the observation made in the standard model.

A.9   Model run SHG

Model run SHG (fig.A.9) was created with lower eustatic sea level amplitude compared to the standard model. The model confirms all the observation made in the standard model.

(a) Cross section and chrono-strat section
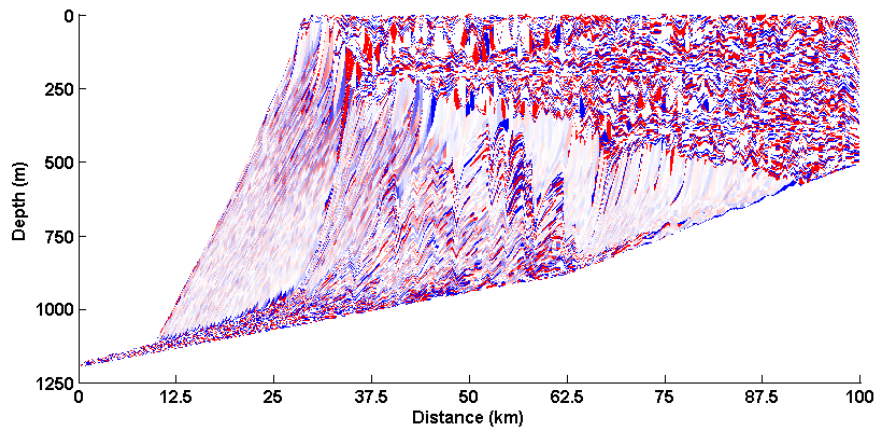
(b) Synthetic seismic image with textural impedance

248
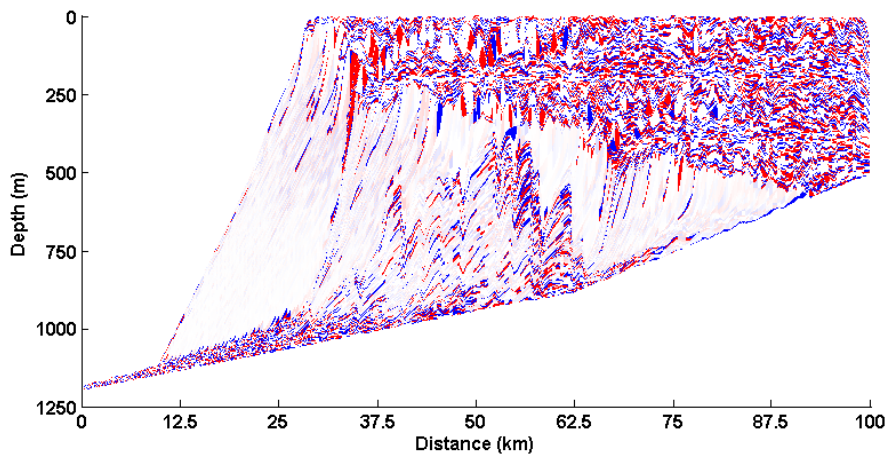
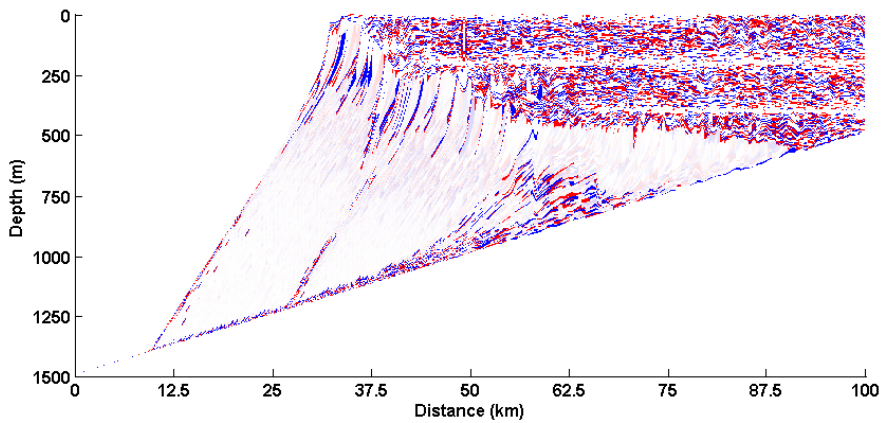(c) Synthetic seismic image with average impedance

Figure A.7: (a) Stratigraphic model and chrono-stratigraphic model of the SHD model run. The interior is dominated by low energy, fine material and the margin by high energy, in-situ produced (b) Synthetic seismic image generated with the textural impedance reflectivity method. (c) The sysnthetic seismic image generated with the average impedance reflectivity method

(a) Cross section and chrono-strat section

(b) Synthetic seismic image with textural impedance

(c) Synthetic seismic image with average impedance

249
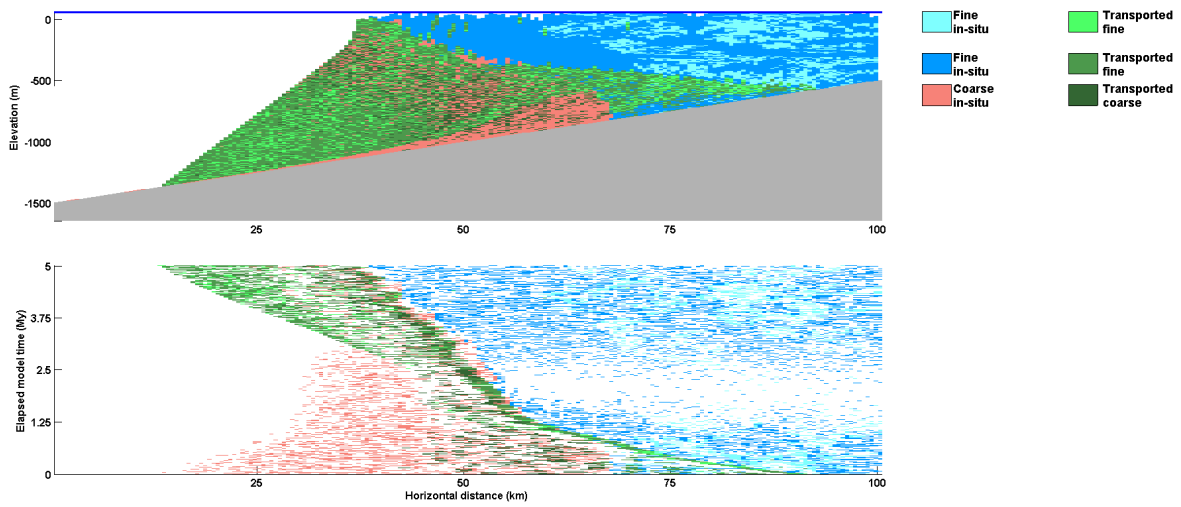
Figure A.8: (a) Stratigraphic model and chrono-stratigraphic model of the SHF model run. The interior is dominated by low energy, fine material and the margin by high energy, in-situ produced (b) Synthetic seismic image generated with the textural impedance reflectivity method. (c) The sysnthetic seismic image generated with the average impedance reflectivity method

(a) Cross section and chrono-strat section

(b) Synthetic seismic image with textural impedance

(c) Synthetic seismic image with average impedance

250

Figure A.9: (a) Stratigraphic model and chrono-stratigraphic model of the SHG model run. The interior is dominated by low energy, fine material and the margin by high energy, in-situ produced (b) Synthetic seismic image generated with the textural impedance reflectivity method. (c) The sysnthetic seismic image generated with the average impedance reflectivity method

B Appendix B - Effects of cross platform sediment transportation model runs

B.1 MS1-Deposition threshold 0.5m and random path transportation direction.

Model runs with water depth depositional threshold of 0.5m and random path transportation direction show that the random path sediment transportation mainly effects the horizontal dimensions of the generated geobodies. For low transported fraction (0.1) relatively small shoals are formed that mainly aggrade and quickly disappear. The autocycles are composed mainly by in-situ material (Fig.B.1a). As the transported fraction increases to medium (0.3, Fig.B.1b) and high (0.5, Fig.B.1c) the generated shoals prograde towards more proximal (0km horizontal distance), with the autocycles dominated by transported material.

The number of isolated geobodies on the interior decreases and the geobodies become volumetrically bigger as the transported fraction increases (Table 7.5). Because transportation includes a random step along the depositional strike not all sediment flow paths that initiate more proximal than a shoal deposit on the proximal part of the shoal. Some flow paths deposit on the sides along the strike of the shoals. As a result of less sediment being deposited on the proximal part(along the dip) of the shoal and more sediment deposited on the strike part, dimensional ratios show an slow increase (Table 7.5).

Spatial entropy on the interior increases for the 0.5-1My EMT when shoals can form. The increase in spatial entropy is related to the transported fraction, with higher fractions generate higher spatial entropy (Fig.B.2).
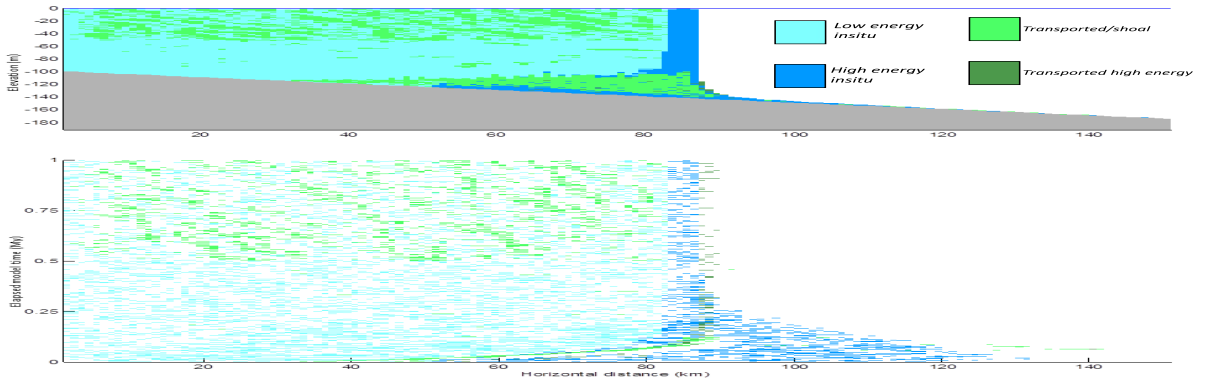
B.2 MS1-Deposition threshold 0.5m and bathymetry controlled transportation direction.
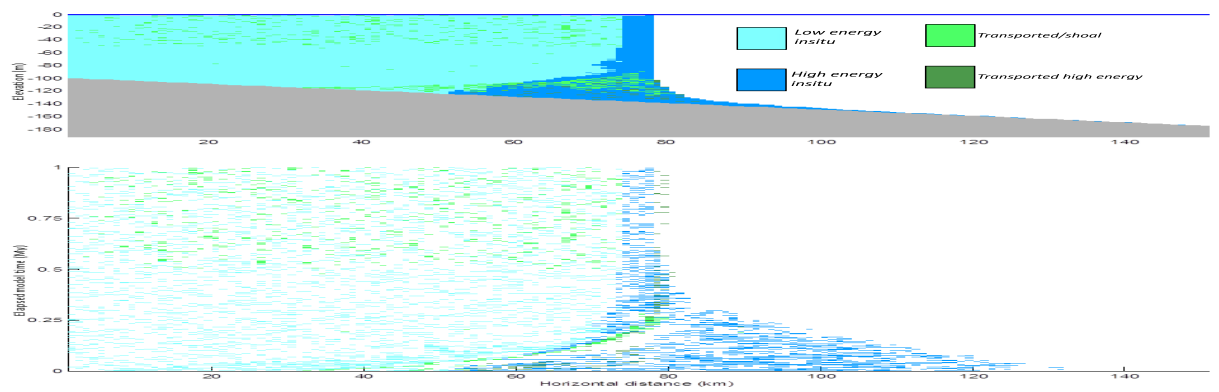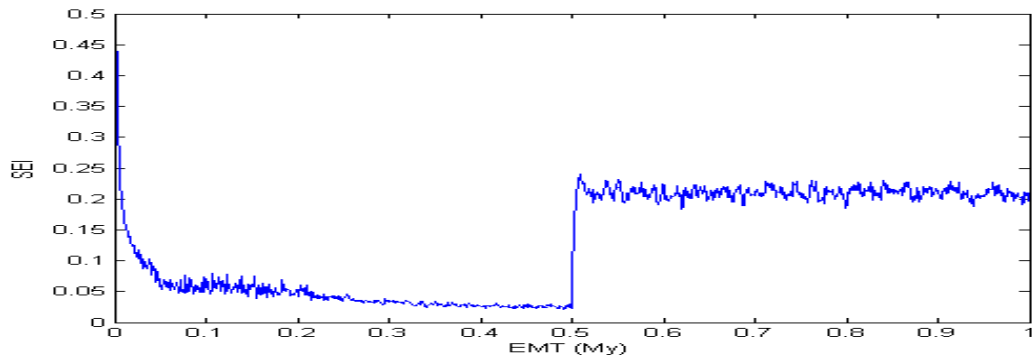
(a) Transported fraction 0.1.
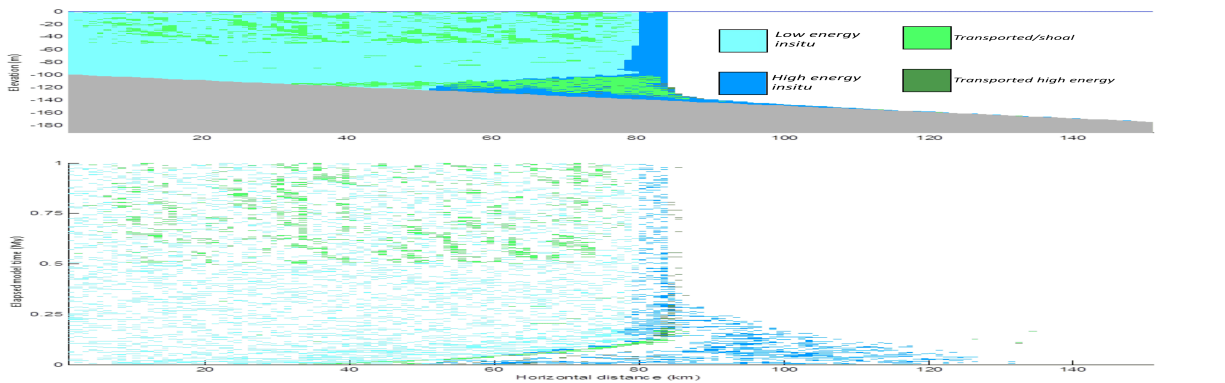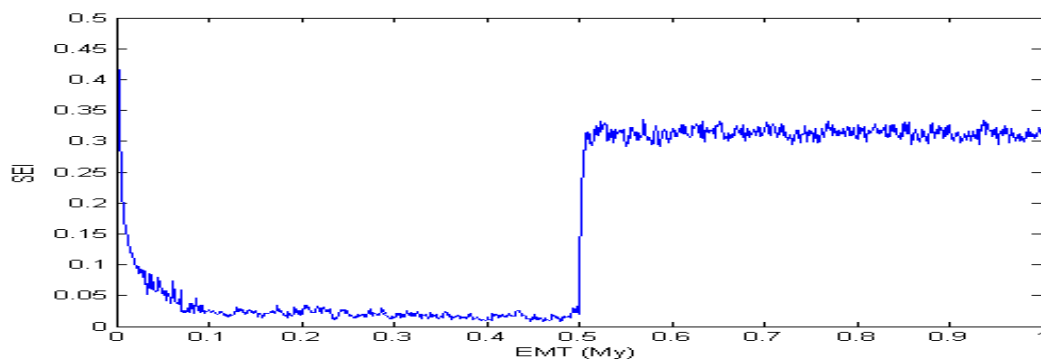

(b) Transported fraction 0.3
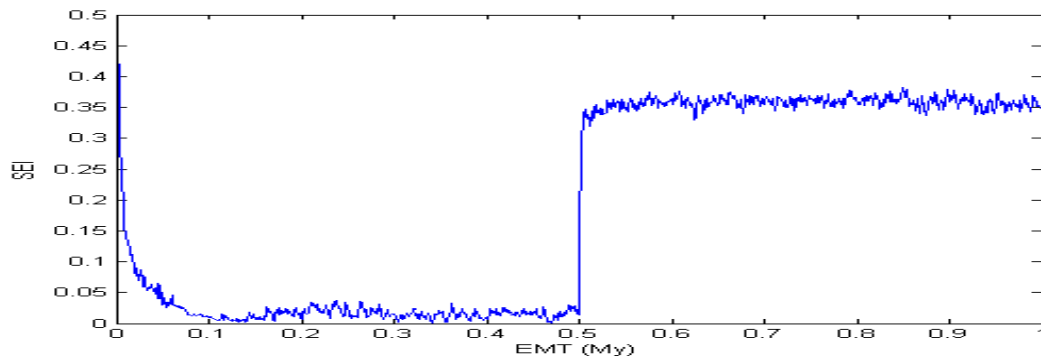

(c) Transported fraction 0.5

Figure B.1: Cross section (TOP) and chrono-stratigraphic section (BOTTOM) of the model runs with 0.5m water depositional threshold and random path transportation direction towards higher values horizontal distance. (a) 0.1 transported fraction. Realtively small, short lived, aggrading shoals are formed. (b) 0.3 transported fraction. Most of the shoals aggrade with a few prograding examples. (c) 0.5 transported fraction. All geobodies slowly prograde towards proximal areas (0km horizontal distance).

252

(a) Transported fraction 0.1.

(b) Transported fraction 0.3

(c) Transported fraction 0.5

Figure B.2: Spatial entropy with time for the model runs with 0.5m water depositional threshold and random path transportation direction towards higher values horizontal distance. The spatial entropy increases with the addition of an extra factory and with transported fraction. (a) Transported fraction 0.1, entropy increases to 0.20. (b)Transported fraction 0.3, entropy increases to 0.31 and (c) transported fraction 0.5, entropy increases to 0.35.

Model runs with water depth depositional threshold of 0.5m and bathymetry controlled transportation direction show that the sediment transportation direction effects the behaviour of the shoals. For all transported fractions the generated shoals mainly aggrade where they form. Cases of shoal progradation (Fig.B.3b and Fig.B.3c) do not show any prefer progradation direction.

The number of isolated geobodies on the interior decreases and the geobodies become volumetrically bigger as the transported fraction increases (Table 7.5). Because transportation does not have any preferred direction, geobodies grow with the same rate in both along the dip and along the distance directions. Dimensional ratios slightly decrease with increasing transported fractions (Table 7.5).

Spatial entropy on the interior increases for the 0.5-1My EMT when shoals can form. The increase in spatial entropy is related to the transported fraction, with higher fractions generate higher spatial entropy (Fig.B.4).

B.3 MS2-Deposition threshold 1m and random path transportation direction.

Model runs with water depth depositional threshold of 1m and random path transportation direction show that due to higher available accommodation, shoals aggrade for the low (0.1, Fig.B.5a) and the medium (0.3, Fig.B.5b) transportation fractions. Only the highest transportated fraction (0.5, Fig.B.5c) generates some geobodies that prograde in the opposite direction of the transportation.

The number of isolated geobodies on the interior decreases and the geobodies become volumetrically bigger as the transported fraction increases (Table 7.6). Because sediment transportation includes a random step along the depositional strike, not all transportation paths initiated more proximal than a shoal deposit on the proximal part of the shoal. Some sediment is deposited on the sides of the shoal along the strike. As a result geobody lengths along the strike grow too and thus the dimensional ratio increases slowly (Table 7.6).

Spatial entropy on the interior increases for the 0.5-1My EMT when shoals can form. Spatial entropy increases more with increasing transported fractions (Fig.B.6).

B.4 MS2-Deposition threshold 1m and bathymetry controlled transportation direction.

Model runs with water depth depositional threshold of 1m and bathymetry controlled transportation show that due to higher available accommodation, shoals aggrade for the all transported fraction (Fig.B.7). A few geobodies that prograde

for the higher transported fraction (0.5, Fig.B.7c) do not seem to have a preferred progradation direction.

The number of isolated geobodies on the interior decreases and the geobodies become volumetrically bigger as the transported fraction increases (Table 7.6). Because sediment transportation does not have any preferred direction, sediment is deposited both along the dip and along the strike areas of the shoals. As a result, geobody lengths increase with similar rates in both directions and the dimensional ratio is not effected by the transported fraction (Table 7.6).

Spatial entropy on the interior increases for the 0.5-1My EMT when shoals can form. The increase in spatial entropy follows the increase in the transported fraction (Fig.B.8).

B.5 MS3-Deposition threshold 0.5m and random path transportation direction.

Low transported fraction (0.1, Fig.B.9a) generates relatively small, relatively short lived, aggradational geobodies. Medium transported fraction (0.3, Fig,B.9b) generates an almost equal number of aggrading and prograding geobodies. The high transported fraction (0.5, Fig.B.9c) generates mainly prograding geobodies. The progradation direction is opposite of the transportation direction.

Similar to the previous examples, the number of isolated geobodies decreases and their volume increases with the transported fraction. The random path transportation direction deposits material both on the most proximal part of the shoal, along the depositional dip and the side areas of the shoals, along the depositional strike. As a result, the shoal geobodies grow in length along the dip and the strike and their dimensional ratios increase slowly with increasing transported fractions (Table 7.7).

Spatial entropy on the interior increases with the addition of two extra facies (transported material from the in-situ factories) relative to the spatial entropy values before the formation of the shoals (0-0.5My EMT). The increase in the spatial entropy is higher with higher transportation rates (Fig.B.10). The increase in spatial entropy with transported fraction implies that as more volume of transported is deposited on the interior, the spatial connectivity of the facies decreases.

Calculation of Markov metric, m, shows that formation of autocycles increases the strata order. Strata with low transportation rates have a m value of 0.14 and probability finding a m value equal to or greater than the observed within the PDF of random shuffling, of 0.4644 (Fig.B.11b).

Shoal formation due to medium transported fractions results to increased strata order with $m = 0.29$ and $p = 0.0083$ (Fig.B.11b). As the transported fraction increases, the shoals grow bigger and the strata order also increases $()m = 0.3$ and

$p = 0.0042$ for 0.5 transported fraction, Fig.B.11c).

TP matrices calculated for the facies successions on the interior show that in-situ produced facies tend to vertically pass to the other in-situ produced facies. Transported facies (shoals) also tend to pass to transported facies and the probability of transported to transported facies transition increases with increasing transported fraction.

B.6   MS3-Deposition threshold 0.5m and bathymetry controlled transportation direction.

The number of isolated geobodies on the interior decreases and the geobodies become volumetrically bigger as the transported fraction increases (Table 7.7). Because transportation moves material onto bathymetric highs, sediment is deposited all around a shoal body. As a result, geobody lengths grow with similar rates both along the dip and the strike directions and thus their dimensional ratios change very little and are independent of transported fraction (Table 7.7).

Spatial entropy on the interior increases for the 0.5-1My EMT when shoals can form. The increase in spatial entropy follows the increase in transported fraction from low (0.1, Fig.B.14a) to medium (0.3, Fig. B.14b). Further increase in the transported fraction seems to have no effect on the spatial entropy of the interior (Fig.B.14c).

The similar values of spatial entropy on the interior for the medium and high transported fractions indicate that for the specific model parameters used here and the specific transportation direction, there is a maximum value of spatial entropy on the interior relative to the volume of the transported material. Further increase in the volume of the transported material deposited on the interior, has no effect on spatial entropy and the spatial connectivity of the facies.

Formation of autocyclic shoals increases the strata order in the generated model runs. Facies distributions for low transported fraction have $m = 0.11$ and high probability to have been formed by chance ($p = 0.49$) (Fig.B.15a). As the transported fraction increases, more transported material is deposited on the interior under the specific conditions controlling shoal formation and strata order increases.

Strata distributions for medium transported fraction (0.3) have $m = 0.24$ and $p = 0.274$ (Fig.B.15b) and for high transported fraction (0.5), $m = 0.38$ and $p = 0$ (Fig.B.15c).

TP matrices for the model runs generated with the specific model parameters indicate that model facies 3 (the transported factory from in-situ producing factory 1) tends to be on the top of the shoal formations. Model facies 3, more than 60% of the cases, passes vertically to in-situ produced facies, for all transported fractions (Fig.B.16).

The same trend of facies 3 passing vertically to in-situ facies and thus appearing on the top of the autocyclic shoal, is repeated for several other points that were tested on the platform (the results from these measurements are not shown here). Further testing is required to examine if this is a general trend and identify its controls or only related to the specific parameters used here.

B.7 Spatial distribution of supratidal and subtidal areas

Spatial distribution and form of supratidal (islands) and subtidal areas do not show any clear relationship with neither transportation direction nor transportation rate (Fig.B.17). Similar to the model runs with one producing factory on the interior, the effect of processes not included in the model is implied.
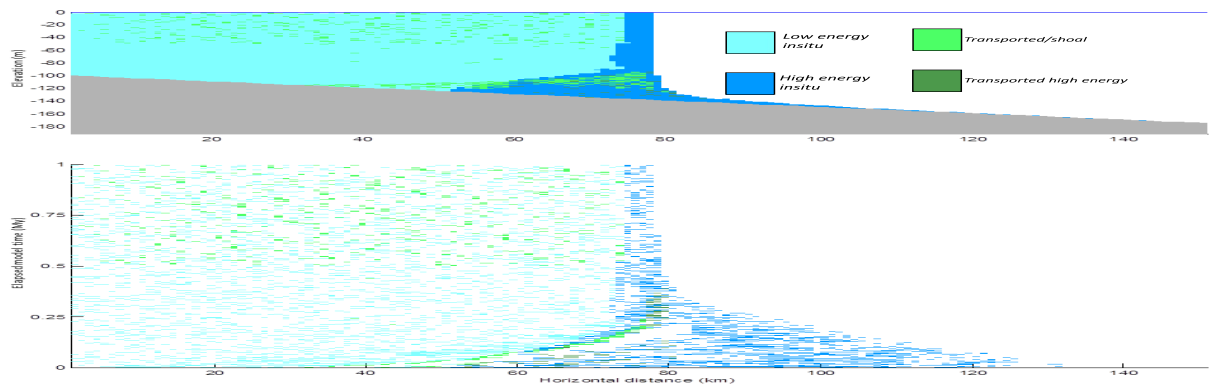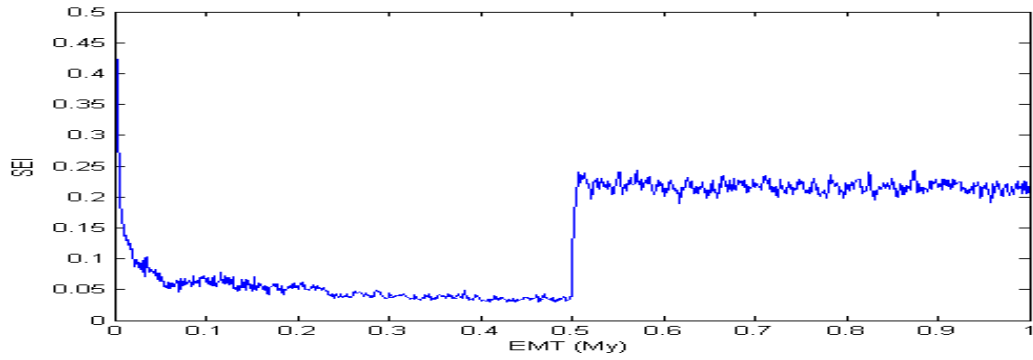
(a) Transported fraction 0.1.
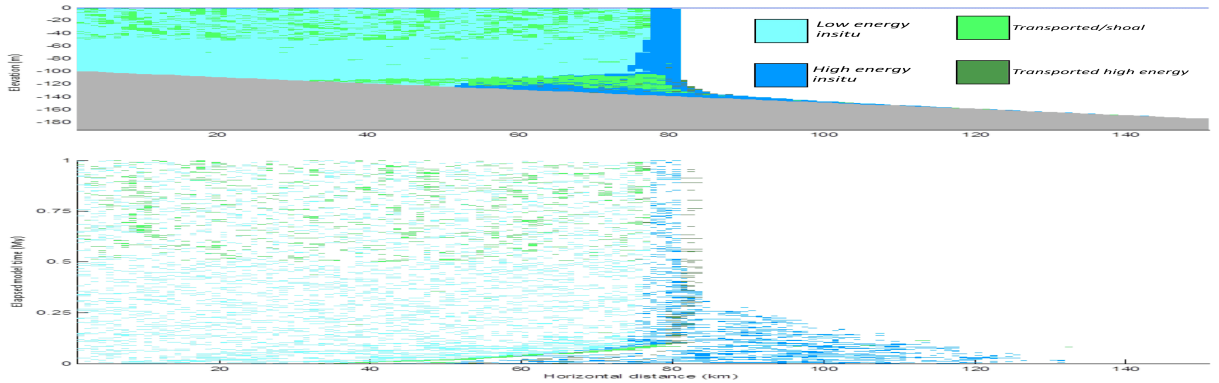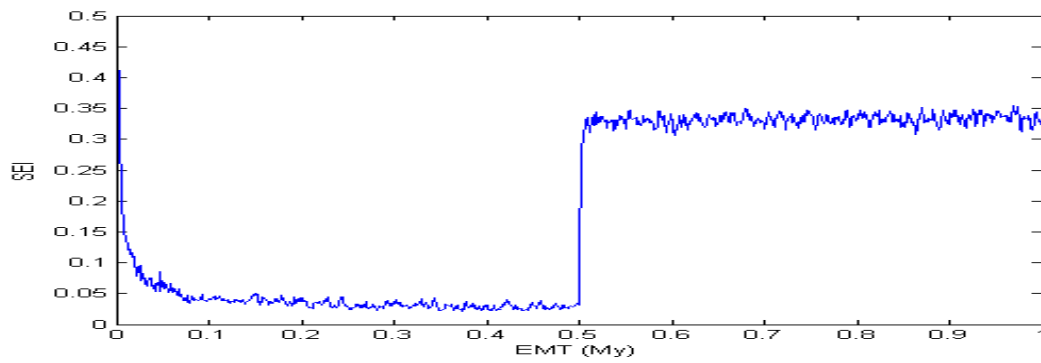

(b) Transported fraction 0.3
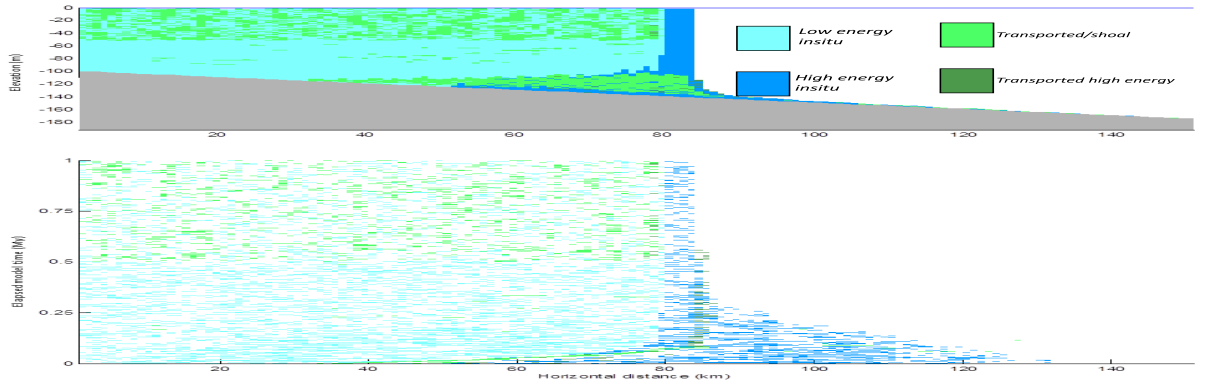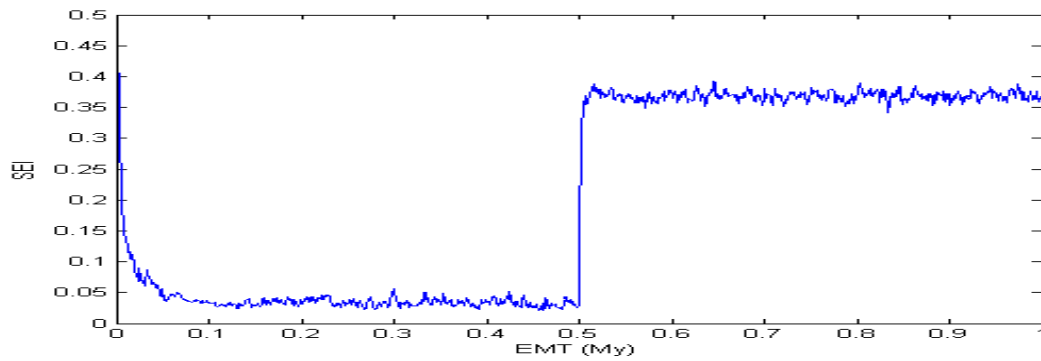

(c) Transported fraction 0.5

Figure B.3: Cross section (TOP) and chrono-stratigraphic section (BOTTOM) of the model runs with 0.5m water depositional threshold and bathymetry controlled transportation direction. (a) 0.1 transported fraction. Realtively small, short lived, aggrading shoals are formed. (b) 0.3 transported fraction. Most of the shoals aggrade with a few prograding examples with progradation direction both more distal (high values horizontal distance) and more proximal (0km horizontal distance). (c) 0.5 transported fraction. The majority of the geobodies aggrade. When progradation is observed, does not have any prefered direction.

(a) Transported fraction 0.1.

(b) Transported fraction 0.3

(c) Transported fraction 0.5

Figure B.4: Spatial entropy with time for the model runs with 0.5m water depositional threshold and bathymetry controlled transportation direction. The spatial entropy increases with the addition of an extra factory and with transported fraction. (a) Transported fraction 0.1, entropy increases to 0.21. (b)Transported fraction 0.3, entropy increases to 0.34 and (c) transported fraction 0.5, entropy increases to 0.36.

(a) Transported fraction 0.1.

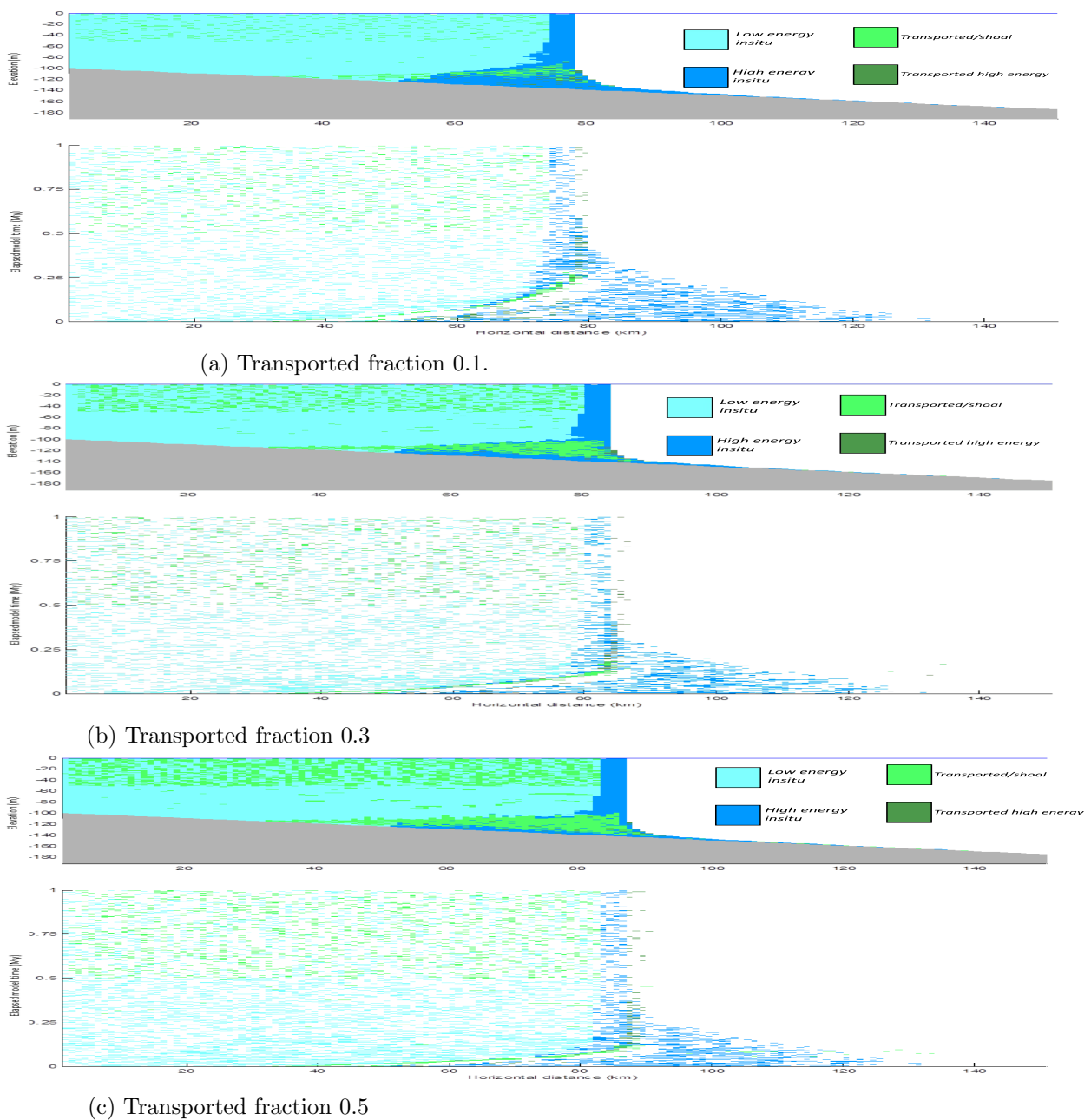(b) Transported fraction 0.3
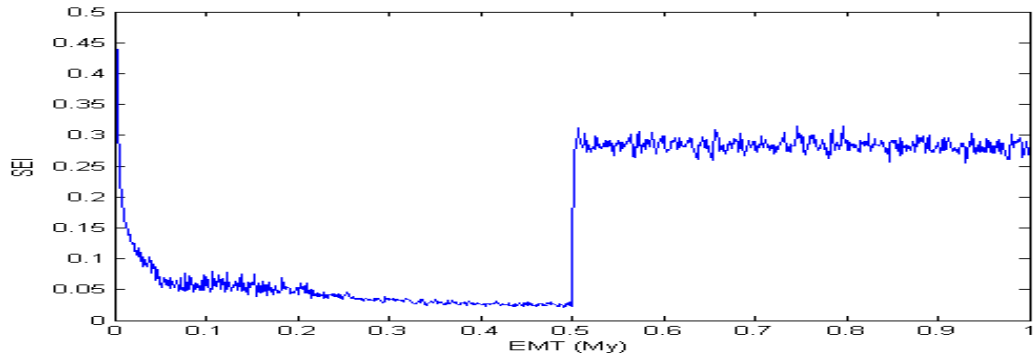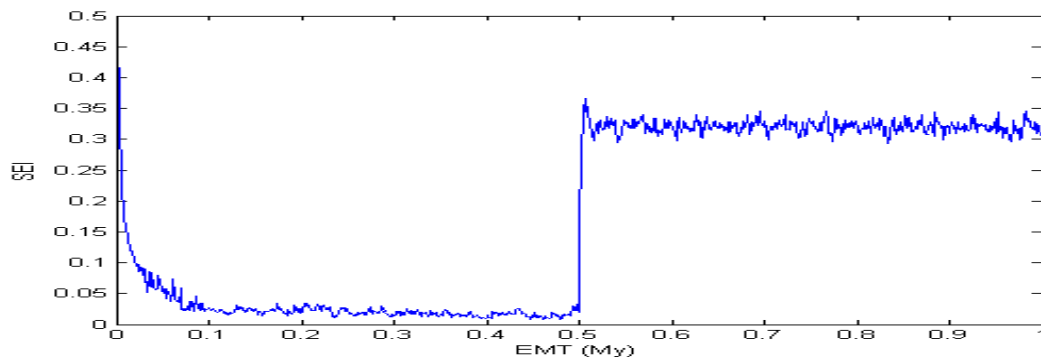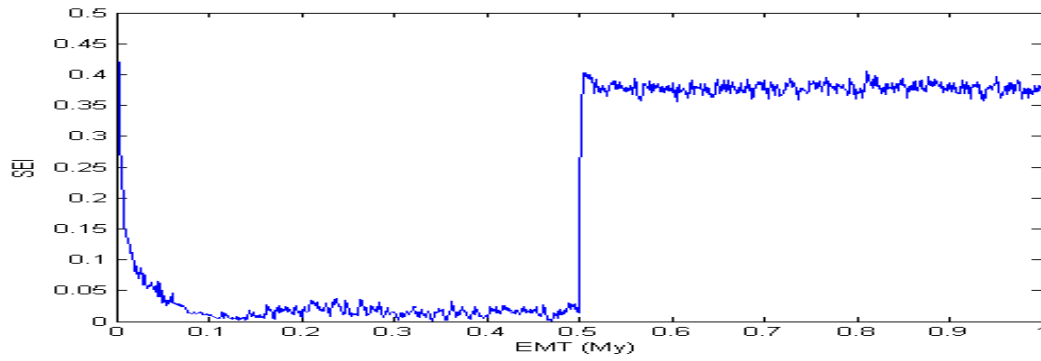

(c) Transported fraction 0.5

Figure B.5: Cross section (TOP) and chrono-stratigraphic section (BOTTOM) of the model runs with 1m water depositional threshold and random path transportation direction towards more distal (higher values horizontal distance). (a) 0.1 transported fraction. Realtively small, short lived, aggrading shoals are formed. (b) 0.3 transported fraction. Mainly aggrading geobodies with a few prograding in the opposite direction of transportation (c) 0.5 transported fraction. The majority of the geobodies aggrades with a few prograding examples in the opposite direction of transportation.
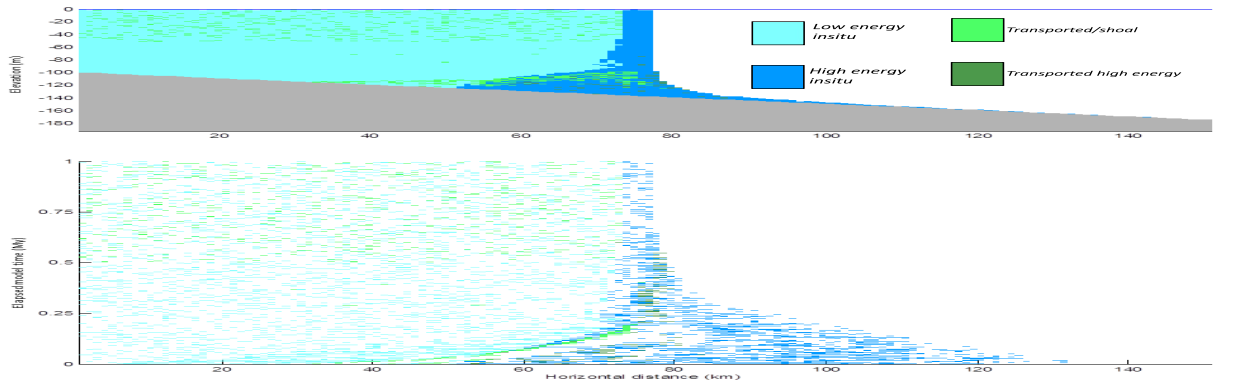
(a) Transported fraction 0.1.

(b) Transported fraction 0.3

(c) Transported fraction 0.5

Figure B.6: Spatial entropy with time for the model runs with 1m water depositional threshold and random path transportation direction towards more distal (higher values horizontal distance). The spatial entropy increases with the addition of an extra factory and with transported fraction. (a) Transported fraction 0.1, entropy increases to 0.27. (b)Transported fraction 0.3, entropy increases to 0.30 and (c) transported fraction 0.5, entropy increases to 0.37.

261

(a) Transported fraction 0.1.

(b) Transported fraction 0.3

(c) Transported fraction 0.5

Figure B.7: Cross section (TOP) and chrono-stratigraphic section (BOTTOM) of the model runs with 1m water depositional threshold and bathymetry controlled transportation direction. (a) 0.1 transported fraction. Realtively small, short lived, aggrading shoals are formed. (b) 0.3 transported fraction. Mainly aggrading geobodies. (c) 0.5 transported fraction. The majority of the geobodies aggrades with a few prograding examples without preferred progradation direction.
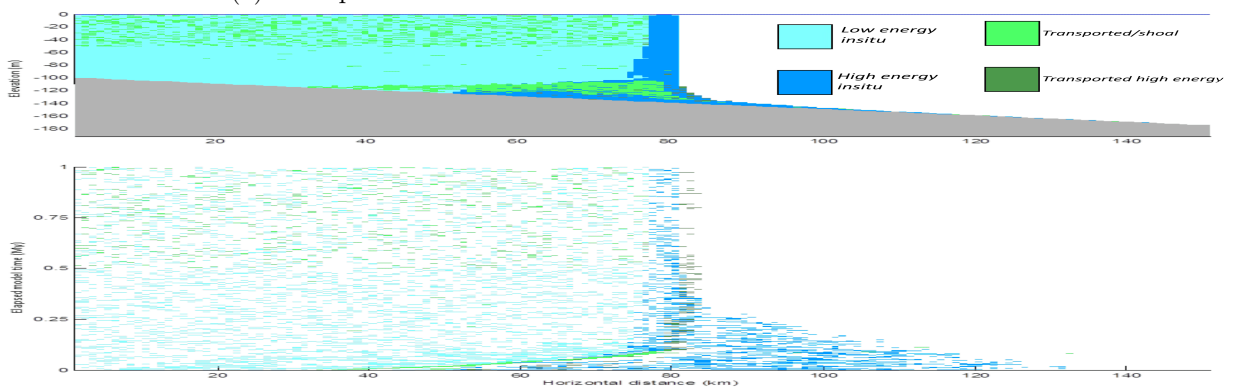
262

(a) Transported fraction 0.1.

(b) Transported fraction 0.3
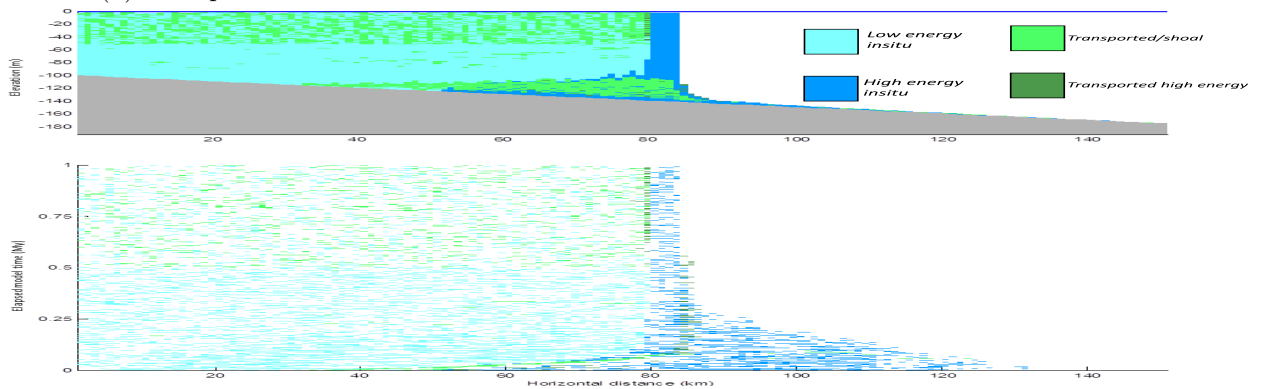

(c) Transported fraction 0.5

Figure B.8: Spatial entropy with time for the model runs with 1m water depositional threshold and bathymetry controlled transportation direction. The spatial entropy increases with the addition of an extra factory and with transported fraction. (a) Transported fraction 0.1, entropy increases to 0.3. (b)Transported fraction 0.3, entropy increases to 0.32 and (c) transported fraction 0.5, entropy increases to 0.4.
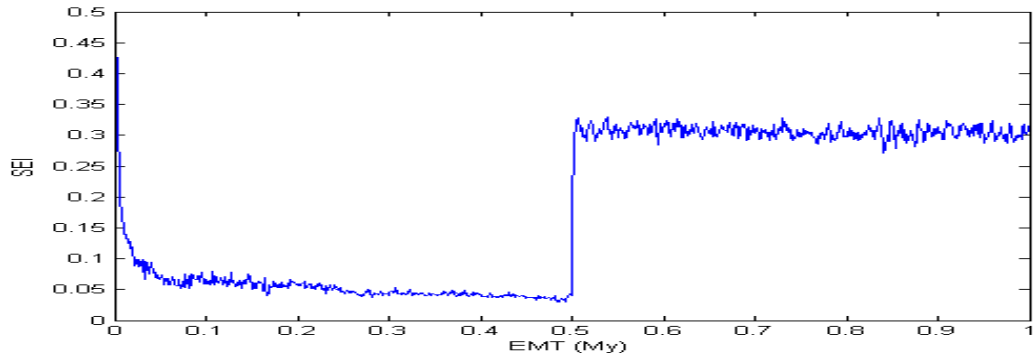
263

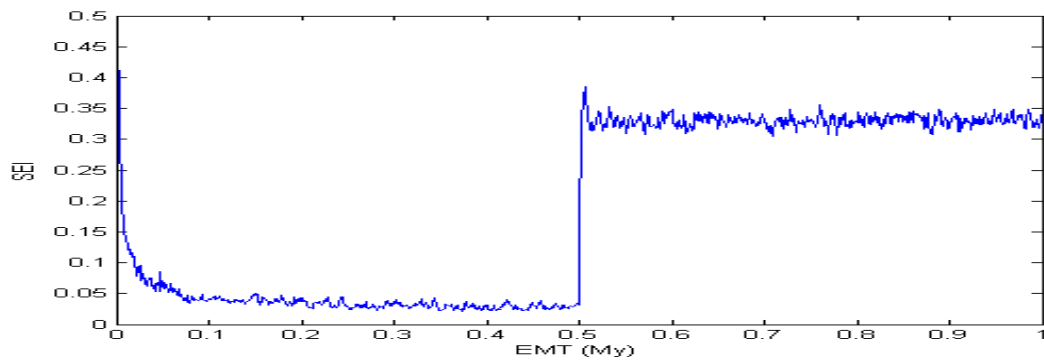(a) Transported fraction 0.1.

(b) Transported fraction 0.3
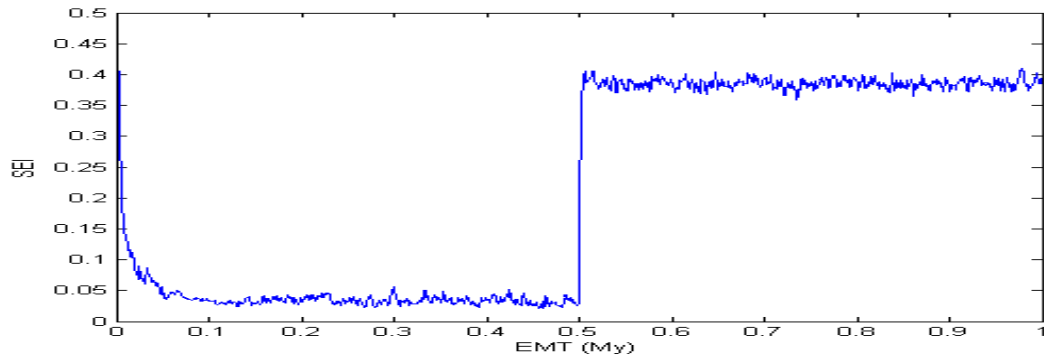

(c) Transported fraction 0.5

Figure B.9: Cross section (TOP) and chrono-stratigraphic section (BOTTOM) of the model runs with 0.5m water depositional threshold, random path transportation direction towards more distal (higher values horizontal distance) and two in-situ producing factories on the interior. (a) 0.1 transported fraction. Realtively small, short lived, aggrading shoals are formed. (b) 0.3 transported fraction. Almost equal number of aggrading and prograding geobodies. Progradation towards more distal (c) 0.5 transported fraction. Mainly geobodies prograde in the opposite direction of transportation.
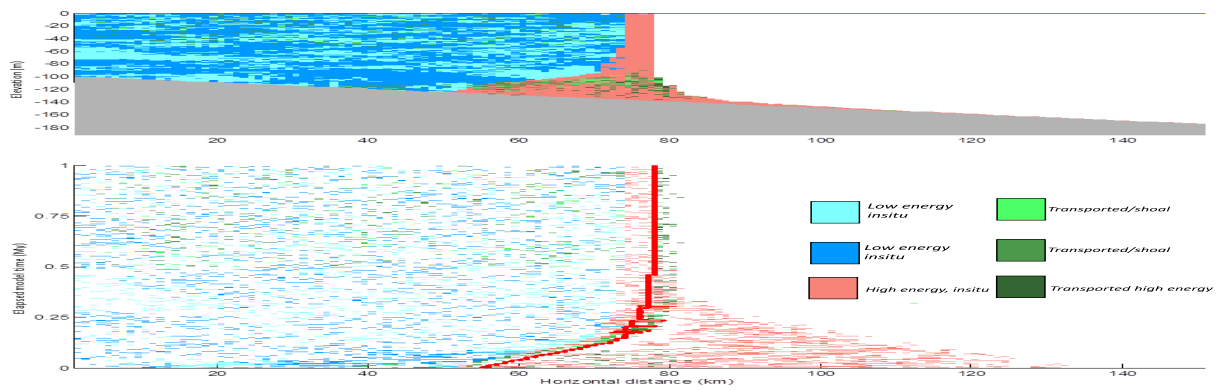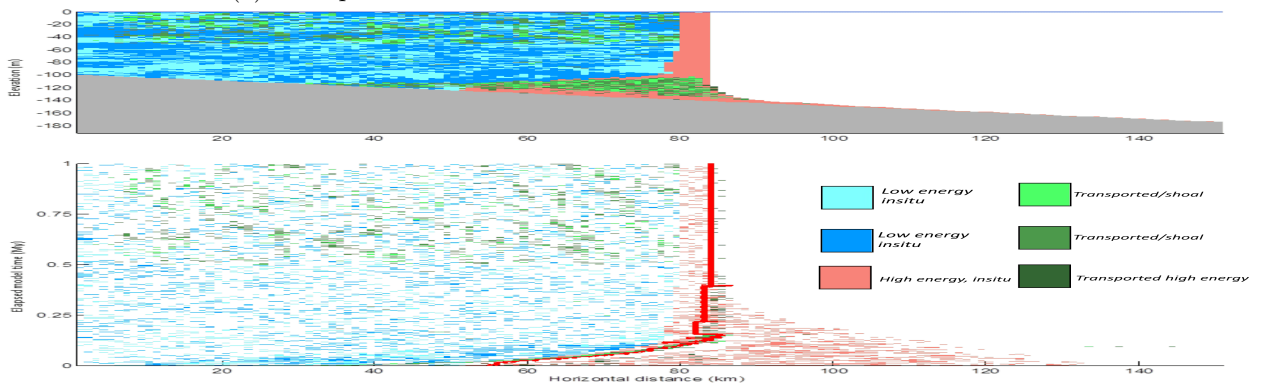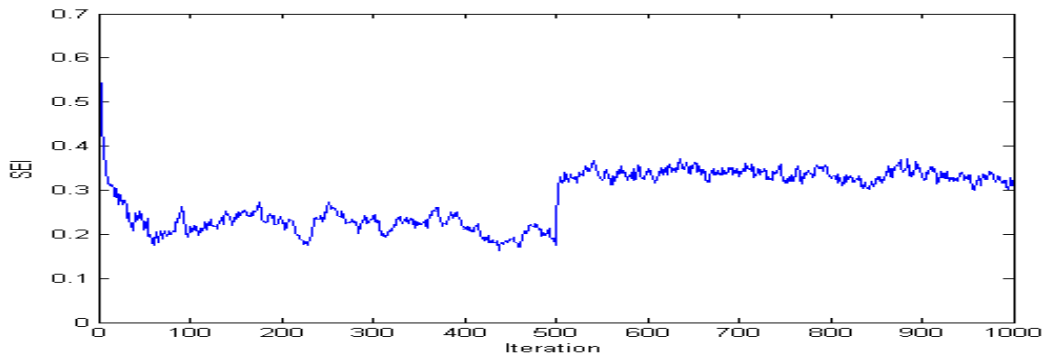
(a) Transported fraction 0.1.
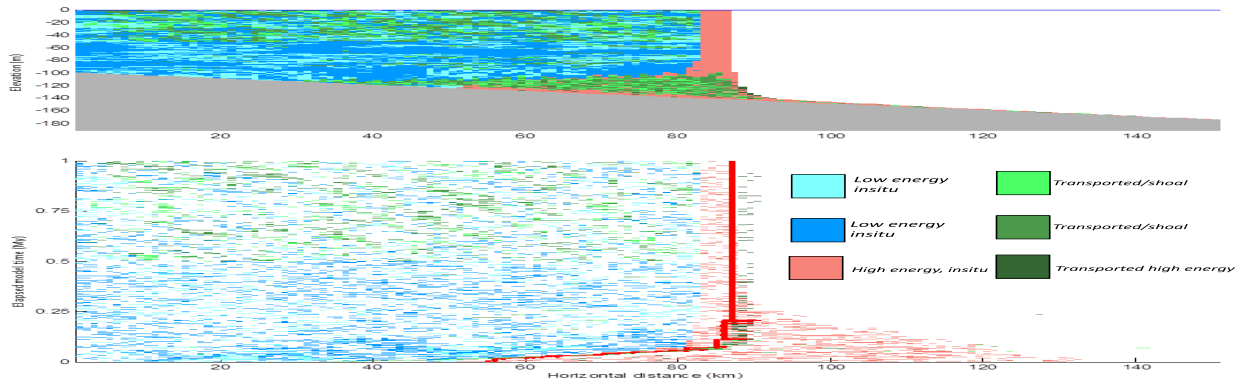

(b) Transported fraction 0.3
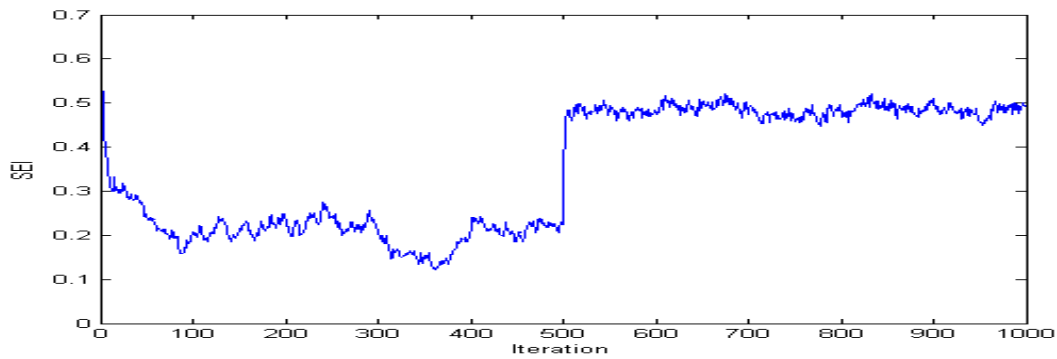
(c) Transported fraction 0.5

Figure B.10: Spatial entropy with time for the model runs with 0.5m water depositional threshold, random path transportation direction towards more distal (higher values horizontal distance) and two in-situ producing factories on the interior. The spatial entropy increases with the addition of an extra factory and with transported fraction. (a) Transported fraction 0.1, entropy increases to 0.31. (b)Transported fraction 0.3, entropy increases to 0.41 and (c) transported fraction 0.5, entropy increases to 0.5.

265

(a) Transported fraction 0.1.

(b) Transported fraction 0.3

(c) Transported fraction 0.5

Figure B.11: Calculated m values of the model run facies distribution (vertical red line) and a histogram (blue) showing the probability density function of m values from 5000 iterations of random shuffling of strata. (a) Transported fraction 0.1, the m value is 0.14 and is located within the PDF of the random shuffles. (b) Transported fraction 0.3, m is 0.29 and lies very close to the right edge of the PDF. (c) transported fraction 0.5, with m 0.3, very close to the right edge of the PDF.

(a) Transported fraction 0.1.

(b) Transported fraction 0.3

(c) Transported fraction 0.5

Figure B.12: Transition probability matrices of the strata successions in model runs with two in-situ producing factories in the interior, 0.5m water depth deposition threshold and random path transportation direction towards more distal (higher values horizontal distance). Facies 1 and 2 correspond to the two in-situ producing factories on the interior. Facies 3 correspond to the transported material of factory 1 and facies 4 the transported material for factory 2. The in-situ factory on the margin and its transported material have been excluded from the calculations. (a) Transported fraction 0.1. (b)Transported fraction 0.3. (c) transported fraction 0.5.

267

(a) Transported fraction 0.1.

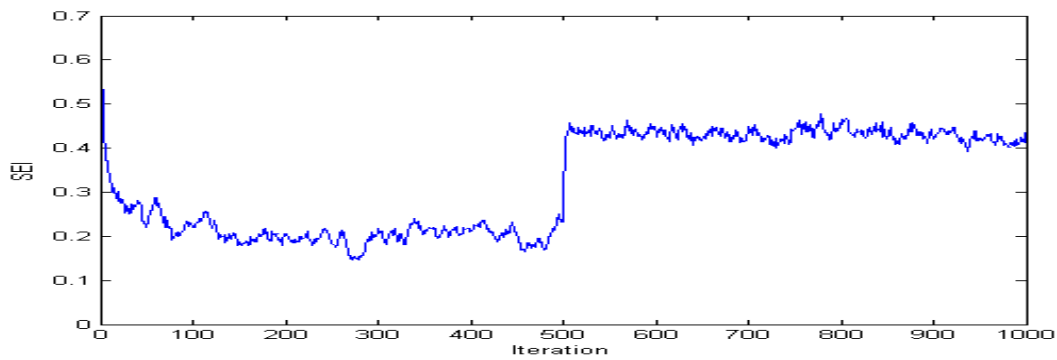(b) Transported fraction 0.3

(c) Transported fraction 0.5

Figure B.13: Cross section (TOP) and chrono-stratigraphic section (BOTTOM) of the model runs with 0.5m water depositional threshold, bathymetry controlled transportation direction and two in-situ producing factories on the interior. (a) 0.1 transported fraction. Realtively small, short lived, aggrading shoals are formed. (b) 0.3 transported fraction. Almost equal number of aggrading and prograding geobodies. Progradation without preferred direction (c) 0.5 transported fraction. Mainly geobodies prograde without preferred direction.
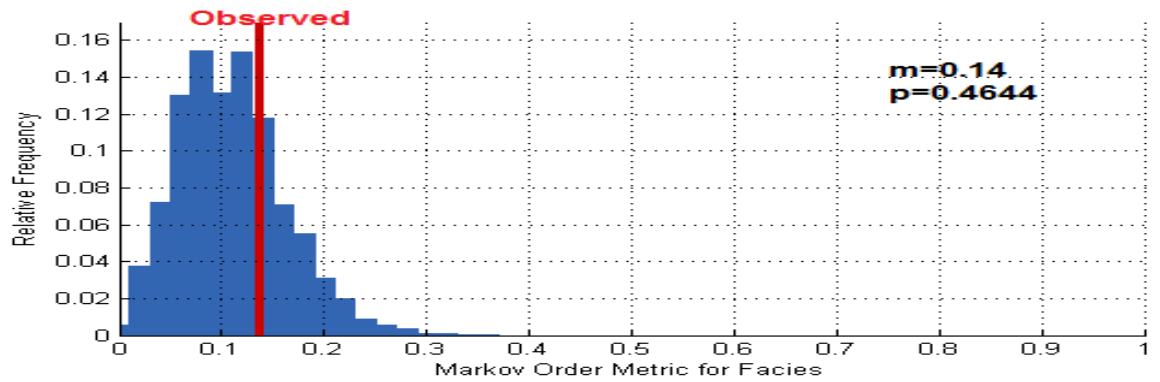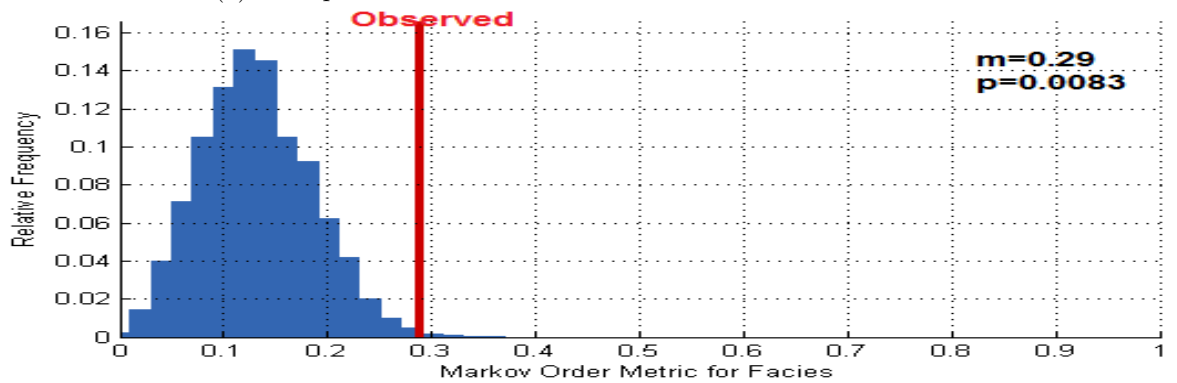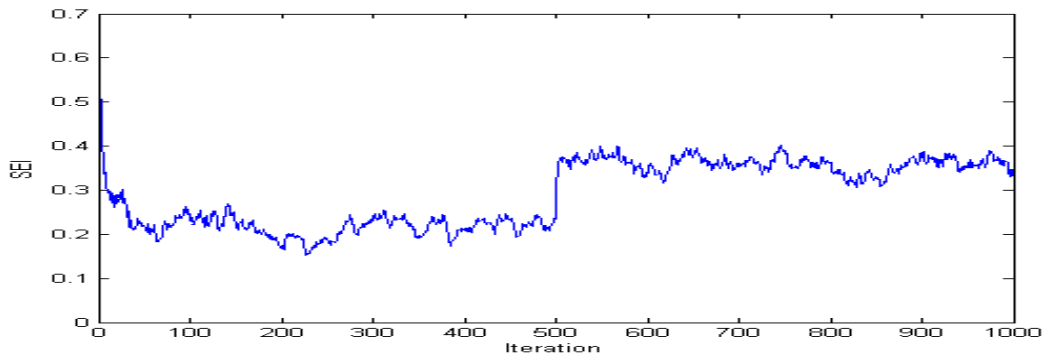
(a) Transported fraction 0.1.
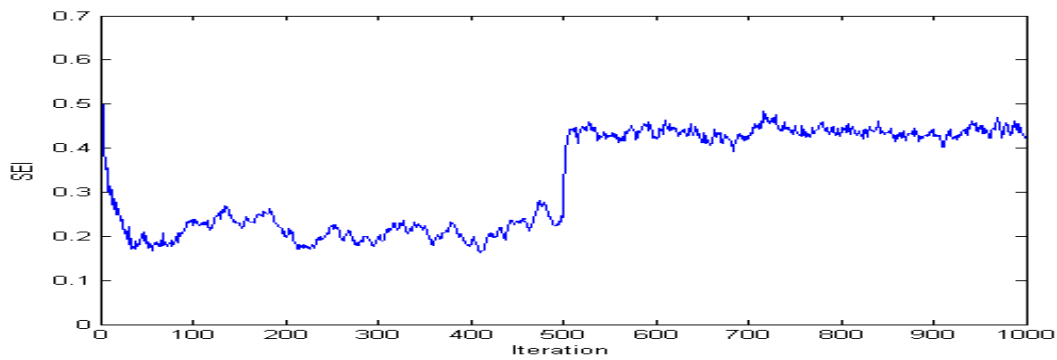
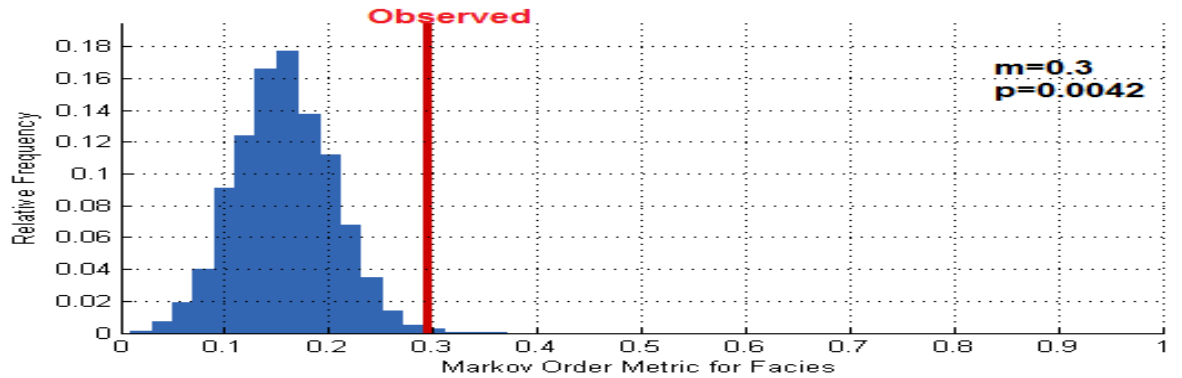(b) Transported fraction 0.3
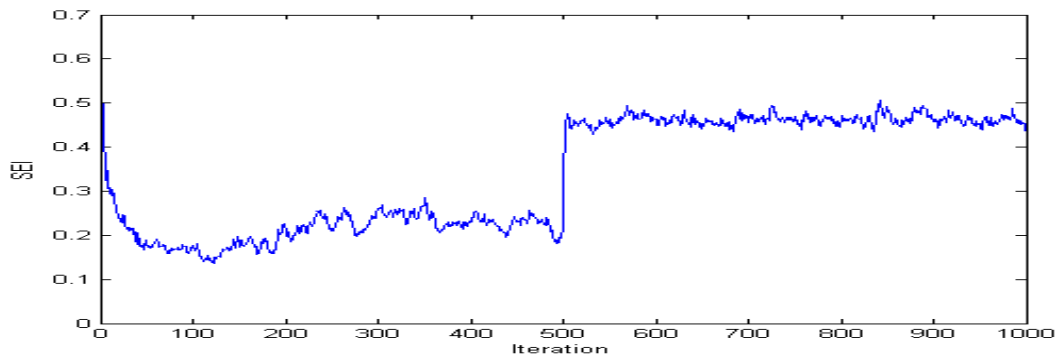
(c) Transported fraction 0.5

Figure B.14: Spatial entropy with time for the model runs with 0.5m water depositional threshold, bathymetry controlled transportation direction and two in-situ producing factories on the interior. The spatial entropy increases with the addition of an extra factory and with transported fraction. (a) Transported fraction 0.1, entropy increases to 0.33. (b)Transported fraction 0.3, entropy increases to 0.42 and (c) transported fraction 0.5, entropy increases to 0.42 which appears to be the maximum entropy value for the specific model parameters and transportation direction.

269
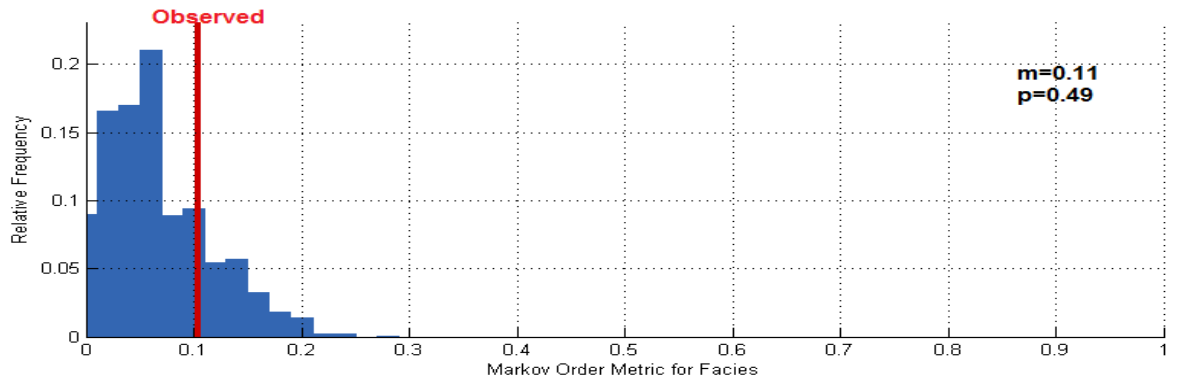
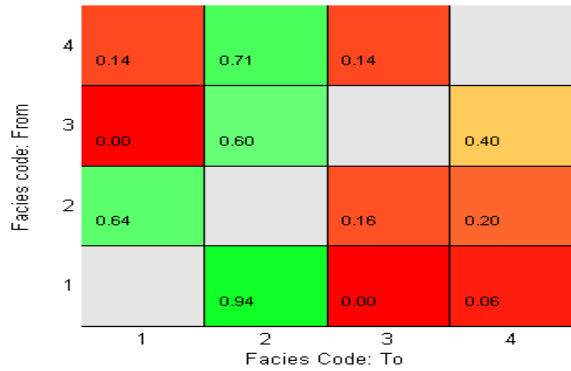(a) Transported fraction 0.1.
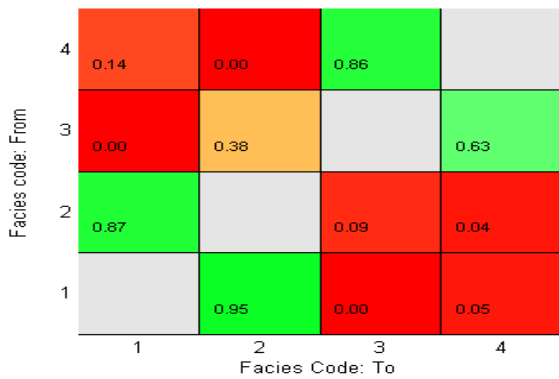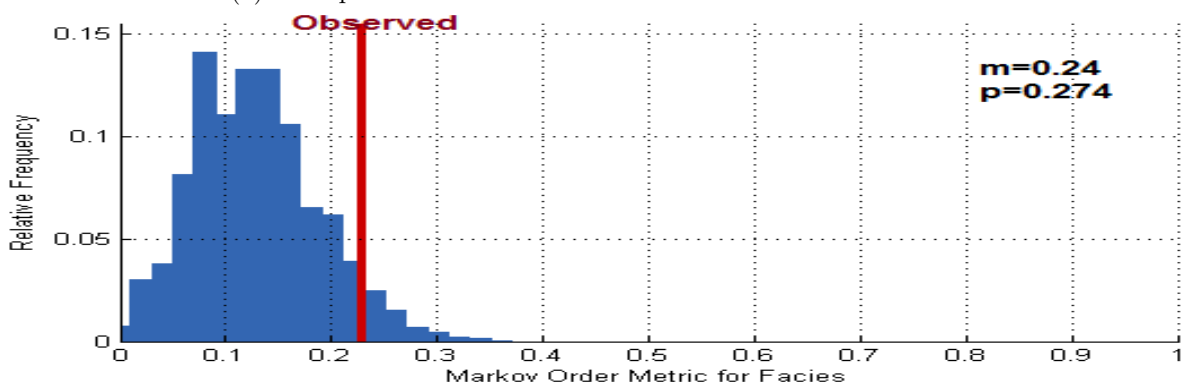

(b) Transported fraction 0.3
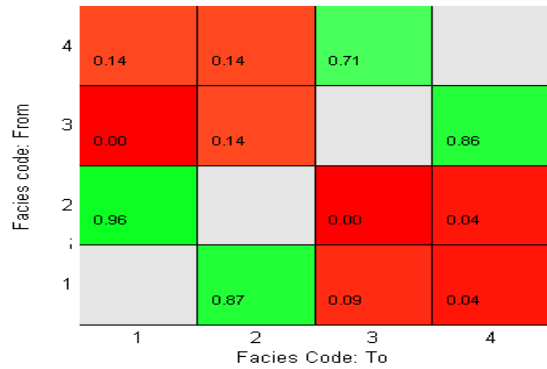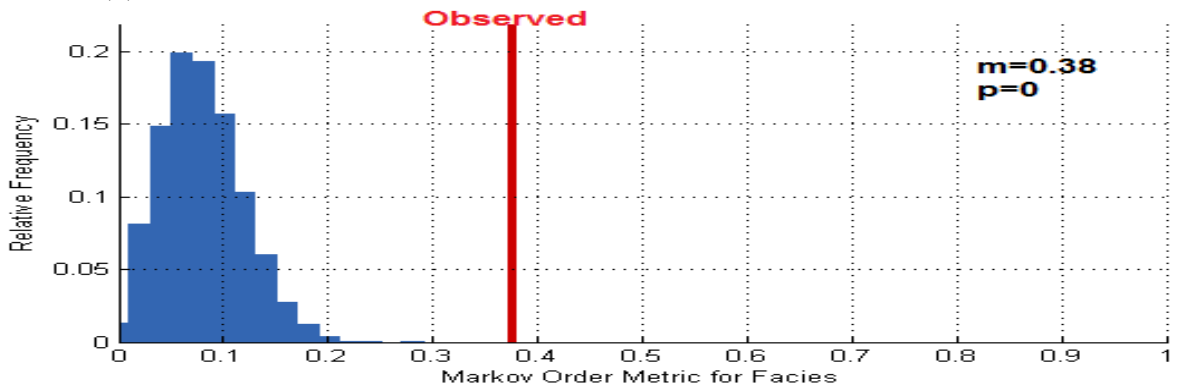

(c) Transported fraction 0.5

Figure B.15: Calculated m values of the model run facies distribution (vertical red line) and a histogram (blue) showing the probability density function of m values from 5000 iterations of random shuffling of strata. (a) Transported fraction 0.1, the m value is 0.11 and is located within the PDF of the random shuffles. (b)Transported fraction 0.3, m is 0.24 which lies to the right side of the PDF. (c) transported fraction 0.5, with m 0.38, outside of the PDF.
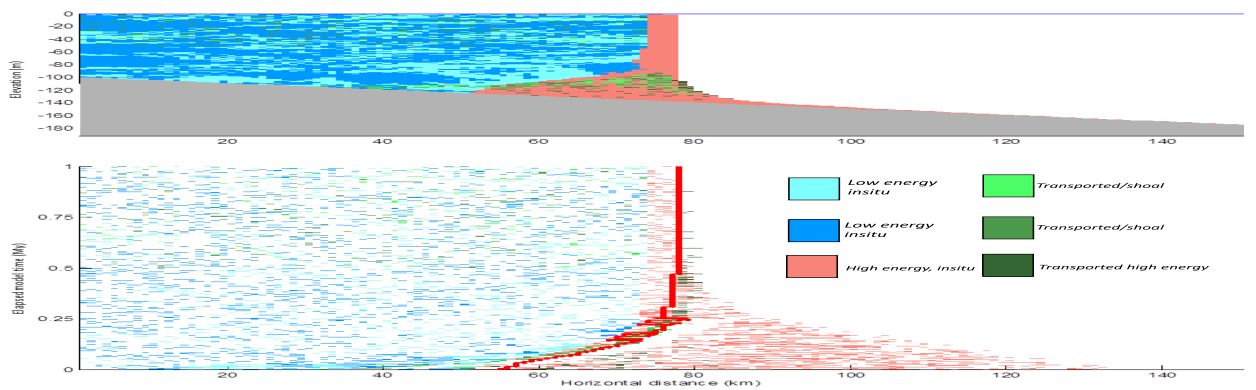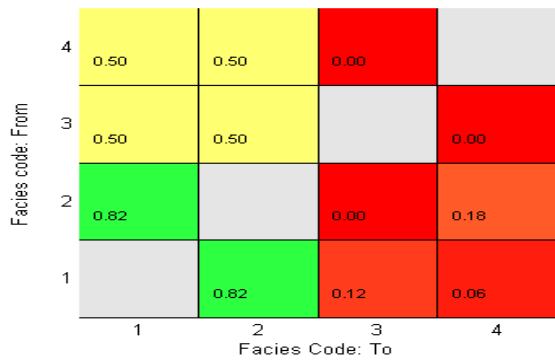
(a) Transported fraction 0.1.
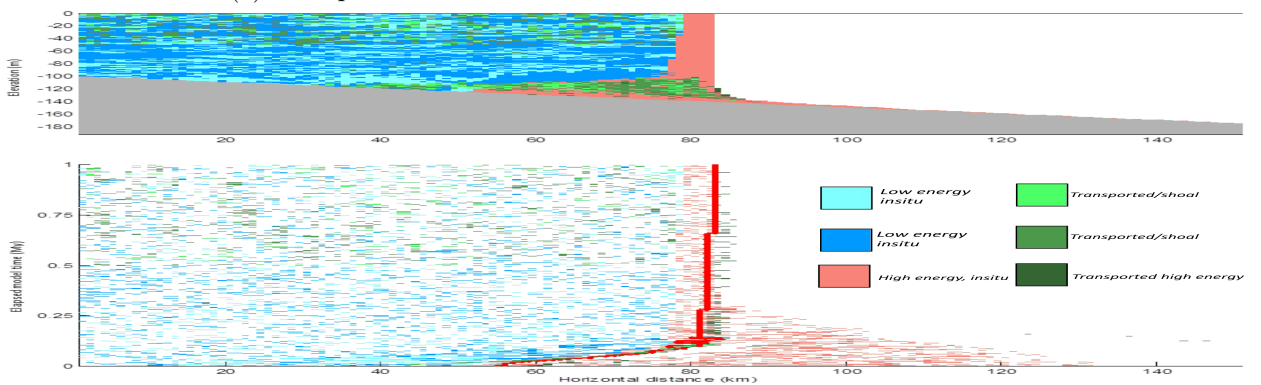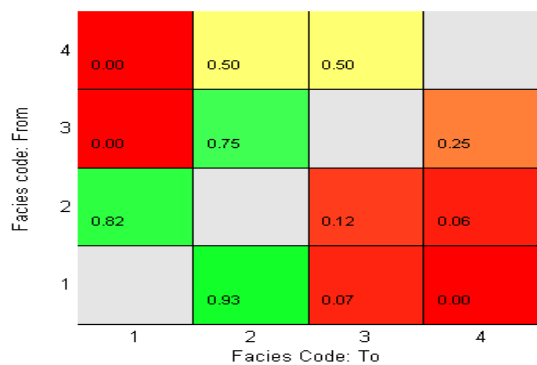

(b) Transported fraction 0.3
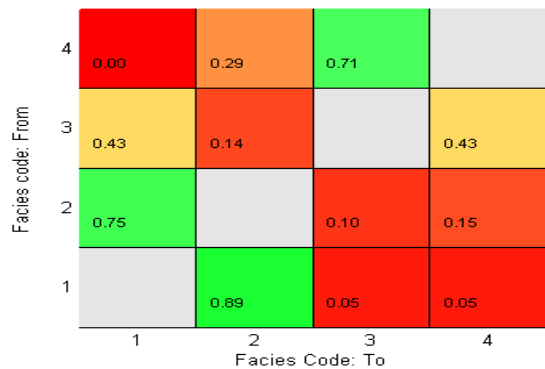
(c) Transported fraction 0.5

Figure B.16: Transition probability matrices of the strata successions in model runs with two in-situ producing factories in the interior, 0.5m water depth deposition threshold and bathymetry controlled transportation direction. Facies 1 and 2 correspond to the two in-situ producing factories on the interior. Facies 3 correspond to the transported material of factory 1, and facies 4 the transported material for factory 2. The in-situ factory on the margin and its transported material have been excluded from the calculations. (a) Transported fraction 0.1. (b)Transported fraction 0.3. (c) transported fraction 0.5.

271

(a) Straight line transportation

(b) Random step transportation

(c) Bathymetry controlled transportation
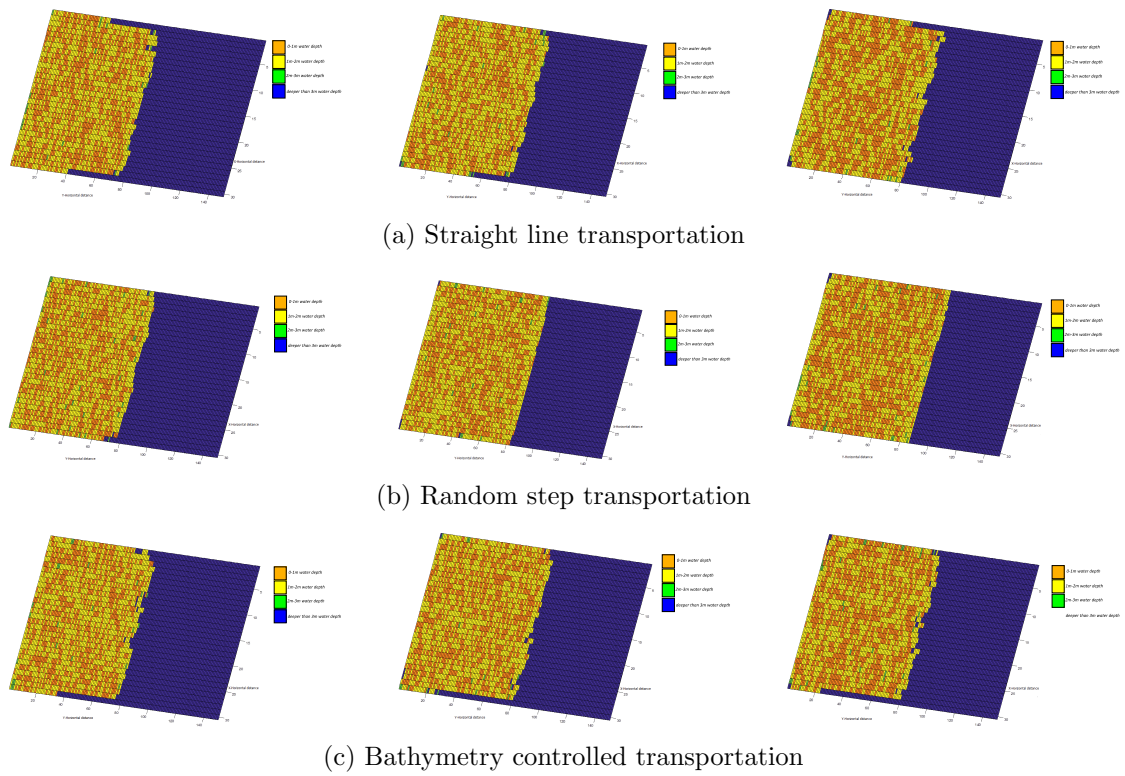
Figure B.17: Map view of model runs with transported fraction 0.1(LEFT), 0.3(MIDDLE) and 0.5(RIGHT) and water depth deposition threshold 1m, showing the spatial distribution and form of supratidal and subtidal areas at 1My EMT. Sediment transportatin direction and rate do not effect the distribution and shape of the islands. The stripes of deep water at the edges of some model runs are temporaray features and are generated by the boundary conditions at the platform edges.

C Appendix C - Bastus stratigraphic forward modelling results

Stratigraphic forward modelling results of the Bastus platform

C.1 EH-A1

Fig.C.1 and Fig.C.2 show a mainly aggradational platform without any sequences. Once the platform margin has been established (0.6 My), it progrades for 7 km total for the whole EMT. All formations show aggradational stacking patterns. Platform interior is dominated by packstones with patch reefs. The platform margin shows reefs with some fragments, while the upper slope is dominated by foraminifera and shell fragments. The dimensions of each platform segment and the strata thickness in each segment are shown in Table.C.1.

Comparison of the model run with the interpreted stratigraphic section reveals that model run EH-A1 fails to properly model the interpreted platform geometry. The numerical model generates a number of features that are not supported by field data. The model run does not show any sequences or facies transitions as shown in the interpreted stratigraphic section. Moreover, the numerical model shows sub-aerial exposure of the platform interior which exposure has not been observed anywhere in the field. It is possible though, that some exposure that has not been mapped might have occurred at the siliciclastic part of the platform. Overall the model run might be probable but it is not a good representation of the Bastus platform.

Table C.1: Length and thickness of EH-A1 model run

Platform segment	Field values	Numerical model
Siliciclastics length	18km	18km
Siliciclastics thickness	60m	60m
Carbonate interior length	28km	30km
Carbonate interior thickness	450m	427m
Margin length	5km	5km
margin thickness	280m	300m
slope thickness	250m	300m
platform type	low angle	0.48^o

Figure C.1: 3D plot of the EH-A1 model run.

Interior packstones
Interior patch reefs
Margin coral/rudists
Pelagic muds

Transported interior
Transported margin

Siliciclastics

Subaerial exposure

Z(m)
0
-200
-400

Y(km)
10
20
30
40
50
60
70
80
90
100

X(km)
5
10
15
20
25
30
35
40
45
50

N

274

Figure C.2: (A) Cross section along the x=25 of the 3D model. The cross section shows siliciclastic dominating the most proximal part (0-18 km), extensive platform interior (18-48 km), aggrading platform margin and upper slope extending to 70 km. (B) Chrono-strat section at the same position as (A) with the platform margin position (red line) superimposed. The platform margin progrades for 7 km once it gets established (0.6 My). (C) Eustatic sea level oscillations with period 0.5 My and amplitude 5m. Interpreted platform geometry for comparison on the top.

Figure C.3: 3D plot of the EH-A2 model run.

Interior packstones

Interior patch reefs

Margin coral/rudists

Pelagic muds

Transported interior

Transported margin

Siliciclastics

Subaerial exposure

Z(m)

Y(km)

X(km)

N

Figure C.4: (A) Cross section along the x=25 of the 3D model. The cross section shows siliciclastic dominating the most proximal part (0-18 km), extensive platform interior (18-48 km), aggrading platform margin and upper slope extending to 69 km. (B) Chrono-strat section at the same position as (A) with the platform margin position (red line) superimposed. The platform margin progrades for 9 km once it gets established (0.6 My). (C) Eustatic sea level oscillations with period 0.5 My and amplitude 10m. Interpreted platform geometry for comparison on the top.

C.2 EH-A2

Fig.C.3 and Fig.C.4 shows a mainly aggradational platform with some progradation and only one sequence. Once the platform margin has been established (0.6 My), the margin progrades for 9km total for the whole EMT. All formations show aggradational stacking patterns. Platform interior is dominated by packstones with patch reefs. The platform margin shows reefs with some fragments, while the upper slope is dominated by foraminifera and shell fragments. The dimensions of each platform segment and the strata thickness in each segment are shown in Table.C.2.

Comparison of the model run with the interpreted stratigraphic section reveals that model run EH-A2 fails to properly model the interpreted geometry. The numerical model generates a number of features that are not supported by field data. The model run does not show any sequences or facies transitions as shown in the interpreted stratigraphic section. Moreover, the numerical model shows extensive sub-aerial exposure of the platform interior which exposure has not been observed anywhere in the field. Furthermore, model run EH-A2 suggests much more progradation of the platform margin than in the interpreted geometry.

Table C.2: Length and thickness of EH-A2 model run

Platform segment	Field values	Numerical model
Siliciclastics length	18km	18km
Siliciclastics thickness	60m	60m
Carbonate interior length	28km	34km
Carbonate interior thickness	450m	442m
Margin length	5km	5km
margin thickness	280m	297m
slope thickness	250m	280m
platform type	low angle	0.45^o

C.3 EL-B1

Fig.C.5 and Fig.C.6 shows a mixed progradational, aggradational platform with one sequence. Once the platform margin has been established (0.6 My EMT), it progrades for 6 km. Most of the progradation occurs before 1.5 My EMT. Platform interior is dominated by packstones with patch reefs. The platform margin shows reefs with few fragments, while the upper slope is dominated by foraminifera and shell fragments. The dimensions of each platform segment and the strata thickness in each segment are shown in Table.C.3.
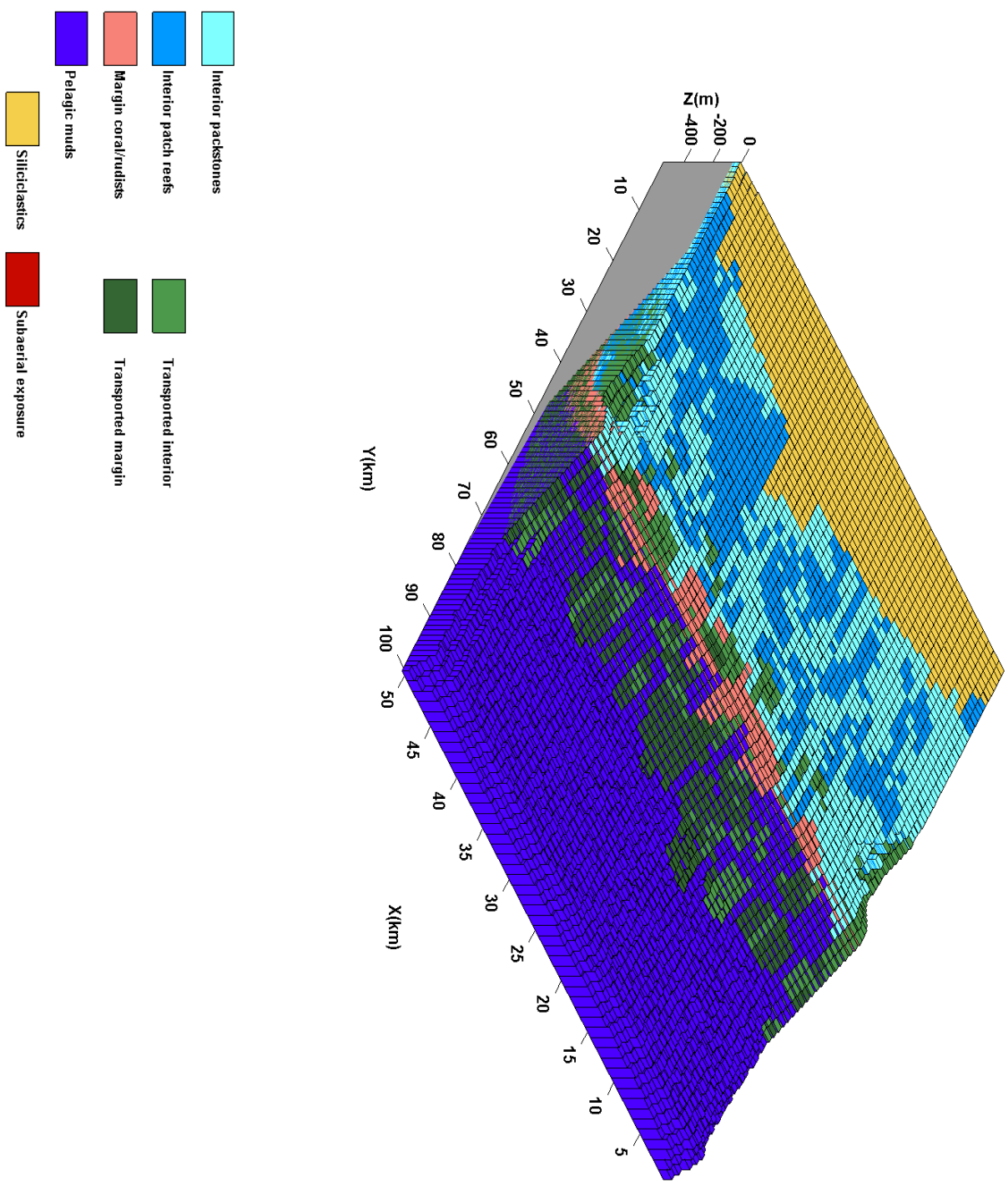
Figure C.5: 3D plot of the EL-B1 model run.

Figure C.6: (A) Cross section along the x=25 of the 3D model. The cross section shows siliciclastic dominating the most proximal part (0-18 km), extensive platform interior (18-48 km), aggrading platform margin and upper slope extending to 71 km. (B) Chrono-strat section at the same position as (A) with the platform margin position (red line) superimposed. The platform margin progrades for 6 km once it gets established (0.6 My). (C) Eustatic sea level oscillations with period 2 My and amplitude 10 m. Interpreted platform geometry for comparison on the top.

Comparison of the interpreted stratigraphic model to model run EL-B1 shows that there is only sequence on model run EL-B1, the platform margin trajectory does not agree with the interpreted stratigraphic section. The model run also shows some sub-aerial exposure on the most proximal areas. Model run EL-B1 does not represent the interpreted geometry.

Table C.3: Length and thickness of EL-B1 model run

Platform segment	Field values	Numerical model
Siliciclastics length	18km	18km
Siliciclastics thickness	60m	60m
Carbonate interior length	28km	30km
Carbonate interior thickness	450m	421m
Margin length	5km	5km
margin thickness	280m	296m
slope thickness	250m	274m
platform type	low angle	0.47^o

C.4   EL-B2

Fig.C.7 and Fig.C.8 shows two sequences and a mixed progradational, aggradational margin. The platform margin progrades for 10 km the first 1.5 My EMT (lower sequence) and at the sequence boundary aggrades for the remaining EMT. Platform interior is dominated by packstones with patch reefs. The platform margin shows reefs with few fragments, while the upper slope is dominated by foraminifera and shell fragments. Significant parts of the platform interior get exposed during ESL lowstands. The dimensions of each platform segment and the strata thickness in each segment are shown in Table.C.4.

Comparing the interpreted stratigraphic section to the EL-B2 model run shows that even though two sequences can be assumed, the nature of the margin trajectory (progradation followed by aggradation), the extensive subaerial exposure and the lack of facies transition make model run EL-B2 not a good model for the Bastus platform.

C.5   EN-C1

Fig.C.9 and Fig.C.10 shows a mainly aggradational platform with only one sequence. Once the platform margin has been established (0.6 My EMT), the margin aggrades for the remaining EMT (total progradation 6km). Platform interior is dominated by packstones with patch reefs. The platform margin shows reefs with

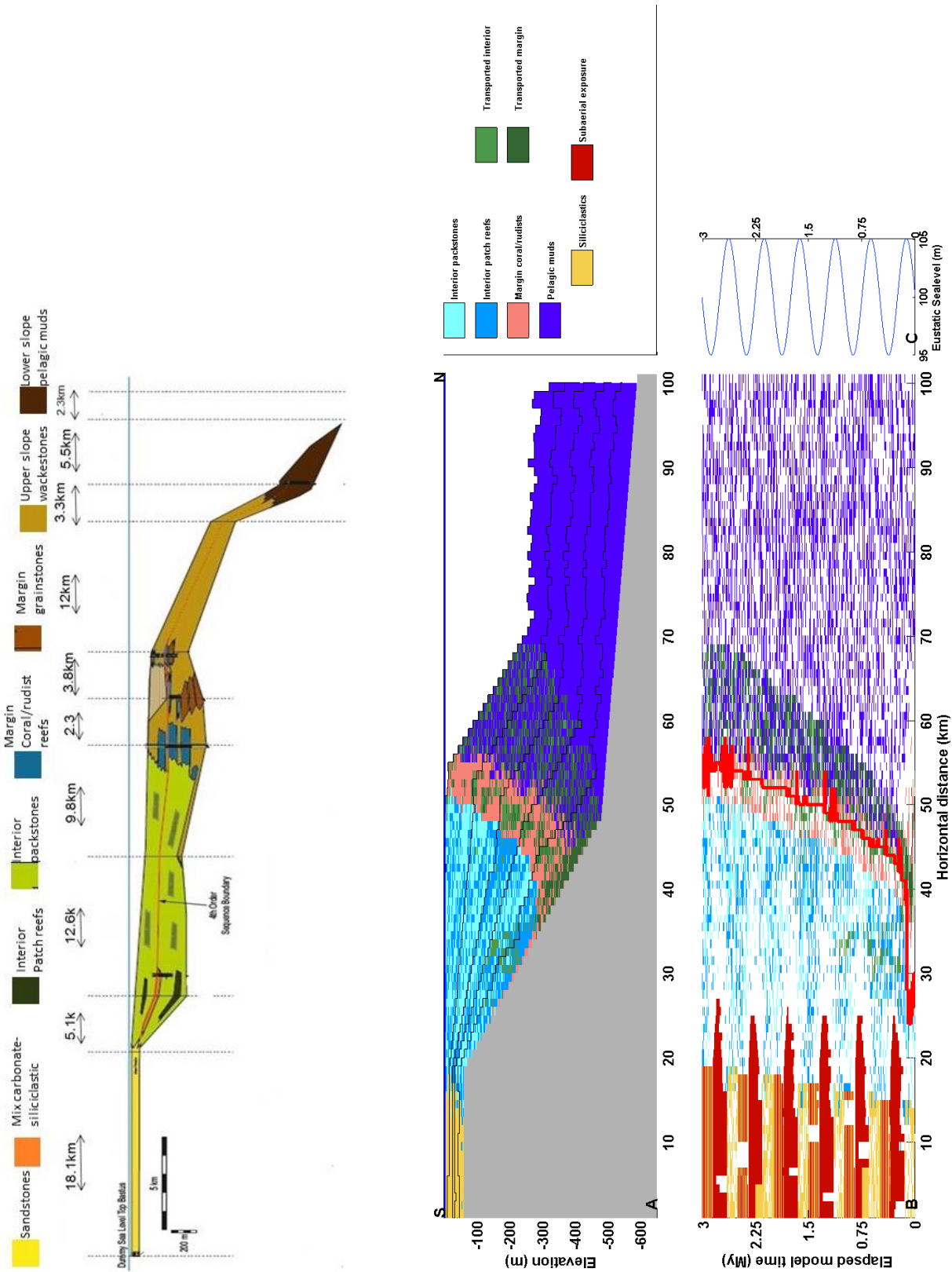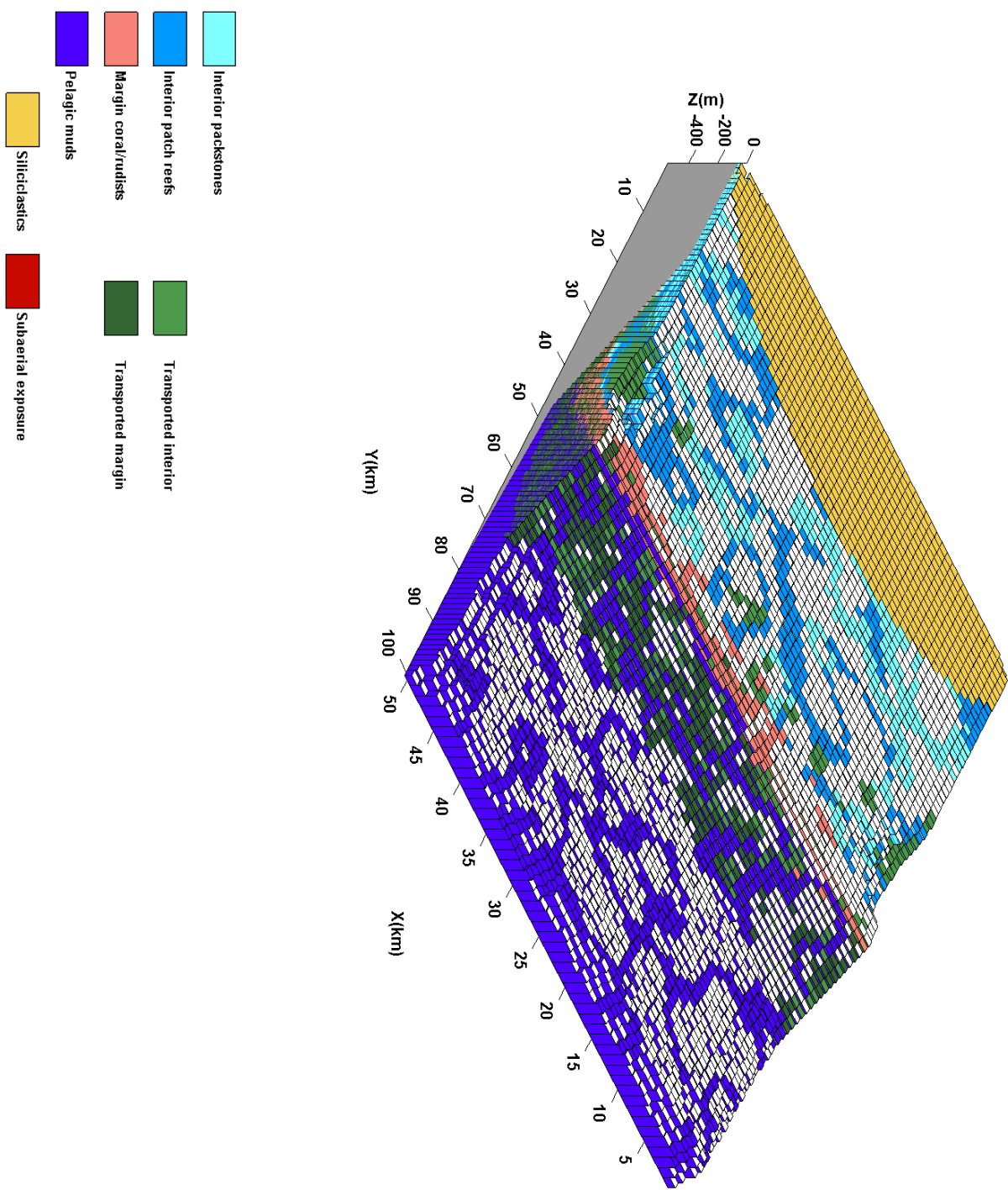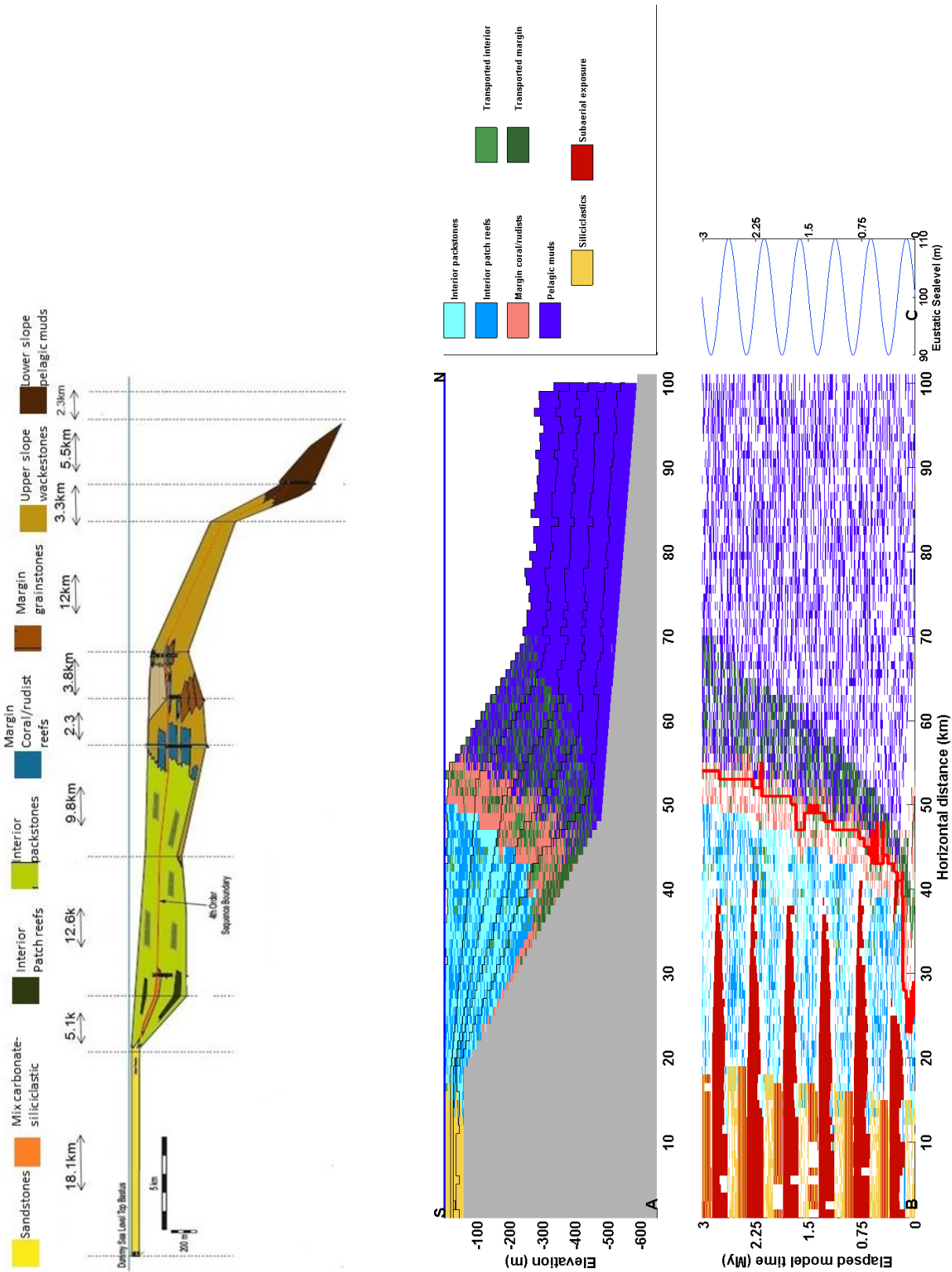281
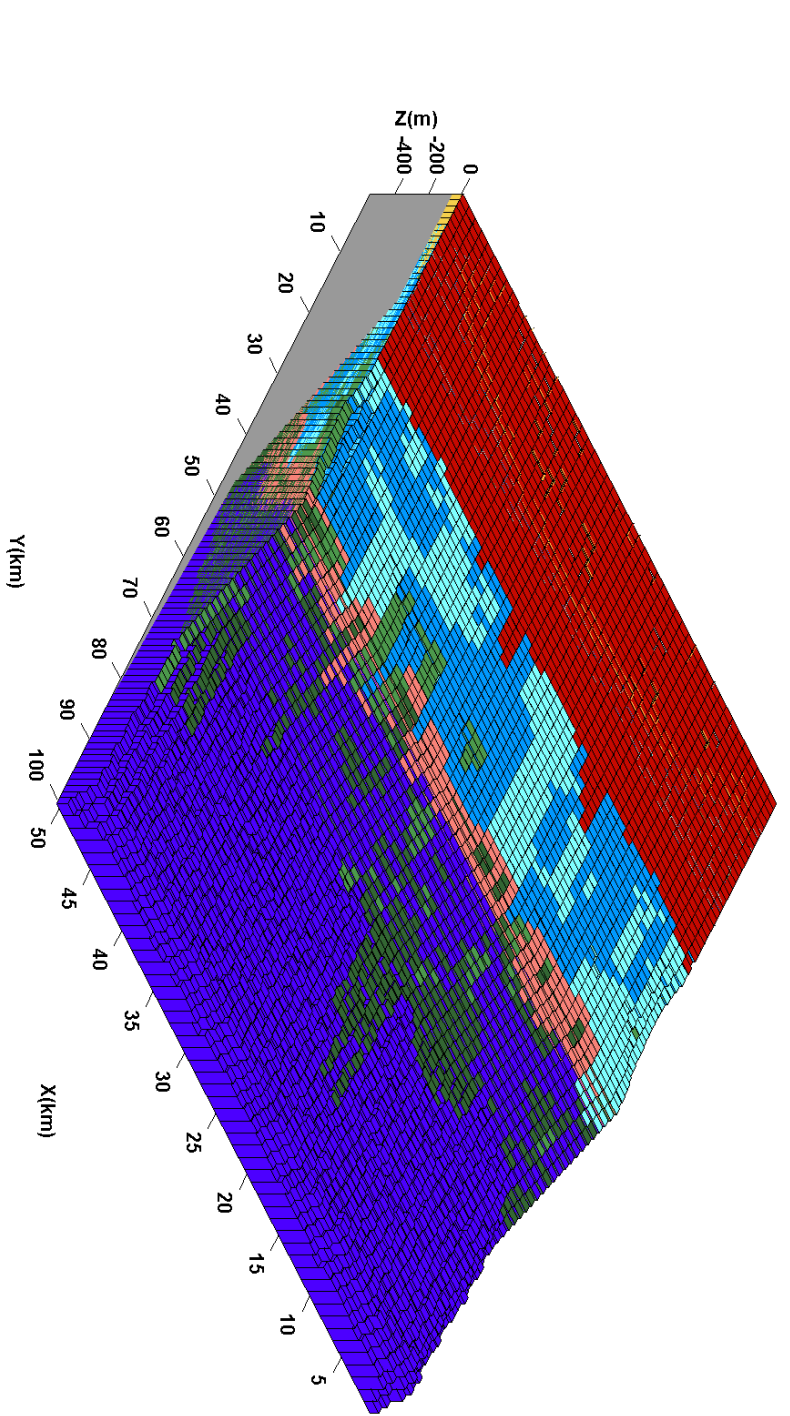
Figure C.7: 3D plot of the EL-B2 model run.
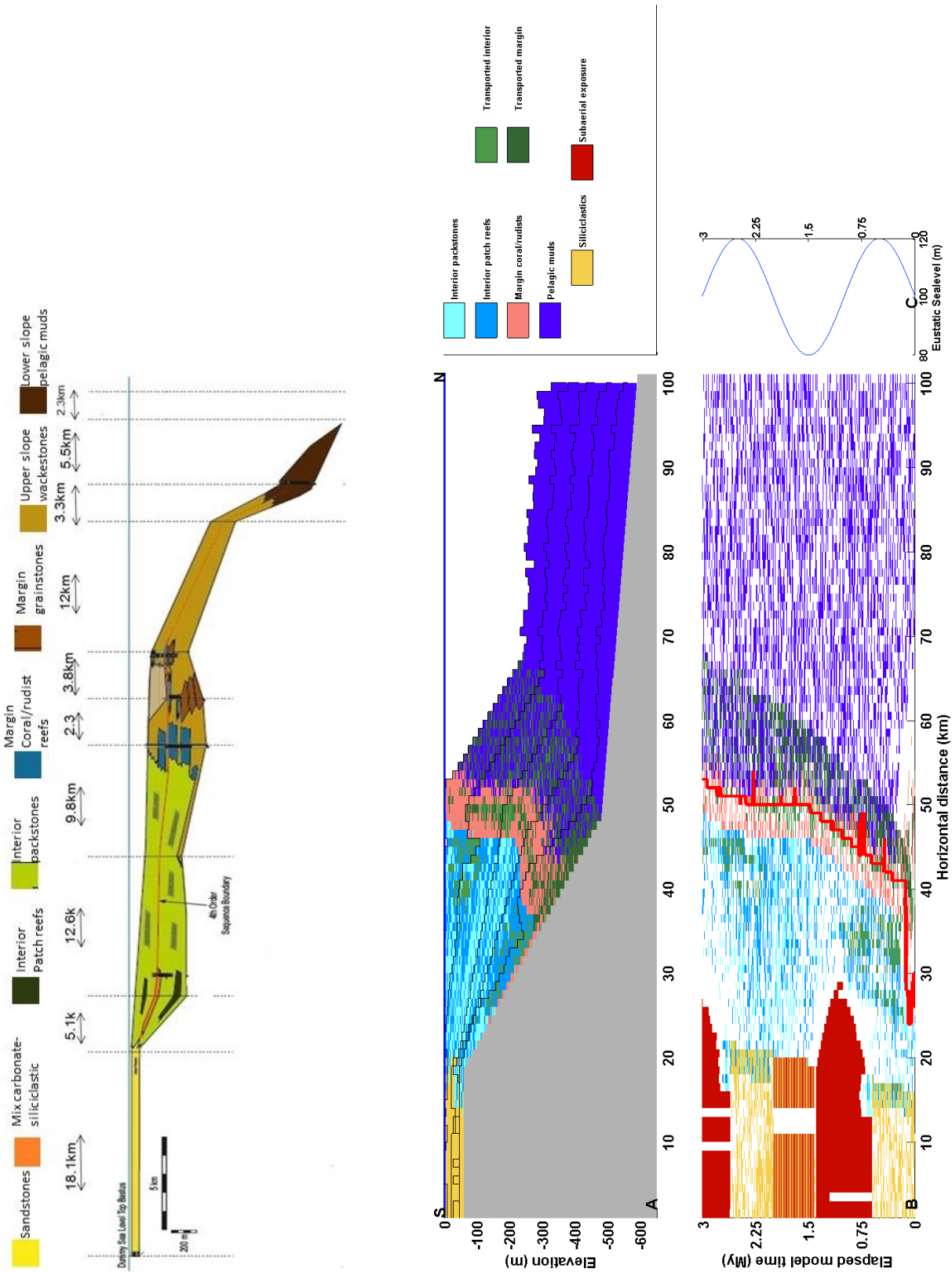
Figure C.8: (A) Cross section along the x=25 of the 3D model. The cross section shows siliciclastic dominating the most proximal part (0-18 km), extensive platform interior (18-48 km), aggrading platform margin and upper slope extending to 71 km. (B) Chrono-strat section at the same position as (A) with the platform margin position (red line) superimposed. The platform margin progrades for 6 km once it gets established (0.6 My). (C) Eustatic sea level oscillations with period 2 My and amplitude 20 m. Interpreted platform geometry for comparison on the top.

Figure C.9: 3D plot of the EN-C1 model run.

Interior packstones

Interior patch reefs

Margin coral/rudists

Pelagic muds

Transported interior

Transported margin

Siliciclastics

Subaerial exposure

Z(m)

X(km)

Y(km)

N

284

Figure C.10: (A) Cross section along the x=25 of the 3D model. The cross section shows siliciclastic dominating the most proximal part (0-18 km), extensive platform interior (18-48 km), aggrading platform margin and upper slope extending to 61 km. (B) Chrono-strat section at the same position as (A) with the platform margin position (red line) superimposed. The platform margin progrades for 6 km once it gets established (0.6 My). (C) Eustatic sea level movement. Interpreted platform geometry for comparison on the top.

Table C.4: Length and thickness of EL-B2 model run

Platform segment	Field values	Numerical model
Siliciclastics length	18km	18km
Siliciclastics thickness	60m	60m
Carbonate interior length	28km	29km
Carbonate interior thickness	450m	448m
Margin length	5km	5km
margin thickness	280m	304m
slope thickness	250m	291m
platform type	low angle	1.26^o

fragments, while the upper slope is dominated by foraminifera and shell fragments. The stacking patterns in both platform interior and margin remain aggradational. The dimensions of each platform segment and the strata thickness in each segment are shown in Table.C.5.

Comparison of the interpreted stratigraphic section with the EN-C1 model run reveals that model run EN-C1 is a fully aggradational model. There are no clear sequences defined anywhere in the numerical model. EN-C1 matches the interpreted geometry and stacking patterns but fails to show any sequences or facies transitions. Overall the model run might be probable but it is not a good representation of the interpreted geometry of the Bastus platform.

Table C.5: Length and thickness of EN-C1 model run

Platform segment	Field values	Numerical model
Siliciclastics length	18km	18km
Siliciclastics thickness	60m	60m
Carbonate interior length	28km	29km
Carbonate interior thickness	450m	400m
Margin length	5km	5km
margin thickness	280m	307m
slope thickness	250m	269m
platform type	low angle	0.51^o

C.6   EN-C2

Fig.C.11 and Fig.C.12 shows a mainly aggradational platform with one sequence. Once the platform margin has been established (0.6 My EMT), the margin aggrades for the remaining EMT (total progradation 6km). Due to the rising ESL
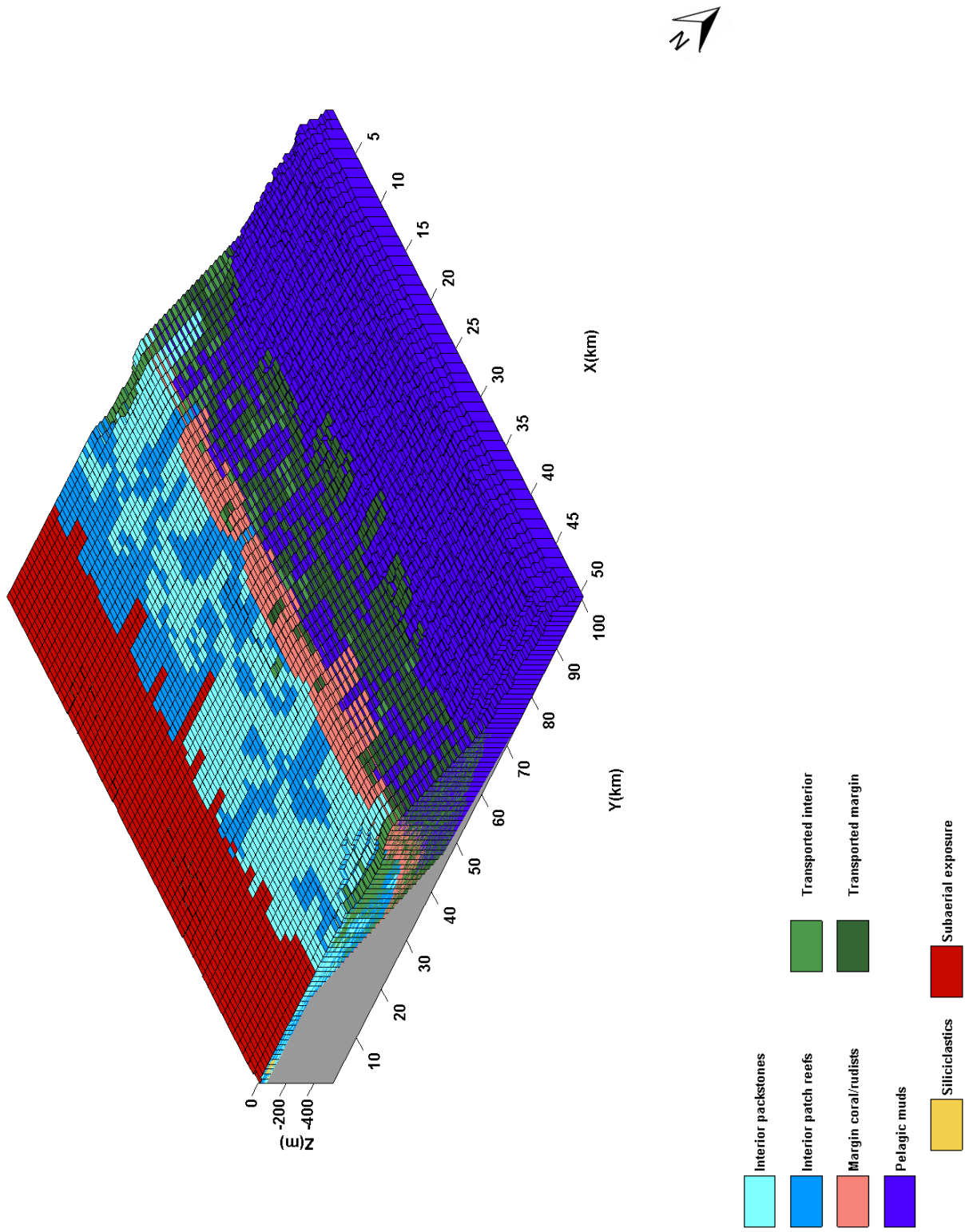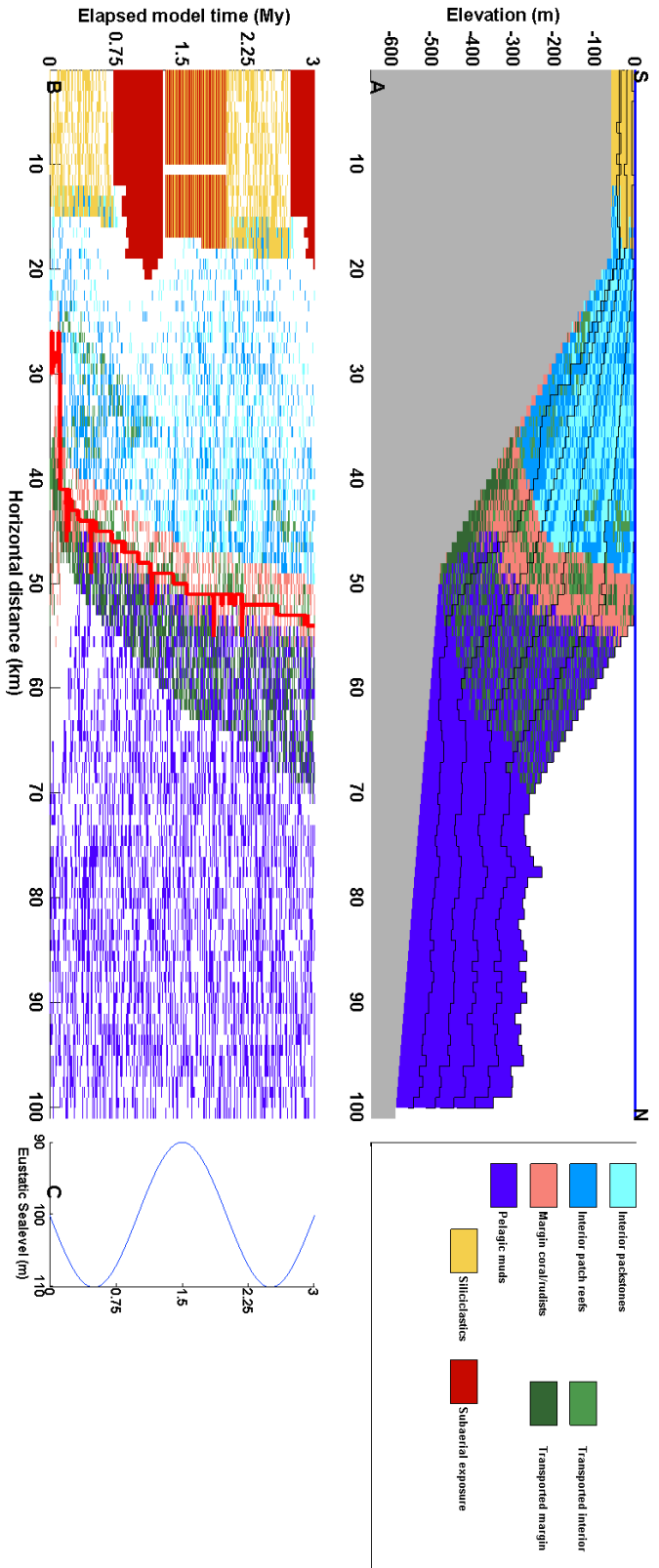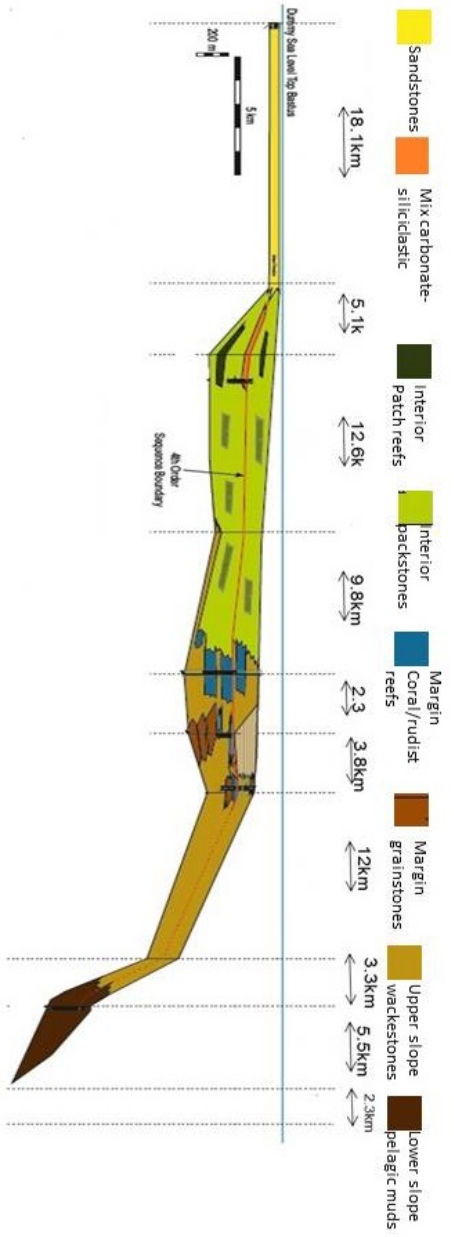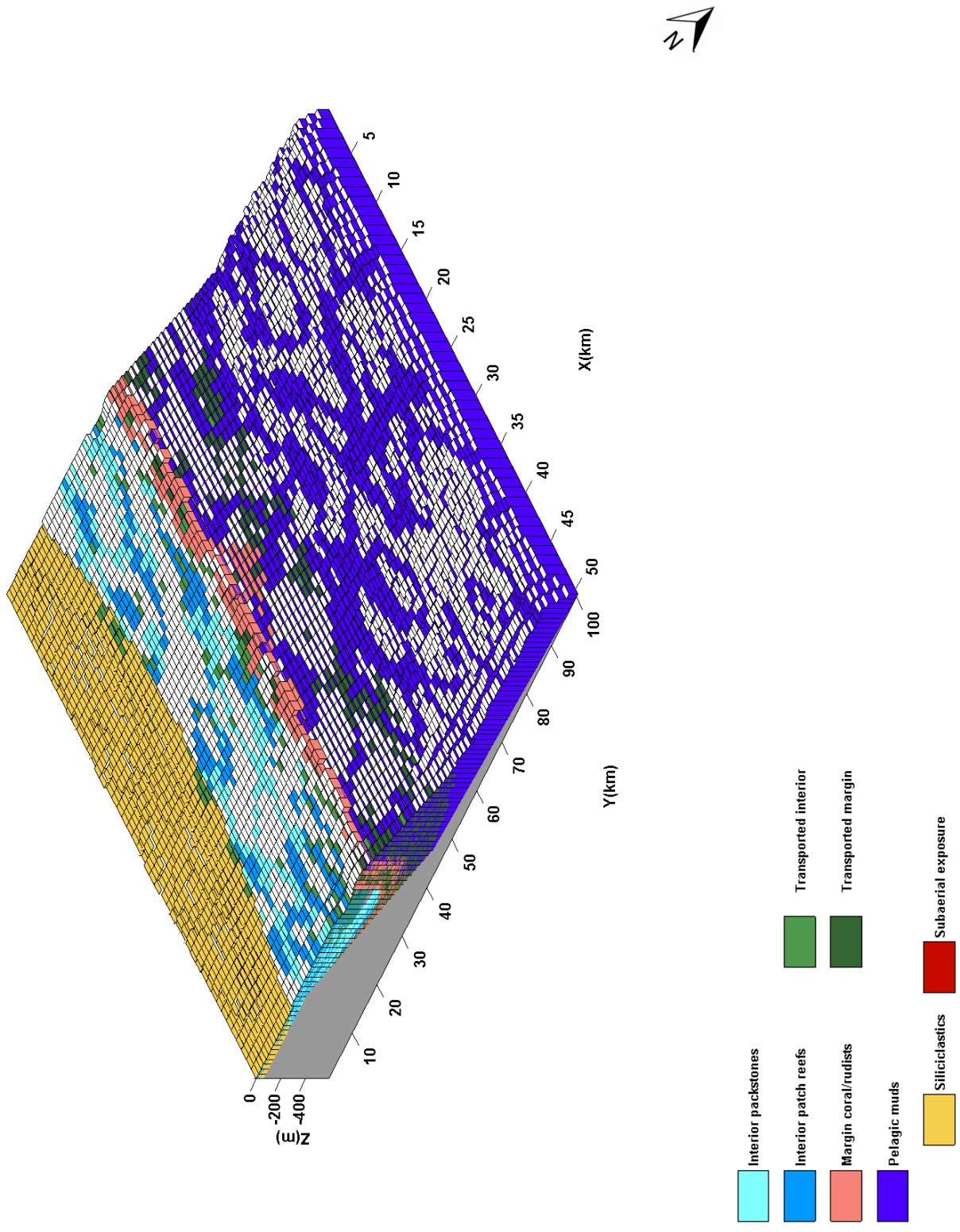
Figure C.11: 3D plot of the EN-C2 model run.

Figure C.12: (A) Cross section along the x=25 of the 3D model. The cross section shows siliciclastic dominating the most proximal part (0-18 km), extensive platform interior (18-48 km), aggrading platform margin and upper slope extending to 61 km. (B) Chrono-strat section at the same position as (A) with the platform margin position (red line) superimposed. The platform margin progrades for 6 km once it gets established (0.6 My). (C) Eustatic sea level movements. Interpreted platform geometry for comparison on the top.

288

at 1.5 My EMT, high energy margin material slightly retrogrates on the platform interior. The dimensions of each platform segment and the strata thickness in each segment are shown in Table.C.6.

Comparison of the interpreted stratigraphic model with the EN-C2 model run shows that model run EN-C2 is a mainly aggradational. EN-C2 model run matches the interpreted geometry and stacking patterns but fails to show any sequences or facies transitions as shown in the interpreted section. Overall the model run is probable but it is not a good representation of the interpreted geometry of the Bastus platform.

Table C.6: Length and thickness of EN-C2 model run

Platform segment	Field values	Numerical model
Siliciclastics length	18km	18km
Siliciclastics thickness	60m	60m
Carbonate interior length	28km	24km
Carbonate interior thickness	450m	400m
Margin length	5km	5km
margin thickness	280m	327m
slope thickness	250m	270m
platform type	low angle	0.96^o

C.7 R-B

Fig.C.13 and Fig.C.14 shows a model with two sequences and a complex platform trajectory. The platform margin slowly progrades for 7 km once the platform has been established (0.6-1.5 My EMT). At 1.5 My EMT and under the effect of the tectonic tilting, the platform margin retrogrades (12 km), followed by 7 km of progradation when the rotation effect has been seized (1.506-1.9 My EMT). From there, (1.9-3 My EMT) the platform margin aggrades. The dimensions of each platform segment and the strata thickness in each segment are shown in Table.C.7.

Model run R-B recreates the interpreted geometry with two sequences and a facies transition at the margin. Furthermore, the numerical model suggests a second facies transition in the platform interior that has not been mapped. Despite this, the numerical model shows some features that are not supported by the field observations.

The 5 km backstepping of the platform margin are much bigger than what has been observed in the field. Furthermore, the numerical model suggests that the high energy platform margin facies backsteps all the way back to most proximal part of the platform. If an interior/margin facies transition might be missed (as in case of model run R-A), high energy, coral/rudists reef boundstones next to siliciclastic strata clearly is not supported by field observations. Model run R-B is not a good representation of the interpreted stratigraphic model but it should be considered the upper limit of the tectonic tilting value.

Table C.7: Length and thickness of R-B model run

Platform segment	Field values	Numerical model
Siliciclastics length	18km	18km
Siliciclastics thickness	60m	60m
Carbonate interior length	28km	23km
Carbonate interior thickness	450m	412m
Margin length	5km	5km
margin thickness	280m	Hard to define
slope thickness	250m	281m
platform type	low angle	0.86^o

C.8 R-C

Fig.C.15 and Fig.C.16 shows a numerical model with two sequences and a complex platform margin trajectory. The platform margin slowly progrades (6km) once the platform has been established (0.6-1.5My EMT). At 1.5My EMT and under the
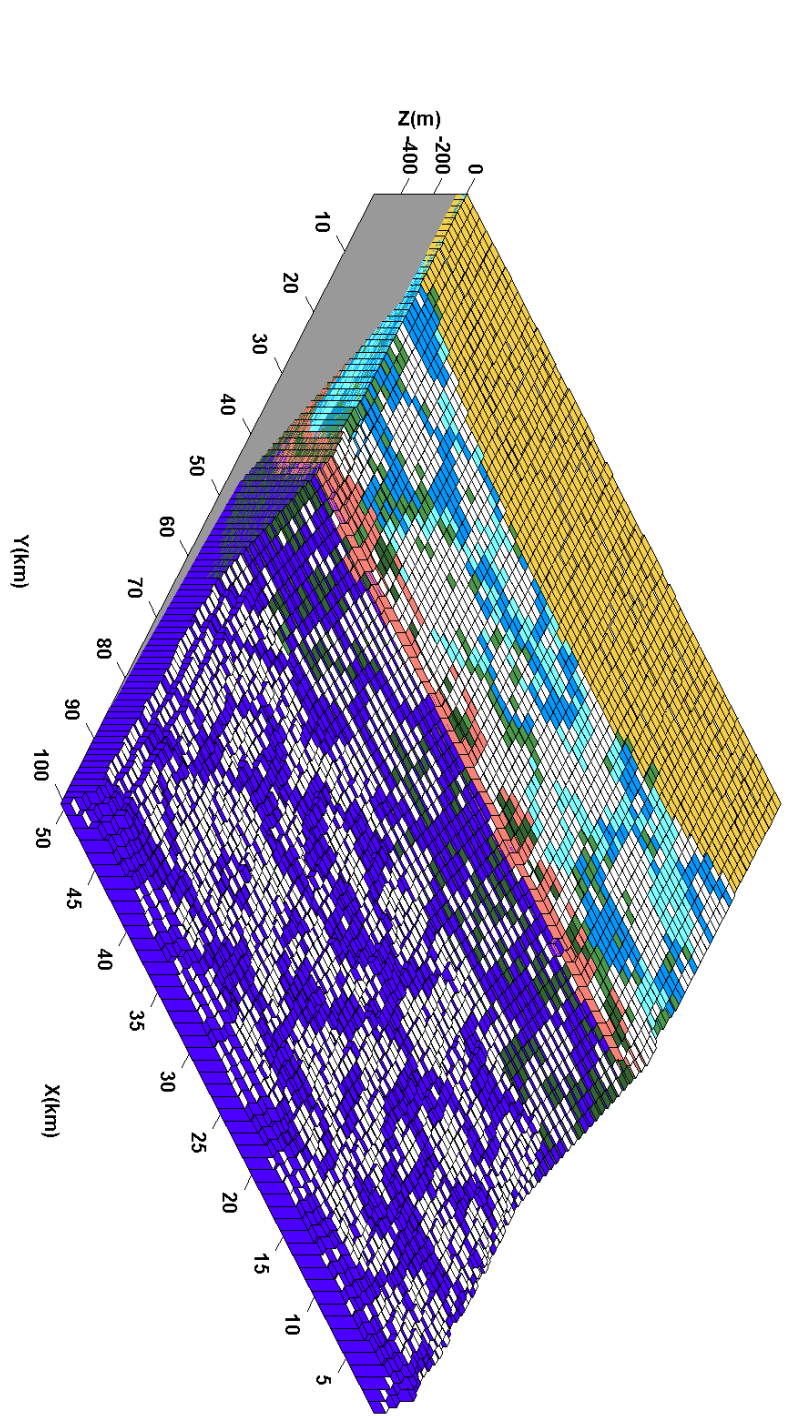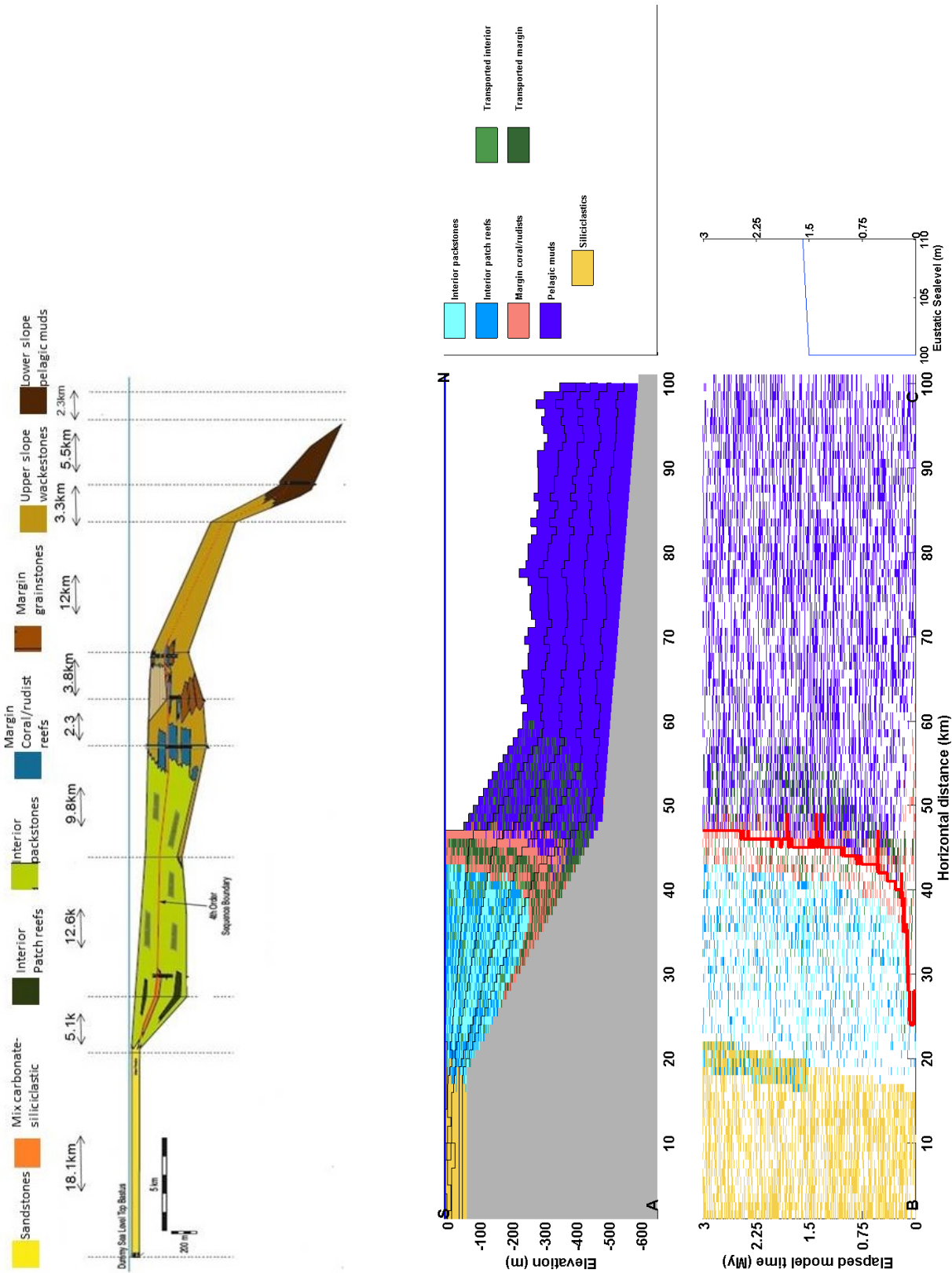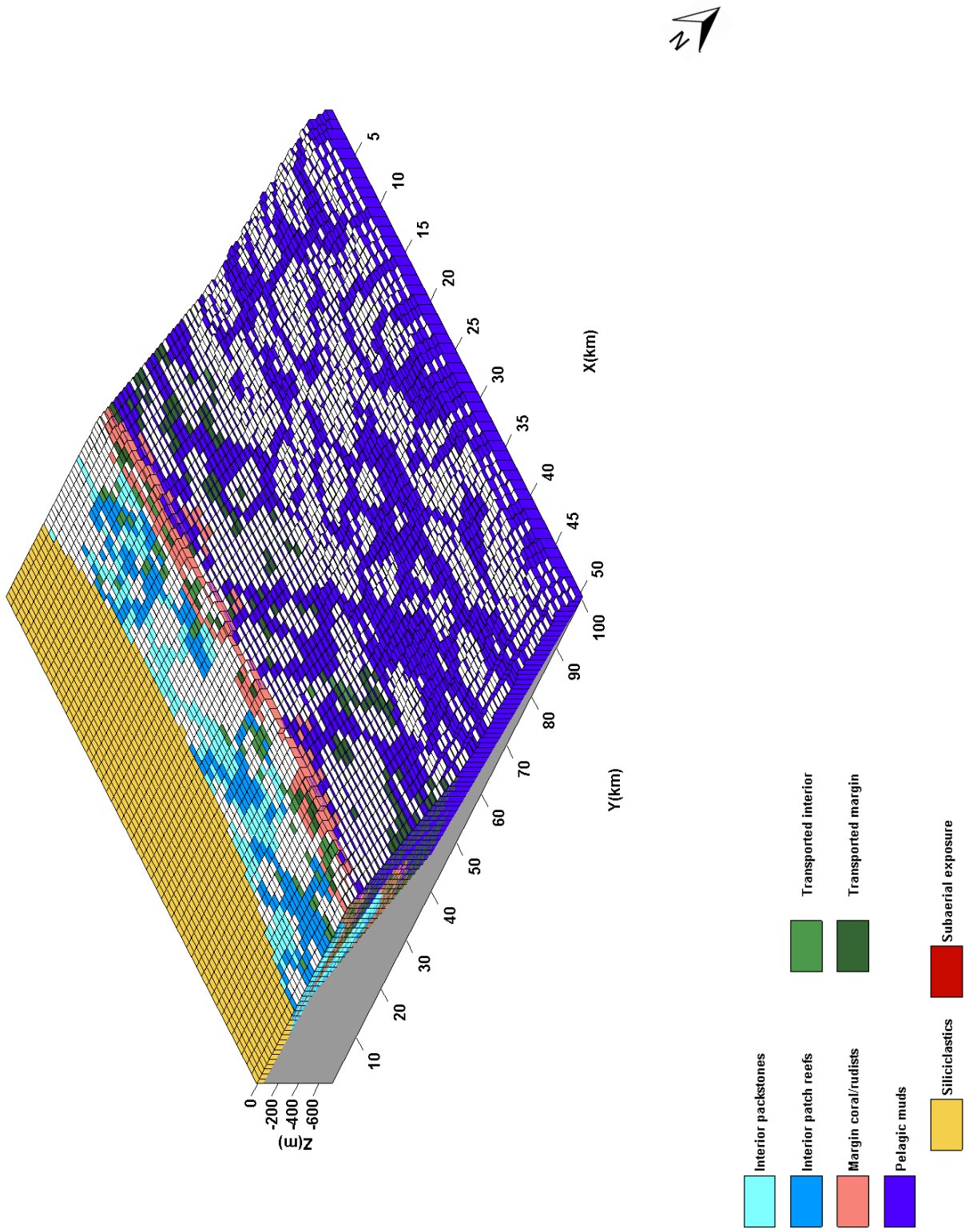
Figure C.13: 3D plot of the R-B model run.

291

Figure C.14: (A) Cross section along the x=25 of the 3D model. The cross section shows siliciclastic dominating the most proximal part (0-18 km), extensive platform interior (18-48 km), aggrading platform margin and upper slope extending to 61 km. (B) Chrono-strat section at the same position as (A) with the platform margin position (red line) superimposed. The platform margin progrades for 6 km once it gets established (0.6 My). (C) Relative sea level movements. Interpreted platform geometry for comparison on the top.

292
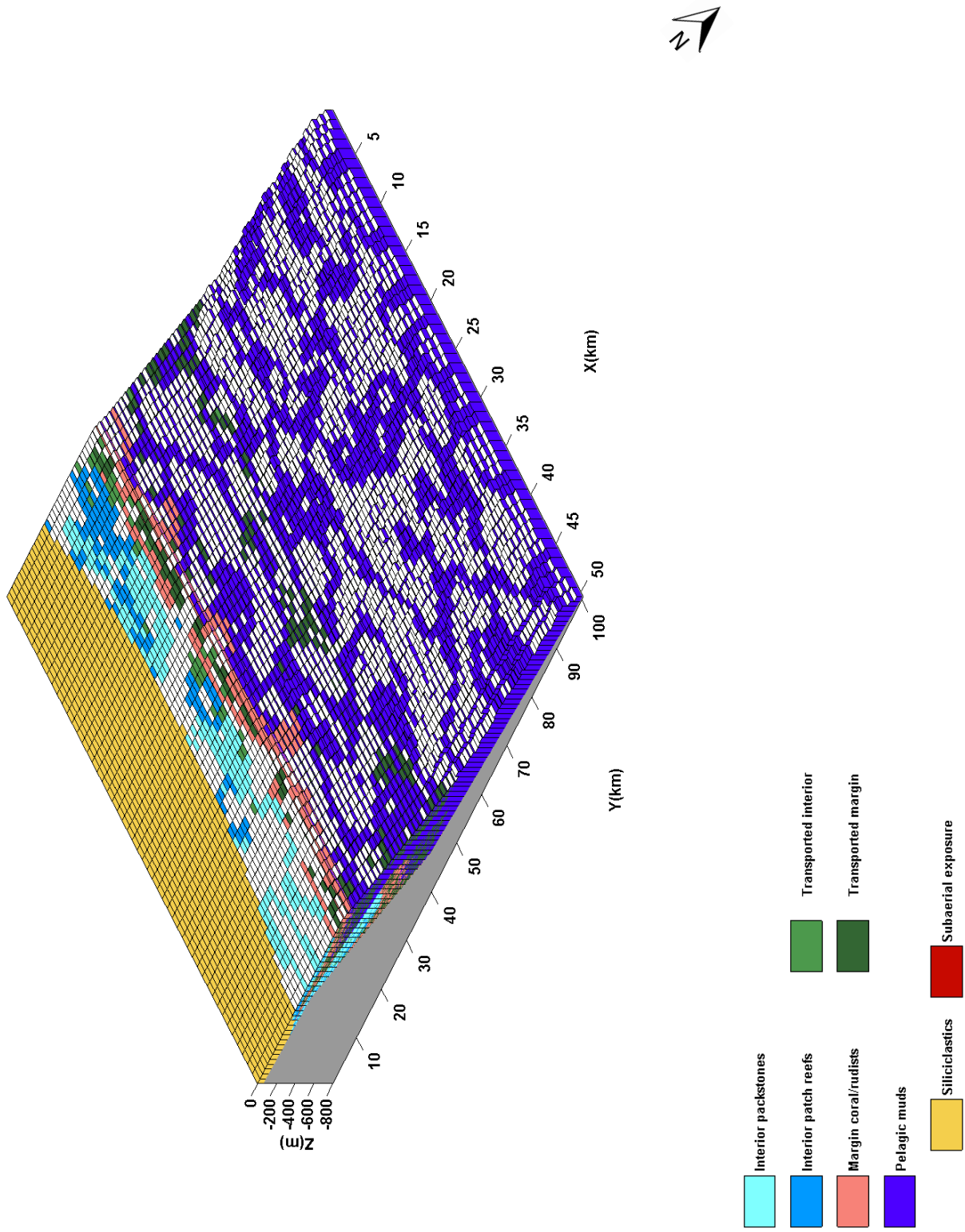
Figure C.15: 3D plot of the R-C model run.
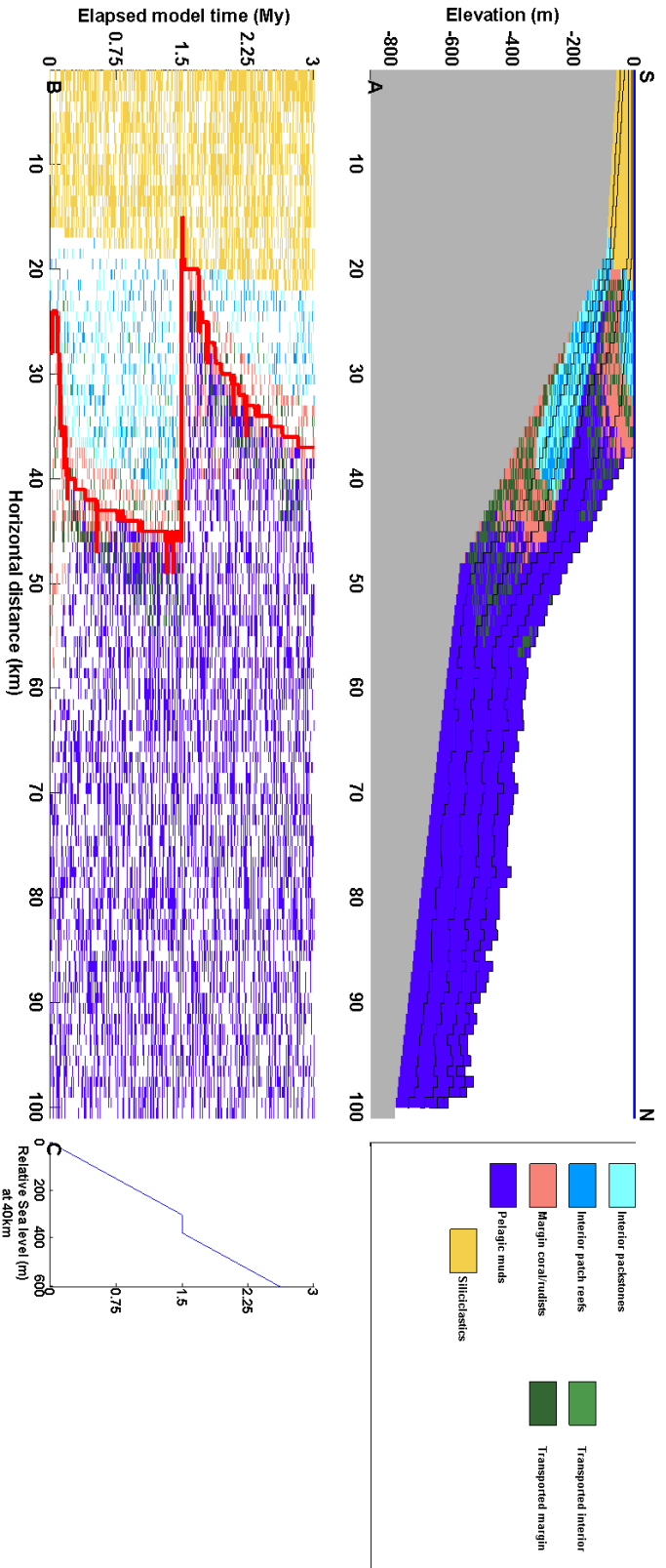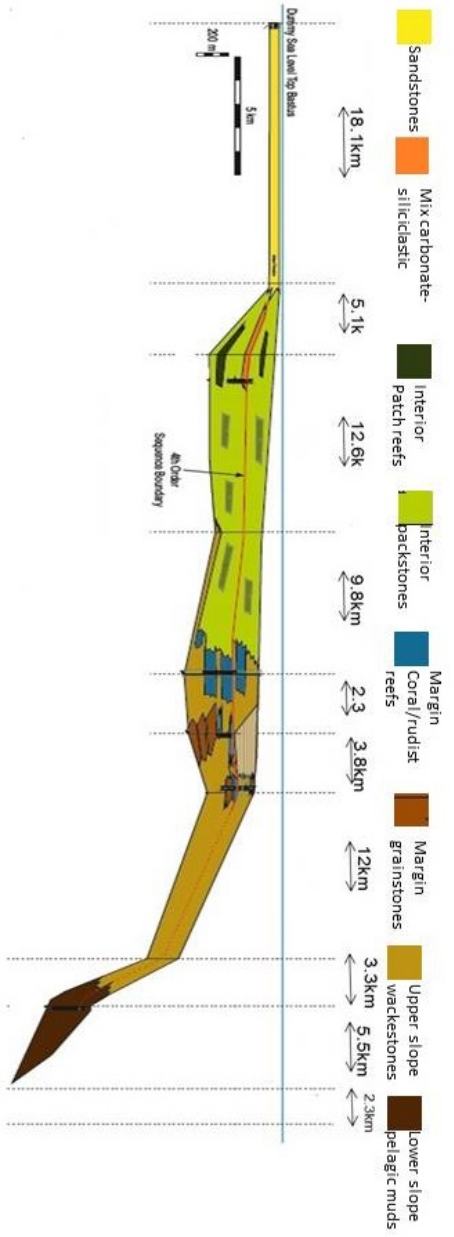
Figure C.16: (A) Cross section along the x=25 of the 3D model. The cross section shows siliciclastic dominating the most proximal part (0-18 km), extensive platform interior (18-48 km), aggrading platform margin and upper slope extending to 61 km. (B) Chrono-strat section at the same position as (A) with the platform margin position (red line) superimposed. The platform margin progrades for 6 km once it gets established (0.6 My). (C) Relative sea level movements at 40km along the dip. Interpreted platform geometry for comparison on the top.

effect of rotation, the platform margin retrogrades (20km), followed by progradation (16km) for the remaining model time (1.506-3My EMT). The total length to the geomorphic margin is 39km, much shorter than the interpreted length. Two sequences are defined with the upper sequence having a much shorter interior. Facies transition from high energy platform margin and low energy interior facies of the lower sequence to the pelagic, below wave base facies of the upper sequence occurs on the platform.

The significant backstepping of the platform margin at 1.5My EMT is not consistent with the interpreted stratigraphic section. Furthermore, the numerical model suggests high energy platform margin strata next to siliciclastic strata in the interior at the boundary of the two sequences which is also inconsistent with the field observations. Model run R-C does not represent the interpreted geometry.

C.9 P-A

Fig.C.17 and Fig.C.18 shows a mainly aggradational platform with one sequence. The platform margin mainly aggrades once the platform has been established (0.6-3 My EMT). Platform interior is dominated by packstones with patch reefs. The platform margin shows reefs with some fragments, while the upper slope is dominated by foraminifera and shell fragments. The dimensions of each platform segment and the strata thickness in each segment are shown in Table.C.8.

Comparison of the interpreted stratigraphic section with the P-A model run reveals that model run P-A is a fully aggradational model. There are no clear sequences defined anywhere in the model. P-A matches the interpreted geometry and stacking patterns but fails to show any sequences or facies transitions. Overall the model run might be probable but it is not a good representation of the interpreted geometry of the Bastus platform.

Table C.8: Length and thickness of P-A model run

Platform segment	Field values	Numerical model
Siliciclastics length	18km	18km
Siliciclastics thickness	60m	60m
Carbonate interior length	28km	25km
Carbonate interior thickness	450m	421m
Margin length	5km	5km
margin thickness	280m	302m
slope thickness	250m	267m
platform type	low angle	1.12^o

Figure C.17: 3D plot of the P-A model run.

Legend:
- Interior packstones
- Interior patch reefs
- Margin coral/rudists
- Pelagic muds
- Transported interior
- Transported margin
- Siliciclastics
- Subaerial exposure
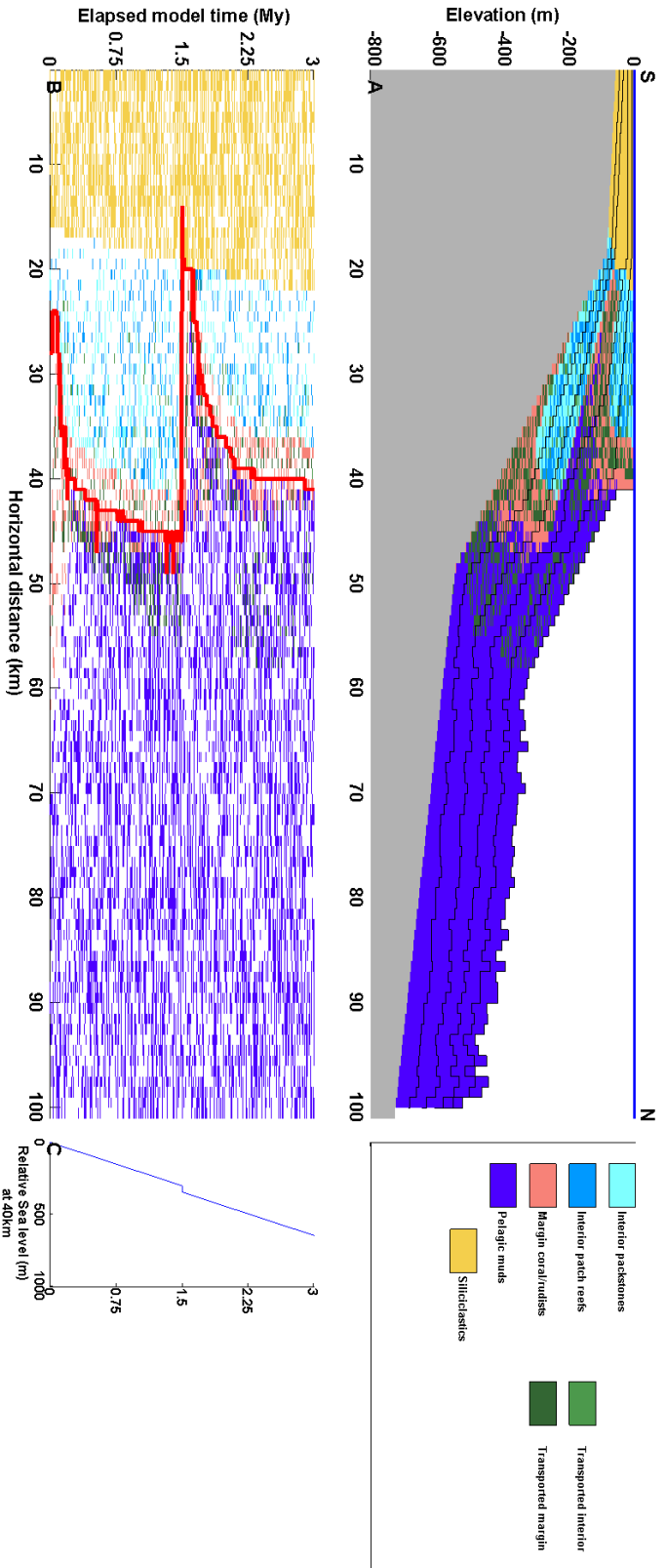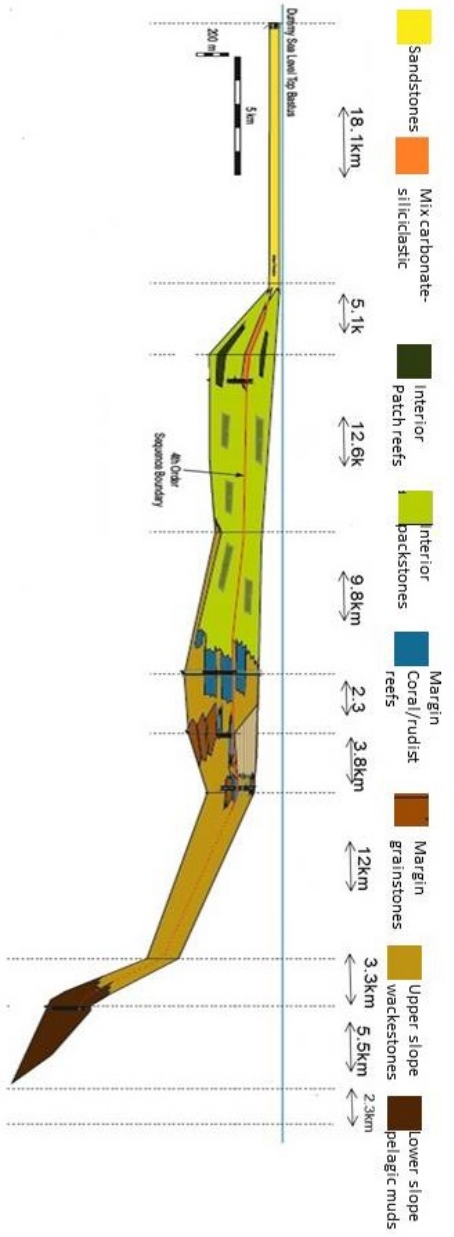
296

Figure C.18: (A) Cross section along the x=25 of the 3D model. The cross section shows siliciclastic dominating the most proximal part (0-18 km), extensive platform interior (18-48 km), aggrading platform margin and upper slope extending to 61 km. (B) Chrono-strat section at the same position as (A) with the platform margin position (red line) superimposed. The platform margin progrades for 6 km once it gets established (0.6 My). (C) Fraction of the carbonate production. Interpreted platform geometry for comparison on the top.

297

C.10 P-B1

Fig.C.19 and Fig.C.20 shows a mainly aggradational platform with two sequences. The platform margin mainly aggrades once the platform has been formed (0.6-3 My EMT). At 1.5 My to 1.8 My EMT no production occurs generating a depositional hiatus. Once production returns to initial values (1.8 My EMT) and for the remaining EMT the margin aggrades. Water depth and wave energy conditions have changed due to production shut down and when production resumes (1.8 My EMT) the margin retrogrades for 3 km generating a facies transition from high energy, margin facies in the lower sequence to below wave base, pelagic facies of the upper sequence. Similar transition occurs between low energy interior and high energy margin facies. The dimensions of each platform segment and the strata thickness in each segment are shown in Table.C.9.

The backstepping of the platform margin at 1.5 My EMT generates a facies transition and two sequences consistent with the interpreted stratigraphic model. The interpreted geometry is well represented with model P-B1. However, the numerical model requires a 300 ky depositional hiatus which even though is quite probable to exist, has not been observed in the field.

Table C.9: Length and thickness of P-B1 model run

Platform segment	Field values	Numerical model
Siliciclastics length	18km	18km
Siliciclastics thickness	60m	60m
Carbonate interior length	28km	23km
Carbonate interior thickness	450m	405m
Margin length	5km	5km
margin thickness	280m	294m
slope thickness	250m	276m
platform type	low angle	1.18^o

C.11 P-C1

Fig.C.21 and Fig.C.22 shows a mainly aggradational platform with two sequences. The platform margin mainly aggrades once the platform has been established (0.6-1.5 My). Production ceases completely for 450 ky at the sequence boundary generating an extensive depositional hiatus. Once production resumes (1.95 My) the margin retrogrades for 6 km and for the remaining EMT the margin aggrades. The back-stepping generates two facies transitions from the lower to the upper sequence. One between high energy margin and below wave base, pelagic facies on the margin and one between low energy interior and high energy margin facies on
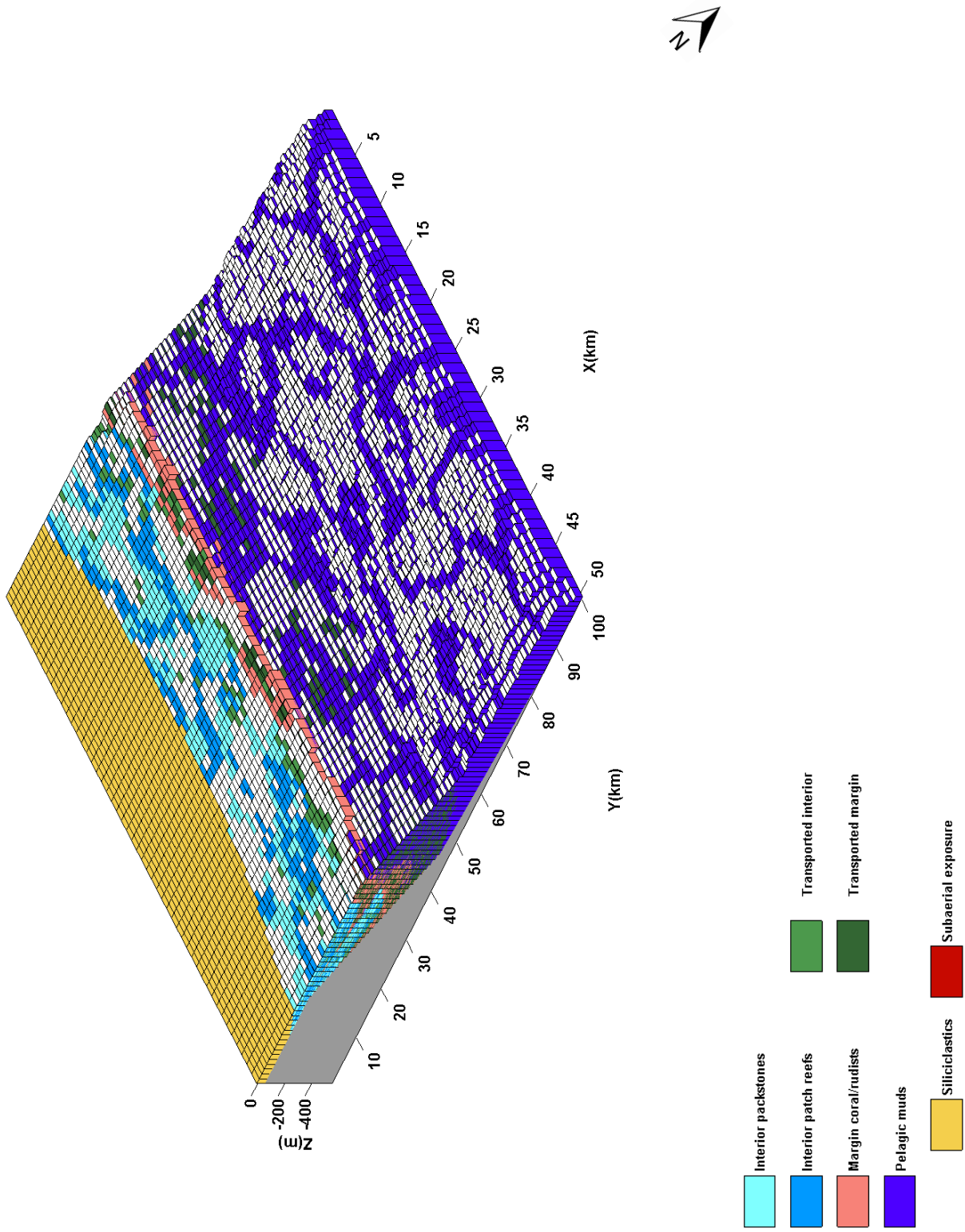
Figure C.19: 3D plot of the P-B1 model run.

Elevation (m)

-600 -500 -400 -300 -200 -100 0

S

A

N

10 20 30 40 50 60 70 80 90 100

Elapsed model time (My)

0 0.75 1.5 2.25 3

B

10 20 30 40 50 60 70 80 90 100

Horizontal distance (km)

C

Fraction of initial production rate

0 0.5 1

0 -0.75 -1.5 -2.25 -3

Sandstones

Mix carbonate-siliciclastic

Interior Patch reefs

Interior packstones

Margin Coral/rudist reefs

Margin grainstones

Upper slope wackestones

Lower slope pelagic muds

Pelagic muds

Margin coral/rudists

Interior patch reefs

Interior packstones

Siliciclastics

Transported margin

Transported interior

18.1km 5.1k 12.6k 9.8km 2.3 3.8km 12km 3.3km 5.5km 2.3km

4th Order Sequence Boundary

Datum Sea Level Top Batala

200 m

5 km

Figure C.20: (A) Cross section along the x=25 of the 3D model. The cross section shows siliciclastic dominating the most proximal part (0-18 km), extensive platform interior (18-48 km), aggrading platform margin and upper slope extending to 61 km. (B) Chrono-strat section at the same position as (A) with the platform margin position (red line) superimposed. The platform margin progrades for 6 km once it gets established (0.6 My). (C) Fraction of the carbonate production. Interpreted platform geometry for comparison on the top.
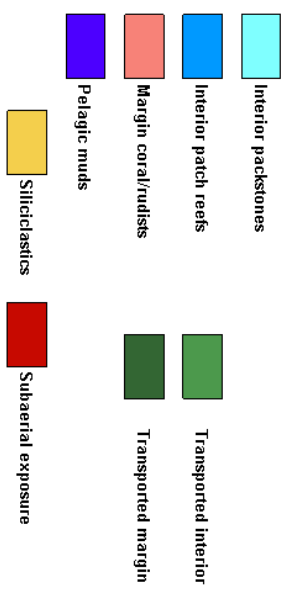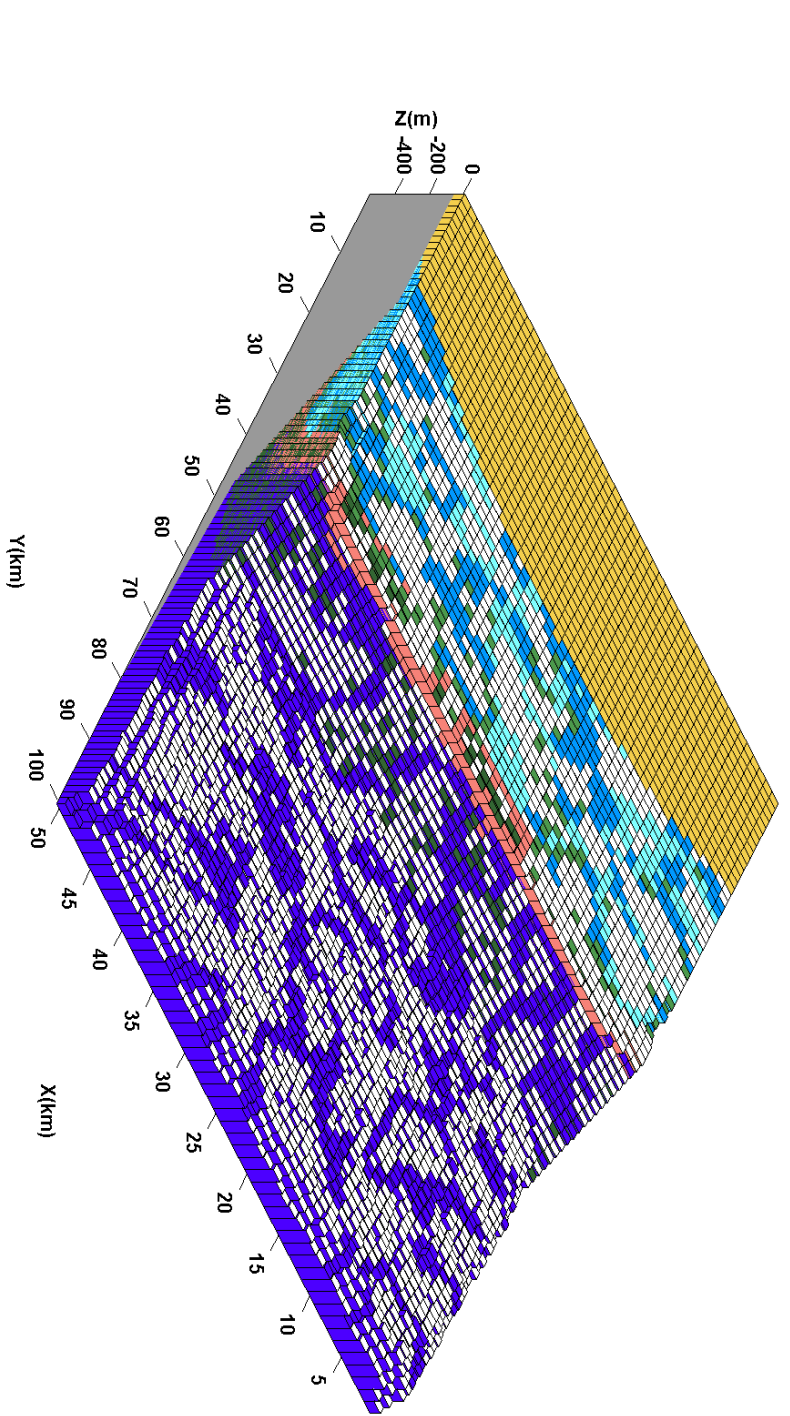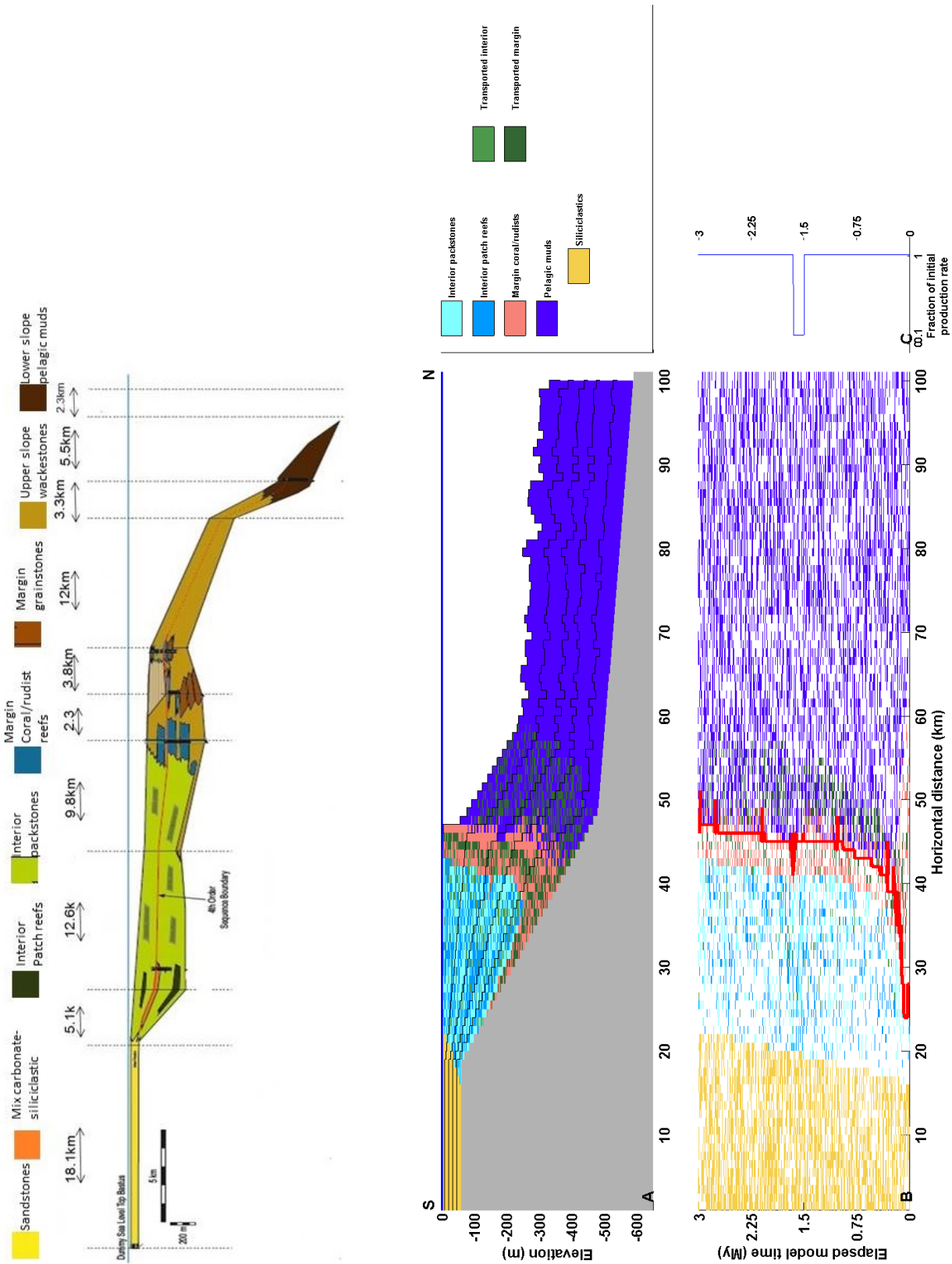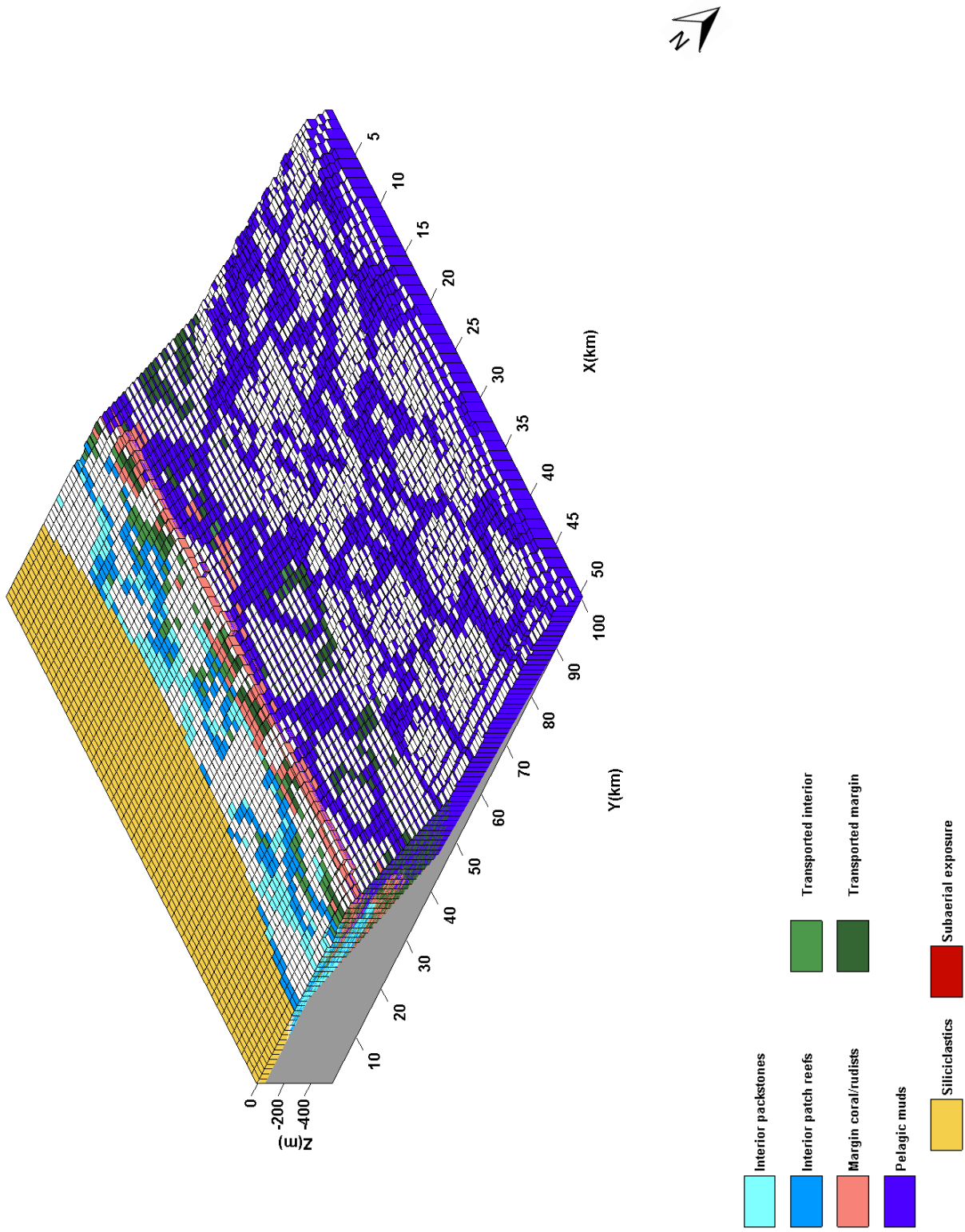
Figure C.21: 3D plot of the P-C1 model run.
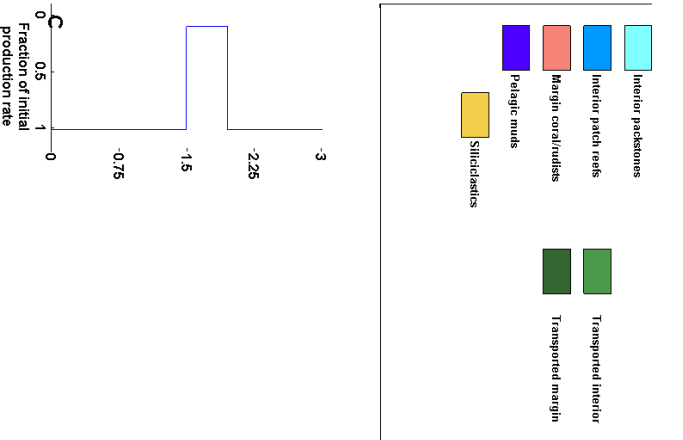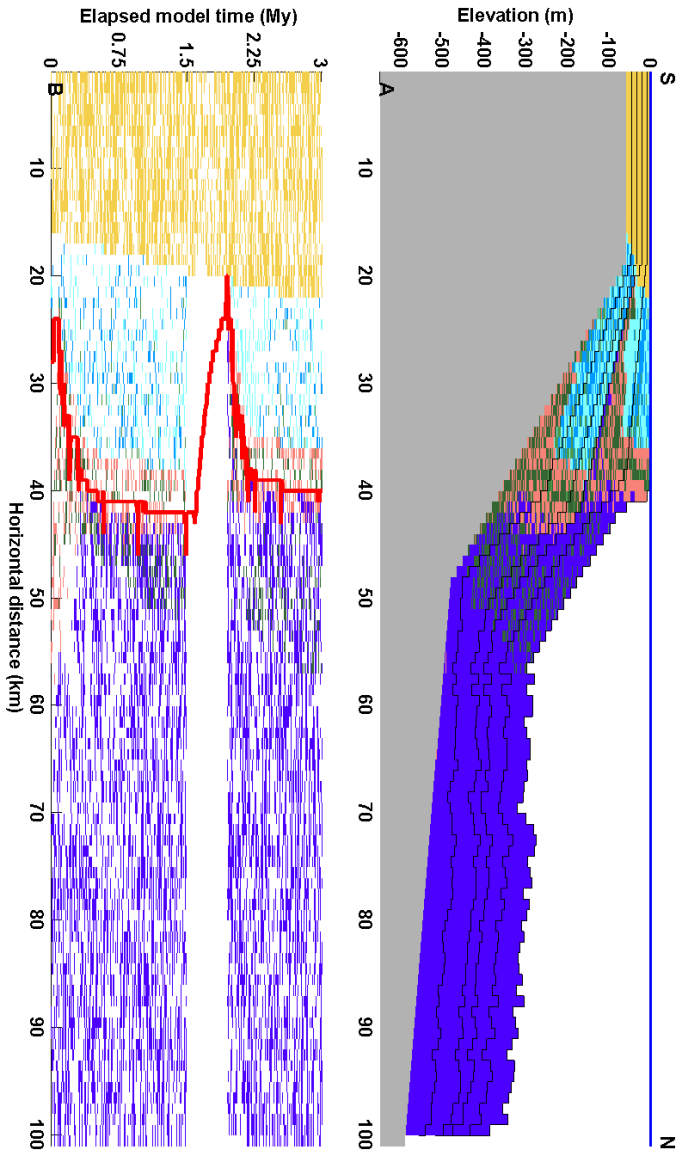
Figure C.22: (A) Cross section along the x=25 of the 3D model. The cross section shows siliciclastic dominating the most proximal part (0-18 km), extensive platform interior (18-48 km), aggrading platform margin and upper slope extending to 61 km. (B) Chrono-strat section at the same position as (A) with the platform margin position (red line) superimposed. The platform margin progrades for 6 km once it gets established (0.6 My). (C) Fraction of the carbonate production. Interpreted platform geometry for comparison on the top.

the interior. The platform interior is shorter than the interpreted. The dimensions of each platform segment and the strata thickness in each segment are shown in Table.C.10.

The backstepping of the platform margin at 1.5 My EMT generates a facies transition and two sequences consistent with the interpreted geometry. The magnitude of the backstepping (6 km) which is slightly bigger than the interpreted and the extensive depositional hiatus do not agree with the field observations.

Table C.10: Length and thickness of P-C1 model run

Platform segment	Field values	Numerical model
Siliciclastics length	18km	18km
Siliciclastics thickness	60m	60m
Carbonate interior length	28km	20km
Carbonate interior thickness	450m	421m
Margin length	5km	5km
margin thickness	280m	302m
slope thickness	250m	281m
platform type	low angle	1.43^o

C.12   P-C2

Fig.C.23 and Fig.C.24 shows a mainly aggradational platform with thwo sequences. The platform margin mainly aggrades once the platform has been established (0.6-1.5 My). At 1.5 My to 1.95 My EMT and under the effect of significantly lower production, the margin retrogrades (3 km). Once production returns back to initial values (1.95 My) and for the remaining EMT the margin aggrades. The back-stepping generates two sequences and facies transitions. One between high energy margin and below wave base, pelagic facies on the margin and one between low energy interior and high energy margin facies on the interior. The dimensions of each platform segment and the strata thickness in each segment are shown in Table.C.11.

The back-stepping of the platform margin at 1.5 My EMT generates a facies transition and two sequences consistent with the interpreted section. The magnitude of the back-stepping is marginally consistent with the interpreted section and the platform segments dimensions are slightly shorter than the the interpreted. Model run P-B2 represent the interpreted geometry well but it should me considered the upper limit for the duration of production hiatus.

303
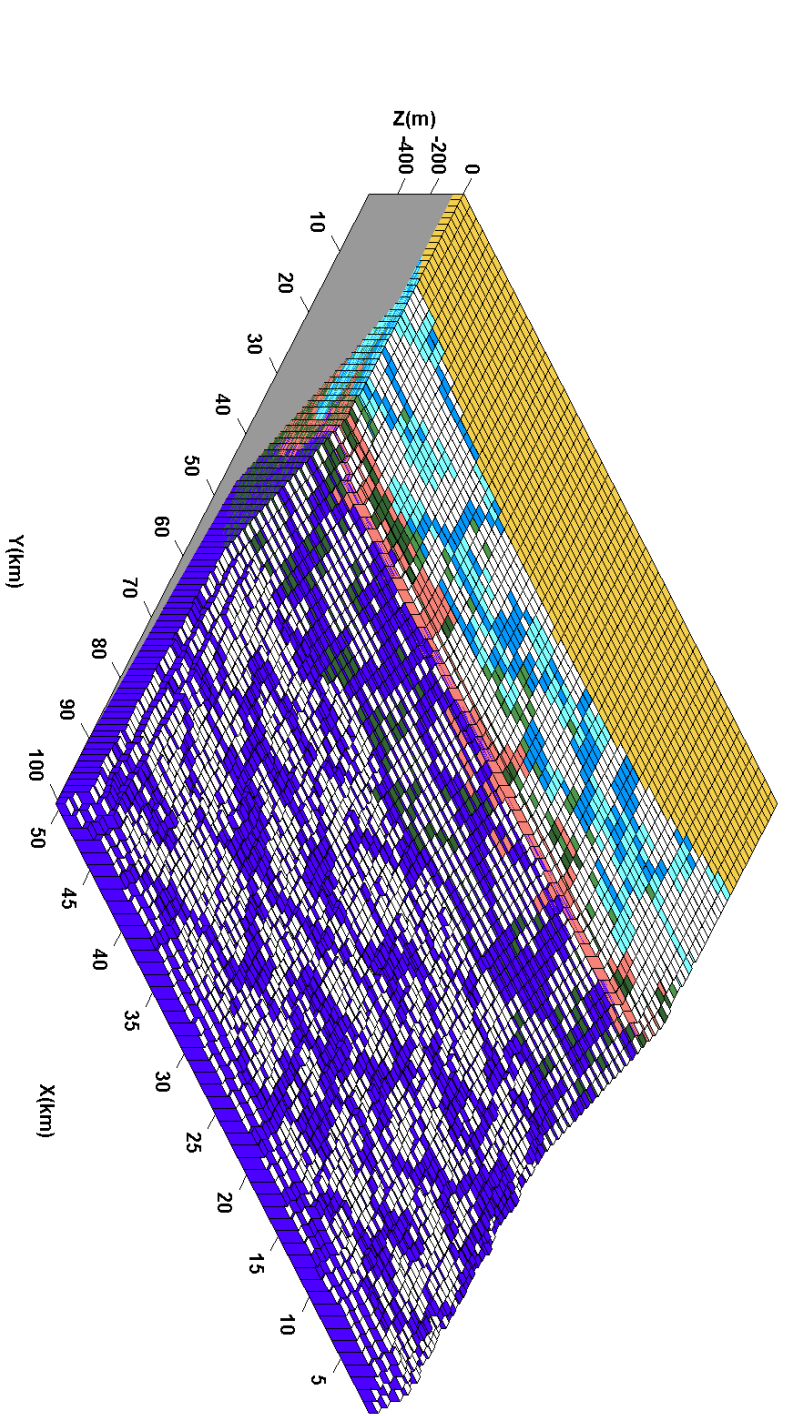
Figure C.23: 3D plot of the P-C2 model run.

Interior packstones

Interior patch reefs

Margin coral/rudists

Pelagic muds

Transported interior

Transported margin
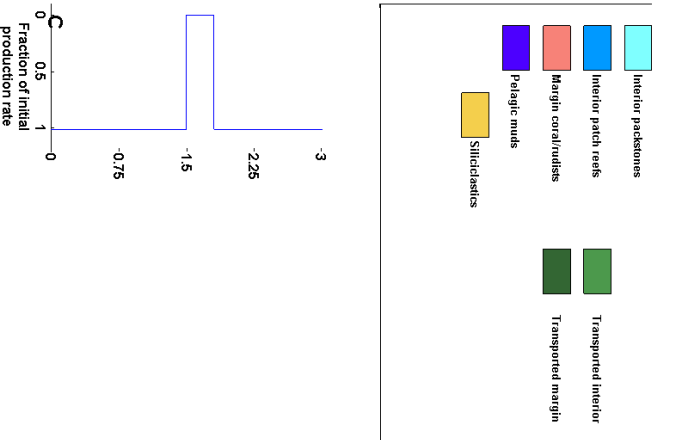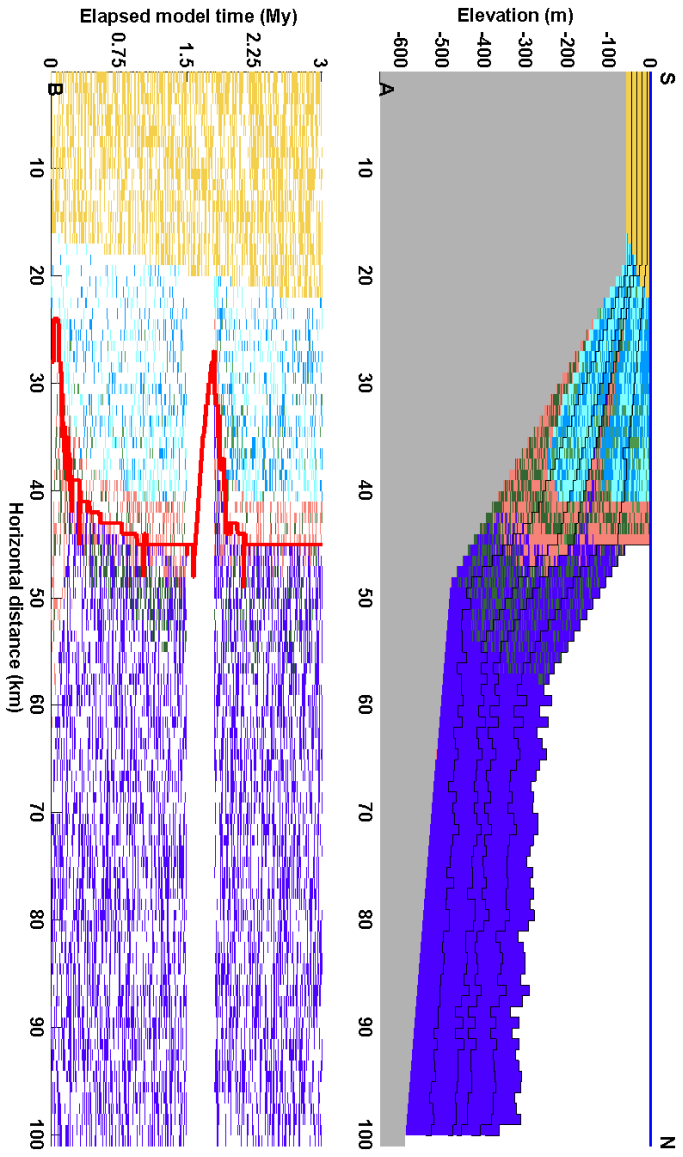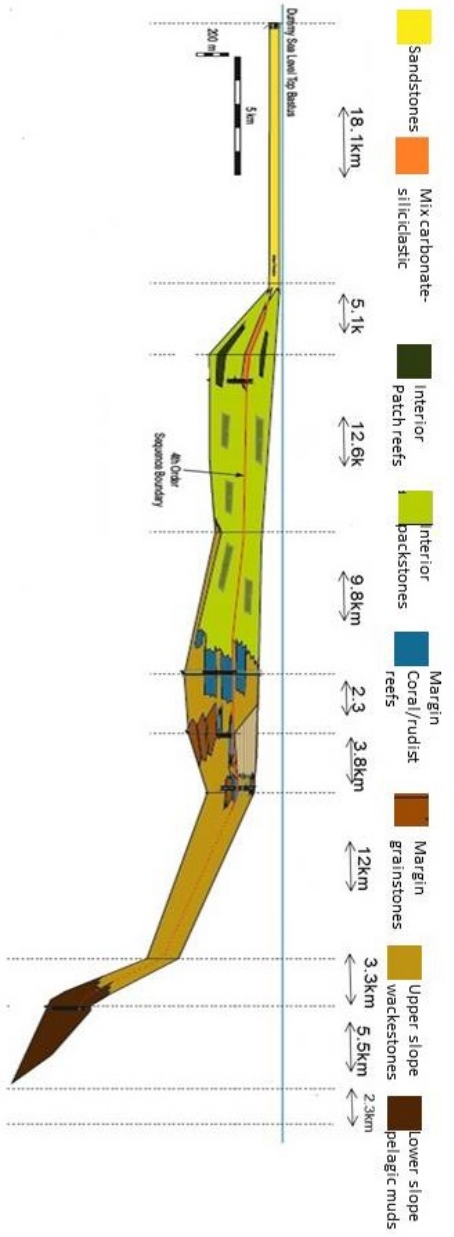
Siliciclastics

Subaerial exposure

Z(m)

Y(km)

X(km)
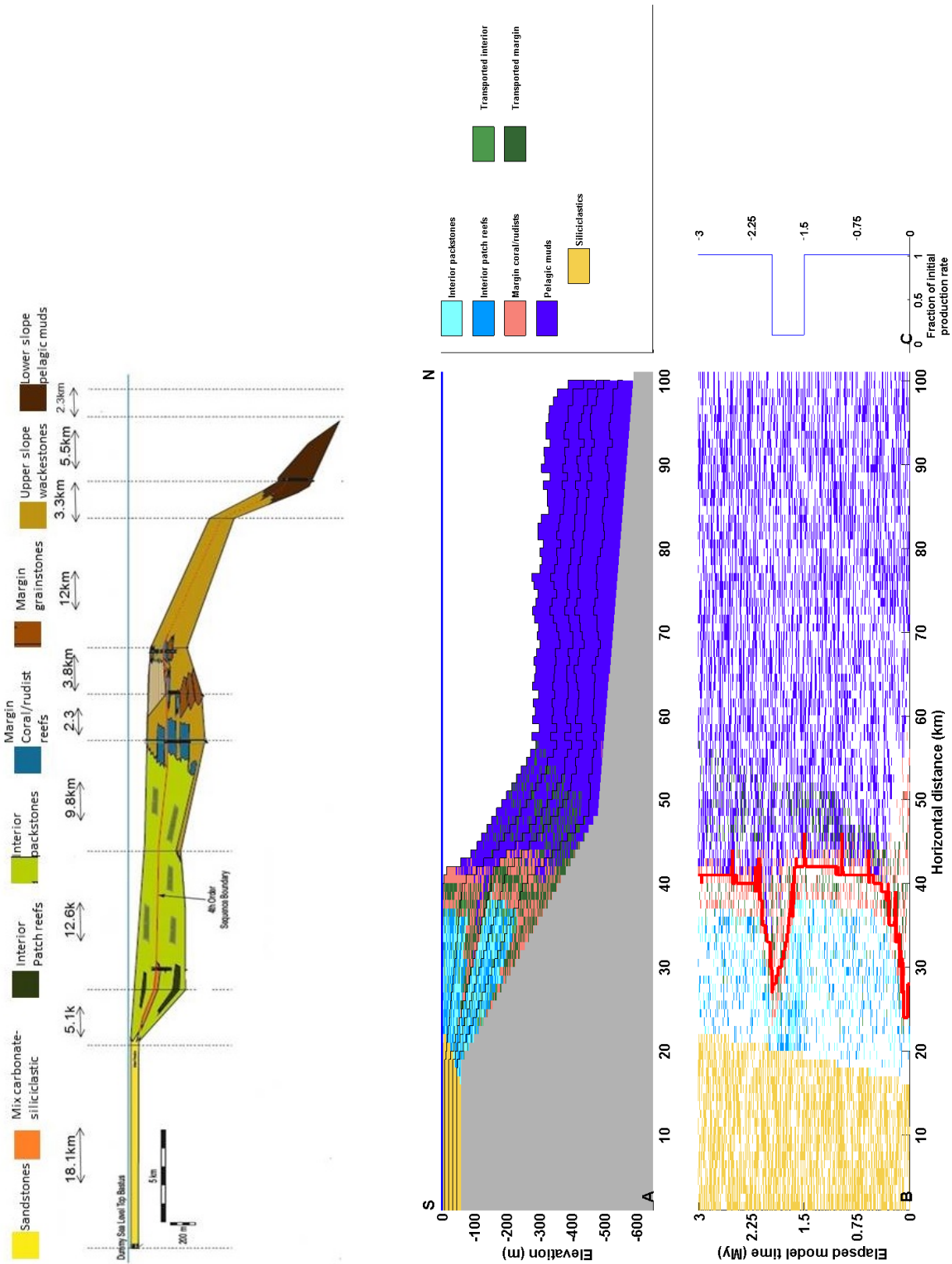
Figure C.24: (A) Cross section along the x=25 of the 3D model. The cross section shows siliciclastic dominating the most proximal part (0-18 km), extensive platform interior (18-48 km), aggrading platform margin and upper slope extending to 61 km. (B) Chrono-strat section at the same position as (A) with the platform margin position (red line) superimposed. The platform margin progrades for 6 km once it gets established (0.6 My). (C) Fraction of the carbonate production. Interpreted platform geometry for comparison on the top.

Table C.11: Length and thickness of P-C2 model run

Platform segment	Field values	Numerical model
Siliciclastics length	18km	18km
Siliciclastics thickness	60m	60m
Carbonate interior length	28km	20km
Carbonate interior thickness	450m	423m
Margin length	5km	5km
margin thickness	280m	302m
slope thickness	250m	274m
platform type	low angle	1.42^o

Bibliography

Adam, L. and Batzle, M. L., 2008. Elastic properties of carbonates from laboratory measurements at seismic and ultrasonic frequencies. The leading edge, 27(8), pp. 1026-1032.

Adams, E. and Kenter, J. A. M., 2012. So Different, Yet So similar: Comparing and Contrasting Siliciclastic and Carbonate Slope.. s.l., s.n.

Adams, E. et al., 2002. Quantifying the geometry and sediment fabric of linear slopes: examples from the Tertiary of Italy (Southern Alps and Gargano Promontory). Sedimentary Geology, Volume 154, pp. 11-30.

Adams, E. and Schlager, W., 2000. Basic types of submarine slope curvature. Journal Of Sedimentary Research, 70(4), pp. 814-828.

Adams, E. W. et al., 2011. Improving reservoir models of Cretaceous carbonates with digital outcrop modelling (Jabal Madmar, Oman): static modelling and simulating clinoforms. Petroleum Geoscience, 17(3), pp. 309-332.

Ahr, W., 2008. Geology of carbonate reservoirs: the identification, description and characterization of hydrocarbon reservoirs in carbonate rocks. s.l.:Hoboken, NJ : Wiley.

Aki, K. and Richards, P. G., 1980. Quantitative Seismology; Theory and Methods. s.l.:W. H. Freeman and Company.

Al-Ameri, T. K., Al-Khafaji, A. and Zumberge, J., 2009. Petroleum system analysis of the Mishrif reservoir in the Ratawi, Zubair, North and South Rumaila oil fields, southern Iraq. GeoArabia, 14(4), pp. 91-108.

Aleardi, M. and Ciabarri, F., 2017. Assessment of different approach to rock-physics modeling. A case study from offshore Nile Delta.. Geophysics, 82(1), pp. MR15-MR25.

Alsharhan, A., 1995. Facies variation, diagenesis and exploration potential of the Cretaceous Rudist-bearing carbonates of the Arabian Gulf. AAPG Bulletin, 79(4), pp. 531-550.

Amaru, M., Sun, T., Goggin, L. and Harris, A., 2017. Integration of computational stratigraphy models and seismic data for subsurface characterization. The leading edge, 36(11), pp. 947b1–947b7.

Anderson, N. and Cardimona, S., 2000. Forward Seismic Modeling: The Key to Understanding Reflection Seismic and Ground Penetrating Radar (GPR) Techniques. Geophysics, Volume 65, pp. 11-15.

Anell, I. and Midtkandal, I., 2015. The quantifiable clinothem – types, shapes and geometric relationships in the Plio-Pleistocene Giant Foresets Formation,Taranaki Basin,New Zealand.. Basin Research, pp. 1-12.

Anon., 1984. Shore Protection Manual., Waterways Experiment Station, Vicksburg, Mississippi: s.n.

Anon., 2013. National Oceanographic and Atmospheric Admnistration. s.l.:s.n.

Anon., n.d. Geosciences Australia. s.l.:s.n.

Anon., n.d. Oilfield Glossary. s.l.:s.n.

Anon., n.d. Stratigraphic Forward Modelingdelling as a Tool in Hydrocarbon Exploration,. s.l.:s.n.

Ansalmetti, F. and Eberi, G., 1993. Controls on sonic velocity in carbonates. Pure and Applied Geophysics, 141(2-4), pp. 287-323.

Appela, D. and Petersson, N. A., 2009. A stable finite difference method for the elastic wave equation on complex geometries with free surfaces.. Communications in Computational Physics, 5(1), pp. 84-107.

Aqrawi, A., Thehni, G., Sherwani, G. and Kareem, B., 1998. Mid-Cretaceous rudists-bearing carbonates of the Mishrif formation: An important reservoir sequence in the Mesopotamian basin, Iraq. Journal of Petroleum Geology, 21(1), pp. 57-82.

Assefa, S., McCann, C. and Sothcott, J., 2003. Velocities of compresional and shear waves in limestones. Geophysical Prospecting, Volume 51, pp. 1-13.

Azeredo, A., Silva, R., Duarte, L. and Cabral, C., 2009. Subtidal stromatolites from the Silnemurian of the Lusitanian Basin (Portugal). Facies, Volume 56, pp. 211-230.

Backus, G., 1962. Long-Wave Elastic Anisotropy Produced by Horizontal Layering. Journal of Geophysical Research, 67(11), pp. 4427-4440.

Badenas, B. and Aurell, M., 2010. Facies models of a shallow-water carbonate ramp based on distribution of non-skeletal grain (Kimmeridgian, Spain).. Facies, Volume 56, pp. 89-110.

Baechle, G., Colpaert, A., Eberli, G. and Weger, R., 2008. Effects of microporosity on sonic velocity in carbonate rocks. The leading edge, 27(8), pp. 1012-1018.

Bagrintseva, K., 2015. Carbonate reservoir rocks. s.l.:Wiley,.

Bal, G. and Moscoso, M., 2000. Polarization effects of seismic waves on the basis of radiative transport theory. Geophysical Journal International, 142(2), pp. 571-585.

Baniak, G. M. et al., 2014. Sbakha and Burrow-Mediated Dolomitization in the Mississippian Debolt Formation, NorNorthwest Alberta, Canada. Ichnos, Volume 21, pp. 158-174.

Ban, S., Graham, N. and Connolly, S., 2014. Evidence for multiple stress interactions and effects on coral reefs. Global Change Biology, Volume 20.

Barnaby, R. and Read, J., 1990. Carbonate ramp to rimmed shelf evolution: Lower to Middle Cambrian continental margin, Virginia Appalachians. Geological Society of America Bulletin, Volume 102, pp. 391-404.

Bauer, S., Olson, D. B. and Hitchcock, G. L., 1991. Influence of monsoonally-forced Ekman dynamics upon surface layer depth and plankton biomass distri-

bution in the Arabian Sea. Deep Sea Research Part A, Oceanographic Research Papers, 38(5), pp. 531-553.

Beavington-Penney, S., Wright, J. D. and Racey, A., 2005. Sediment production and dispersal on foraminifera-dominated early Teriary rramp: the Eocene El Garcia Formation, Tunisia. Sedimenntology, 52(3), pp. 537-569.

Berger, A. and Loutre, M., 1991. Insolation values for the climate of the last 10 million years. Quaternary Science Revies, Volume 4, pp. 297-317.

Beydoun, W. B. and Mendes, M., 1989. Elastic ray-Born l (sub 2) -migration/inversion. Geophysical Journal of the Royal Astronomical Society, 97(1), pp. 151-160.

Beylkin, G., 1985. Imaging of discontinuities in the inverse scattering problem by inversion of a causal generalized Radon transform. Journal of Mathematical Physics, Volume 26, p. 99.

Bice, D., 1988. Synthetic stratigraphy of carbonate platfrom and basin systems. GEOLOGY, Volume 16, pp. 703-706.

Bissell, H. J. and Chilingar, G. V., 1967. Chapter 4 Classification of Sedimentary Carbonate Rocks. In: G. V. Chilingar, H. J. Bissell and R. W. Fairbridge, eds. Carbonate Rocks Origin, Occurrence and Classification. s.l.:Elsevier, pp. 87-168.

Bitzer, K. and Salas, R., 2001. Geologic modelling and Simulations.. s.l.:Kluwer Academic / Plenum Publishers.

Bitzer, K. and Salas, R., 2002. SIMSAFADIM: Three- dimensional simulation of stratigraphic architecture and facies distribution modeling of carbonate sediments. Computers and Geosciences, 28(10), pp. 1177-1192.

Bleistein, N., 1987. On the imaging of reflectors in the Earth. Geophysics, 52(7), pp. 931-942.

Bosellini, A., 1984. Progradation geometries of carbonate platforms: examples from the Triassic of the Dolomites, northern Italy.. Sedimentology, Volume 31, pp. 1-24.

Bosence, D., 2005. A genetic classification of carbonate platforms based on their basinal and tectonic settings in the Cenozoic. Sedimentary geology, Volume 175, pp. 49-72.

Bosence, D., 2008. Randomness or order in the occurrence and preservation of shallow-marine carbonate facies? Holocene, South Florida. Palaeogeography, Palaeoclimatology, Palaeoecology, Volume 270.

Bosence, D., Pomar, L., Waltham, D. and Lankester, T., 1994. Computer Modeling a Miocene Carbonate Platform, Mallorca, Spain. AAPG Bulletin, 78(2), pp. 247-266.

Bosence, D., Rowlands, R. and Quine, M., 1985. Sedimentology and budget of a Recent carbonate mound, Florida Keys. Sedimentology, Volume 32, pp. 317-343.

Bosence, D. and Waltham, D., 1990. Computer modeling the internal archi-

tecture of carbonate platforms. Geology, Volume 18, pp. 26-30.

Bosscher, H. and Schlager, W., 1992. Computer simulation of reef growth. Sedimentology, Volume 39, pp. 503-512.

Bowers, D., K.M.Braithwaite, W.A.M.Nimmo-Smith and G.W.Grahamb, 2009. Light scattering by particles suspended in the sea: The role of particle size and density. Continental Shelf Research, Volume 29.

Boylan, A. L. et al., 2002. Digital rocks: linking forward modelling to carbonate facies. Basin Research, 14(3), pp. 401-415.

Bretschneider, C., 1958. Revisions in Wave Forecasting; Deep and Shallow Water. Proceedings of the Sixth Conference on Coastal Engineering, ASCE, Counsil on Wave Research.

Burchette, T., 1993. Mishrif Formation (Cenomanian-Turonian), southern Arabian Gulf: carbonate platform growth along a Cratonic basin margin. AAPG Memoir, Volume 56, pp. 185-200.

Burchette, T. and Wright, V., 1992. Carbonate ramp depositional systems. Sedimentary Geology, Volume 79, pp. 3-57.

Burgess, P. M., 2001. Modeling carbonate sequence development without relative sea-level oscillations. Geology, 29(12), pp. 1127-1130.

Burgess, P. M., 2006. The signal and the noise: Forward modeling of allocyclic and autocyclic processes influencing peritidal carbobate stacking patterns. Journal of Sedimentary Research, Volume 76, pp. 962-977.

Burgess, P. M., 2008. The nature of shallow-water carbonate lithofacies thickness distributions. Geology, 36(3), pp. 235-238.

Burgess, P. M., 2013. CarboCAT; A cellular automata model of heterogeneous carbonate strata. Computers and Geosciences, Volume 53, pp. 129-140.

Burgess, P. M., 2016. Identifying ideal stratigraphic cycles using a quantitative optimization method. Geology, 44(6), pp. 443-446.

Burgess, P. M., 2016. Identifying ordered strata: Evidence, method and meaning. Journal of Sedimentary Research, Volume 86, pp. 148-167.

Burgess, P. M., 2016. The future of the sequence stratigraphic paradigm: Dealing with a variable third dimension. Geology, 44(4), pp. 335-336.

Burgess, P. M. and Allen, P., 1996. A forward-modelling analysis of the controls on sequence stratigraphical geometries. Geological Society London Special Publications, Volume 103, pp. 9-24.

Burgess, P. M., Allen, P. and Steel, R., 2016. Introduction to the future of sequence stratigraphy: evolution or revolution?. Jornal of the Geological Society.

Burgess, P. M. and Emery, D., 2004. Sensitive dependence, divergence and unpredictable behaviour in a stratigraphic foward model of a carbonate system.. Geological Prior Information: Informing Science and Engineering., Geological Society, London, Special Publications,(239), pp. 77-94.

Burgess, P. M. and Emery, D., 2005. Sensitive dependence, divergence and unpredictable behaviour in a stratigraphic forward model of a carbonate system. Geological society, London, Special Publications, Issue 239.

Burgess, P. M., Lammers, H., va Oosterhout, C. and D., G., 2006. Multivariate sequence stratigraphy: Tackling complexity and uncertainty with stratigraphic forward modeling, multiple scenarios, and conditional frequency maps.. AAPG Bulletin, 90(12), pp. 1883-1901.

Burgess, P. M. and Prince, G. D., 2015. Non-unique sstrata geometries: implications for sequence stratigraphic interpretations. Basin research, Volume 27, pp. 351-365.

Burgess, P. M. and Wright, P. V., 2003. Numerical forward modelling of carbonate platform dynamics: An evaluation of complexity and completeness in carbonate strata. Journal of ssedimentary research, 73(5), pp. 637-652.

Burgess, P. M., Wright, V. and Emery, D., 2003. Numerical forward modelling of peritidal carbonate parasequence developmet: implications for outcrop interpretation. Basin, Volume 13, pp. 1-16.

Burgess, P. M., Wright, V. P. and Emery, D., 2001. Numerical forward modelling of peritidal carbonate parasequence development: implications for outcrop interpretation. Basin Research, Volume 13, pp. 1-16.

Burgess, P. and Prince, G., 2017. Reply to Comment of O.Catuneanu and M.Zecchin on Non-unique stratal geometries: implications for sequence stratigraphic interpretations, by:P.M. Burgess and G.D.Prince,Basin Research (2015) 27, 351–365. Basin Research, Volume 29, pp. 630-635.

Burgess, P. and Steel, R., 2017. How to interpret, understand and predict stratal geometries using stratal-control spaces and stratal-control-space trajectories. Journal of Sedimentary Research, Volume 87, pp. 325-337.

Burgess, P., Wright, V. and Emery, D., 2001. Numerical forward modelling of peritidal carbonate parasequence development:implications for outcrop interpretation. Basin Research, Volume 13, pp. 1-16.

Buxton Latimer, R., Davison, R. and van Riel, P., 2000. An interpreter's guide to understanding and working with seismic-derived acoustic impedance data. The leading edge, 19(3), pp. 242-256.

C., C. et al., 2001. Elastic of single crystal calcite and rhodochrosite by Brillouin spectroscopy. American Mineralogist, Volume 86.

Campbell, A. E., 2005. Shelf-geometry response to changes in relative sea level on a mixed carbonate–siliciclastic shelf in the Guyana Basin. Sedimentary Geology, Volume 175, pp. 259-275.

Castagna, J. P., Batzle, M. L. and Eastwood, R., 1985. Relationships between compressional wave and shear wave vlocities in clastic silicate rocks. Geophysics, 50(4), pp. 571-581.

Castagna, J. P., Swan, H. W. and Foster, D., 1998. Framework for AVO gradient and intercept interpretation. Geophysics, 63(3), pp. 948-956.

Catuneanu, O., 2002. Sequence stratigraphy of clastic systems: concepts, merits and pitfalls. Journal of African Earth Sciences, Volume 35, pp. 1-43.

Catuneanu, O. et al., 2009. Towards the standardization of sequence stratigraphy. Earth Science Reviews, Volume 92, pp. 1-33.

Catuneanu, O., Willis, A. J. and Miall, A. D., 1998. Temporal significance of sequence boundaries. Sedimentary Geology, Volume 121, pp. 157-178.

Catuneanu, O. and Zecchin, M., 2016. Unique vs. non-unique stratal geometries: Relevance to sequence stratigraphy. Marine and Petroleum Geology, Volume 78, pp. 184-195.

Catuneanu, O. and Zecchin, M., 2017. Comment on Non-unique stratal geometries: implications for sequence stratigraphic interpretations, by:P.M.Burgess and G.D.Prince, Basin Research (2015) 27, 351–365. Basin Research, Volume 29, pp. 625-629.

Cheng, J. and Kang, W., 2014. Simulating propagation of separated wave modes in general anisotropic media, Part 1: qP-wave propagators. Geophysics, 79(1), pp. C1-C18.

Chereskin, T. and Roemmich, D., 1991. A comparison of Measured and Wind Derived Ekman Transportation at 11o N in the Atlantic Ocean. Journal of Physical oceanography, 21(21), pp. 869-878.

Choquette, P. and Pray, L., 1970. Geological nomenclature and classification of porosity in sedimentary cabonates.. American Association of Petroleum Geologists Bulletin, 54(2), pp. 207-250.

Chung, H. and Lawton, D., 1995. Amplitude responces of thin beds: Simnusoidal approximation versus Ricker approximation. Geophysics, 60(1), pp. 223-230.

Chung, H. and Lawton, D., 1999. Approximation study of the effects of tuning on AVO effects for thin beds. Canadian Journal of exploration geophysics, Volume 35, pp. 36-42.

Churl-Hyun, J., Changsoo, S. and Jung Hee, S., 1996. An optimal 9-point, finite-difference frequency-space, 2-D scalar wave extrapolator. Geophysics, 61(2), pp. 529-537.

Connolly, P., 1999. Elastic impedance. The leading edge, 18(4), pp. 438-452.

Craig, P. D. and Banner, M. L., 1994. Modeling wave-enhanced turbulance in the ocean surface layer. Journal of physical oceanography, Volume 24.

Culling, W. E. H., 1960. Analytical Theory of Erosion. The Journal of Geology, Volume 3, pp. 336-344.

Cumings, E. R., 1932. Reefs or bioherms. Geological Society of America Bulletin, Volume 43, pp. 331-352.

de Bakker, D. M. et al., 2017. 40 years of benthic community change on the Caribbean reefs of Curacao and Bonaire: the rise of slimy cyanobacterial mats. Coral reefs, Volume 36, pp. 355-367.

Demicco, R., 1998. Cycopath 2D - A two dimensional, forward model of cyclic sedimentation on carbonate platforms. Computers and Geosciences, 24(5), pp. 405-423.

Driscoll, N. W. and Karner, G. D., 1999. Three- dimensional quantitative modeling of clinoform development. Marine Geology, 154(1-4), pp. 383-398.

Drummond, C. and Dugan, P., 1999. Self-organising models of shallow-water carbonate accumulation.. Journal of Sedimentary Research, Volume 69, pp. 939-946.

Dunham, R. J., 1962. Classification of carbonate rocks according to depositional texture. American Association of Petroleum Geologists, Volume Memoir 1, pp. 108-121.

Dvorkin, J. and Wollner, U., 2017. Rock-physics transforms and scale investigation. Geophysics, 82(3), pp. MR75-MR88.

Eberli, G., Baechle, G., Anselmetti, F. and Incze, M., 2003. Factors controlling elastic properties in carbonate sediments and rocks. The leading edge, 22(7), pp. 654-660.

Ehrenberg, S. N., 2006. Porosity destruction in carbonate platforms. Journal of Petroleum Geology, 29(1), pp. 41-52.

Embry, A. F. and Klovan, J. E., 1971. A Late Devonian reef tract on northeastern Banks Island, Northwest Territories.. Bulletin Canadian Petroleum Geologists, Volume 33, pp. 730-781.

Emery, D. and Myers, K., 1996. Sequence srtratigraphy. First edition ed. s.l.:Blackwell Science Ltd.

Enge, H. D., Howell, J. A. and Buckley, S. J., 2010. Quantifying clinothem geometry in a forced regressive rive-dominated delta, Panther Tongue Member, Utah, USA. Sedimentology, Volume 57, pp. 1750-1770.

Enos, P., 1991. Sedimentary parameters for computer modelling.. Sedimentary Modeling: Computer Simulations and Methods for Improved Parameter Definition, Kansas Geological Survey, Bulletin(233), pp. 63-99.

Erftemeijer, P. A., Riegl, B., Hoeksema, B. and P.A., T., 2012. Environmental impacts of dredging and other sediment disturbances on corals: A review. Marine Pollution Bulletin, Volume 64, pp. 1737-1765.

F., F. et al., 2011. Elastic properties of microporous cemented grainstones. Geophysics, 76(6), pp. 211-226.

Fabricius, I., Bachle, G. and Eberi, G., 2010. Elastic moduli of dry and water-saturated carbonates - Effect of depositional texture, pororsity and permeability. Geophysics, 75(3), pp. N65-N78.

Fabricius, K., 2005. Effects of terrestrial runoff on the ecology of corals and coral reefs: review and synthesis. Marine Pollution Bulletin, Volume 50, pp. 125-146.

Folley, M., Whittaker, T. J. T. and Henry, A., 2007. The effect of water depth on the performance of a small surging wave energy converter. Ocean Engineering, 34(8), pp. 1265-1274.

Fournier, F. and Borgomano, J., 2009. Critical porosity and elastic properties of microporous mixed carbonate-siliciclastic rocks. Geophysics, 74(2), pp. E93-E109.

Fournier, F. et al., 2014. Pore space evolution and elastic properties of platform carbonates (Urgonian limestone, Barremian-Aptian, SE France). Sedimentary Geology, Volume 308, pp. 1-17.

G., B., G., E., R., W. and J., M., 2009. Changes in dynamic shear moduli of carbonate rocks with fluid substitution. Geophysics, 74(3), pp. E135-E147.

G., B. et al., 2005. Changes of shear moduli in carbonate rocks:Implication for Gassmann applicability. The leading edge, 24(5), pp. 507-510.

Galloway, W., 1987. Depositional and structural architecture of prograding clastic continental margins: tectonic inftuence on patterns of basin filling. Norsk Geologisk Tidsskrift, Volume 67, pp. 237-251.

Gardner, G., Gardner, L. and Gregory, A., 1974. Formation velocity and density - The diagnostic basics for stratigraphic traps. Geophysics, 39(6), pp. 770-780.

Gebauer, D., Volel, A. and Colfen, H., 2008. Stable prenuclation calcium carbonate clusters. Science, Volume 322, pp. 1819-1822.

Gelis, C., Virieux, J. and Grandjean, G., 2007. Two-dimensional elastic full waveform inversion using Born and Rytov formulations in the frequency domain. Geophysical Journal International, 168(2), pp. 605-633.

Gerber, T. P. et al., 2008. Clinoform progradation by turbidIty current: Modeling and experiments. Journal of Sedimentary Research, Volume 78, pp. 220-238.

Ginsburg, R. N., 1971. Landward movement of carbonate mud: new model for regressive cycles in carbonates (Abstract). American Association of Petroleum Geologists, Annual Meeting Abstract Programs, Volume 55, p. 340.

Goldhammer, R., Dunn, P. and Hardie, L., 1990. Depositional cycles, composite sea-level changes, cycle stacking patterns, and the hierarchy of stratigraphic forcing: Examples from Alpine Triassic platform carbonates. Geological Societty of American Bulletin, Volume 102, pp. 535-562.

Goldhammer, R., E.J., O. and Dunn, P., 1991. Hierarchy of stratigraphic forcing: example from Middle Pennsylvanian shelf carbonates of the Paradox Basin. Sedimentary Modeling: Computer Simulations and Methods for Improved Parameter Definition, Kansas Geological Survey, Volume Bulletin 233, pp. 361-413.

Goldhammer, R., Lehmann, P. and Dunn, P., 1993. The origin of high-frequency platform carbonate cycles and third-order sequences (Lower Ordovician, El Pao GP, west Texas): Constraints from outcrop data and sytratigraphic modeling. Journal of Sedimentary Petrology, Volume 63, pp. 318-359.

Gold, N., Shapiro, S. A., Bojinski, S. and Muller, T., 2000. An approach to upscaling for seismic waves in statistically isotropic heterogeneous elastic media. Geophysics, 65(6), pp. 1837-1850.

Graham, G., Jackson, M. and Hampson, G., 2015. Three-dimensional modeling of clinoforms in shallow-marine reservoirs: Part 1. Concepts and application. AAPG Bulletin, 99(6), pp. 1013-1047.

Granjeon, D. and Joseph, P., 1999. Concepts and applications of a 3-D multiple lithology, diffusive model in stratigraphic modeling. Numerical Experiments in Stratigraphy: Recent Advances in Stratigraphic and Sedimentologic Computer Simulations:SEPM, Issue 62, pp. 197-210.

Gratacos, O., Bitzer, K., Cabrera, L. and Roca, E., 2009. SIMSAFADIM-CLASTIC: A new approach to mathematical 3D forward simulation modelling for terrigenous and carbonate marine sedimentation. Geologica Acta, 7(3), pp. 311-322.

Hahn, D., 2006. Light scattering theory.. Aerospace Engineering.

Hallock, P., 2005. Global change and modern coral reefs: New oportunities to understand shallow water carbonate deposiotional processes. Sedimentary Geology, Volume 175, pp. 19-33.

Hampson, G., 2016. Towards a sequence stratigraphic solution set for autogenic processes and allogenic controls: Upper Cretaceous strata, Book Cliffs, Utah, USA. Journal of Geological Society, Volume 173, pp. 817-836.

Hampson, G. and Storms, J., 2003. Geomorphological and sequence stratigraphic variability in wave-dominated, shore-shelf parasequences. Sedimentology, Volume 50, pp. 667-701.

Hanford, C. and Loucks, R., 1993. Carbonate Depositional Sequences and System Tracts - Responces of Carbonate Platform to Relative Sea Level Changes. American Association of Petroleum Geologists.

Hart, D. E. and Kench, P. S., 2007. Carbonate production of an emergent reef platform, Warraber Island, Torres Strait, Australia. Coral reefs, Volume 26, pp. 53-68.

Hastings, F., Schneider, J. B. and Broschat, S. L., 1996. Application of the perfectly matched layer (PML) absorbing boundary condition to elastic wave propagation.. The Journal of the Acoustical Society of America, 5(100), pp. 3061-3069.

Helland-Hansen, W. and Gjelberg, J. G., 1994. Conceptual basis and variability in sequence stratigraphy: a different perspective. Sedimentary Geology, 92(1), pp. 31-52.

Helland-Hansen, W. and Hampson, G., 2009. Trajectory analysis: concepts and applications. Basin Research, Volume 21, pp. 454-483.

Helland-Hansen, W. W. and Martinsen, O., 1996. Shoreline trajectories and sequences: Description of variable depositional-dip scenarios. Journal Of Sedimentary Research, 66(4), pp. 670-688.

Hine, A. C. et al., 1981. Offbank transport of carbonate sands along open, leeward bank margins: Northern Bahamas. Marine Geology, 42(1), pp. 327-348.

Hjulstrom, F., 1939. Transportation of Detritus by Moving water. AAPG Special Volumes, Volume Sdimentology, Recent Marine Sediments, pp. 5-31.

Hoegh-Guldberg, O. et al., 2007. Coral Reefs Under Rapid Climate Change and Ocean Acidification. Science, Volume 318, pp. 1737-1742.

Horn, B. K. P., 1981. Hill shading and the Reflectance Map. Proceedings of the IEEE, 69(1), pp. 14-47.

Huang, X., Griffiths, C. M. and Liu, J., 2015. Recent development in stratigraphic forward modelling and its application in petroleum exploration.. Australian Journal of Earth Sciences, Volume 62, pp. 903-919.

Hudson, J. A. and Heritage, J. R., 1981. The use of the Born approximation in seismic scattering problems. Geophysical Journal, Royal Astronomical Society, 66(1), pp. 221-240.

Hughes, T., 1999. Off-reef transport of coral fragments at Lizard Island, Australia. Marine Geology, Volume 157, pp. 1-6.

Hunt, D. and Tucker, M. E., 1992. Stranded parasequences and the forced regressive wedge systems tract: deposition during base-level fall. Sedimentary Geology, Volume 81, pp. 1-9.

Hurd, G., Kerans, C., Fullmer, S. and Janson, X., 2016. Large-scale inflections in slope angle below the shelf: a first order control on the stratigraphic architecture of carbonate slopes: Cutoff formation, Guadalupe mountains national park, West Texas, USA. Journal of Sedimentary Research, Volume 86, pp. 336-362.

Hurdle, D. P. and Stive, R. J. H., 1989. Revision of SPM 1984 wave hindcast model to avoid inconsistencies in engineering applications. Coastal Engineering, 12(4), pp. 339-351.

Husseiny, A. and Vanorio, T., 2015. The effect of micrite content on the acoustic velocity of carbonate rocks. Geophysics, 80(4), pp. L45-L55.

Hustedt, B., Operto, S. and Virieux, J., 2004. Mixed-grid and staggered-grid finite-difference methods for frequency-domain acoustic wave modelling. Geophysical Journal International, 157(3), pp. 1269-1296.

Immenhauser, A., 2005. High rate sea level change during the Mesozoic: New appraoches to an old problem. Sedimentary Geology, Volume 175, pp. 277-296.

Immenhauser, A., 2009. Estimating palaeo- water depth from the physical rock record. Earth-Science Reviews, 96(1-2), pp. 107-139.

316

Immenhauser, A., 2009. Estimating paleo-water depth from the physical rock record. Earth Science Reviews, Volume 96, pp. 107-139.

Insalaco, E., 1998. The descriptive nomenclature and classification of growth fabrics in fossil scleractinian reefs. Sedimentary Geology, Volume 118, pp. 159-186.

Jackson, D., Briggs, K., Williams, K. and Richardson, M. D., 1996. Tests of models for high- frequency seafloor backscatter. Ieee Journal Of Oceanic Engineering, 21(4), pp. 458-470.

Jervey, M., 1988. Quantitative geological modeling of siliciclastic rock sequences and their seismic expression. The Society of Economic Paleontologists and Mineralogists (SEPM), Special Publication n42(42), pp. 47-69.

Johanessen, E. P. and Steel, R., 2005. Shelf-margin clinoforms and prediction of deepwater sands. Basin Research, Volume 17, pp. 521-550.

Jones, K. H., 1998. A comparison of algorithms used to compute hill slope as a property of the DEM. Computers and Geosciences, 24(4), pp. 315-323.

Jones, N. L. and Monismith, S. G., 2008. Modelling the influence of wave-enhanced turbulence in a shallow tide- and wind-driven water column. Journal of geophysical research, Volume 113.

Jones, N., Ridgwell, A. and Hendy, E., 2015. Evaluation of coral reef carbonate production models at a global scale. Biogeosciences, Volume 12, pp. 1339-1356.

Julien, P., 2010. Erosion and Sedimentation. 2 ed. s.l.:Cambridge University Press.

Julien, P. and Simons, D., 1985. Sediment transport capacity of overland flow. Transactions of the ASAE, 28(3), pp. 755-762.

Kajishima, T. and Taira, K., 2017. Computational Fluid Dynamics. 1 ed. s.l.:Springer International Publishing.

Kallweit, R. S. and Wood, L., 1982. The limits of resolution of zero-phase wavelets. Geophysics, Issue 7, pp. 1035-1046.

Karakul, H. and Ulusay, R., 2013. Empirical Correlations for Predicting Strength Properties of Rocks from P-Wave Velocity Under Different Degrees of Saturation. Rock Mech Rock Eng, 46(5), pp. 981-999.

Kaser, M. and Dumbser, M., 2006. An arbitrary high-order discontinuous Galerkin method for elastic waves on unstructured meshes - I. The two-dimensional isotropic case with external source terms. Geophysical Journal International, 166(2), pp. 855-877.

Kaufman, P., Grotzinger, J. and McCormick, D., 1991. Depth dependent diffusion algorithm for simulation of sedimentation in shallow marine depositional systems. Kansas Geological Survey Bulletin, Volume 233, pp. 489-508.

Kausel, E. A. and Roesset, J. M., 1981. Stiffness matrices for layered soils. Bulletin of the Seismological Society of America, 71(6), pp. 1743-1761.

Kausel, E., Roesset, J. M. and Bouckovalas, G., 1980. A stiffness matrix

approach for layered soils. Proceedings of the World Conference on Earthquake Engineering, Issue 7, Vol. 3, pp. 265-272.

Kendal, C. and Schlager, W., 1981. Carbonate and relative changes in sea level. Marine Geology, Volume 44, pp. 181-212.

Kenter, J. A. M., 1990. Carbonate platform flanks: Slope angle and sediment fabric. Sedimentology, Volume 37, pp. 777-794.

Kenter, J. A. M. and Schlager, W., 1989. A comparison of shear strength in calcereous and siliciclastic marine sediments. Volume 89, pp. 145-152.

Kenter, J., Braaksma, H., Verwer, K. and Lanen, X., 2007. Acoustic behavior of sedimentary rocks: Geologic properties versus Poisson's ratios. The leading edge, Volume 26, pp. 436-444.

Kenter, J. and Ivanov, M., 1995. Parameters controlling acoustic properties of carbonate and volcaniclastic sediments at sites 866 and 869. Proceedings of the ocean program. Scientific results, 143(18).

Kertznus, V. and Kneller, B., 2009. Clinoform quantification for assessing the effects of external forcing on continentalmargin development. Basin Research, Volume 21, pp. 738-758.

Kleipool, L., Reijmer, J., Badenas, B. and Aurell, M., 2015. Variations in petrophysical properties along a mixed siliciclastic carbonate ramp (Upper Jurassic, Ricla, NE Spain). Marine and Petroleum Geology, Volume 68, pp. 158-177.

Knighton, D., 1998. Fluvial forms and processes : a new perspective. London: London : Arnold.

Kominz, M. A. et al., 2008. Late Cretaceous to Miocene sea-level estimates from the New Jersey and Delaware coastal plain coreholes: an error analysis. Basin Research, Volume 20, pp. 211-226.

Konta, J., 1968. Classification of sedimentary rocks. s.l.:Academia Prague.

Kozlowski, E. N., 2017. Multi-scale forward modelling of microbial lacustrine carbonates, s.l.: s.n.

Lavi, J., 2017. Controls on Basin-scale and Platform-scale Architecture of Upper Cretaceous Carbonate Platforms, s.l.: s.n.

Lay, T. and Wallace, T., 1995. Modern Global Seismology. s.l.:Academin Press.

Lee, C. M., Jones, B. H., Brink, K. H. and Fischer, A. S., 2000. The upper-ocean response to monsoonal forcing in the Arabian Sea: Seasonal and spatial variability. Deep-Sea Research Part II: Topical Studies in Oceanography, 47(7-8), pp. 1177-1226.

Lehrmann, D. and Goldhammer, R., 1999. Secular variation in parasequence and facies stacking patterns of platform carbonates: A guide to application of stacking-patterns analysis in strata of diverse ages and settings.. Advances in Carbonate Sequence Stratigraphy: Applications to Reservoirs Outcrops and Models.

SEPM, Volume 63, pp. 187-225.

Leonard, J. and Richard, G., 2004. Estimation of runoff critical shear stress for soil erosion from soil shear strength. CATEN, 57(3), pp. 233-249.

Lima Neto, I. et al., 2015. Evaluation of carbonate pore system under texture control for prediction of microporosity aspect ratio and shear wave velocity. Sedimentary Geology, Volume 323, pp. 43-65.

Liu, T. and Zhao, C., 2013. Dynamic analyses of multilayered poroelastic media using the generalized transfer matrix method. Soil Dynamics and Earthquake Engineering, Volume 48, pp. 15-24.

Lopez, H. A. and Dvorkin, J., 2017. Rock-physics diagnostic of a turbidite oil reservoir offshore nortwest Australia. Geophysics, 82(1), pp. MR1-MR13.

Lucia, F. J., 1999. Carbonate Reservoir Characterization. s.l.:Springer - Verlag Berlin Heidelberg.

Lund-Hansen, L. C., Hai, D. N., Lam, N. N. and Nielsen, M. H., 2010. Optical properties of a tropical estuary during wet and dry conditions in the Nha Phu estuary, Khanh Hoa Province, south-east Vietnam. Hydrobiologia, Volume 644, pp. 207-216.

M., C., 2003. Frequency-dependent anisotropy due to meso-scale fractures in the presense of equant porosity.. Geophysical Prospecting, Volume 51.

Madariaga, R., 2007. Seismic Source Theory. Treatise on Geophysics, Issue 4, pp. 59-82.

Madof, A. S., Harris, A. D. and Connell, S. D., 2016. Nearshore along-strike variability: Is the concept of the systems tract unhinged?. Geology, 44(4), pp. 315-318.

Mahdi, T. A. and Aqrawi, A., 2014. Sequence stratigraphic analysis of the mid-Cretaceous Mishrif Formation, southern Mesopotamian Basin, Iraq. Journal of Petroleum Geology, 37(3), pp. 287-312.

Mahdi, T. A., Aqrawi, A., Horbury, A. D. and Sherwani, G., 2013. Sedimentological characterization of the mid-Cretaceous Mishrif reservoir in southern Mesopotamian Basin, Iraq. GeoArabia, 18(1), pp. 139-174.

Maina, J., Venusb, V., McClanahana, T. R. and Ateweberhana, M., 2008. Modelling susceptibility of coral reefs to environmental stress using remote sensing data and GIS models. Ecological Modelling, Volume 212, pp. 180-199.

Mallela, J., 2007. Coral reef encruster communities and carbonate production in cryptic and exposed coral reef habitats along a gradient of terrestrial disturbance. Coral Reefs, Volume 26, pp. 775-785.

Maloof, A. C. and Grotzinger, J., 2012. The Holocene shallowing-upwards parasequence of north-west Andros Island, Bahamas. Sedimenntology, Volume 59, pp. 1375-1407.

Mao-Jones, J., Ritchie, K. B., Jones, L. E. and Ellner, S. P., 2010. How micro-

bial community composition regulates coral disease development. PLoS Biology, 8(3), p. e1000345.

Marion, D., Mukerji, T. and Mavko, G., 1994. Scale effects on velocity dispersion: From ray to effective medium theories in stratified media.. Geophysics, 59(10), pp. 1613-1619.

Martin, J. et al., 2009. Sequence stratigraphy of experimental strata under known conditions of differential subsidence and variable base level. AAPG Bulletin, 93(4), pp. 503-533.

Mavko, G., Mukerji, T. and Dvorkin, J., 2009. Rock physics handbook,. Second ed. s.l.:Cambridge university press.

Mazler, C., 2002. MATLAB functions for Mie scattering and absorption, version 2., s.l.: s.n.

McNeill, D., 2005. Accumulation rates from well-dated late Neogene carbonate platforms and margins. Sedimentary geology, pp. 73-87.

Miller, K. G. et al., 2005. The phanerozoic record of global sea- level change. Science, 310(5752), pp. 1293-1298.

Mitchum, R. M., Vail, P. r. and S., T., 1977. Seismic stratigraphy and global changes of sea level, Part 2: The depositional sequence as a basic unit for stratigraphic analysis. American association of Petroleum Geologists Memoir, Volume 26, pp. 53-62.

Mitchum, R. M., Vail, P. R. and Sangree, J. B., 1977. Seismic Stratigraphy and Global Channges of Sea Level, Part 6: Stratigraphic Interpretation of Seismic Reflection Patterns in Depositional Sequences. American Association of Petroleum Geologists, Volume Memoir 26, pp. 117-133.

Moore, C., 2001. Carbonate reservoir. Porosity evolution and diagenesis in a sequence stratigraphic framework. First Edition ed. s.l.:Elsevier Science.

Morgan, K. M. et al., 2016. Evidence of extensive reef development and high coral cover in nearshore environments: implications for understanding coral adaptation in turbid settings. Nature Scientific Reports — 6:29616.

Morse, J. and Mackenzie, F., 1990. Geochemistry of Sedimentary Cabonates. s.l.:Elsevier Science.

Moulton, J., Knapek, S. and Dendy, J., 1998. Mulseismic upscaling in heterogeneous porous media. http://citeseer.ist.psu.edu/212257.html.

Munoz, J., Martinez, A. and Verges, J., 1986. Thrust sequences in the eastern Spanish Pyrenees. Journal of Structural Geology, 8(3/4), pp. 399-405.

Muto, T. and Steel, R., 1997. Principles of regression and transgression. The nature of interplay between accommodation and sediment supply. Journal of Sedimentary Research, 67(6), pp. 994-1000.

Muto, T. and Steel, R., 2000. The accommodation concept in sequence stratigraphy: some dimensional problems and possible redefinition. Sedimentary Geol-

ogy, Volume 130, pp. 1-10.

Muto, T. and Steel, R., 2014. The autostratigraphic view of responses of river delats to external forcing: A review of the concepts.. International Association of Sedimentologists, Volume 46, pp. 139-148.

Muto, T., Steel, R. J. and Burgess, P. M., 2016. Contributions to sequence stratigraphy from analogue and numerical experiments. Journal of Geological Society, Volume 173, pp. 837-844.

Muto, T., Steel, R. and Swenson, J. B., 2007. Autostratigraphy: A framework norm for genetic stratigraphy. Journal of Sedimentary Research, Volume 77, pp. 2-12.

Neal, J. and Abreu, V., 2009. Sequence stratigraphy hierarchy and the accommodation succession method. Geology, 37(9), pp. 779-782.

Neal, J. E. et al., 2016. Accommodation succession sequence stratigraphy: observational method, utility and insights into sequence boundary formation. Journal of Geological Society, Volume 173, pp. 803-816.

Palaz, I. and Marfurt, K. eds., 1997. Carbonate Seismology. s.l.:Society of Exploration Geophysicists.

Paola, C., 2000. Quantitative models of sedimentary basin filling. Sedimentology, Volume 47, pp. 121-178.

Paracer, S. and Ahmadjian, V., 2000. Symbiosis, An introduction to biological associations. s.l.:Oxford Press.

Paterson, R. J. et al., 2006. Accommodation and sedimentary architecture of isolated icehouse carbonate platforms: Insights from forward modeling with CARB3D +. Journal of Sedimentary Research, 76(10), pp. 1162-1182.

Payton, C., ed., 1977. Seismic Stratigraphy - applications to hydrocarbon exploration. s.l.:American Association of Petroleum Geologists.

Peel, F. J., 2014. The engines of gravity-driven movement on passive margins: Quantifying the relative contribution of spreading vs. gravity sliding mechanisms. Tectonophysics, Volume 633, pp. 126-142.

Perry, C. T. et al., 2012. Estimating rates of biologically driven coral reef framework production and erosion: a new census-based carbonate budget methodology and applications to the reefs of Bonaire. Coral Reefs, Volume 31, p. 853.

Peters, S. and Loss, D., 2012. Storm and fair-weather wave base: A relevant distinction?. Geology, 40(6), pp. 511-514.

Philip, J. and Gari, J., 2005. Late Cretaceous heterozoan carbonates: Palaeoenvironmental setting, relationships with rudist carbonates (Provence, south-east France). Sed, Volume 175, pp. 315-337.

Pidwirny, M., 2006. "Erosion and Deposition". Foundamentals of Physical Geography. s.l.:s.n.

Pirmez, C., Steckler, M. S. and Pratson, L. F., 1998. Clinoform development by

advection- diffusion of suspended sediment: Modeling and comparison to natural systems. Journal of Geophysical Research: Solid Earth, 103(10), pp. 24141-24157.

Pollitt, D. A., Burgess, P. M. and Wright, V. P., 2015. Investigating the occurance of hierarchies of cyclicity in platform carbonates. Strata and Time: Probing the Gaps in Our Understanding, Geological Society, London, Special Publications, Volume 404, pp. 123-150.

Pomar, L., 2001. Ecological control of sedimentary accommodation: evolution from a carbonate ramp to rimmed shelf, Upper Miocene, Balearic Islands. Palaeogeography, Palaeoclimatology, Palaeoecology, Volume 175, pp. 249-272.

Pomar, L., 2001. Types of carbonate platforms: a genetic approach. Basin Research, Volume 13, pp. 313-334.

Pomar, L., Brandano, M. and Westphal, H., 2004. Environmental factors infuencing skeletal grain sediment associations: a critical review of Miocene examples from the weswest Mediterranean. Sedimentology, Volume 51, pp. 627-651.

Pomar, L., Gili, E., Obrador, A. and Ward, W. C., 2005. Facies architecture and high- resolution sequence stratigraphy of an Upper Cretaceous platform margin succession, southern central Pyrenees, Spain. Sedimentary Geology, Volume 175, pp. 339-365.

Pomar, L. and Hallock, P., 2008. Carbonate factories: A conundrum in sedimentary geology. Earth Science Reviews, Volume 87, pp. 134-169.

Pomar, L. and Kendal, C., 2008. Architecture of Carbonate platforms: A response to hydronamics and evolving ecology. Controls on Carbonate Platform and Reef Development, Volume SEPM Special Publication, 89, pp. 187-216.

Pomar, L. and Ward, W. C., 1999. Reservoir-Scale Heterogeneity in Depositional Packages and Diagenetic Patterns on a Reef-Rimmed Platform, Upper Miocene, Mallorca, Spain. AAPG Bulletin, 83(11), pp. 1759-1773.

Potter, C. and Stewart, R., 1998. Density predictions using Vp and Vs sonic logs, s.l.: s.n.

Pratt, R. G., Shin, C. and Hicks, G. J., 1998. Gauss-Newton and full Newton methods in frequency-space seismic waveform inversion. Geophysical Journal International, 133(2), pp. 341-362.

Puigdefabregas, C. and Souquet, P., 1986. Tecto-sedimentary cycles and depositional sequences of the Mesozoic and Tertiary from the Pyrenees. Tectonophysics, pp. 173-203.

Purkis, S., Riegl, B. and Andrefouet, S., 2005. Remote sensing of geomorphology and facies patterns on a modern carbonate ramp (Arabian gulf, Dubai, U.A.E.). Journal of Sedimentary Research, Volume 75, pp. 861-876.

Purkis, S., Rowlands, G. and Kerr, J., 2015. Unravelling the influence of water depth and wave energy on the facies diversity of shelf carbonates. Sedimenntology, Volume 62, pp. 541-565.

Purkis, S. and Vlaswinkel, B., 2012. Visualizing lateral anisotropy in modern carbonates. AAPG Bulletin, 96(9), pp. 1665-1685.

Purkis, S., Vlaswinkel, B. and Gracias, N., 2012. Vertical to Lateral Transitions Among Cretaceous Carbonate Facies - A mean to 3D Framework Construction Via Markov Analysis. Journal of Sedimentary Research, Volume 82, pp. 232-243.

Quintal, B., Schmalholz, S. and Podladchikov, Y., 2011. Impact of fluid saturation on the reflection coefficient of a poroelastic layer. Geophysics, 76(2).

Rankey, E., 2004. On the interpretation of shallow shelf carbonate facies and habitats: How much does water depth matter?. Journal of Sedimentary Research, 74(1), pp. 2-6.

Rankey, E., Riegl, B. and Steffen, K., 2006. Form, function and feedbacks in a tidally dominated ooid shoal, Bahamas. Sedimenntology, Volume 53, pp. 1191-1210.

Rao, R. R., Molinari, R. L. and Festa, J. F., 1989. Evolution of the climatological near-surface thermal structure of the tropical Indian Ocean: 1. Description of mean monthly mixed layer depth, and sea surface temperature, surface current, and surface meteorological fields. JOURNAL OF GEOPHYSICAL RESEARCH, 94(C8), pp. 10,801–10,815.

Rasolofosaon, P., Lucet, N. and Zonszner, B., 2008. Petroacoustics of carbonate reservoir rocks. The leading edge, 27(8).

Read, J., 1982. Carbonate platforms of passive (extensional) continental margins: Types, characteristics and evolution. Tectonophysics, Volume 81, pp. 195-212.

Reeder, S. and Rankey, E., 2008. Interactions between tidal flows and ooid shoals, Northern Bahamas. Journal of Sedimentary Research, Volume 76, pp. 175-186.

Regnet, J. et al., 2015. Acoustic and reservoir properties of microporous carbonate rocks:Implication of micrite Paparti size and morphology. Journal of Geophysical Research: Solid Earth, Volume 120, pp. 790-811.

Reis, H. L. and Suss, J. F., 2016. Mixed carbonate-siliciclastic sedimentation in forebulge grabens: An example from the Ediacaran Bambui Group, Sao Francisco Basin, Brazil. Sedimentary Geology, Volume 339, pp. 83-103.

Rich, J., 1951. Three critical environments of deposition, and criteria for recognition of rocks deposited in each of them. Bulletin of the Geological Society of America, 62(1), pp. 1-20.

Rogen, B. et al., 2005. Ultrasonic velocities of North Sea chalk samples: influence of porosity, fluid content and texture. Geophysical Prospecting, Volume 53, pp. 481-496.

Rowlands, G. et al., 2012. Satellite imaging coral reef resilience at regional scale. A case-study from Saudi Arabia. Marine Pollution Bulletin, pp. 1222-1237.

Ruf, M., Link, E., Pross, J. and Aigner, T., 2005. Intergrated sequence stratigraphy: Facies, stable isotope and palynofacies analysis in a deep epicontinental carbonate ramp (Late Jurassic, SW Germany).. Sedimentary Geology, Volume 175, pp. 391-414.

Ryther, J., 1956. Photosynthesis in the Ocean as a Function of Light Intensity. Limnology and Oceanography, 1(1), pp. 61-70.

Sadler, P., 1981. Sediment accumulation rates and the completeness of stratigraphic sections. Journal of Geology, 89(5), pp. 569-584.

Sadooni, F. N., 2005. The nature and origin of Upper Cretaceous basin-margin rudists buildups of the Mesopotamian Basin, southern IIraq with consideration of possible hydrocarbon stratigraphic entrapment.. Creataceous Research, Volume 26.

Saenger, E. H., Gold, N. and Shapiro, S. A., 2000. Modeling the propagation of elastic waves using a modified finite- difference grid. Wave Motion, 31(1), pp. 77-92.

Sanders, D., 1998. Upper Cretaceous rudist formations. Geol. PalÃont. Mitt. Innsbruck, Volume 23, pp. 37-59.

Sanders, D. and Pons, J. M., 2001. Stratigraphic Architecture of a Santonian Mixed Siliciclastic-Carbonate Succession (Catalonian Pyrenees, Spain). Facies, Volume 44, pp. 105-136.

Sangree, J. and Windmier, J. M., 1977. Seismic stratigraphy and global changes of sea level, Part 9: Seismic interpretation of clastic depositional facies. Seismic stratigraphy: Applications to hydrocarbon Exploration. American Association of Petroleum Geologists, Memoir(26), pp. 168-184.

Sayers, C. M., 2008. The elastic properties of carbonates. The leading edge, 27(8).

Sayers, C. M. and Rickett, J. E., 1997. Azimuthal variation in AVO response for fractured gas sands. Geophysical Prospecting, 45(1), pp. 165-182.

Scales, J. A., 1997. Theory of Seismic Imaging. 2.2 ed. s.l.:Samizdat Press.

Schlager, W., 1981. The paradox of drowing rreef and carbonate platforms. Geological Society of America Bulletin, 92(Part 1), pp. 197-211.

Schlager, W., 1999. Scaling of sedimentation rates and drowing of reef and carbonate platforms. Geology, 27(2), pp. 183-186.

Schlager, W., 2003. Benthic carbonate factories in the Phanerozoic. International Journal of Earth Sciences, 92(445-464).

Schlager, W., 2004. Fractal nature of stratigraphic sequences. Geology, 32(3), pp. 185-188.

Schlager, W., 2005. Carbonate sedimentology and sequence Stratigraphy. s.l.:SEPM (Society for Sedimentary Geology).

Schlager, W. and Camber, O., 1986. Submarine slope angle, drowning un-

comformities and self-erosion of limestone escrapments. Geology, Volume 14, pp. 762-765.

Schlager, W., Reijmer, J. and Droxler, A., 1994. HighsHigh shedding of carbonate platforms. Journal of sedimentary research, B64(3), pp. 270-281.

Schwing, F., O'Farrell, M., Steger, J. and Baltz, K., 1996. Coastal up-welling indices west coast of North America 1946-1995. s.l.:U.S. DEPARTMENT OF COMMERCE National Oceanic and Atmospheric Administration National Marine Fisheries Service.

Sech, R. P., Jackson, M. D. and Hampson, G., 2009. Three dimensional modeling of a shore-shelf parasequence reservoir analog: Part 1. Surface based modeling to capture high resolution facies architecture.. AAPG Bulletin, 93(9), pp. 1155-1181.

Seeling, W. N. and Ahrens, J. P., 1981. Estimation of wave reflection and energy dissipation coefficients for beaches, revetments, and breakwaters.. DTIC, US ARMY, CORPS OF ENGINEERS.

Shackleton, J. R., Cooke, M. L., Verges, J. and Simo, A., 2011. Temporal constrains on fracturing associated with fault related folding at Sant Corneli anticline, Spanish Pyrenees. Journal of Structural Geology, Volume 33, pp. 5-19.

Shanley, K. and McCabe, P., 1994. Perspectives on the sequence stratigraphy of continental strata.. AAPG Bulletin, Volume 78, pp. 544-568.

Shearer, P., 2009. Introduction to seismology. Second ed. s.l.:Cambridge university press.

Sheriff, R. E. and Geldart, L. P., 1995. Exploration Seismology. Second ed. s.l.:Cambridge university press.

Simmons, G. and Brace, W. F., 1965. Comparison of static and dynamic measurements of compressibility of rocks. Journal of Geophysical Research, 70(22), pp. 5649-5656.

Simo, A., 1986. Carbonate platform depositional sequences, Upper Cretaceous, south- central Pyrenees (Spain). Tectonophysics, Volume 129, pp. 205-231.

Simo, A., 1989. Upper Cretaceous platform to basin depositional sequence development, Tremp Basin, South-Central Pyrenees, Spain. SEPM, Issue 44.

Simo, A., 1993. Cretaceous carbonate platforms and stratigraphic sequences, south-central Pyrenees, Spain.. Cretaceous carbonate platforms: AAPG Memoir, Volume 56, pp. 325-342.

Skelton, P. W., 1978. The evolution of functional design in rudists (Hippuritacea) and its taxonomic implications. Philosophical Transactions of the Royal Society B: Biological Sciences, 284(1001), pp. 305–318.

Skelton, P. W., Gili, E., Obrador, A. and Lopez, G., 2003. Revised lithostratigraphy of the Upper Cretaceous (Santonian) carbonate succesion on the nortern flank of Sant Corneli, southern Central Pyrenees. Journal of Iberian geology, Vol-

ume 29, pp. 73-87.

Slaney, M., Kak, A. C. and Larsen, L. E., 1984. LIMITATIONS OF IMAGING WITH FIRST- ORDER DIFFRACTION TOMOGRAPHY. IEEE Transactions on Microwave Theory and Techniques, 32(8), pp. 860-874.

Sloss, L., 1962. Stratigraphic models in exploration. Journal of Sedimentary Petrology, Volume 32, pp. 415-422.

Smith, T., Sondergeld, C. and Rai, C., 2003. Gassmann fluid substitutions: A tutorial. Geophysics, 68(2).

Snieder, R. and Lomax, A., 1996. Wavefield smoothing and the effect of rough velocity perturbations on arrival times and amplitudes. Geophysical Journal International, 125(3), pp. 796-812.

Steuber, T., 2000. Skeletal growth rates of Upper Cretaceous rudist bivalves: Implications for carbonate production and organism- environment feedbacks. Geological Society Special Publication, Volume 178, pp. 21-32.

Storlazzi, C. D., Norris, B. K. and Rosenberger, K. J., 2015. The influence of grain size, grain color, and suspended-sediment concentration on light attenuation: Why fine-grained terrestrial sediment is bad for coral reef ecosystems. Coral Reefs, Volume 34, pp. 967-975.

Strobel, J. et al., 1989. Interactive (SEDPAK) simulation of clastic and carbonate sediments in shelf to basin settings. Computers and Geosciences, 15(8), pp. 1279-1290.

Sutherland, K. P., Porter, J. w. and Torres, C., 2004. Disease and immunity in Caribbean and Indo-Pacific zooxanthellate corals. Marine and ecology progess series, Volume 266, pp. 273-302.

Terray, E. et al., 1995. Estimates of kinetic energy dissipation under breaking waves. Journal of physical oceanography, Volume 26, pp. 792-807.

Thamer, K., Al-Khafaji, A. and Zumberge, J., 2009. Petroleum system analysis of the Mishrif reservoir in the Ratawi, Zubair, North and South Rumaila oil fields, southern Iraq. GeoArabia, 14(4), pp. 91-108.

Tipper, J. C., 2016. Measured rates of sedimentation: What exactly are we estimating and why?. Sedimentary Geology, Volume 339, pp. 151-171.

Tiwary, D., Bayuk, I., Vikhorev, A. and Chesnokov, E., 2009. Comparison of seismic upscaling methods: From sonic to seismic. Geophysics, 74(2), pp. WA3-WA14.

Torquato, S., 2000. Random heterogeneous materials: Microstructure and macroscopic properties. s.l.:Springer.

Turchin, P., 2003. Complex Population Dynamics: A Theoritical/Empirical Synthesis. 41 William Street, Princeton: Princeton University Press.

Turley, S., 2006. Acoustic scattering from a sphere. s.l.:s.n.

Valero, L. et al., 2017. Linking sedimentation rates and large scale architec-

ture for facies prediction in nonmarine basins (Paleogene, Almazan Basin, Spain). Basin Research, 29(Suppl.1), pp. 213-232.

Van Wagoner, J., 1995. Sequence Stratigraphy of Foreland Basin Depsoits: Terminology, Summary of Papers and Glossary of Sequency Stratigraphy. AAPG Memoir, Volume Memoir 64.

Van Wagoner, J. C., 1990. Siliciclastic sequence stratigraphy in well logs, cores, and outcrops : concepts for high-resolution correlation of time and facies. s.l.:Tulsa : American Association of Petroleum Geologists.

Vanoni, V. A., 1964. Measurements of critical shear stress for entraining fine sediments in a boundary layer. California Institute of Technology.

Vanorio, T., Elbert, Y. and Grombacher, D., 2013. What laboratory-induced dissolution trends tell us about natural trends of carbonate rocks. Geological Society London, Volume Special Publications, 406, pp. 311-329.

Vanorio, T. and Mavko, G., 2011. Laborratory measurements of the acoustic and transport properties of carbonate rocks and their link with the amount of microcrystalline matrix. Geophysics, 76(4).

Vanorio, T., Scotellaro, C. and Mavko, G., 2008. The effect of chemical and physical processes on the acoustic properties of carbonate rocks. The leading edge, 27(8).

VanWagonwer, J. and Bertram, G. T. eds., 1995. Overview of Sequence Stratigraphy of Foreland Basin Deposits: Terminology, Summary of Papers, and Glossary of Sequence Stratigraphy. s.l.:AAPG Memoir.

Verwer, K., Braaksma, H. and Kenter, J., 2008. Case History. Acoustic properties of carbonates: EEffect of rock texture and implications for fluid substitution. Geophysics, 79(2), pp. B51-B65. Verwer, K., Eberli, G., G., B. and R., W., 2010. Effect of carbonate pore structure on dynamic shear moduli. Geophysics, 75(1).

Villalba-Breva, S. and Martin-Closaa, C., 2013. Upper Cretaceous paleogeography of the Central Southern Pyrenean Basins (Catalonia, Spain) from microfacies analysis and charophyte biostratigraphy. Facies, Volume 29, pp. 213-232.

Virieux, J., Etienne, V. and al, e., 2012. Modelling seismic wave propagation for geophysical imaging. Seismic Waves-Research and Analysis.

Virieux, J. and Operto, S., 2009. An overview of full- waveform inversion in exploration geophysics. Geophysics, 74(6), p. WCC1.

Waltham, A. L. et al., 2002. Digital rocks: Linking forward modelling to carbonate facies. Basin Research, 14(3), pp. 401-415.

Wang, Z., 2001. Y2K Tutorial: Fundamentals of seismic rock physics. Geophysics, 66(2).

Wang, Z., Wang, R., Wang, F. Q. H. and Li, T., 2015. Experiment study of pore structure effects on velocities in synthetic carbonate rocks. Geophysics, 80(3).

Warrlich, G. et al., 2008. 3D stratigraphic forward modelling for analysis and prediction of carbonate platform stratigraphies in exploration and production. Marine and Petroleum Geology, 25(1), pp. 35-58.

Warrlich, G. M. D., Waltham, D. A. and Bosence, D. W. J., 2002. Quantifying the sequence stratigraphy and drowning mechanisms of atolls using a new 3-D forward stratigraphic modelling program (CARBONATE 3D). Basin Research, 14(3), pp. 379-400.

Watney, L., Rankey, E. and J.W, H., 1999. Perspectives on stratigraphic simulation models: current approaches and future opportunities. Numerical Experiments in Stratigraphy: Recent Advances in Stratigraphic and Sedimentologic Computer Simulations:SEPM, Special Publication(62).

Wear, S. L. and Thurber, R. V., 2015. Sewage pollution: mitigation is key for coral reef stewardship. Annals of the New York academy of sciences, Volume 1355, pp. 15-30.

Weger, R. et al., 2009. Qauantification of pore structure and its effect on sonic velocity and permeability in carbonates. AAPG Bulletin, 93(10).

Whitcombe, D. N., Connolly, P. A., Reagan, R. L. and Redshaw, T. C., 2002. Extended elastic impedance for fluid and lithology prediction. Geophysics, 67(1), pp. 63-67.

Widess, M., 1973. How thin is a thin bed?. Geophysics, 38(6), pp. 1176-1180.

Wilcock, P. R., 2001. Toward a practical method for estimating sediment-transport rates in gravel- bed rivers. Earth Surface Processes and Landforms, 26(13), pp. 1395-1408.

Wilkinson, B., Drummond, C., Diedrich, N. and Rothman, E., 1999. Poisson processes of carbonate accumulation on Paleozoic and Holocene platforms. Journal Of Sedimentary Research, 69(2), pp. 338-350.

Wilkinson, B., Merill, G. and Kivett, S., 2003. Stratal order in Pennsylvanian cyclothems. GSA Bulletin, 115(9).

Williams, H. et al., 2011. Investigating carbonate platform types: Multiple controls and a continuum of geometries. Journal of Sedimentary Research, 81(1), pp. 18-37.

Willliams, G. D., 1985. Thrust tectonic in the south central Pyrenees. Journal of structural geology, 7(1), pp. 11-17.

Wilson, J. L., 1975. Carbonate Facies in Geologic History. s.l.:Berlin : Springer-Verlag.

Wilson, M. E. and Lokier, S. W., 2002. Siliciclastic and volcanoclastic infuences on equatorial carbonates: insights from the Noegene of Indonesia. Sedimentology, Volume 49, pp. 583-601.

Wolfram, S., 1984. Universality and complexity in cellular automata. Physics D: Nonlinear Phenomena, 10(1), pp. 1-35.

Wolfram, S., 2002. A new kind of science. s.l.:Wolfram Media, Inc.

Wollner, U. and Dvorkin, J., 2016. Effect fluid and grain bulk moduli for heterogeneous thinly layered poroelastic media. Geophysics, 81(6).

Woodward, M. J. et al., 2008. A decade of tomography. s.l.:s.n.

Wright, V. P. and Burgess Peter, M., 2005. The carbonate factory continuum, facies mosaics and microfacies: An appraisal of some of the key concepts underpinning carbonate sedimentology. Facies, 51(1-4), pp. 17-23.

Wu, R. S. and Aki, K., 1988. Introduction: Seismic Wave Scattering in Three-dimensionally Heterogeneous Earth. Aki K., Wu RS. (eds) Scattering and Attenuations of Seismic Waves, Part I. Pageoph Topical Volumes., Volume 128.

Xu, S. and Payne, M., 2009. Modelling elastic properties in carbonate rocks. The leading edge, 28(1), pp. 66-74.

Yi, L. and Schuster, G., 1990. Parsimonious staggered grid finite-differencing of the wave equation. Geophysical Research Letters, 17(2), pp. 155-158.

Zachos, J. et al., 2001. Trends, rhythms, and aberrations in global climate 65 Ma to present. Science, Volume 292, pp. 686-693.

Zadooni, F., 2005. The nature and origin of Upper Creataceous basin-margin rudists buildups of the Mesopotamian Basin, southern Iraq, with consideration of possible hydrocarbon stratigraphic entrapment. Cretaceous Research, Volume 26, pp. 213-224.

Zaneveld, J. R. et al., 2016. Overfishing and nutrient pollution interact with temperature to disrupt coral reefs down to microbial sscale.. Nature Communications, Volume 7:11833.

Zeng, H. and Marfurt, K., 2015. Recent progress in analysis of seismically thin beds. Interpretation, 3(3).

Zhang, R., Daley, T. and Vasco, D., 2015. Improving thin-bed resolution: Application of a sparse-layer inversion on 3D seismic observations from the In Salah carbon dioxide storage project. Interpretation, 3(3).